Numerical analysis of nonlinear soil behavior and heterogeneity effects on railway track response

Vinicius Alves Fernandes

ÉCOLE CENTRALE DES ARTS ET MANUFACTURES « ÉCOLE CENTRALE PARIS »

THÈSE

présentée par

Vinicius ALVES FERNANDES

pour l'obtention du

GRADE DE DOCTEUR

Spécialité : Modélisation numérique, Mécanique des Sols

Laboratoire d'accueil : Mécanique des Sols, Structures et Matériaux

SUJET: NUMERICAL ANALYSIS OF NONLINEAR SOIL BEHAVIOR AND HETEROGENEITY EFFECTS ON RAILWAY TRACK RESPONSE

Soutenue le: 10 novembre 2014

devant un jury composée de:

M. DUHAMEL Denis	Président
M. GOMES CORREIA Antônio	Rapporteur
M. WOODWARD Peter	Rapporteur
M. BRESSOLETTE Philippe	Examinateur
M. ROBINET Alain	Invité
Mme. MODARESSI Arézou	Directrice de Thèse
M. LOPEZ-CABALLERO Fernando	Co-encadrant de Thèse
Mme. COSTA d'AGUIAR Sofia	Co-encadrante de Thèse

2014-ECAP0055

Remerciements

Après cette longue étape de plus de 3 ans de travail, je voudrais dans ces quelques lignes remercier tous ceux qui y ont participé et contribué.

En premier lieu, je voudrais remercier mes encadrants Sofia Costa d'Aguiar et Fernando Lopez Caballero. La réussite de ce travail est grâce à votre engagement et à la confiance que vous avez eu en moi. Ce fut un immense plaisir de pouvoir travailler avec vous et de partager mes idées et difficultés. Je remercie également ma directrice de thèse Arézou Modaressi, pour vos précieux conseils et discussions.

Je remercie M. Duhamel d'avoir présidé le jury de cette thèse ainsi que M. Bressolette d'avoir accepté d'éxaminer mon travail de thèse. Je remercie également M. Gomes Correia et M. Woodward d'avoir accepté de rapporter ce travail.

Je tiens particulièrement à remercier mes collègues d'Innovation et Recherche SNCF, avec qui j'ai pu partager l'aventure du ferroviaire. Merci pour la convivialité et les moments partagés ensemble toutes ces années. Je garderai pour toujours un très bon souvenir des moments passés à St. Lazare et à Cour St. Emilion.

Je voudrais aussi remercier mes collègues du laboratoire MSSMat. J'ai beaucoup apprécié les discussions scientifiques et encore plus les non scientifiques. Merci de me faire sentir partie intégrante de la vie du laboratoire, malgré ma présence intermittente.

Merci également à mes amis. Je suis heureux de vous avoir à mes côtés pendant toutes ces années.

Aproveito estas linhas para agradecer o apoio incondicional da minha familia ao longo de todos estes anos. Obrigado por estarem sempre ao meu lado, apesar da distância, e por me apoiarem nas minhas escolhas professionais e pessoais. Vocês sabem que os tenho comigo sempre.

Tania, tu es mon soleil et ma tranquillité. Ensemble, nous découvrons le vrai bonheur dans la vie, merci pour tout.

Abstract

An increasing demand for railway transportation is observed in many countries around the world. Achieving higher network capacity requires the evaluation of the existing structure regarding the required traffic, speed and axle load, as well as the reduction of maintenance interventions. A higher track performance in terms of these metrics can be achieved by enhanced design standards and predictive tools accounting for the whole structure's life span.

Within this context, this thesis aims to provide a global framework for combining geotechnical perspective and numerical modeling for the railway infrastructure. A rational approach for railway track modeling is proposed. It is composed by three main aspects: (i) railway track dynamics, (ii) probabilistic analysis and (iii) geomaterials' non linear behavior. This approach allows assessing the track behavior during different instants of its life span.

The first step of this thesis is the development of a dynamic numerical model of the railway track for both probabilistic and non linear analysis. For this purpose, the Finite Element method in time domain is chosen as general modeling framework. A 2D plane-strain model with a modified width is used in this thesis, the out-of-plane width being calibrated from 3D static analysis. The advantages and drawbacks of such methodology are discussed in the light of the representativeness of the in-plane stress field and associated computational cost for probabilistic analysis. A loading methodology for reducing spurious wave generation is also discussed and implemented. With the developed model, the track structural response and the crossed influence of speed and subgrade stiffness are first analyzed under linear elasticity hypothesis.

The influence of track properties variability in the track stiffness measurement is discussed in the second part of this thesis. Spatial variations are introduced by considering the rigidity of each track layer as an invariant scalar random field. The first-order marginal probability distributions are calibrated from statistical analysis of *in situ* measurements. By considering different theoretical correlation structures, the crossed influence of the discrete sleeper support and the input correlation length on the track stiffness field is highlighted. In order to verify the importance of each input parameter in the track stiffness' variability, a global sensitivity analysis is conducted for different track configurations. It is shown that track stiffness variations are primarily caused by variations of subgrade stiffness and possible variations of rail pad stiffness.

Furthermore, the importance of geomaterials' non linear behavior is discussed in the last part of the thesis. A suitable framework for the description of geomaterials' behavior under cyclic loading, for a large range of stress paths, is provided by a fully elastoplastic multimechanism model. This approach is well adapted for assessing the track behavior

during the so-called “conditioning phase”, or the the first cycles when high track settlements are observed and materials cumulate high plastic strains.

The model parameters are calibrated from triaxial test results available in the literature for different track materials (ballast, interlayer, subgrade soil). The model is able to capture the main mechanisms acting during the conditioning phase: densification and increase in stiffness of the different materials by accumulation of plastic strains. The load transfer mechanisms and the stress-strain response of the materials are then analyzed. Different stress-strain paths and plastic strains are observed in the ballast layer according to the position of the control point relative to the sleepers. The load speed influence on track permanent settlement and ballast stress-strain response is also studied. Finally, the influence of both interlayer and subgrade behavior on the track response is assessed via a parametric analysis.

Keywords: ballasted railway track, finite element method, moving loads, probabilistic analysis, soil mechanics, advanced elastoplastic constitutive model

Résumé

Une forte progression du transport ferroviaire est observée les dernières années dans plusieurs pays. L'augmentation de la capacité du réseau ferroviaire demande à la fois l'évaluation de l'infrastructure existante selon le trafique attendu, la vitesse des trains, la charge à l'essieu, ainsi que la réduction des interventions de maintenance. Une performance accrue de la voie ferrée par rapport à ces critères nécessite l'amélioration des normes de conception et des outils de prédiction qui puissent prendre en compte toute la durée de vie de la structure.

Dans ce contexte, l'objectif de cette thèse est d'apporter un point de vue géotechnique à la modélisation numérique du comportement des voies ferrées sous charge mobile. Un modèle numérique rationnel est developpé dans la thèse, composé de trois aspects principaux: (i) comportement dynamique de la voie ferrée, (ii) analyse probabiliste et (iii) comportement non linéaire des géomatériaux. Cette approche permet d'appréhender le comportement mécanique de la voie ferrée à différents instants de son cycle de vie.

La première partie de cette thèse est consacrée au développement d'un modèle numérique en dynamique de la voie ferrée, adapté à l'analyse probabiliste et au comportement non linéaire. Une modélisation par Eléments Finis dans le domaine temporel est choisie pour cadre général. Ainsi, un modèle 2D en déformation plane avec épaisseur est proposé dans cette thèse, l'épaisseur hors plan étant calibrée à partir des calculs 3D en statique. Les avantages et inconvéniants de cette méthodologie sont discutés selon la répresentativité du champ de contraintes dans le plan et du temps de calcul associé, paramètre important pour l'analyse probabiliste. Une méthodologie pour la mise en charge est discutée et implementée afin de réduire la génération d'ondes parasites. La réponse dynamique de la voie ferrée et l'influence croisée de la vitesse de la charge et de la rigidité de la platforme sont évaluées sous hypothèse de comportement élastique linéaire.

L'influence de la variabilité des propriétés mécaniques de la voie ferrée dans la mesure de la raideur de voie est discutée dans la deuxième partie de cette thèse. Des variations spatiales du module d'Young des couches ferroviaires sont modélisées par des champs aléatoires invariants scalaires. La densité de probabilité de la loi marginale d'ordre 1 associée au champ est obtenue grâce à une analyse statistique des mesures *in situ*. L'influence croisée du support discret et de la distance de corrélation des champs d'entrée dans les variations de la raideur de voie est mise en évidence à partir de différentes structures de corrélation. Afin de vérifier l'importance de chaque paramètre d'entrée sur les variations de raideur de voie, une analyse de sensibilité globale est effectuée pour différentes configurations de voie. La raideur de voie est principalement affectée par des variations de rigidité de la plateforme et des semelles.

L'importance du comportement non linéaire des géomatériaux est soulignée dans la

dernière partie de la thèse. Le modèle de comportement élastoplastique développé à l'Ecole Centrale Paris fournit un cadre approprié pour l'étude du comportement des géomatériaux sous chargement cyclique. Cette approche est bien adaptée au comportement des matériaux pendant leur "conditionnement initial", ou les premiers cycles de charge, quand les tassements permanents sont plus importants et les matériaux cumulent des déformations plastiques élevées.

Les paramètres du modèle sont calibrés pour les différents géomatériaux ferroviaires (ballast, couche intermédiaire, sol de la platforme) à partir d'essais triaxiaux disponibles dans la littérature. Les résultats obtenus illustrent les mécanismes prépondérants dans cette phase : densification et augmentation de la rigidité des différents matériaux par accumulation des déformations plastiques. Les mécanismes de transfert de charge et la réponse en contrainte-déformation pendant le conditionnement et le cyclage des matériaux sont discutés. Les résultats obtenus montrent que le ballast est soumis à différents chemins de contrainte selon la position observée par rapport à la traverse. En outre, l'influence de la vitesse de la charge dans le tassement permanent et dans les déformations plastiques est aussi étudié. Finalement, la sensibilité du comportement obtenue pour le ballast par rapport aux matériaux de la couche intermédiaire et de la plateforme est estimée à partir des simulations numériques.

Mot-clés: voie ferrée ballastée, méthode des éléments finis, charge mobile, analyse probabiliste, mécanique des sols, modèle de comportement élastoplastique avancé

Contents

Notations

Latin Alphabet

a	acceleration
$\dot{a}$	jerk
a_1, a_2	deviatoric hardening parameters (ECP model)
A	rail cross section (Chapter 3)
A^{3D}, A^{2D}	influence area of loading for width optimization on 2D plane-strain approach (Chapter 3)
A_L	area enclosed by hysteresis loop
A_T	area enclosed by the triangle defined by maximum strain and maximum stress for a hysteresis loop
b	yield surface shape parameter (ECP model)
b	width of the soil slide considered in equivalent 2D plane-strain approach (Chapter 3)
c_1, c_2	isotropic hardening parameter (ECP model)
d	distance between critical state line and isotropic consolidation line (ECP model)
D	damping ratio
D_r	relative density
D_{50}	mean grain size
e	void ratio
e_{max}	maximum void ratio
e_{min}	minimum void ratio
E	Young's Modulus
E_{sec}	secant Young's Modulus
E_{ref}	Young's Modulus under the reference pressure
F, F_1, F_2	load applied by an axle
f	frequency
f_k, f_{iso}	yield surfaces (ECP model)
F_k	yield function (ECP model)
g	gravity acceleration
G	shear modulus
G_{sec}	secant shear modulus

G_{max}	maximum shear modulus
G_{ref}	maximum shear modulus under the reference pressure
G_s	specific gravity
$\underline{\underline{I}}$	second-order unit tensor
I	rail inertial moment
I_d	density index for sands
k	track global stiffness
k_0	earth pressure coefficient
K	track bogie-stiffness (Chapter 4)
K	bulk modulus
K_{ref}	bulk modulus under the reference pressure
l_c	scale of fluctuation
m	coefficient for nonlinear evolution of deviatoric behavior domains (ECP model)
M	slope of the critical stat line in the plane $(q - p')$
M_r	resilient modulus
n	soil porosity
n_{el}	exponent of nonlinear elastic laws
$\underline{n}$	normal vector
N	number of load cycles
PI	plasticity index (Chapter 2)
p	total mean stress
p'	effective mean stress
p_c	critical mean stress (ECP model)
p_{c0}	initial critical mean stress (ECP model)
p'_{ref}	effective reference pressure
q_d	dynamic cone resistance
q_c	static cone resistance
q	deviatoric stress
r_k^m, r_k^c	friction mobilization degree (ECP model)
r_k^{ela}, r_k^{hys}, r_k^{mob} r_{iso}^{ela}	threshold domains parameters (ECP model)
R	autocorrelation matrix
S_i	first-order sensitivity indices
S_r	degree of saturation
t	time
t_o	time spent on first loading phase
$\underline{t}$	stress vector
T	specific period of the model
$\underline{u}_b$	displacement field in the superstructure domain
$[u_N]$	normal interface jump

$\underline{u}_s$	displacement field of soil domain
$[\underline{u}_T]$	tangent interface jump vector
C_u	coefficient of uniformity
u_w	pore water pressure
u_z^p	permanent settlement
v, v_t	load nominal speed
v_s	shear wave velocity
$\mathbb{V}_b$	set of kinematically acceptable displacement fileds for the superstructure domain
$\mathbb{V}_s$	set of kinematically acceptable displacement fileds for the soil domain
$\underline{w}_b$, $\underline{w}_s$	virtual displacement fields
$\underline{x}$	material point coordinates
x	spatial coordinate
X	random variable (Chapter 4)
y	spatial coordinate
z	spatial coordinate

Greek Alphabet and other symbols

α_k	hardening evolution function (ECP model)
α_ψ	constant parameter for volumetric behavior (ECP model)
α_{yz}	principal stress axes rotation angle in the (y, z) plane
β	Newmark integration parameter (Chapter 3)
β	plastic compressibility (ECP model)
γ	Newmark integration parameter (Chapter 3)
γ	shear strain
γ_d	dry density
Γ_s, Γ_b	mechanical boundaries of soil and superstructure domains
Γ_{sym}	symmetry boundary
Γ_{s_σ}, Γ_{b_σ}	parts of boundaries where stresses are imposed
Γ_{s_u}, Γ_{b_u}	parts of boundaries where displacements are imposed
Δh	layer thickness
$\Delta p'$	effective mean stress increment
Δt	time step
Δu_z	layer settlement
Δx	mesh discretization in the x direction
Δy	mesh discretization in the y direction
Δz	mesh discretization in the z direction
ϵ_b	estimation error for width optimization on 2D plane-strain approach
ϵ_k	estimation error between track global stiffness and Winkler foundation stiffness
$\underline{\underline{\varepsilon}}$	strain tensor
ε_v	volumetric strain
ε_d	deviatoric strain
ε_v^p	volumetric plastic strain
ε^p	plastic strain
ε^r	resilient strain
ζ	numerical damping
η	stress ratio
θ	correlation length
λ	compression index (Chapter 5)
$\dot{\lambda}^p$	plastic multiplier
μ	mean value
ν	Poisson's ratio
ν_r	resilient Poisson's ratio
ρ	volumetric mass density
ρ	autocorrelation function (Chapter 4)
ρ_b	superstructure's mean density

ρ_d	dry volumetric mass density
ρ_s	density of soil's solid phase
σ	standard deviation (Chapter 4)
$\underline{\underline{\sigma'}}$	effective stress tensor
$\underline{\underline{\sigma}}$	total stress tensor
σ_1, σ_2, σ_3	principal stresses
Σ_{bs}, Σ	interfaces between domains
τ	shear stress
ϕ	friction angle
ϕ'_{pp}	friction angle at critical state (ECP model)
ψ	characteristic angle (ECP model)
ω_i	assigned generation frequencies for FAST
ω_n	water content
Ω_b, Ω_s	superstructure and soil domains

Tensorial notation and operators

$[\cdot]$	jump of a quantity
$\cdot$	scalar product
$:$	contracted product
$\underline{a}$	vector a
$\underline{\underline{a}}$	second-order tensor a
$\|\cdot\|$	modulus of a vector
a^0	initial value of a
a_N, a_n	normal component of vector $\underline{a}$
$\underline{a}_T$, $\underline{a}_t$	tangential projection of vector $\underline{a}$
$\Delta(\cdot)$	variation of a quantity
$\mathrm{grad}(\cdot)$	gradient operator
$\mathrm{div}(\cdot)$	divergence operator
$\triangle(\cdot)$	Laplace operator
$E[\cdot]$	expectation
$\sum$	sum

Abbreviations

ANOVA	ANalysis Of VAriance
AREMA	American Railway Engineering and Maintenance-of-Way Association
BEM	Boundary Element Method
CBR	California Bearing Capacity
CCP	triaxial test at Constant Confining Pressure
cdf	cumulative density distribution
CSL	Critical State Line
CV	coefficient of variation
DAF	Dynamic Amplification Factor
DCP	Dynamic Cone Penetrometer
DEM	Discrete Element Method
ECP	*Ecole Centrale Paris*
EMW	swiss vehicle for track stiffness measurement
ESs	Evolution Strategies
FAST	Fourier Amplitude Sensitivity Test
FWD	Falling Weight Deflectometer
FE	Finite Element
FEM	Finite Element Method
FFT	Fast Fourier Transform
GEFDyn	*Géomécanique Eléments Finis DYNamique*
GPR	Ground Penetrating Radar
HCA	Hollow Cylinder Apparatus
KLE	Karhunen-Loève Expansion
LHS	Latin Hypercube Sampling
MCS	Monte Carlo Sampling
MISS3D	*Modélisation de l'Interaction Sol Structure en 3D*
NSCD	Non Smooth Contact Dynamics
OMC	Optimum Moisture Content
PCA	Principal Component Analysis
PCE	Polynomial Chaos Expansions
pdf	probability density function

PML	Perfectly Matched Layer
POD	Proper Orthogonalization Decomposition
RSMV	Rolling Stiffness Measurement Vehicle
SED	Specific Energy Density
SNCF	*Société Nationale des Chemins de Fer Français*, French national railway company
TER	*Trains Express Régionaux*, French regional trains
TGV	*Train à Grande Vitesse*, French high-speed train
UIC	*Union Internationale des Chemins de Fer*, International Union of Railways
USP	Under Sleeeper Pads
VCP	triaxial test at Variable Confining Pressure

Chapter 1

Introduction

Contents

1.1 Background and Motivations

Railway tracks are common structures in many countries, as passenger and freight railroads have proved to be a reliable and cost-effective transportation mode. Nowadays, the increasing demand for both freight and passenger railway transportation has motivated infrastructure managers to seek for higher capacity of the existing network by increasing traffic frequency, maximum allowed train speed and maximum allowed axle load for freight trains. To meet this challenge, one key aspect is to increase the network availability by reducing the number of maintenance interventions. This can only be achieved by pushing forward the limits of the actual structures and by proposing new design standards and predictive tools accounting for the dynamic behavior of the track.

A large program of rehabilitation and renewal of existing conventional tracks in the French network is being performed since 2009. This is accompanied by a research program conducted by the French national railway company SNCF in different domains such as:

- Development of *in situ* diagnostic tools;
- Laboratory characterization of track geomaterials;
- Development of numerical models and methods adapted for a geotechnical description of the track;
- Assessment of new materials and design concepts influence on the short-term (one vehicle passage) and long-term (lifespan of the structure) behavior of the structure;
- Assessment of new materials and design concepts influence on the short-term (one vehicle passage) and long-term (lifespan of the structure) behavior of the structure;
- Evaluation of the main maintenance operation parameters controlling the subsequent response of the track.

In the context of the present thesis two scientific challenges can be highlighted:

1. Different time scales: the short-term and long-term behavior of the structure depends on the materials' behavior subjected to cyclic dynamic loading. It is well understood that soil behavior depends on stress history, moisture content, drainage conditions and the characteristics of the applied cyclic load (Biarez and Hicher, 1994). After track construction or maintenance operations, a rapid accumulation of track settlement is observed during the first 100 or 1000 cycles (Shenton, 1984; Jeffs and Marich, 1987). This phase can be related to the so-called "conditioning phase" observed on laboratory tests results of specimens under cyclic load (Brown, 1974). It is well-known that the accumulation of plastic strains in granular materials during this phase influences the material's further response (Kolisoja, 1997; Balay et al., 1998; Suiker et al., 2005, among others). Although some insights have been brought by these laboratory characterization and track feedback, taking these phenomena into account for the prediction of the structure's mechanical response at different instants of its lifespan is an open challenge.

2. Stochastic characteristics of the system: railway networks are composed of long linear structures passing by different soil formations, which are submitted to variable train loads, maintenance operations and environmental conditions. It is well known from *in situ* measurements that both track geometry (Perrin, 2013) and track layers thickness and mechanical properties (Duong et al., 2014b) are inhomogeneous along the track. Therefore, the main challenge is in effectively characterizing this variability in tracks and assessing the importance on the long-term response of the structure.

1.2 Objectives

The main objective of this work is to propose a global framework for combining both geotechnical and numerical approaches in the railway field. The above scientific challenges are tackled by independently considering the nonlinear constitutive model ECP for the mechanical behavior of geomaterials and spatial variations of mechanical properties along the track.

The main objectives of this work can be summarized by the following points:

- Development of a numerical model of the railway track adapted for dynamic moving loads, nonlinear behavior and stochastic analysis;
- Assessment of the impact of mechanical properties variability on the track stiffness measurement;
- Improvement of the knowledge of the main mechanisms controlling the conditioning phase of the track and how train speed affects the cyclic response of the materials.

1.3 Outline

This thesis is organized in four main chapters:

Chapter 2 is devoted to a literature review on different aspects concerning the mechanical behavior of railway tracks. It is broadly divided in 3 main topics: a global description of the railway structure and the usual used materials, followed by the main *in situ* diagnostic tools used in French railway network, whose results are used in the thesis; an overview of soil behavior under cyclic load, both in terms of laboratory test results and modeling techniques; and finally, an overview of the different modeling strategies usually implemented for studying the track mechanical response.

Chapter 3 describes the numerical model developed in this thesis. The choice of the numerical model strategy in this work considers a 2D FE model with a modified width in plane-strain condition coupled with adapted boundary conditions. To calibrate the out-of-plane width from a 3D static model, the method proposed by Ribeiro (2012) is used. Different numerical aspects developed within the model are discussed. Results for a parametric study under linear elastic hypothesis are given in order to give a first insight of stress and strains developed in the materials during loading.

Chapter 4 is devoted to the study of how spatial variations of mechanical properties of the track geomaterials affect the track stiffness. A probabilistic nonintrusive framework is

considered, under which the mechanical properties are modeled as invariant scalar random fields. The probabilistic description is obtained from an extensive *in situ* cone penetration test campaign performed by SNCF, from which Young's Modulus of the geomaterials are obtained by applying empirical relations available in the literature. The influence of the input field's correlation length on the track stiffness measure is analyzed both in terms of the first and second-order marginals. The influence of moving load speed on the track stiffness variability is assessed under the model hypothesis. Global sensitivity analysis is performed and the influence of different track configurations and model hypothesis is discussed under this approach.

Chapter 5 is dedicated to the description of the conditioning phase of the materials in track. The nonlinear constitutive model developed at *Ecole Centrale Paris*, ECP model, is chosen for representing the ballast, interlayer and subgrade soil responses under cyclic load. In the first part of the chapter, the laboratory test results obtained from the literature for the different materials are presented, followed by the methodology for calibrating the model parameters for ballast and interlayer. Then, the importance of the nonlinearity is discussed in the light of the influence of speed, loading history, subgrade soil characteristics and the interlayer material on the mechanical response of the structure.

Conclusions arising from this work and suggestions for future research are presented in the last chapter, followed by the appendices.

Chapter 2

Mechanical behavior and modeling aspects of the railway structure

Contents

2.1 Introduction

The assessment of the mechanical response of the track requires a good comprehension of the different phenomena taking place in the railway structure and soil subjected to dynamic moving loads. On one hand, the track is subjected to variable static and dynamic loading conditions according to vehicle type, speed, track geometry irregularities and changes in track stiffness.

On the other hand, geomaterials in place have different scales of complexity and heterogeneity. From the coarse grained ballast material to the subgrade soil, grain size, geometry and nature vary not only between layers but also inside each layer. Geomaterial's mechanical response is known to be nonlinear and influenced by the initial state, stress history, plastic deformation rate and water content, according to the grain size and/or nature. Within this context, aspects such as the characterization of track materials' state and their variability; the prediction of their response under train load and the evaluation of their evolution with train traffic loading, and to better anticipate maintenance operations, are key aspects for a rational approach of track modeling.

This chapter gives a briefly overview of these different aspects. The railway track structures present in the French network are discussed in the first section, followed by an overview of the railway materials and train loading characteristics. The second section is devoted to the different tools used for characterization and diagnostic of the materials *in situ*. Although track maintenance is mainly based on the track geometry measurement, these tools provide valuable information for better analyzing the encountered geometry problems and planning future track renewal works. For instance, results from Panda cone penetration tests are used in Chapter 4 in order to estimate the Young's Modulus of geomaterials and their variability.

The third section presents an overview of the laboratory characterization of the soil behavior under cyclic loading. The main physical phenomena taking place on soil are discussed in the light of the soil mechanics concepts developed for monotonic loading. These concepts are used in Chapter 5 as the theoretical basis in order to better identify the mechanical load transfer mechanisms on railway tracks. The approach chosen in pavement engineering for describing the cyclic response of soils is presented as a complementary view of the described cyclic behavior of soils. The main modeling strategies associated with the observed laboratory test responses are presented as possible ways of describing the materials in the track.

In the last section, the different numerical modeling strategies used for studying the railway response to moving loads are presented. The advantages and drawbacks of each method are discussed in the light of the considered hypothesis, possible observed phenomena and train-track interaction strategies.

2.2 The railway track

Different track configurations are exploited by the French national railway company SNCF in the French railway network. These can be principally divided into two groups: conventional and high-speed lines. Conventional lines were built prior to the high-speed lines and

both followed different design specifications. These two track configurations are presented in a comparative form in Figure 2.1. The main difference between them is the fact that historically, ballast on conventional lines was laid down directly over the natural ground, while in high-speed lines a subballast layer and eventually a capping layer exists in order to prevent ballast from penetrating in the subgrade. According to SNCF (2009), conventional lines represent around 91% of the 32000 km of French railway network exploited by SNCF and high-speed lines only 9%.

The major points in order to increase the industrial performance of both structures are different, reflecting the construction age, design and the different operation requirements of each structure. For the high speed line network, the main concern is in improving the performance of ballasted tracks by decreasing the maintenance interventions. Research in this case is mainly focused on applying new components (under sleeper pads (USP), geosynthetics, etc) and materials (bituminous layer for example) that may contribute to this performance. The conventional line network is undergoing massive renewal works in order to improve its performance in terms of increasing train speed, axle load and track availability. In this case, research effort in France is concentrated on two different main points:

- characterizing the materials in place both by *in situ* and laboratory tests and understanding different specific phenomena occurring in these structures, such as the interlayer creation and mud pumping appearing in some sites (Trinh et al., 2012; Duong et al., 2013, among others).

- studying the influence of critical design specifications for renewal works, such as the thickness of ballast layer to be renewed and the need of installing a drainage system due to the presence of water in the interlayer and the subgrade.

In this work, the choice is made of studying the conventional line structure. It is motivated by the increasing importance in France of understanding the mechanical response of this structure. Besides being representative of the largest portion of the French railway network, conventional lines present the actual challenge of modernizing a centenary structure to nowadays objectives and performance. In the following sections, the main components of the structure will be briefly described as well as the load characteristics of trains transiting in these lines.

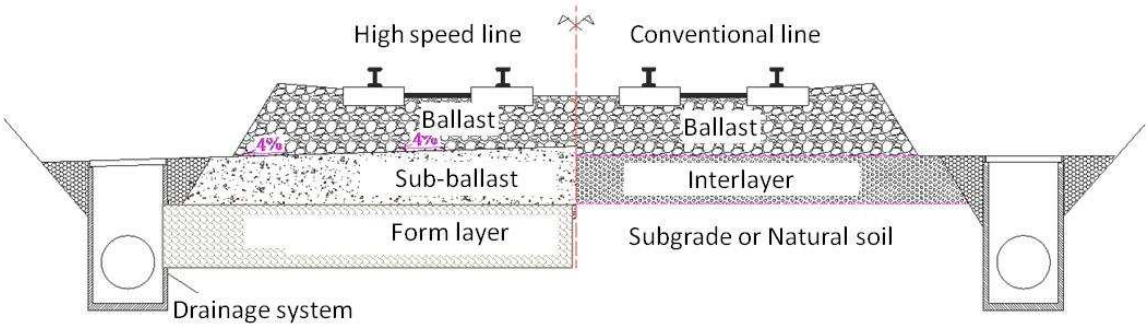

Figure 2.1: Schematic representation of the two track structures of the French railway network (adapted from Cui et al., 2014).

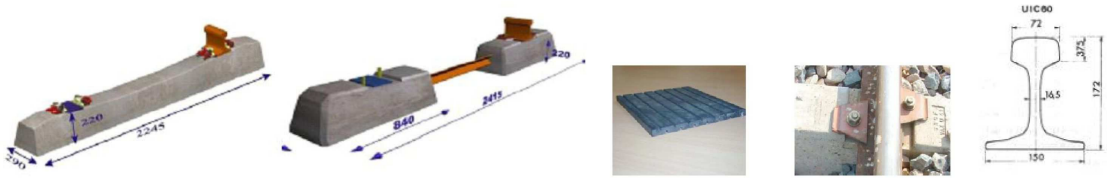

Figure 2.2: Sleepers, rail pad, fastening system and rail (from Rhayma, 2010).

2.2.1 Railway track materials and components

The rail is the element assuring the contact between the train and the track. It guarantees the wheelset guidance along the track and aslo vertical and lateral load distribution along the sleepers and subsequent track components (Alias, 1984). The rail profile and geometry determines the guidance and vehicle stability in curves. The UIC60 is the standard rail in France for high-speed lines and conventional lines with high traffic. The rail cross section is chosen in order to provide a high flexural strength and good internal stresses repartition during load.

The fastening system guarantees the positioning of the rail over the sleepers. The rail pad is a viscoelastic component of 9 mm width present within the fastening system, which allows for an increased elasticity of the rail-sleeper mechanical coupling. It also guarantees damping the high frequency content of the contact forces transmitted to the track (Kaewunruen and Remennikov, 2009).

Historically made of wood, nowadays sleepers are mainly made of reinforced pre-stressed concrete both in conventional and high-speed lines. Sleepers main functions are to transmit the static and dynamic loads to the ballast layer and to guarantee the track geometry, mainly the track gauge (distance between rails) and the rail inclination. Two sleeper's type exists: mono and duo block sleepers. Duo block sleepers are present in high-speed lines, while mono block are present in conventional lines, although Le Pen (2008) argues that it is not clear which type of sleeper is more advantageous in terms of lateral resistance and stress distribution. All these elements are schematically showed in Figure 2.2.

The ballast layer is composed of a coarse granular material traditionally obtained from angular, crushed, hard stones and rocks, such as crushed granite, basalt, limestone, slag and gravel (Selig and Waters, 1994). Although ballast specifications varies from country to country depending on materials locally available, they are usually based on the rock petrology, hardness, abrasion resistance and grain morphology. The main objectives of the ballast layer are:

- Attenuate the stress developed at the vicinity of the sleeper to an acceptable value to the subgrade materials, limiting the track permanent settlement;
- Ensure vibration damping from dynamic loads;
- Guarantee drainage capacity from pluvial water;
- Provide easy installation and maintenance.

The standard ballast particle size distribution in France is 31.5/50 mm. The ballast layer thickness depends mainly on the type of railway line, characterized by the UIC group (*Union Internationale des Chemins de fer*, International Union of Railways), train speed and the sleeper type. The layer thickness is usually between 15 cm and 35 cm, although higher thicknesses may be found in conventional lines.

During the track lifespan, grain attrition and breakage due to both train load and usual maintenance operations lead to smaller rounded grains and fines (Aursudkij, 2007; Paderno, 2010; Indraratna et al., 2011). Fine material can also migrate to the ballast layer from the interaction with the layer below and from outside conditions, e.g. fines from coal transportation in Australia (Indraratna et al., 2011). In France, ballast in conventional lines is then classified in fresh or clean ballast and fouled ballast, the former being composed of ballast following the prescribed granulometry and angularity and the latter composed of the smaller rounded grains and fines. Laboratory tests presented by Indraratna et al. (2011) show that fresh and fouled ballast present different mechanical responses, the fine content influencing the response of fouled ballast as expected.

In high-speed lines, a subballast layer built of well-graded gravel (grain size distribution of 0/31.5 mm) exists under the ballast layer. Its thickness varies between 15 cm and 55 cm depending to the soil bearing capacity. Besides assuring a better load transmission from the ballast layer to the subgrade, it protects the subgrade against the rain water flow and frost. The form layer allows adapting the embankment to the designed characteristics of the substructure. It can either be composed of the same natural soil in place or by a different soil with lower deformability.

For the conventional track configuration, these layers are not always present as the ballast was directly posed over the natural soil in place. What is nowadays called interlayer in France is the heterogeneous material formed by the mix of ballast fine particles and the soil (either natural ground or a combination of fill material and natural ground) with cyclic loading cycles (Trinh et al., 2012; Duong et al., 2014a).

Concerning the subgrade, the bearing capacity is the main design characteristic of new lines. The subgrade has a relatively larger deformability than the other track layers, depending on the geotechnical characteristics of the soil and the hydrological and hydrogeological conditions of the site. For conventional lines, the subgrade or natural soil has already been subjected to a larger number of cycles. Assessing the bearing capacity in this case is not straightforward and the design of renewal works is mainly based on the geotechnical analysis tools presented in Section 2.3.1.

2.2.2 Train load characteristics

The train load is usually divided into static and dynamic loads. The static load corresponds to the train weight and it is usually discussed in terms of maximum wheelset load. For instance, the TGV (*Train à Grande Vitesse*) is limited to a maximum of 17 tonnes per axle. Freight trains are allowed for a maximum of 22.5 tonnes per axle in the French railway network. However, heavy-haul transportation is allowed in different countries (e.g. Brazil, Australia, United States). One of the main questions discussed by authors in this case is how to estimate the adequacy and long-term response of existing lines to the increased static load, very often higher than 30 ton per axle (Paulsson and Berggren, 2005; Roney,

2005; Korpanec et al., 2005; Singh, 2005).

An analytical function of the vehicle static load applied by the sleeper over the ballast is proposed by Al Shaer et al. (2008) (Equation 2.1), based on the numerical simulation results obtained by Profillidis (1982) and Sauvage (1993). It represents the "double M wavelet" cycle characteristic of a TGV bogie (Figure 2.3).

$$F(t,Q,v) = \frac{QY}{2}\left[X^{\frac{(vt-a)^2}{d^2}} + X^{\frac{(vt-a-L)^2}{d^2}}\right] \tag{2.1}$$

where Q is the load supported by an axle, v is the train speed, t is the time, d the distance between two sleepers, a is a critical distance, L the distance between two axles of a bogie and X and Y are dimensionless parameters varying between 0 and 1 which depend on the subgrade stiffness.

From the railway vehicle dynamics point of view, dynamic loads appear when the vehicle passes over track irregularities, changes in track stiffness or in curves. In this case, the dynamic loads can be viewed as vehicle's response to the different above track excitations. The wheel-rail contact forces can be directly measured from the wheel strains in the laboratory. However, the contact forces cannot be measured directly in trains and have to be estimated by the contact theory. Hertz (1896) was the first to provide a solution of the contact between two elastic bodies, by considering the contact surface much smaller than the surface of the bodies in contact and also of their respective curvatures. A hertzian contact is then characterized by an ellipsoidal contact surface and a semi-elliptical pressure distribution. Creep appears when one body rotates relatively to the other, their tangential speeds at the contact surface no longer being equivalent. As discussed by Wickens (2003), Carter (1916) was the first to use this concept in order to explain the mechanism of

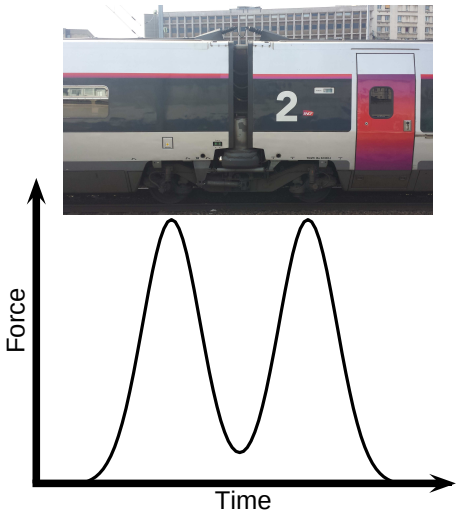

Figure 2.3: Typical "double M wavelet" cycle characteristic of a TGV bogie (adapted from Al Shaer et al., 2008).

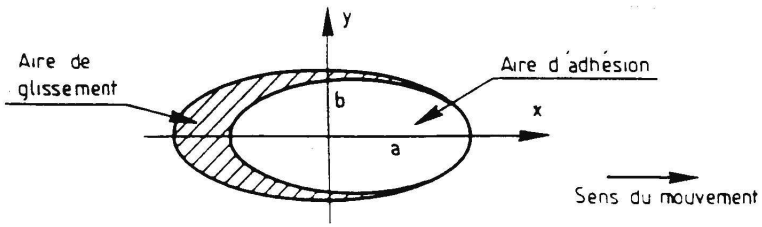

Figure 2.4: Ellipsoidal rolling contact (from Sauvage, 1993).

lateral dynamics of the railway wheelset, by linking the variations of creep appearing in the wheel-rail contact to the tangential contact forces. Kalker (1990) proposed a general solution of the wheel-rail contact problem and showed that the contact surface is divided in an adhesion surface and a creep surface (Figure 2.4). The tangential contact forces are obtained from the nonlinear geometrical and mechanical properties of the wheel-rail contact and creep.

The importance of the train-track interaction and dynamic loads increase with increasing speed. In conventional lines, passenger train speed is limited at a maximum of 220 km/h. However, different passenger train vehicles transit at the same line at different speeds, such as TER (regional trains) and TGVs. High speed lines are used exclusively by TGV trains at a maximum speed of 320 km/h. Freight trains are only allowed in conventional lines and their speed is limited to 80 km/h.

The aspects related to train-track interaction and vehicle dynamics should be taken into account in a fine modeling of loads applied by the train on the track. Even if the static load remains the highest part, the variations of the dynamic load can be understood as consequence of track differential settlement and track irregularities. However, linking the track geometrical aspects and variations of dynamic loads to the mechanical response of the track materials is outside the scope of this thesis.

From the geomaterials point of view, the stress path induced by a moving load is well understood in pavement engineering (Chan and Brown, 1994; Brown, 1996; Balay et al., 1998; Lekarp et al., 2000a). Both normal (vertical and lateral) and shear stresses varies during loading as represented in Figure 2.5. Rotation of the principal stress axes happens as a consequence of the variations of the shear stress component. For a tridimensional stress path, two main parameters are thus defined: α_{yz}, which is the rotation angle in the load propagation (y, z) plane, and b, which characterizes the role of the intermediate principal stress. These are defined by Equations 2.2 and 2.3. The influence of the rotation of principal stress axes on the cyclic behavior of soils is discussed in Section 2.4.

$$\alpha_{yz} = \frac{1}{2}\tan^{-1}\left(\frac{2\sigma_{yz}}{\sigma_{zz}-\sigma_{yy}}\right) \tag{2.2}$$

$$b = \frac{\sigma_2 - \sigma_3}{\sigma_1 - \sigma_3} \tag{2.3}$$

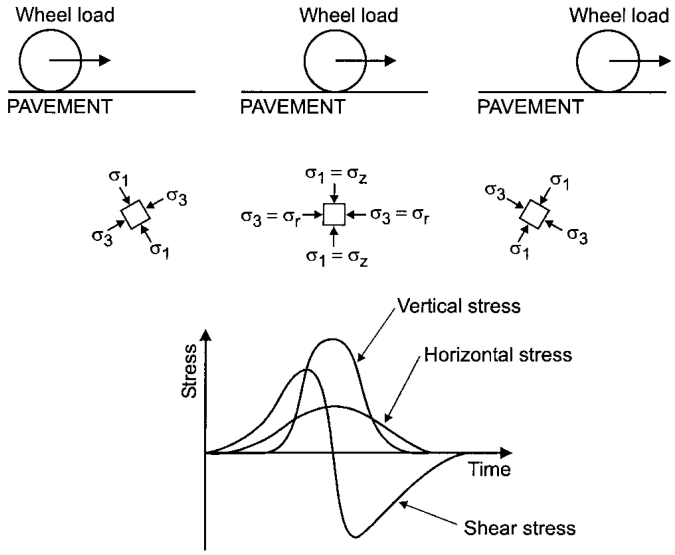

Figure 2.5: Stress beneath a rolling wheel load (obtained from Lekarp et al., 2000a).

2.3 *In situ* analysis: characterization and diagnostic of the railway track

Track irregularities are historically characterized by their geometrical aspect and in this sense railway quality and maintenance indicators are based on the track geometry. Besides earthquakes, slope failure and other possible soil failures, it is broadly accepted that the evolution of the track geometry is caused by the train-track interaction and by the dynamic forces that the train imposes in the track due to track irregularities. This is a complex mechanism putting together different time scales and wavelengths. One of the necessary bricks in order to better evaluate the risk and possible roots of track geometry degradation is the characterization and diagnosis of the geomaterials in place, and more broadly the mechanical characterization of the track response.

From this background, several methods and tools are currently available in order to characterize the materials *in situ* and the mechanical response of the railway track structure. These can be divided in punctual or discrete diagnostic tools and continuous diagnostic tools. In the first case, very often the characterization is based on geotechnical and pavement engineering tools adapted for the railway domain, such as the core sample train and the dynamic cone penetration test Panda. In the second case, geophysical tools, such as the Ground Pentetrating Radar (GPR) (Jack and Jackson, 1999; Olhoeft and Selig, 2002; Su et al., 2010, among others), have been successfully applied in the last years in coarse granular media such as ballast. Specific tools for measuring the mechanical response of the track to moving loads have been also developed and from them a measure of the track stiffness is assessed. These different tools are discussed in the next sections.

Figure 2.6: Typical core sample from conventional lines (obtained from Duong et al., 2014b).

2.3.1 Discrete analysis tools of track materials

Geotechnical tools are commonly used for the characterization of the railway materials. The specific characteristics of railways in terms of track availability and materials currently favored using two main diagnostic tools: the core sample train and the Panda dynamic cone penetrometer. These are presented in the following sections.

2.3.1.1 Core sample train

The core sample train is an adapted train with a drilling equipment. A continuous core sample of the track layers is obtained by dynamically driving a tube into the track, which is shown in Figure 2.6. The thickness of each layer can be estimated from the obtained sample as well as the nature of the soil, which are important parameters in the assessment of conventional track substructure (Brough et al., 2003, 2006; Duong et al., 2014b). Although complete samples of track layers can be obtained by the core sample train, it has the disadvantage of being a relatively slow procedure, not adapted to face the needs for increasing the quantity of renewed track sections. Moreover, the core sample is an intrusive method and subsequent filling of the drilled hole is necessary.

These drawbacks lead to adapt lighter and faster diagnostic tools from the pavement engineering to the railway context. In France, the dynamic cone penetrometer test Panda is used coupled with a geoendoscopic analysis as a fast and effective way of characterizing the track layers' width and materials.

2.3.1.2 Panda dynamic cone penetrometer (DCP) and Geoendoscopic analysis

The dynamic cone penetrometers are largely used for pavement evaluation after construction in order to assure the prescribed compaction level (Zhou, 1997; Chaigneau, 2001). The test consists in driving a standard cone into the soil by manual hamming the head of

the tip. For each hammer blow, an automatic numerical procedure is implemented which allows to record both the vertical displacement and the cone resistance q_d. The cone resistance is obtained by the Hollandais formula, which links the blow energy and vertical displacement of the tip to the soil resistance.

$$q_d = \frac{E}{A.e}\frac{M}{M+P} \tag{2.4}$$

where M is the hammer weight (2.35 kg), P is the dead weight, e is the plastic vertical displacement at each blow (normally between 0.5 and 2 cm), A is the cone cross section and E is the kinetic energy given by the hammer blow.

Panda is a lightweight cone penetrometer of variable energy developed by Gourvès (1991). It has been adapted for railway track configuration and materials, presenting the advantages of being portable and easily installed on the railway track. It allows then a fast characterization of the dynamic cone resistance q_d of the track layers. Quezada (2012) particularly discussed the use of the Panda cone penetration test in the ballast layer as an effective way for characterizing the material in the track.

The Panda test is usually coupled with a geoendoscopic analysis. It consists of passing a camera through the hole previously obtained from the cone penetration test (or any other drilling test). These images help on defining the thickness of each layer and allow a qualitative characterization of both the subgrade soil nature and the presence of water within the interlayer and the subgrade. Figure 2.7 presents a typical result of the dynamic cone resistance and the geoendoscopic images.

Coupling the Panda and geondoscopic analysis is a standard procedure for the geotechnical characterization prior to the renewal works in the French network since 2009. These informations contribute on the design and decision making process, specially when the soil presents a poor drainage capacity and a drainage system should be installed.

2.3.2 Continuous analysis of track stiffness parameter

Different definitions exist for the track stiffness (k). The straightforward definition is the ratio of the applied load ($F(s)$) by the vertical rail displacement ($u_z(s)$) at the point of the applied load, i.e. both are functions of the considered load application position (s).

$$k(s) = \frac{F(s)}{u_z(s)} \tag{2.5}$$

From quasi-static moving load measurements, Berggren (2005) and Hosseingholian et al. (2011) showed that the applied load is not a linear function of the rail vertical displacement and presents an hysteresis loop (Figure 2.8). The measured static track stiffness value depends on the applied load and on the considered slope. For instance, Hosseingholian et al. (2011) propose to calculate the secant track stiffness from the loading path between 30% and 90% of the maximum applied force (Equation 2.6) as shown in Figure 2.8.

$$k_{90\%-30\%F_{max}}(s) = \frac{F_{90\%}(s) - F_{30\%}(s)}{u_{z90\%}(s) - u_{z30\%}(s)} \tag{2.6}$$

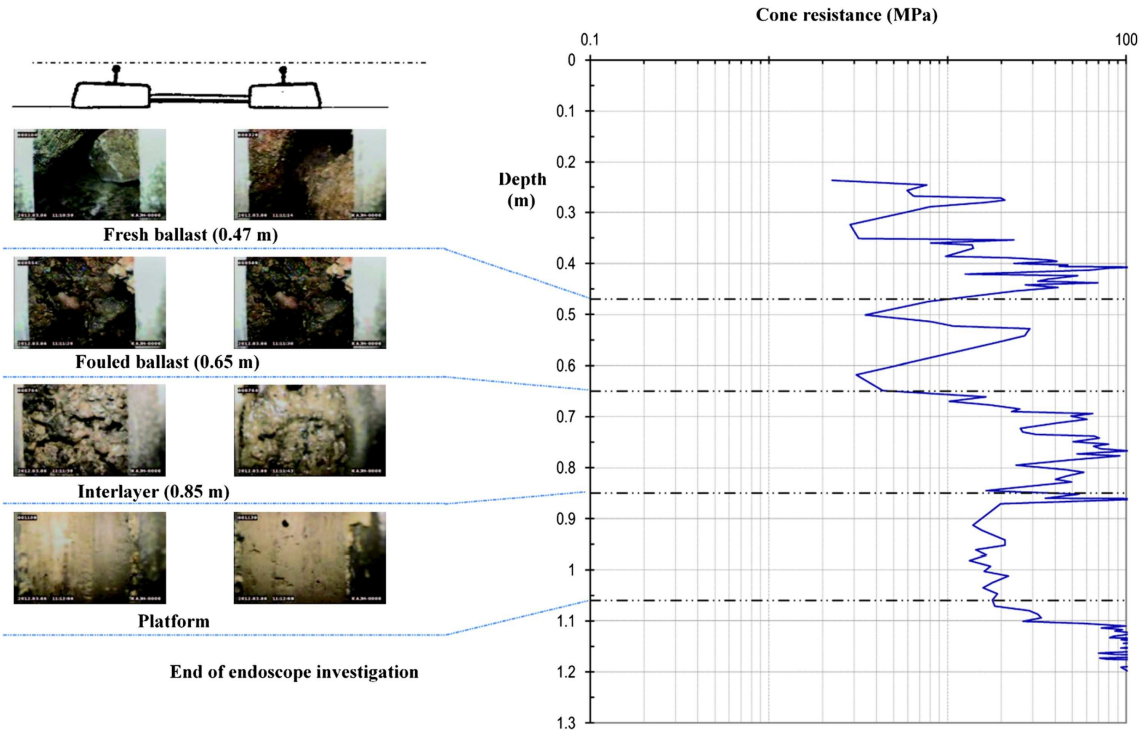

Figure 2.7: Typical result of Panda and geoendoscopic analysis (obtained from Duong et al., 2014b).

The track stiffness is also frequency dependent, which means that both the excitation frequency and the vehicle speed will affect the measured value. In this sense, although the definition of a dynamic track stiffness can be used, the receptance or dynamic flexibility concept is preferably used in the literature. It represents the transfer function between the applied force and displacement and is simply the inverse of a dynamic track stiffness.

According to Nielsen et al. (2013), the track stiffness characterization can be applied as a criteria for verifying the accordance of newly built tracks or after renewal operations, or for track maintenance purposes. In the last case, track stiffness measurement can be used in order to detect hanging sleepers, soft soils and possible causes of track irregularities. It can be used for evaluation of transition zones and soil vibration and possibly the causes of rail bending or crack propagation according to the latter authors. As discussed by Berggren (2005) and Berggren et al. (2010), although track stiffness measurement tools are being used for some years, there is no common agreement on how carrying out the measurement and how interpreting the results. For instance, Berggren (2005) and Nielsen et al. (2013) describe the main aspects which may differ for different track stiffness measurement methods:

- Static preload;
- Excitation frequency and vehicle speed;
- Spatial resolution of the measurement;

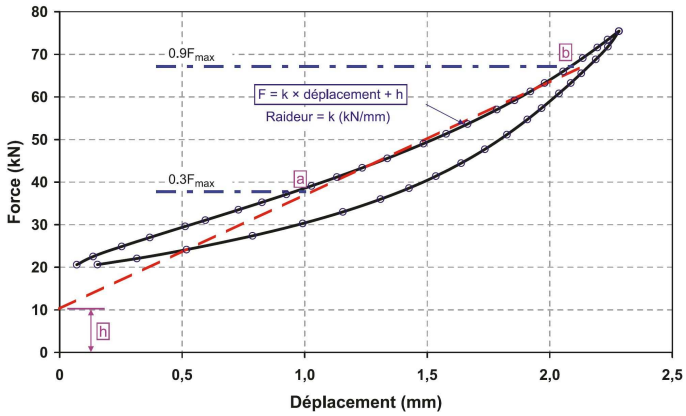

Figure 2.8: Nonlinear displacement of the rail under quasi-static moving load excitation (obtained from Hosseingholian et al., 2011).

- Model dependency if the rail deflection is measured at some distance away from the applied load, as in this case a model for the rail bending has to be used;
- Influence of track irregularities.

Some of the available tools characterize the dynamic track stiffness by means of an oscillating mass. A very good review of the different track stiffness measurement strategies is given by Berggren (2005) and Nielsen et al. (2013). In the following, the EMW and the Rolling Stiffness Measurement Vehicle (RSMV) equipments will be briefly described as the commonly used tools for continuous quasi-static and dynamic track stiffness estimation, respectively.

2.3.2.1 EMW

The EMW vehicle developed by the the Swiss Federal Railways allows obtaining track deflections at the speed range of 10 - 15 km/h, which can be linked to the quasi-static track stiffness. The measurement method consists in obtaining the track deflection for a loaded axle of 20 ton and an unloaded axle, i.e. negligible load. The total track deflection is given by the difference of the two measures. The track deflection is measured each 5 cm and the associated error is of $\pm$ 0.2 mm for the rail deflection and $\pm$ 1 mm for the longitudinal position. The used equipment is shown in Figure 2.9a.

According to Nielsen et al. (2013), low-pass filter is normally used with cut-off wavelength of 10-20 m. The use of a low-pass filter appears to be justified by the fact that even low levels of wheel out-of-roundness can significantly influence the measurement. The track deflection can then be linked to the track stiffness by one of the presented above formulations.

An example of the EMW measurements in a high speed line is given in Figure 2.9b. The track vertical deflection and the associated track stiffness present a large range of values and important variations at both small and large wavelengths. Although track stiffness variations are much discussed in the literature in terms of transition zones, e.g. bridge - embankment and ballasted - slab track (Dimitrovová and Varandas, 2009; Ribeiro, 2012;

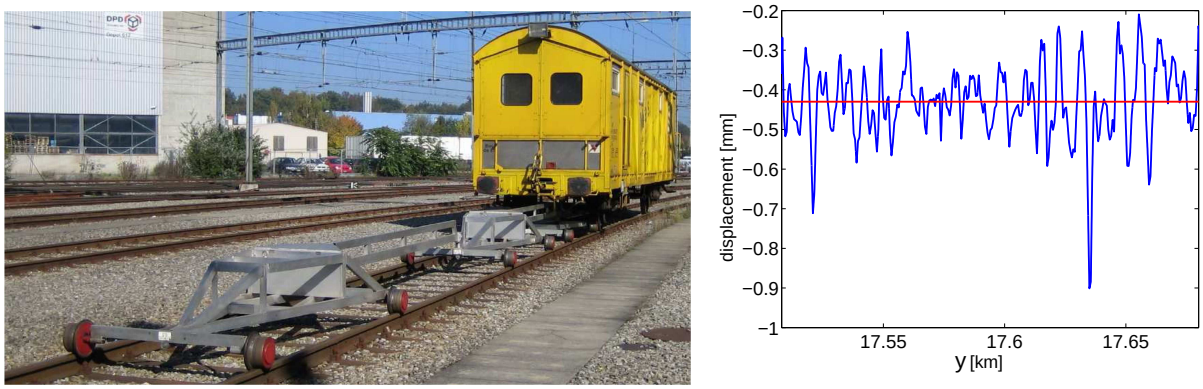

(a) (b)

Figure 2.9: EMW track stiffness measurement. a) EMW equipment (obtained from Nielsen et al., 2013); b) EMW measure at a portion of high speed line. Red line represents the mean displacement value along a certain distance y.

Ang and Dai, 2013; Shan et al., 2013, among others), variations appearing in the same track structure are seldom discussed. On transition zones, authors have showed that the abrupt track stiffness variation is responsible for an important increase in dynamic train-track interaction force, leading to rapid development of track irregularities and hanging sleepers (Dahlberg, 2010). On current track zones, the observed track stiffness variations can possibly lead to track irregularities, by the same process as observed in transition zones. Studying the importance of this aspect in the mechanical response of the track and train-track interaction is an important subject which has not yet been addressed in the literature.

2.3.2.2 Rolling Stiffness Measurement Vehicle (RSMV)

The Rolling Stiffness Measurement Vehicle (RSMV) measures the dynamic track stiffness at frequencies up to 50 Hz (Berggren, 2005; Berggren et al., 2010). The equipment is a rebuilt two-axle freight wagon (Figure 2.10a). The proposed method consists in dynamically excitating the track by two oscillating masses and measuring the corresponding accelerations, as schematically represented in Figure 2.10b. The method compensates the vertical deflection due to the wheel-rail contact and filters the excitation frequency of the signal before resampling in the spatial domain. Measurements at speeds up to 60 km/h can be done with sinusoidal excitation frequency. Results of track stiffness measurements performed by Berggren (2005) using RSMV presented good correlations with the depth of clay layer, obtained from borehole investigation (Figure 2.11), high values of track stiffness corresponding to lower depth of the clay layer.

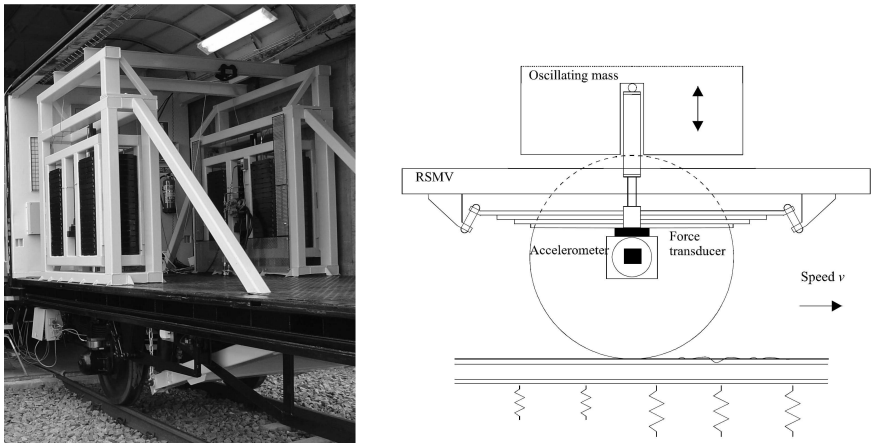

(a) (b)

Figure 2.10: RMSV measurement equipment. a) Photo of the equipment; b) Schematic representation (one side only) (obtained from Berggren, 2005).

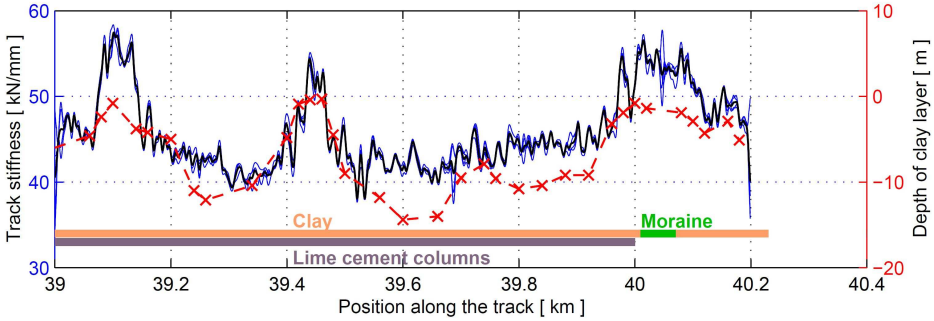

Figure 2.11: RSMV measure at a track section of 1.2 km with speed of 20 km/h and excitation frequency of 5.7 Hz. The dark line represents the mean of 4 conducted measurements of the track stiffness and the x-mark represents the depth of the clay layer present in the site (obtained from Berggren, 2005).

2.4 Soil behavior under cyclic load

In pavement engineering and railway applications, geomaterials are subjected to cyclic loads at different magnitudes and frequencies. During the construction phase, cyclic loading is applied as an effective way of compacting the material. It is well understood that this phase is critical in improving the performance of the structure to future loads (Martins, 2011). In this sense, a large range of equipments and technologies exist both in compaction techniques and in compaction control. However, compaction is not the only physical phenomena that soil can experiment during cyclic loading. Although seldom discussed in the railway field, liquefaction and cyclic mobility can also occur during cyclic loading, depending mainly on the drainage conditions as well as the load amplitude.

The experimental results and modeling strategies presented in this section consider that the soil is fully saturated with water or completely dry. Under these hypotheses, the soil behavior can be explained in the light of the effective stress concept introduced by Terzaghi:

$$p = p' + u_w \tag{2.7}$$

where $p = (\sigma_1 + 2\sigma_3)/3$ is the total mean stress, p' is the effective mean stress and u_w is the pore water pressure. The effective mean stress and the deviatoric stress $q = \sigma_1 - \sigma_3$ are used in order to define the main aspects of the soil's stress response.

In the following, an overview of soil behavior under cyclic loading is presented. The main laboratory equipments used in soil mechanics are presented followed by the main concepts used to describe the soil behavior under monotonic load. The physical phenomena taking place during cyclic loading are then discussed in the light of these concepts. In pavement engineering, very often the deformational response of unbound aggregates during loading is characterized by recoverable (resilient) and residual (permanent) deformations. An example of this approach is presented in Figure 2.12. Uncoupling the resilient and the permanent responses and considering the soil response only resilient relies in the hypothesis that during loading, the increment of permanent deformation is insignificant regarding the observed resilient deformation. Under these hypothesis, an overview of the different aspects affecting the resilient and permanent response of soil are presented. Finally, an overview of the numerical models used for studying the cyclic behavior of soils are presented in the last section based on these experimental evidences.

2.4.1 Current laboratory equipments

Different experimental devices are used in soil mechanics in order to characterize the soil behavior under cyclic loading. The loading characteristics can be divided between quasi-static and dynamic loading, the difference being considering or not inertial forces during loading. Among quasi-static cyclic loading, the main used equipments are the triaxial cell, the simple shear cell and the torsional shear device. The triaxial cell is probably the most used equipment for soil testing. From an isotropic initial state, total lateral stress (σ_r or σ_3) is kept constant while cyclically varying the total vertical stress (σ_a or σ_1). Both drained and undrained conditions can be used and they are representative of different loading characteristics simulating two opposites cases:

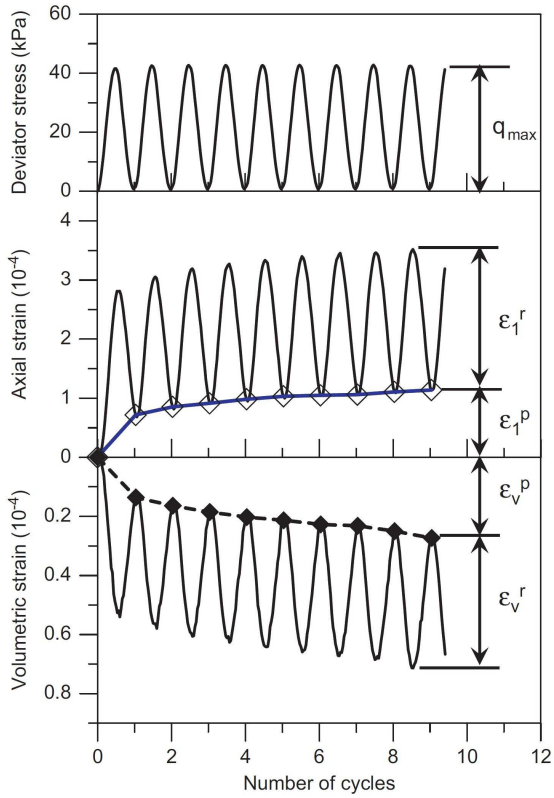

Figure 2.12: Cyclic triaxial test results obtained by Trinh et al. (2012). Evolution of resilient (ε_1^r and ε_v^r) and permanent (ε_1^p and ε_v^p) strains with cycles.

- Drained condition: volume change takes place and no increment in pore water pressure is allowed;
- Undrained condition: volume is kept constant and in this case the soil skeleton deformation during the test leads to changes in the pore water pressure.

Both are idealized conditions, as in many applications fully drained or undrained conditions are not verified and both pore water pressure and volume changes are likely to occur.

Concerning the applied load, sinusoidal cycles at different stress levels are usually applied, although the "double M wavelet" cycle presented in Section 2.2.2 is also used (Al Shaer et al., 2008).

In pavement engineering, a modification of the standard triaxial test at constant confining pressure (CCP) is the variable confining pressure (VCP) equipment. In this case, the variations of lateral stress during load passage can be taken into account. However, none of these allows applying shear stress, thus not representing the continuous principal stress axes rotation observed in pavements and railways (Tutumluer and Seyhan, 1999).

In the case of the simple shear test, from an oedometric initial state, shear stress is cyclically varied. In this case, under drained conditions the stress path imposed by the loading in the (q, p') plane is purely deviatoric, $\Delta p'$=0. This is considered as an idealized stress path followed by soil layers during seismic events.

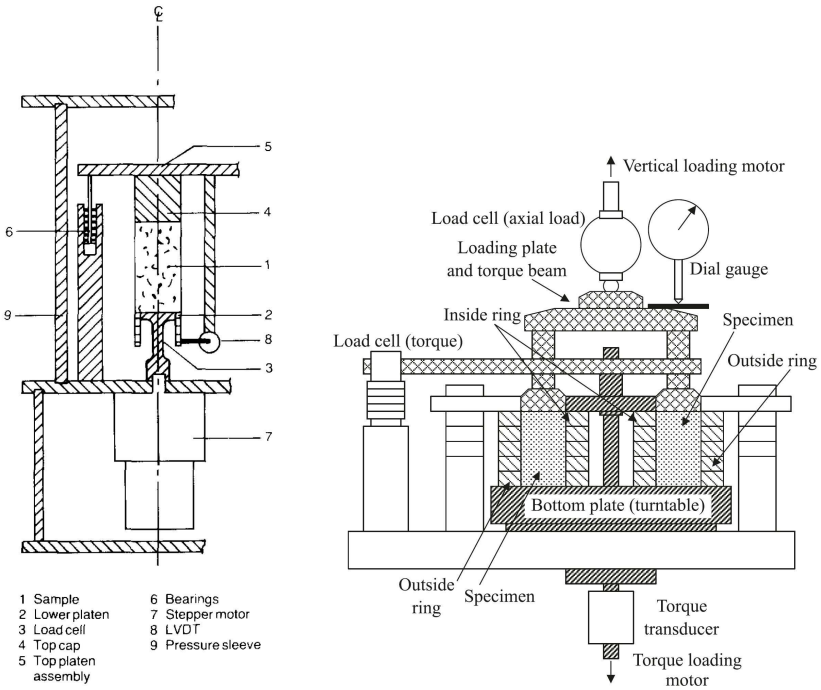

(a) (b)

Figure 2.13: Different configurations of torsional shear tests. a) Wilson equipment (from Bolton and Wilson, 1989); b) Hollow cylinder (from Ishikawa et al., 2011).

Torsional shear test allows applying a torque momentum on the upper or lower plate of the equipment, which is superimposed to a triaxial state also controllable during the test. In this class of equipments, samples shape can either be of a filled or hollow cylinder. Examples of the first and second class are given in Figures 2.13a and 2.13b. The hollow cylinder apparatus (HCA) is usually preferred as it allows testing the soil in a large range of stress paths and the stress and strain fields can be considered as almost homogeneous. Particularly to pavement engineering, the HCA allows correctly modeling the stress path and the rotation of principal stress axes imposed by the moving load (Ishikawa et al., 2011; Caicedo et al., 2012). By independently controlling the inner and outer pressure, the stress rotation and the state of stress can be completely decoupled (Miura et al., 1986), i.e. parameters α_{yz} and b are decoupled (Equations 2.2 and 2.3). When the inner and outer pressures are the same, parameters α_{yz} and b are linked by the following relationship $b = \sin^2 \alpha_{yz}$. As discussed by Caicedo et al. (2012), very few HCAs are adapted for unbounded aggregates, as the particle size requires very large equipments.

For dynamic loading, the resonant column device is the main used equipment. It consists of a triaxial cell equipped with a cyclic torsional loading system. Figure 2.14 represents the Stokoe apparatus described by Bolton and Wilson (1989). From an initial triaxial stress state, cyclic shear stress is imposed by the torsional loading system, while the lateral and vertical stresses are kept constant. By continuously varying the loading frequency, the specimen's resonance can be obtained and this can be well approximated as a function of the soil specimen's mass and the shear stiffness (G). By varying the imposed

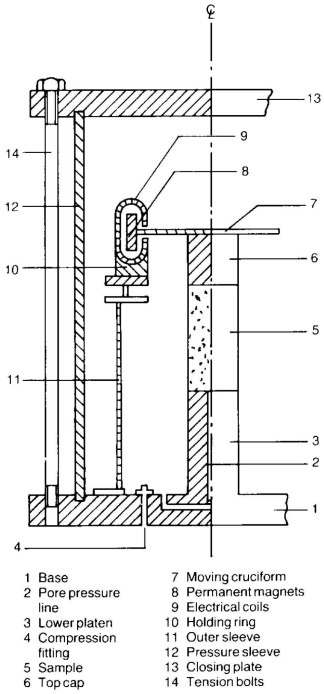

Figure 2.14: Resonant column (Stokoe apparatus) (from Bolton and Wilson, 1989).

shear stress, the specimen's resonance frequency changes and this allows characterizing the shear stiffness at different shear strains. Damping can be studied by the decaying vibrations obtained by switching off the loading system at the resonant frequency (Bolton and Wilson, 1989).

2.4.2 Main concepts from monotonic loading tests

Three main concepts used in soil behavior modeling are defined for explaining the soil behavior from monotonic test results. These concepts are used as envelopes for explaining the soil behavior under cyclic load. These are:

- The critical state: it is a fundamental concept in soil mechanics first proposed by Roscoe et al. (1958). It can be defined as a state when the soil continues to deform without any variations of stress and volume. The critical state line (CSL) in the (q, p') plane can be viewed as the perfect plastic behavior obtained by the Mohr-Coulomb failure criterion (Figure 2.15a). Any state of the soil can thus be defined relatively to the CSL in the (e, p') plane (Figure 2.15b), e being the void ratio. The volumetric behavior (contraction, dilatancy) can be explained according to the distance of the initial state (A,B in Figure 2.15b) to the critical state line. For undrained samples, the steady state (Poulos, 1981) can be supposed as being the same as the critical state if the behavior is independent of the strain rate (Sladen et al., 1985; Canou et al., 2002).

- The characteristic state: it represents the change from the contractive to the dilative behavior in sands and defines the characteristic line in the (q, p') plane. It can be

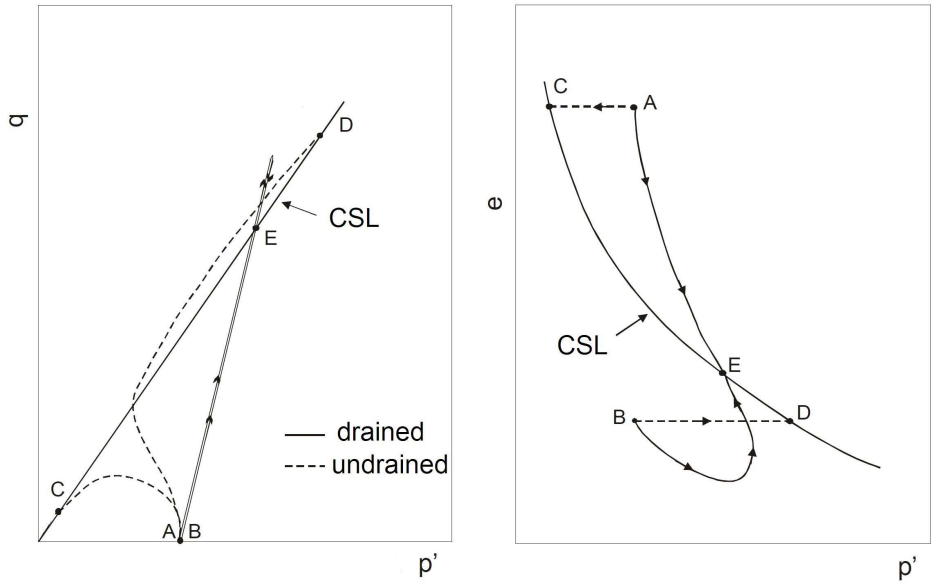

(a) (b)

Figure 2.15: Typical behavior of soils for monotonic drained and undrained triaxial tests with projection of the critical state line (CSL). (adapted from Canou et al., 2002). a) Effective stress paths; b) Variation of void ration during the tests.

graphically interpreted as in Figure 2.16a. For undrained tests, the characteristic state is called phase transformation or quasi-steady state (Ishihara, 1993) and in this case it also represents the locus of minimum effective mean stress p'. Some authors have argued, however, that the critical state and characteristic states in sands present the same slope in the (q, p') plane.

- The instability line: it is the locus of peak deviatoric stress for an initial void ratio obtained for undrained tests (Figure 2.16b). This also called in the literature as collapse line or flow line. In elasto-plasticity models, these are related to maximum value of plastic potential surface and of the yield surface, respectively. The phase transformation line and instability line are distinctly different for sands, while for normally consolidated and insensitive clays these two lines coincide (Lade and Ibsen, 1997).

These concepts can be used for explaining both the behavior of granular and fine soils, the degree of consolidation of clays playing an analogous role as the density index $(I_d = (e_{max} - e)/(e_{max} - e_{min}))$ for sands.

2.4.3 Experimental results of the cyclic behavior of soils

When performing cyclic triaxial loading under drained conditions, volume changes are allowed to happen. In this case, the cyclic loading can either lead to reduction or increase of the specimen volume. In the first case, cyclic compaction takes place, volume reduction being associated with the increase of the specimen relative density during cycles. Whereas

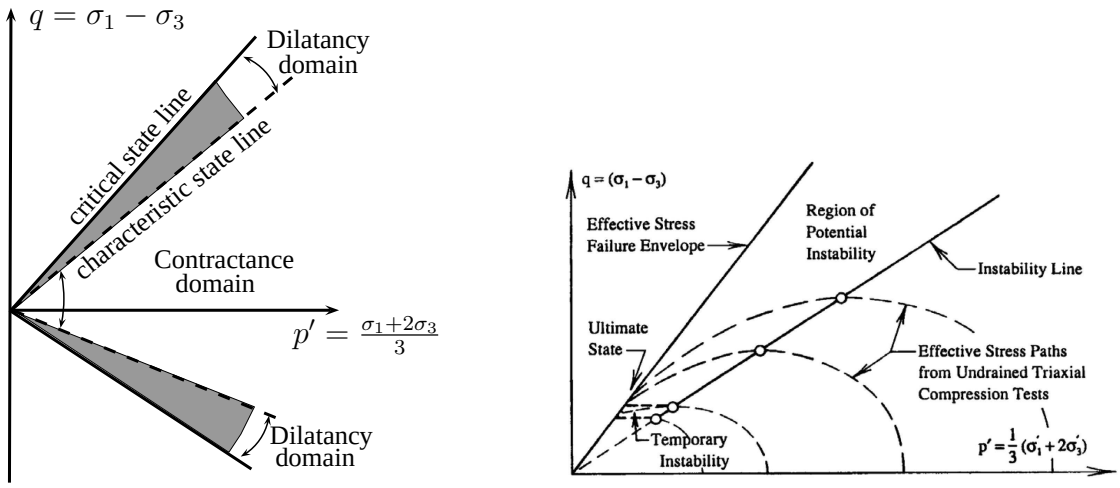

Figure 2.16: Schematic representation of different lines in the effective stress plane. a) Critical state and characteristic state lines (adapted from Luong, 1980); b) Instability line (from Lade, 1992).

in the second case, cyclic dilation and failure of the specimen after a certain number of cycles could be observed. According to Prisco and Zambelli (2003), the two main factors affecting this behavior are the initial state of the specimen and the cycle amplitude. Luong (1980) performed a comprehensive study of volume change characteristics of sand drained samples under cyclic loading. By performing cycles of small amplitude at different initial states (Figure 2.17), the author showed that cycles of maximum deviatoric stress lower than the characteristic state lead to compaction and stiffening of the sample. Dilation of the soil specimen takes place when values higher than the characteristic state are imposed.

Luong (1980) also showed that different final states can be achieved by performing cycles of different amplitudes and that densification of the sample can be maximized by performing cycles of compression and extension exceeding the characteristic state, cycles of great amplitude rather than small amplitude. In this case, the increase in volume observed after the characteristic state is exceeded leads to important fabric rearrangement and helps in the rapid densification of the material. Similar results can be found in Biarez and Hicher (1994).

When performing cyclic triaxial or torsional stress under undrained conditions, volume changes in the specimen are not allowed to happen. In this case, the pore water pressure (u_w or p_w) changes as a consequence of the tendency of the soil skeleton to suffer volumetric deformation, which implies in a reduction of effective mean stress (p') at each cycle. When the pore water pressure approaches total pressure (p), a sudden important increase of axial strain is observed, characterizing softening of the specimen. According to Ishihara (1993), initial liquefaction or simply liquefaction can be defined as the soil state when a 100% build-up of the water pore pressure is observed or alternatively when axial strain is about 5% in double amplitude (Ishihara, 1993). Two main cases can be then observed, depending on the initial state of the soil specimen:

- the volume change tendency of the soil skeleton is only contractive. In this case, the effective mean stress p' drops to very low values, a complete loss of strength

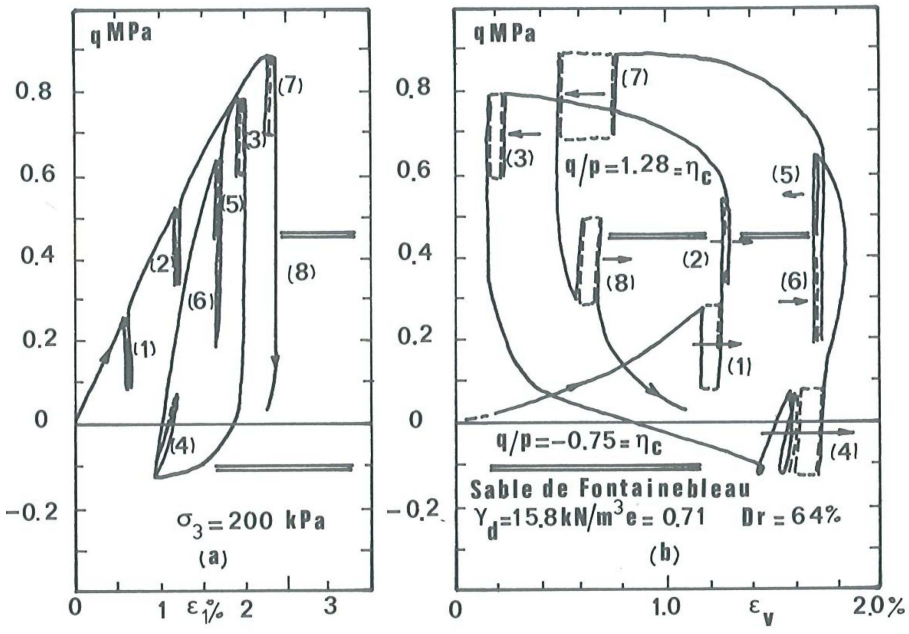

Figure 2.17: Cyclic loading at different initial states at drained triaxial test performed by Luong (1980).

is observed and infinitely large deformations are produced. The typical stress path obtained in this case is presented in Figure 2.18a.

- the volume change tendency of the soil skeleton is contractive at low strains and dilative at higher strains. In this case, the effective mean stress p' does not drop to zero as the dilatancy tendency presented by the soil skeleton at high strains counterbalances the pore water pressure build-up. The sample then does not present a complete loss of strength and continuing applying cyclic load does not lead to infinite large deformations. This case is often described as cyclic mobility in the literature, although some authors define both states as liquefaction. The corresponding stress path for this case is presented in Figure 2.18b.

According to Sladen et al. (1985), the liquefaction potential is usually studied with monotonic undrained triaxial tests on very loose samples. This is mainly due to the triaxial equipements being widely available, loose samples remaining contractive and in this case nonuniformities due to the shear plane appearing during dilatancy phase are avoided. Constant volume condition of the undrained test also helps avoiding nonuniformities of the sample. According to Ishihara et al. (1975), the state defined by the phase transformation line has to be reached at least once for a sample in order to attain liquefaction.

The lines obtained from the monotonic response and discussed in Section 2.4.2 define three different zones for liquefaction potential in the stress plane defined by the stress invariants $t = (\sigma_1 - \sigma_3)/2$ and $s = (\sigma_1 + \sigma_3)/2 = s' + u_w$. These are shown in Figure 2.19 and can be defined as:

- Zone A: the cyclic shear stress levels are lower than the steady state deviatoric stress t_{ss} and in this case liquefaction cannot happen,

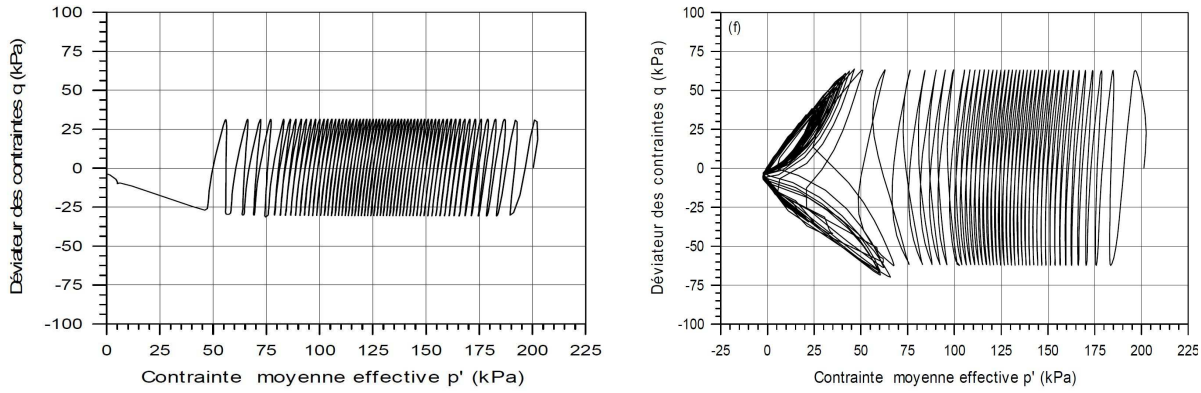

(a) (b)

Figure 2.18: Typical stress paths for cyclic undrained tests on Houstun RF sand performed by Canou et al. (2002). a) Liquefaction; b) Cyclic mobility.

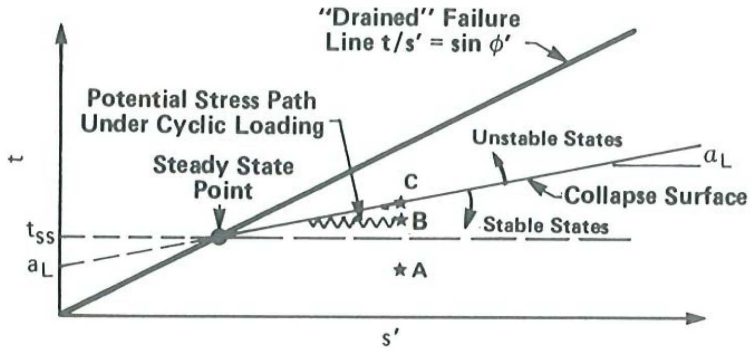

Figure 2.19: Effect of soil state on liquefaction potential (from Sladen et al., 1985).

- Zone B: liquefaction is possible under cyclic loading, depending on the cycle amplitude, deviatoric mean value and the number of cycles, Liquefaction takes place once the soil state during loading intercepts the collapse line.
- Zone C: in this case soil failure occurs under static loading.

As showed by Lanier et al. (1991), liquefaction can also be observed under other stress paths, for example at a hollow cylinder apparatus by rotating the principal stress axes and keeping constant both mean pressure and the second invariant of stress. Moreover, isotropic and anisotropic samples can present different liquefaction potential (Ishihara, 1993).

In real applications, cyclic increase of pore water pressure in sands depends in general on the permeability boundary conditions, i.e. the possibility of the material to evacuate the pore water pressure during loading relatively to the loading characteristics. Undrained conditions can be observed for instance when a sand layer is surrounded by a clay formation during earthquakes and liquefaction is indeed one of the main concerns on geotechnical earthquake engineering. In the railway field, liquefaction of the soil as defined above is unlikely to occur. However, some experimental evidence on the interlayer formation

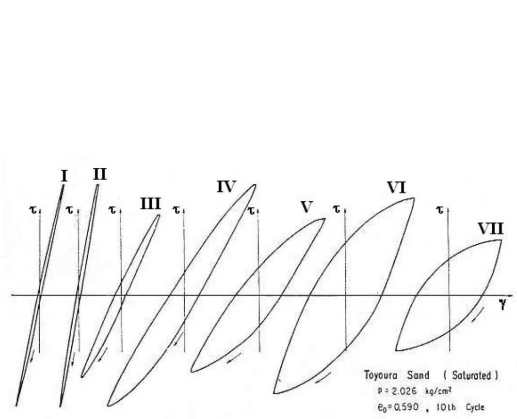

(a)

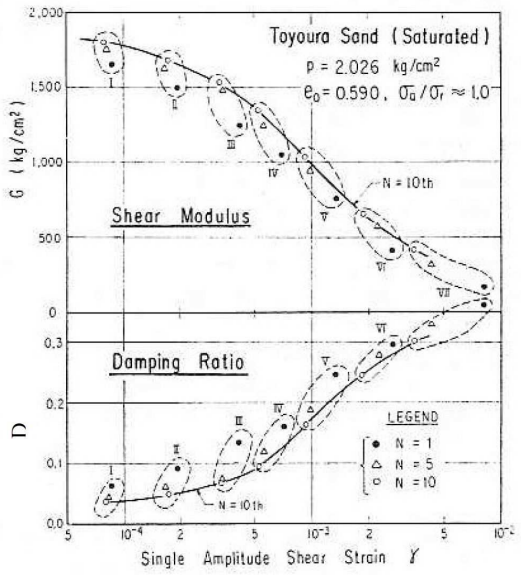

(b)

Figure 2.20: Torsional shear tests on Toyoura sand (from Iwasaki et al., 1978). a) Stress-strain records; b) Shear modulus and damping ratios.

on conventional lines and possibly mud-pumping formation presented by Duong et al. (2014a) is linked to the increase of pore water pressure in the subgrade soil. Liquefaction as defined by Ishihara (1993) does not occur in the subgrade soil but migration of fines to the ballast layer takes place during the dissipation of the excess of pore water pressure.

Another phenomena influencing the soil behavior under cyclic loading is the nonlinear dependency of the shear stiffness (G) and damping ratio (D) with the shear strain (γ). Figure 2.20 presents the results from Iwasaki et al. (1978) on drained torsional shear tests on isotropically consolidated Toyoura sand. Increasing the shear strain amplitude leads to higher hysteresis loops and lower secant modulus. The damping ratio is defined for a hysteresis loop as (Hardin and Drnevich, 1972):

$$D = \frac{A_L}{4\pi A_T} \tag{2.8}$$

where A_L is the area enclosed by the hysteresis loop and A_T the area enclosed by the triangle defined by the maximum strain and the maximum stress. By normalizing G by its maximum value G_{max}, obtained at γ=10^{-4}% or less for different laboratory results on fine and granular soils, at different confining pressures, Seed and Idriss (1970) showed that the influence of the shear strain on the shear modulus and the damping ratio defines a narrow area, as shown in Figure 2.21.

Vucetic and Dobry (1991) compared different results available in the literature and showed that plasticity index for fine materials is one of the most influencing parameters in the shape of the shear modulus reduction and damping increase. The documented curves are presented in Figure 2.22. Highly plastic soils present an increased linear domain and lower damping ratio than low plastic soils.

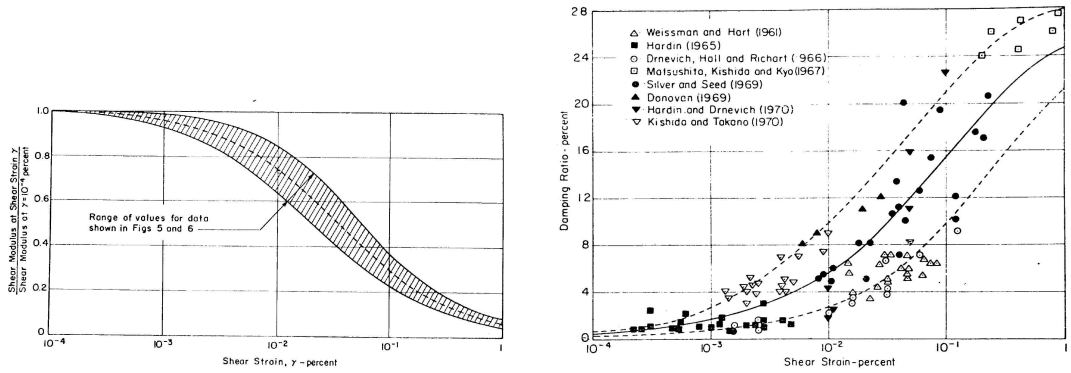

(a) (b)

Figure 2.21: Influence of the shear strain amplitude on cyclic load (from Seed and Idriss, 1970). a) Shear modulus; b) Damping ratio.

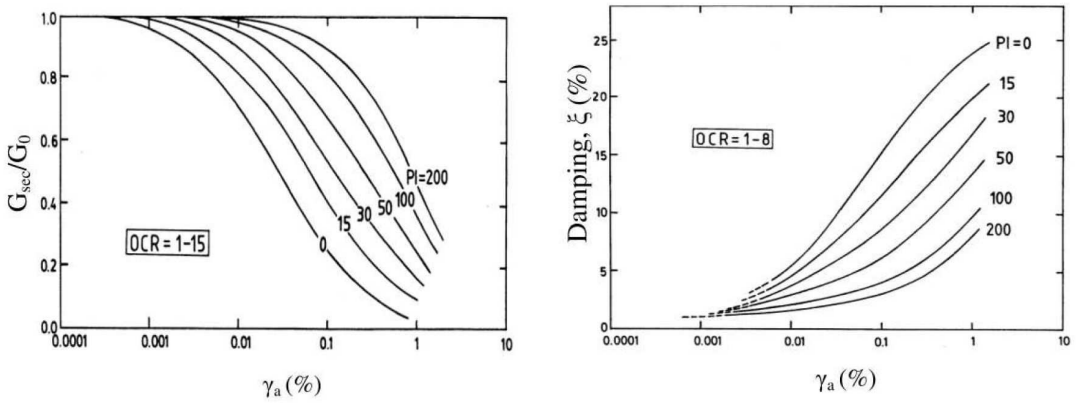

(a) (b)

Figure 2.22: Effect of plasticity index (PI) on soil response (from Vucetic and Dobry, 1991). a) Shear modulus; b) Damping ratio.

According to Bolton and Wilson (1990b), soil damping should be divided in two components: one related to the hysteresis loop, (hysteretic damping), and one related to the pore fluid (viscous damping). The first term is solely related to the used aggregate, whether the second varies according to the viscosity of the considered pore fluid. Comparing the behavior of dry and saturated with water Leighton Buzzard sand on resonant column tests, Bolton and Wilson (1989) showed that for maximum soil strains of 0.07%, steady state conditions and loading frequencies from 0.001 to 120 Hz, the soil behavior is independent of the frequency. As discussed by Bolton and Wilson (1990a), the cyclic behavior of the soil can thus be assessed by quasi-static tests. Using silicone oil as pore fluid instead of water, whose viscosity is 100 times larger, Bolton and Wilson (1990a) showed that the damping ratio increases by 2 to 3 times. According to the authors, it is then necessary to consider the viscosity of the pore fluid in order to assess its influence on soil damping. From the above results, damping on dry sand and saturated sand with

water can be considered as hysteretic and not viscous.

These results have an important impact on how train speed affects the response of granular materials. The soil strain and load frequency range tested by Bolton and Wilson (1990b) are representative of those encountered in tracks and in this sense the cyclic behavior of the materials is not expected to change with the train speed. Therefore, the effect of load speed is suitably measured by the impact on stresses and strains during load.

2.4.4 Resilient and permanent response of unbound aggregates

When splitting the mechanical behavior into a resilient and permanent responses (Figure 2.12), the elasticity hypothesis for the resilient behavior is considered and it is characterized by a resilient modulus (M_r), also called secant Young's Modulus (E_{sec}), and the resilient Poisson's ratio (ν_r). Brown and Hyde (1975) suggested characterizing the resilient properties by bulk (K) and shear (G) moduli instead of resilient modulus and resilient Poisson's ratio. The authors provide the following reasons: they do not rely on elasticity assumptions in their calculation, the volumetric and shear components are uncoupled and they have a more realistic meaning in three-dimensional stress regime. However, many results are still published in terms of resilient modulus (Heelis et al., 1999; Christie et al., 2007; Fortunato et al., 2010; Trinh, 2011, among others).

The Rankine Lecture and the subsequent paper from Professor Brown (Brown, 1996) establishes a milestone on the techniques and main results of soil mechanics applied in pavement engineering. A literature review of different aspects affecting the resilient and permanent deformational behavior of unbound aggregates is given by Lekarp et al. (2000a) and Lekarp et al. (2000b), respectively. More recently, Brecciaroli and Kolisoja (2006) made a specific literature review of this approach for railway embankment materials. Further elements are given hereafter.

2.4.4.1 Resilient behavior

According to Brecciaroli and Kolisoja (2006), the resilient response is mainly affected by the level of applied stress and moisture content. The resilient modulus increases with increasing confining pressure and the sum of principal stresses, but only slightly with increasing deviator stress. Brown and Hyde (1975) have showed that similar resilient modulus can be obtained by both triaxial tests at constant confining pressure (CCP) and variable confining pressure (VCP), when the mean lateral stress of the VCP test is used in the CCP test (Figure 2.23a). The resilient Poisson's ratio increases with decreasing confining pressure and increasing deviator stress according to Brown and Hyde (1975) and Kolisoja (1997). However in this case, the CCP and VCP tests give opposite trends for the resilient Poisson's ratio. These aspects are represented in Figure 2.28.

Concerning the moisture content, not all materials present the same dependence as it is mainly affected by the amount and mineralogy of fines present in the material. Dry and saturated materials present the same resilient properties under effective stress analysis (Pappin et al., 1992).

For partially saturated materials, a comprehensive study was performed by Wu et al.

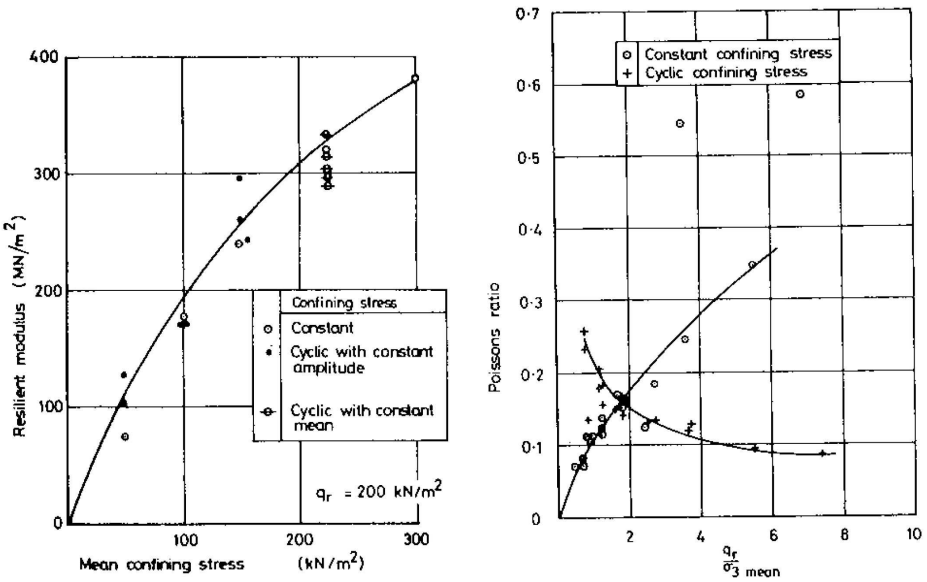

(a) (b)

Figure 2.23: Difference results for CCP and VCP test results (from Brown and Hyde, 1975). a) Resilient modulus; b) Resilient Poisson's ratio.

(1984) on resonant column tests for five different materials at different degrees of saturation. Figure 2.24 presents the results of shear modulus variation with the degree of saturation and confining pressure, and it is clearly showed that the degree of saturation plays an important role in the evolution of the resilient properties. According to Pappin et al. (1992) and Brown (1996), the resilient modulus of partially saturated materials could also be explained by an effective stress analysis, but in this case estimating the effective stress from the measured total stress is not straightforward.

According to the Brecciaroli and Kolisoja (2006), it is not yet clear in the literature the impact on the resilient characteristics of other factors, such as the soil density, the considered strain level and the loading characteristics.

For unbound aggregates, a type of anisotropy called cross-anisotropy appears from the stratification and compaction applied during construction and the structure life (Tutumluer and Seyhan, 1999). In laboratory tests, the cross-anisotropy is obtained by highly compacting the material; very dense samples are obtained and the cross-anisotropy appears as a consequence from the strain history. Authors have showed that in this case the resilient modulus increases up to a certain axial strain level before decreasing (Kolisoja, 1997; Tatsuoka et al., 1999; Coronado Garcia, 2005, among others). Figure 2.25 shows the results obtained by Tatsuoka et al. (1999) for virgin and prestrained Houston sand samples. The modulus increases for axial strain between 0.01% and 0.7%, the latter being characteristic of the volumetric behavior changing from contractive to dilative. The appeareance of a cross-anisotropy on railway materials due to cyclic loading is less discussed in the railway literature.

Regarding the effect of principal stress axes rotation on the resilient response, Brown (1996) stated that there is no impact. According to the author, both principal stress and

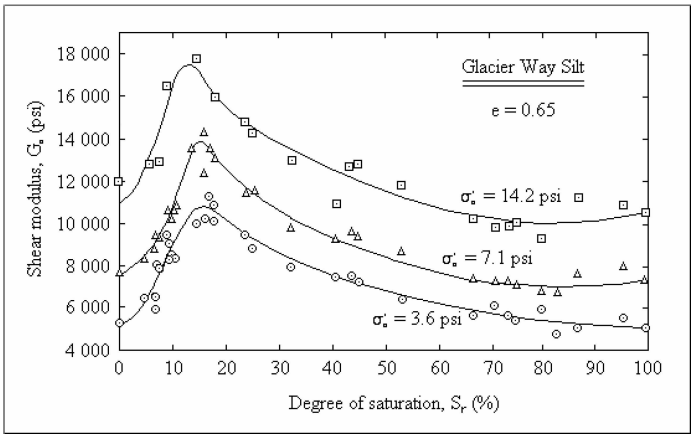

Figure 2.24: Variation of shear modulus with the imposed degree of saturation and the confining pressure for Glacier Way Silt material tested by Wu et al. (1984).

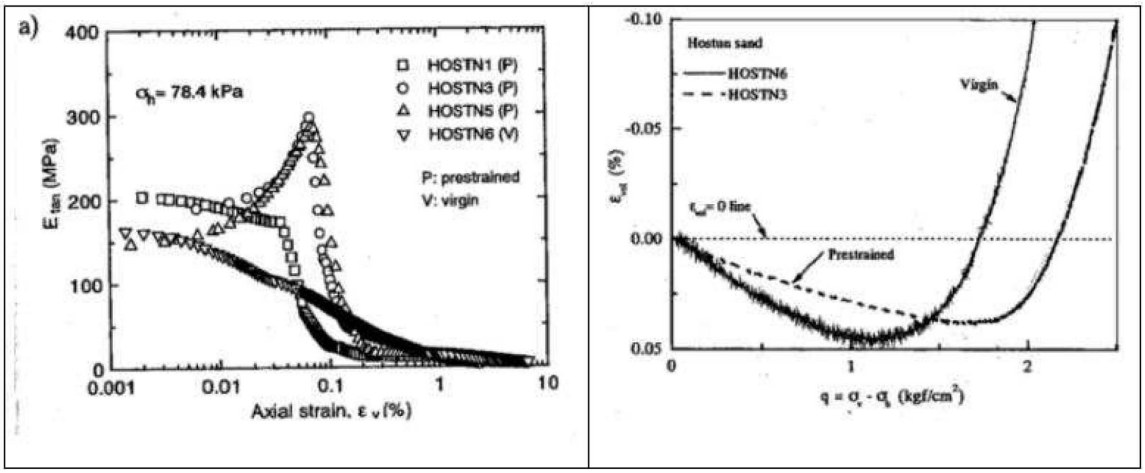

Figure 2.25: Variation of the tangent modulus with the axial strain for virgin (V) and prestrained (P) Houston sand samples (left); evolution of q and ε_v on small strains (right) (from Tatsuoka et al., 1999).

strain axes rotate together during the moving load cycle.

2.4.4.2 Permanent behavior

Differently from the resilient response, whereas the level of applied stress and moisture content are the most contributing factors affecting the mechanical response, the development of permanent strains is affected by several factors (Brecciaroli and Kolisoja, 2006). These are:

- soil state;
- stress level;
- number of load applications;

- principal stress rotation;
- moisture content;
- grading and aggregate type;
- physical properties of aggregate particles.

Some of these aspects are highlighted in the following. The reader is invited to refer to the following references (Brown, 1996; Lekarp et al., 2000a,b; Brecciaroli and Kolisoja, 2006) for further results.

The analysis of the permanent behavior of unbounded aggregates generally relies on measuring the axial permanent strain on drained cyclic triaxial tests. The importance of volume behavior and compaction/dilation mechanisms is seldom discussed in the literature, although (Chan, 1990) discuss the influence of soil dilatancy on the increase of permanent strains. Maybe this intrinsic assumption that cyclic compaction is the main mechanism of volume behavior mainly relies on the empirical evidence that pavements and railroads settle. However, this does not guarantee volume reduction, as lateral strains are allowed to develop. Increase in volume, liquefaction and cyclic mobility can also occur during cyclic loading, depending on the stress level, soil initial state, moisture content and drainage conditions. In the case of studying moisture's content influence, undrained tests are performed, but in this case liquefaction is avoided by performing cyclic loading of small amplitude. Besides the shakedown concept, there seems to be a gap between the permanent deformation analysis and the concepts and different defined locus from static failure.

In pavement engineering, the effect of soil state is generally studied separately in terms of the soil density and stress history. Regarding soil density, which is usually described by the degree of compaction, it has been showed that accumulated permanent deformation decreases as a consequence of increased soil density. Barksdale (1972) showed for instance that compacting unbound granular materials at 95% instead of 100% of the maximum compaction density leads to higher permanent axial strains on cyclic triaxial tests (Figure 2.26) .

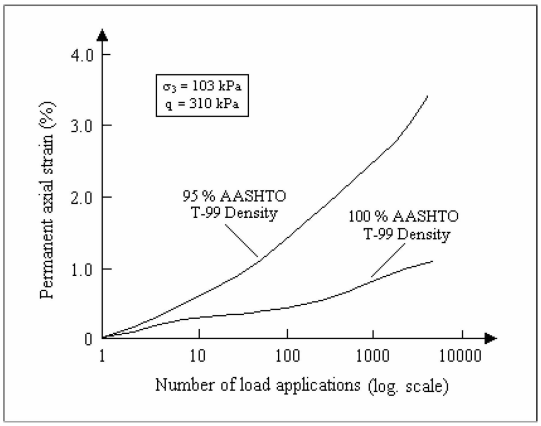

Figure 2.26: Effect of density on permanent strains (from Barksdale, 1972).

Regarding the stress history, it has been showed that the stress level of the first cycle determines the subsequent plastic strain accumulation. In this sense, applying low stresses before higher stresses leads to lower permanent strains than directly applying higher stresses. The tests conducted by Brown and Hyde (1975) on granular materials showed in Figure 2.27 exemplifies this behavior: higher permanent strains are obtained when the highest stress level is immediately applied. This is due to progressive compaction and stiffening of the material obtained during the incremental loading.

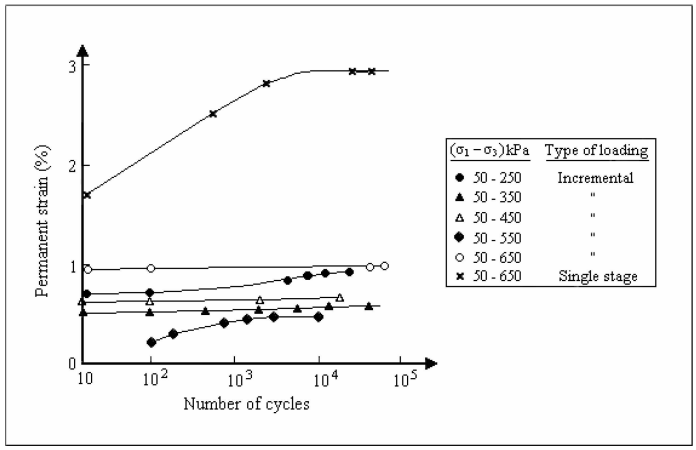

Figure 2.27: Effect of loading history for different type of loading on permanent strain (from Brown and Hyde, 1975).

The level of applied stress and the number of applied cycles play an important role on the accumulation of permanent strain. Concerning the level of cyclic stress, Barksdale (1972) stated that the permanent axial deformation is directly related to the deviatoric stress and inversely related to the mean stress. In contrast, Brown and Hyde (1975) stated that the permanent axial strain is governed by some form of stress ratio between deviatoric and confining stress. Moreover, Brown and Hyde (1975) discussed that using CCP or VCP apparatus lead to similar permanent axial strain if the mean value of the applied confining stress in the VCP test is used in the CCP test. This result is revised by Rondon et al. (2009), who obtained larger permanent axial strain values for VCP tests than CCP (Figure 2.28b). According to the authors, the ratio of permanent axial strain obtained by the VCP and CCP tests increases as the slope of the VCP test in the (q, p') plane decreases, e.g. tests VCP1 and VCP2 in Figure 2.28a.

Concerning the number of applied cycles at the same cyclic stress, rapid increase in the first cycles is always observed, followed by three different responses depending on the material, its initial state and the cyclic stress amplitude:

- Asymptotic stabilization of the accumulation of plastic strain at a certain number of cycles;
- Linear (Barksdale, 1972) or hyperbolic (Chan, 1990) increase of plastic strain with the logarithm of the number of cycles;
- Continuous rapid increase of plastic strains and failure of the soil specimen.

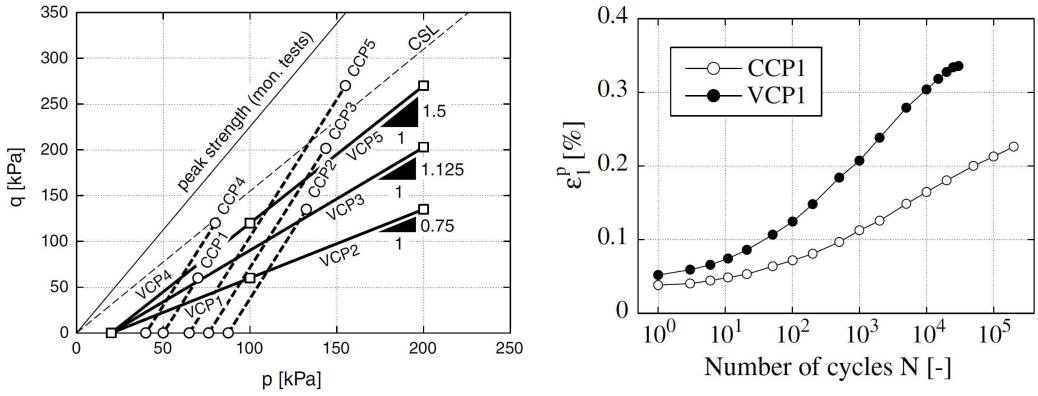

(a) (b)

Figure 2.28: Laboratory test results on VCP and CCP tests performed by Rondon et al. (2009). a) Considered stress paths; b) Permanent axial strain with cycles for VCP1 and CCP1 stress paths.

Kolisoja (1997) performed cyclic loading at a large number of cycles and observed that permanent strain became unstable after approximately reaching a stable condition. The author argues that these instabilities come from grain attrition and crushing during the test. Suiker et al. (2005), Karraz (2008) and Indraratna et al. (2011) showed that grain attrition is the main cause of granulometric evolution of ballast material under cyclic load.

Using hollow cylinder apparatus, Chan (1990) showed that principal stress axes rotation increases the plastic strain accumulation during cyclic loading when compared to tests when no principal stress axes rotation occurs. Figure 2.29a from Chan and Brown (1994) illustrates this fact by showing the increase in the rate of strain when shear reversal is applied after the specimen had been subjected to triaxial cyclic loading. Similar results were obtained by Grabe and Clayton (2009) on subballast material at different clay contents (Figure 2.29b).

Higher shear stress and stresses close to failure lead to higher difference in the cumulated plastic strain. Inversely, when the shear stress is low compared to the normal stress, only slightly differences are observed. Differences between unidirectional and bidirectional shear reversal (representing one-way or two-way load reversal) are also observed by Chan (1990); Brown (1996); Kolisoja (1997, among others), one-way load leading to lower strains. This aspect is illustrated in Figure 2.30.

Drainage conditions can also play an important role on the plastic strain accumulation. It is reminded that in the resilient and permanent strain decoupling approach, the amplitude of loading cycles is low and increase of pore water pressure is limited. Otherwise, liquefaction takes place and uncoupling the resilient and permanent behavior is no longer valid. With this aspect in mind, Figure 2.31 shows that undrained conditions lead to higher permanent strains as the increase in pore water pressure reduces the effective stress in the material. Guaranteeing good drainage conditions seems essential in order to limit the permanent deformation development on railway tracks.

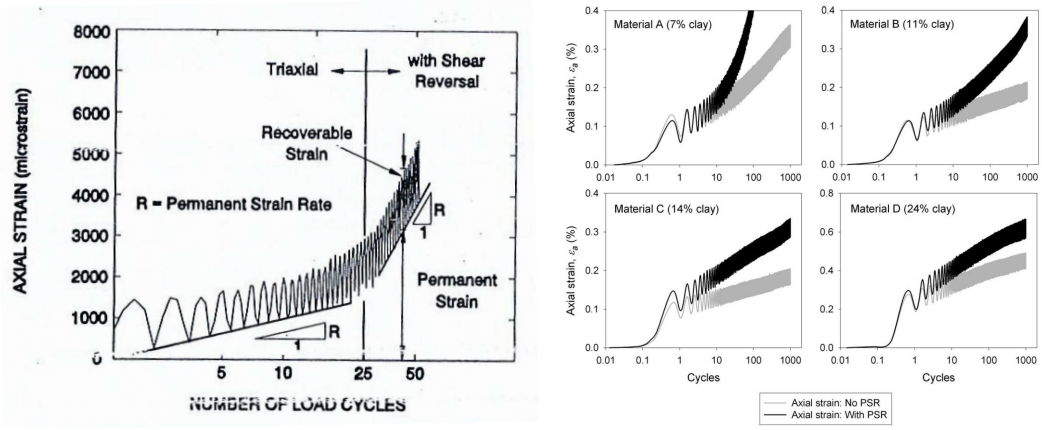

(a) (b)

Figure 2.29: Influence of shear stress reversal (principal stress axes rotation) on plastic strain accumulation. a) Results from Chan and Brown (1994); b) Results from Grabe and Clayton (2009) (PSR: Principal stress rotation).

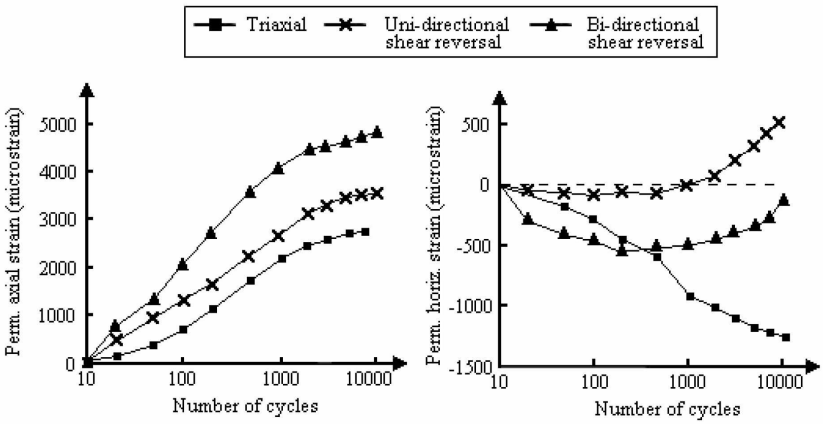

Figure 2.30: Variation of permanent axial and horizontal permanent strains with cycles (from Chan, 1990).

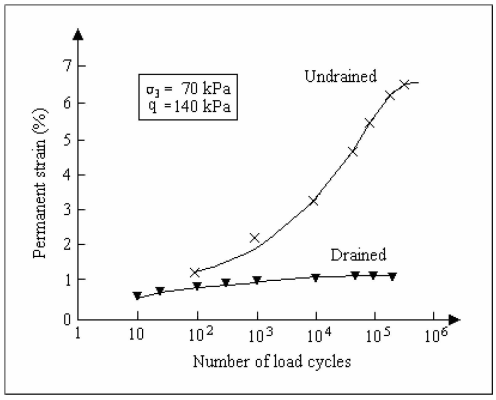

Figure 2.31: Influence of drainage on permanent deformation development (cited by Lekarp et al., 2000b).

2.5 Modeling the cyclic behavior of soils

Different modeling strategies exist in the literature for the cyclic behavior of soils, depending on the hypothesis and considered physical phenomena. In the following, three different modeling strategies are presented as representative of the mechanical models used in pavement and railway engineering. The first class are elastic models accounting for the shear modulus reduction and damping in soils during cyclic load. The second class are developed based on the resilient response of the soil and have been developed mainly for pavement engineering. Finally, the general framework given by the plasticity theory is briefly presented as an effective way of modeling the cyclic behavior of soils under different stress paths.

2.5.1 Models adapted for the cyclic shear response

Within the elasticity framework, the equivalent linear analysis (Madshus and Kaynia, 2000; Costa et al., 2010; Cunha, 2013) is the simplest way in order to take into account the reduction of stiffness and increase of damping with the induced cyclic shear strain. In this case, an iterative procedure is defined based on linear elastic calculations where the shear stiffness and damping are updated according to the obtained effective shear strain in the previous step. The procedure continues until no relevant change in the shear strain is observed. The main question in applying this approach is in obtaining an equivalent shear strain from the shear strain time signal. According to Cunha (2013), in earthquake engineering the effective shear strain has been empirically obtained as between 50% and 70% of the strain peak value; 65% of the strain peak value is commonly used.

Viscoelastic models relying in arrangements of spring and dashpots are also commonly used, such as the Kelvin model and the Maxwell model (Adam et al., 2010; Ansari et al., 2011). However, the main drawback of such arrangements is that they are frequency-dependent, contradicting the laboratory evidence previously discussed in Section 2.4.

Correctly modeling the energy dissipation appearing in the soil during cyclic loading requires specific models that take into account hysteretic and not viscous damping. Cyclic nonlinear elastic models relying in the description of the hysteresis curve seem to be more adapted than both the equivalent linear approach and viscoelastic models in reproducing the shear behavior and damping. According to Kramer (1996), these models usually follow the extended Masing Rules:

1. In the initial load, the stress-strain curve follows a prediscribed backbone curve;
2. When stress reversal takes place at a point (γ_a, τ_a), the stress-strain curve follows the path described by Equation 2.9.

$$\frac{\tau - \tau_a}{2} = F_{bb}\left(\frac{\gamma - \gamma_a}{2}\right) \tag{2.9}$$

   The unloading and reloading curves have the same shape but they are increased by a factor of 2;
3. When the unloading or the reloading exceeds the maximum past strain and intersects the backbone curve, it follows the backbone curve until the next stress reversal;

4. If during an unloading or reloading curve crosses an unloading or reloading curve from the previous cycle, the stress-strain curve follows the one from the previous cycle.

Figure 2.32 schematically represents these rules for a given stress time signal. A popular model intrinsically taking into account these assumptions is the Iwan model (Iwan, 1966, 1967). It relies in the assumption that the backbone curve can be represented by a parallel arrangement of Jenkin elements, each composed of linear spring in series with a frictional slider (Figure 2.33a). The main idea is to set different yield levels for each Jenkin element, the backbone curve being approximated by a series of lines according to the representation in Figure 2.33b.

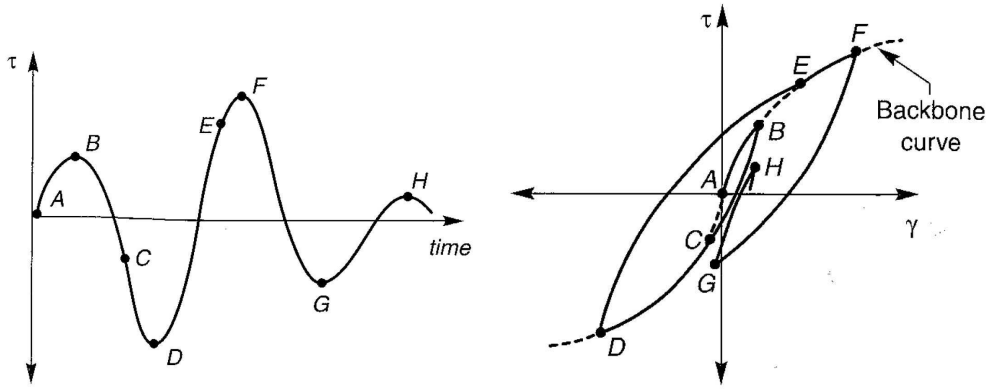

(a) (b)

Figure 2.32: Extended Masing rules (from Kramer, 1996). a) Variation of shear stress with time; b) Stress-strain behavior.

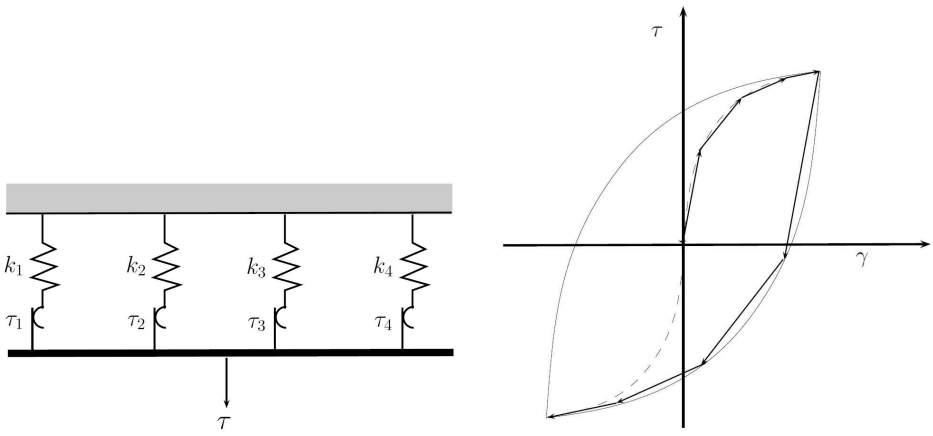

(a) (b)

Figure 2.33: Iwan model (from Cunha, 2013). a) Arrangement of Jenkin elements; b) Approximated stress-strain behavior.

2.5.2 Models for the resilient response of unbound aggregates

The idea of splitting the resilient and the permanent behavior in the mechanical response of unbound aggregates lead researchers to separately modeling the resilient and the permanent deformation. From the above discussed experimental results, the resilient behavior is usually modeled by a nonlinear elastic and inelastic models. The difference of these models is either accounting or not for energy dissipation at each loading cycle. Among nonlinear elastic models, a first class of models considers the resilient modulus (M_r) as a function of the sum of principal stresses or the bulk stress $\theta{=}\sigma_1 + \sigma_2 + \sigma_3$ normalized by a reference pressure p_o. In this sense, different authors (Seed et al., 1967; Hicks, 1970, among others) first suggested a hyperbolic relationship called K-θ model:

$$M_r = k_1 \left(\frac{\theta}{p_o}\right)^{k_2} \tag{2.10}$$

where k_1 and k_2 are model constants which have to be calibrated from experimental results. The simplicity of the model contrasts with two main drawbacks: first, considering a constant Poisson's ratio is not representative of the experimental findings; secondly, the resilient modulus M_r is not only dependent on the bulk stress but also of the shear strain induced by the deviatoric stress. The Uzan model (Uzan, 1985) described by Equation 2.11 is a modification of the K-θ model that better captures the variations of the resilient modulus.

$$M_r = k_1 p_o \left(\frac{\theta}{p_o}\right)^{k_2} \left(\frac{q}{p_o}\right)^{k_3} \tag{2.11}$$

A second class of models considers splitting the resilient deformational behavior in volumetric ε_{vr} and deviatoric ε_{qr} components instead of only considering the axial response, which is represented by the resilient modulus. Boyce (1980) proposes a nonlinear elastic model with no net loss of strain energy described by Equations 2.12 and 2.13.

$$\varepsilon_{vr} = \frac{1}{K_a} \frac{p'^n}{p'^{n-1}_a} \left[1 - \beta \frac{q^2}{p'^2}\right] \tag{2.12}$$

$$\varepsilon_{qr} = \frac{1}{3G_a} \frac{p'^n}{p^{n-1}_a} \left(\frac{q}{p'}\right) \tag{2.13}$$

where p' is the effective mean normal stress, q the deviator stress and n, G_a and K_a are the model parameters, p_a a reference pressure for which bulk K_a and shear modulus G_a are measured and $\beta = (1-n)K_a/6G_a$. The Boyce model requires only 3 parameters and accounts for different volume behavior depending on the stress path (Hornych et al., 1998).

An important modification of the Boyce model is proposed by Hornych et al. (1998) in order to account for soil cross-anisotropy appearing from the compaction. Anisotropy is introduced by considering a coefficient of orthotropy γ multiplying the major principal stress σ_1, which is considered as the vertical direction. The stress-strain relationships are then written as Equations 2.14 and 2.15. The value of γ is usually lower than 1, which leads to higher stiffness in the vertical than the lateral direction.

$$\varepsilon^*_{vr} = \frac{1}{K_a}\frac{p'^{*n}}{{p'_a}^{n-1}}\left[1 + \frac{(n-1)K_a}{6G_a}\left(\frac{q^*}{p'^*}\right)^2\right] \tag{2.14}$$

$$\varepsilon^*_{qr} = \frac{1}{3G_a}\frac{p'^{*n}}{{p'_a}^{n-1}}\left(\frac{q^*}{p'^*}\right) \tag{2.15}$$

where $p'^* = (\gamma\sigma'_1 + 2\sigma'_3)/3$, $q^* = \gamma\sigma'_1 - \sigma'_3$, $\varepsilon^*_{vr} = \varepsilon_1/\gamma + 2\varepsilon_3$, $\varepsilon^*_q = \varepsilon_1/\gamma - \varepsilon_3$. Hornych et al. (1998) reported good results from cyclic load triaxial test with this model (Figure 2.34).

The inelastic contour model proposed by Brown and Pappins (1985) is also based on the shear and volumetric resilient strains. The model considers the representation of the resilient strains as contours in the (q, p') plane proposed by Pappin and Brown (1980) and shown in Figure 2.35. For a given effective stress path between points (q_1, p'_1) and (q_2, p'_2), resilient strains are obtained by Equations 2.16 and 2.17.

$$\varepsilon_{vr} = \left[\left(\frac{p'_2}{A}\right)^m\left(1 - B\left(\frac{q_2}{p'_2}\right)^n\right)\right] - \left[\left(\frac{p'_1}{A}\right)^m\left(1 - B\left(\frac{q_2}{p'_2}\right)^n\right)\right] \tag{2.16}$$

$$\varepsilon_{sr} = C\left[\frac{q_2}{p'_2 + D} - \frac{q_1}{p'_1 + D}\right]\left[\frac{\sqrt{{p'_r}^2 + q_r^2}}{p'_m}\right]^r \tag{2.17}$$

where A, B, C, D, m, n and r are model parameters, $q_r = q_{max} - q_{min}$, $p_r = p_{max} - p_{min}$ and $p_m = (p_{max} + p_{min})/2$. The shear resilient strain in this case depends only on the stress values whereas the volumetric resilient strain depends also of the length of the induced stress path in the (q, p') plane.

2.5.3 Advanced constitutive models for cyclic soil behavior

A general framework in order to model the different aspects of soil behavior under cyclic loading must include the importance of initial state, volume behavior, drainage conditions, stress-path dependency and possibly rotation of principal stress axes. Models accounting

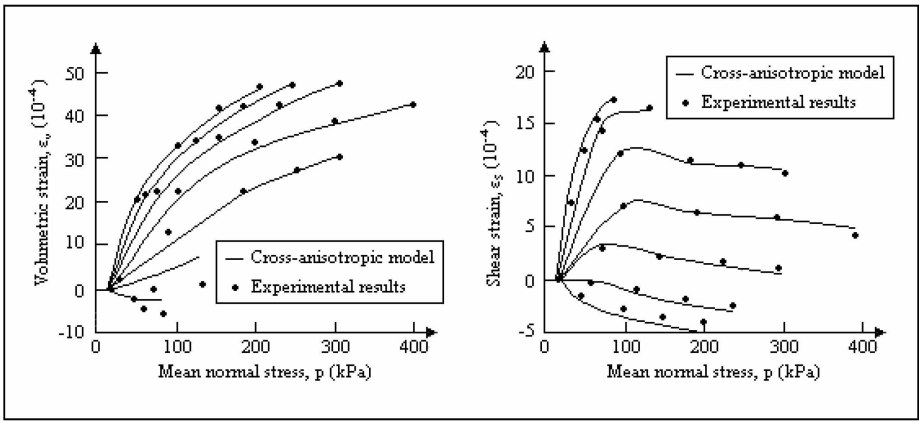

Figure 2.34: Example of cross-anisotropic Boyce model results (from Hornych et al., 1998).

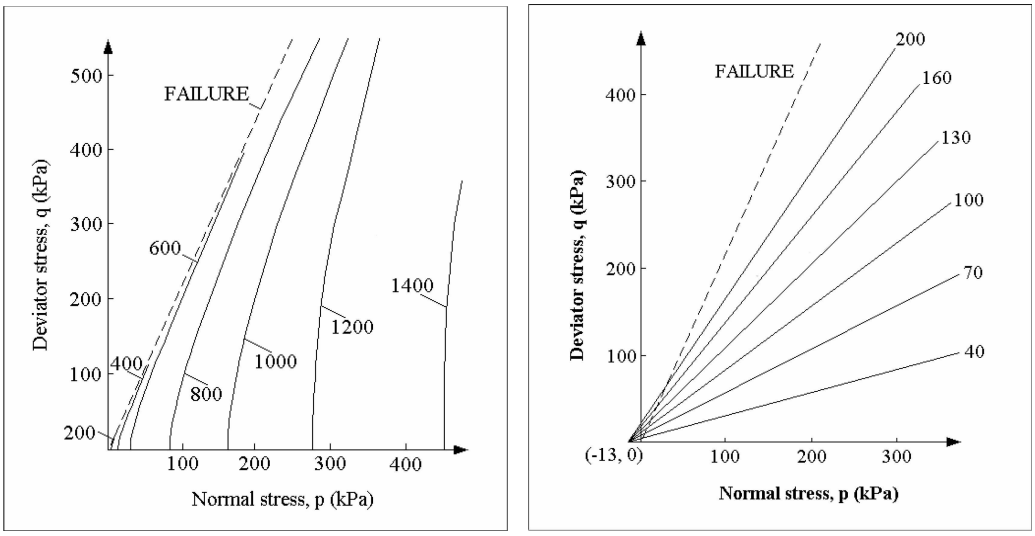

(a) (b)

Figure 2.35: Contour representation of resilient strains in the (q, p') space (from Pappin and Brown, 1980). a) Resilient volumetric strain; b) Resilient shear strain.

for these aspects are called advanced constitutive models (Kramer, 1996). The plasticity theory gives a suitable framework to model the different aspects of soil behavior previously discussed. In this case the following aspects are present:

- Partition of the total strain rate $\dot{\underline{\underline{\varepsilon}}}$ in independent elastic $\dot{\underline{\underline{\varepsilon}}}^e$ and plastic $\dot{\underline{\underline{\varepsilon}}}^p$ strain rates:

$$\dot{\underline{\underline{\varepsilon}}} = \dot{\underline{\underline{\varepsilon}}}^e + \dot{\underline{\underline{\varepsilon}}}^p \tag{2.18}$$

- The elastic domain, which corresponds to stress state which can be attained without producing plastic deformation. Hyperelastic and hypoelastic models can be used, the former corresponding to admissible thermodynamic potentials and the latter related to empirical formulations.

- The yield surface $f(\underline{\underline{\sigma}}, k)$, which depends on the stress state and the hardening variables k. It defines the threshold splitting the elastic and plastic domains. Three cases can be defined:

  - If $f(\underline{\underline{\sigma}}, k) < 0$, the stress state is inside the elastic domain;
  - if $f(\underline{\underline{\sigma}}, k) = 0$, the stress state is on the yield surface and plastic strain appears if the loading direction is outside the domain, i.e. $\frac{\partial f}{\partial \underline{\underline{\sigma}}} \dot{\underline{\underline{\sigma}}} > 0$; otherwise, $\frac{\partial f}{\partial \underline{\underline{\sigma}}} \dot{\underline{\underline{\sigma}}} \leq 0$ and no plastic strain is obtained;
  - $f(\underline{\underline{\sigma}}, k) > 0$ is impossible to attain.

- The hardening law, which defines how the yield surface evolves with hardening. Two categories exist: isotropic and kinematic (also called anisotropic). Isotropic hardening controls the size of the yield surface by a scalar parameter, while kinematical

laws permit to impose rotations, translations and distortions to the yield surface. These are schematically represented in Figure 2.36.

- The plastic flow rule, which gives the direction of plastic strain rates and links the increase in the plastic strains to the stress state and the hardening variables:

$$\dot{\underline{\underline{\varepsilon}}}^p = \dot{\lambda} \frac{\partial g}{\partial \underline{\underline{\sigma}}} \tag{2.19}$$

where $g(\underline{\underline{\sigma}}, k)$ is the plastic potential and $\dot{\lambda}$ is the plastic multiplier. When $g(\underline{\underline{\sigma}}, k) = f(\underline{\underline{\sigma}}, k)$ the plastic flow rule is considered associated, otherwise it is considered nonassociated.

Within this general framework, different models emerged in soil mechanics, among which the most probably known are Cam-Clay, modified Cam-Clay and subsequent adaptations. Among these, the nonlinear constitutive model developed at *Ecole Centrale Paris* called ECP model, also known as Hujeux model, is adapted for both monotonic and cyclic loading of soils (Aubry et al., 1982; Hujeux, 1985). It is based on the critical state concept and written in effective stress. It considers 3 plane-strain deviatoric hardening mechanisms and one isotropic, and hardening is controlled by the plastic strain evolution. Cyclic behavior uses kinematical hardening and a double memory approach. This model is chosen in Chapter 5 for describing the mechanical behavior of track geomaterials. More on the mathematical formulation of the ECP model is presented in Appendix A.

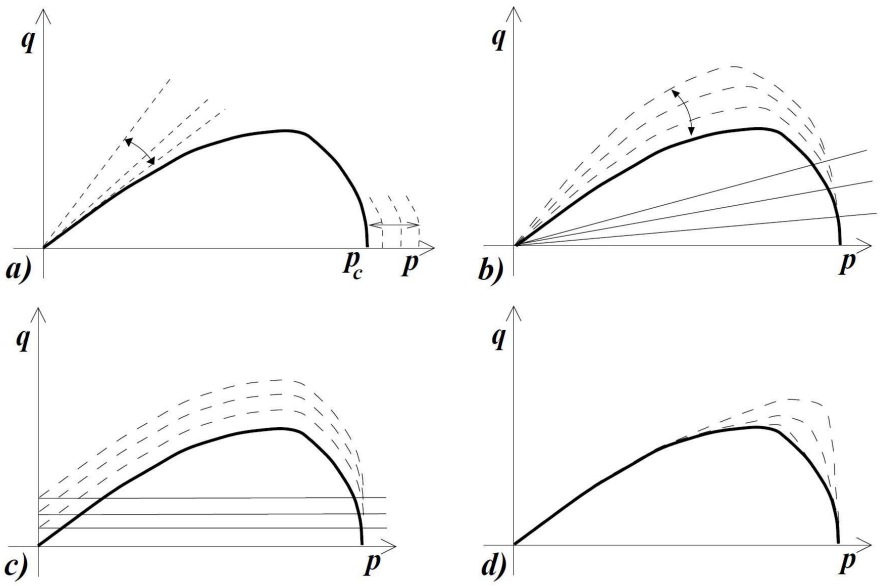

Figure 2.36: Effect of various types of hardening law on the yield surface (from Jeremic and Yang, 2002). a) Isotropic; b) Rotational; c) Translational; d) Distortional.

2.6 Modeling strategies of the railway track response to moving loads

Different modeling strategies exist in order to account for the mechanical response of the railway track. A very good review of available methods at the time is given by Knothe and Grassie (1993). According to the authors, two major differences exist among numerical models: considering or not the sleeper discrete support and finite or infinite domain size. The latter is closely connected to the solution technique, whereas analytical solutions and frequency domain solutions consider infinite domain and time domain solutions consider a finite domain. More recently, Beskou and Theodorakopoulos (2011) presented an exhaustive literature review of the modeling strategies for moving loads on road pavements. The following model classification is proposed, which can be analyzed in the view of railway track models:

- Modeling strategy: beam over Winkler foundation and related strategies, beam over homogeneous or layered half-spaces and mixed strategies, spatial discretization techniques (FEM, BEM);
- Material mechanical behavior: linear elasticity or viscoelasticity, equivalent linear analysis and shear stiffness degradation models, nonlinear models;
- Solution strategy: analytical or numerical in frequency or time domain;
- Load methodology: concentrated or distributed, constant or varying magnitude and speed.

In the following, an overview of the different strategies is presented. These are classified by their increasing aptitude in completely reproducing the geometrical and mechanical behavior of the railway track.

2.6.1 Beam resting on Winkler foundation and related models

Consider an infinite Euler-Bernoulli beam on a viscoelastic Winkler-type foundation being loaded by a constant force P moving at constant speed v from the infinite to infinite. The differential equation of the above problem may be written as follows:

$$EI\frac{\partial^4 \nu(x,t)}{\partial x^4} + \mu\frac{\partial^2 \nu(x,t)}{\partial t^2} + 2\mu\omega_b\frac{\partial \nu(x,t)}{\partial t} + k\nu(x,t) = P\delta(x-vt) \tag{2.20}$$

where x is the length coordinate with the origin at the left-hand end of the beam, t is the time coordinate, $\nu(x,t)$ is the beam deflection at a point x at the instant t, E is the Young's Modulus of the beam, I is the constant moment of inertia of the beam cross section, μ is constant mass per unit length of the beam, ω_b is the circular frequency of damping of the beam, P is the concentrated force of constant magnitude, v is the constant speed of the load motion, k is the coefficient of the Winkler foundation and $\delta(x-vt)$ is the Dirac function. Fryba (1972) proposed an analytical solution for the quasi-stationary state, i.e. the beam is at rest in relation to the moving coordinate system. Appendix B

Author	Equation
Vesic (1963)	$k = \frac{0.65E_s}{1-\nu_s^2}\sqrt{\frac{E_sB^4}{EI}}$
Biot (1937)	$k = \frac{0.95E_s}{1-\nu_s^2}\left(\frac{E_sB^4}{(1-\nu_s^2)EI}\right)^{0.108}$
Vlaslov and Leontiev (1956)	$k = \frac{E_s(1-\nu_s)}{(1+\nu_s)(1-2\nu_s)}\frac{\mu B}{2}$

Table 2.1: Different methods in estimating the foundation stiffness k (adapted from Heelis et al., 1999).

presents the mathematical development of the solution, which is based on the Fourier integral method and the Cauchy's residue theorem.

As discussed by Heelis et al. (1999), the difficulty in using this model is in relating the coefficient of the Winkler foundation k to measurable mechanical parameters and in defining which components are considered as being part of the "beam" and which are part of the foundation. For the first point, analytical relations given by different authors and showed in Table 2.1 can be used, where E_s and ν_s are the considered Young's Modulus and Poisson's ratio of the foundation and B is the effective width of the beam. For the second point, most authors consider the beam as being the rail only, and the foundation stiffness as the combination of stiffness from all other materials, from the rail pads to the subgrade (Fryba et al., 1993; Frohling, 1997; Krylov et al., 2000; Steenbergen, 2008; Dimitrovová and Varandas, 2009; Ang and Dai, 2013, among others). However, some authors also considered different configurations, as obtaining the flexural stiffness of the beam (EI) from a combination of different track layers (Hunt, 1994) or adding the mass of the sleepers and ballast to the total mass of the beam, but considering the flexural stiffness of the rail only (Fortin, 1983).

From the idea of the Winkler foundation, discrete models based on a combination of springs, dashpots and lumped masses are proposed in the literature (Nielsen, 1995; Lei and Noda, 2002; Sun, 2002; Zhai et al., 2004; Xie and Iwnicki, 2008; Zhai et al., 2009; Kouroussis et al., 2011a; Sadeghi and Fesharaki, 2013, among others). An example from the work of Xie and Iwnicki (2008) is given in Figure 2.37. These are usually more realistic than the Winkler foundation only, as they allow to reproduce different track vibration modes. Either discrete or continuous rail support can be considered, the first being solved in the time domain and the second in the frequency domain. As pointed out by Knothe and Grassie (1993), the support conditions lead to important differences for rail receptance on frequencies higher than 500 Hz, which is shown in Figure 2.38 for the rail receptance results obtained by Xie and Iwnicki (2008).

On all cases, model parameters can be obtained by calibrating the track receptance from *in situ* measurements. Although in some cases the obtained parameters are representative of certain materials due to the modeling strategy (rail pads, sleepers), global coefficients for ballast and other layers are usually obtained. Moreover, these can be only representative of the vertical vibration modes of the track and do not take into account the wave propagation in the medium caused by the moving train. In this sense, these models do not seem adapted for studying soil vibration and the mechanical behavior of

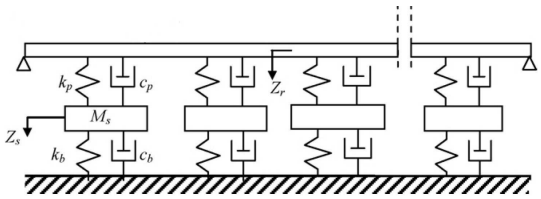

Figure 2.37: Track model proposed by Xie and Iwnicki (2008).

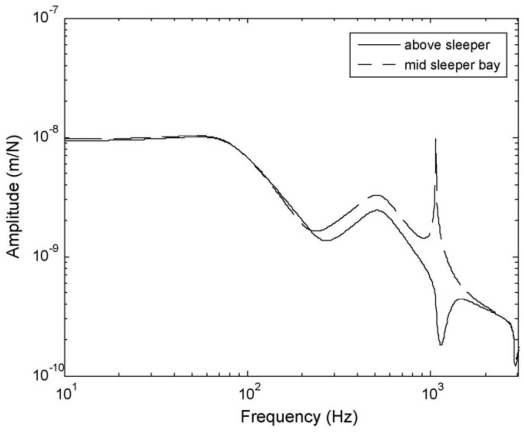

Figure 2.38: Amplitude of rail receptance above sleeper and at mid-sleeper bay (adapted from Xie and Iwnicki, 2008).

track components and the geomaterials composing the railway track. Nonetheless, some of these models consider shear development in the ballast layer by adding stiffness and damping elements between ballast masses (Zhai et al., 2004; Kouroussis et al., 2011a).

The Winkler foundation and related models are usually the most adapted strategy for train-track interaction analysis (Xie and Iwnicki, 2008; Steenbergen, 2008; Zhai et al., 2009; Kouroussis et al., 2011a; Sadeghi and Fesharaki, 2013), as they are sufficiently representative of the track mechanical response at the rail level for a large range of frequencies. This strategy is also applied on studies about stiffness variation (Fryba et al., 1993; Frohling, 1997; Oscarsson, 2002; Andersen and Nielsen, 2003) and transition zones (Dimitrovová and Varandas, 2009; Ang and Dai, 2013), although in this case other modeling techniques can be also applied.

2.6.2 Beam resting on half-space and related models

In this case the Winkler foundation is replaced by a half-space or layered half-space in order to better represent wave propagation effects in the soil. Different mathematical approaches for solving the beam over a half-space problem are proposed in the literature. They are all based on a Fourier transform in the frequency-wavenumber domain of the elastodynamics or Navier equation:

$$\mu \triangle \underline{u} + (\lambda + \mu)\, \underline{\mathrm{grad}}\, (\mathrm{div}\underline{u}) = \rho \frac{\partial^2 \underline{u}}{\partial^2 t^2} \tag{2.21}$$

where $\underline{u}$ is the displacement field, μ and λ are the Lamé coefficients, ρ is the mass density and t is the time. The Navier equation describes the mechanical response of a linear elastic medium under infinitesimal strain hypothesis. For infinite medium, Sommerfeld or radiation conditions are also necessary to describe the behavior of the medium at infinity.

A fundamental solution of the medium, also called Green's function of the medium, is obtained when a concentrated impulsive load is considered (Luco and Apsel, 1983; Apsel and Luco, 1983). A first approach to obtain the Green's functions of a layered half space is given by Thomson (1950) and Haskell (1953), based on transfer matrices accounting for the exact solution of the wave equation. A second approach of obtaining the Green's function called direct stiffness formulation was given by Kausel and Roesset (1981). In this case, stiffness matrices are proposed instead of transfer matrices, which relates the Fourier transform of stresses and displacements at the upper and lower surfaces of each layer. These present the advantage of being symmetric and allowing for faster numerical implementation (Lombaert, 2001) by means of the Boundary Element Method (BEM) formulation. The BEM for railway applications is discussed in the next section, as it is based on space discretization by shape functions. For all cases, the numerical evaluation of the Green's functions by the Fast Fourier Transform (FFT) or more adapted quadrature rules must be carried out.

In railway track applications, the beam can be either considered as characteristic or equivalent to the whole track system (rail, pads, sleepers and ballast) (Dieterman and Metrikine, 1997; Auersch, 2008) or only to the rail (Sheng et al., 1999). Rail pads are usually modeled as distributed stiffness, sleepers as distributed mass and ballast as both distributed stiffness and mass. An example of this type of model is given in Figure 2.39. Hysteretic damping is used for rail pads and ballast by considering complex stiffness properties (Sheng et al., 1999), as well as complex Lamé coefficients for the soil. Cosserat material model (Suiker et al., 1999) is also considered by some authors (Cai et al., 2008, 2010) under this approach, although it can also be used for other modeling techniques. Slab tracks are also considered by some authors (Steenbergen et al., 2007), and in this case the discrete support hypothesis is only related to rail pad distributed stiffness. Poroelastic half-space (Xu et al., 2007) and poroviscoelastic layered half-spaces (Lefeuve-Mesgouez and Mesgouez, 2010) for the soil can be considered based on Biot's theory.

Considering a half-space, smooth contact and uniform stress distribution along the cross section of the beam, Dieterman and Metrikine (1996) analytically obtained an "equivalent stiffness" coupling the beam and the half-space. This concept allows to obtain a reduction of the 3D half-space to a 1D wavenumber-dependent complex stiffness, although only the vertical reaction of the half-space can be studied. This approach was further developed by Vostroukhov and Metrikine (2003) for the case of a beam on periodically positioned supports of a spring-dashpot (rail pads) and mass (sleeper), which is in contact with the half-space. Takemiya and Bian (2005) also worked under a similar concept, but in this case a substructure technique was employed in order to obtain the "equivalent stiffness" from the Green's function of a layered half-space, which is used on a second model of the track. The main advantage of these models rely in the fact that discrete support can be considered, although Vostroukhov and Metrikine (2003) do not obtain relevant differences between the discrete support model and the homogenized one.

This technique has been mostly used in order to estimate soil vibration and track-soil

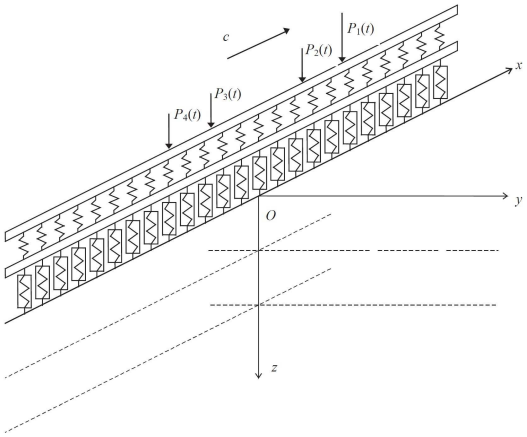

Figure 2.39: Model for track and ground proposed by Sheng et al. (1999).

receptance and dispersion characteristic curves (Sheng et al., 2003, 2004a,b; Steenbergen et al., 2007). Train-track interaction is considered in some works (Sheng et al., 2003; Cai et al., 2008), and rail irregularities can be studied (Sheng et al., 2004b; Cai et al., 2010). Time signals can be studied by applying the inverse Fourier transform (Xu et al., 2007; Cai et al., 2010). Noise and vibration problems in environing structures are the usual application of these models. However, this technique depends on the invariant homogeneous structure hypothesis, not being adapted for studying track stiffness variations or material nonlinearity for example.

2.6.3 Finite Elements, Boundary Elements and other spatial discretization techniques

The last class of railway models proposed in the literature relies on spatial discretization techniques such as the Finite Element Method (FEM) and the Boundary Element Method (BEM). FEM has been extensively used in the different engineering applications, as it allows for modeling complex geometries and can naturally consider different material constitutive models. Modeling unbounded domains by FEM requests a special attention on the boundary conditions in order to avoid wave reflection. In this sense, different strategies are proposed in the literature, such as absorbing boundaries, infinite elements, paraxial elements, PML, among others. A review of these methods is presented in Appendix C.

Another way of dealing with the unbounded domain is by the Boundary Element Method: the unbounded domain is modeled as a half-space or layered half-space with complex Lamé coefficients and using the associated fundamental solution or Green's function. On both FEM and BEM the numerical solution relies in an Galerkin approximation of an integral equation by shape functions. While the geometrical support for FEM is the whole considered domain, for BEM only the surface of the unbounded domain is discretized.

These models represent a very large class, mainly because of the model dimensions (2D, 2.5D and 3D), time or frequency domain and material properties. In the following the main implemented strategies are discussed in the light of the capabilities and drawbacks

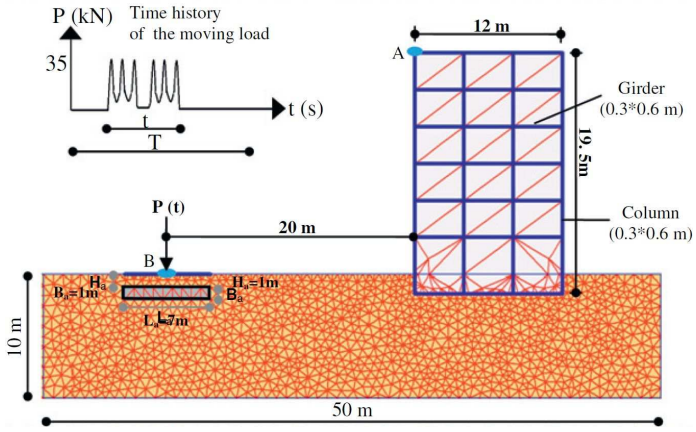

Figure 2.40: 2D FE model proposed by Çelebi and Göktepe (2012).

of each methodology. Some examples of models proposed in the literature are given in order to illustrate these strategies.

2.6.3.1 Finite Element models

Different domain sizes and symmetry planes are considered by the FEM models proposed in the literature. A first class of models are 2D models solved in the time domain and considering either the lateral (Figure 2.40) or the longitudinal plane (Figure 2.41) under plane-strain condition. In the first category, Çelebi and Göktepe (2012) uses a 2D model in order to study the impact of surface waves induced by railway traffic on nearby buildings. Suiker (2002) considers the same symmetry plane for studying the cumulated cyclic plastic strains of ballast and subballast materials. For this case the plane-strain condition cannot take into account the sleeper discrete support and authors need to consider a hypothetical load function obtained from an analytical expression or a simplified model.

In the second category, Yang et al. (2009) study the effect of track imperfections, acceleration, break and hanging sleepers on the stress path in different track materials. This model is further confronted with *in situ* measurements by Priest et al. (2010). Rhayma et al. (2011, 2013) also considers a 2D model in order to study the impact of uncertainty and variability of the railway geomaterials mechanical properties on different maintenance operations. Ribeiro (2012) proposed a 2D model with variable width in the third dimension. The width can thus be optimized in order to match the static vertical strain under the load regarding the obtained value from a 3D model. The model is then used for studying different types of transition zones. For the second category, the discrete support is taken into account but the plane-strain condition with variable thickness supposes a repeatable mono-rail structure in the dimension perpendicular to the moving load direction, as shown in Figure 2.41.

Although computationally intensive, different 3D models in the time domain are proposed in the literature (Kumaran et al., 2003; Hall, 2003; Ju and Lin, 2004; Powrie et al., 2007; Banimahd, 2008; Araújo, 2010; El Kacimi et al., 2012; Connolly et al., 2013; Thach et al., 2013; Shan et al., 2013; Cunha, 2013, among others). In this case, the full geometry characteristics of the railway track can be correctly modeled. However, in order

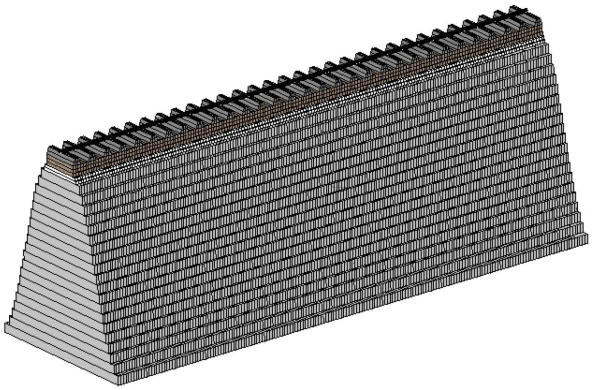

Figure 2.41: 3D representation of the 2D FE model accounting for variable width in the third direction proposed by Ribeiro (2012).

to give an idea of the involved computational cost, Ju and Li (2011) report a computer time requirement of 9 days using a personal computer for a 3D finite element mesh containing around 13 million degrees-of-freedom and 4000 time steps. An example of a 3D model proposed in the literature is given in Figure 2.42. This technique is particularly adapted for complex geometries such as pile-supported embankments (Thach et al., 2013) and transition sections between bridges and embankments (Shan et al., 2013). Authors have studied surface vibration characteristics for trans-Rayleigh train speeds (Ju and Lin, 2004; El Kacimi et al., 2012) and more generally ground vibrations (Hall, 2003; Connolly et al., 2013). Powrie et al. (2007) conducted static analysis in order to verify the effect of increasing stiffness with depth, variations of Poisson's ratio, soil anisotropy and initial stress state conditions on the mechanical response of the geomaterials.

Some authors consider simplified models for the railway vehicle (Kumaran et al., 2003; Ju and Lin, 2004; El Kacimi et al., 2012; Connolly et al., 2014, among others), which account only for the vertical vehicle dynamics. More recently, Ju and Li (2011) propose a 3D train model accounting for both vertical and lateral vehicle dynamics. This is used in order to study the derailment risk during earthquakes. Kouroussis et al. (2011c) propose a substructure technique by decoupling the train-track interaction model (beam over elastic

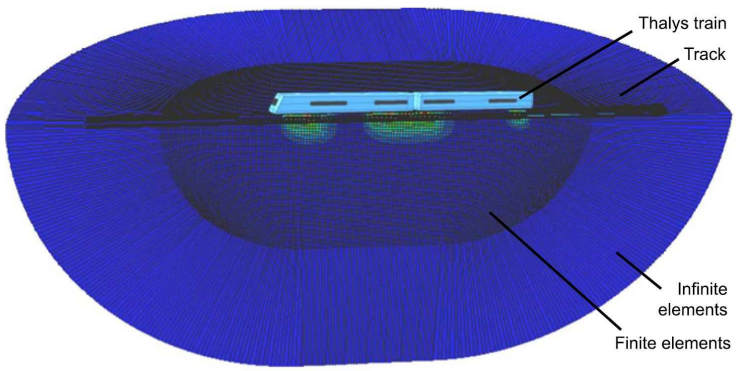

Figure 2.42: 3D FE model used by Connolly et al. (2013) for ground vibration studies.

foundation) and the soil (FEM). In this case the train can be finely modeled and the reaction of the foundation in the first model is applied as a load under sleeper in the second model. Maglev trains are also considered by Ju et al. (2012).

The main advantage of FEM models in the time domain is the possibility to account for constitutive laws adapted for geomaterials. On numerical modeling applied in the railway field, authors have used different classes of models besides linear elasticity and viscoelasticity. The first class is based on the resilient behavior of soils discussed in Section 2.5.2 and are nonlinear elastic models: $K - \theta$ model (Ferreira, 2013), Uzan model and Boyce model (Banimahd, 2008). The second class are elastic models based on soil dynamic results obtained on cyclic response and they consider mainly the evolution of the shear stiffness G with the increase of cyclic shear strain γ, e.g. equivalent linear (Costa et al., 2010), Iwan model (Cunha, 2013). The third class is based on mechanical models adapted for the monotonic response of soils and account for plastic deformations, e.g. linear elastic perfect plastic with a Mohr Coulomb yield criteria (Çelebi and Göktepe, 2012) and modified approaches (Cunha, 2013), Drucker-Praguer, Cam-Clay and modified Cam-Clay (Desai and Siriwardane, 1982), an adapted version of the model developed by Pender (1978) for ballast accounting for particle breakage (Indraratna and Nimbalkar, 2011). However, this class is not always adapted for cyclic loading, as kinematical hardening is not considered. A fourth class considers the cyclic plastic strains cumulated for a large number of cycles under an approach called "overstress formulation", similar to the viscoplastic model of Perzyna (1966) (Suiker, 2002). Finally, some authors (Paderno, 2010; Araújo, 2010) considered advanced cyclic constitutive models as presented in Section 2.5.3, which can correctly consider the soil behavior under monotonic and cyclic loading.

Considering the frequency-wavenumber domain, the 2.5D approach is the most adapted technique for finite elements. In this case, by considering the 3D railway structure invariant in the longitudinal direction, i.e. continuously supported, the equilibrium equation can be posed in the frequency-wavenumber domain and only the 2D lateral plane is discretized. The main advantage of this technique is the computational cost reduction compared to a 3D model while being able to consider a 3D structure. The main drawback is that the discrete support characteristic is lost, but differently from 2D models considering the same lateral plane under plane-strain conditions, the loading function is independent from the support characteristics. Using this approach, authors have considered poroelastic materials (Gao et al., 2012), vibration caused by underground moving trains (Yang and Hung, 2008), reduction of shear stiffness with shear strain by "equivalent linear" analysis (Costa et al., 2010), vibration caused by rail irregularities (Hung et al., 2013). Concerning boundary conditions, the infinite element approach adapted for 2.5D calculation is a very popular technique (Yang and Hung, 2001), although other strategies based on the hypothesis that the wave propagates in a semi-cylindrical form are developed in the literature (Gao et al., 2012). An example of 2.5D FE model is given in Figure 2.43.

It is important to highlight that a different technique is also proposed in the literature based on the Floquet transform of periodic structures under moving loads (Chebli et al., 2006). In this case, a 3D periodic cell can be studied and the discrete support characteristics maintained while solving a smaller and more computational cost efficient model. In this sense, Clouteau et al. (2013) present a literature review of different numerical modeling techniques applied in soil-structure interaction. Using the Fourier or the

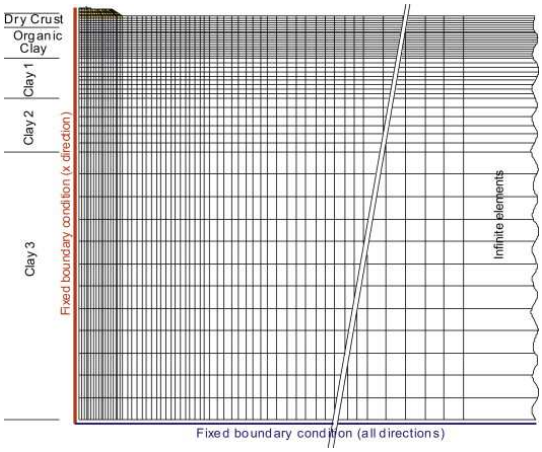

Figure 2.43: 2.5D FE model proposed by Costa et al. (2010).

Floquet transform with Finite Element models present the main disadvantage of loosing the possibility of directly considering nonlinear constitutive laws.

2.6.3.2 Beam resting on Boundary Elements

The Boundary Element Method presents the advantage of correctly accounting for wave propagation in the considered half-space or layered half-space, but it is not adapted for complex structures and nonlinearities (Kausel and Roesset, 1981). In this sense, it is often used for modeling the soil and another technique is used for the track structure. A first approach is to consider the rail, rail pads, sleepers and ballasted layers as a series of springs and dashpots or more complex arrangements, as discussed in Section 2.6.1. In this case, the frequency-wavenumber domain is preferred and the hypothesis of continuous support is made. The main difference with the case of beam resting on half-space discussed in Section 2.6.2 lies in the fact that in the present case, the railway track lateral plane can be correctly modeled, e.g. 2 parallel rails, sleeper finite length in the lateral direction. The model developed by Lombaert et al. (2006) is shown in Figure 2.44 and it is used in order to study the free field response due to the passage of high speed trains.

Models based on this approach are scarce in the literature as authors prefer to couple a Finite Element model for the track with a Boundary Element model for the soil. This approach is discussed in the next section.

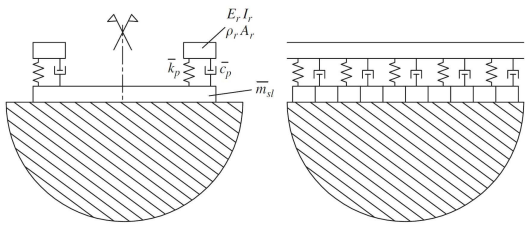

Figure 2.44: Track-soil model proposed by Lombaert et al. (2006).

2.6.3.3 Coupling Finite Elements and Boundary Elements

Coupling FE and BE strategies is a very promising field, as one can expect to benefit from the advantages of both methods: modeling complex geometries and nonlinear mechanical behavior for the track materials thanks to FEM and considering wave dissipation in the soil thanks to BEM.

In the railway track domain, two main class of models are proposed in the literature: 2.5D models or 3D models. Concerning 2.5D models, some are very similar to 2.5D FE models and the Boundary Elements are considered as simple absorbing elements, specially on railway over embankment applications (Costa et al., 2012a,b; Galvín et al., 2010a). When studying surface vibration caused by underground trains, the 2.5D FE-BE methodology seems very adapted as wave propagation from the tunnel to the surface can be correctly captured (François et al., 2010; Galvín et al., 2010a). However, these models are developed in the frequency-wavenumber domain and the capability of considering nonlinear mechanical behavior in the FE structure is lost. The Floquet transform is also developed for FE-BE models and in this case the Green-Floquet fundamental solution is computed in the periodic cell (Clouteau et al., 2005; Chebli et al., 2008). An example of this approach is given in Figure 2.45.

In 3D models, this drawback no longer exists as time domain numerical schemes can be used. However, the FEM-BEM coupling in this case is more laborious and the stability of the numerical scheme is not guaranteed (Clouteau et al., 2013). The model developed by Galvín and Domínguez (2009) and shown in Figure 2.46 considers an iterative algorithm proposed by Estorff and Hagen (2005) for coupling the FE and BE domains and the model is used for studying vibration induced in the soil. Transition zones are considered in a secondary paper from the authors (Galvín et al., 2010b). Nonlinear mechanical behavior is not considered and as it seems, this aspect was not yet addressed by the railway researchers using this approach.

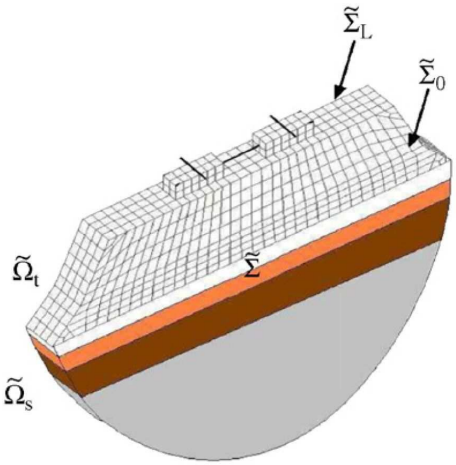

Figure 2.45: 3D FE-BE model accounting for track periodicity using the Floquet transform (from Chebli et al., 2008).

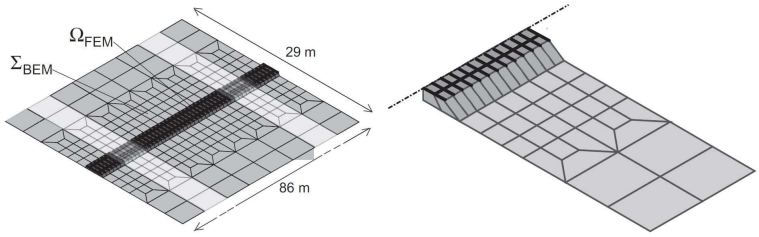

Figure 2.46: 3D FE-BE model in the time domain proposed by Galvín and Domínguez (2009). The right-hand side figure presents a closer zoom on a track section.

2.6.4 Discrete Element Models

Particularly to the ballast layer, the Discrete Element Method (DEM) has being successfully applied by many authors (Lim and McDowell, 2005; Saussine et al., 2006; Zhou et al., 2013, among others) in order to better capture the granular and discrete characteristics of the ballast material in the railway track. The main advantage of this method is that the micromechanics of the ballast layer is well represented, this approach being particularly suitable for studying granular thin layers and the localized rigid structures appearing during loading (Saussine et al., 2006). Two main algorithms are proposed in the literature:

1. The Distinct Element Method, first developed by Cundall and Strack (1979), which is characterized by a regular treatment of the contact forces and an explicit time integration scheme,

2. The Non Smooth Contact Dynamics (NSCD), developed by Jean and Moreau (1992), which considers unilateral contact conditions and permits an implicit time integration scheme.

In both cases contact characteristics between grains must be assessed, but no constitutive law is necessary. Figure 2.47 gives an overview of the actual track model developed at SNCF by using a DEM approach. Rail and rail pads are usually neglected as for instance only rigid bodies are considered. When studying moving load applications, the load is directly applied at the sleeper and in this sense an assumption of load repartition over the sleepers is necessary.

Simulating maintenance procedure such as tamping (Azéma, 2007; Saussine et al., 2008; Perales et al., 2011; Zhou et al., 2013; Voivret et al., 2013) and ballast flight phenomenon (Saussine et al., 2011) are possible within this framework. Grain cracking (Donzé et al., 2009) and ballast layer reinforcement by geogrid interaction (Kwan, 2006; Ferellec and McDowell, 2012; Chen et al., 2013) can also be suitably studied by discrete element models. However, applying these methods in real track applications has a high computational cost. Domain decomposition using parallel computing strategies can be implemented (Hoang et al., 2012), but nowadays a distance corresponding only of a few sleepers can be studied. Moreover, these models usually considers an infinitely rigid subgrade, which is not representative of real track applications. Coupling Discrete Element Models with Finite Elements (Ricci et al., 2005; Nitka et al., 2011, among others) in order to better capture the subgrade mechanical behavior is a promising field still in progress.

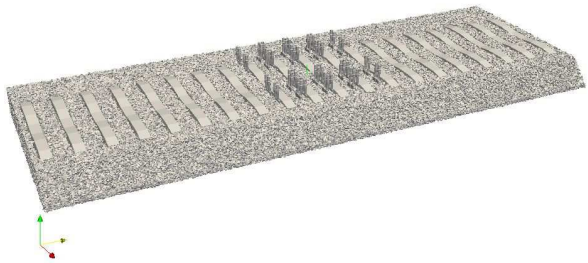

Figure 2.47: Track model obtained by DEM (obtained from Voivret et al., 2013).

2.7 Background on railway track models accounting for track properties variability

In this section, a brief overview of different railway track models accounting for track properties variability is given. The implemented methodologies and main results obtained by different authors are also discussed.

Frohling (1997) considers the railway track degradation with vehicle loading and non-linear spatially varying track stiffness. The author proposes a dynamic and static track deterioration prediction models. These are based on an experimental work focused on the dynamic behavior of the railway vehicle and the corresponding response of the track. In these models, settlement equations are based on measurable parameters of the different track layers and wheel loading. Particularly for the dynamic prediction model, it also considers vehicle/track dynamic interaction. The obtained results show that the spatial variations of the track stiffness contributes significantly to track deterioration, in terms of differential settlement and increase in vehicle's dynamic loading.

In this sense, Steenbergen (2013) discusses the physical mechanisms leading to track degradation and mainly the role of mechanical properties variability. The dynamic stiffness concept introduced by Dieterman and Metrikine (1996) is used by the later author in order to discuss the influence of damping on track degradation. According to the author, viscoelastic drag (from material damping) and dynamic drag (from radiation damping) are responsible for track degradation. Some conceptual track designs taking into account these concepts for track transitions are given and the use of geogrids as increasing the waveguide characteristic of the track is discussed.

Oscarsson (2002) considers the influence of track properties variability on the wheel-rail contact force, the wheel vertical acceleration and the sleeper vertical displacement. Two techniques are used: the Latin Hypercube Sampling with correlation control and the perturbation method, the former being a nonintrusive technique and the later an intrusive one. The variability in a particular set of input parameters of the considered model (sleepers spacing, rail pad stiffness, ballast stiffness and the dynamic ballast-subgrade mass) is obtained through *in situ* measurements and laboratory tests. Small coefficients

of variation are found for ballast stiffness, rail pad stiffness and sleeper spacing. However, the dynamic ballast-subgrade mass coefficient of variation is high. The author argues that the sleeper support stiffness probably varies significantly from one sleeper to the other while the fundamental track resonance is basically constant along the track.

From these results, Oscarsson (2002) argues that although the perturbation technique has the advantage of being simple and fast when compared with other stochastic methods, it has the important disadvantage of being restricted to cases where the random properties exhibit small scatter around mean values. In this sense, Kleiber and Hien (1992) state that perturbation techniques can be used for a maximum coefficient of variation of 10%, which is small compared to the scatter encountered on mechanical properties of geotechnical materials (Phoon and Kulhawy, 1999a,b). Therefore, Monte Carlo methods seem to be better suited for numerical models accounting for the encountered variations of the railway track properties. By using Latin Hypercube Sampling with correlation control, Oscarsson (2002) shows that the contact force is hardly affected by input variability, as its quasi-static part remains almost constant, but wheel vertical acceleration and sleeper vertical displacement are strongly affected.

More recently, Rhayma et al. (2011) uses the collocation method (Bressolette et al., 2010) to study the impact of uncertainty on railway track mechanical properties. Linear elastic mechanical behavior is considered and Young's Modulus are calibrated from *in situ* data obtained from the project Innotrack (Ekberg and Paulsson, 2010). The authors show that the encountered Young's Modulus variability is more influential than track layers's width variability regarding different indicators, such as rail and sleeper vertical maximum deflection. Current maintenance operations are studied in order to verify their effectiveness in terms of reducing the scatter on model's response. However, one drawback from the chose stochastic method, the influence of spatial variations along the track are not considered.

An additional source of uncertainty is the variability on the moving load amplitude applied by the vehicle on the track. In his classical book, Fryba (1972) discusses the randomly effect of the moving load as caused by track irregularities, train speed or traffic flow, random motions of vehicles, effects of vehicle engines, among others. The perturbation method is used to account for an infinite beam on random elastic foundation, i.e. Winkler foundation, subjected to a random moving load.

In a later work from the same author (Fryba et al., 1993), spatial variations of the elastic and viscous properties of the foundation are considered. The perturbation method is used in order to evaluate the variance of the deflection and bending moment of a beam model. Two types of covariance functions are used: cosine and exponential. Correlation length influence is studied at small speed and the variance of the deflection and bending moments seems to stabilize at 5 m and 3 m, respectively. At higher speeds (near or greater than the critical speed of the foundation), the variance of the rail deflection and bending moment reduces and then increases, stabilizing at higher values of the correlation length. The final values are higher for higher speed than at small speeds, the coefficient of variation of the beam deflection is greater than the beam bending moment. Moreover, random beam stiffness variations result on greater variance of the output than random beam damping variations.

More generally, Elkateb et al. (2003) discuss that soil heterogeneity may be classi-

fied as lithological heterogeneity and inherent spatial soil variability. According to the later authors, the main elements to be identified in order to be able to account for spatial variability are: classical statistical characteristics, spatial correlation structure, the limit of spatial continuity and the volume-variance relationships. One important remark concerning the first point is that high variability is usually associated with soil's strength parameters. There is no clear evidence for choosing *a priori* a particular probabilistic density function (pdf) or a correlation structure for soil's physical properties (Popescu et al., 2005a; Griffiths et al., 2009, among others). However, physical properties are nonnegative quantities and this condition must be satisfied by the considered pdf. In this sense, lognormal, beta and gamma distributions are usually chosen for fitting *in situ* data.

The results summarized above show the increasing importance of performing probabilistic analysis in the railway domain. There is a common understanding that variations in the track support can lead to track geometry degradation, even though the mechanical mechanisms are not yet completely understood. Nonintrusive techniques based on sampling strategies seem to be more adapted for considering the expected variation range and spatial variations along the track. Moreover, variations of material's stiffness and load speed seem to be important parameters to be taken into account. Concerning the probabilistic parameters, no particular probability density function or correlation structure is expected for railway materials.

2.8 Concluding remarks

The present chapter gives an overview of the different aspects regarding railway tracks and materials' mechanical behavior. The large scope of this review reflects the complexity of the topic and the fact that different scientific domains have to be accounted for a complete description of the system.

From the presented *in situ* results obtained from commonly used diagnostic tools, the track mechanical properties present important variations along the track. Track geometry variations are acknowledged as being the most important factor on derailment risk and safety, hence maintenance standards are based on this measure. Track stiffness variations, however, are seldom studied, although it is physically related to the track geometry as representing the support on which the rail is posed. From track transition zones, it seems clear that track stiffness variations play an important role on the evolution of track geometry. Hence, the first step toward better understanding the influence of track stiffness variations on the track geometry is to better understand the variations of the track stiffness itself, and possibly which track layers and materials contribute the most to these variations.

It arises from the different presented laboratory test results that nonlinear mechanical models are better suited for correctly reproducing the different aspects of the behavior of soils. Separately considering a resilient and permanent behavior instead of advanced cyclic constitutive models has the main advantage of considerably simplifying the model. For example, the Boyce model for anisotropic materials requires only 4 parameters. However, no evolution of the material state is considered by such models. Therefore, this hypothesis only holds after several loading cycles, when materials experiment low permanent

deformation. It is clear that the main drawback of such models is in assuming the correct reproduction of the material state from the track to the laboratory test, in order to obtain representative parameters that can be further transposed in a numerical model.

In this sense, when modeling the first loading cycles, it is important to account for the role of initial state and volume variations on the mechanical response. This last cannot be accounted for by resilient models. Using cyclic advanced constitutive models such as the ECP model requires indeed calibrating several parameters, but once this task is done the mechanical model is representative of the material behavior under different conditions. However, it is important to highlight that the ECP model is not expected to be used for large number of cycles. One of the reasons is the considered nonlinear elastic domain, which cannot be written in terms of a thermodynamical potential. Therefore, energy is dissipated within elastic cycles. More generally, according to Gidel (2001), different authors pointed out that advanced constitutive models based on elastoplasticity theory and kinematical hardening lead to higher values of permanent strains for a large number of cycles.

The modeling strategies presented in the previous section give an overview of the possibilities and constraints of the different techniques. The choice of the most adapted modeling strategy depends on the aspect and physical phenomena of interest. When only the rail vertical response is of interest, a beam resting on Winkler foundation and related models give consistent results for a large range of frequencies. Considering discrete support can lead to even better results at high frequency content and the pin-pin frequency can be correctly modeled. Material nonlinearity can be captured depending on the solution technique, but parameters are very often only approximations from the real materials in order to reproduce the track receptance measured at the rail.

When soil vibration and mitigation techniques are of interest, considering the soil as a half-space seems to be the most cost efficient technique. An increasing interest in the Boundary Element Method is observed in the literature, as it is more versatile than analytical or semi-analytical methods. However, in this case the soil constitutive law is restrained to viscoelasticity.

When specific nonlinear material behavior is of interest, the Finite Element Method is the most adapted numerical tool to model the railway track. As in different domains, FEM has imposed itself as a versatile and multi-purpose technique and recent models account for train-track interaction and soil-pile interaction, among other applications, while absorbing boundary conditions are properly implemented in order to avoid spurious wave reflection on boundaries. However, interestingly most part of FEM proposed models do not take advantage of the FEM capabilities and consider only linear elastic material behavior.

From the above discussed points, a representative description of the mechanical response of the track have to account for the effect of speed and dynamic loads, nonlinear behavior of the materials and possible variations of track properties encountered along the track. FEM appears as the most adapted strategy for the numerical tool. The developed model in the thesis accounts for all these aspects and it is presented in the following chapter.

Chapter 3

Numerical model and elastic response of the track

Contents

3.1 Introduction

In the past years, physical and numerical railway track models have allowed a better understanding of the railway infrastructure and the different physical mechanisms acting during train loading. Choosing the most adapted model depends on the considered hypotheses and physical parameters as well as the objectives and output quantities of interest. In this chapter, the development of the model proposed in this work respects the different constrains imposed by the three aspects developed in the thesis:

- Wave propagation analysis: in the case of linear elastic material properties, correctly describing the wave propagation up to a certain wavelength in the model imposes a maximum element size given the considered interpolation function, requires applying adapted boundary conditions and considering a numerical integration scheme with an adapted time step. In the case of moving loads, it will be shown that the initialization procedure can also play an important role in avoiding spurious waves in the results.

- Stochastic analysis: in this case, the main constrain is the computational time, as a large number of simulations are required. In this work, this constrain is considered by optimizing the model size and dimensions. Moreover, the chosen representation of mechanical properties variations in the model imposes also a maximum element size.

- Nonlinear analysis: in this case, considering higher order for FE basis function is necessary as well as correctly capturing the sleeper kinematics. These aspects will be further addressed in Chapter 5.

The numerical model of the railway track used in this work is presented in this chapter. Some key aspects of the track's mechanical response to moving loads are also discussed under linear elasticity mechanical behavior.

The chapter is composed of three main sections. In the first section, the mathematical formulation of the present railway track mechanical problem is rapidly revisited in the general framework of a soil-structure interaction problem. Then, in the second section the optimized characteristics of the proposed numerical model are developed, namely: model dimension, domain size and finite element discretization, boundary conditions and loading procedure.

The third section presents the main characteristics of stress and strain response of the railway track subjected to one bogie loading cycle. The role of speed and subgrade stiffness is assessed from a series of numerical simulations. This analysis provides a comparative basis for further discussion in Chapter 5, when mechanical nonlinearity is considered. Concluding remarks are given in the end of the chapter.

3.2 Formulation of the dynamic mechanical problem

The schematic representation of a single line on a conventional railway track in France, considered in this work, is presented in Figure 3.1. The structure is composed from top to bottom of two rails, which are connected to the sleepers by a fastening system presenting an elastic rail pad component. Around the sleepers, unconfined ballast is present, which helps maintaining the sleeper in the lateral and longitudinal positions. Under the sleepers, fresh ballast, fouled ballast and the interlayer material forms the three observed track layers, which are followed by the subgrade soil or natural ground, above which the track is constructed. Standard track gauge of 1.435 m is considered. The geometrical characteristics are typical from conventional lines in France. The layer thickness Δh of the different track materials are also showed in Figure 3.1.

The loading conditions are modeled by punctual forces over the rails representing the load carried by the two wheelsets of a train bogie, F_1 and F_2, which move forward in the y direction at the same speed $v(y)$.

This problem can be viewed in the framework of soil-structure interaction, under which the structure domain Ω_b composed of the rail, rail pads and the sleepers is embedded in a multilayer semi-infinite soil domain Ω_s. The problem is complex due to the geometrical aspects imposed by the soil-structure interface Σ_{bs} and the fact that both the structure and the soil are infinite in the longitudinal direction. Artificial boundaries Γ_b and Γ_s are then introduced in both the structure and the soil domains in order to tackle this problem in a finite element formulation. These boundaries can be further partitioned into imposed

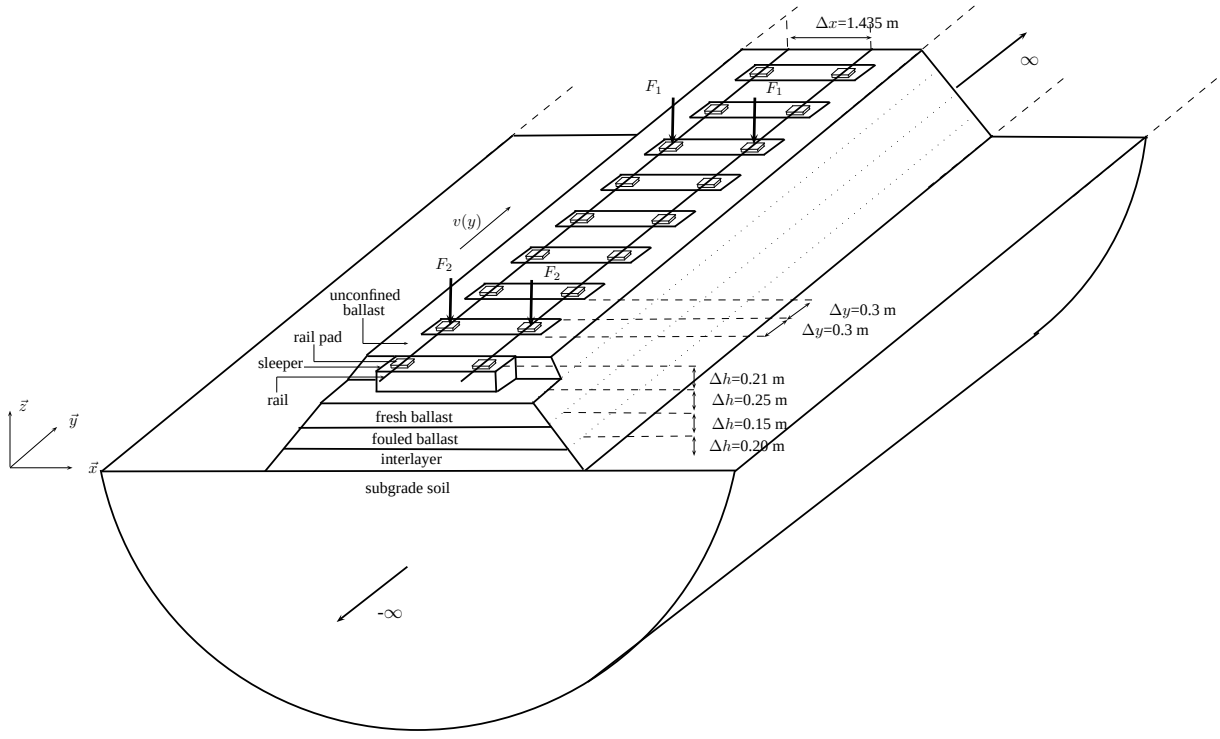

Figure 3.1: Complete model of the the railway track.

displacement or Dirichlet conditions $\Gamma_{._u}$ and imposed tractions or Neumann conditions $\Gamma_{._\sigma}$, where the subscript . denotes either b or s. Moreover, the following conditions hold: $\Gamma_{._u} \cup \Gamma_{._\sigma} = \Gamma_.$ and $\Gamma_{._u} \cap \Gamma_{._\sigma} = \emptyset$. Finally, the considered system presents a full symmetry boundary Σ_{sym} at the (y, z) plane defined at the center of the track.

The dynamic mechanical problem consists thus in obtaining the stress field $\underline{\underline{\sigma}}_s(\underline{u})$ and the displacement field $\underline{u}_s(\underline{x}, t)$ in both domains. In the soil domain, the total stress field $\underline{\underline{\sigma}}_s$ is usually decomposed in an effective stress tensor $\underline{\underline{\sigma'_s}}$ and the pore pressure u_w according to Terzaghi's principle:

$$\underline{\underline{\sigma}}_s = \underline{\underline{\sigma}}'_s - u_w \underline{\underline{I}} \tag{3.1}$$

where $\underline{\underline{I}}$ is the identity tensor. In this work, the pore pressure is neglected. Therefore, $\underline{\underline{\sigma}}_s = \underline{\underline{\sigma}}'_s$. Under small strain hypothesis, the momentum conservation in the soil domain can be written as:

$$\underline{\text{div}}\ \underline{\underline{\sigma}}'_s + \rho \underline{g} = \rho \underline{\ddot{u}}_s, \ \forall \underline{x} \in \Omega_s \tag{3.2}$$

where $\underline{\underline{\sigma}}'_s$ is the effective stress tensor, $\underline{g}$ is the gravity, $\underline{\ddot{u}}_s$ is the absolute acceleration vector of the soil and ρ is the specific mass obtained as:

$$\rho = (1 - n)\rho_s \tag{3.3}$$

where n is the soil porosity and ρ_s is the volumetric weight of soil grains. Evidently, the equilibrium equation must be satisfied at each track layer.

In the structure domain, the momentum conservation (Equation 3.4) takes the same formulation as in the soil, the difference being that in this case $\underline{\underline{\sigma}}_b$ is the stress tensor in the structure, ρ_b is the specific mass of the structure elements and $\underline{\ddot{u}}_b$ is the absolute acceleration vector of the structure.

$$\underline{\text{div}}\ \underline{\underline{\sigma}}_b + \rho_b \underline{g} = \rho \underline{\ddot{u}}_b, \ \forall \underline{x} \in \Omega_b \tag{3.4}$$

Specifically to the rail, the Bernoulli beam kinematics is considered. In this case, under linear elastic hypothesis Equation 3.4 can be reduced to:

$$\sigma_{rr} = E\varepsilon_{rr} \tag{3.5}$$
$$\sigma_{rs} = 2G\varepsilon_{rs} \tag{3.6}$$
$$\sigma_{rt} = 2G\varepsilon_{rt} \tag{3.7}$$

where r,s and t are the principal local system of axes, E is the Young's Modulus and G the shear stiffness. Please refer to Sáez (2009) for the full mathematical development of the beam formulation used in this work.

The weak form of the the momentum conservation (Equations 3.1 and 3.4) can be obtained using the Variational formulation. A set of kinematically acceptable displacement fields $\mathbb{V}_b$ for the Ω_b domain and $\mathbb{V}_s$ for the Ω_s are defined as:

$$\mathbb{V}_b = \{\underline{w}_b \mid \underline{w}_b \text{ regular in } \Omega_b,\ \underline{w}_b(\underline{x}) = 0 \text{ on } \Gamma_{bu}\}$$
$$\mathbb{V}_s = \{\underline{w}_s \mid \underline{w}_s \text{ regular in } \Omega_s,\ \underline{w}_s(\underline{x}) = 0 \text{ on } \Gamma_{su}\}$$

Using the Stoke's formula the following expressions are obtained:

$$\int_{\Omega_b} \underline{\underline{\sigma}}_b : \underline{\underline{\varepsilon}}_b(\underline{w}_b)dV + \int_{\Omega_b} \rho_b \underline{\ddot{u}}_b \cdot \underline{w}_b dV = \int_{\Omega_b} \rho_b \underline{g} \cdot \underline{w}_b dV + \int_{\Sigma_{bs}} \underline{t}_b \cdot \underline{w}_b dS + \int_{\Gamma_{b_\sigma}} \underline{t}_b \cdot \underline{w}_b dS + \int_{\Gamma_{b_u}} \underline{t}_b \cdot \underline{w}_b dS,\ \forall \underline{x} \in \Omega_b \tag{3.8}$$

$$\int_{\Omega_s} \underline{\underline{\sigma}}'_s : \underline{\underline{\varepsilon}}_s(\underline{w}_s)dV + \int_{\Omega_s} \rho_s \underline{\ddot{u}}_s \cdot \underline{w}_s dV = \int_{\Omega_s} \rho \underline{g} \cdot \underline{w}_s dV + \int_{\Sigma_{bs}} \underline{t}_s \cdot \underline{w}_s dS + \int_{\Gamma_{s_\sigma}} \underline{t}_s \cdot \underline{w}_s dS + \int_{\Gamma_{s_u}} \underline{t}_s \cdot \underline{w}_s dS,\ \forall \underline{x} \in \Omega_s \tag{3.9}$$

where $\underline{\underline{\varepsilon}}_b$ and $\underline{\underline{\varepsilon}}_s$ are the strain tensors associated with the virtual displacement fields $\underline{w}_b$ and $\underline{w}_s$ at the structure and soil domains, respectively, and the stress vectors $\underline{t}_b$ and $\underline{t}_s$ are obtained as follows:

$$\underline{t}_b(\underline{x}, t) = \underline{\underline{\sigma}}_b \cdot \underline{n}_b \tag{3.10}$$
$$\underline{t}_s(\underline{x}, t) = \underline{\underline{\sigma}}'_s \cdot \underline{n}_s \tag{3.11}$$

where $\underline{n}_b$ and $\underline{n}_s$ are the exterior normal vector of Ω_b and Ω_s with respect to the interface Σ_{bs}, respectively. Thus, the continuity of the stress vector at the interface Σ_{bs} is assured by introducing the coupling between the structure and soil given by Equation 3.12.

$$\int_{\Gamma_{bs}} \underline{t}_b \cdot \underline{w}_b dS + \int_{\Gamma_{bs}} \underline{t}_s \cdot \underline{w}_s dS = \int_{\Gamma_{bs}} \underline{t}_{bs} \cdot [\underline{w}] dS \tag{3.12}$$

where [w] represents the jump in the displacement field $[\underline{w}] = \underline{w}_b - \underline{w}_s$ at the interface Σ_{bs}. If $[\underline{w}] = 0$, then the displacement fields $\underline{w}_b$ and $\underline{w}_s$ are equivalents at the interface Σ_{bs}.

3.2.1 Boundary conditions

Concerning the model boundary conditions, the main focus is in avoiding wave reflexion caused by the dynamic moving load. This is a large research topic and different strategies exist (boundary approximations, viscous elements, among others) in order to proper decompose infinite media into a finite domain. A review of different methods is presented in Appendix C.

The imposed boundary conditions can be defined as follows:

- In the soil domain, normal displacements on the bottom boundaries are set to zero:

$$u_n = 0, \ \forall \underline{x} \in \Gamma_{s_u} \tag{3.13}$$

  In the soil lateral boundaries, absorbing boundaries conditions are applied, which will be further described in Section 3.3.4.

  The free surface condition at the unconfined ballast elements is given as:

$$\underline{\underline{\sigma'_s}} \cdot \underline{n} = 0, \ \forall \underline{x} \in \Gamma_{s_\sigma} \tag{3.14}$$

- In the structure domain, normal displacements to lateral boundaries are also set to zero:

$$u_n = 0, \ \forall \underline{x} \in \Gamma_b \tag{3.15}$$

  Specifically to the rail, no particularly boundary condition is imposed (free displacement condition).

- At the soil-structure interface Σ_{bs}, displacement continuity is imposed:

$$\underline{u}_s = \underline{u}_b, \ \forall \underline{x} \in \Sigma_{bs} \tag{3.16}$$

  This boundary condition is modified for the nonlinear model by considering interface elements.

- At the symmetry boundary Σ_{sym}, normal displacements are set to zero:

$$u_n = 0, \ \forall \underline{x} \in \Sigma_{sym} \tag{3.17}$$

- Wheelset load application is conducted by prescribing a stress at the rail:

$$\underline{\underline{\sigma_b}} \cdot \underline{n} = \underline{F}, \ \forall \underline{x} \in \Gamma_{b_\sigma} \tag{3.18}$$

  The moving load function is further described in Section 3.3.3.

3.2.2 Domain discretization

The space discretization is conducted by Finite Element approach, and linear shape functions are considered both for the soil and the structure domains. The obtained 3D finite element model is presented in Figure 3.2. The dashed line represents the symmetry plane existing in the rail track structure.

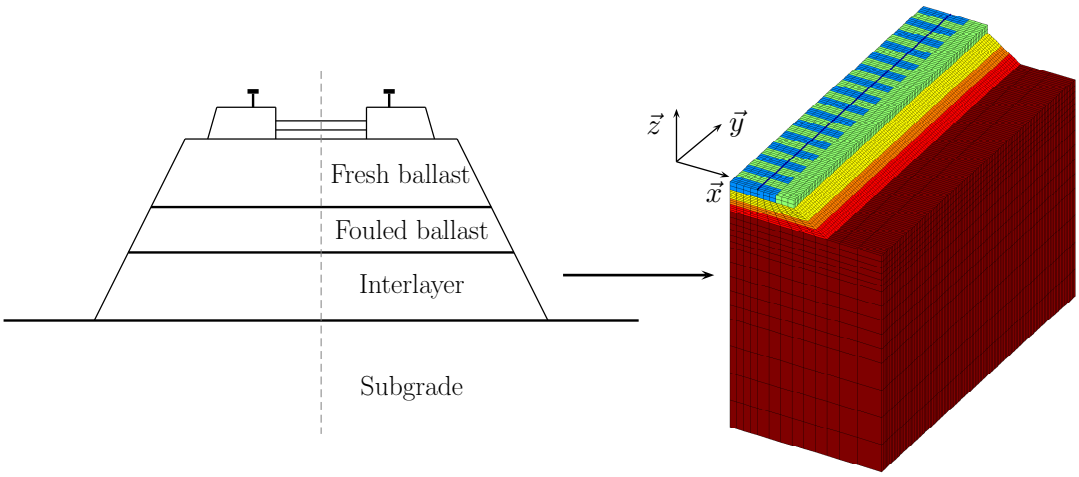

Figure 3.2: Schematic representation of track layers and the associated 3D model. Left-hand side: cut at the (x, z) plane. Right-hand side: associated 3D model.

3.2.3 Material properties

For the linear model, isotropic linear elastic mechanical properties are considered, which are characterized by the Young's Modulus E and the Poisson's ratio ν. Table 3.1 presents these physical properties values and the mass density ρ of the different components. Particularly for the rail, the Euler-Bernoulli beam hypothesis requires the definition of the inertial moment I and the cross-sectional area A. These are taken from the UIC60 rail standard, I=3.05·10^{-5} m^4 and A=0.007686 m^2. Particularly to the rail pad, the vertical stiffness is usually given rather than the Young's Modulus and Poisson's ratio. In this work stiff rail pads are considered, k_{RP}=120 kN/mm, which are characteristic of conventional lines in France. By considering the Poisson's ratio ν_{RP} equal to 0.25, it is possible to obtain an equivalent Young's Modulus by the following relation:

$$E_{RP} = k_{RP}\frac{\Delta h_{RP}}{A_{RP}}\frac{(1+\nu_{RP})(1-2\nu_{RP})}{(1-\nu_{RP})} \tag{3.19}$$

where Δh_{RP}=0.009 m is the thickness of the rail pad element and A_{RP} ≈0.0225 m^2 is the considered contact surface between the rail and the rail pad.

The Young's Modulus of the granular materials are estimated from the methodology further discussed in Chapter 4.

In the following sections, soft and stiff soils are considered in order to verify the role of the subgrade's mechanical characteristics on the numerical aspects of the model. In this case, stiff soil corresponds to E=100 MPa and soft soil to E=20 MPa.

3.2.4 Time integration and numerical damping

The time integration scheme used is implicit Newmark with the following parameters $\gamma = 0.625$ and $\beta = 0.375$ (Katona and Zienkiewicz, 1985). These are unconditionally stable as $2\beta \geq \gamma \geq 0.5$ and induce numerical damping. The choice of inducing numerical damping in the model is based on the fact that better results can be obtained by

Component	Young's Modulus E [MPa]	Poisson's ratio ν [.]	Mass density ρ [kg/m^3]
Rail	$210 \cdot 10^3$	0.25	7850
Rail pads	40	0.25	900
Sleeper	$30 \ . \ 10^3$	0.25	1300
Unconfined ballast	50	0.20	1500
Fresh ballast	150	0.20	1600
Fouled ballast	250	0.30	1600
Interlayer	80	0.30	2000
Subgrade	20 - 100	0.40	1800

Table 3.1: Mechanical properties of different components of the structure and soil.

removing the participation of high frequency modes induced by the spatial discretization (Hughes, 2000), even if second-order accuracy is lost. It is important to highlight that no viscous damping or Rayleigh matrix is used, and numerical damping comes only from chosen time integration scheme. When elasticity is considered, this is then the only factor affecting damping in the model. For the nonlinear model, damping can be induced by the constitutive equations once strains are higher than the elastic domain.

From a series of simple one dimensional wave propagation tests of a single elastic homogenous layer overlying an elastic half-space bedrock, Sáez (2009) verified that this set of parameters induce numerical damping of order of magnitude ζ=0.8%. In this work, the expression given by Hughes (2000) in order to estimate the numerical damping is prefered:

$$\zeta = \pi \left(\gamma - \frac{1}{2}\right) \frac{\Delta t}{T} + O\left(\left(\frac{\Delta t}{T}\right)^2\right) \tag{3.20}$$

where T is the specific period of the model.

The time step used in this work is Δt=5.10^{-4} s, and neglecting the quadratic terms for low $\Delta t/T$ values leads to a good approximation of the numerical damping induced by the numerical scheme. It is a linear function of the frequency given by $\zeta \approx 0.0002 f$.

3.3 Optimized characteristics of the FE model

The modeling framework presented in the previous section provides a general basis in order to study the mechanical response of the railway track under moving loads. However, different aspects can be enhanced in order to reduce the numerical simulation time. This can become an important issue for very large models, specially when dealing with 3D models, or when a large number of simulations are required, as in stochastic analysis. In the next sections the following main points of the optimized dynamic linear numerical model are discussed:

- model dimension (3D and 2D);

- domain size and finite element discretization;
- load application methodology;
- appropriate boundary conditions.

In Chapter 5, some of these aspects are revisited when the influence of nonlinear mechanical behavior is considered.

3.3.1 Modeling approaches for the 3D railway track domain

Different classical geotechnical problems present an important 3D component, such as pile-soil interaction for a group of piles, finite slope stability, among others. Nonetheless, hypothesis on considered dimensions and symmetries are usually necessary in order to carry out numerical simulations. The moving load problem over the railway track structure is a 3D problem, mainly because of the sleeper discrete support. In the finite element framework, although some authors (Hall, 2003; Kouroussis et al., 2011c; El Kacimi et al., 2012; Shan et al., 2013; Thach et al., 2013; Connolly et al., 2014) propose to use directly 3D models, these are computationally intensive both in terms of CPU time and memory, therefore not being suitable in order to perform probabilistic calculations. Modal substructure reduction strategies can lead to significantly simulation time reduction (Balmès, 1996; Ferreira, 2010). However, considering nonlinear mechanical properties within a reduced model is a current challenge. In the railway track framework, different modeling assumptions regarding the considered dimensions are discussed in the literature:

- Simplifying the load propagation dimension (y) (in Figure 3.2) by considering it invariant by translation. This approach is also called 2.5D approach. In this case, only the lateral (x) and vertical (z) planes are considered. This approach is usually implemented when nearby soil vibration caused by wave propagation in the lateral direction is of interest (Galvín et al., 2010a; Costa et al., 2012b,a; Gao et al., 2012; Hung et al., 2013). A continuous sleeper support is considered, which is an important drawback as the discrete support plays an important role on the stress distribution and its role on ballast response.

- Simplifying the load propagation direction (y) by considering an invariant periodical reference structure and using the Floquet theorem to solve the mechanical problem in the convective reference frame (Clouteau et al., 2005; Chebli et al., 2006, 2008; Ferreira, 2010). In this case, the periodical structure is well represented, but no variations of the material parameters in the load propagation direction (y) can be considered in this case.

- Simplifying the lateral direction (x) by using a plane deformation hypothesis with variable lateral width. In this case, lateral width can be optimized regarding a certain quantity of interest. Ribeiro (2012) proposes to match the vertical deformation from the 3D and 2D models for all points under load, under linear elasticity hypothesis.

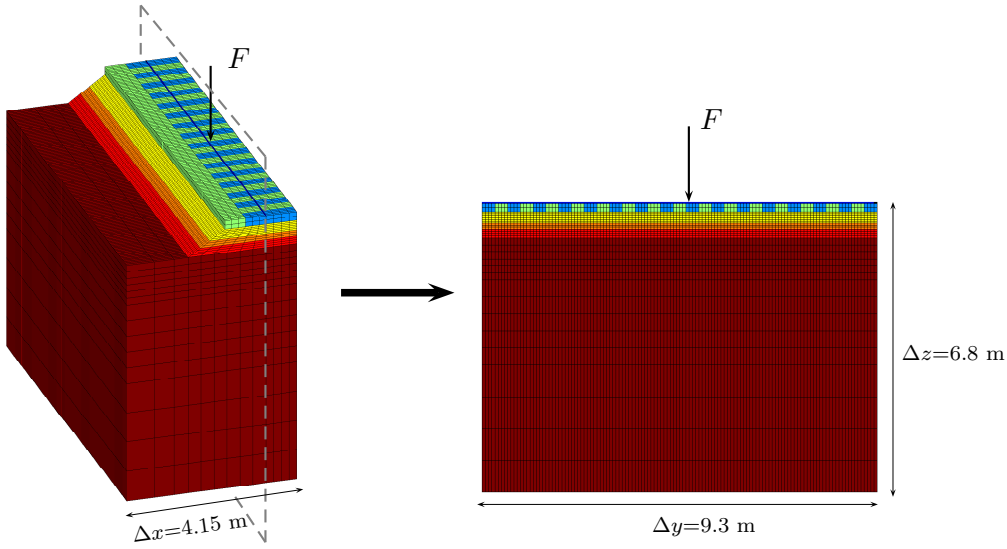

Figure 3.3: 3D mesh and simplification to 2D mesh.

Sáez et al. (2013) presented a 2D plane-strain approach with modified width in order to take into account periodicities in the out-of-plane direction, which is in the x direction in the model. Normal stress in the x plane is obtained by considering a mean value over a certain out-of-plane width (b). The value of b can be optimized in order to match the vertical strain (ε_{zz}) of both 3D and 2D models for the column of soil directly under the load. Moreover, Ribeiro (2012) showed an iterative procedure for calibrating b values, which is briefly presented as follows. A schematic representation of the proposed simplification is exposed in Figure 3.3.

Consider ε_{zz}^{3D} the vertical strain of the column of soil in the 3D model directly beneath the applied load, ε_{zz}^{2D} the vertical strain of the column of soil in the 2D model also directly beneath the load, the out-of-plane width (b) of the soil column at iteration i can be defined as:

$$(b)_{i+1} = f(\varepsilon_{zz}^{3D}, (\varepsilon_{zz}^{2D})_i) \tag{3.21}$$

where i is the index from the iterative process defined hereafter. From a FE perspective, the out-of-plane width (b) is constant at each FE soil element, while strains are obtained at each Gauss point and their location depends on the considered degree of the polynomial approximation. From the FE solution obtained both by the 3D and 2D models, the vertical strains $\varepsilon_{zz}^{3D}{}_n$ and $\varepsilon_{zz}^{2D}{}_n$ are defined as the vertical strains interpolated at the middled of the nth FE element among the N FE elements in the discretized soil column. b_n is defined as the out-of-plane width of the nth FE element, which is considered constant for all soil elements at the same depth. The index n is dropped from the following equations in order to simplify the mathematical notation. Under linear elastic hypothesis and a sufficiently small element size for the finite element mesh, the vertical strain under load for both the 3D and the 2D models can be expressed by the following relation:

$$\varepsilon_{zz}^{3D} \cdot A^{3D} = \varepsilon_{zz}^{2D} \cdot A^{2D} \tag{3.22}$$

where A^{3D} and A^{2D} are the influence area of the loading in the considered soil element. It is then convenient in this case to impose the same discretization in both the 2D and 3D models in the (y, z) plane. Equation 3.22 can be approximated by:

$$\varepsilon_{zz}^{3D} \cdot b^{3D} = \varepsilon_{zz}^{2D} \cdot b^{2D} \tag{3.23}$$

where b^{3D} is an equivalent width for the 3D model and b^{2D} is the width to be used in the 2D model in order to match the vertical strain of the 3D model. Equation 3.23 can be solved iteratively by considering the following relation:

$$(b^{2D})_{i+1} = \frac{(\varepsilon_{zz}^{2D} b^{2D})_i}{\varepsilon_{zz}^{3D}} \tag{3.24}$$

Equation 3.24 is verified at each node of the finite element mesh for points under the load. The estimation error (ϵ_b) based on an L_2 norm defined in Equation 3.25 is used in order to control the convergence of the approximation algorithm. Convergence is achieved when $(\epsilon_b)_i$<0.1.

$$(\epsilon_b)_i = \sqrt{\sum_{n=1}^{N} (\varepsilon_{zz}^{3D}{}_n - \varepsilon_{zz}^{2D}{}_n)^2} \tag{3.25}$$

The above formulation allows to correctly characterize the vertical strain and displacement in the soil elements under the applied load in the 2D model. An example is conducted for both soft and stiff soils. The considered domain size for this application is presented in the Figure 3.3. The obtained out-of-plane width (b) for both cases are presented in Figure 3.4a. The initial width profile is chosen equal to the values of the used 3D mesh. Values are very close, despite the important differences of stiffness on both discussed cases. The error is presented in Figure 3.4b, the threshold proposed value is reached for both cases after 5 iterations. Good agreement is obtained for both vertical strain (ε_{zz}) (Figure 3.5a) and vertical displacement (u_z) (Figure 3.5b) of soil elements under the loaded sleeper. However, both initial vertical stress (σ_{zz}^0) (Figure 3.6a) and during load vertical stress (σ_{zz}) under the application point (Figure 3.6b) are higher in the 2D model for elements in the upper half of the model, the difference being higher for soft soils than stiff soils.

One important drawback emerges from the fact that the out-of-plane width (b) is kept constant for all elements at the same depth: values at both sides of the the load are the same, therefore not optimized. The shear component of stress and strain tensor is mainly concerned, as under the load elements present null shear. The representation of the difference between the 3D and 2D calculations after width calibration on shear stress (σ_{yz}) in the considered plane is presented in Figure 3.7 for soft and stiff soil. It is shown that mainly differences occur in the ballast layer and between the sleepers, these being attenuated in the subgrade.

3.3.2 Domain size and finite element discretization

Considering large domains in the FE formulation require intensive computational effort, while the result's accuracy can be undermined by considering small domains. In order to

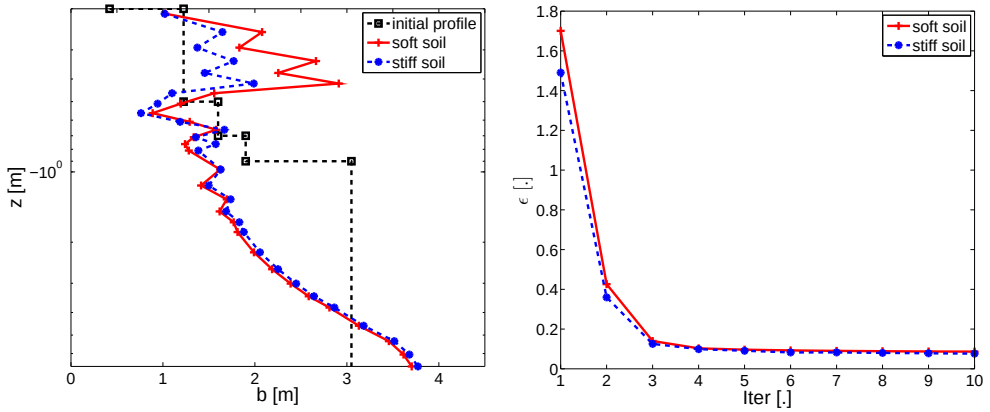

(a) (b)

Figure 3.4: Width calibration procedure for soft and stiff soils. a) Calibrated width (b); b) Estimation error (ϵ).

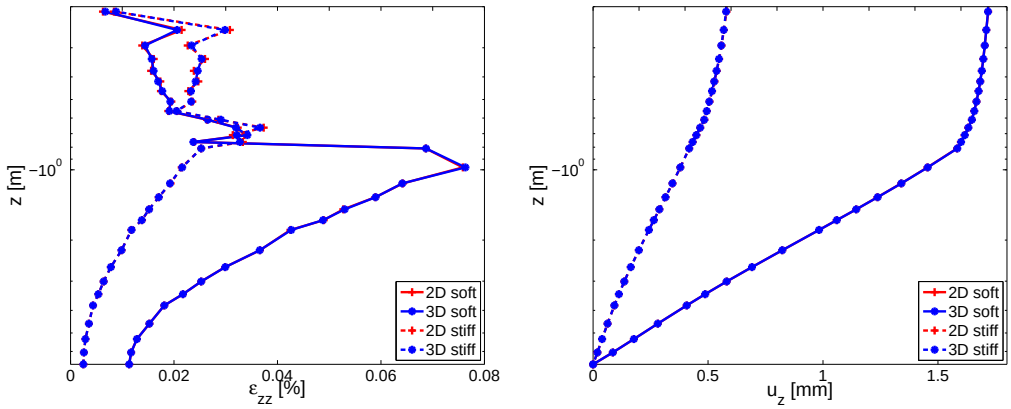

(a) (b)

Figure 3.5: Width calibration procedure for soft and stiff soils. a) Vertical strain (ε_{zz}); b) Vertical displacement (u_z).

control the adequacy of the model's dimension, a sensitivity study on the length and the width of the necessary domain size is performed in this section.

Modeling unbounded domains by the finite element method requires to decide where to place the model boundaries and how to ensure that the effect of the boundaries in the model can be neglected. The main concern is to ensure that the boundaries do not affect the results. In static models, the influence of both bottom and lateral boundaries are to rigidify the structure as a consequence from the Dirichlet condition imposed on the normal direction to the boundary. In the case of dynamic models, boundaries are also responsible for wave reflection appearing from the dynamic loading. In this case, special boundary conditions must be applied in order to reduce their impact on the obtained results. The paraxial approximation and viscous boundaries based on a Kelvin-Voigt model are used in this work as effective ways of preventing wave reflection at lateral boundaries. Their

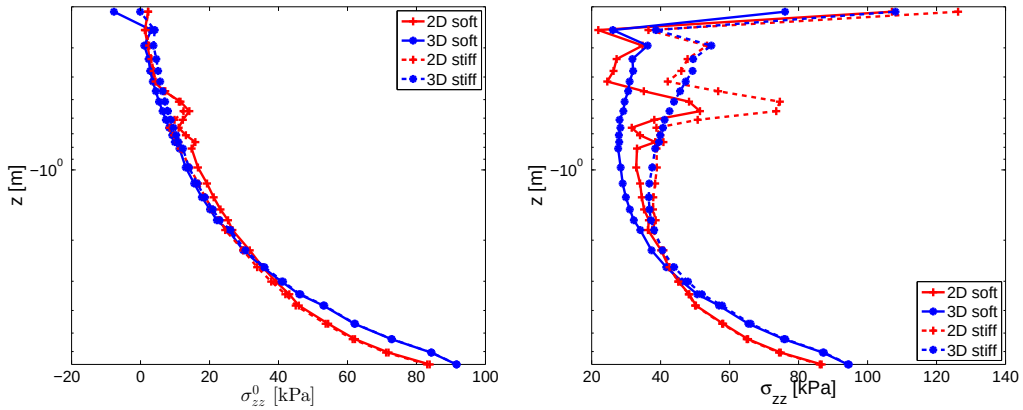

Figure 3.6: Width calibration procedure for soft and stiff soils. a) Initial vertical stress (σ^0_{zz}); b) Vertical stress (σ_{zz}) after the application of the vertical load.

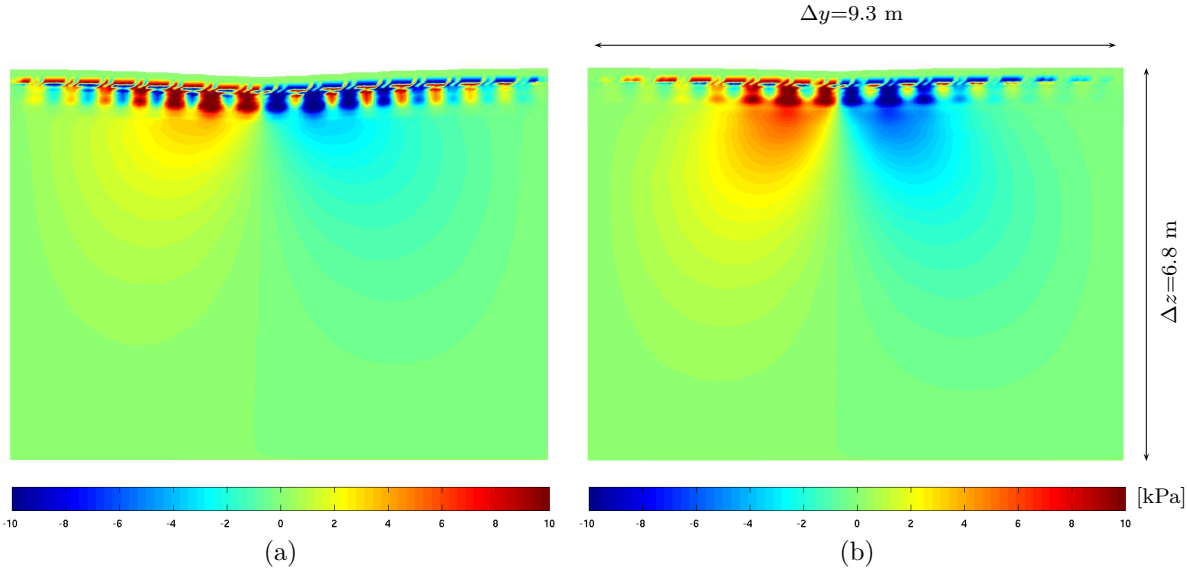

Figure 3.7: Difference between shear stress (σ_{yz}) in the 2D and 3D models obtained after out-of-plane width (b) calibration. a) Soft soil; b) Stiff soil.

performance is further compared in Section 3.3.4.

The element size is also an important issue when dealing with finite element models. On the dynamic models, the element size defines up to which wavelength, i.e. frequency, the model provides reliable values. It is widely accepted on finite element modeling that at least 10 elements per wavelength is sufficient to describe the considered wavelength. In this case the following rule of thumb may be applied:

$$10\Delta y = \frac{v_{min}}{f_{max}} \tag{3.26}$$

$$f_{max} = \frac{v_{min}}{10\Delta y} \tag{3.27}$$

v_{min} is the minimum speed of waves traveling in the medium, which can be approximated by the shear wave velocity (v_s). For a given FE discretization, soft soils present lower maximum frequency than stiff soils. For example, in the case of a shear wave velocity v_s=120 m/s (G=25.9 MPa and E=67.4 MPa, considering ρ=1800 kg/m^3 and Poisson's ratio ν=0.3), the maximum representative frequencies are 400 Hz for an average element size of Δy=0.03 m.

3.3.2.1 Vertical size and mesh discretization

The position of the bottom boundary as well as the discretization of the subgrade soil in the model are optimized from static track stiffness results of a single static load. The track stiffness is defined as:

$$k_{static} = \frac{F_{st}}{u_{st}} \tag{3.28}$$

where F_{st} is the nominal static load for the EMW test, F_{st}=100 kN, and u_{st} is the vertical displacement of the rail where F_{st} is applied.

For this study the reference mesh is 20 m × 12 m. The soil depth is then optimized in order to reduce the necessary mesh size. Three vertical mesh discretizations for the soil are considered: fine (Δz=0.15 m), regular (Δz=0.30 m) and coarse (Δz=0.50 m) for both stiff and soft soil cases. All other layers are discretized with elements presenting $\Delta z \approx$0.05m. Figure 3.8a shows how the track stiffness varies when increasing the soil depth for the two considered soil types. The track stiffness is a nonlinear decreasing function of the soil depth. This is a direct result from the considered linear elastic mechanical behavior for the soil. In this case, increasing the considered mesh depth always leads to higher displacements thus lower stiffness. This condition is not physically possible, as soil stiffness increases with increasing depth due to higher confining stress. Rather than the track stiffness, its numerical derivative in respect to the increasing considered soil depth is preferentially used, which is defined by Equation 3.29. The numerical derivative has the main advantage of providing an approximation measure relative to the influence of the constant drift observed on the track stiffness. Figure 3.8b shows that variations of Δk are more important in soft soil case rather than stiff soil. The value of Δk=0.3% is considered as the acceptable variation in this work, which is obtained for Δh=6 m. On the other hand, no influence of the soil vertical discretization is observed for this measure.

$$\Delta k = \frac{k(i) - k(i-1)}{k(i)} \cdot 100 \qquad [\%] \tag{3.29}$$

In order to further analyze the model bottom boundary influence, the vertical strain (ε_{zz}) at all layers and their numerical derivatives ($\Delta\varepsilon_{zz}$) as defined by applying Equation 3.29 are verified. Results are presented in Figure 3.9 and Figure 3.10, where solid line represents stiff soil results and dashed line the soft soil results. Vertical strain at the fresh and fouled ballast layers are not affected by the soil vertical discretization, as they present higher Young Modulus values than the interlayer and the subgrade. The interlayer is more affected by subgrade vertical discretization for stiff soil case, and the subgrade is more affected for the soft soil case. In all cases convergence in terms of the $\Delta\varepsilon_{zz} \leq$0.3% is

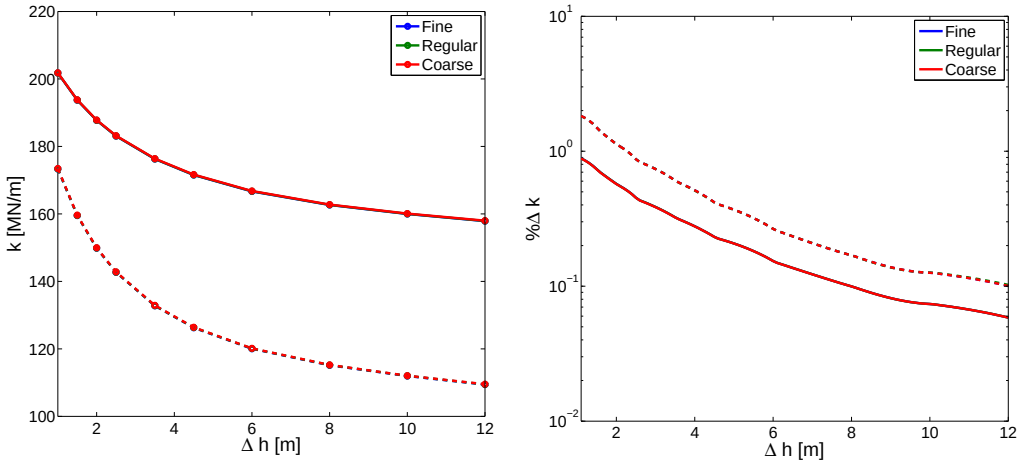

(a) (b)

Figure 3.8: Influence of considered subgrade thickness Δh on track stiffness. Solid line represents stiff soil results and dashed line the soft soil results. a) Subgrade thickness' influence on the track stiffness; b) Subgrade thickness' influence on the derivative of the track stiffness.

obtained for a subgrade thickness Δh=6 m, which is kept as the reference value for the numerical model.

3.3.2.2 Lateral size and mesh discretization

The lateral size of the mesh is chosen based on the loading characteristics and different mesh lengths are used in this work. The reference case is a track section of 84 m long, which corresponds to 140 sleepers. The sleeper discrete support introduces a periodicity in the railway track structure which must be correctly modeled, as well as the rail pad geometry and position on the sleeper. These geometrical constrains lead to a maximum lateral discretization of 0.075 m. The chosen value in this work is 0.06 m, as it allows to correctly describe the longitudinal dimension of the rail pad (0.18 m) and its position on the sleeper.

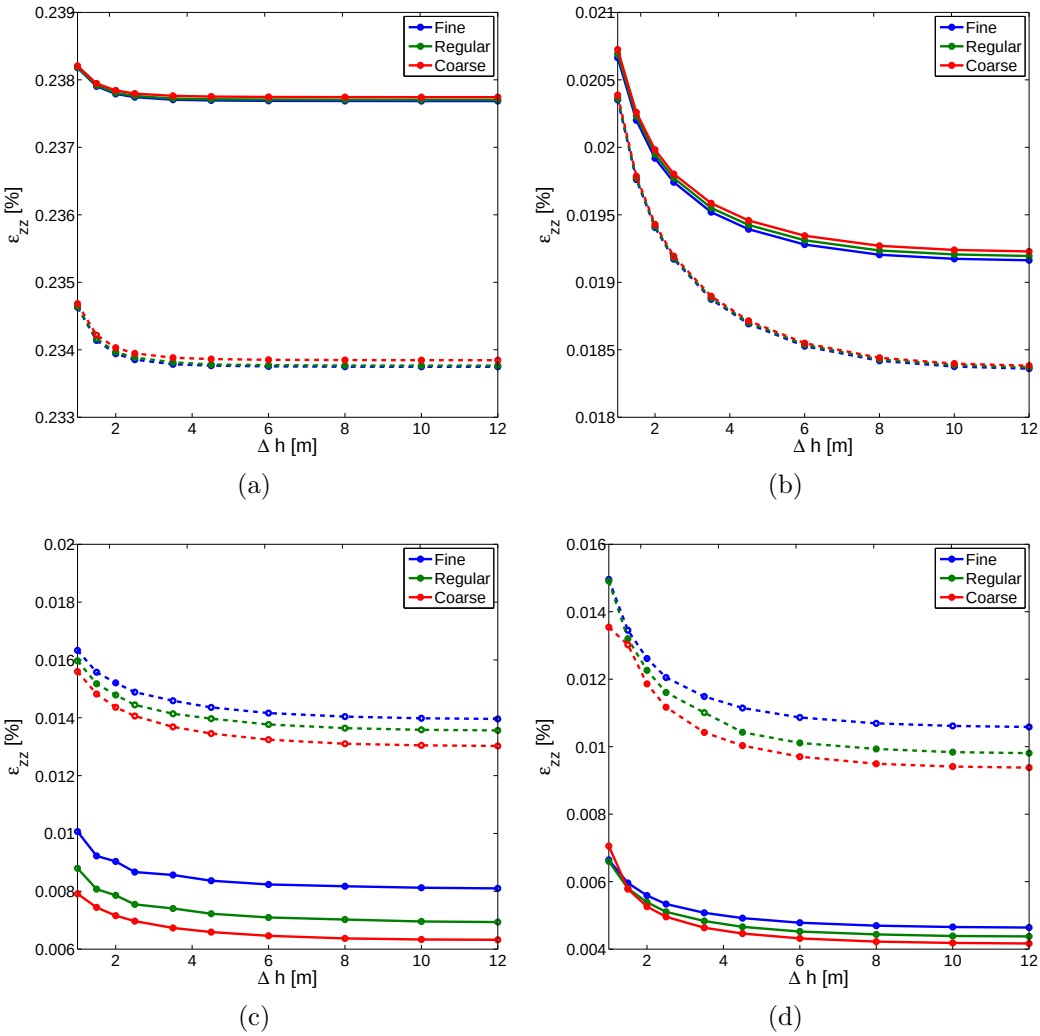

Figure 3.9: Evolution of vertical strain (ε_{zz}) with increasing considered subgrade thickness (Δh). Solid line represents stiff soil results and dashed line the soft soil results. a) Fresh ballast; b) Fouled ballast; c) Interlayer; d) Subgrade.

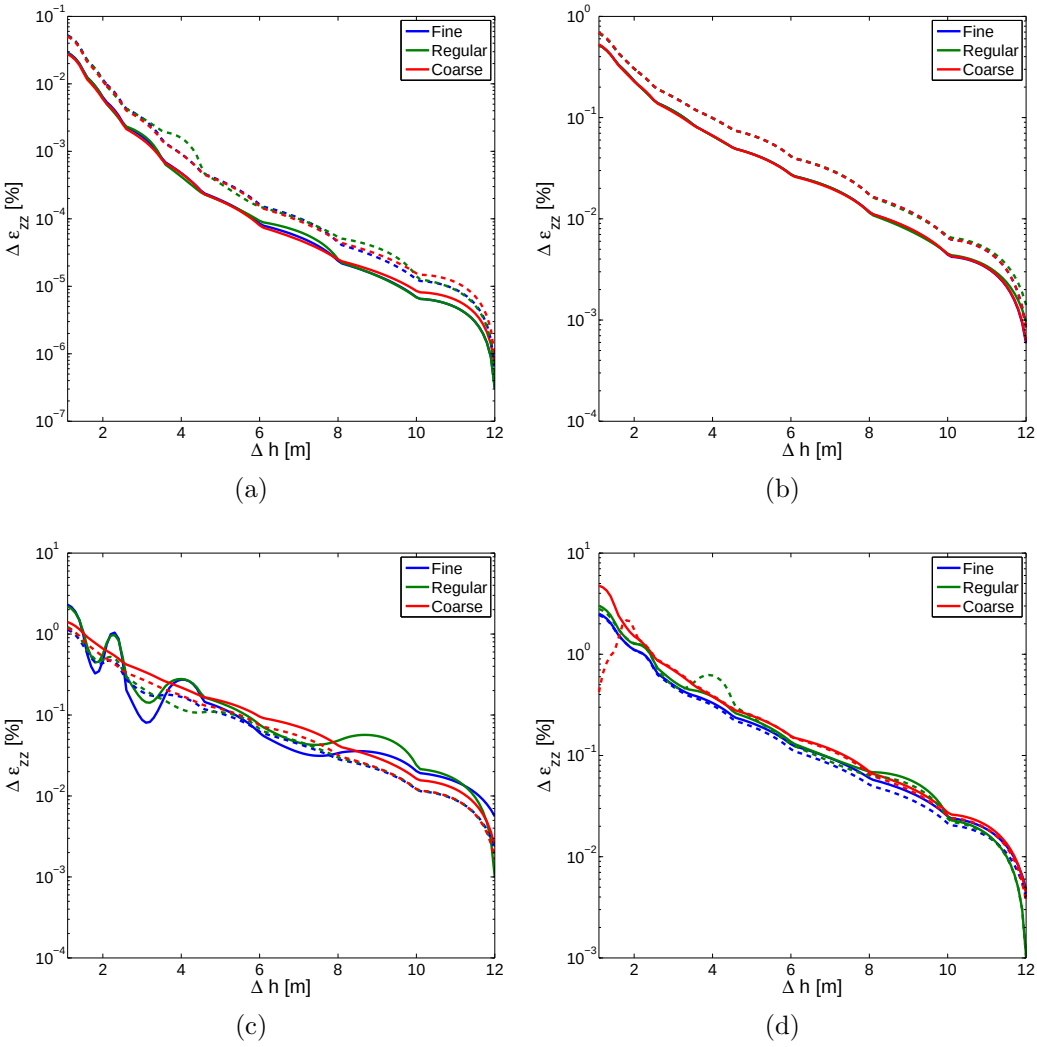

Figure 3.10: Convergence of vertical strain (ε_{zz}) in terms of $\Delta\varepsilon_{zz}$ for different track layers. Solid line represents stiff soil results and dashed line the soft soil results. a) Fresh ballast; b) Fouled ballast; c) Interlayer; d) Subgrade.

3.3.3 Moving load application methodology

The way to start dynamic moving load calculations on finite element models are still an open point of discussion in the scientific community. Different methods of load application on the scope of railway track modeling by the finite element method are proposed in the literature. In the case of linear elastic mechanical behavior, some authors have tried to apply full load at maximum speed and only to observe the point in the middle of the track (Hall, 2003; Rhayma, 2010) as to avoid errors arising from the finite domain. On the nonlinear case, Araújo (2010) applied full load and waited for wave dissipation through the medium and then full speed was applied. On all these cases no boundary condition was implemented to deal with wave reflexion. Some authors have also used viscous boundaries with infinite elements, although in this case no special attention was paid on the load application methodology (Kouroussis et al., 2011c; Connolly et al., 2013).

A more consensual point is how to apply the loading on a discretized beam element modeling the rail. Most authors use a triangle loading principle, which is presented in Figure 3.11. In this case, the maximum load is applied on a specific node and it moves forward to the next node according to a specified time-displacement function. When the load is between two nodes, the parallelogram principle is applied in order to equilibrate the load respective to the distance to each node.

In this work, the load application phase is decomposed in two steps: load magnitude initialization and speed initialization. The first phase consists of increasing the load magnitude on a fixed point y_o of the track. Without loss of generality, in the following development it is considered that y_o=0. During this phase, the load increases from 0 to the nominal applied load (F_{max}) on a given time t_o. The second phase consists of increasing the speed of the load gradually, from 0 to the nominal speed (v_t). The parametrization of the load acceleration ($a(t)$), speed ($v(t)$) and displacement ($y(t)$) functions is given by:

$$\begin{aligned} 0 < t < t_o \quad & a(t) = 0 \\ t_o \leq t < \tau_o/2 + t_o \quad & a(t) = \dot{a}t + C_1 \\ \tau_o/2 + t_o \leq t < \tau_o + t_o \quad & a(t) = -\dot{a}t + D_1 \\ t \geq \tau_o + t_o \quad & a(t) = 0 \end{aligned} \tag{3.30}$$

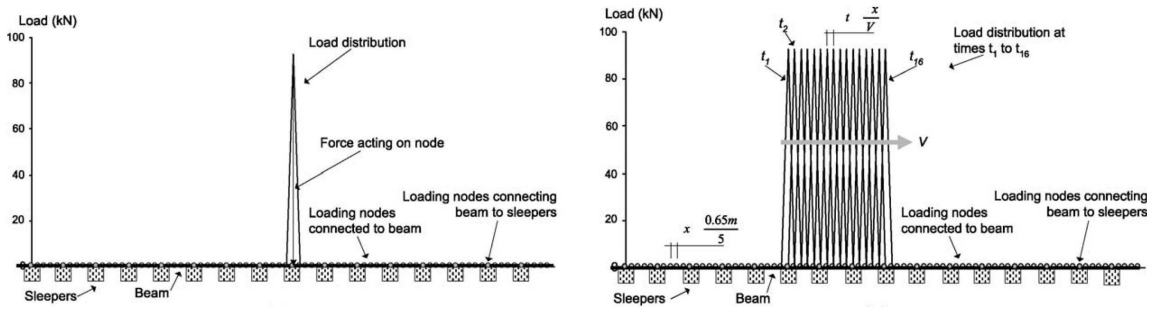

Figure 3.11: Triangle principle used on load application over rail nodes (from Hall, 2003).

$$
\begin{aligned}
0 < t < t_o \qquad & v(t) = 0 \\
t_o \leq t < \tau_o/2 + t_o \qquad & v(t) = \frac{\dot{a}t^2}{2} + C_1 t + C_2 \\
\tau_o/2 + t_o \leq t < \tau_o + t_o \qquad & v(t) = -\frac{\dot{a}t^2}{2} + D_1 t + D_2 \\
t \geq \tau_o + t_o \qquad & v(t) = v_t = \frac{\dot{a}\tau_o^2}{4}
\end{aligned}
\tag{3.31}
$$

$$
\begin{aligned}
0 < t < t_o \qquad & y(t) = y_o = 0 \\
t_o \leq t < \tau_o/2 + t_o \qquad & y(t) = \frac{\dot{a}t^3}{6} + \frac{C_1 t^2}{2} + C_2 t + C_3 \\
\tau_o/2 + t_o \leq t < \tau_o + t_o \qquad & y(t) = -\frac{\dot{a}t^3}{6} + \frac{D_1 t^2}{2} + D_2 t + D_3 \\
t \geq \tau_o + t_o \qquad & y(t) = v_t t + E_3
\end{aligned}
\tag{3.32}
$$

with:

$$
\begin{aligned}
C_1 &= -\dot{a}t_o \\
C_2 &= \frac{\dot{a}t_o^2}{2} \\
C_3 &= -\frac{\dot{a}t_o^3}{6} \\
D_1 &= \dot{a}(t_o + \tau_o) \\
D_2 &= -\frac{\dot{a}t_o^2}{2} - \dot{a}t_o\tau_o - \frac{\dot{a}\tau_o^2}{4} \\
D_3 &= \frac{\dot{a}t_o^3}{6} + \frac{\dot{a}t_o^2\tau_o}{2} + \frac{\dot{a}t_o\tau_o^2}{4} + \frac{\dot{a}\tau_o^3}{24} \\
E_3 &= -\frac{\dot{a}(t_o + \tau_o)^3}{6} + \frac{D_1(t_o + \tau_o)^2}{2} + D_2(t_o + \tau_o) + D_3 - v_t(t_o + \tau_o) \\
\tau_o &= 2\sqrt{\left(\frac{v_t}{\dot{a}}\right)}
\end{aligned}
$$

The function $a(t)$ described by Equations 3.30 is a triangular function. It is fully parametrized by three parameters:

- t_o: time spent on the first phase (loading),
- v_t: nominal speed,
- $\dot{a}$: rate of change of the acceleration, also called *jerk*.

Figure 3.12 shows the acceleration ($a(t)$), speed ($v(t)$) and displacement ($y(t)$) functions using the described methodology, where the given set of parameters is considered: $\dot{a}$=150 m/s^3, t_o=0.5 s and v_t=220 km/h.

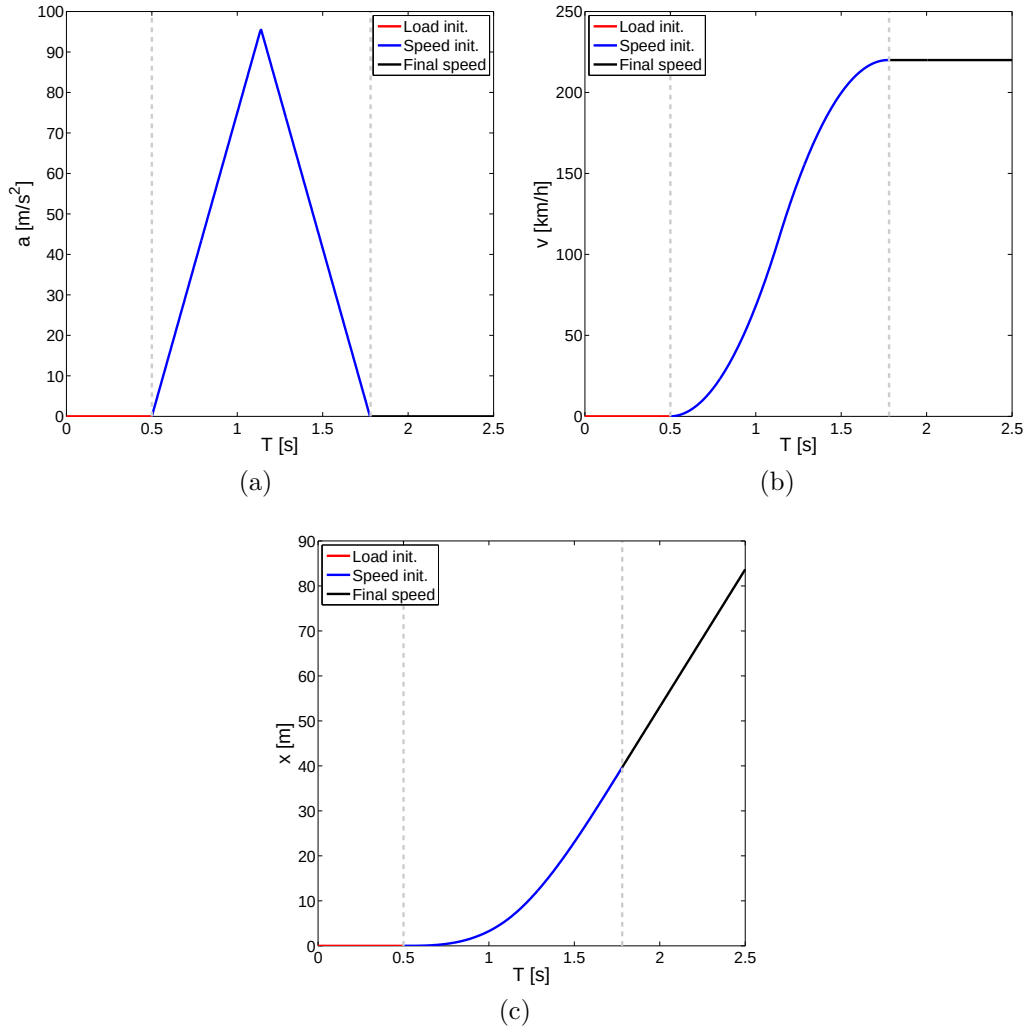

Figure 3.12: Load application method. a) Acceleration function ($a(t)$); b) Speed function ($v(t)$); c) Displacement function ($y(t)$).

From the proposed parametrization, the load function ($F(y(t),t)$) can be written as:

$$0 < t < t_o \qquad F(y(t),t)) = F_{max}\frac{t}{t_o}$$

$$t \geq t_o \qquad F(y(t),t) = F_{max}$$

For the given parameters, this methodology implies on a load sequence as presented in Figure 3.13. The first phase ends when F_{max} is applied on the first considered node. Then the load moves forward at increasing speed as defined by Equation 3.30, until it reaches its nominal value (v_t), at some point further at the track. Starting from this point, any numerical study may be performed considering the load F_{max} at speed v_t. Moreover, applying multiple loads is easy to implement.

The first parameter (t_o) is only related on the first phase, while the second (v_t) and third ($\dot{a}$) parameters are related only to the second phase. It is worth observing that increasing the final speed increases also the necessary displacement in order to reach a given

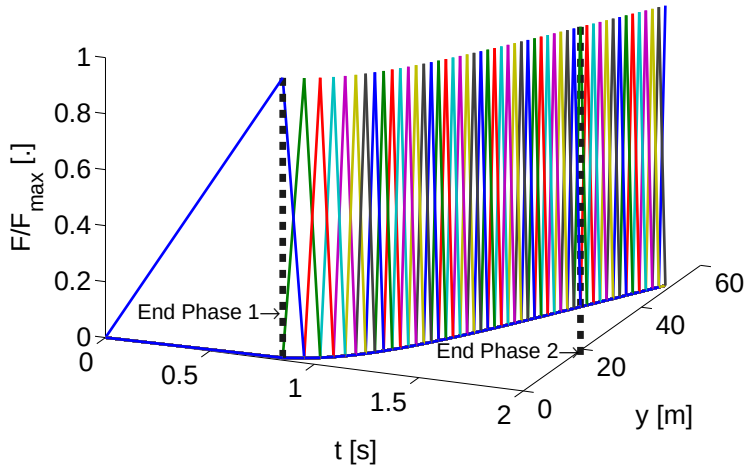

Figure 3.13: Triangle principle used on load application over rail nodes.

final speed, for a given jerk ($\dot{a}$). Increasing the jerk reduces the necessary displacement, but then the dynamic perturbation imposed in the model by the loading methodology is increased. A compromise between the jerk and the necessary load displacement must be found in order to be able to model high speeds on a relatively small mesh. Applying full speed corresponds to the worst case, as modeled by a Dirac on the acceleration.

It is important to highlight that the time step (Δt) must be carefully chosen in order to allow a correct description of the loading function at each node. The maximum Δt can be obtained as:

$$\Delta t_{max} = \frac{\Delta y_{min}}{2v_t} \tag{3.33}$$

where Δy_{min} is the minimum discretization size of the rail (which is constant for all performed simulations, Δy_{min}=Δy=0.06 m) and v_t is the nominal speed, which characterizes the highest speed. A factor of 2 is chosen as the minimal number in order to let the load to smoothly move forward from node to node. For example, simulating v_t=220 km/h requires a minimum time-step of around 5.10^{-4} s.

Coupling the proposed methodology with an appropriate boundary condition and the numerical damping from the time integration scheme allows to improve the model dynamic results and to obtain more robust and reliable values. These results are presented in the next sections.

3.3.3.1 Comparison for dynamic loads *before* using proper boundary conditions

In this section the considered loading methodology considering parameters t_o=0.5 s and $\dot{a}$=150 m/s^3 is compared with a traditional full-load full-speed method (t_o=0 s and $\dot{a}$=∞), hereafter called "No method", for the case of v=120 km/h. Figure 3.14 compares the

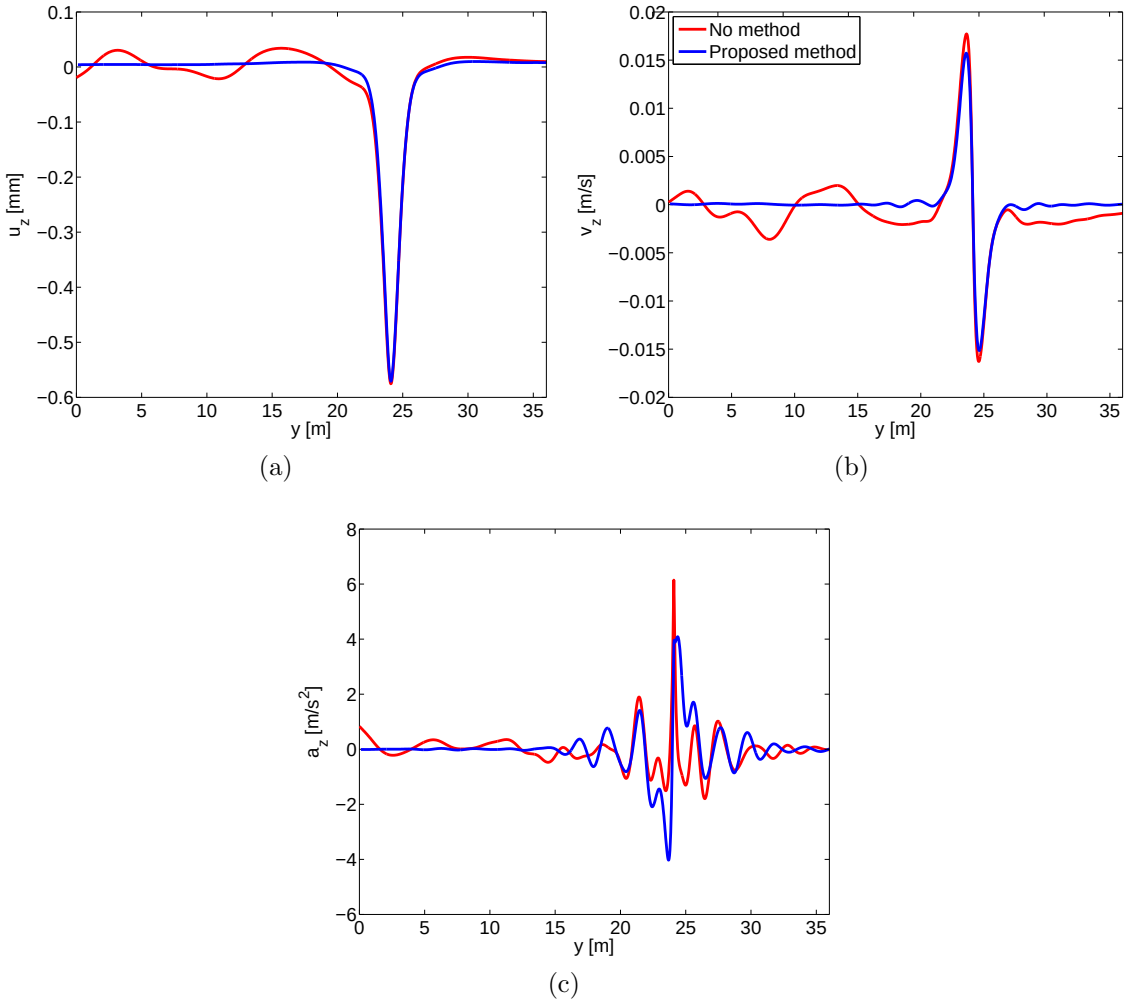

Figure 3.14: Comparison of different loading strategies on the vertical rail response for a moving load at 120km/h. a) Vertical displacement (u_z); b) Vertical speed (v_z); c) Vertical acceleration (a_z).

vertical response of the rail the two cases. The considered model is 36 m long and the comparison is made at the instant when the moving load is at the same point for both cases. The proposed methodology permits to obtain better results on displacement, speed and acceleration curves *before* implementing any appropriate boundary.

In order to have a more global view of the improvement on the dynamic calculation, a criteria based on the energy arriving on and reflected by the boundaries is used. It is based on the Specific Energy Density (SED) used in earthquake engineering and it is defined by Equation 3.34.

$$SED(z) = \int_0^t v^2(z)dt \qquad [m^2/s] \tag{3.34}$$

Figure 3.15 compares the SED for the case when no method is used, i.e. force is applied at maximum value and maximum speed, and the proposed method. In the Figure

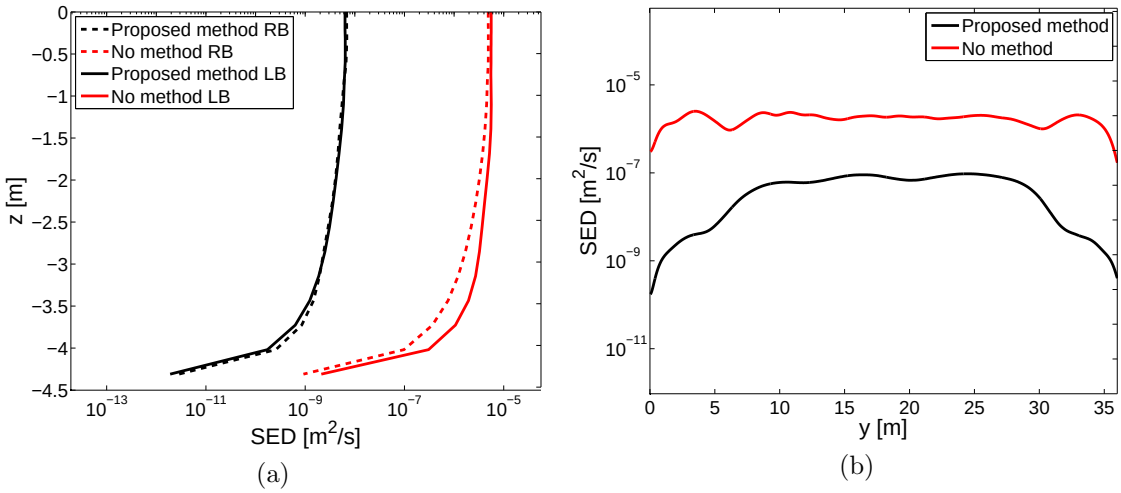

(a) (b)

Figure 3.15: SED for the proposed method and no method loading cases for a moving load at 120 km/h. a) Right boundary (RB) / Left boundary (LB); b) Bottom boundary.

PM stands for proposed method and NM for no method. SED values reduce with depth for the left and right boundaries, SED_{PM}, being almost 1000 times smaller than SED_{NM} (Figure 3.15a). Improvement is also obtained on the bottom boundary (Figure 3.15b), although in this case SED_{PM} is only 10 times smaller than SED_{NM}. It is expected that $SED_{PM} < SED_{NM}$, as in the proposed methodology less energy is introduced in the system.

The proposed loading methodology reduces the dynamic effects of the loading procedure and yields better results. Wave reflection on boundaries is then addressed by appropriate boundary conditions discussed in the next section.

3.3.4 Comparison of different boundary conditions for moving loads

The viscous elements with Kelvin-Voigt mechanical model and the paraxial approximation are used in this work. Both are implemented in the lateral boundaries of the railway track model in order to reduce wave reflection due to the moving load. More on their mathematical formulation can be found in Appendix C. Their performance is compared by considering the results of a model composed of 60 sleepers (36 m), schematically represented in Figures 3.16 and 3.17. A very long model composed of 140 sleepers (84 m), denoted as 140SLP hereafter, is considered to yield sufficiently undisturbed results from lateral boundaries and is used reference model for the comparisons. A bogie load composed of two wheelsets of 85 kN and at final speed of 120 km/h is applied, following the proposed loading methodology. The following two cases are defined:

- Case I: absorbing boundary with Kelvin-Voigt model (60SLP KV). Elastic parameters are kept the same as the nearest layer, and the viscous parameter η is equal to 10^5 s^{-1} on all layers.

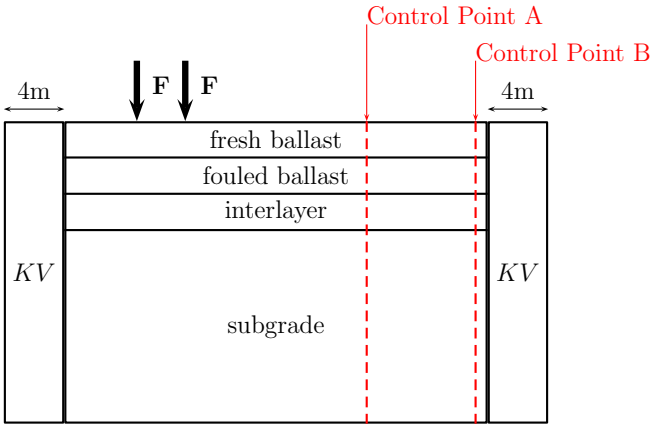

Figure 3.16: Case I: Absorbing elements on boundaries (60SLP KV).

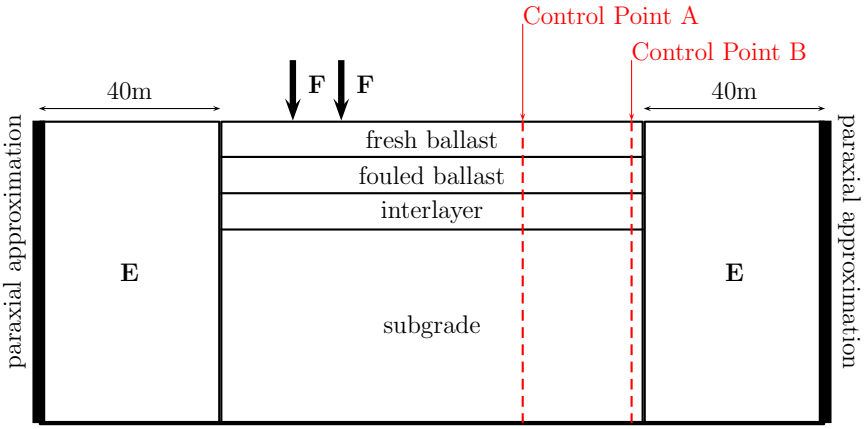

Figure 3.17: Case II: Paraxial approximation on boundaries (60SLP PARX).

- Case II: paraxial approximation with elastic domain E of 40 m at each side, which follows the same elastic parameters as the nearest layer (60SLP PARX).

Two control points are verified: control point A, which is fully loaded and unloaded, and control point B, which is not loaded during the simulation and is just next to the boundary on cases I and II. The vertical displacements and accelerations at all layers are only slightly affected at control point A as shown in Figure 3.18 for the interlayer material. However, the lateral response in terms of lateral velocity is better approximated by the paraxial solution rather than the Kelvin-Voigt boundary before and after loading (Figure 3.19). During loading, the maximum values are only slightly affected and in the case where only these values are of interest both approaches give similar results.

On the control point B, however, both vertical and lateral responses are very different depending on the considered boundary solution. A comparison is shown in Figure 3.20. The paraxial solution in this case better approximates the response of the 140 sleeper

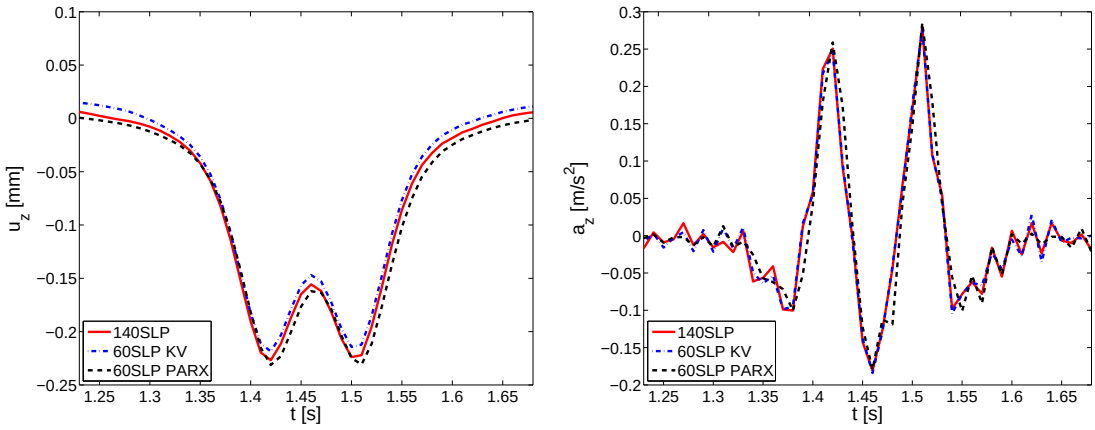

(a) (b)

Figure 3.18: Comparison of the interlayer vertical response at control point A for different boundary conditions for a bogie load at 120 km/h. a) Vertical displacement (u_z); b) Vertical acceleration (a_z).

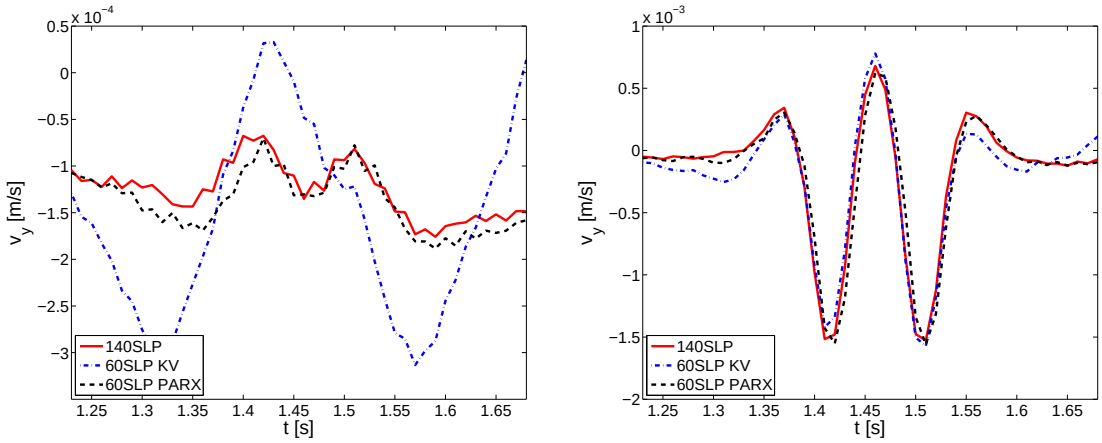

(a) (b)

Figure 3.19: Comparison of the lateral speed (v_y) at control point A for different boundary conditions for a bogie load at 120 km/h. a) Rail; b) Interlayer.

model, presenting even a better description of the vertical response (zero before load arrival). The viscous Kelvin-Voigt boundary imposes rather a constrained motion, as the lateral displacements are almost zero next to the boundary.

Figure 3.21 compares the SED as defined by Equation 3.34 for the three considered cases on control point A. On the topmost layers the values are the same, although deeper in the subgrade the paraxial approximation leads to lower levels of energy. On control point B, however, the paraxial approximation is the one allowing the most energy to leave the model through the elastic boundaries and to be absorbed by the paraxial elements.

These comparisons show that both boundary solutions yield similar results when only the vertical maximum values are of interest, i.e. only the values beneath the moving load

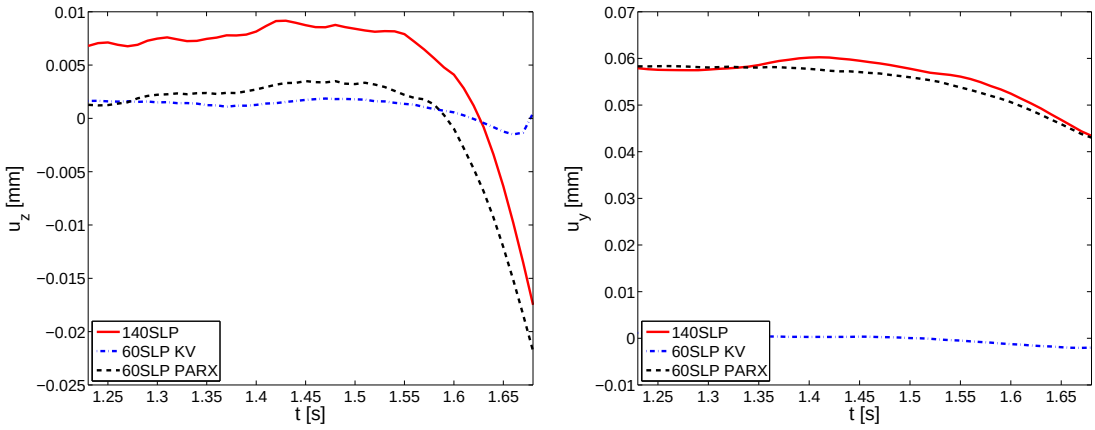

(a) (b)

Figure 3.20: Comparison of the interlayer vertical response at control point B for different boundary conditions for a bogie load at 120 km/h. a) Vertical displacement (u_z); b) Lateral displacement (u_y).

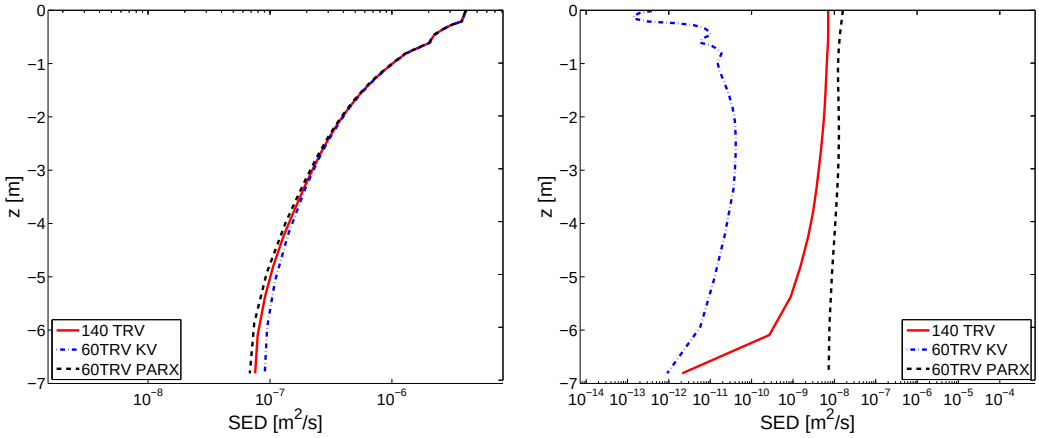

(a) (b)

Figure 3.21: Comparison of different boundary conditions: SED values at different control points for a bogie load at 120 km/h. a) Control Point A; b) Control Point B.

at the moment of the applied force. This is often the case when measuring maximum displacement or stress on layers. Although the lateral behavior is poorly approximated by the viscous Kelvin-Voigt boundary, this solution can be used when the vertical track response is of interest.

3.4 Elastic response of the railway track

In this section, the dynamic response of a conventional track structure subjected to moving load at speeds up to 270km/h is analyzed. The geometrical and mechanical characteristics of the conventional track structure considered in the previous sections is maintained (Table 3.1). It is composed of three layers (fresh ballast, fouled ballast and interlayer) and the subgrade (stiff soil, E = 100 MPa). A total length of 84 m is modeled, corresponding to 140 sleepers' bay. The mesh is composed of 56082 nodes, 60625 4-node bilinear qudrilateral elements and 1405 beam elements modeling the rail.

Two moving loads of 85kN are applied, which are 3 m apart in order to model the passage of a TGV bogie on a conventional line. The remaining load parameters are t_o=0.5 s and $\dot{a}$=150 m/s^3. The maximum necessary displacement imposed by the load methodology is of 53 m, obtained for the 270 km/h case. The chosen zone of interest is under the 100^{th} sleeper, or between y=60 m and y=60.6 m. Under sleeper points are at position y=60.12 m and between sleeper at position y=60.42 m. These characteristics are summarized in a schematic representation in Figure 3.22.

3.4.1 Mechanical response at small speed

The track response for a bogie passing at 15 km/h is first analyzed for elements under the sleeper. The choice of first characterizing the small speed response is motivated by providing a basis for the study of the influence of speed on the track response showed in the next section. Figure 3.23a presents the vertical displacement profile of points under the sleeper on the different layers. At the subgrade, the considered point is at a total depth of 1.10 m under the sleeper. All other points represent the middle point of the respective track layer. The rail vertical maximum displacement is around 0.6 mm, which is coherent with observed values on highly compacted conventional lines. Rail pads are responsible for 50% of the total maximum displacement of the rail (difference between the rail and sleeper vertical maximum displacement, Figure 3.23a), which highlights the importance of this elastic component on load distribution. All track layers are sensible

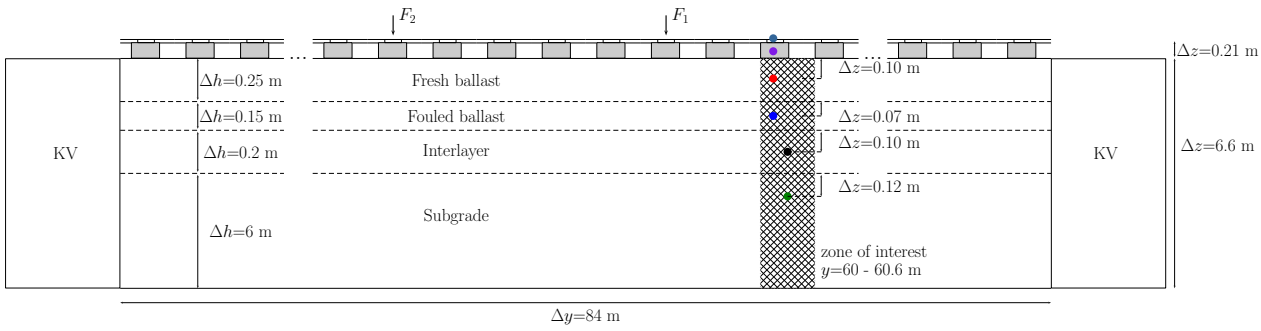

Figure 3.22: Schematic representation of the conventional track for linear elastic results

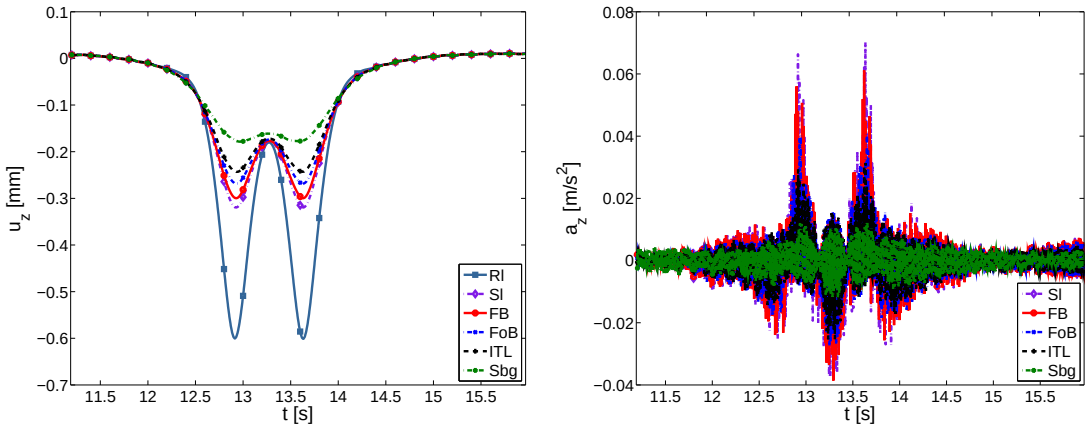

(a) (b)

Figure 3.23: Kinematic response of the track components for bogie load passing at 15 km/h. a) Vertical displacement (u_z); b) Vertical acceleration (a_z). Rl: Rail, Sl: Sleeper, FB: Fresh ballast, FoB: Fouled ballast, ITL: Interlayer, Sbg: Subgrade.

to the loading/unloading imposed by the axle distance, the subgrade in a smaller degree than the other layers. The vertical acceleration is shown from the sleeper to the subgrade in Figure 3.23b. As values are very small ($\approx$0.1 m/s^2) due to the considered low speed, the numerical noise is of the same order of magnitude of the acceleration levels, specially at the subgrade. The 15 km/h can thus be considered as a quasi-static loading. On higher speeds the observed numerical noise can be neglected, as will be shown in the next sections.

Stress and strain on materials are also obtained from the model. Figures 3.24a, 3.24b and 3.24c show the evolution of lateral, vertical and shear stress with loading, respectively. The fresh ballast material is the one presenting the highest increase in vertical stress, passing from 5kPa to 35kPa during loading. Moreover, two loading cycles almost independent are observed on the vertical applied stress (Figure 3.24b). Lateral stress showed to be very dependent regarding material layer and depth (Figure 3.24a). The lateral stress of fresh and fouled ballast layers is sensitive to the different axles, although these layers presented out-of-phase maximums. On the contrary, lateral stress of the interlayer and the subgrade is less sensitive to axles, i.e. a global increase and decrease of lateral stress is observed at the bogie scale rather than the axle scale. This could be explained by the lower Young's Modulus values and higher Poisson's ratio of the subgrade material. Shear stress is not very sensitive with depth, which is a direct result from linear elasticity hypothesis.

Principal stress axes rotation in the moving load problem has been already discussed by many authors (Chan and Brown, 1994; Grabe and Clayton, 2009; Chang et al., 2012, among others). This phenomenon is characterized by the nonalignment between principal stress axes and vertical/horizontal axes. Thus, principal stress rotation is controlled by shear stress variations compared with normal stress variations. As the moving load approaches a certain point, the major stress axis points to the loading and follows it along its trajectory. During loading, the principal stress axes are only aligned with vertical and horizontal axis when the load is exactly over the considered point, thus the vertical stress is maximum and shear stress is null, as observed in Figure 3.24d, where the principal

stress axes rotation angle (α_{yz}) is presented. It is obtained by Equation 3.35. Maximum and minimum values are not obtained at maximum values of shear stress but rather at certain combinations of normal and shear stress.

$$\alpha_{yz} = \frac{1}{2}\tan^{-1}\left(\frac{2\sigma_{yz}}{\sigma_{zz}-\sigma_{yy}}\right)\cdot\frac{180}{\pi} \qquad [^\circ] \tag{3.35}$$

The same characteristics can be studied in terms of the stress and strain invariants. As the in-plane stresses and strains are fully considered by the 2D model, mean (p_x) and deviatoric (q_x) stress invariants and volumetric (ε_v^x) and deviatoric (ε_d^x) strain invariants defined in the plane (y, z) are used. These are defined as:

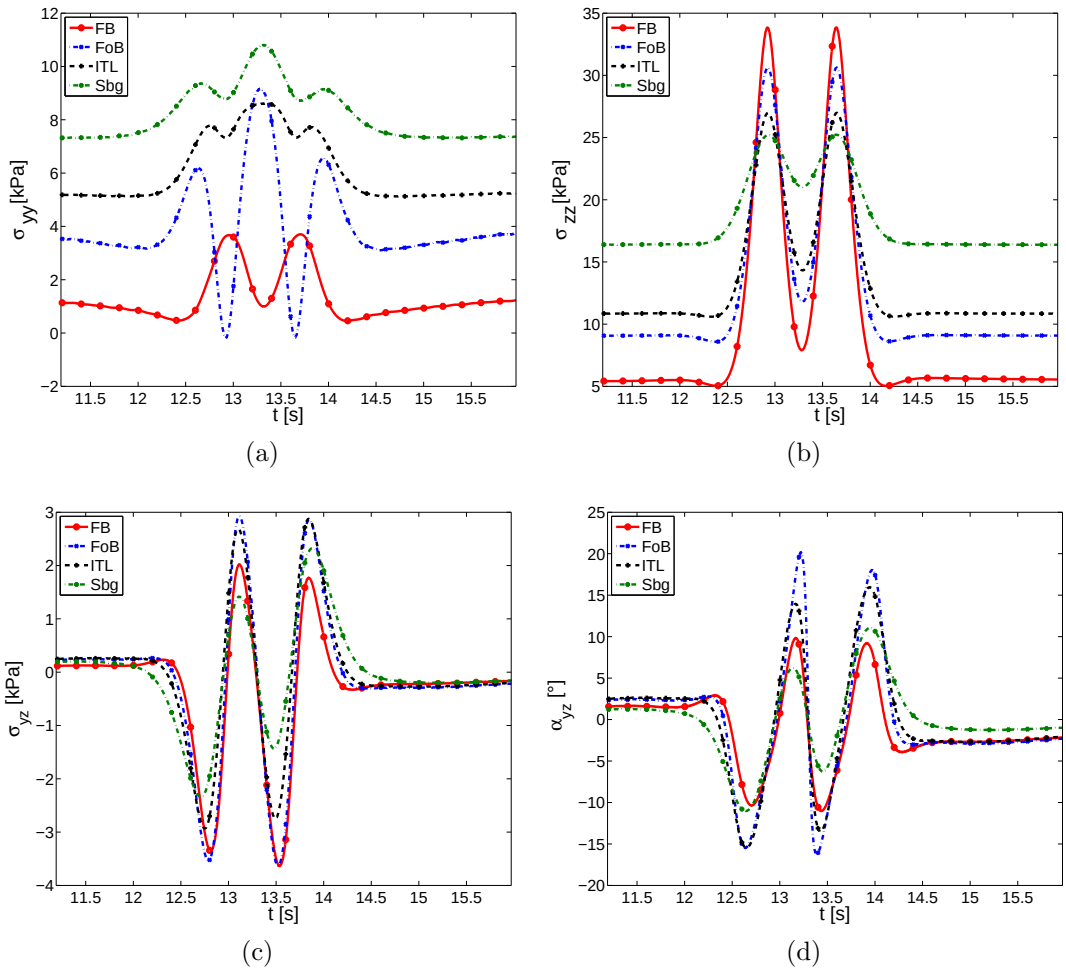

Figure 3.24: Time response of stresses on track layers a) Lateral stress (σ_{yy}); b) Vertical stress (σ_{zz}); c) Shear stress (σ_{yz}); d) Principal stress rotation angle (α_{yz}). FB: Fresh ballast, FoB: Fouled ballast, ITL: Interlayer, Sbg: Subgrade.

$$p_x = \frac{\sigma_{yy} + \sigma_{zz}}{2} \tag{3.36}$$

$$q_x = \sqrt{\left(\frac{\sigma_{yy} - \sigma_{zz}}{2}\right)^2 + \sigma_{yz}^2} \tag{3.37}$$

$$\varepsilon_v^x = \varepsilon_v = \varepsilon_{yy} + \varepsilon_{zz} \tag{3.38}$$

$$\varepsilon_d^x = \sqrt{\left(\frac{\varepsilon_{yy} - \varepsilon_{zz}}{2}\right)^2 + \varepsilon_{yz}^2} \tag{3.39}$$

Figures 3.25a and 3.25b present these results in terms of stress invariants p_x and q_x. Both mean and deviatoric stresses increase when the load approaches and their maximum values occur when the load is exactly over the considered point. Following vertical stress response, fresh and fouled ballast layers present the highest increase on deviatoric stress during load, from 2-3 kPa to 15 kPa at each axle passage. At the subgrade, mean stress is less sensitive to the combination of axles on the considered case, while deviatoric stress is sensitive to each axle passage. As the axle loads spread by the sleepers through the ballasted layers over the subgrade, their effects are added over larger distances and reduction on mean stress is thus less pronounced between axles. In this sense, the characteristic distance between axles defining a bogie is a key parameter on the reduction/increase of stresses in the track layers.

Figures 3.25c and 3.25d present the results in terms of strain invariants ε_v and ε_d^x. These results give an insight of strain levels which the materials are submitted to. Ballast layer present the highest values of both volumetric and deviatoric strain. In the considered case, the deviatoric strain in the other layers presents a two-pic response for each axle passage, due to the out-of-phase response of lateral and vertical strains. This effect is caused by the discrete sleeper support, each pic being representative of the action of the load over the track when the load is at the sleeper just before and then just after the considered sleeper.

Figure 3.26a presents the stress response in the (p_x, q_x) plane. The first interesting finding is that increase and decrease of stresses do not happen through the same slope once the two axle loads spread and interconnect, below the fresh ballast layer. Moreover, each material is subjected to a different stress slope at each cycle. In the (p_x, q_x) plane the triaxial test condition is obtained at the 1/2 slope (45°). The fouled ballast is the only one following this condition, while other materials are subjected to slopes lower than the triaxial and in some cases even lower than the unitary slope.

The previous analysis considered points under the sleeper, thus fully loaded during the moving load passage. However, the fresh ballast material is not equally loaded: points under the sleeper and between sleeper present different stress paths. Between sleepers points are laterally loaded by the action of ballast elements under the sleeper directly receiving the load. In this case, both mean and deviatoric stress levels are lower, but they follow a different stress path. Indeed, as shown in Figure 3.26b, the stress path is characterized by increase of p_x and q_x, followed first by a decrease of q_x with p_x constant and then a decrease of p_x with low variation of q_x. This cycle is repeated for the second axle of the bogie. Fouled ballast material presents also different stress path, although in this

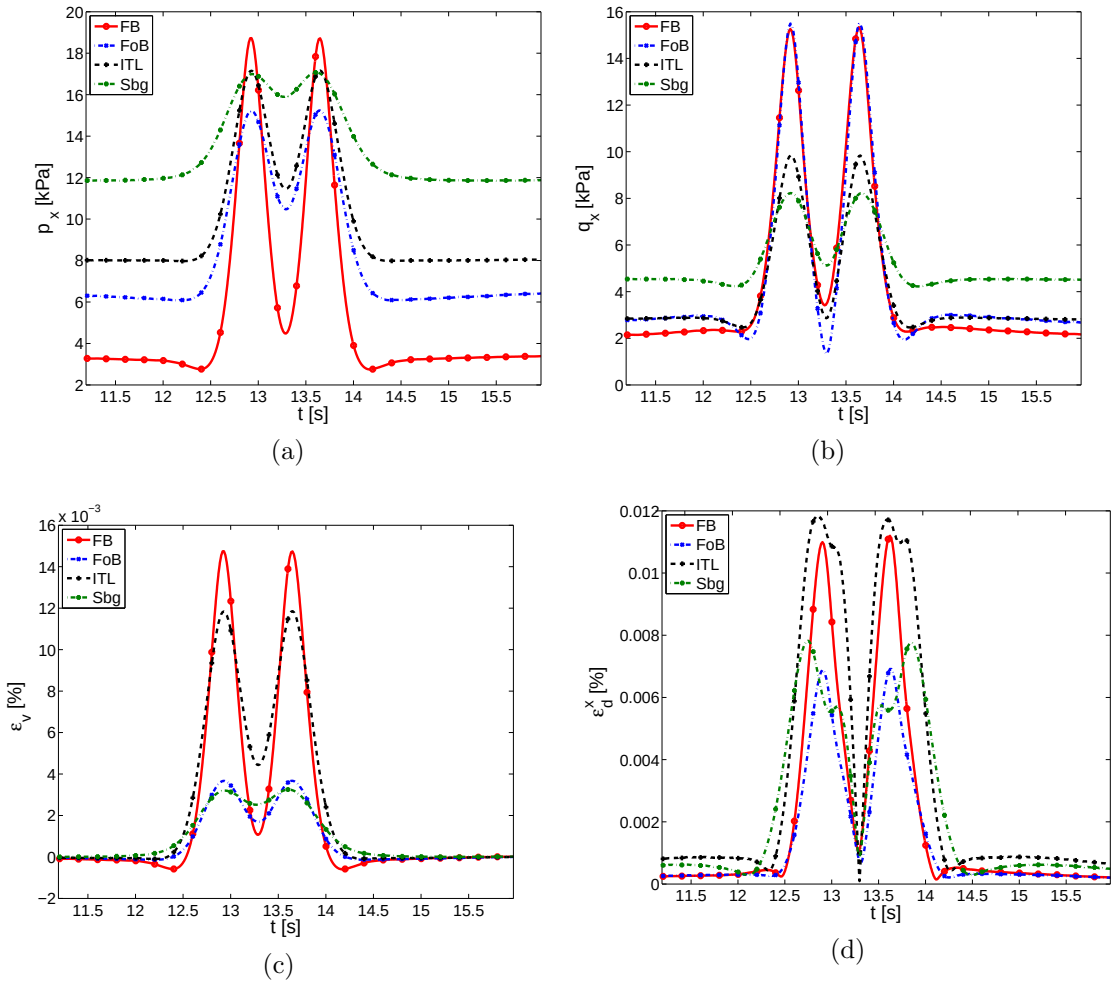

Figure 3.25: Time response of stress invariants on track layers. a) Mean stress (p_x); b) Deviatoric stress (q_x); c) Volumetric strain (ε_v); d) Deviatoric strain (ε_d^x). FB: Fresh ballast, FoB: Fouled ballast, ITL: Interlayer, Sbg: Subgrade.

case the differences are less pronounced. These differences were already discussed by Bodin (2001) on modeling aspects of the mechanical response of ballast on the track. However, Bodin (2001) provided a point of view of differences on stiffness between under sleeper and between sleeper ballast, without discussing the role of the stress path imposed by the load on different representative points of the ballast layer. At further depth, the discrete support characteristics are less important thus, do not lead to significant differences in the interlayer and the subgrade soil.

3.4.2 Influence of speed on the track response

In this section the influence of load speed on the considered railway track structure is assessed for speeds from 15 km/h to 270 km/h. Figures 3.27a and 3.27b show the increase on maximum vertical displacement and accelerations, normalized by the maximum value obtained at 15 km/h, respectively. The relative increase over the speed shows that the

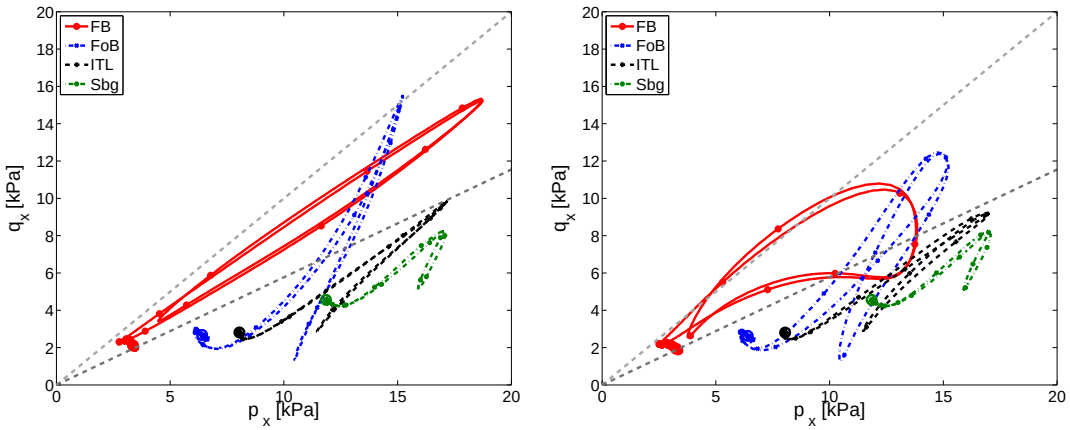

Figure 3.26: Stress paths at different materials for load at 15 km/h and stiff soil. FB: Fresh ballast, FoB: Fouled ballast, ITL: Interlayer, Sbg: Subgrade. Slopes of 30° and 45° are drawn in gray in order to better identify friction angle. a) Under the sleeper points; b) Between sleepers points.

maximum displacements are slightly affected by the increase of speed in the considered case, maximum values at 270 km/h are only 14% higher on the subgrade than the 15 km/h speed case. Maximum displacement at the rail level seems to be even less sensitive to the increse of speed. Accelerations, however, increase significantly as the speed of the moving load increases.

The influence of speed on vertical stress is shown in Figure 3.28a. Vertical stress increase is more pronounced in the subgrade than in the other layers, for a maximum increase of around 8% compared to the 15 km/h case. From the performed simulations,

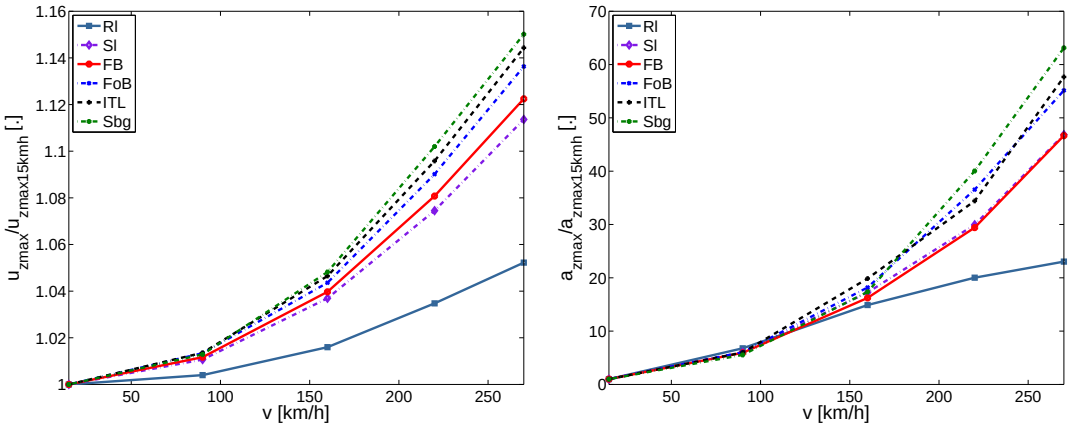

Figure 3.27: Normalized kinematic response of the track materials with increasing moving load speed. a) Vertical displacement (u_z); b) Vertical acceleration (a_z). Rl: Rail, Sl: Sleeper, FB: Fresh ballast, FoB: Fouled ballast, ITL: Interlayer, Sbg: Subgrade.

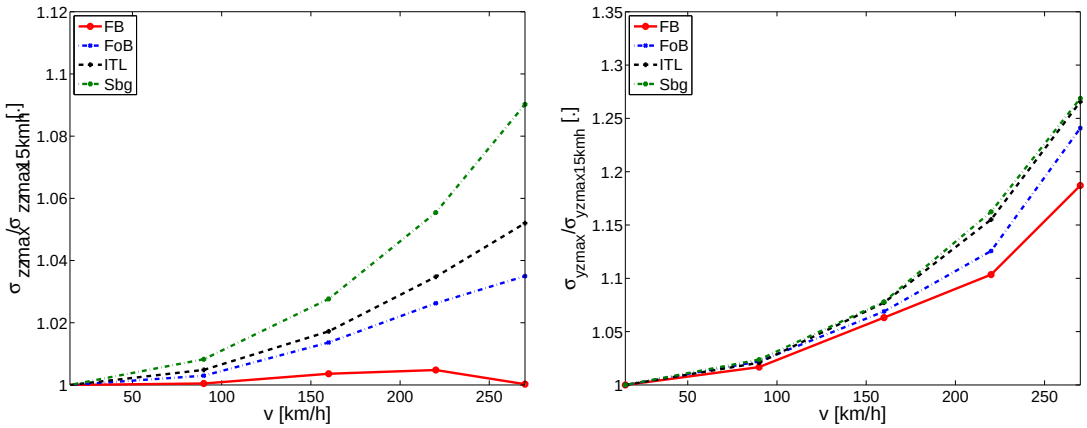

Figure 3.28: Normalized mechanical response of the track materials with increasing moving load speed. a) Vertical stress (σ_{zz}); b) Shear stress (σ_{yz}). FB: Fresh ballast, FoB: Fouled ballast, ITL: Interlayer, Sbg: Subgrade.

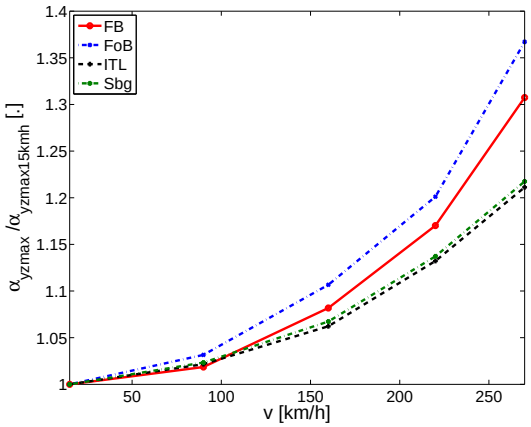

Figure 3.29: Maximum rotation angle (α_{yz}) of principal stress axes with increasing moving load speed. FB: Fresh ballast, FoB: Fouled ballast, ITL: Interlayer, Sbg: Subgrade.

the fresh ballast layer does not present any increase in vertical stress with the load speed increase. Shear stress variation with speed is presented in Figure 3.28b. In this case, a more notable increase is observed for all layers. This result endorses the low increase of vertical displacements and shows that the increase of speed has an effect more prononced on shear stress rather than on vertical stress. Increase of speed imposes thus higher values of shear stress, leading to higher principal stress rotation angles, which are presented in Figure 3.29. This is an interesting preliminarly result, as the principal stress rotation is usually related in the literature to higher plastic deformation. This last could be one of the mechanisms leading to higher values of track settlement observed on conventional lines when nominal speed is increased.

The invariants p_x and q_x do not give the same perspective of these results. Figures 3.30a and 3.30b show the influence of increasing speed on the maximum values of p_x

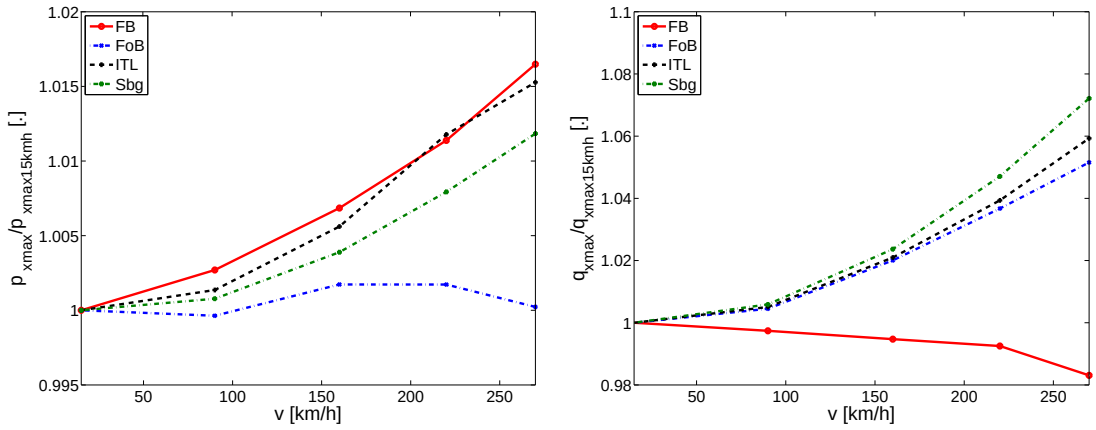

Figure 3.30: Normalized mechanical response of the track materials with increasing moving load speed. a) Mean stress (p_x); b) Deviatoric stress (q_x). FB: Fresh ballast, FoB: Fouled ballast, ITL: Interlayer, Sbg: Subgrade.

and q_x, respectively. The maximum mean stress p_x is quasi insensitive to increase of speed, in all layers, as maximum values increase at most of 1.5%. This increase could be neglected for pratical pourpuses or for calibration of laboratory test conditions reproducing different load speeds. Even if the deviatoric stress is more sensitive, the maximum observed increase is of around 8% on the subgrade. Interestingly, maximum deviatoric stress in the fresh ballast layer slightly decreases with increasing speed, which can be explained by the concurrent effect of increase of shear and vertical stress during the load passage.

From these results, load speed mainly influences the shear stress component developed in the materials during loading. and thus principal stress rotation angles. The mean stress is insensitive to load speed and the deviatoric response is influenced by the concurrent effects of increase on lateral and vertical stress.

3.4.3 Crossed influence of moving load speed and subgrade stiffness

A parametric study concerning the influence of the subgrade stiffness with increasing moving load speed is conducted. In order to be able to compare different temporal signals at different moving load speeds, the temporal axis is multiplied by speed of the considered moving load. Considering the convective axis t.v [m] is a direct method to superpose signals at different speeds. Figure 3.31a presents the rail vertical displacement (u_z) during loading. Increasing speed leads to higher vertical displacements on soft soils rather than stiff soils, the train speed not affecting the vertical displacement profile in this case. Figure 3.31b shows the sleeper vertical acceleration (a_z) during loading. Although soft soils condition leads to higher accelerations, the observed increase in values can be mainly attributed to the moving load speed.

The influence of the subgrade stiffness on the stress and strain characteristics of the fresh ballast is presented in Figures 3.32 and 3.33. Volumetric characteristics (p_x and

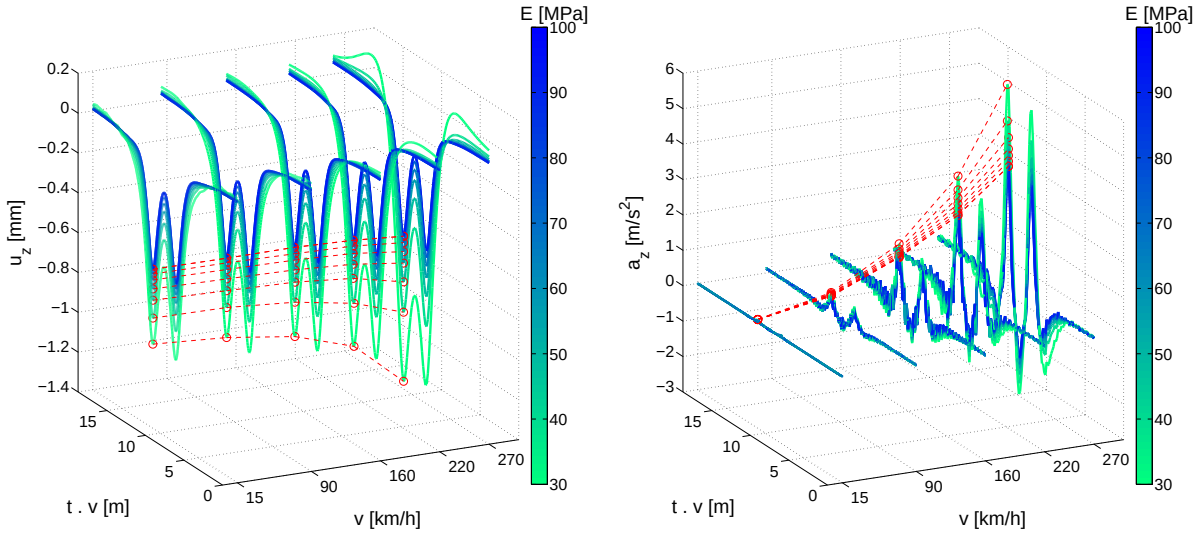

(a) (b)

Figure 3.31: Influence of subgrade stiffness and moving load speed on the kinematic response of the track materials. a) Rail vertical displacement (u_z); b) Sleeper vertical acceleration (a_z).

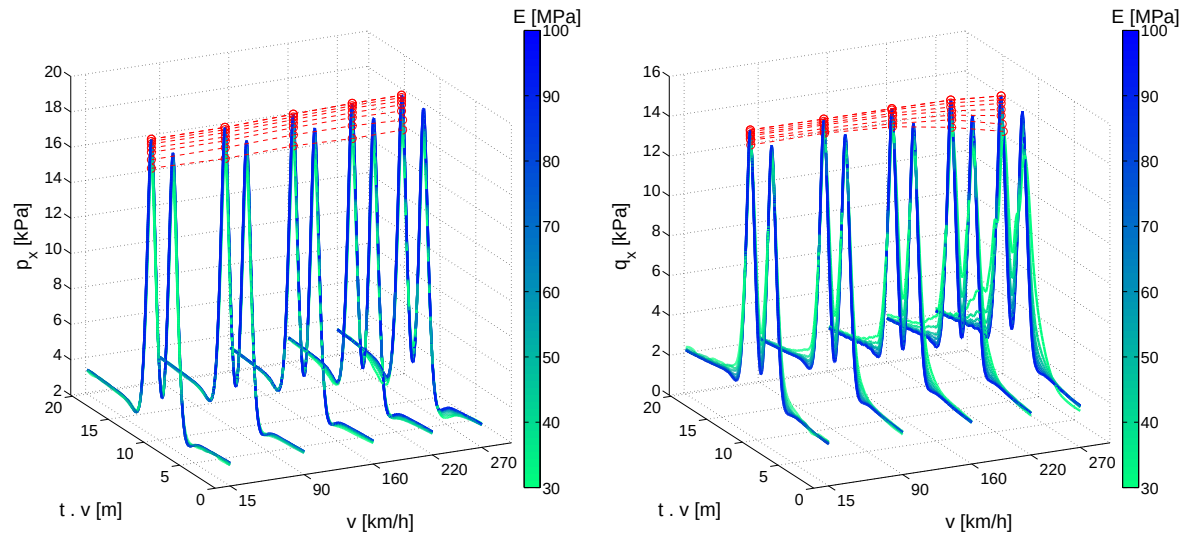

(a) (b)

Figure 3.32: Influence of subgrade stiffness and moving load speed on the stress response of the fresh ballast layer. a) Mean stress (p_x); b) Deviatoric stress (q_x).

ε_v) are insensitive to variations on moving load speed and subgrade stiffness, while q_x decreases and ε_d^x increases with increasing speed and decreasing subgrade stiffness. On the other materials, increase in load speed leads to higher deviatoric stress and strain, the effect being more pronounced for low stiffness. Deviatoric stress and strain in the subgrade are presented in Figure 3.34. While maximum deviatoric stress increases slightly from 15

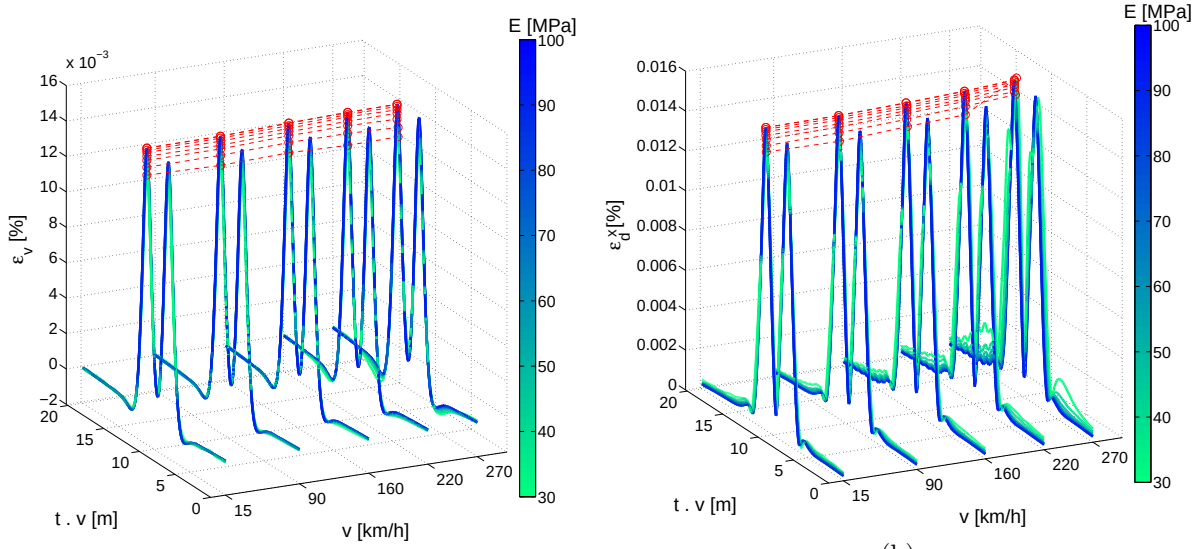

(a) (b)

Figure 3.33: Influence of subgrade stiffness and moving load speed on the strain response of the fresh ballast layer. a) Volumetric strain (ε_v); b) Deviatoric strain (ε_d^x).

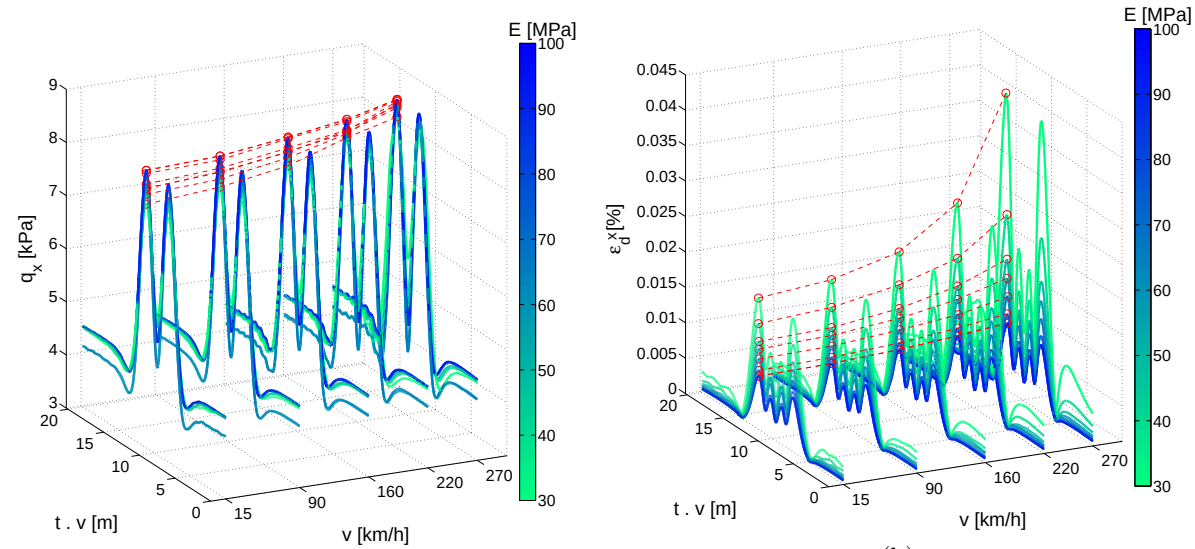

(a) (b)

Figure 3.34: Influence of subgrade stiffness and moving load speed on the deviatoric response of the subgrade soil. a) Deviatoric stress (q_x); b) Deviatoric strain (ε_d^x).

km/h to 270 km/h, maximum deviatoric strain values increase more than two times in the case of low stiffness of the subgrade soil.

3.4.3.1 Influence of speed and subgrade stiffness on rotation of the principal stress axes

As discussed in Section 2.4, rotation of the principal stress axes is a key issue on the deformation characteristics of soil materials. In this section, some insights on the stress rotation characteristics of different materials is discussed, and the role of the subgrade stiffness in this case is assessed. Figures 3.35a and 3.35b present the rotation stress angle (α_{yz}) as a function of the deviatoric and the mean stresses for points under the sleeper at the fresh ballast layer, for both soft and stiff subgrades. The projections of each two variables from the 3D representation is also presented in the figures in order to facilitate the comprehension of the described 3D path. Some of the key features already presented are once again observed: low influence of speed at stiff subgrades, low variation of maximum p_x with increasing speed, reduction of maximum q_x with increasing speed for soft soils and increase of maximum rotation angles with increasing speed also for soft soils. These variations result from a change in the imposed stress path in the (p_x, q_x) plane and in the curve characteristics in the (α_{yz}, q_x) plane. The maximum obtained rotation angle values are of 15° for stiff soils and as high as 30° for soft soils for the 270 km/h case.

Between sleeper points in the fresh ballast layer are also verified. As previously discussed, they are submitted to a different stress path as the loading characteristics are essentially different from under sleeper points. Figure 3.36 presents the results for soft and stiff soils in this case. Rotation angles α_{yz} are higher for points between sleepers than under the sleeper (Figure 3.35). Moreover, the differences on deviatoric stress on positive and negative values of α_{yz} are more pronounced, as the characteristic stress path is different from the under sleeper case. The maximum obtained values of α_{yz} are in this case of 30° for the stiff soil case and as high as 40° for the soft soil case.

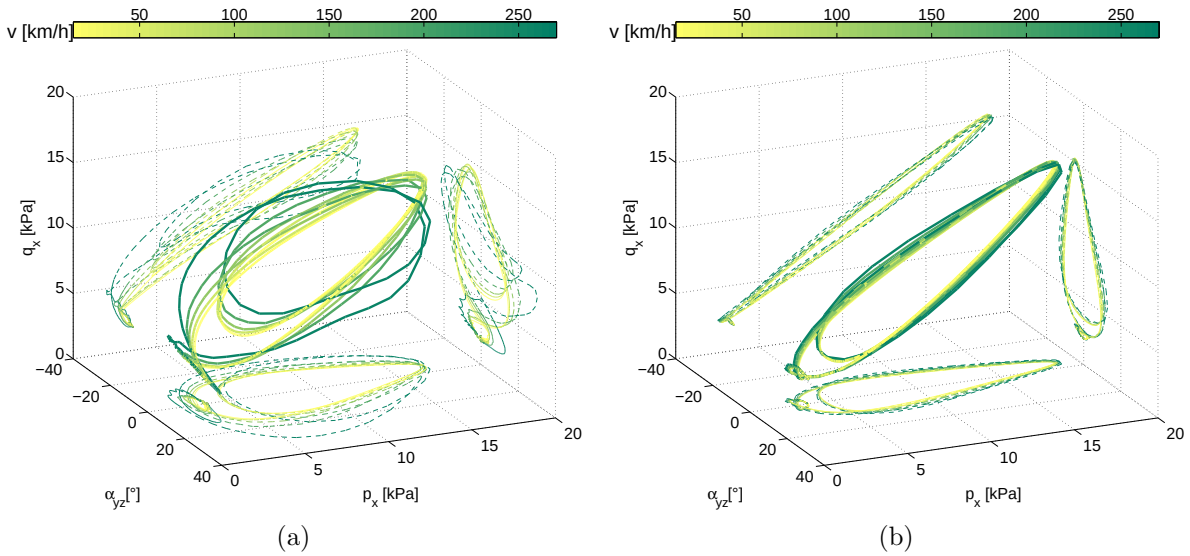

Figure 3.35: Rotation of the principal stress axes at the for points at the fresh ballast layer under the sleeper as a function of both deviatoric and mean stresses. a) Soft soil; b) Stiff soil.

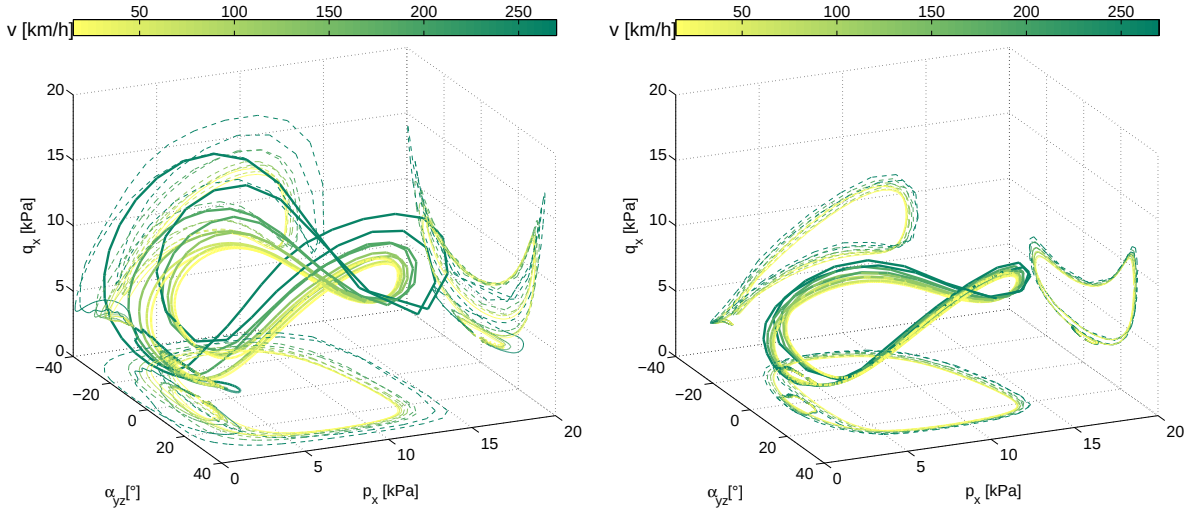

Figure 3.36: Rotation of the principal stress axes for points at the fresh ballast layer between sleepers as a function of both deviatoric and mean stresses. a) Soft soil; b) Stiff soil.

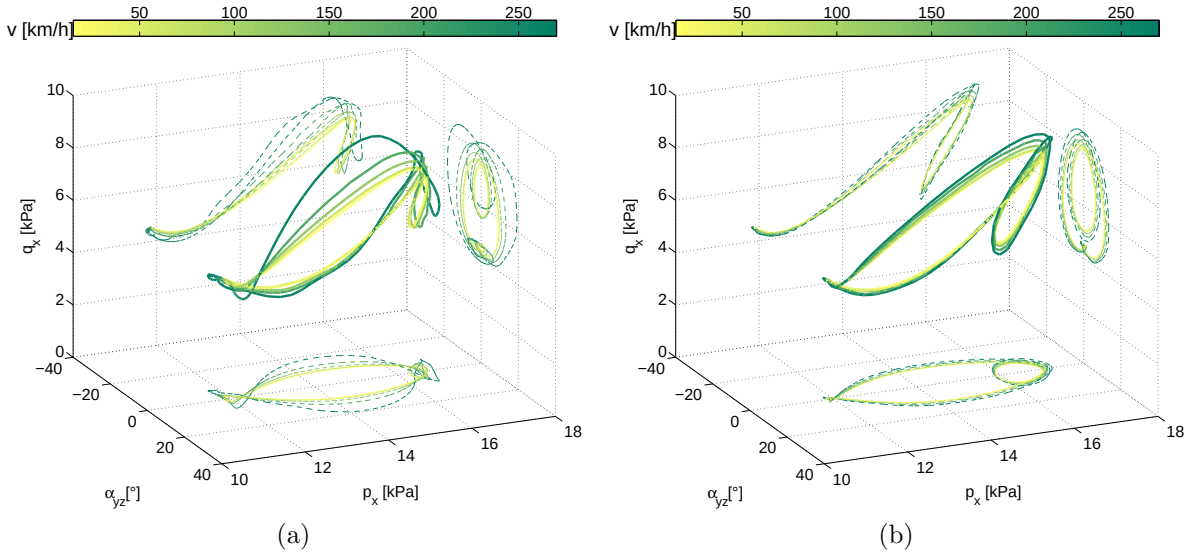

Figure 3.37: Rotation of the principal stress axes (α_{yz}) at the subgrade as a function of both deviatoric and mean stresses. a) Soft soil; b) Stiff soil.

At the subgrade level, the influence of the smaller reduction in p_x compared to q_x between axles characterizes the upper circles in the (α_{yz}, p_x) and (α_{yz}, q_x) planes. From the obtained results, the influence of speed on soft soils is to impose higher slopes in the (q_x, p_x) plane, characterizing as an anticlockwise rotation around its initial value. Maximum rotation angle is 15° for all cases except the soft soil at 270 km/h, for which 20° is obtained.

3.5 Concluding remarks

The main aspects of the numerical model used in this work are presented and discussed in this chapter. Mechanical and geometrical parameters representing a conventional railway line are used. A 2D finite element model with a modified width plane strain condition is proposed. Width calibration by matching the vertical strain of the 2D and 3D models subjected to static loading is performed. This procedure leads to good approximations on vertical strain and displacements, but differences exist in both vertical stress and mainly shear stress. The 2D model is not capable of correctly defining the radiation condition existing in the 3D medium, as widths are constant at each depth. This is showed by the variations in the shear stress obtained for the static load condition. However, it is considered as a good approximation of the mechanical response in the (y, z) plane and it is certainly more adapted to perform stochastic calculations, as the computational cost is lower than the 3D model.

Domain size and discretization are verified by both static and dynamic considerations and tests. Absorbing boundary conditions based on a viscous elastic Kelvin-Voigt model and the paraxial approximation are implemented and their performance compared. For the linear elastic model, both presented comparable results in loaded points. Numerical damping on high frequencies is considered by using a particular set of parameters of the Newmark numerical scheme. A two-step loading strategy, composed on load initialization and speed initialization phases is proposed in order to reduce spurious wave generation in the model. All these aspects are the basis for the numerical model used in the following chapter. Some of them are rediscussed in Chapter 5, when the nonlinear numerical model is presented.

A first analysis of the mechanical response of the railway track model is made for a bogie passing at 15 km/h and discussed in terms of stress and strain invariants for a stiff subgrade soil. The role of the discrete support on load repartition over sleepers and stress in layers is assessed. It is then noted that under sleeper and between sleepers control points at the fresh ballast layer do not follow the same stress path. Principal stress axes rotation occurs as a natural consequence of shear stress in the layers caused by the moving load.

One of the studied aspects is the influence of load speed. It mainly affects the vertical acceleration levels and the maximum shear stress thus, the maximum principal stress axes rotation angle. However, this effect is less important in terms of stress invariants.

In addition, the subgrade stiffness influence is verified for different speeds and as expected, soft soils are more sensitive to moving load speed than stiff soils. Deviatoric stress and strains are more sensitive to variations in the subgrade stiffness than volumetric stress and strains. The coupled effect of volumetric and deviatoric stress at the principal stress axes rotation angle is verified for soft and stiff soils. Once again, different paths are obtained for ballast depending if under sleeper or between sleepers control points are considered. Between sleeper points are those presenting the highest values of rotation angle, specially when soft soils are considered. In this case, speed significantly affects the stress path and maximum rotation angles.

Four main conclusions are drawn from these results:

1. The importance of the discrete support on the ballast mechanical response. While

considerations from static load are mainly based on load repartition over sleepers, the discrete support also plays an important role in the moving load case, imposing different stress paths on materials depending on their position. This is an important aspect, as deformation characteristics of geomaterials are stress path dependent. With cycles, variations of the mechanical properties are expected to appear, as at each position a different stress path is mobilized.

2. It is also shown that materials are subjected to stress paths different from the one imposed by the triaxial apparatus (1/2 slope in the (p_x, q_x) plane). Assessing the long-term behavior in terms of settlement laws from cyclic loading using this device does not seem appropriate, as it is not representative of the imposed stress variations the track materials are subjected by the moving load.

3. The influence of the moving load speed and subgrade stiffness on the mechanical response of the track. From the model response, speed influences mainly shear stress and deviatoric stress and strain. In this work, no increase in load magnitude is considered with speed, as only the dynamic influence of speed is of interest and not the train-track dynamic interaction. In this sense, the volumetric response is seldom affected, as it depends more on the load magnitude than load speed.

4. Principal stress axes rotation is expected in moving load problems, as the shear stress component is related to the moving load speed. The obtained maximum values (between 15° and 40°) depend on the stress state of materials, the rotation angle being higher for the same shear stress for low vertical and lateral stresses. In the literature, the occurrence of principal stress axes rotation is often related to higher plastic strains when compared to stress paths not presenting this aspect, i.e. not presenting shear stress.

In the next chapter, the impact of stiffness variations of the different geomaterials on the track stiffness is discussed. A nonintrusive probabilistic framework is considered and spatial variability is modeled by the random field theory. These aspects give a close look on how stiffness variations are captured by the track stiffness measurement and the conducted global sensitivity analysis gives a better insight of the relative importance of each material in the global response.

Chapter 4

Impact of mechanical properties variability over the track response[1,2]

Contents

[1]Sections 4.2, 4.3 and 4.4 are based on the work that has been published by the author in Alves Fernandes, V., Lopez-Caballero, F., & Costa d'Aguiar, S. (2014). Probabilistic analysis of numerical simulated railway track global stiffness. *Computers and Geotechnics*, 55(1): 267-276.

[2]Most of the mathematical formulations used in this chapter are given in Appendix D and E. Only the necessary information is given in the present chapter in order to lighten the text.

4.1 Introduction

Railway track geomaterials present different scales of complexity and heterogeneity. From the coarse grained ballast material to the subgrade, grain size, geometry and nature vary not only between layers but also inside each layer. Random variations of the mechanical properties of railway materials have been verified both *in situ* and in laboratory tests (Shenton, 1984; Jacobsson, 1998; Baessler and Ruecker, 2003; Duong et al., 2014b, among others). Authors seem to agree that spatial variations of track properties may contribute to track degradation (Dahlberg, 2010; Steenbergen, 2013), although more *in situ* data in this sense seems necessary in order to consolidate this result.

Further insight in the impact of track properties variability on the mechanical response of the railway track is given in this chapter. A probabilistic nonintrusive methodology is considered and the influence of mechanical properties variations is studied in terms of different track stiffness measures and track layers settlement during train passage at different speeds.

This chapter is organized in five sections. A background on railway track models accounting for track properties' variability is given in the first section. Then, the probabilistic nonintrusive methodology used in this work is summarized. In the third section, the input data obtained from an extensive cone penetration test Panda campaign performed on a classical line by SNCF is discussed. Hypothesis of how to link the cone resistance to the Young's Modulus are presented.

The fourth section is devoted to main results regarding track global stiffness as measured by a point load force, either with spatial variability or not. Global sensitivity analysis is performed and conclusions are drawn regarding model hypothesis and mechanical properties of each layer. These results are further compared to those obtained from high-speed line parameters. The influence of rail pads variability on the global analysis is also assessed on a parametric basis. Finally, the influence of the deterministic rail bending stiffness on the obtained values is assessed by means of the analytical solution proposed by Fryba (1972) of a beam resting on an elastic foundation subjected to moving loads. The speed influence on the track global stiffness as observed by a train bogie is discussed in the fifth section. The impact of the different boundary solutions implemented in the model and discussed in Chapter 3 is assessed and some conclusions are drawn in terms of modeling characteristics. Final remarks are presented in the last section.

4.2 Probabilistic nonintrusive methodology

A probabilistic nonintrusive methodology is applied in this work in order to characterize the mechanical response of the railway track. This approach is largely used on risk analysis for different scientific and industrial domains (Sudret, 2007; Helton et al., 2006, among others). It is a robust and versatile method, as it allows to keep the model description in a classical deterministic way, and concentrate the uncertainties in input variables and their influence on the output variability. It can be presented as in Figure 4.1 (adapted from Sudret, 2007). Phase A consists on obtaining a numerical model which correctly reproduces the physical phenomena in question. This may be, in some cases, a simplified

numerical model (or surrogate model) which was previously compared and validated with a more complex model or existing data. The model is often already available from previous developments. Phase B consists on obtaining a full probabilistic description of the input variables, in terms either of random variables or random fields if a spatial description is available or needed. This probabilistic description may be obtained either by available data (*in situ* or laboratory test), or from expert analysis and previous experience. This step is a crucial one for the probabilistic analysis. Results of numerical simulations will depend strongly on the input variability and correlations that may exist between them. Once this probabilistic description is obtained, Phase C consists on propagating the input's uncertainties through the model, in order to estimate a certain quantity of interest's variability. Moreover, failure analysis may be conducted based on existing or proposed failure thresholds. Finally, conducting both local and global sensitivity analysis may reveal which inputs impact the most the quantity of interest's variability. In this case, the sources of uncertainty may be reduced to only those that play an important role on the quantity of interest's variability.

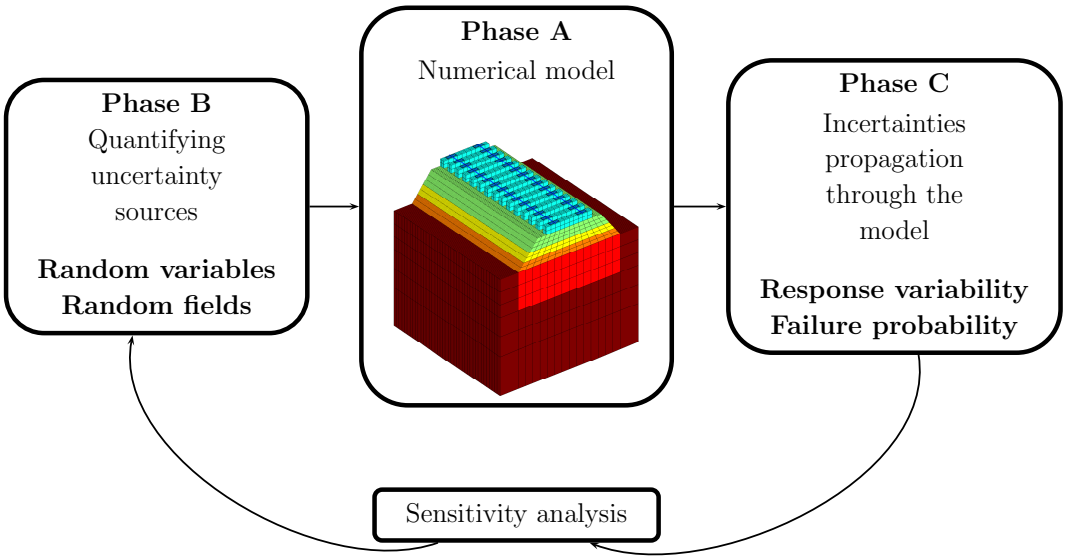

Figure 4.1: Nonintrusive methodology (adapted from Sudret, 2007).

4.3 Probabilistic characterization of materials' stiffness

The characterization of the railway track layers' stiffness in classical lines using the dynamic cone penetration test Panda (Gourvès, 1991) has become a standard procedure in France since 2009. These tests are usually coupled with a geoendoscopic analysis, which consists in passing a camera through the bore-holes obtained from the Panda tests. A quantitative characterization of material's resistance is obtained from the dynamic cone resistance measure (q_d) and a full qualitative characterization of the soil nature is obtained from the geondoscopic images. These tests are prescribed previously to renewal track works, as different useful engineering parameters can be estimated, such as layers thickness, soil nature and water presence (useful if the soil presents a poor drainage capacity and when a drainage system should be installed). The Panda test and adjacent parameters are described in more details in Appendix F.

In this work, *in situ* data coming from a conventional railway line (used by both regional trains and high speed trains at reduced speeds) is considered. Figure 4.2 presents a global scheme of a conventional line in France. Usually, conventional lines are composed by three layers, from top to bottom: fresh ballast, fouled ballast and the interlayer. The interlayer layer is composed of crushed ballast grains and soil fines (Trinh et al., 2012), which was not initially built but was created due to repeated loading over the years. In many classical lines the subgrade is the natural soil already in place when the track was built.

The Panda tests used in this work were made at irregular distances, from 30 m to 600 m along the track, in order to characterize more than 60 km of the railway track. Measures were made indistinctly on either the left and right side or in the middle of the track. The mean thickness values obtained for the fresh ballast, fouled ballast and interlayer were 25 cm, 15 cm, 20 cm, respectively. Interlayer and subgrade were identified as sandy material by the geoendoscopic analysis.

From these tests, a statistical description of the dynamic cone resistance is made under the hypothesis of invariance of each soil layer on the longitudinal direction. This hypothesis holds as a first approach to verify the influence of mechanical properties variability on the railway track response.

The empirical histograms obtained are presented in Figure 4.3. The total number of Panda tests considered on the analysis is presented in Table 4.1. All four layer were not always observed at each test. It is noted that the coefficient of variation is particularly high for the fresh ballast layer, as it is composed of a highly coarsed granular material. Interlayer layer also presents a high coefficient of variation, as it is a very heterogeneous material. Nevertheless, all four layers present coefficients of variation higher than 40%, which endorse with the strong variability encountered on geomaterials. The Kolmogorov-Sminorv test was carried out for each empirical distribution and the lognormal probability distribution was accepted for all layers with a 5% level of rejecting the null hypothesis.

Even if the dynamic cone resistance (q_d) is used to evaluate *in situ* soil strength, soil mechanical behavior parameters are needed in order to carry out numerical simulations. In this sense, researchers have worked on characterizing empirical relations between useful

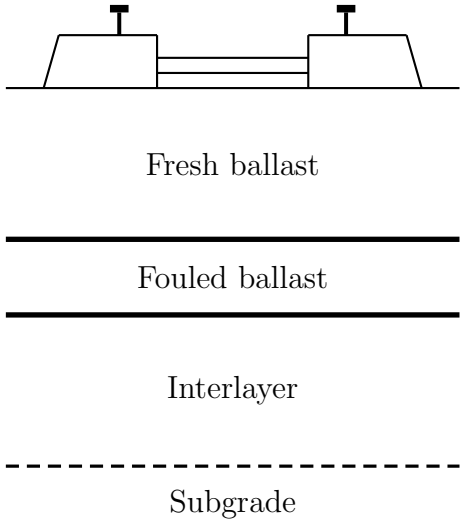

Figure 4.2: Material layers in a conventional railway line in France (adapted from Trinh et al., 2012).

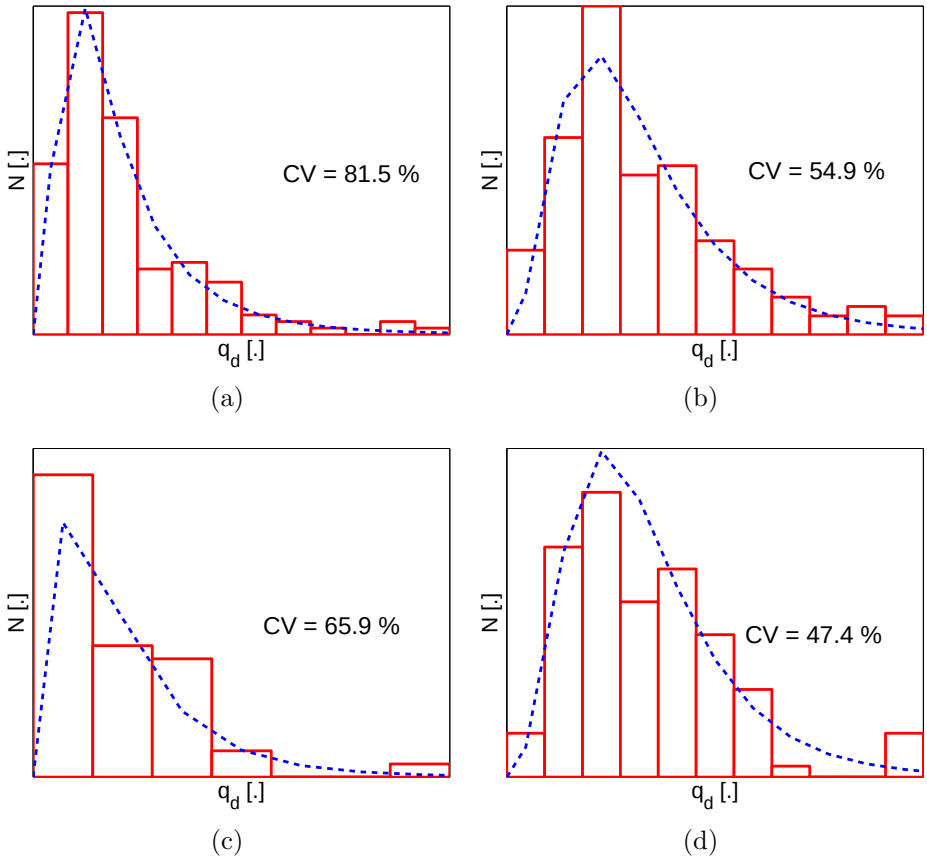

Figure 4.3: Histograms of q_d for the four layers. a) Fresh ballast; b) Fouled ballast; c) Interlayer; d) Subgrade.

Layer	N° measurements
Fresh ballast	146
Fouled ballast	128
Interlayer	45
Subgrade	112

Table 4.1: Number of measurements for each layer.

mechanical parameters, as the California Bearing Ratio (CBR), the static cone penetration resistance, and the soil stiffness, among others. More on the different analytical and empirical relations between the Young's Modulus and the dynamic cone resistance are discussed in Appendix F. In this work fresh ballast and fouled ballast are considered as gravel/crushed stones material and the interlayer and subgrade follows their characterization obtained from the geondoscopic tests. The relations used are summarized in Equations 4.1 and 4.2.

Gravel/crushed stones (Chua, 1988):

$$E = 67.8 \cdot q_d^{0.55} \qquad [\text{MPa}] \tag{4.1}$$

Sand (Lunne et al., 1997):

$$\begin{aligned} E &= 4 \cdot q_d \qquad \forall q_d \leq 10 \qquad [\text{MPa}] \\ E &= 2 \cdot q_d + 20 \qquad \forall 10 \leq q_d \leq 50 \ [\text{MPa}] \end{aligned} \tag{4.2}$$

These relations are based on the secant modulus in order to account for the fact that the physical phenomenon taking place are of small "plastic deformation" and the deformation levels are beyond the elastic domain of the soils (i.e. $\varepsilon > 10^{-5}$). These assumptions are based on the numerical simulations presented in Chapter 3, which showed that soil experiments strains greater than the elastic limit. They are further discussed in Chapter 5, when the results from the nonlinear mechanical model are presented.

Applying these equations on the obtained distributions of cone resistance (q_d), the probabilistic description of the Young's Modulus for all layers in terms of its probability density function (pdf) is obtained (Figure 4.4). As Equation 4.1 is nonlinear, statistical moments of the q_d distributions of fresh and fouled ballast are not conserved by the transformation. These functions depend on the soil nature and in this sense they amplify the input data uncertainty, although this fact could not be taken into account on this study.

It must be pointed out, however, that empirical relations established in the literature must be applied with caution, as they were obtained for a particular set of conditions (initial stresses, loading path, soil nature). Moreover, these parameters are not always fully related (as the physical phenomena may not be the same), and uncertainty in obtaining these relations always exists. Nevertheless, this approach is considered as a relevant one

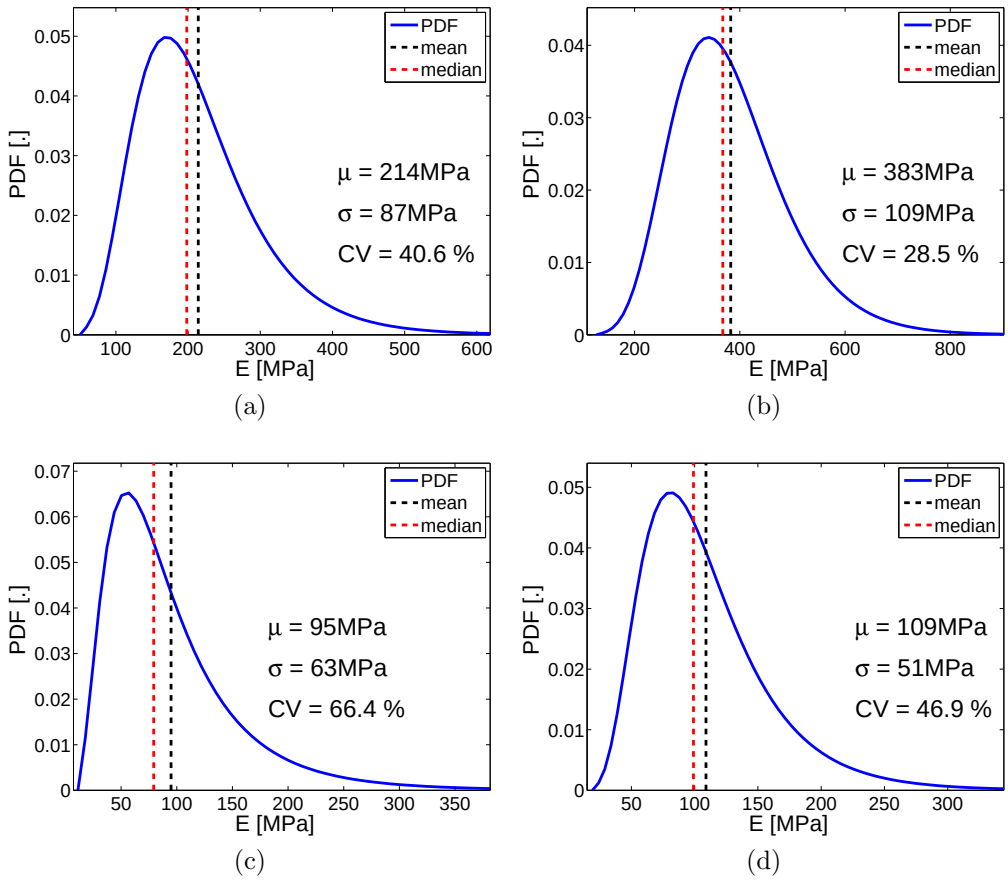

Figure 4.4: Probability density function (pdf) of the Young Modulus E for the four layers. a) Fresh ballast; b) Fouled ballast; c) Interlayer; d) Subgrade.

as it permits to characterize the variability on the Young's Modulus of track materials directly from *in situ* tests.

The spatial variations are modeled by an independent and invariant random fields associated with each material. More details on the stochastic methods used in this work are discussed in the Appendix D. No correlation structure was identified from the test results, as they were performed on long distances thus considered in this analysis as independent. A theoretical correlation function is imposed in order to verify the influence of the correlation structure on the variability of the response. Random fields are generated by the decomposition of the correlation structure. The squared exponential autocorrelation function (Equation 4.3) was chosen to describe the correlation structure of the random field.

$$\rho_{ij}(\tau) = \exp\left(-\pi\frac{\tau_y^2}{\theta_y^2} - \pi\frac{\tau_z^2}{\theta_z^2}\right) \tag{4.3}$$

The correlation lengths θ_y and θ_z in Equation 4.3 are a measure of the common influence between two points distant of $\tau_y = y_i - y_j$ and $\tau_z = z_i - z_j$, respectively, y being the longitudinal axis and z the vertical axis of the railway track. In this chapter, different

correlation lengths θ_y are studied. The limiting case $\theta_y = \infty$ is also considered in order to model when no spatial variability is present. Thus, the considered random field being fully described by the first marginal distribution and being equivalent to a random variable formulation. This approach is useful for the sensitivity analysis performed in Section 4.4.4.

The correlation length θ_z is considered as infinite on the vertical direction, so each column of soil at the same layer assumes the same value of elastic modulus at each simulation. This hypothesis holds as the width of track layers is much smaller than track length. In the case of the subgrade, the same assumption is maintained, as only the variability over the track length is of interest rather than over layer's width. Each layer is assumed to be independent of each other, although the presented formulation can take into account correlated random fields.

4.4 Variability of track global stiffness

In this section the track global stiffness measure k is studied using the proposed numerical model. A moving force of magnitude F_z=100 kN at constant speed v=15 km/h is applied on the track, following the characteristics of the EMW vehicle discussed in Chapter 2. The track global stiffness (k) is then defined as being the vertical force applied by the wheel on the rail (F_z) over the rail vertical displacement (u_z) at the point of the applied force, $k = F_z/u_z$. Although being a local measure, it is expected to give an insight of the complete structure's response as the track structure distributes the wheel load over several sleepers.

The followed methodology in this section is: first, a deterministic case is defined and the railway track global stiffness k_{det} is compared to one obtained when random fields have no spatial variability (i.e. $\theta_y = \infty$). Then the impact of the spatial variability and inhomogeneities (i.e. $\theta_y < \infty$) existing in track geomaterials is taken into account and their influence is assessed by comparing it to the homogeneous case. The adopted simulation scheme/procedure is the following:

1. A given value of cone resistance (q_d) is considered for each layer at each finite element. These may be all assume the same value ($\theta_y = \infty$) along y or be dependent upon the position y along the railway track ($\theta_y < \infty$). In all cases cone resistance values are the same for any depth, in the same layer, at a given position y ($\theta_z = \infty$).

2. Young's Modulus (E) is obtained from the cone resistance (q_d) from the relationship functions presented on Section 4.3. Their values are used on numerical calculations but only the cone resistance field at each layer is characterized probabilistically. In this sense the cone resistance field is subjected to linear or nonlinear deterministic transformation in order to obtain the Young's Modulus, which is used on the numerical model.

3. The railway track global stiffness at each position along the track (y) is obtained from each calculation of the numerical model.

4. Statistical analysis of the results is performed.

The numerical model used in this section has the same geometrical characteristics as the one discussed in Section 3.4. The full track system is composed of rail, pads, sleepers, unconfined ballast between sleepers and the four identified layers (fresh and fouled ballast, interlayer and subgrade soil). The model is composed of 25468 nodes, 850 beam elements for the rail and 23982 4-node bilinear qudrilateral elements for the track infrastructure. Track mesh is 24m long, modeling 40 sleepers bay. Linear elastic mechanical behavior is considered for all materials (i.e. solid and structural ones). The mesh is kept the same on all simulations in this section in order to prevent variabilities due to the numerical procedure. Dirichlet boundary condition is imposed on the normal direction to boundaries (i.e. $u_y = 0$ over lateral boundaries and $u_z = 0$ over bottom boundary). Track is loaded from 6m to 18m in order to avoid boundary effects.

4.4.1 Random variables

As recalled before, the deterministic case is defined by considering only the mean values of the cone resistance (q_d) at each layer. A comparative result of the deterministic case and 500 Monte Carlo simulations of the random fields with no spatial variability is given in Figure 4.5. Rails, pads, sleepers and unconfined ballast are kept deterministic.

Results of the railway track stiffness random field are presented between 8 m and 17 m. The sleeper's discrete support is well observed from both the deterministic and probabilistic simulations. In this sense, depending upon the position along the track (considering over sleeper or between sleepers) the value of k is not the same. The obtained track stiffness random field is thus nonhomogeneous, as its values depend on the sleeper positioning. So, although supposing homogeneity of input random fields, elastic mechanical behavior and perfectly horizontal layers, the geometry of the railway track impose a nonhomogeneous probabilistic result. Indexing the track stiffness random field in the relative position in the unitary cell simplifies the field to the homogeneous case, i.e. constant mean values.

As depicted in Figure 4.5a, k_{det} differs from the mean values of the random fields with no spatial variability case, which is a characteristic of nonlinear models. In the present case, the nonlinearity between the layers Young's Modulus and the track global stiffness (k) can be viewed as intrinsic of the modeled problem: beam vertically loaded and discretely supported over a multilayer medium. Although the degree of nonlinearity can be considered small, as the obtained values are close, this result demonstrates that considering only the input mean values is not equivalent to mean values of the output.

In this work, as two transformations are considered (from cone resistance (q_d) to Young's Modulus (E) and then numerical simulation of railway track global stiffness k, as explained above), this effect is even more pronounced. However, when no homogeneities are considered, the same value of k is obtained at the same position of the railway track periodic cell. The case with spatial variability will further reveal the impact of the correlation length on the variance of the railway track global stiffness.

Figure 4.5b represents the coefficient of variation for both mean ($CV_{\hat{\mu}_k}$) and standard deviation ($CV_{\hat{\sigma}_k}$) estimators. It was considered that convergence was achieved when $CV_{\hat{\mu}_k}$ and $CV_{\hat{\sigma}_k}$ were smaller than 1%.

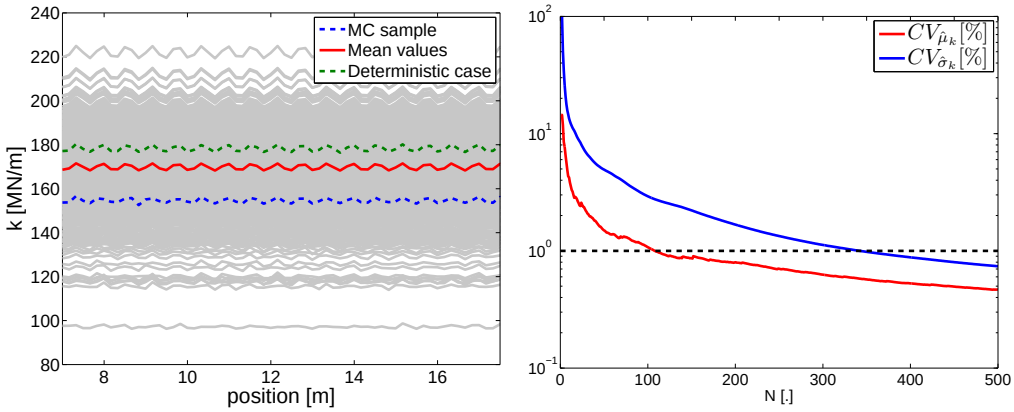

(a) (b)

Figure 4.5: Results of track global stiffness for the homogeneous case. a) Railway track global stiffness (k) computed at each position. Green dashed line represents the deterministic case (k_{det}), red solid line represents the mean values of the random fields case, blue dashed line represents a random sample and gray represent all obtained results; b) Evolution of the coefficient of variation of mean and standard deviation estimators.

4.4.2 Spatial variability

The first step when considering spatial variability is obtaining Young's Modulus random fields for each layer from cone resistance fields. Figure 4.6 represents 500 Monte Carlo samples of the Young's Modulus fields considering a correlation length of 0.5 m, where a random sample generated with a squared exponential autocorrelation function (Equation 4.3) is shown in blue solid line and all samples are represented on gray. These Young's Modulus fields are used as input parameters for finite element calculations.

The mechanical simulations' results for the cases θ_y=0.5 m and θ_y=5.0 m are presented in Figure 4.7. Convergence was verified and achieved under the same criteria proposed in the previous case. The blue dashed line represents one random sample, the red solid line is the spatial mean and gray lines represent all obtained results. It is observed that spatial variability may be captured by random samples, which can be interpreted as a possible value of the track stiffness for the considered part of the track.

Results regarding variance reduction for correlation lengths from 0.25 m to 5.0 m obtained by 500 Monte Carlo simulations are presented in Figure 4.8, as well as for the case where all points are fully correlated (i.e. random field with infinity correlation length). Dashed lines represents the minimum and maximum values obtained at each considered case. These variations are due mainly to the sleeper's presence: minimum values correspond to the position between sleepers and maximum values to the position over sleeper. The correlation length (θ_y) plays an important role on the variance of the global stiffness field. Figure 4.8a shows that the mean values of the field are almost unaffected with the reduction of the correlation length, excepted for small correlation lengths, when an increase is observed. The coefficient of variation (Figure 4.8b), reduces with the reduction of the correlation length. It can be noticed that random spatial variability reduces the variability of the output as a whole, as letting some variability to exist at each sample.

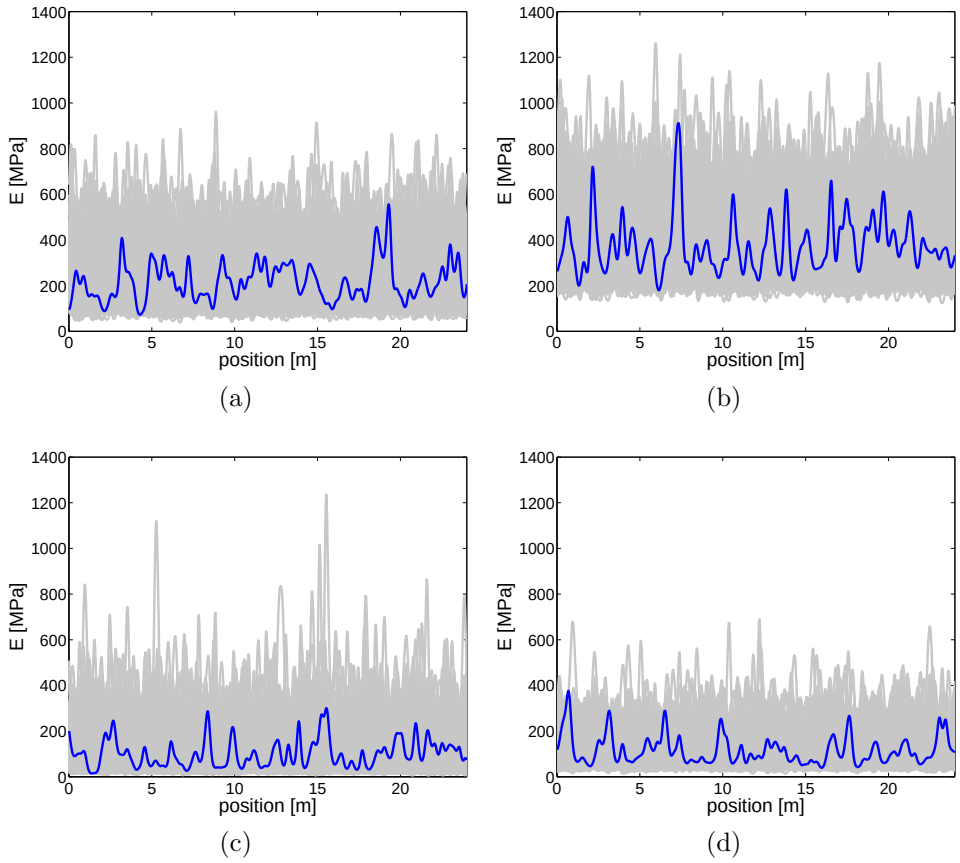

Figure 4.6: Young's Modulus stochastic fields, blue solid line represents one random sample of the field. Squared exponential autocorrelation function with correlation length θ_y=0.5 m. a) Fresh ballast; b) Fouled ballast; c) Interlayer; d) Subgrade.

In the railway context, this result is only half of the necessary information on how the track variability will impact the railway system. The vehicle dynamic behavior will certainly not be the same if spatial variability exists or not, and its response to the obtained global railway track stiffness fields must be assessed. However, this analysis was not conducted in this thesis and remains as a proposition for further works.

Another important point is that the variability on the global track stiffness is smaller than the input's one. Comparing the cone resistance coefficient of variation (shown in Figure 4.3, $47.0\% < CV < 81.5\%$) and the ones obtained for the railway track global stiffness (shown in Figure 4.8, $4.0\% < CV < 10.5\%$), it is observed that the spatial coefficient of variation is much smaller for all cases than the variability obtained on the measured data (and imposed on the model's input). Two main key factors are proposed as to explain this reduction. Firstly, the geometry of the system (specifically the force distribution over sleepers) would play a role on homogenizing the applied forces and then accounting for less variation for this global result. Secondly, the fact that the superstructure was kept deterministic during simulations reduced the output variations. Indeed, rail pads are the less stiff element on the track and they are responsible for much of the total rail deflection, as discussed in Section 3.4.1.

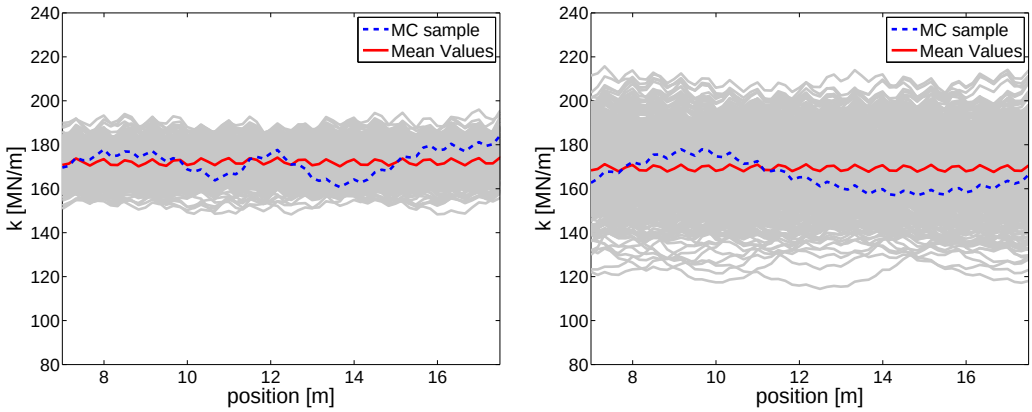

Figure 4.7: Track global stiffness k computed at each position. Blue dashed line represents a random sample, red solid line is the spatial mean and gray represent all obtained results. a) Correlation length of input fields θ_y=0.5 m; b) Correlation length of input fields θ_y=5.0 m.

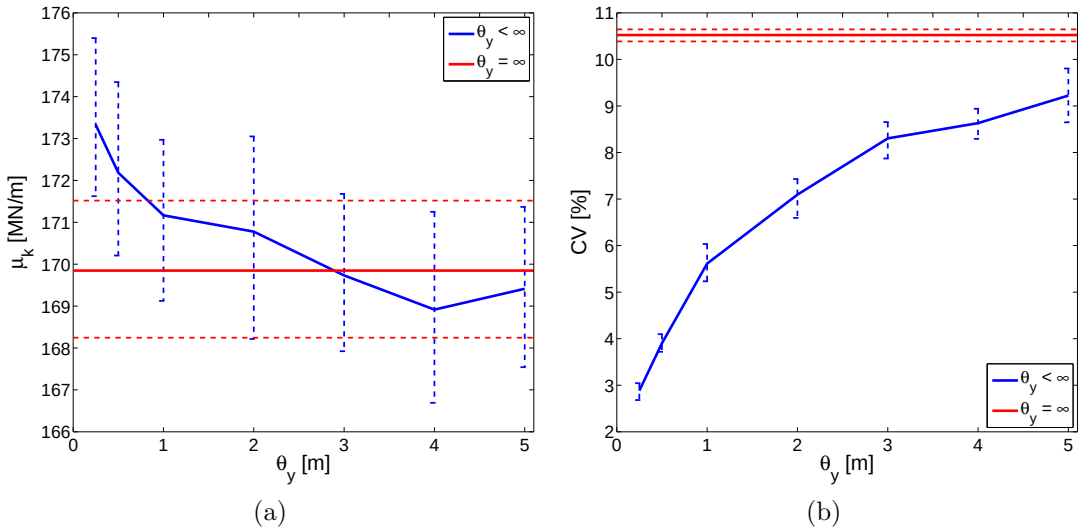

Figure 4.8: Variance reduction of track stiffness. Red line represents the fully correlated case and blue lines the different correlation lengths. Maximum and minimum obtained values are represented by dashed lines. a) Mean values (μ_k); b) Coefficient of variation (CV).

The homogenizing role of the force distribution over the sleepers can be further studied by the autocorrelation structure of the global track stiffness random field. In this case, it is not the variance reduction that is of interest but rather the importance of the railway structure on how the imposed correlation lengths on the input field will be measured by the track global stiffness. Figure 4.9 presents the autocorrelation coefficient (ρ) of the first considered position relative to the other positions. Higher input correlation lengths

(θ_y) lead to strongly correlated output fields, i.e. the global stiffness is self-correlated to a longer distance. In order to evaluate it more precisely, the global stiffness random field can also be characterized by its scale of fluctuation (l_c), which is obtained by the following expression (Vanmarcke, 1983):

$$l_c(x) = \int_{-\infty}^{\infty} R(x, x')dx \tag{4.4}$$

where $R(x, x')$ is the autocorrelation matrix of the random field. For the exponential autocorrelation function used in this work (Equation 4.3), the scale of fluctuation (l_c) and the correlation length (θ_y) represent the same quantity. In the following, the term scale of fluctuation will be used for the output field and correlation length for the input field.

The obtained values of l_c for the track global stiffness at each considered case are represented in Figure 4.10a. As the simulated track global stiffness field is finite, values near the boundaries must not be considered as they do cannot take into account both sides of the correlation structure. In this case smaller values are obtained as the integrand from 4.4 is finite. In order to keep the second-order hypothesis, this effect can be neglected starting the analysis from l_c meters from each boundary. Figure 4.10b represents the values of l_c using this methodology. Bars are plotted as to show minimum and maximum values obtained of the scale of fluctuation at each case. The unitary slope is also plotted in order to better verify the variations of l_c according to θ_y. As expected, the scale of fluctuation increases with increasing correlation length. As the correlation length (θ_y) reduces, a limiting value of 3 m is obtained, which corresponds to 5 sleepers bay. This result means that superstructures homogenizes the variability on the track layers in such a way that the global track stiffness field presents at least a scale of fluctuation equal to the distance on which the forces spreads over the structure. Moreover, the force spread over the structure is much related to the rail pad stiffness. Reducing rail pad stiffness increases the importance of the environing sleepers, which can in turn increase the limiting value of l_c of the track global stiffness field and probably change the slope of the curve in Figure 4.10b, although these hypothesis were not verified during this work.

From another point of view, Figure 4.10b also shows that a limiting value of θ_y is

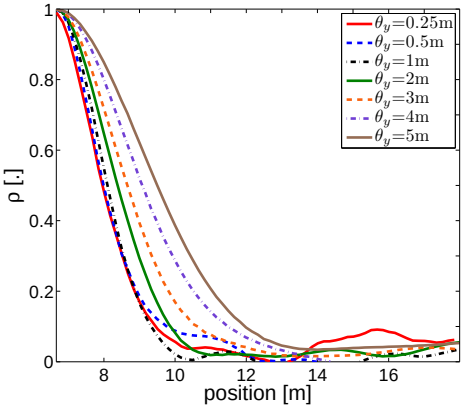

Figure 4.9: Autocorrelation coefficient (ρ) for the track global stiffness random field of the first position relative to the others.

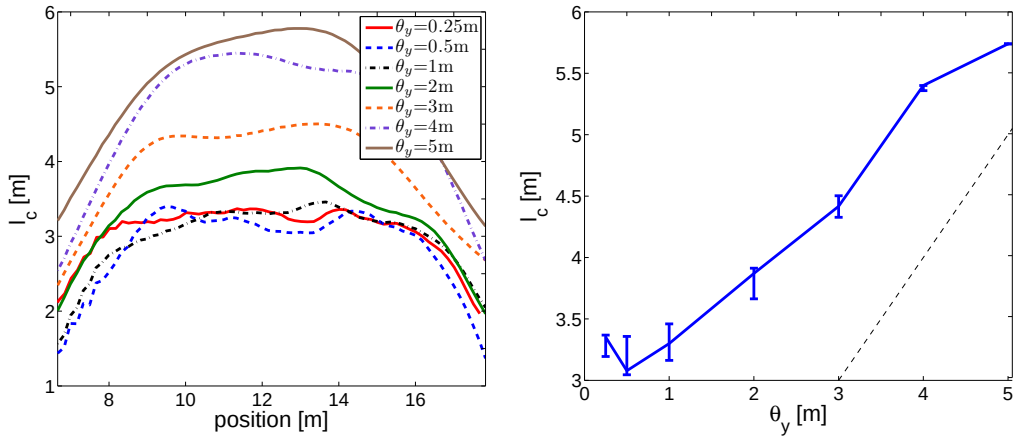

(a) (b)

Figure 4.10: Scale of fluctuation (l_c) of the global stiffness random field. a) Full representation of l_c according to the position; b) Increase of l_c with the correlation length of the input fields.

obtained, for which no further reduction of l_c is obtained. Although this value is not completely characterized in this work, it can be seen that variations of l_c are irelevant for θ_y <0.5 m. The work from Cottereau et al. (2011) showed that the scale of fluctuation of the ballast material is in the order of magnitude of the grain size, approximately 3 cm. From the presented results, such small correlation lengths cannot be measured by the track global stiffness. Considering random fields with such small correlation lengths seen to not be appropriate in this case, as a limiting distance higher than the grain size exists in the track global stiffness field.

4.4.3 Influence of the structural response on the output variability

In the case of homogeneous layers, the railway global stiffness values can be compared with the analytic solution of a beam resting on a Winkler foundation proposed by Fryba (1972), whose mathematical derivation is presented on Appendix B. In this sense, the structural influence of the rail bending stiffness on the calculated value of track global stiffness can be assessed.

An iterative procedure is used in order to solve the inverse problem posed by imposing a certain vertical displacement of the rail ($u_{z_{FEM}}$) under the moving load (calculated by the finite element model) and obtaining the corresponding stiffness of the Winkler foundation ($k_{Winkler}$). A first trial value of $k_{Winkler}$ is considered and as the response of the analytical solution is linear with respect to k, a fixed direction of convergence is determined. The maximum error (ϵ_k^{max}) is fixed at 10^{-6} m between the vertical displacement of the rail obtained from the analytical solution ($u_{z_{Winkler}}$) and the finite element model ($u_{z_{FEM}}$), $\epsilon_k = u_{z_{Winkler}} - u_{z_{FEM}}$. These operations are schematically represented in Figure 4.11. This procedure is repeated for each longitudinal position and each simulation.

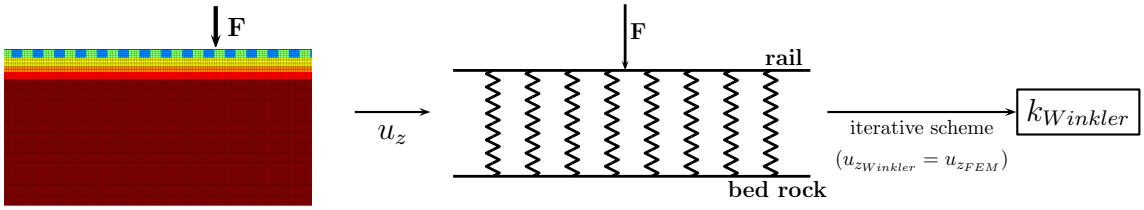

Figure 4.11: Schematic representation of the implemented algorithm for solving the inverse problem posed by imposing a vertical displacement under the load and obtaining the corresponding stiffness of the soil foundation.

The comparison of the track global stiffness and the soil stiffness calculated from the analytic solution of Fryba (1972) is presented in Figure 4.12 for stiff and soft soil, where $k_{Winkler}$ stands for stiffness of the Winkler foundation and k_{FEM} is the track global stiffness. The downscript $_{FEM}$ is used in this section in order to clearly differentiate the stiffness measurement value. It can be observed that the finite element model and the analytical solution present different displacement profiles, specially in the case of stiff soil (Figure 4.12b). Load distribution is more concentrated on the near sleepers in the case of the finite element model. This is mainly caused by the difference between the analytical approach and the finite element model concerning the discrete support. An idealized unique attach point is considered in the first, while in the finite element model different nodes link the rail to the rail pads and further to the sleeper. In the case of soft soils (Figure 4.12a), the rail deflection profiles are almost the same for both cases, even if positive vertical displacement of the rail is not obtained near the load in the finite element model. Indeed, once again, support conditions are the main reason for these differences. Therefore, the rail bending stiffness plays an important role on the measured value of the track global stiffness.

The results presented in Figure 4.8 are reanalyzed in the view of the analytical solu-

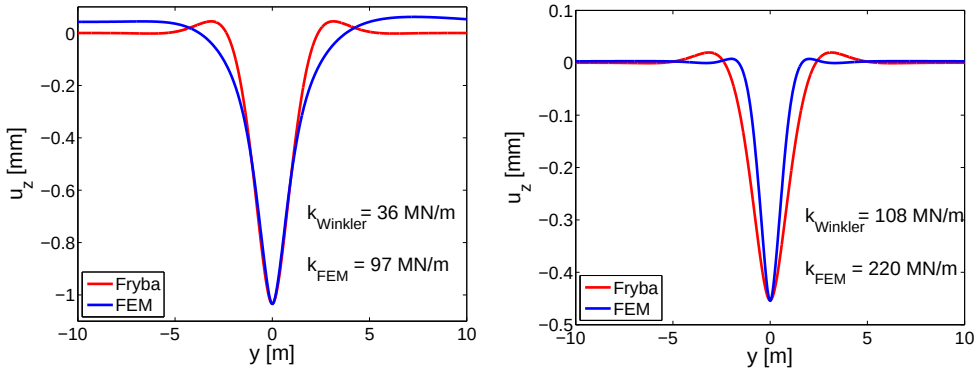

Figure 4.12: Comparison of the rail vertical displacement u_z obtained from the finite element calculation and the analytical solution of a beam over Winkler fondation proposed by Fryba (1972). a) Soft soil; b) Stiff soil.

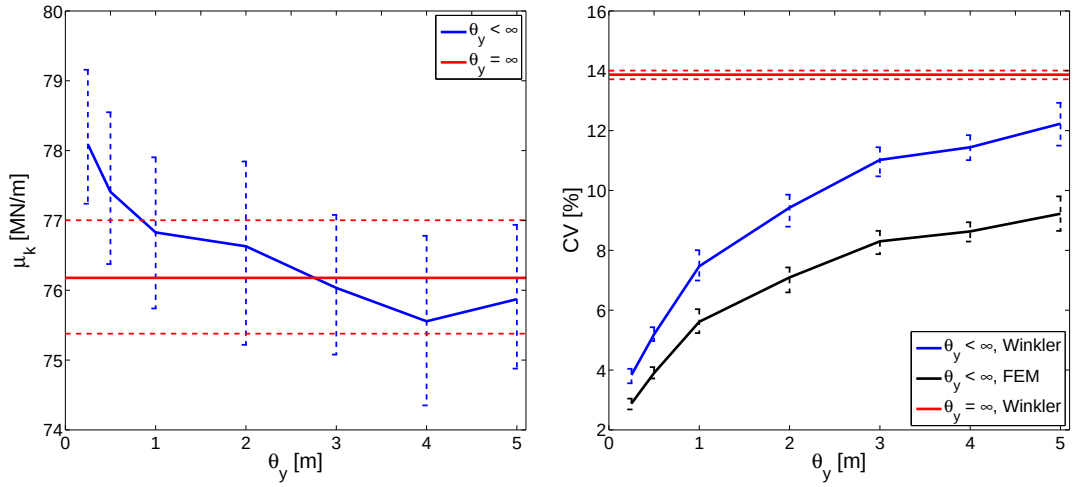

Figure 4.13: Variance reduction of track stiffness after considering rail bending by the analytical solution proposed by Fryba (1972). Red line represents the fully correlated case and blue lines the different correlation lengths. Maximum and minimum obtained values are represented by dashed lines. a) Mean values (μ_k); b) Coefficient of variation (CV).

tion in order to verify the importance in the variance reduction of the deterministic rail bending stiffness in Figure 4.13. It is important to point out that a local homogeneity hypothesis is made when dealing with spatial variability results, as the analytical solution is described only for constant values of $k_{Winkler}$. The curve showed in Figure 4.8b is re-plotted (downscript $_{FEM}$) in Figure 4.13b in order to compare the variance reduction in both cases. A constant relation of 0.75 is obtained when dividing the obtained coefficient of k_{FEM} and $k_{Winkler}$, i.e. $CV_{k_{FEM}}$=0.75$CV_{k_{Winkler}}$. The role of the rail bending can thus be viewed as constantly reducing the variability of the track materials measured by the track global stiffness.

An important aspect of the proposed analysis is to be able to study the relation between the proposed measure obtained from the numerical simulations and the possible applications of the track global stiffness in other railway engineering fields. Train-track interaction models used to study the train dynamic behavior on tracks usually relies on simplified models for the track mechanical behavior, such as the analytical solution discussed above. In this sense, transposing the track global stiffness measure presented in this work to such a model must take into account the rail bending stiffness.

4.4.4 Sensitivity analysis

In order to verify the importance of the variability of each layer on the variability of the railway track global stiffness, a global sensitivity analysis is performed using the Fourier Amplitude Sensitivity Test (FAST). The FAST method was developed only for the case of independent random variables, thus only the case with no spatial variability is assessed in this section (i.e. $\theta_y = \infty$). The method is based on a multidimensional

Fourier transform. Independent frequencies are assigned for each variable and a space-filling harmonic function is used in order to explore the space spanned by each variable. Cukier et al. (1973) showed that the the Fourier transform of the response can be used in order to estimate the first-order sensitivity indices (S_i) by calculating the contribution of each assigned frequency and its harmonics. More details on local and global sensitivity analysis and the FAST methodology are given in Appendix E. The generation frequencies (w_i) assigned for each random variable X are shown in Table 4.2. Input frequencies are taken as proposed by Saltelli et al. (1999).

Even if noninterference is assured for a minimum sample size of 281 points, 350 simulations are performed using the same set of parameters discussed in Section 4.3. Results are shown in Figures 4.14a and 4.14b. Figure 4.14a shows the power spectrum obtained from FAST and mainly the effect of the first harmonic of each assigned frequency to each random variable is observed. Figure 4.14b shows a histogram for the first-order sensitivity indices (S_i), and two main features must be highlighted: first of all, 98% the output variance may be explained by first order variances, which means that only 2% of the total variance is due to higher order effects imposed by the model; secondly, the variance of the subgrade is responsible for 82% of the variance of the global track stiffness. This is a direct result from the linear elastic hypothesis, as the subgrade layer is the largest layer on the multilayer system and it presents lower Young's Modulus values than fresh and crushed ballast layers (see Figure 4.4). Inversely, the fouled ballast layer do not contribute at all to the variance of the track global stiffness, as it is a thin very stiff layer. The fresh ballast is responsible for 4% and the interlayer for 12% of the output's total variance.

In order to further understand the influence of the subgrade variability on the track stiffness, the same analysis was performed but in this case considering a nonlinear elastic model for the subgrade. In this case, the following expression (Biarez and Hicher, 1994) is considered:

$$E(p') = E_{ref} \left(\frac{p'}{p_{ref}} \right)^{n_{el}} \tag{4.5}$$

where $E(p')$ is the Young's Modulus at a certain mean stress $p' = (\sigma_1 + \sigma_2 + \sigma_3)/3$. E_{ref} is the Young's Modulus obtained at a predefined mean stress p_{ref} and n_{el} is the degree of nonlinearity.

Indeed, according to expression 4.5, the Young's Modulus will increase as confining stress increases thus with increasing depth, as shown in Figure 4.15 for different nonlinear coefficients (n_{el}). It is considered that the Young's Modulus value is obtained at 20 cm depth from the interface with the interlayer, which represents the half of the mean values

Layer	w_i [Hz]
Fresh ballast	11
Fouled ballast	21
Interlayer	27
Subgrade	35

Table 4.2: Assigned frequencies for FAST.

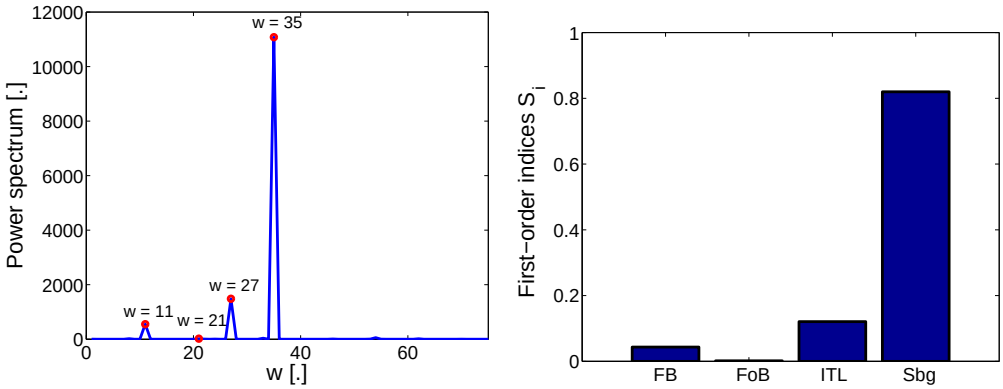

(a) (b)

Figure 4.14: Results of Global Sensitivity Analysis FAST of the railway track global stiffness (k). a) Power spectrum; b) First-order sensitivity indices (S_i). FB: Fresh Ballast, FoB: Fouled Ballast, ITL: Interlayer, Sbg: Subgrade.

of the maximum measured depth of the Panda test. Indeed, the cone penetration tests considered in this work usually stopped at after the measured interface between the interlayer and the subgrade. At this point, all lines crosses at the value of 109 MPa, which is the mean value obtained from the empirical relations used (Figure 4.4d). The case $n_{el} = 0$ is the linear elastic case previously addressed.

Figure 4.16 presents the results of the first-order sensitivity indices (S_i) for all considered models. Results of the linear elastic model are also presented as to compare with the nonlinear case. Subgrade's influence on the total variance reduces as the nonlinear coefficient (n_{el}) increases. However, it is still responsible for a large amount of the variability of the track stiffness. Interlayer as well as the fresh ballast layer present an increase on their respective importance as the nonlinear elasticity of the subgrade mechanical behavior increases, as a consequence of the their relative importance in the total vertical displacement of the rail. As for the linear elastic case, the total sum of the first-order index represents more than 95% of the total variance, although a slight reduction is observed as n_{el} increases.

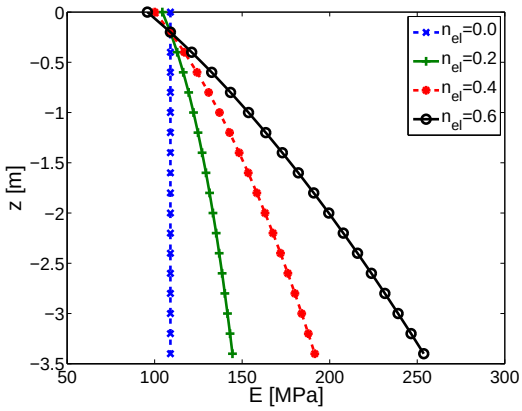

Figure 4.15: Evolution of Young's Modulus with depth.

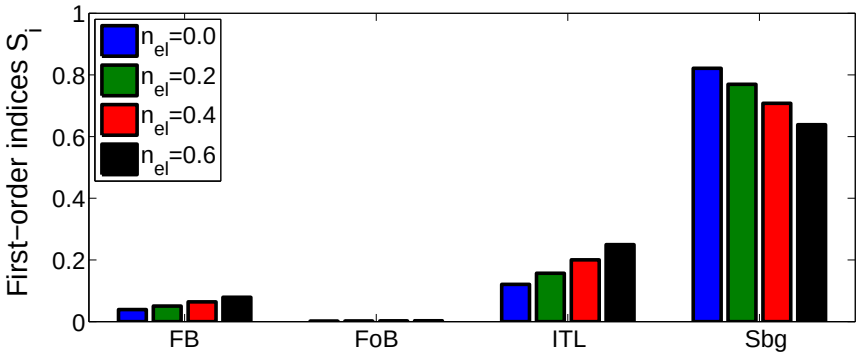

Figure 4.16: First-order sensitivity indices (S_i) for nonlinear elastic subgrade. FB: Fresh Ballast, FoB: Fouled Ballast, ITL: Interlayer, Sbg: Subgrade.

To summarize the sensitivity analysis performed on the proposed track structure, subgrade quality plays an important role on assuring good track quality, both in terms of its mechanical resistance and homogeneity. Reducing the uncertainty on the mechanical parameters of subgrade materials is a very important issue in order to correctly predict the railway track response, both on design and maintenance phases.

4.4.4.1 Influence of rail pads variability

Although the focus of this section is on the variability of mechanical properties of railway geomaterials on global track stiffness, rail pads play an important role on the mechanical response of the track measured at the rail on classical lines. As shown in Section 3.4.1, this component is responsible for 50% of all the measured vertical deflection of the rail in the case of stiff soils. Variability of the mechanical response of this component is expected to be lower than from granular materials, as they are industrially manufactured and quality control are easier to be implemented and achieved. However, some variability is to be expected, and in this section a parametric study of the impact of rail pads variability on the balance of first-order index is conducted, in the linear elastic case (i.e. n_{el}=0 in Equation 4.5).

Rail pads Young's Modulus are considered to follow a lognormal distribution whose mean value is unchanged from the previous analysis (μ_E=40 MPa), and the coefficient of variation is considered either of 5%, 10% or 20%. It is important to highlight that for each numerical simulation, all rail pads are considered as presenting the same mechanical properties, just as the railway track layers when no spatial variability is present. The considered case is then different from considering variable rail pads mechanical properties inside each numerical simulation, which is not treated in this work.

As shown in Figure 4.17, the rail pad variability impacts greatly the first-order indices balance observed in Figure 4.14b. The uncertainty in the rail pads Young's Modulus directly affects the track global stiffness, as the load balance between sleepers is directly affected when rail pads variability is introduced. As the uncertainty in the Young's Modulus grow, i.e. higher CV_{RP} values, the importance of rail pad on the track global stiffness variance increases. Quality control on rail pad production and correct characterization of their mechanical properties are then important aspects in order to reduce the influence of

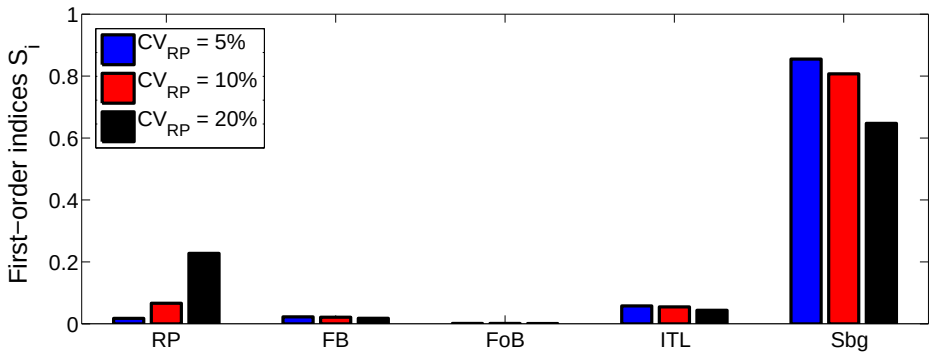

Figure 4.17: First-order sensitivity indices (S_i) with variable rail pad's properties. RP: Rail Pads, FB: Fresh Ballast, FoB: Fouled Ballast, ITL: Interlayer, Sbg: Subgrade.

rail pad uncertainty on the mechanical response of the track.

4.4.4.2 Comparative results with other track configurations

The aim of this analysis is to compare the conclusions of Section 4.4.4, which are based on a set of mechanical parameters adapted to a classical railway line, with the results obtained from a set of parameters describing the high-speed line between Brussels and Paris/London (Kouroussis et al., 2011c; Connolly et al., 2013). The Young's Modulus of all track layers are supposed to follow a lognormal distribution of mean value (μ_E) according to the values presented by the respective authors. Two different cases are considered depending on the hypothesis made on the coefficient of variation value:

- Case 1 (C1): The coefficient of variation is supposed to be the same as the one obtained in Section 4.3,
- Case 2 (C2): All layers are supposed to have the same coefficient of variation of 40%.

The mechanical and geometrical parameters of different materials are shown in Table 4.3. Moreover, case 2 provides a theoretical case where the differences on the variability characteristics of each layer are not considered thus, the role of the mechanical response of each layer on the railway track stiffness can be evaluated.

A sensitivity analysis of the numerical model for both Cases 1 and 2 is performed using the FAST methodology, considering linear elastic material behavior. The results for Case 1 are summarized in Figure 4.18, where the first-order sensitivity indices (S_i) are represented. In this case the first soil layer is responsible for 61% of the track stiffness variance. Ballast layer is responsible for 17% and the subgrade for 8.5% of the track stiffness variance. Subballast does not contribute to track stiffness variance, as it is very stiff compared to the other layers. The second soil layer contributes to 6.5% and the last soil layer marginally contributes to the track stiffness variance. These results agree entirely to those previously obtained on Section 4.4.4, i.e. variability encountered on the stiff layers of the railway track system contribute very little to the variability of the track stiffness and the subgrade soil is responsible for most of the measured variance. Moreover, the first meters of the subgrade soil play a major role on the output's variance, as it presents the

Component	Young's Modulus			Poisson's ratio	Mass density	Layer thickness
	μ_E[MPa]	CV_E^{C1}[.]	CV_E^{C2}[.]	ν [.]	ρ [kg/m^3]	Δh [m]
Rail	210.10^3	-	-	0.25	7900	-
Sleepers	30.10^3	-	-	0.40	2400	-
Ballast	100	0.41	0.40	0.35	1800	0.3
Subballast	300	0.28	0.40	0.35	2200	0.2
Subgrade	127	0.66	0.40	0.35	2100	0.5
Soil layer 1	129	0.47	0.40	0.30	1600	2.7
Soil layer 2	227	0.47	0.40	0.30	2000	3.9
Soil layer 3	659	0.47	0.40	0.30	2000	3.4

Table 4.3: Data obtained from Connolly et al. (2013) and adapted for the current analysis.

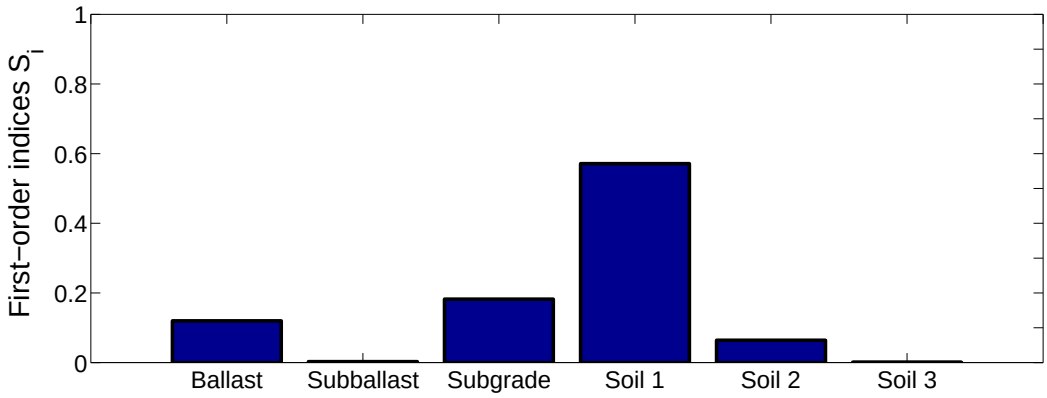

Figure 4.18: First-order sensitivity indices (S_i) for Case 1.

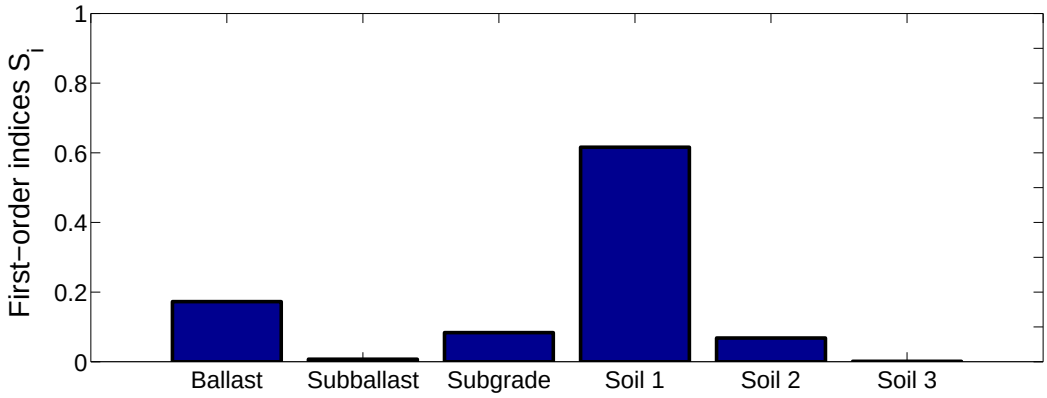

Figure 4.19: First-order sensitivity indices (S_i) for Case 2.

lower mechanical resistance and is subjected to higher deformation levels compared to the other subgrade soil layers.

Case 2 results are summarized in Figure 4.19. In this case, reduction of 5% of the first-order indices of both the first soil layer and ballast layer are observed. These 10%

are directly attributed to the subgrade layer, although its coefficient of variation reduces from Case 1 to Case 2. One reason for this increase is that the imposed variability on the subballast layer imposed larger deformations on the subgrade (which is just below and is softer than the subballast layer), increasing its importance on the railway track stiffness variance.

4.5 Dynamic analysis for train loading

In the previous section, the probabilistic characteristics of the mechanical response of the railway track subjected to a single moving load at low speed (i.e. 15 km/h) were discussed. Different aspects relating to material's variability and the structural and homogenizing role of the rail bending stiffness were discussed. This section focus on verifying the influence of the load speed on the probabilistic characteristics of the railway track response obtained at different speeds. In order to reproduce the railway vehicle load, a bogie loading type is hereafter considered, which means that a moving load consisting of two loads 3 m apart is applied on the track. Load magnitude is of 85 kN, representing half of the wheelset weight. Track structure is kept the same from the previous analysis, but a longer mesh is considered, as a consequence of the load methodology discussed in Section 3.3.3. Material properties and its probabilistic description are also kept the same as presented in Section 4.3. Three load speeds are considered: 15 km/h, 120 km/h and 220km/h, representing both quasi-static and dynamic moving loads. Viscous boundaries are used as to avoid spurious wave reflection on lateral boundaries.

The output quantities of interest are in this case the track bogie-stiffness (K), measured as the force applied by a the first wheelset divided by the vertical displacement of the rail at the point of the applied force. Clearly, the value of K is smaller than the value of k defined in 4.4.4.2 for the same track structure, as in this case higher settlements are expected due to the mutual interaction of deflection zones of each wheelset. This effect is evidently dependent of the distance between wheelsets, smaller distances leading to lower values of K. Further studying the dynamic impact of the wheelset distance is outside the scope of this work.

The layer settlement (Δu_z) is also studied in this section, defined as:

$$\Delta u_z = \frac{u_z^t - u_z^b}{h} \tag{4.6}$$

where u_z^t is the vertical displacement at the top, u_z^b is the vertical displacement at the bottom and h is the width of the considered layer. This is similar to a local measure of the deformation level to which the material is subjected to.

Random field generation and discretization is obtained by decomposition of the correlation structure reduced by the Proper Orthogonalization Decomposition (POD). As discussed in the Appendix D, this method allow to reduce to probabilistic dimension of the problem and to ensure a good description of the imposed correlation structure. This technique is chosen in this section as the model is significantly longer than the one discussed in Section 4.4, in order to achieve the desired speed following the methodology proposed in Section 3.3.3. Sampling strategy is based on Latin Hypercube Sampling

(LHS) with correlation control. The formulation, hypothesis and results obtained in Section 4.3 are considered in order to describe the probabilistic description of the input data. The squared exponential autocorrelation structure (Equation 4.3) is considered for three different correlation lengths θ_y, 2 m, 5 m and 8 m.

4.5.1 Random variables and spatial variability analysis

Figure 4.20 presents the results of 300 Latin Hypercube samples for bogie speed of 120 km/h for the cases where θ_y equal to infinity and 2 m. As already observed in the case of single moving load discussed in Section 4.4.1, variations in mean values are due to the sleeper positioning in the track. The mean value of the output field is different from the result obtained when considering the input mean values, which is called as deterministic value in Figure 4.20a. This highlights the importance of conducting a probabilistic analysis rather than a deterministic one. In the case of spatial variability, a random sample captures again the variations in the track bogie stiffness value.

The autocorrelation structure of the output random field is studied, in order to highlight the importance of the railway structure on how the imposed correlations on the input field are measured by the track bogie-stiffness (K). Figure 4.22 presents the autocorrelation coefficient (ρ) of the first considered position relative to the others, for the three considered speeds (15 km/h, 120 km/h and 220 km/h) and correlation lengths (2 m, 5 m and 8 m). Higher input correlation lengths (θ_y) lead to strongly correlated output fields, i.e. K is autocorrelated to a longer distance.

The scale of fluctuation (l_c) of the output field is studied, as defined by Equation 4.4. The values of l_c are represented in Figure 4.21a. As previously discussed, values near the boundaries must not be considered. Figure 4.21b represents the values of l_c using this methodology. Bars are plotted in order to show minimum and maximum values obtained of the scale of fluctuation (l_c) at each case. This result is considerably similar

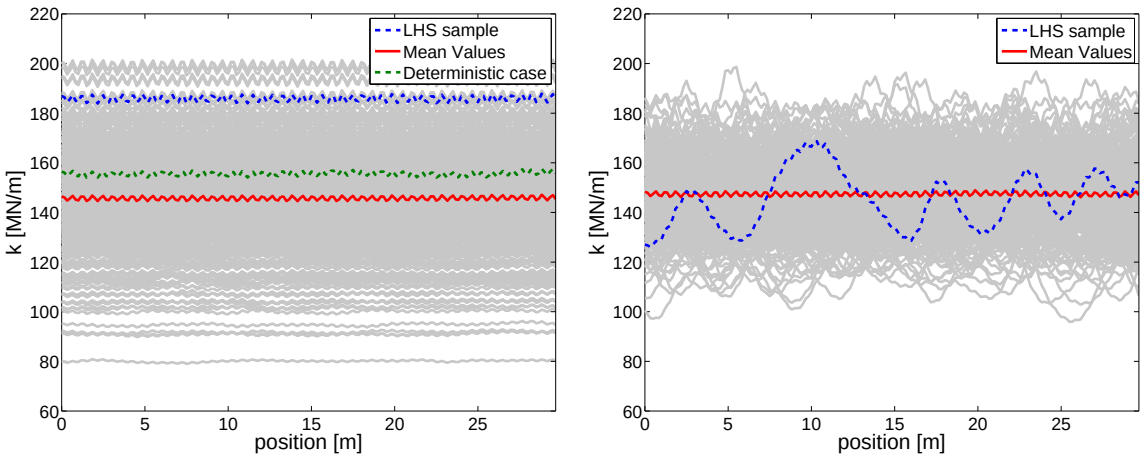

(a) (b)

Figure 4.20: Results of track bogie-stiffness (K) measured at 120 km/h. a) Correlation length θ_y=∞ case; b) Correlation length θ_y=2 m.

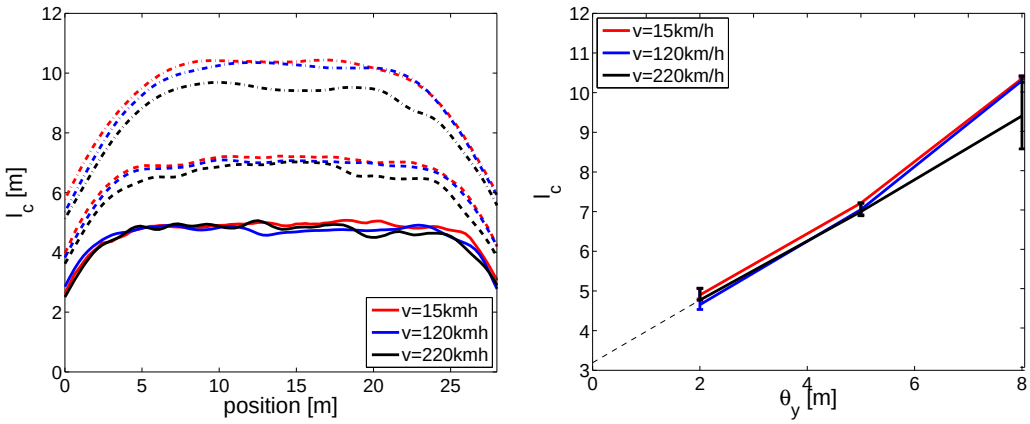

Figure 4.21: Scale of fluctuation (l_c) of the track bogie-stiffness random field. Solid line represents θ_y=2 m, dashed line represents θ_y=5 m and dash-dot line represents θ_y=8 m. a) Full representation of l_c according to the position; b) Increase of l_c with the correlation length of the input fields.

to the case discussed in Section 4.4.2. The scale of fluctuation increases with increasing correlation length and lower limiting value of around 3 m is once again expected to be obtained. Therefore, speed seems to play a minor role in the above results, even if l_c is smaller in the case of 220 km/h comparatively to the other two speeds, in all considered autocorrelation lengths. The structural characteristics of the structure is for the considered set of parameters preponderant than the moving load speed.

Figure 4.22 presents the autocorrelation coefficient (ρ) of the first considered position relative to the others, for the three considered speeds (15 km/h, 120 km/h and 220 km/h) and correlation lengths (2 m, 5 m and 8 m), and for the squared exponential autocorrelation function considering a correlation length defined by the mean value of the scale of fluctuation of the output field, i.e. values presented in Figure 4.21b. The output field keeps some of the second-order characteristics of the input field, the load spread among sleepers does not leading to an important change in the correlation structure of the field.

The same simulations are also analyzed in terms of each layer settlement (Δu_z). In this case, the maximum settlement of the fresh ballast layer and the subgrade are analyzed during train passage. Figures 4.23 and 4.24 present the settlement under load as obtained by Equation 4.6. Once again, mean values are only affected by sleeper positioning in both cases. The amplitude characteristics of a random sample are different from the fresh ballast layer and the subgrade: while the first is influenced both by the sleeper positioning and the input field, the second is mainly affected only by the input random field characteristics.

The scale of fluctuation characteristics in the case of track layers settlement are presented in Figures 4.25a and 4.25b for the fresh ballast layer and the subgrade. The input correlation length and the output scale of fluctuation and variations are the same for the fresh ballast layer settlement thus, its settlement characteristics being directly proportional to the local mechanical properties variations. In the case of the subgrade, a certain spread as with track stiffness characteristics is obtained, although in a smaller degree

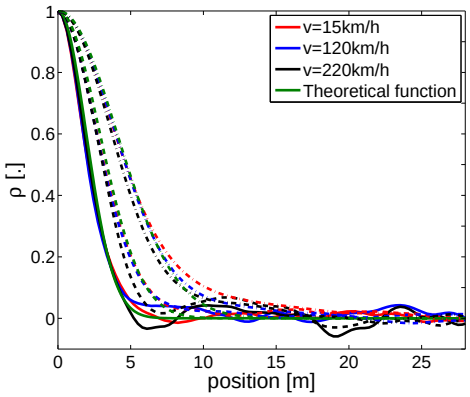

Figure 4.22: Autocorrelation coefficient (ρ) of the first position relative to the others. Solid line represents θ_y=2 m, dashed line represents θ_y=5 m and dashed-dotted line represents θ_y=8 m. Green lines represents the autocorrelation coefficients obtained by considering the squared exponential autocorrelation function with correlation length defined by the mean value of the scale of fluctuation of the output field.

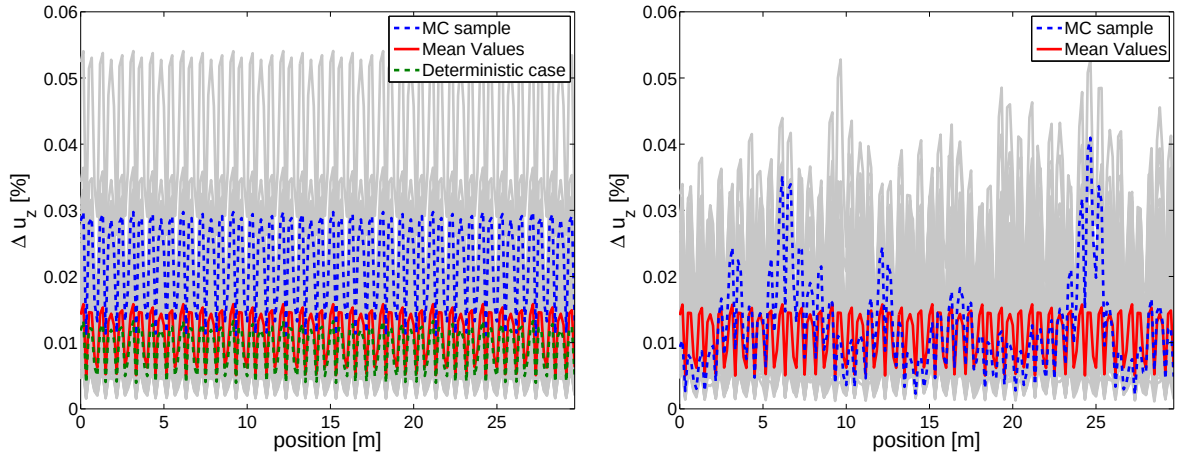

Figure 4.23: Results of settlement of the fresh ballast layer at 120 km/h. a) Random variables case; b) Spatial variability with θ_y=2 m for all track layers.

compared to the track bogie-stiffness (K).

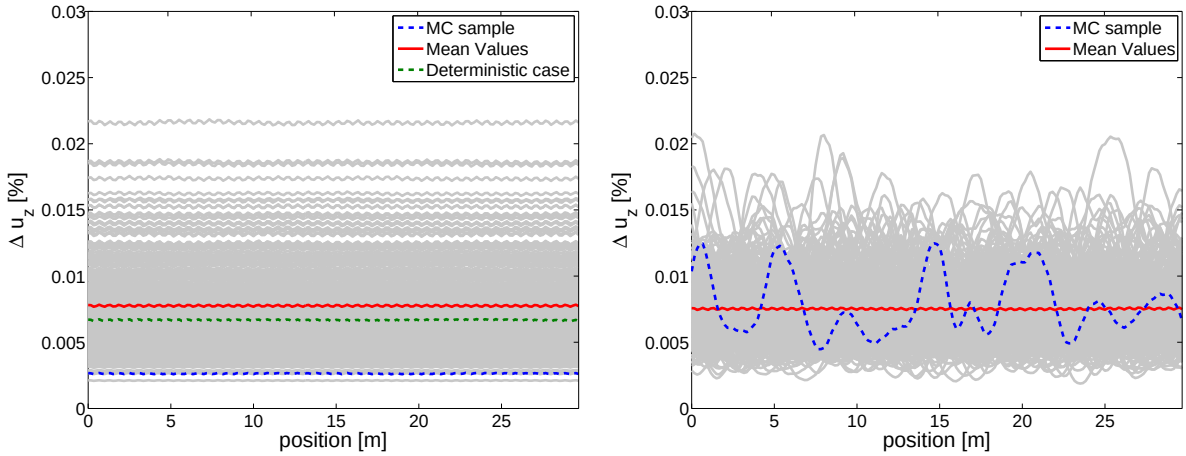

Figure 4.24: Results of settlement of the subgrade at 120 km/h. a) Random variables case; b) Spatial variability with θ_y=2 m for all track layers.

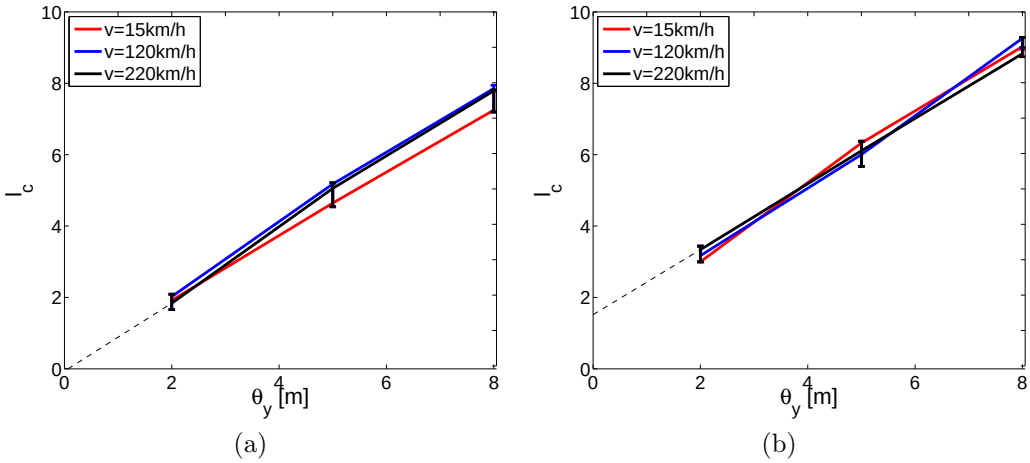

Figure 4.25: Scale of fluctuation (l_c) of the track layers settlement. a) Fresh ballast layer; b) Subgrade soil.

4.5.2 Sensitivity analysis

The FAST methodology is applied in this section in order to verify the role of increasing moving load speed on the variance of both track bogie-stiffness (K) and layers settlement (Δu_z). It is reminded that only the random variables case is considered, i.e. θ_y=∞.

As shown in Figure 4.26, moving load speed presents little effect on the first-order sensitivity indices (S_i). The subgrade is responsible for more than 80% of the output variance, as previously observed in Section 4.4.4. From the numerical results presented in Section 3.4.3 for the influence of speed and subgrade stiffness on the mechanical response of the railway track, the subgrade material in the studied site is stiff (μ_E=109 MPa) thus, leading to small influence of moving load speed on the measured vertical displacement of the rail and the measured track stiffness under linear elasticity mechanical behavior.

The first-order sensitivity index of track layers' settlement are presented in Tables 4.4 and 4.5 for the fresh ballast layer and the subgrade, respectively. The settlement being a local measure of deformation, its variance is mainly influenced by the mechanical properties of the considered layer. Higher order effects (i.e. interaction between layers) is responsible for around 8% of the total variance. In this sense, although reducing the uncertainty in the subgrade mechanical properties can certainly reduce the obtained variance in the track stiffness, only better characterizing the mechanical properties of the ballast material can reduce uncertainty in the ballast settlement.

Layer	15 km/h	120 km/h	220 km/h
Fresh Ballast	91.7%	91.6%	91.4%
Fouled Ballast	0.0%	0.0%	0.0%
Interlayer	0.2%	0.2%	0.2%
Subgrade	0.3%	0.4%	0.6%

Table 4.4: First-order sensitivity indices (S_i) of fresh ballast layer settlement.

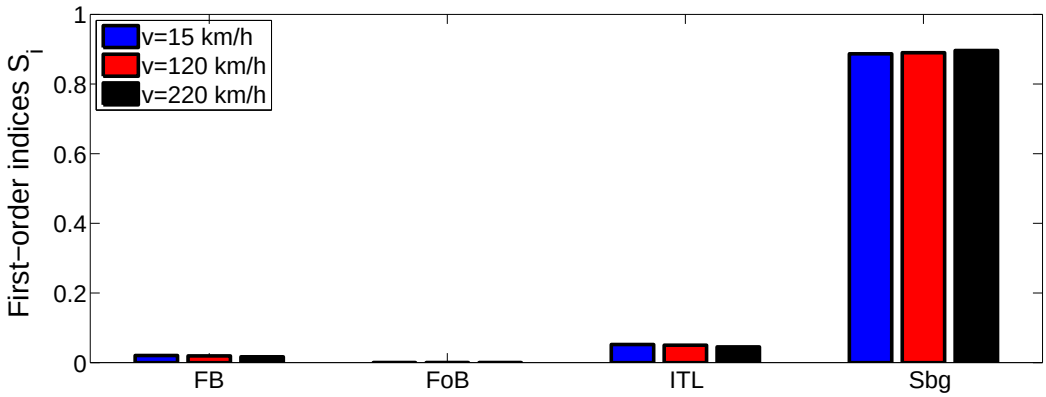

Figure 4.26: First-order sensitivity indices (S_i) of track bogie-stiffness (K). FB: Fresh Ballast, FoB: Fouled Ballast, ITL: Interlayer, Sbg: Subgrade.

Layer	15 km/h	120 km/h	220 km/h
Fresh Ballast	0.3%	0.3%	0.4%
Fouled Ballast	0.0%	0.0%	0.0%
Interlayer	0.0%	0.0%	0.1%
Subgrade	92.7%	92.5%	92.0%

Table 4.5: First-order sensitivity indices (S_i) of subgrade settlement.

4.5.3 Impact of boundary conditions on the output field

In this section the impact of using either the paraxial approximation or absorbing boundaries is assessed in the case where spatial variability is present. Both solutions are considered as rather approximative in this case, as Rayleigh waves are expected to appear in wave propagation in heterogeneous media. However, this is still an open question in the literature and are outside the scope of this thesis. Please refer to Appendix C.1.1 for a discussion of the paraxial approximation for random media.

The analysis is performed in the case of input fields with squared exponential correlation structure, correlation length of 2 m and speed of 120 km/h. A lower correlation length is chosen as it is expected to be the one leading to more differences on the output responses. The same data (i.e. same seed) is used in both cases, as to avoid differences appearing from the statistical convergence. Comparisons are made by using the following proposed field:

$$H(x) = \frac{K_{abs}(x)}{K_{parx}(x)} \tag{4.7}$$

where K_{abs} is the output random field obtained with absorbing boundaries and K_{parx} with the paraxial approximation. If both calculations are exactly the same at every point, then $\mu_{H(x)}$=1 and $\sigma_{H(x)}$=0 at every point. Both K_{parx} and K_{abs} are not expected to be zero as they represent stiffness, which is physically bounded to positive values. This representation allows to better take into account the differences brought about by each modeling option on the dynamic results.

Mean and standard deviation values of H are represented in Figures 4.27a and 4.27b, respectively. Comparatively, results are very consistent using either boundary solution, as $\mu_H \approx$1 and $\sigma_H \approx$0, although using the viscous boundary lead to higher values of K and differences are higher near the mesh left boundary. It can be concluded that both boundary solutions yield similar results in the considered case.

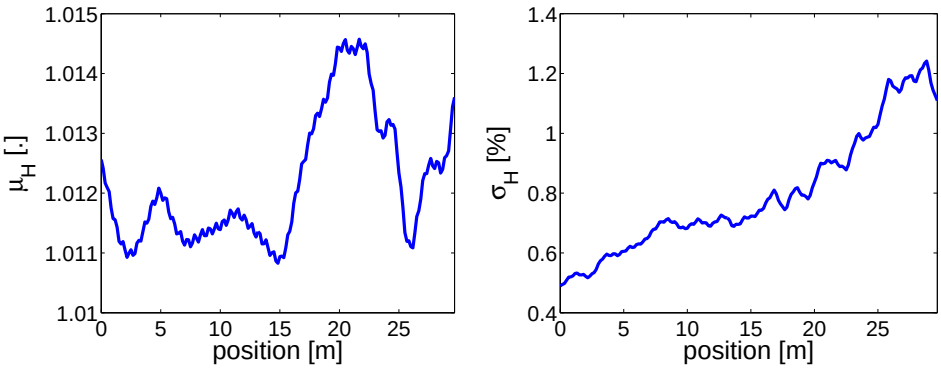

(a) (b)

Figure 4.27: Analysis of $H(x)$. a) First-order moment (μ_H); b) Second-order moment (σ_H).

4.6 Concluding remarks

A probabilistic nonintrusive methodology is applied in order to characterize the variability of the track stiffness based on Panda tests (i.e. dynamic cone penetration tests). Cone resistance is considered as being a random field characterized by its marginal probability density function and a theoretical autocorrelation function. Young's Modulus of each layer is obtained from empirical/analytical relations proposed in the literature. This approach allowed to obtain a probabilistic description of the Young's Modulus considering spatial variability along the track. According to the performed simulations and for the used configurations, the following conclusions can be drawn:

1. The railway track global stiffness variability showed to be smaller than the input's variability. Two main key factors are proposed to explain this reduction. First, the sleeper's positioning and load distribution over the track would play a role on homogenizing the track stiffness measure. Secondly, track superstructure was kept deterministic for all simulations (except in Section 4.4.4.1). The analytical solution of a moving load over a beam resting on a elastic foundation is used in order to verify the rail bending influence on the track global stiffness variance. It is showed that higher coefficient of variations are obtained after excluding the rail bending from the track global stiffness measure.

2. Correlation length θ_y plays an important role on the variance of the track stiffness. Reduction of variance is observed, which means that smaller correlation lengths leads to smaller variance of output field. Interestingly, this property means that allowing more variability at smaller distances leads to less variability on the output field. However, the full impact on the railway system of such spatial variability can only be assessed by a train-track coupled system as to verify the impact of track stiffness variability on the vehicle dynamic response. This analysis is proposed as further work from this thesis based on the obtained track stiffness.

3. Both the track global stiffness field k the track bogie stiffness K present a minimum scale of fluctuation around 3 m, which corresponds to the load spread among the

sleepers. In this sense, a direct *in situ* measurement of the track global stiffness seems to be unable to characterize fluctuations smaller than this distance. Although in the case of track bogie stiffness K no simulations was performed with small correlation lengths (θ_y<0.5m), it is expected that such minimum also exists.

4. Global sensitivity analysis was performed based on the Fourier Amplitude Sensitivity Test (FAST), in the case of no spatial variability. For the analysed field case, first-order sensitivity indices were obtained and in the case of linear elastic behavior, the subgrade is responsible for more than 80% of track stiffness variance. Nonlinear elasticity was also verified as to better model the increase of soil's stiffness in depth compared to a linear elastic model. Its influence reduces as the nonlinearity increases, however its influence is of more than 60% on the simulations performed. This result stresses the importance of taking into account the subgrade's mechanical behaviour coherently with soil mechanics on track models. Rail pads variability also contributes to the variance of the output field, although their variability is expected to be low as quality control on industrial production can prevent scatter in the mechanical properties of this equipement. Performing laboratory tests on rail pads can confirm this hypothesis.

These results emphasize the importance of the subgrade soil behavior on the response of the railway track. After track construction, the subgrade is considered to be homogeneously compacted and presenting the same mechanical characteristics at every point along the track. However, the *in situ* test results presented in this chapter showed the different results obtained at the same track. In this sense, correcting evaluating the mechanical response of the subgrade soil seems to be of great interested in order to correctly characterize the mechanical response of the railway track system.

Chapter 5

Nonlinear railway track model

Contents

5.1 Introduction

In the previous chapters, the mechanical behavior of the different track materials was modeled as linear and nonlinear elastic (Section 4.4.4). The Young's Modulus in this case was approximated by secant modulus at a strain level of 0.1%. The elastic limit of soils, i.e. reversible strain during shear, is very small and usually considered around 0.001%. Ballast, interlayer and the subgrade soil experiment higher strains during load (Selig and Waters, 1994). Although the elasticity hypothesis is used for many applications, e.g. train-track interaction problems and soil vibration, it is not representative of the soil and granular materials behavior during loading. Indeed, once the elastic limit is exceeded, irreversible volume changes take place leading to an evolution of stress and strains which cannot be accounted for by elastic models.

As discussed in Section 2.4, it is common practice in highway applications to split the soil behavior into two different parts: resilient and permanent responses (Brown, 1996). These are considered as representative of both short-term (one train passage) and long-term behavior (track's lifespan) of the railway track. The resilient response is considered elastic and a resilient modulus M_r can be defined. This last is obtained by unloading and reloading the material at different strain levels during the drained triaxial test, for example. The permanent response is characterized by the evolution of the plastic strains with loading cycles. In this case, instead of considering a secant modulus at a certain strain level, a resilient modulus is used as representative of the soil stiffness for cyclic loading applications at a certain strain level. This approach supposes the strain level during each loading cycle to be very small and not contributing to state evolution of the materials after each cycle.

However, soil behavior depends on the stress history and the subsequent resilient response depends on the so-called "conditioning phase", or the first 100 or 1000 load cycles when the material is subjected to larger permanent deformation. Therefore, assessing the state of materials in the railway structure and the influence of stress history and load speed during this phase is an important step toward establishing a modeling approach based on the resilient behavior.

Capturing the main mechanical mechanisms of the different track layers response during the conditioning phase can be achieved by advanced nonlinear mechanical models, which can account for the different aspects of soil's mechanical response. In this chapter, the elastoplastic multimechanism constitutive law developed at *Ecole Centrale Paris*, called ECP model (Aubry et al., 1982; Hujeux, 1985), is used to capture the different irreversible phenomena and the cyclic hardening and softening appearing in soil during cyclic load. Different authors have implemented nonlinear railway track models using the ECP model (Paderno, 2010; Araújo, 2010). However, the latter authors pointed out difficulties in obtaining a coherent set of parameters for the ballast material.

These different aspects are discussed in this chapter. The first section is devoted to the mechanical response of the different railway geomaterials. The mechanical parameters of the ECP model for ballast and the interlayer are calibrated from drained triaxial shear test results available in the literature (Suiker et al., 2005; Indraratna et al., 2011; Trinh et al., 2012). The methodology used in calibrating the different materials is presented and follows the proposed method discussed by Lopez-Caballero (2003). Two subgrade soils are

considered and their ECP model parameters are directly obtained from the literature. In the second section, the nonlinear track model is presented along with different numerical strategies used for considering nonlinear behavior. The response of a conventional track structure subjected to a bogie load at different speeds is presented in the third section. The influence of stress history and load speed on cyclic response is also discussed. The fourth section is devoted to verify the influence of the subgrade's initial density and the interlayer material on the response of the track materials. Finally, the main conclusions and mechanisms observed from the numerical simulations are highlighted at the end of this chapter.

5.2 Railway geomaterials and associated mechanical model

In this section, the parameters of the ECP model for ballast and the interlayer material are calibrated from standard triaxial test results available in the literature. These are considered representative of the mechanical response of these materials in the complete model of the railway track used in the subsequent sections.

In this thesis, using a constitutive law from continuum mechanics is considered a valid hypothesis for ballast and the interlayer. However, it is important to keep in mind that ballast and interlayer are thin layers, for which the mean grain-size relative to the track layer's width is very high (e.g. around 10 grains for ballast layer in France). As discussed in Section 2.6.4, Discrete Element Method (DEM) is an effective way of considering the grain-size scale on the mechanics of thin granular layers. However, coupling DEM and FEM models (Nitka et al., 2011) can be computationally intensive and it is still not completely developed for railway applications.

5.2.1 Ballast material

Mechanical tests on ballast material have been performed by different authors (Lim, 2004; Suiker et al., 2005; Fortunato, 2005; Aursudkij, 2007; Paderno, 2010; Indraratna et al., 2011, among others). Ballasted track design is still very common in many countries. However, the ballast material itself comes from different gravel materials, such as dolomite, rheolite, gneiss, granite, basalt, quartzite (Raymond, 1979), and the grain-size specifications change in different countries depending on the used standards.

In this work, standard triaxial shear tests performed by Suiker et al. (2005) (Netherlands) and Indraratna et al. (2011) (Australia) on ballast are analyzed and compared, in order to have a better insight of its different mechanical characteristics. The grain-size distribution curves of both materials are presented in Figure 5.1, along with the actual French standard for ballast material (SNCF, 2010). Ballast tested by Suiker et al. (2005) is composed of smaller grains comparatively to ballast tested by Indraratna et al. (2011) and the French standard. The maximum particle size from Suiker et al. (2005) corresponds to only the 60% passing of the ballast grains tested by Indraratna et al. (2011).

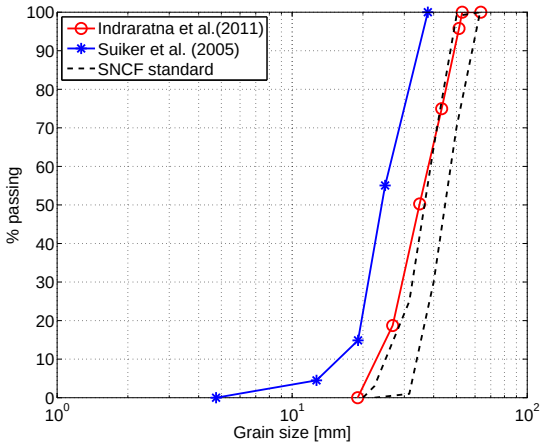

Figure 5.1: Grain-size distribution curves for ballast specimens tested by Suiker et al. (2005) and Indraratna et al. (2011).

5.2.1.1 Ballast tested by Suiker et al. (2005)

Ballast grains tested by Suiker et al. (2005) followed the requirements of gradation No. 4 from the AREMA Manual for Railway Engineering (AREMA, 2002). The authors tried to follow the characteristics of the ballast present in the test track in Pueblo, Colorado (Selig et al., 1981). The obtained samples presented a mean dry density γ_d between 16.1 and 17.0 kN/m^3. The triaxial cell used is presented in Figure 5.2a. It has 645 mm height and diameter of 254 mm, which corresponds to a mean ratio of 7 grains per diameter. Three different radial measurement points were installed at H/3, H/2 and 2H/3, where H is the total height of the triaxial cell, as shown in Figure 5.2a. Three different confining pressures are considered: 10.1, 41.3 and 68.9 kPa. According to the authors, these are representative of the applied stress at the layer during a train passage. The tests were carried out with a prescribed displacement and the obtained results are plotted in Figure 5.3.

As expected, higher deviatoric stresses are developed by specimens subjected to higher initial confining stress (Figure 5.3a). The volumetric behavior of all three specimens is first contractant, then dilatant for larger strains (Figure 5.3c). However, the developed volumetric strain is lower for the sample at initial confining pressure of 41.3 kPa relatively to the the sample at 68.9 kPa. This is inconsistent with the expected volumetric behavior of soils during drained triaxial test. Although the author does not discuss this particular point, Araújo (2010) points out that probably problems with the radial strain measurements occurred.

5.2.1.2 Ballast tested by Indraratna et al. (2011)

Indraratna et al. (2011) also conducted different laboratory tests in order to characterize the mechanical behavior of the ballast used in Australian railways. The mean dry density γ_d obtained for the samples was between 15.4 and 15.6 kN/m^3. The triaxial cell is shown in Figure 5.2b. It measures 600 mm height and has a diameter of 300 mm, which corresponds to a ratio of around 8 grains per diameter. Indraratna et al. (2011) tested ballast under 5

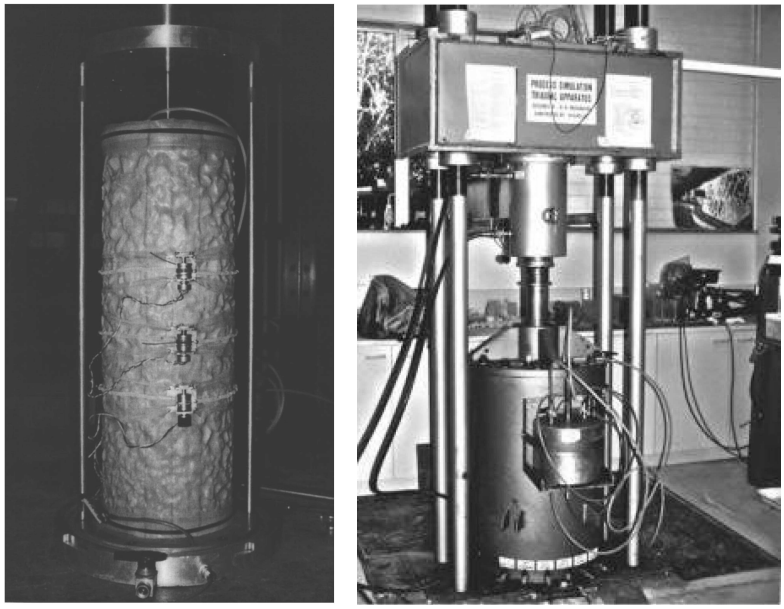

(a) (b)

Figure 5.2: Triaxial cells used for testing ballast material. a) Triaxial cell used by Suiker et al. (2005); b) Triaxial cell used by Indraratna et al. (2011).

different confining pressures: 10, 50, 100, 200 and 300 kPa. The obtained drained triaxial test results are plotted in Figure 5.4. In the present work, only the 10, 50 and 100 kPa initial confining pressures are used for the calibration procedure further presented in Section 5.3.1, as being more representative of the confining pressures which the ballast material is submitted to.

5.2.1.3 Discussion about laboratory test results on ballast material

As a coarse granular material, the ballast presents two main characteristics at low confining stress: it develops high stress ratio (η=q/p') and presents significant volume increase during shear. These characteristics were observed in the test results from Suiker et al. (2005) and Indraratna et al. (2011). However, the stress ratio evolution during the tests are very different for both material (Figures 5.3b and 5.4b). A constant value of η around 1.98 is obtained by Suiker et al. (2005) for all the considered confining pressures, while the results from Indraratna et al. (2011) present high values of η (maximum around 2.7) at the lowest confining pressure (10 kPa). These different evolutions of the stress ratio during the drained triaxial test can be related to the different grain-size distributions, the sample preparation procedure and the obtained relative density. Indeed, while Suiker et al. (2005) prepared the ballast specimen by compacting eight layers of equal thickness, each one tamped 40 strokes with a steel rod, Indraratna et al. (2011) divided the specimen in 4 layers of equal thickness and compacted each one with a hand-held vibratory hammer. Moreover, it has been showed for soils that not only the grain assembly but also grain shape and geometry can result in differences in the mechanical response (Biarez and Hicher, 1994). The results obtained by both authors at the lowest confining pressure show

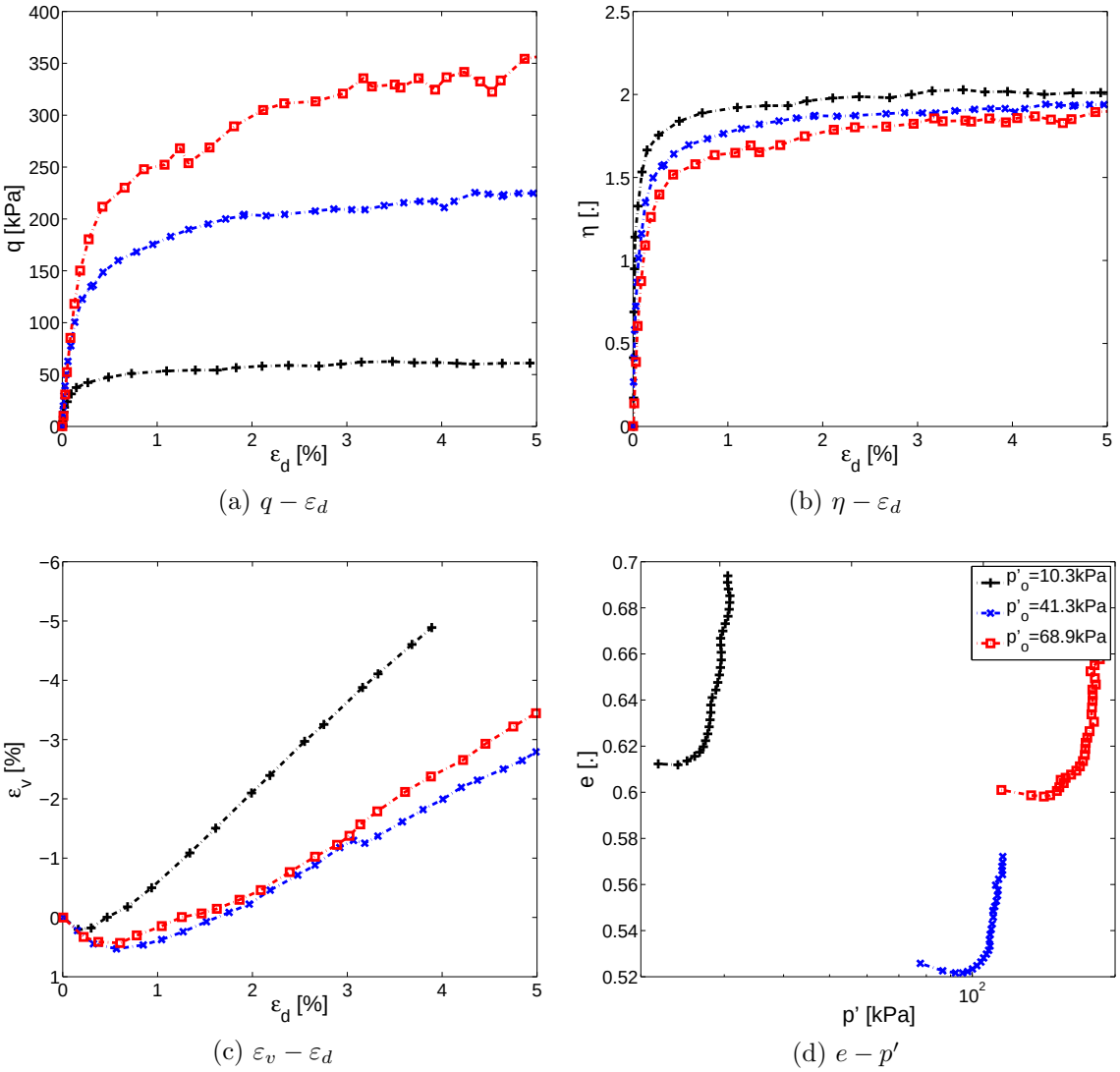

(a) $q - \varepsilon_d$ (b) $\eta - \varepsilon_d$

(c) $\varepsilon_v - \varepsilon_d$ (d) $e - p'$

Figure 5.3: Results of drained triaxial tests performed by Suiker et al. (2005) on ballast material.

completely different behaviors in terms of mobilized internal friction. η can be related to the friction angle ϕ for a Mohr-Coulomb failure criterion at the critical state (η=M) by the following relation:

$$\phi = \arcsin \frac{3\eta}{6+\eta} \tag{5.1}$$

Indraratna et al. (2011) analyzed these test results from a peak friction angle (ϕ_p) point of view, i.e. friction angle obtained from η at the highest deviatoric stress q and not at the critical state. The authors argue that in this case a nonlinear relation exists between the peak friction angle and the confining pressure at low pressures for crushed basalt and other rockfill materials. High values of peak friction at low confining pressures are thus obtained, which decreases with increase in confinement and stabilizes at more

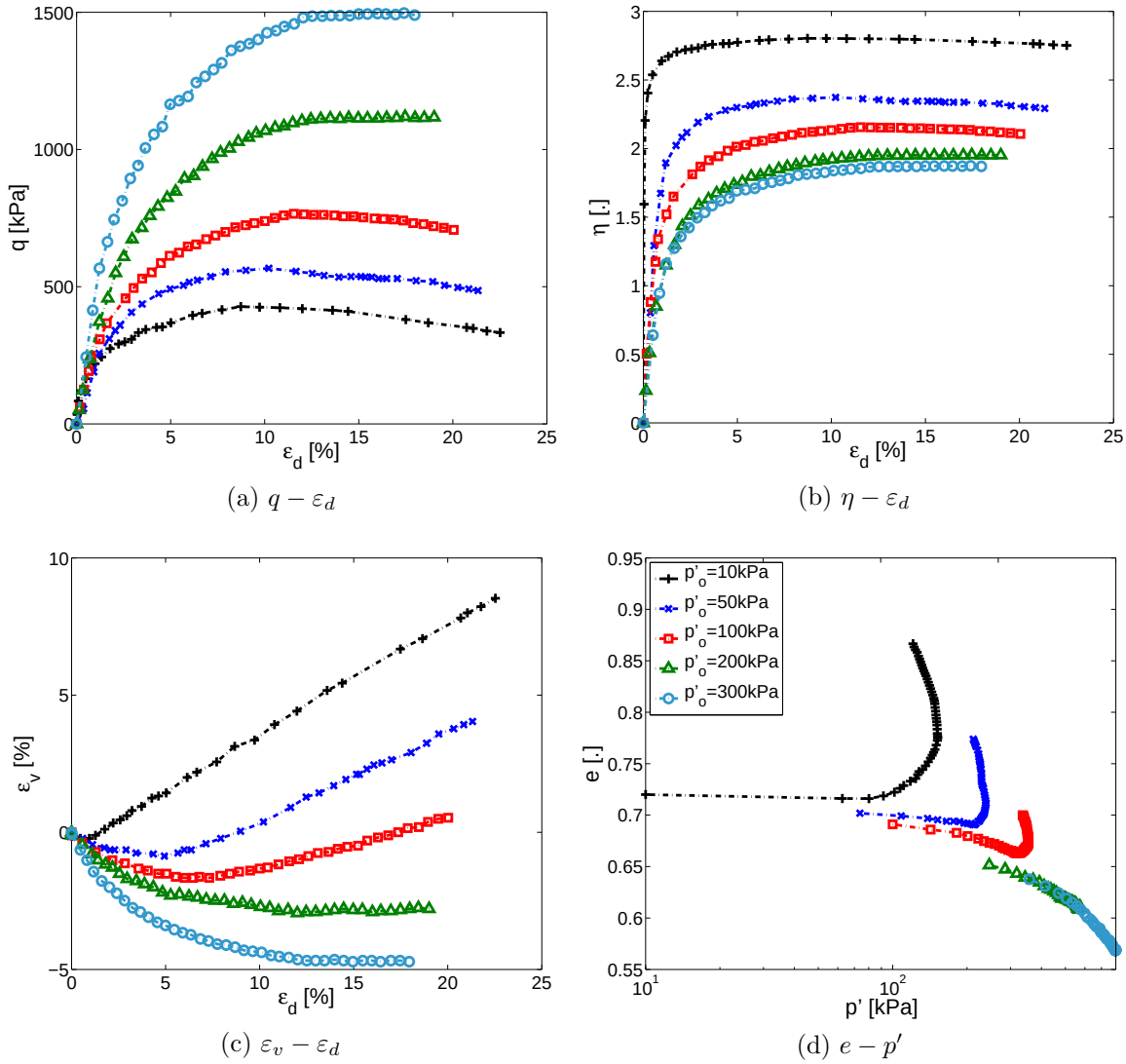

(a) $q - \varepsilon_d$ (b) $\eta - \varepsilon_d$

(c) $\varepsilon_v - \varepsilon_d$ (d) $e - p'$

Figure 5.4: Results of drained triaxial tests performed by Indraratna et al. (2011) on ballast material.

usual values around 35 ° for high confining pressures. This reflects the influence of the initial state and particle size on the stress state evolution during triaxial load.

5.2.2 Interlayer material

Trinh et al. (2012) characterized the interlayer material of a conventional railway track and investigated both mechanical and hydraulic properties in the laboratory by a series of drained triaxial tests, at different water contents, and infiltration tests. The grain-size distribution curve for the material directly obtained from *in situ* material and tested by Trinh et al. (2012) is presented in Figure 5.5. A dry volumetric mass density ρ_d of 2.39 Mg/m^3 and water content of ω_n=5.13% was measured in the *in situ* material. The dry volumetric mass density ρ_d achieved in the laboratory was of 2.01 Mg/m^3, showing

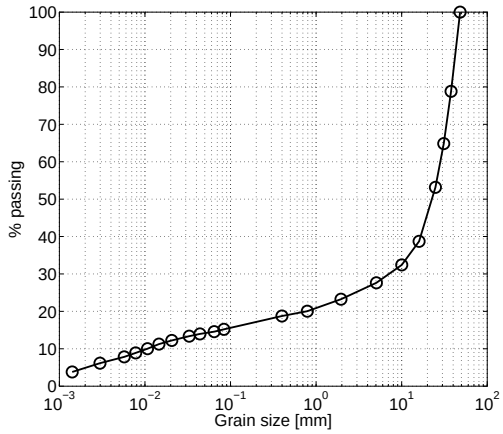

Figure 5.5: Grain-size distribution curve for interlayer material tested by Trinh et al. (2012).

how compact this material is in the railway track. Trinh et al. (2012) characterized the mechanical response of the material using the drained triaxial test for two different water contents: ω_n=4% and ω_n=12%. The first is representative of the obtained Optimum Moisture Content (OMC) by modified Proctor compaction tests and is characterized by an initial degree of saturation S_{ri}=32%; the second is representative of the saturated state, S_r=100%. The obtained results are plotted in Figure 5.6.

Trinh et al. (2012) showed that the water content influences considerably the mechanical response of the intermediate layer material. In the saturated state, the material develops lower deviatoric stress during the triaxail test and does not present increase in volume for the considered initial confining stresses. More recently, Duong et al. (2013) also studied the mechanical response of the interlayer material and similar results were obtained.

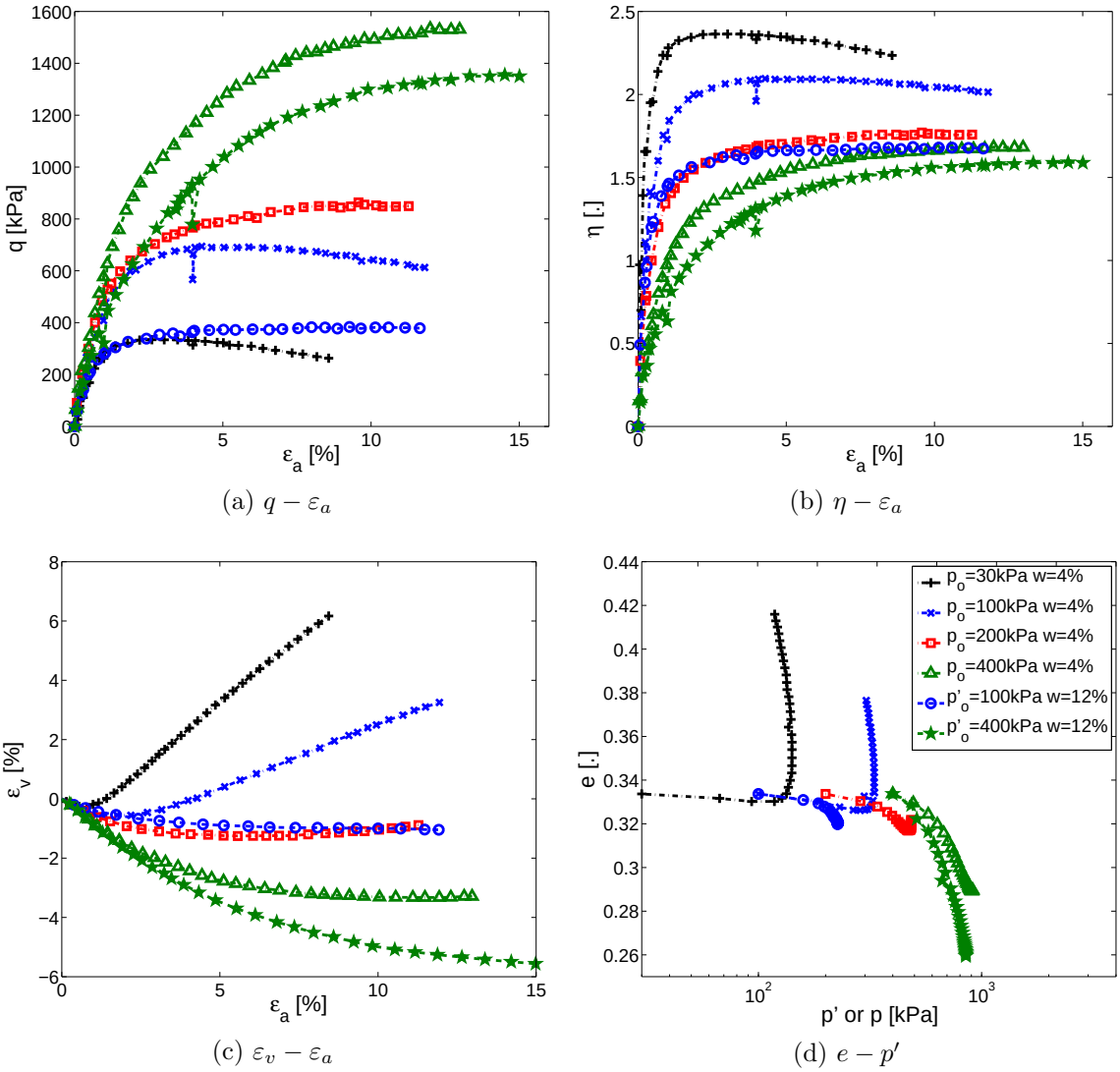

(a) $q - \varepsilon_a$ (b) $\eta - \varepsilon_a$

(c) $\varepsilon_v - \varepsilon_a$ (d) $e - p'$

Figure 5.6: Results of drained triaxial tests performed by Trinh et al. (2012) on interlayer material at ω_n=4% and ω_n=12%.

5.3 Calibration of ECP model parameters

The ECP model, also called Hujeux model, is an elastoplastic multimechanism model developed at *Ecole Centrale Paris* (Aubry et al., 1982; Hujeux, 1985). It considers the effective stress concept developed by Terzaghi and is based on a Coulomb type failure criterion and the critical state concept. All irreversible phenomena is modeled by four coupled elementary plastic mechanisms: one isotropic and three plane-strain deviatoric on three orthogonal planes. Hardening is controlled by plastic strain: volumetric plastic strain for the isotropic mechanism and both deviatoric and volumetric plastic strains for the three deviatoric ones. Cyclic behavior uses kinematical hardening based on the state variables at the last load reversal. This model is chosen for representing the mechanical behavior of the different track geomaterials. The model's mathematical formulation is

presented in Appendix A.

Optimization algorithms are commonly used in order to obtain a set of mechanical parameters of a constitutive law reproducing laboratory tests. The choice of the best algorithm to use depends on both the available data and the constitutive model. An elastoplastic multimechanism model as the ECP model can correctly capture the mechanical response of soil on different stress paths, however its complexity and number of parameters increase the difficulty on the parameter calibration procedure. Regarding the ECP model, Cekerevac et al. (2006) proposed an optimization strategy based on a combination of stochastic and quasi-Newton methods, which combines the advantages of both direct search algorithms and gradient-based algorithms. The procedure is implemented in order to optimize a set of parameters adapted for triaxial tests results on isotropically consolidated and overconsolidated clays. Gamboa (2011) used a combination of quasi-Newton and line search algorithms (Bonnans et al., 2006) for numerical modeling of rockfill dam materials. Lopez-Caballero et al. (2011) used a similar approach for obtaining the ECP model parameters of highway materials from Falling Weigth Deflectometer (FWD) tests.

In the railway context, Araújo (2010) used an optimization procedure based on the Evolution Strategies (ESs) algorithm proposed by Miranda (2007). Araújo (2010) considered the test results presented by Suiker et al. (2005) for modeling ballast, but the objective function was the cumulative axial plastic strain for cyclic drained triaxial test and not the mechanical response to monotonic loading. Araújo (2010) justified this choice by the inconsistent volumetric response at different initial stresses obtained by Suiker et al. (2005). However, the choice of the cumulative axial plastic strain as objective function is questionable, as the total plastic strain is a product of the different plastic mechanisms and the obtained parameters hardly reflect the response of the soil to monotonic tests.

Lopez-Caballero and Modaressi-Farahmand-Razavi (2008) proposed to classify the ECP model parameters in terms of their estimation method. This approach separates the parameters in two categories: directly measured (either by *in situ* or laboratory tests) and not-directly measured. However, very often not all the necessary tests are performed in order to calibrate the directly measured parameters. In this case, tests on similar soils can be used in order to provide the necessary basis for calibration. In the case of the railway geomaterials, usually only oedometric and triaxial test are performed. The difficulty relies mainly on the necessary equipment to test coarse heterogeneous geomaterials. Although large-scale triaxial cells are available, hollow cylinders or shaking tables are not yet commonly used equipments for these materials. The elastic domain is usually not measured and only parameters related to the critical state can be directly obtained.

In this work, the adopted strategy for parameter calibration did not use any optimization algorithm, but was rather based on a manual and operator-based procedure to control the model parameters. The manual calibration looked for a compromise between a good correspondence for the drained triaxial test response and a coherent response on a large panel of stress paths (e.g. isotropic and oedometric consolidation tests and drained cyclic strain-controlled shear test, presented in Appendix G), which are obtained by direct integration of the constitutive law. The methodology described by Lopez-Caballero (2003) in order to calibrate the model parameters is followed. This choice is motivated by the fact that the model response is stress path dependent.

In Section 3.4.1, it was shown from linear elastic simulations that ballast experiments

different stress paths when loaded, depending on the control point relatively to the sleeper (i.e. under or between sleepers). These will activate both the monotonic and cyclic deviatoric and volumetric mechanisms in different ways from the drained triaxial test. In this sense, good calibration of the drained triaxial tests response does not necessarily correspond to correctly accounting for the material's response on the railway track. Ensuring a consistent behavior at different stress paths is an effective way of obtaining a coherent set of parameters.

5.3.1 Ballast material

The differences in the mechanical response of ballast tested by Suiker et al. (2005) and Indraratna et al. (2011) are described by different sets of parameters of the ECP model (Table 5.2). These are representative of the mechanical behavior observed from the drained triaxial test (Figures 5.7 and 5.8) and give an overall consistent response for a set of drained laboratory tests numerically obtained by the direct integration of the ECP model (isotropic and oedometric consolidation tests and drained cyclic strain-controlled shear test). The numerical test results are presented in Appendix G. In the following, the calibration procedure methodology is presented for both tested materials.

Elasticity parameters are obtained by considering test results on crushed-rock-soil-mixtures from Mok et al. (2011). The choice is made of considering linear elasticity (i.e. n_{el}=0), as ballast layer is thin ($\approx$ 40 cm in conventional lines) and no important variations of the elastic coefficients K and G are expected in depth. In this case, the coefficients K_{ref} and G_{ref} are evaluated by considering a constant mean value p' of 10 kPa. High friction angle ϕ'_{pp} is obtained from the drained triaxial tests and it is representative of the critical state for coarse aggregates.

The critical state line in both cases could not be directly defined, as in the ballast tested from Suiker et al. (2005) the volumetric measurement is not consistent and in the case of ballast tested by Indraratna et al. (2011) the critical state was not reached during the test. In order to estimate the model parameters, it is then considered that the tendency observed in the (e, p') for the ballast tested by Indraratna et al. (2011) is representative

	Directly measured	Not-directly measured
Elastic	K_{ref}, G_{ref}, n_{el}, p_{ref}	
Critical state and plasticity	ϕ'_{pp}, β, p_{c0}, d	b
Flow rule and Isotropic hardening	ψ	a_1, a_2, α_ψ, m, c_1, c_2
Threshold domains		r^{ela}, r^{hys}, r^{mob}, r^{ela}_{iso}

Table 5.1: Classification of ECP elastoplastic model parameters as proposed by Lopez-Caballero and Modaressi-Farahmand-Razavi (2008).

of the slope of the critical state line for both cases.

The plastic compressibility modulus β is estimated from the slope of the critical state line in the (e, p') plane. Neglecting the elastic volumetric strain, β can be determined as:

$$\beta = \frac{1 + e_0}{\lambda} \tag{5.2}$$

where λ is the compression index, which characterizes the slope of the critical state line at the (e, p') plane (as in the Cam Clay model). For both cases $\lambda \approx 0.15$, which leads to $\beta \approx 10$. The estimated value of β in both cases is low, which accounts for the fact that the influence of material densification is low on the observed final resistance, which is to say that the influence of the variation of p_c from its initial state p_{c0} is low.

The initial state defined by the critical mean effective stress p_{c0} is usually related to the overconsolidation ratio for clays and to the relative density D_r for sands. Neglecting the elastic volumetric strain, it can be approximated as the pressure at the critical state line corresponding to the same void ratio as the initial pressure p'_0.

Ballast material		
	Suiker et al. (2005)	Indraratna et al. (2011)
Elasticity		
$K_{ref}(MPa)$	69.4	87.0
$G_{ref}(MPa)$	52.0	60.0
n_{el}	0.00	0.00
$p_{ref}(MPa)$	1.0	1.0
Critical State and Plasticity		
$\phi'_{pp}(^\circ)$	42	43
β	10	8
d	3.00	8.80
b	0.06	0.65
$p_{co}(MPa)$	0.70	0.50
Flow Rule and Isotropic Hardening		
$\psi(^\circ)$	42	43
α_ψ	3.00	1.20
a_1	0.00002	0.00002
a_2	0.00080	0.01500
c_1	0.00200	0.80000
c_2	0.00100	0.40000
m	1.50	1.20
Threshold Domains		
r^{ela}	0.00001	0.00001
r^{hys}	0.01000	0.00400
r^{mob}	0.98000	0.80000
r^{ela}_{iso}	0.00002	0.00002

Table 5.2: ECP model's parameters for ballast.

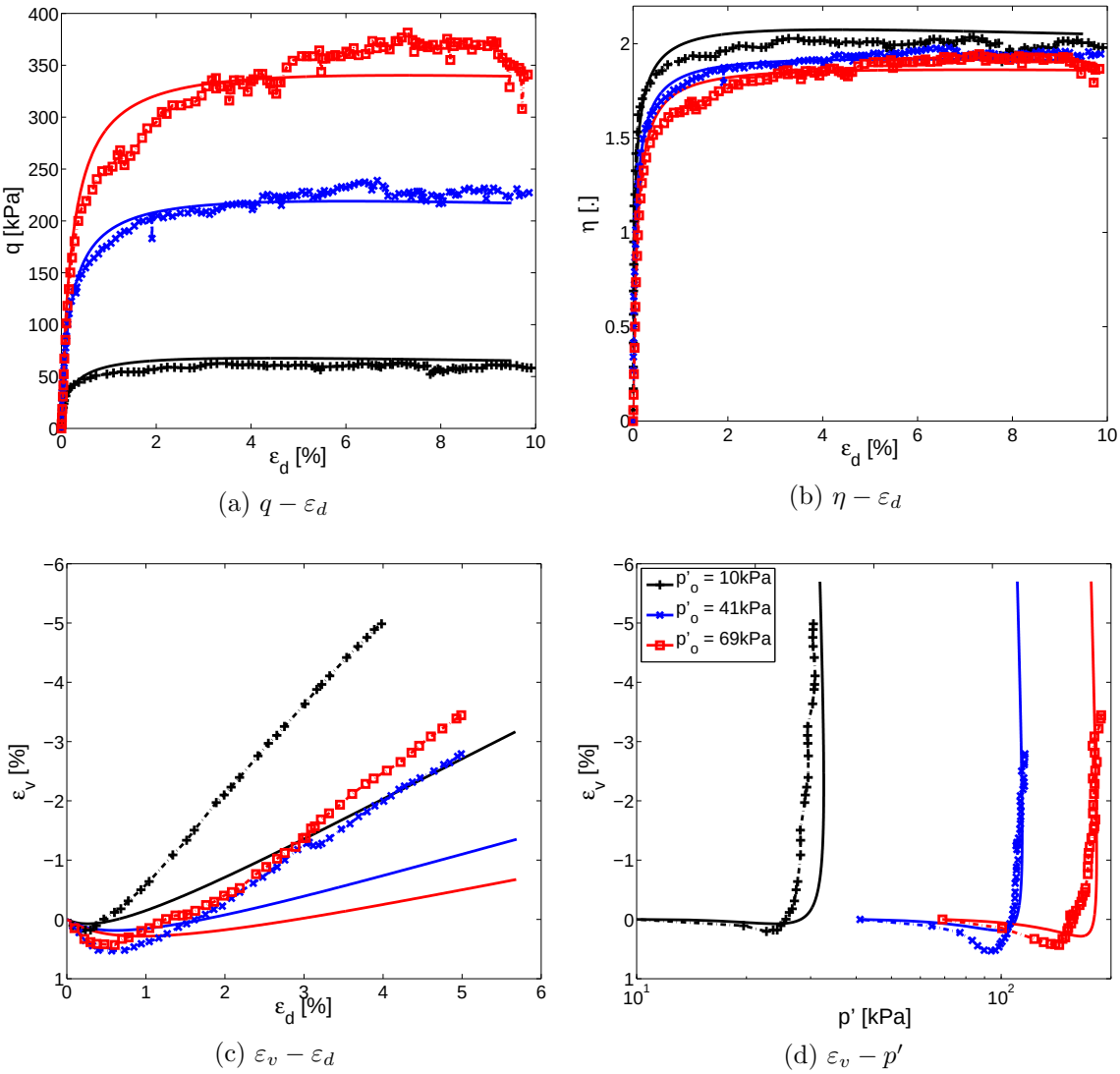

(a) $q - \varepsilon_d$ (b) $\eta - \varepsilon_d$

(c) $\varepsilon_v - \varepsilon_d$ (d) $\varepsilon_v - p'$

Figure 5.7: Comparison of drained triaxial test results performed by Suiker et al. (2005) (dash-dot line) and numerical results obtained by the calibrated model (solid line) for the ballast material.

The parameter d is defined as the distance between the isotropic consolidation line and the critical state line (Equation 5.3). Saïm (1997) proposes to consider $\Delta e \approx 0.1$ for both sands and clays. Nguyen (2006) argued that a higher distance is necessary for coarse grained materials. In this case, the importance of the volumetric mechanism in the volumetric stress evolution is increased.

$$d = \exp\left(\frac{\Delta e}{\lambda}\right) \tag{5.3}$$

The yield functions f_k of the different deviatoric mechanisms are differently considered in both cases: while for ballast tested by Suiker et al. (2005) a small value of b is considered as representative of the stress-strain response obtained from the drained triaxial test and

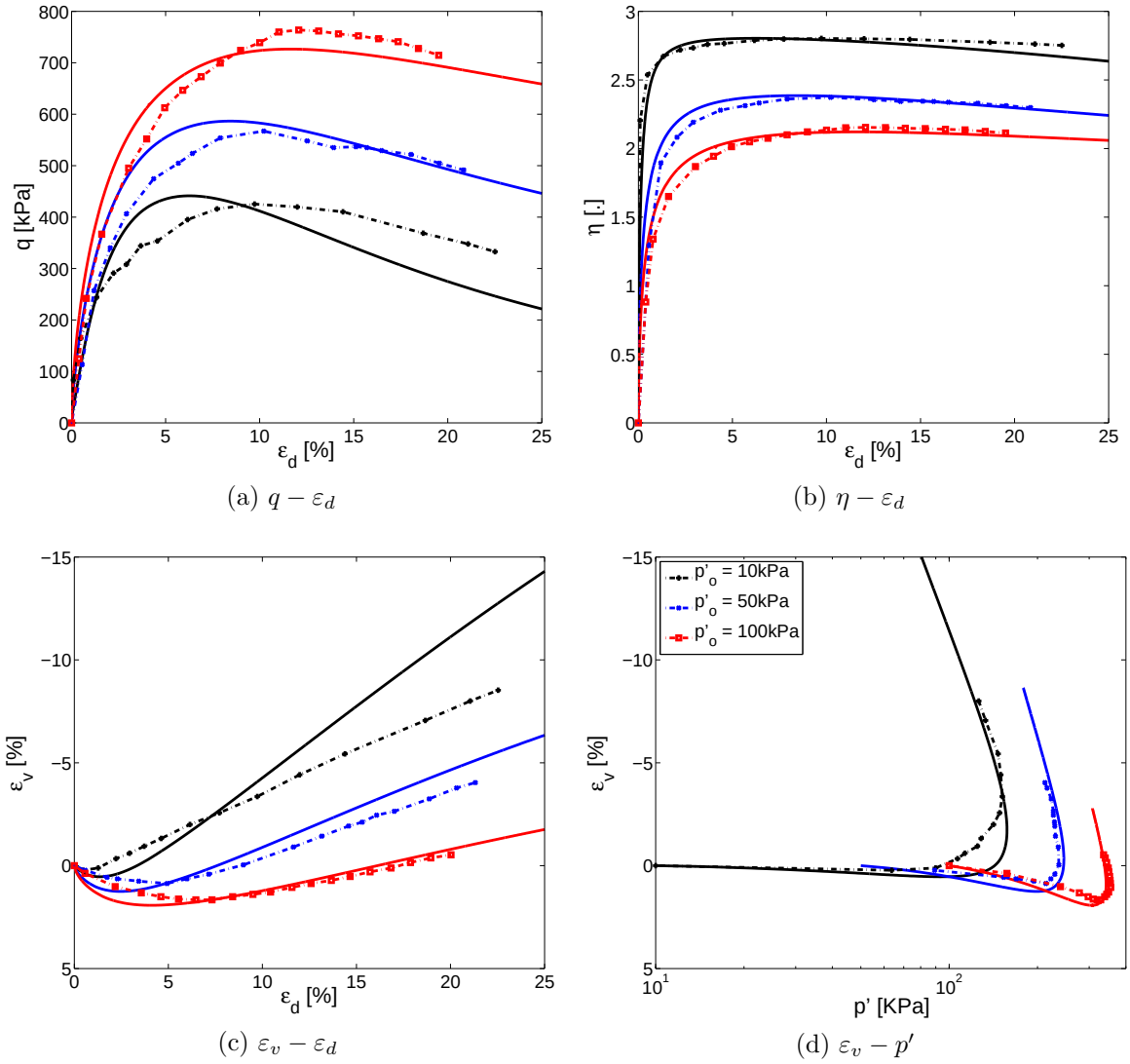

(a) $q - \varepsilon_d$ (b) $\eta - \varepsilon_d$

(c) $\varepsilon_v - \varepsilon_d$ (d) $\varepsilon_v - p'$

Figure 5.8: Comparison of drained triaxial test results performed by Indraratna et al. (2011) (dash-dot line) and numerical results obtained by the calibrated model (solid line) for the ballast material.

represented in the (η, ε_d) plane. In the case of the ballast tested by Indraratna et al. (2011), a higher value of b is considered in order to model the high deviatoric stress obtained at low confining pressure. It is reminded that b=0 represents a Mohr-Coulomb type yield surface and b=1 the Cam Clay yield surface.

Parameters a_1 and a_2 govern the evolution of the deviatoric yield surface of each deviatoric mechanism, controlling the soil rigidity in the plastic domain. These must be calibrated for both monotonic and cyclic response. The domain radius parameters r^{ela}, r^{hys} and r^{mob} are calibrated in order to obtain a coherent response in the $(G/G_{max}, \gamma)$ plane for the drained cyclic strain-controlled shear test (Appendix G). The test curves used in this work are based on large-scale free-free resonant column test results on crushed-rock-soil-mixtures tested by Mok et al. (2011) and presented in Figure 5.9. As expected,

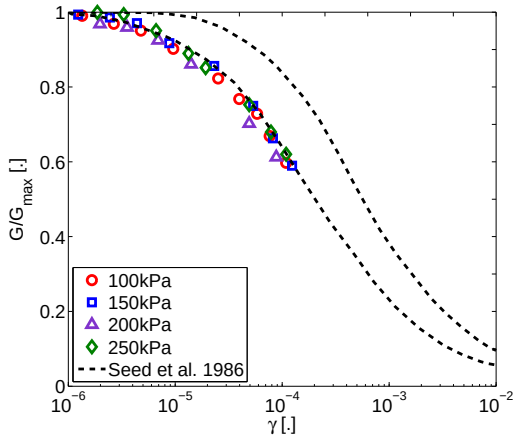

Figure 5.9: Evolution of the shear modulus G with increasing shear strain γ for crushed-rock-soil-mixtures tested by Mok et al. (2011).

these can be interpreted by the *locus* determined by Seed et al. (1986). The considered values for ballast tested by Suiker et al. (2005) and Indraratna et al. (2011) reflect the similarities and differences in their mechanical responses: both present very small elastic domain r^{ela} and small a_1 values, which imposes a rapid evolution of the mobilized friction r_k toward the hysteretic domain. The a_2 value obtained for the ballast material tested by Suiker et al. (2005) is considerably smaller than for the ballast material tested by Indraratna et al. (2011), as the influence of F_k on the deviatoric yield surface is different in both cases. The degree of nonlinearity m in the evolution of $\alpha(r_k)$ is calibrated in order to better capture the evolution of the mobilized friction during shear.

As discussed in Section 2.4.2, the characteristic angle ψ represents the change from the contractive to the dilative behavior in sands and defines the characteristic state line, phase transformation line or quasi-steady state in the (q, p') plane (Ishihara, 1993). Experimental data supports that $\phi'_{pp} = \psi$ and neither are affected by the relative density (Lade and Ibsen, 1997).

The increment of volumetric plastic strain of each deviatoric mechanism depends also on the internal variable α_ψ. In the case of the ballast material tested by Suiker et al. (2005), this parameter is high in order to better capture the volume changes in the drained triaxial test. However, the proposed set of parameters does not completely captures the dilatancy observed in the laboratory test, mainly because b is small and $\psi{=}\phi'_{pp}$. In the case of the ballast tested by Indraratna et al. (2011), this is not necessary as dilatancy is directly obtained from the proposed set of parameters.

The elastic domain radius of the volumetric mechanism r^{ela}_{iso} is taken similar as r^{ela} from the deviatoric mechanism. The parameters c_1 and c_2 govern the evolution of the isotropic hardening mechanism and can be calibrated either by undrained triaxial tests or isotropic consolidation tests. These are not available for the ballast material and the considered values are calibrated for a coherent response of numerical isotropic consolidation tests.

5.3.2 Interlayer material

In this section, two sets of parameters are calibrated for the interlayer material following drained triaxial test results: the first at water content ω_n=4%, which corresponds to an initial degree of saturation S_{ri}=32% and the second of the saturate state, S_r=100%, at water content ω_n=12%. These will be further called as interlayer material A and interlayer material B, respectively. In both cases, test results obtained at a confining stress of 400 kPa are not considered as they are not representative of the stress state of the material *in situ*.

It is important to highlight that for the interlayer material A, no information is given about the evolution of the degree of saturation during the test. Therefore, the ECP model is applied to this material in terms of total stresses, and the capillary cohesion and hardening due to the unsaturated state are neglected. Although the ECP model can further account for unsaturated conditions (Modaressi and Abou-Bekr, 1994), these are not considered in this work. Not considering the degree of saturation evolution during the test is a very strong hypothesis, but the obtained adequacy of the calibrated set of parameters in reproducing the drained triaxial test response is very good, as shown in Figure 5.10. Concerning interlayer material B, effective stress approach is considered.

The obtained set of parameters is presented in Table 5.3 and the comparison between the drained triaxial test response for the numerical parameters are presented in Figure 5.10 and 5.11 for both cases. The mechanical response of both set of parameters under different stress paths is presented in Appendix G.

The calibration procedure is identical to the one presented in the previous section. The main difference in the two set of parameters is the definition of the initial state by parameter p_{c0}, its evolution with the plastic volumetric strain ε_v^p defined by parameter β and the definition of the both deviatoric and volumetric yield surfaces (f_k and f_{iso}) by parameters b and d. The higher value of parameter p_{c0} for material A comparatively to material B reflects the over-consolidation induced by the unsaturated state (Modaressi and Abou-Bekr, 1994). These choices reflect the volumetric and deviatoric responses of the saturated material during shearing: less deviatoric stress is developed for the same initial confining pressure and more pronounced reduction of volume.

Interlayer material		
	A	B
Elasticity		
$K_{ref}(MPa)$	133.0	133.0
$G_{ref}(MPa)$	61.0	61.0
n_{el}	0.00	0.00
$p_{ref}(MPa)$	1.0	1.0
Critical State and Plasticity		
$\phi'_{pp}(^\circ)$	41	41
β	10	30
d	1.00	2.50
b	0.30	0.15
$p_{co}(MPa)$	0.65	0.18
Flow Rule and Isotropic Hardening		
$\psi(^\circ)$	41	41
α_ψ	1.70	1.10
a_1	0.00001	0.00001
a_2	0.00400	0.00120
c_1	0.00800	0.01000
c_2	0.00400	0.00500
m	1.20	1.00
Threshold Domains		
r^{ela}	0.00001	0.00001
r^{hys}	0.02000	0.02000
r^{mob}	0.90000	0.90000
r^{ela}_{iso}	0.00002	0.00002

Table 5.3: ECP model's parameters for interlayer materials.

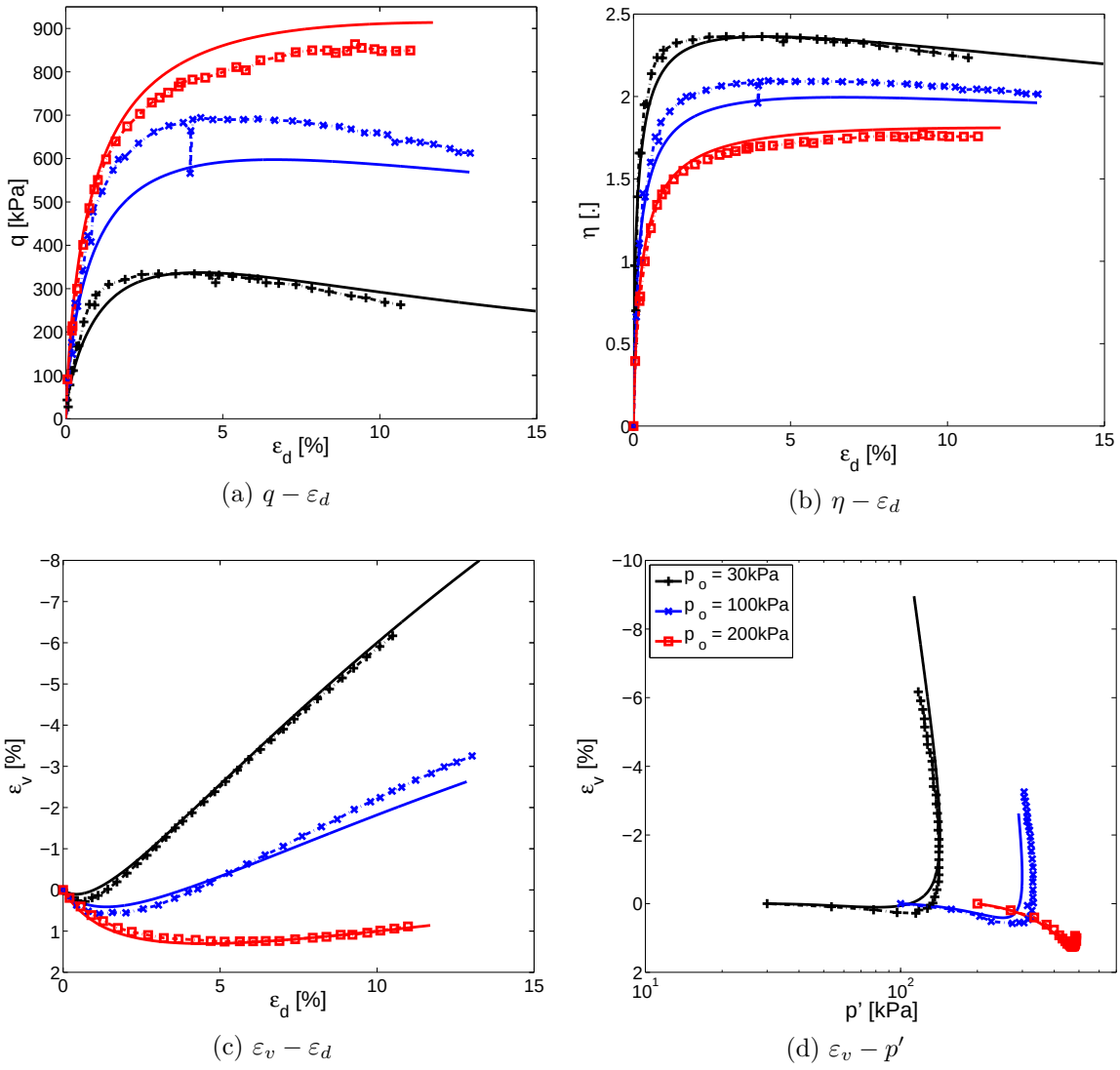

(a) $q - \varepsilon_d$ (b) $\eta - \varepsilon_d$

(c) $\varepsilon_v - \varepsilon_d$ (d) $\varepsilon_v - p'$

Figure 5.10: Comparison of drained triaxial test results performed by Trinh et al. (2012) (dash-dot line) and numerical results obtained by the calibrated model (solid line) for the interlayer material A.

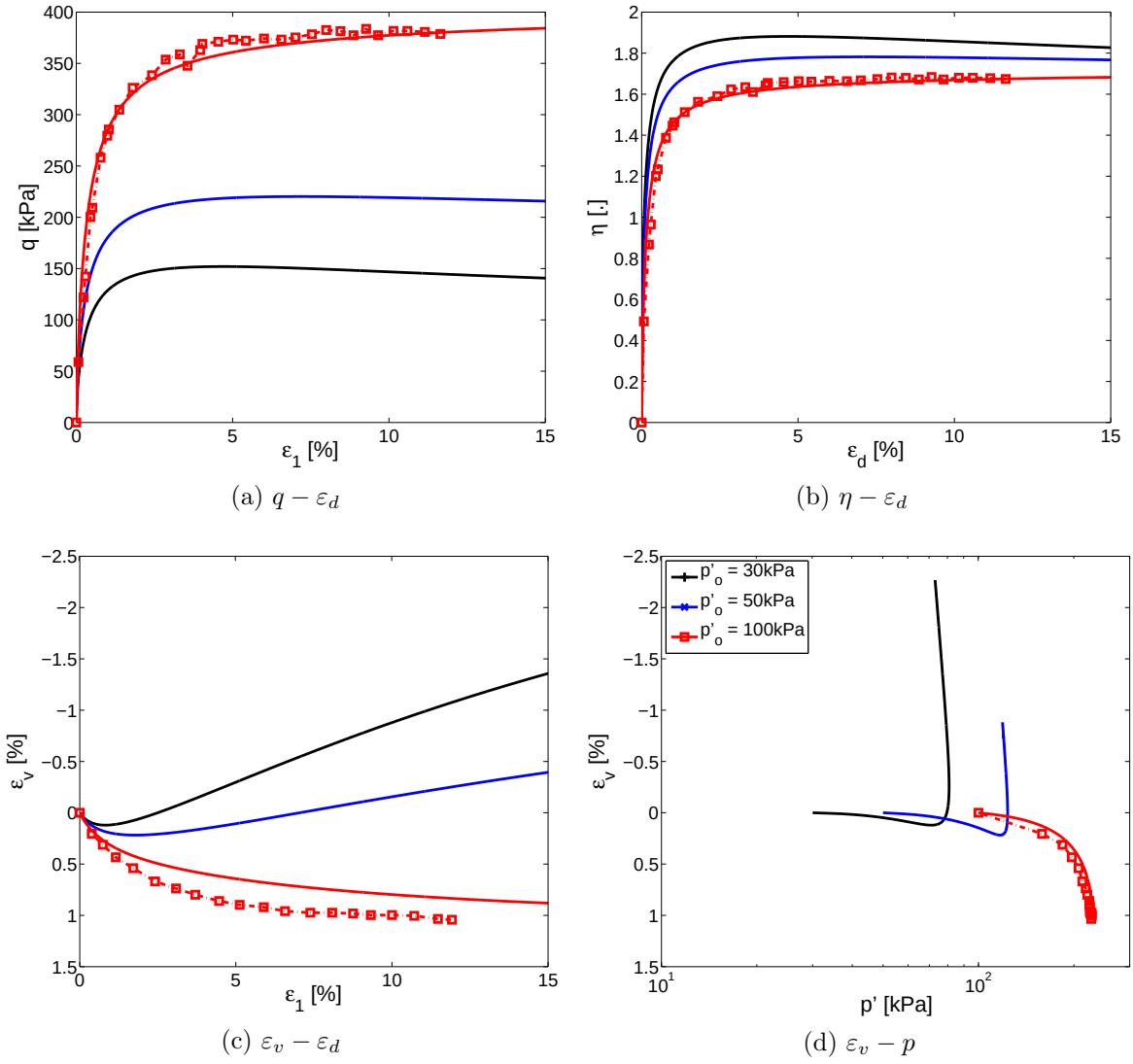

(a) $q - \varepsilon_d$ (b) $\eta - \varepsilon_d$

(c) $\varepsilon_v - \varepsilon_d$ (d) $\varepsilon_v - p$

Figure 5.11: Comparison of drained triaxial test results performed by Trinh et al. (2012) (dash-dot line) and numerical results obtained by the calibrated model (solid line) for the interlayer material B.

5.3.3 Subgrade soil materials

Different subgrade soil materials are studied in this work, the main objective being to verify the differences on track mechanical response regarding the subgrade. Two different soils are considered: dense sand (Toyoura sand at relative dry density D_r=93%) and medium-to-dense sand (Toyoura sand at relative dry density D_r=40%).

The Toyoura sand is a Japanese sand well studied and characterized (Fukushima and Tatsuoka, 1984; Tatsuoka et al., 1986). It is a uniform sand with mean grain size D_{50} of 0.16 mm, coefficient of uniformity C_u of 1.46 and specific gravity G_s of 2.64. The ECP model parameters used in this work have been already calibrated by Lopez-Caballero (2003) and Costa d'Aguiar (2008). The mechanical response of these soils to different stress paths is presented in Appendix G.

A comparative result of numerical drained triaxial tests performed for an initial confining pressure p'_o=20 kPa on the two materials are presented in Figure 5.12. The used set of parameters for the different materials is presented in Table 5.4.

Subgrade soil		
	Dense sand (D_r=93%)	Medium-to-dense sand (D_r=40%)
Elasticity		
$K_{ref}(MPa)$	296.0	296.0
$G_{ref}(MPa)$	222.0	222.0
n_{el}	0.40	0.40
$p_{ref}(MPa)$	1.0	1.0
Critical State and Plasticity		
$\phi'_{pp}(^\circ)$	30	30
β	17	43
d	3.50	3.50
b	0.22	0.22
$p_{co}(MPa)$	4.90	1.40
Flow Rule and Isotropic Hardening		
$\psi(^\circ)$	30	30
α_ψ	1.00	1.00
a_1	0.00010	0.00010
a_2	0.01500	0.01500
c_1	0.00600	0.06000
c_2	0.00300	0.03000
m	1.00	1.00
Threshold Domains		
r^{ela}	0.00500	0.00500
r^{hys}	0.03000	0.03000
r^{mob}	0.80000	0.80000
r^{ela}_{iso}	0.00010	0.00010

Table 5.4: ECP model's parameters for the considered subgrade soils.

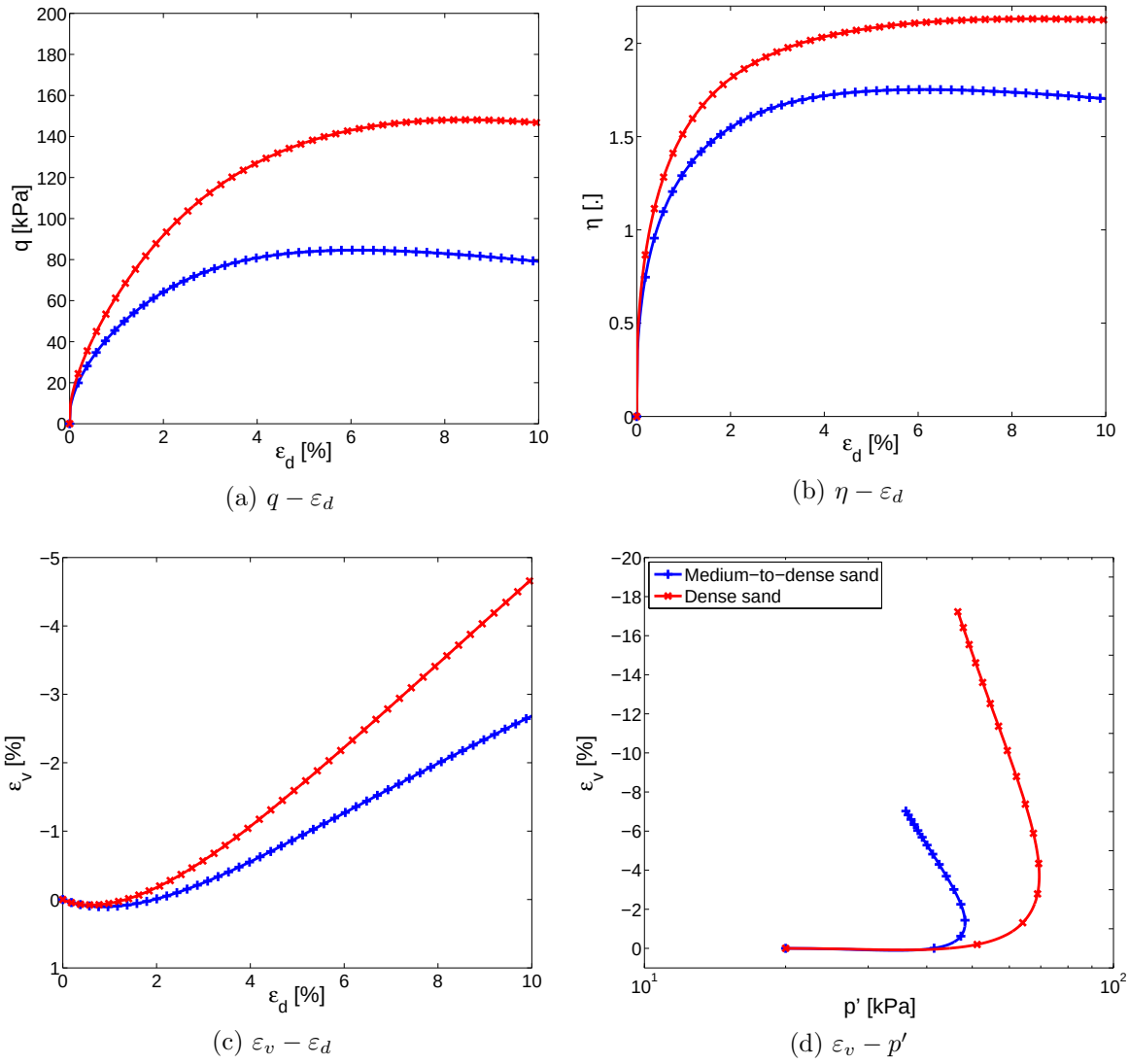

(a) $q - \varepsilon_d$ (b) $\eta - \varepsilon_d$

(c) $\varepsilon_v - \varepsilon_d$ (d) $\varepsilon_v - p'$

Figure 5.12: Comparison of numerical drained triaxial tests performed on considered subgrade materials (p'_o=20 kPa).

5.4 Numerical strategy for the nonlinear railway track model

Considering advanced elastoplastic models for unbounded domain problems is very often a challenge, as at low effective confining stress soil presents high dilative behavior and very low resistance. In many applications (pile resistance, deep foundations, etc) the unbounded layer contributes marginally to the total structure's mechanical resistance. In this case, usually the soil mechanical behavior near the free surface is modified and/or simplified in order to avoid numerical errors due to the singularity of zero mean pressure in the soil constitutive models (Berenguer Todo Bom, 2014).

However, in railway applications and more generally in moving load applications, the structure's response is affected by the mechanical behavior of the materials directly beneath it, which are subjected to low confining pressure at rest. In this context, using the ECP model in a numerical model of the track for railway geomaterials and particularly for ballast presents some issues. These can be related to two factors:

1. Stress initialization conditions. Soil mechanical response depends on the initial conditions and these must be correctly modeled in order to obtain an adequate response. As the ballast layer is the topmost layer, it is subjected to low confining pressures. Stewart et al. (1985) presented laboratory test results on cyclic loading on ballast at a confined trackbox and inferred that confinement may increase during the railway track life (measured as an increase on lateral stress and described in their work by an increase in the ratio $k_0 = \sigma^0_{yy}/\sigma^0_{zz}$, where σ^0_{yy} and σ^0_{zz} are the initial lateral and vertical stresses). However, the boundary conditions used in the test were not representative of the railway track, as ballast was tested on a confined trackbox but on track it presents a free surface at lateral boundaries. In real tracks, a standard procedure after renewal or tamping of ballast is to stabilize it before subjecting the track to train loads, as ballast experiments high settlement and grain rearrangement during the conditioning phase or the first 100 loading cycles (Jeffs and Marich, 1987). In this work, stress initialization considers only material self-weight. A procedure based on layer construction is used in order to correctly model the initial state of the materials on the track.

2. Contact conditions between the sleeper and the ballast layer. Shared nodes between the sleeper and the ballast in the FE mesh are not representative of the real track conditions. The rail bending tends to uplift the sleepers at a certain distance from the load, which depends on the load repartition among sleepers and rail pad stiffness. This uplift is directly applied on ballast material right down the sleepers, which reduces the confining stress to very low values, leading to material failure. Moreover, by considering shared nodes between the sleeper and the ballast, shear stress near the interface is poorly approximated by the model as a consequence from the difference in stiffness of both materials.

These aspects motivated some modifications in the numerical model, regarding the elastic simulations presented in Section 3.4. These are described in next sections.

Particularly for ballast material, the calibrated sets of parameters reflect the high dilative behavior at low confining stress. However, the plane-strain hypothesis in the numerical 2D model leads to incompatible volume changes when increase in volume is obtained, as no lateral strain is allowed, i.e. ε_{xx}=0. From the two sets of parameters, the one representing the ballast tested by Indraratna et al. (2011) is the one presenting highest dilative characteristics. As discussed in Section 5.3.1, the parameter b calibrated from the response in the (ε_d, η) plane plays an important role on increasing the volume change at other stress paths than the triaxial one. The set of parameters representing the ballast tested by Suiker et al. (2005) presented less volumetric strain and lower dilatancy at low confining pressures. Therefore, the latter is the only one considered in the numerical simulations presented in following sections.

5.4.1 Materials initial state on the track

In the linear elastic case presented in Section 3.4, the methodology in obtaining a coherent initial state was not addressed as it is irrelevant regarding the considered mechanical behavior. However, this is an important step for nonlinear models relying on the stress state. The procedure must be coherent with the construction phase of the studied geotechnical structure, as the initial stress state will depend on it. For instance, this initialization phase is particularly necessary in excavation problems, when the stress state of the soil next to the excavated area is influenced by the excavation process.

In GEFDyn software (Aubry et al., 1986; Aubry and Modaressi, 1996), a comprehensive method is implemented, which allows to "construct" the model from the bottom to the top as in real tracks. In order to reach equilibrium, a first initial state is given in terms of the earth pressure coefficient, k_o. For all layers, the value 0.5 was considered for k_o. In this case, the following initial conditions are imposed:

$$\begin{aligned} {\sigma'_{yy}}^o = {\sigma'_{xx}}^o = k_o {\sigma'_{zz}}^o \\ \sigma^o_{yz} = 0 \end{aligned} \tag{5.4}$$

where ${\sigma'_{zz}}^o$ is basically obtained as a function of depth, ${\sigma'_{zz}}^o = \rho g \Delta h$. Equilibrium is then achieved by evolving the different materials from this initial state to the geostatic stress level. Initializing a material means not only considering both its stiffness and mass matrices in the FE methodology but also estimating the internal variables of the constitutive model that ensures plastically admisible states. After all track layers are initialized and equilibrated, sleepers, rail pads and rails are introduced in the model. This procedure allows to install the sleeper after the ballast layer is in place, which reduces initial shear stress in the sleeper-ballast interface due to equilibrium conditions. This aspect is also addressed by interface elements, which are discussed in the section 5.5.

However, it is important to highlight that the construction phase described above does not account for any compaction procedure coming from either specific compaction equipments or by trains used during track construction. In this sense, materials can be considered as still "virgin" to the stress characteristics imposed by the moving load. This is particularly important concerning shear stress and the increase in deviatoric stress due to shearing, as will be shown in the next section.

5.4.2 Sleeper kinematics

In the nonlinear model, it is necessary to correctly model the sleeper kinematical response during the moving load passage. In tracks, the sleeper is posed over the ballast layer and is maintained in place due to: self-weight, ballast weight (in the lateral direction) and volume (in the longitudinal direction) and shear stress developed due to friction with the ballast grains in the lateral and bottom surfaces. In the numerical model presented in Section 3.3, shared nodes are used between the sleeper and the ballast layer in the finite element mesh. This assumption is not representative of the physical characteristics of the sleeper-ballast interface. In order to better capture the sleeper boundary condition, mechanical interfaces are considered. These allow discontinuities in the stress field once uplift is verified. The mathematical formulation and parameters of the mechanical interfaces used in this work is presented in Appendix H. Decoupling the sleeper and ballast in the FE mesh showed to be an important step toward using a nonlinear model for ballast. Indeed, this procedure allowed to significantly reduce the initial shear stress (σ^o_{yz}) appearing at the sleeper-ballast interface after track construction, as shown in Figure 5.13.

In the numerical model, shear stress developed from friction between the sleepers and the ballast layer is neglected (shear modulus G of the interface model is very low), as the main interest in using the mechanical interface is to correctly model the vertical response of the sleeper. The mechanical parameters used can be viewed as penalty factors in both vertical and lateral directions, in order to avoid overlapping of the FE nodes.

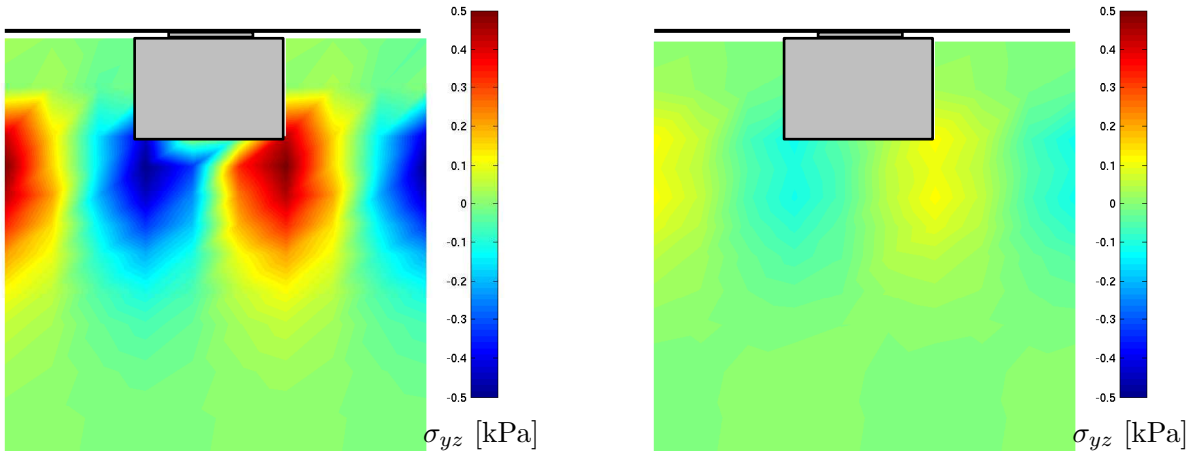

(a) (b)

Figure 5.13: Example of shear stress σ_{yz} around the sleeper-ballast interface according to initialization procedure and interface conditions. a) Sleeper-ballast shared nodes and no initialization procedure; b) Considered methodology (sleeper-ballast interface element and initialization procedure).

5.4.3 Ballast stress path identification and discussion

The numerical simulation results presented in Section 3.4 gave some insights about the stress paths imposed on the materials by the moving load (Figure 3.26). Different stress paths are observed depending on the observation point regarding the sleeper, i.e. directly under or between sleepers. In the particular case of the ballast layer, under sleeper points closely follow a stress path characterized by a unitary slope and between sleepers points are subjected to a more complex stress path. Although these results are obtained considering linear elasticity, they provide an initial basis for further verification of the calibrated set of parameters on stress paths other than the triaxial. Therefore, it is proposed to verify the aptitude of the calibrated set of parameters for ballast in reproducing the material response under cyclic load, for a stress path characterized by a slope lower than the triaxial one. The choice is made of conducting numerical cyclic oedometric tests under initial low confining pressures. The test is performed by numerically integrating the constitutive model for the boundary conditions imposed by the oedometer apparatus (ε_3=0 $\rightarrow$ ε_v=ε_d=ε_1). The test is defined by fours steps:

1. From an isotropic initial state at p'_0=10 kPa, increase and reduction of the vertical stress σ_1 of 10 kPa;
2. Increase and reduction of σ_1 of 40 kPa;
3. Increase and reduction of σ_1 of 70 kPa;
4. Increase and reduction of σ_1 of 100 kPa.

These steps of increasing and reducing σ_1 are defined in order to verify the aptitude of the calibrated parameters on capturing the volumetric evolution during the reloading phases. The reloading phase can be defined in this case when the material is subjected to stresses which it has already been subjected to. This test is considered relevant regarding the stress path imposed by the moving load on the observation points under the sleeper. The main advantage of imposing oedometric conditions instead of directly imposing a numerically obtained stress path from simulations is assuring the numerical convergence of the test.

Two cases are considered for exemplifying the importance of the calibration procedure in the response of the material. These are the following:

- Case 1 is defined by the set of parameters given in Table 5.2 representing the ballast material tested by Suiker et al. (2005);
- Case 2 the same set of parameters as Case 1 is considred, with the slight difference that the elastic domain radius r^{ela} is changed from 1.10^{-5} to 1.10^{-3}.

Figure 5.14 shows the mechanical response to the proposed numerical test for Case 1 and 2, where blue solid line represents Case 1, red dashed line represents Case 2 and $q = \sigma_1 - \sigma_3$ as for the triaxial test. The obtained response for Case 1 is coherent with the oedometric path (Biarez and Hicher, 1994), the hysteresis loop on deviatoric and volumetric responses being correctly represented during the reloading phases. However, by

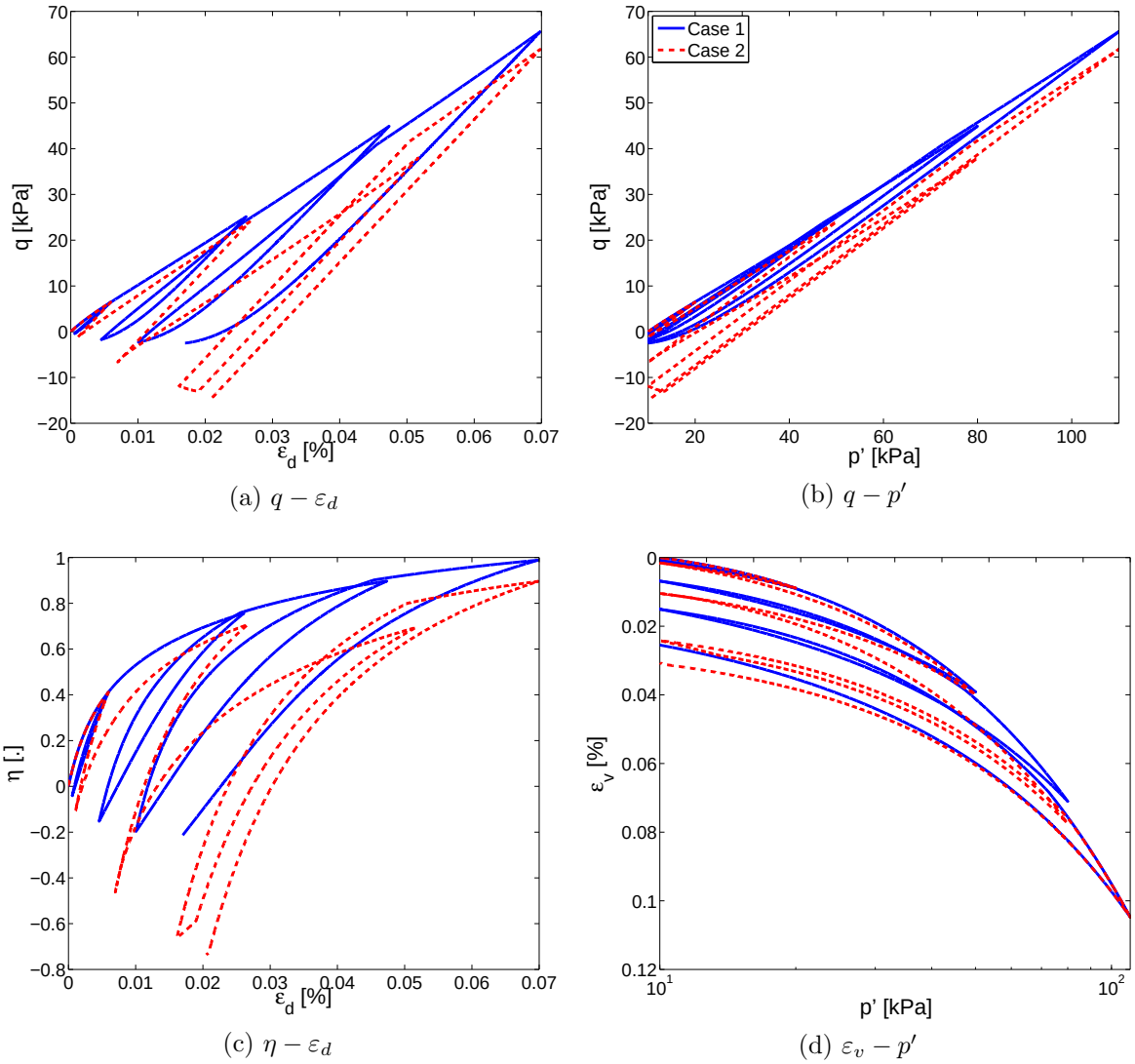

(a) $q - \varepsilon_d$ (b) $q - p'$

(c) $\eta - \varepsilon_d$ (d) $\varepsilon_v - p'$

Figure 5.14: Numerical cyclic oedometric test results for the set of parameters calibrated for the ballast material tested by Suiker et al. (2005). Blue solid line represents Case 1 and red dashed line represents Case 2.

increasing the elastic domain radius of the deviatoric mechanism, the considered set of parameters is not able to correctly capture the unloading/reloading phases and a uncoherent response is obtained.

The ECP model considers a double memory system in order to model the cyclic response. Both monotonic and cyclic mobilized friction parameters r_k^m and r_k^c evolve depending on the load direction to the normal vector to both deviatoric and volumetric yield surfaces. The evolution of these parameters during the oedometric cyclic loading is verified for the different calibrated materials. The results for both monotonic and cyclic degrees of mechanism mobilization for the devatoric and isotropic mechanisms, obtained from the test results shown in Figure 5.14, are presented in Figure 5.15. Dashed gray lines represent the end of increasing σ_1 and dashed black lines represent the end of reducing σ_1

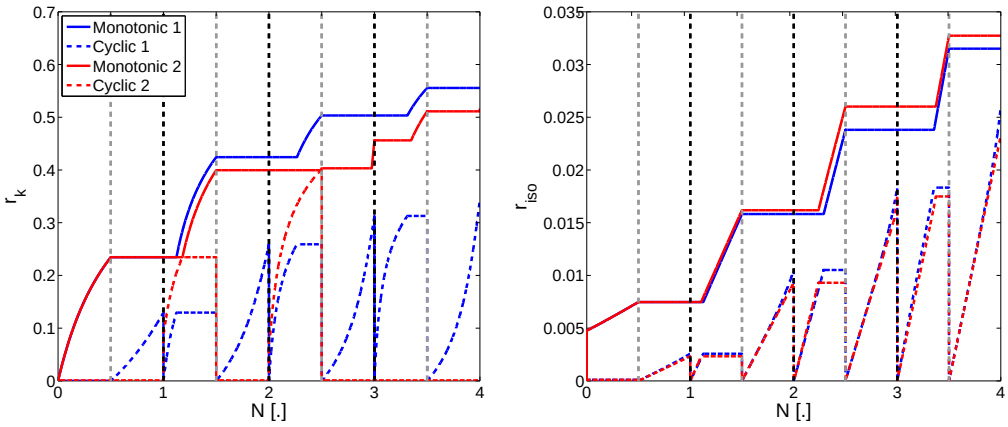

(a) (b)

Figure 5.15: Evolution of monotonic and cyclic degrees of mechanism mobilization during the numerical cyclic oedometric test for the set of parameters calibrated for the ballast material tested by Suiker et al. (2005). N stands for each step of the proposed numerical test. a) Deviatoric yield surface; b) Isotropic yield surface.

thus, the end of the considered step. Correctly triggering the cyclic mechanism during the load reversal has proved to be an essential aspect in order to capture a coherent response for the numerical cyclic oedometric test. The elastic domain radius of both deviatoric and isotropic mechanisms, r^{ela} and r_{iso}^{ela} respectively, are the important parameters in order to correctly capture the unloading/reloading phases. As shown in Figure 5.15, both the deviatoric and isotropic cyclic mobilized friction parameters are triggered for Case 1 during the unloading phase and this aspect is the main point controlling the response in the reloading phase, thus controlling the observed hysteresis in the material behavior.

5.5 Nonlinear response of the railway track

The main advantage of using the proposed nonlinear modeling methodology regarding elastic modeling techniques is the possibility of taking into account initial state evolution of the different materials. This approach is particularly adapted for studying the first loading cycles the railway track is subjected to, when materials develop the highest deviatoric and volumetric strains. Soil behavior depends on the loading history and in this sense considering the influence of permanent strains on the evolution of the soil initial state is essential to study this first phase of the track behavior.

5.5.1 Numerical model characteristics

A schematic representation of the conventional track considered in the following sections is given in Figure 5.16. It is composed of two layers (ballast and interlayer) and the subgrade soil. Differently from the previous sections, the choice is made in the nonlinear model of considering fresh and fouled ballast as one and same material. The total width

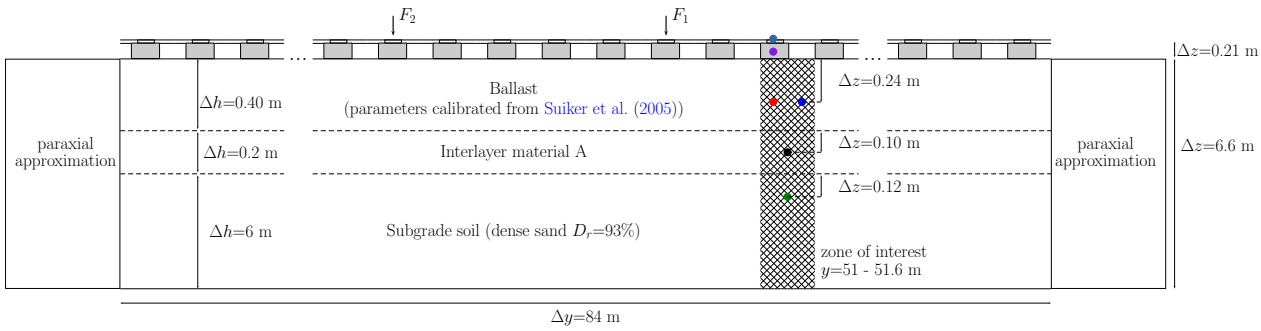

Figure 5.16: Schematic representation of the nonlinear model for a conventional track configuration.

of the ballast layer corresponds thus to 40 cm. The 4-node bilinear quadrilateral elements from the linear model are replaced by 8-node biquadratic quadrilateral elements with 9 integration points. These provide better numerical convergence for the nonlinear model. In order to keep the same computational cost, the mesh elements are bigger, maintaining roughly the same total number of integration points. The element lateral size is increased from 6 cm to 10 cm and elements are two times higher in the vertical direction than in the linear elastic model. The total length of 84 m is maintained, the mesh being composed of 58807 nodes, 16142 8-node biquadratic quadrilateral elements modeling the track and soil, 1686 beam elements modeling the rail and 983 6-node quadratic interface elements modeling the sleeper-ballast interface.

The representative observation points for each layer are also presented in Figure 5.16. It was shown in Section 3.4 that two representative stress paths are observed for the ballast layer depending on the position of the observation point regarding the sleeper. In this sense, two observation points are chosen for the ballast layer, which are called ballast under the sleeper (BUS) and ballast between sleepers (BBS) in the following analysis.

The time integration scheme discussed in Section 3.2.4 is maintained, i.e. numerical damping from the Newmark scheme is considered. However, the time step is reduced in order to assure a better convergence of the nonlinear model, Δt=5.10^{-5} s. In this case, the estimated numerical damping is 10 times smaller than in the linear elastic simulations, $\zeta \approx 0.00002 f$. It is important to highlight that soil damping is considered by the nonlinear model (i.e. material damping). Numerical damping is introduced as a mean to ensure low high frequency energy due to the spatial discretization and damping in the elastic domain.

Concerning the boundary conditions, the paraxial approximation is preferred to the proposed Kelvin-Voigt absorbing boundaries for the nonlinear model, as it can better approximate both vertical and lateral soil responses. Obtaining more adapted boundary conditions for dynamic nonlinear numerical models is a research topic by itself and it is not in the scope of this work. Material damping induced by plastic deformation is also expected to attenuate wave energy before arriving to the boundaries.

In Section 3.4, the mechanical response of the track and materials for different track

conditions was characterized by applying one bogie load. This approach is useful when one train passage can be decomposed in independent bogie loads, as often considered for the passenger cars from TGV high-speed trains. The same simulation strategy is kept in this chapter. The choice is made of presenting separately the results for one bogie load (first loading cycle) and for multiple bogies (cyclic load).

In the following sections, the results of the nonlinear mechanical model are presented. The load transfer mechanisms between layers and the differences appearing in the mechanical response of ballast are highlighted for one bogie load at 15 km/h. The influence of speed on the stress-strain path and shear response of materials is then analyzed by performing numerical simulations for one bogie load at 220 km/h. The cyclic response of materials and the influence of stress histories is then discussed by considering 5 bogie cycles at different speeds.

5.5.2 Mechanical response at small speed

A general view of the model response during the first loading cycle is shown in Figure 5.17, where the vertical displacement is presented over a scaled deformed mesh of a 15 m track section. Rail and rail pad elements are omitted from this representation for the sake of clarity. Forces F_1 and F_2 model the two axle loads applied on the track. These forces represent a train bogie crossing the track from left to right. Permanent settlement, i.e. plastic deformation, is observed at the different materials after loading. The empty spaces observed between sleepers and unconfined ballast are a consequence of the mechanical interfaces used for ensuring the sleeper kinematics.

The time response of vertical displacement (u_z) on the selected control points is shown

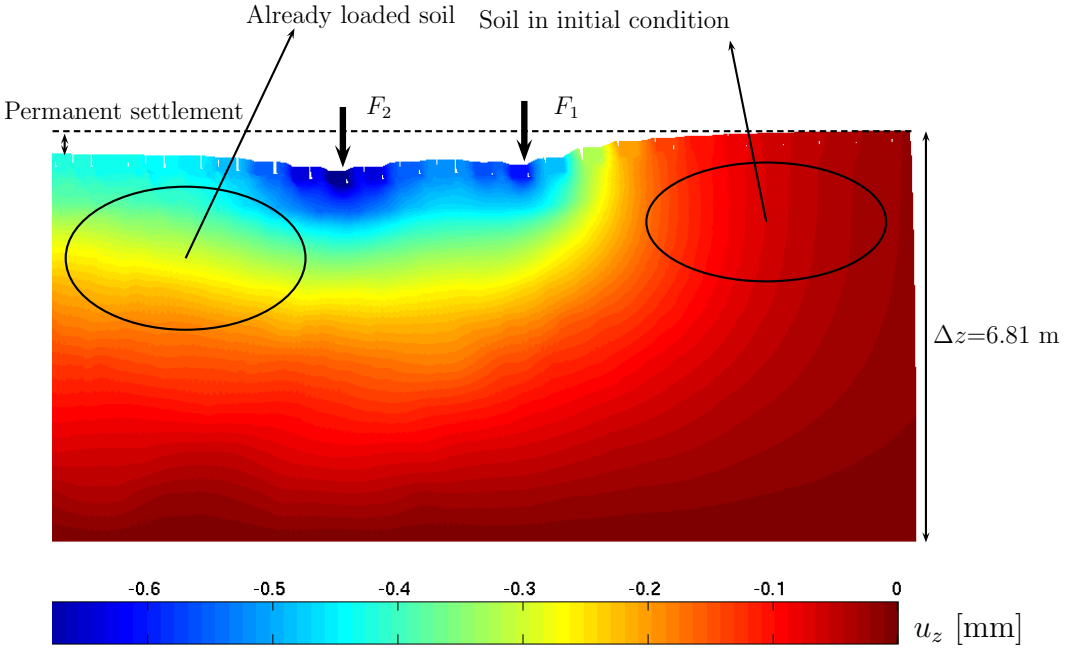

Figure 5.17: Vertical displacements (u_z) obtained by the model (scaled deformation) for a bogie at 15 km/h.

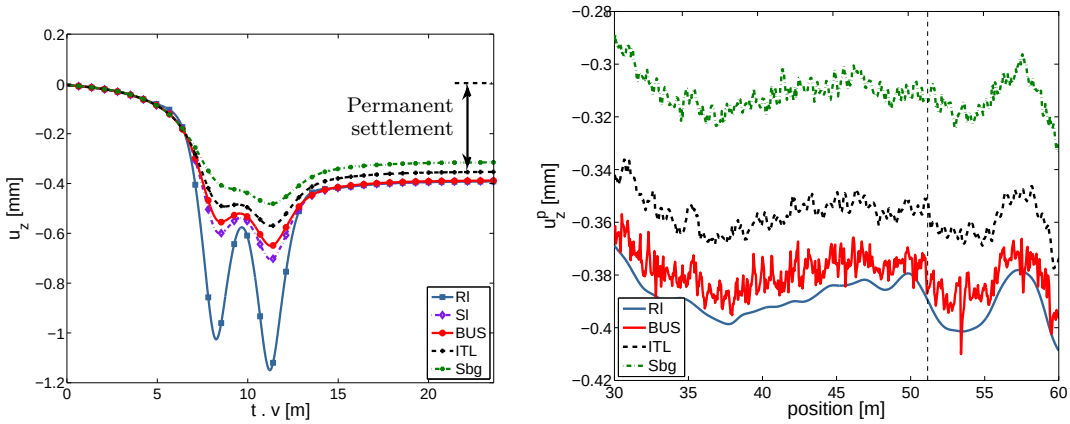

(a) (b)

Figure 5.18: Vertical displacement for different materials at 15 km/h. a) Time scaled response; b) Profile of permanent settlement in a track section (Dashed dark line represents considered points in a)). Rl: Rail; Sl: Sleeper; BUS: ballast under the sleeper; ITL: interlayer; Sbg: subgrade.

in Figure 5.18. The convective axis t.v [m], also used in Section 3.4.3, is an effective way for further comparison of time signals at different speeds. Higher values of vertical displacement are obtained for the second axle passage for all layers, as a consequence of permanent settlement occurring during the first axle passage. At the rail, a total permanent settlement of 0.4 mm is obtained during the first loading cycle. However, as shown from Figure 5.18b, permanent settlements observed in a track section are not homogeneous and depend mainly on the local behavior of the materials.

The obtained vertical stress (σ'_{zz}) in the track is shown in Figure 5.19. A further zoom on the dashed box is presented in Figure 5.20. From a homogeneous initial state of the materials, an inhomogeneous final state is obtained after the load has passed, which is shown in the left hand-side of Figure 5.19. These inhomogeneities in the final state of the materials arise naturally as a consequence of the differences in plastic deformation along the track observed in Figure 5.18b. The main consequence of this process is the occurrence of variations of stiffness at different locations of the track. The effet of such variations in stiffness in the track stiffness measurement has been extensively discussed in Chapter 4. These results highlight one of the motivations for considering material variability in elastic track models.

The vertical load transfer mechanism between layers can be analyzed from Figure 5.20. For this track profile, only 3 sleepers are responsible for distributing the load from the rail to the ballast. Low load spread is observed under the ballast: while points directly beneath the sleeper are subjected to maximum vertical stress of 35 kPa, points between sleepers are subjected to much lower values, the maximum being around 20 kPa for points near the interlayer. The closer look on the first axle presented in Figure 5.20b shows the different layer profiles during load. Differently from static analysis, the vertical load is not equally distributed among the sleepers, as the soil already loaded presents higher stiffness. This effect cannot be observed with a linear elastic model. An uniform vertical

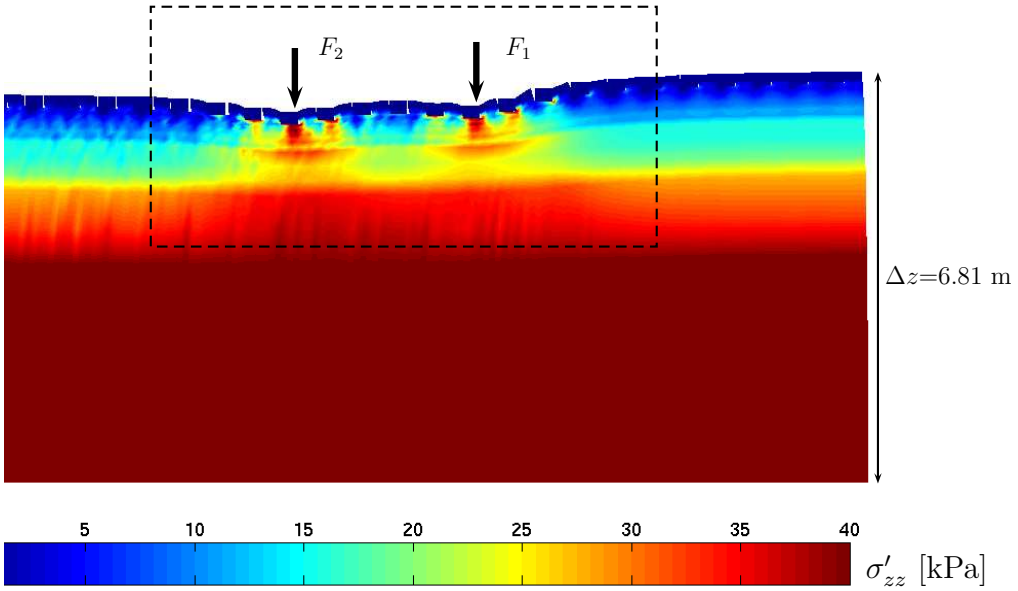

Figure 5.19: Vertical stress (σ'_{zz}) obtained by the model (scaled deformation) for a bogie at 15 km/h.

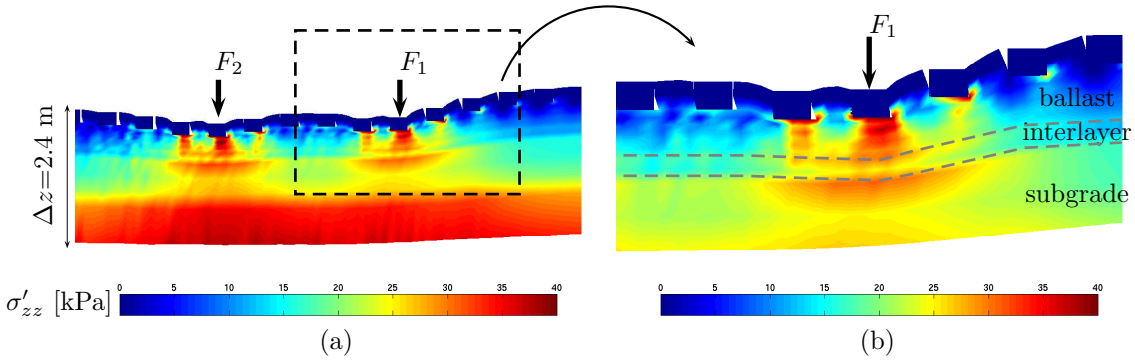

Figure 5.20: Vertical stress (σ'_{zz}) obtained by the model (scaled deformation) for a bogie at 15 km/h. a) Zoom for a small track section; b) Zoom on the first axle passage.

load distribution is obtained at the subgrade, thanks to the interlayer material. As a consequence of the increase of the initial vertical stress in depth, variations imposed by the moving load rapidly decrease below 1 m in the subgrade.

The same track profiles are given for the obtained lateral stress (σ'_{yy}) (Figure 5.21) and shear stress (σ_{yz}) (Figure 5.22). In the ballast layer, higher maximum lateral stress is observed between sleepers than under the sleeper, although the stress levels are lower than for vertical stress. As for the previous case, the interlayer is responsible for homogenizing the stress variations in the lateral direction. However, the subgrade is subjected to the highest maximum lateral stresses. An increase of residual values is observed for all materials, specially at the subgrade.

These two mechanisms are highlighted in Figure 5.23, where the maximum vertical and

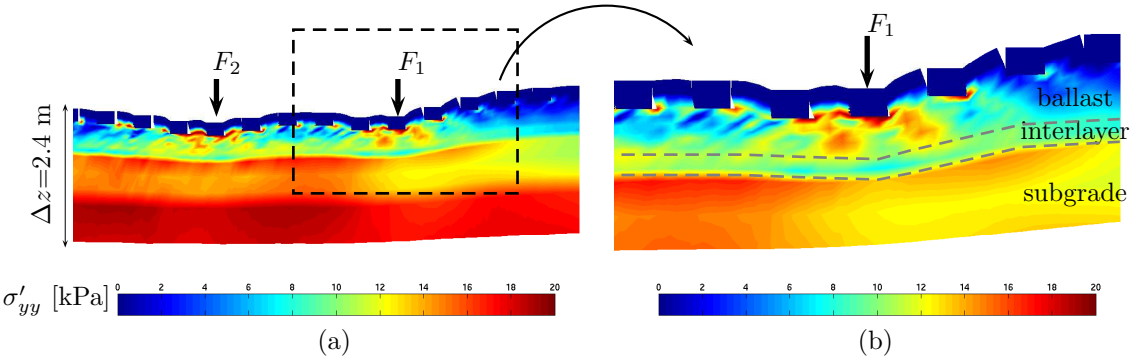

Figure 5.21: Lateral stress (σ'_{yy}) obtained by the model (scaled deformation) for a bogie at 15 km/h. a) Track section; b) Zoom on the first axle passage.

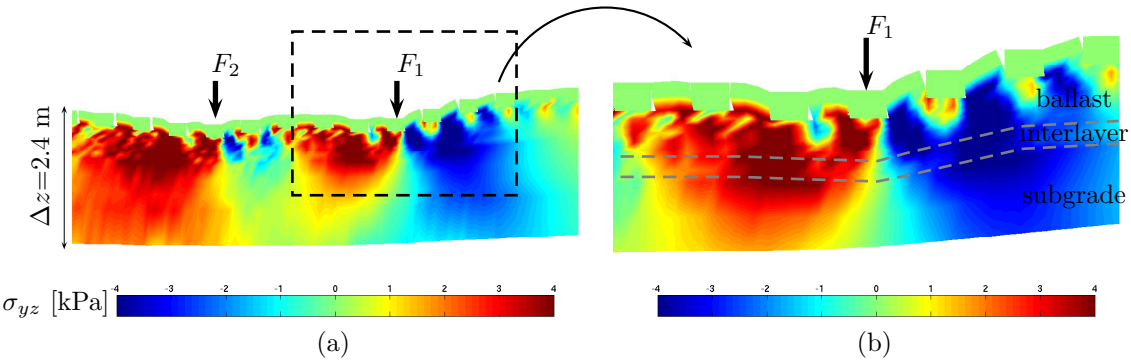

Figure 5.22: Shear stress (σ_{yz}) obtained by the model (scaled deformation) for a bogie at 15 km/h. a) Track section; b) Zoom on the first axle passage.

lateral stresses relative to the initial value for the points at the zone of interest are shown. As expected, the values are higher at lower depth as maximum stresses are higher and initial vertical and lateral stresses are lower. The main differences concerning the position relative to the sleeper are concentrated in the ballast layer, whereas at the subgrade, no differences are observed.

Concerning the obtained shear stress results, once again the importance of the control point position in ballast regarding the sleeper is highlighted, the highest values being obtained for points between sleepers during the loading cycle. A final state of non null shear stress is obtained after load for all materials. Differently from normal stresses, the interlayer does not seem to play a particular role in the shear stress spread to the subgrade.

The same analysis can be performed regarding the deformation characteristics of the track. Figure 5.25 presents the vertical strain (ε_{zz}) on materials during load. It can be seen that a discontinuous strain profile is observed on ballast, vertical strains being concentrated on points under the sleeper. The subgrade presents vertical strain values higher than the interlayer. Therefore, the interlayer can be viewed in this track profile as a low deformable layer, which guarantees its capability in homogenizing vertical stress variations due to discrete sleeper support. The lateral strains (ε_{yy}) developed by the materials

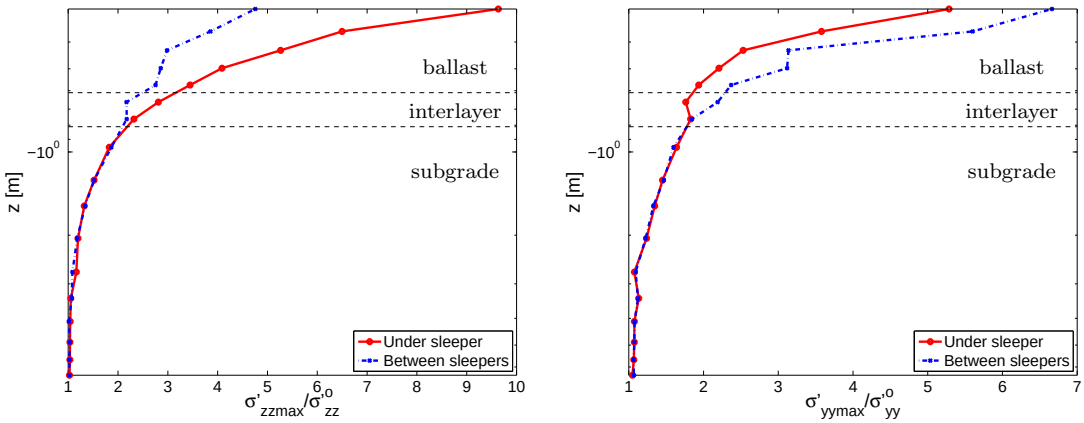

Figure 5.23: Comparison of maximum stresses during load relative to the initial value for a load speed of 15 km/h. a) Vertical stress (σ'_{zz}); b) Lateral stress (σ'_{yy}).

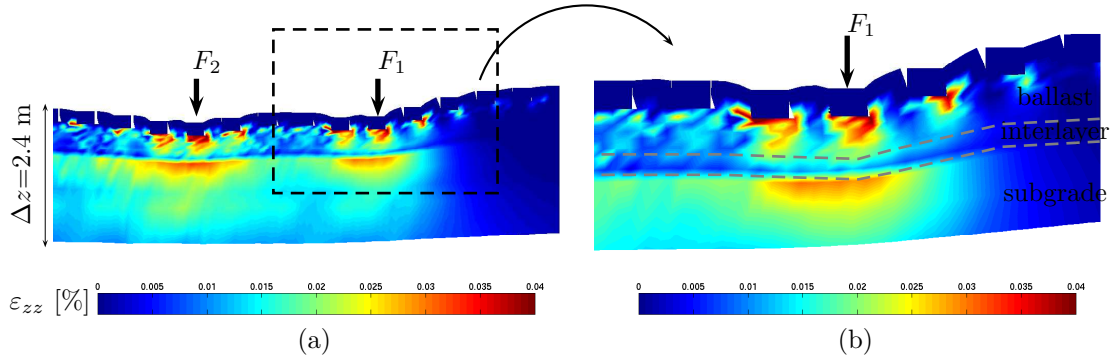

Figure 5.24: Vertical strain (ε_{zz}) obtained by the model (scaled deformation) for a bogie at 15 km/h. a) Track section; b) Zoom on the first axle passage.

during load are approximately 10 times lower than vertical strains (Figure 5.25). For the first axle (F_1), a clear profile of the wave propagation in the soil is observed (Figure 5.24a), although during the second axle passage this is less visible due to different plastic strains cumulated by the materials.

The profiles of maximum vertical and lateral strains in the zone of interested are shown in Figure 5.26. The same conclusions from the stress characteristics regarding the differences on under the sleeper and between sleepers points (Figure 5.23) can be draw for the strain characteristics. Moreover, it can be seen that maximum vertical and lateral strains are higher at the subgrade than at the interlayer.

A local analysis of the mechanical response for the different control points is hereafter discussed. Stresses on the (y, z) plane are presented in Figure 5.27. As expected, maximum vertical stress (σ'_{zz}) is higher for ballast under the sleeper, which presents a stress amplitude ($\Delta\sigma'_{zz}$) of 20 kPa. Interlayer and the subgrade present similar maximum values, although reduction of the final value of vertical stress is observed for the interlayer. Concerning lateral stress (σ'_{yy}), an increase of residual values is observed for all layers,

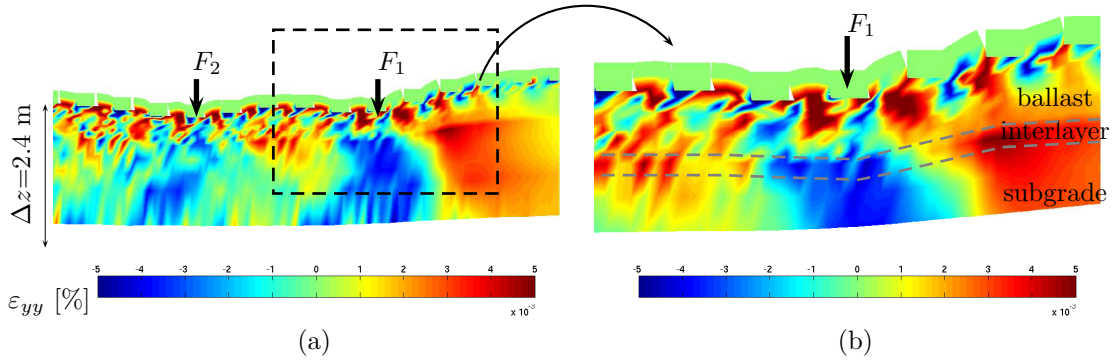

Figure 5.25: Lateral strain (ε_{yy}) obtained by the model (scaled deformation) for a bogie at 15 km/h. a) Track section; b) Zoom on the first axle passage.

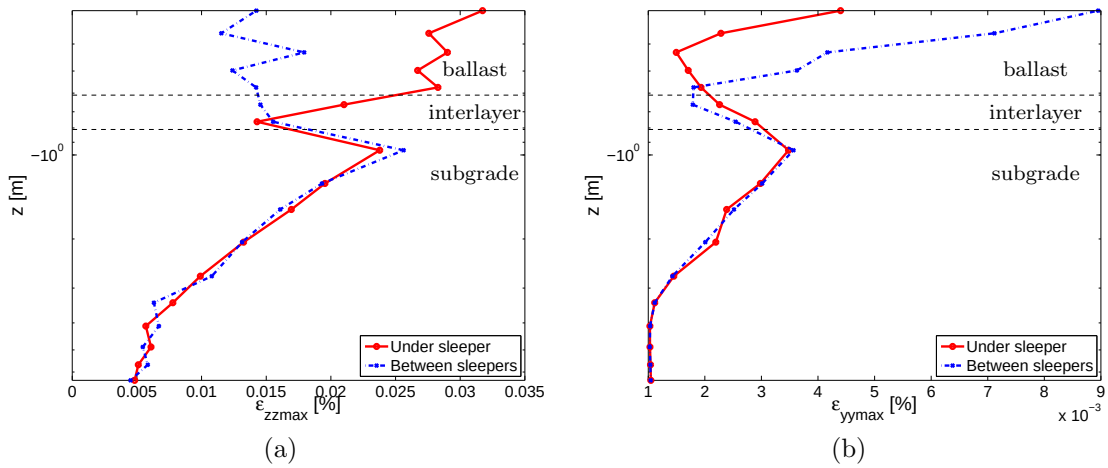

Figure 5.26: Comparison of maximum strains during load for a load speed of 15 km/h. a) Vertical strain (ε_{zz}); b) Lateral strain (ε_{yy}).

which leads to an increased confining pressure.

Concerning shear stress (σ_{yz}), the interlayer presents the highest amplitude and ballast under the sleeper the lowest. Residual shear stress is observed for all layers. The principal stress axes rotation angle (α_{yz}) (Figure 5.27d) varies significantly for all materials after load, reflecting the increase of lateral stress relative to vertical stress and the existence of residual shear stress after the load has passed. The earth pressure coefficient (k_o) is shown in Figure 5.27e for these materials. Values of k_o near the unity are obtained after load for all materials, therefore important variations of α_{yz} can be produced by low variations of shear stress. Even though this is less important at the subgrade, a total amplitude of around 40° is observed during load.

Regarding the strain levels, Figure 5.28 shows the vertical (Figure 5.28a), lateral (Figure 5.28b) and shear strains (Figure 5.28c) on materials during load. Ballast under the sleeper and the subgrade present the highest strain levels, the interlayer presenting lower strain variations. Both vertical and shear strain levels are higher than lateral strains, max-

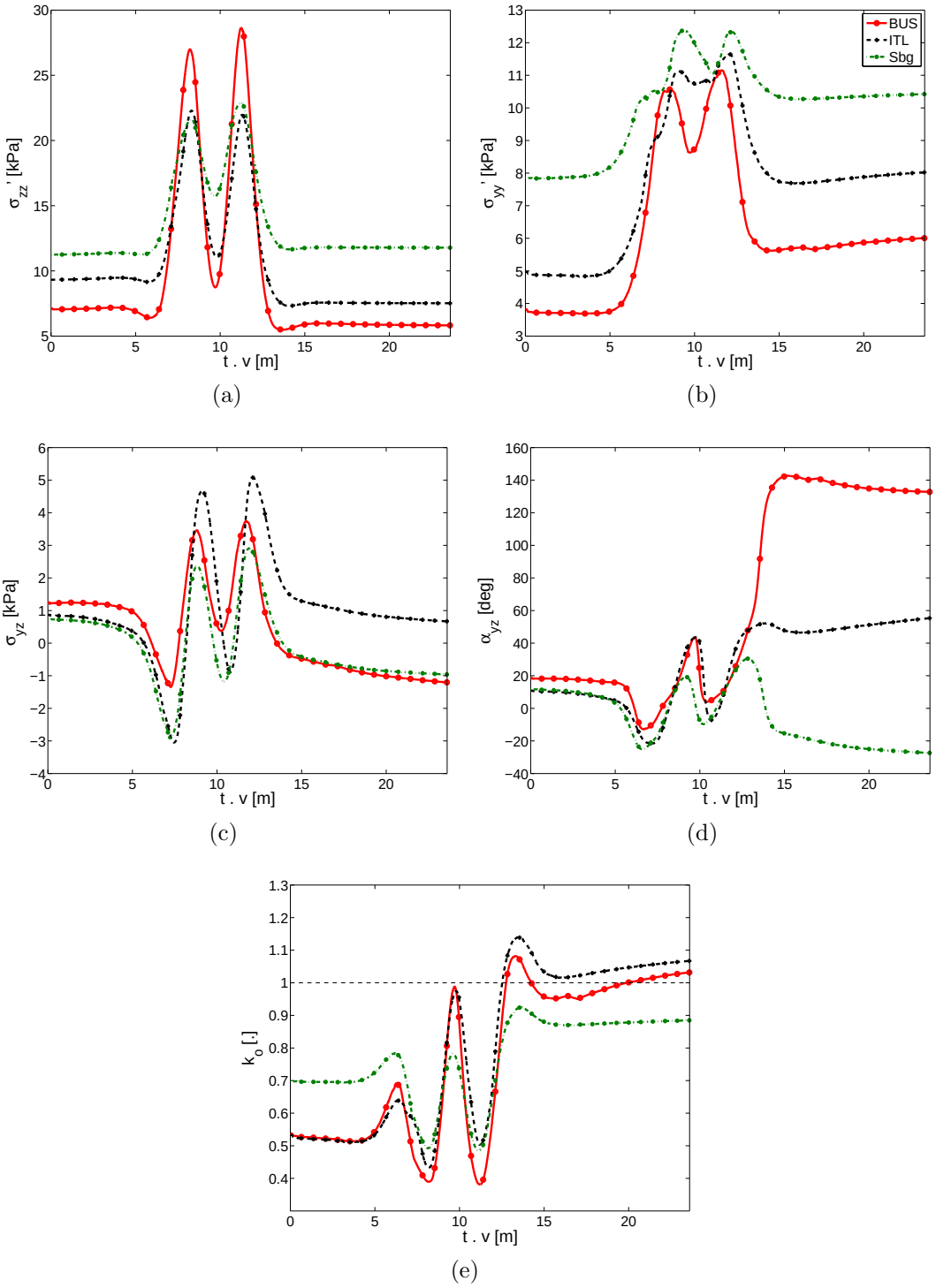

Figure 5.27: Time scaled response of different materials during the first loading cycle at 15 km/h. a) Vertical stress (σ'_{zz}); b) Lateral stress (σ'_{yy}); c) Shear stress (σ_{yz}); d) Principal stress axes rotation angle (α_{yz}); e) Earth pressure coefficient (k_o). BUS: ballast under the sleeper; ITL: interlayer; Sbg: subgrade.

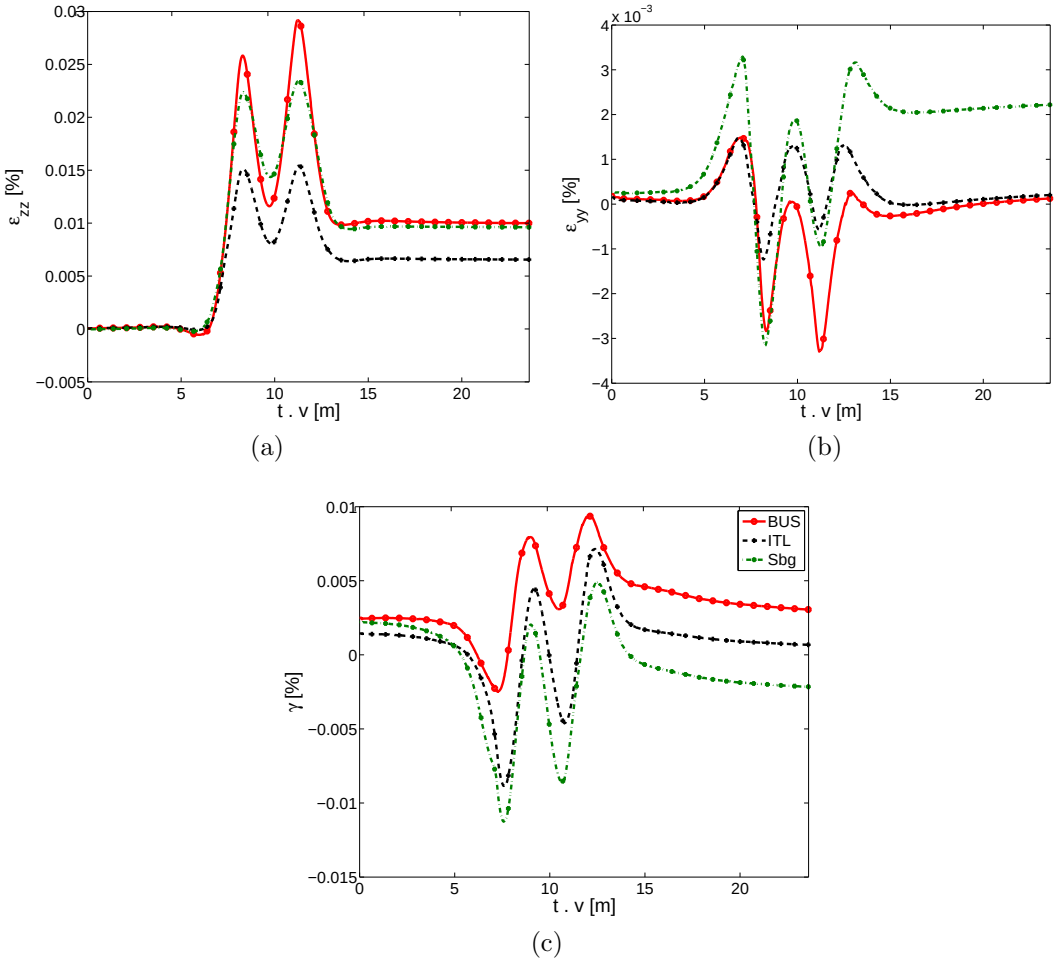

Figure 5.28: Time scaled response of different materials during the first loading cycle at 15 km/h. a) Vertical strain (ε_{zz}); b) Lateral strain (ε_{yy}); c) Shear strain (ε_{yz}). BUS: ballast under the sleeper; ITL: interlayer; Sbg: subgrade.

imum vertical strain being 10 times higher than maximum lateral strain. The second axle imposes on ballast under the sleeper higher total vertical strains than the first axle, as the material cumulates vertical plastic strain during both axle passage. For the interlayer and the subgrade, this effect is less pronounced, plastic vertical strains being cumulated mainly during the first axle passage. Moreover, only the subgrade cumulates lateral plastic strain during the load cycle (Figure 5.28b), as both residual and initial values for ballast under the sleeper and the interlayer are similar. Concerning shear strains, maximum values increase during the second axle passage, as a consequence of material cyclic softening. The interlayer presents similar initial and residual values, while ballast under the sleeper and the subgrade cumulates either positive or negative shear strains. The strain response is further analyzed in details in section 5.5.3.1.

The stress and strain invariants in the (y, z) plane are also analyzed in Figure 5.29. They are defined in Equations 5.5 to 5.8. Ballast presents the highest maximum strains and the maximum stress variations, as previously observed. After loading, a slight increase in

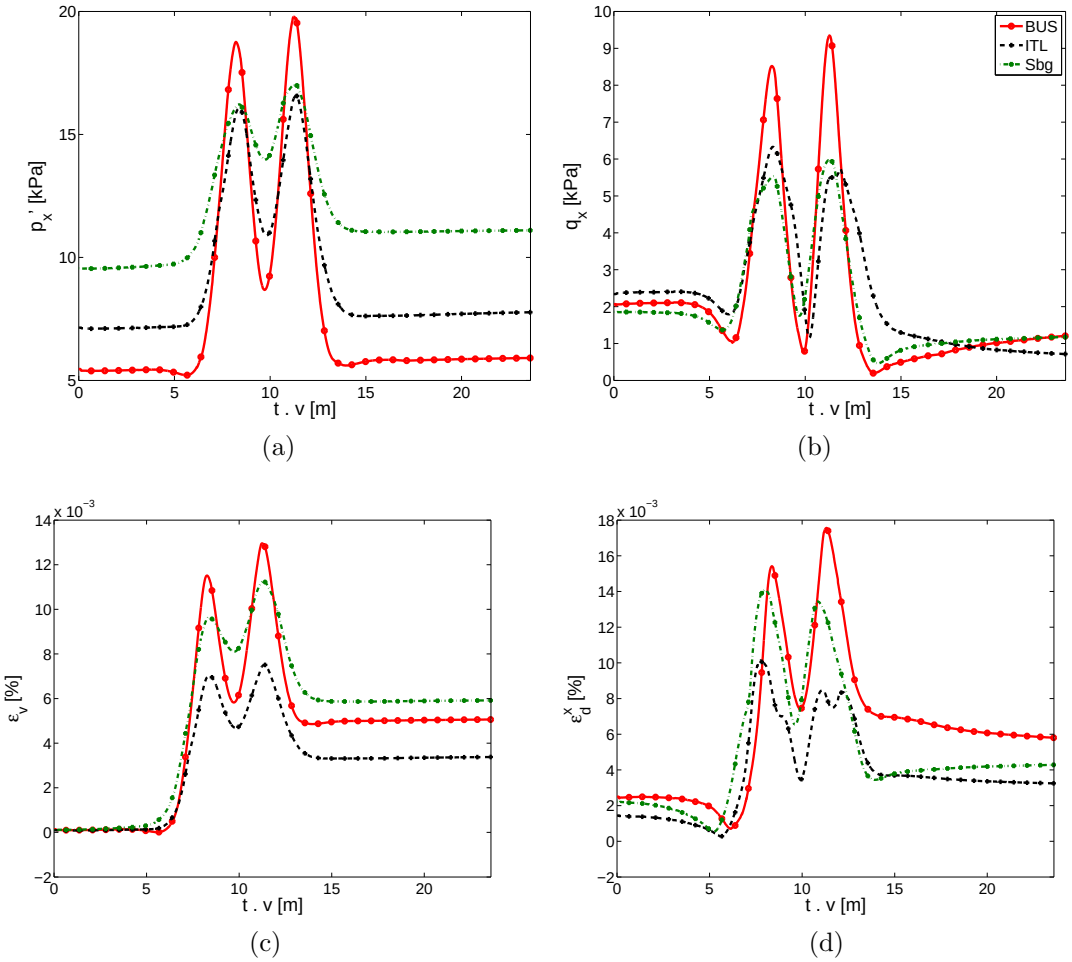

Figure 5.29: Time scaled response of different materials during the first loading cycle at 15 km/h. a) Effective mean stress (p'_x); b) Deviatoric stress (q_x); c) Volumetric strain (ε_v); d) Deviatoric strain (ε_d^x). BUS: ballast under the sleeper; ITL: interlayer; Sbg: subgrade.

the effective mean stress (p'_x) is observed, specially at the subgrade. Inversely, deviatoric stress (q_x) decreases as a consequence of the final lateral stress increase compared to vertical stress. Permanent volume reduction is obtained for all materials, ballast and the subgrade presenting comparable maximum and residual values of volumetric strain (ε_v). The interlayer presents the lowest maximum and residual strain levels.

$$p'_x = \frac{\sigma'_{yy} + \sigma'_{zz}}{2} \tag{5.5}$$

$$q_x = \sqrt{\left(\frac{\sigma'_{yy} - \sigma'_{zz}}{2}\right)^2 + \sigma_{yz}^2} \tag{5.6}$$

$$\varepsilon_v^x = \varepsilon_v = \varepsilon_{yy} + \varepsilon_{zz} \tag{5.7}$$

$$\varepsilon_d^x = \sqrt{\left(\frac{\varepsilon_{yy} - \varepsilon_{zz}}{2}\right)^2 + \varepsilon_{yz}^2} \tag{5.8}$$

These results are replotted in a more convenient stress-strain path in Figure 5.30. The stress path defined in the (q_x, p'_x) plane (Figure 5.30b) can be compared to the one obtained at linear elastic case in Section 3.4.1 (Figure 3.26). On both cases, a stress-path characterized by different slopes at the decrease and increase of stresses is obtained. However, in the present case the material behavior evolves during loading due to plastic volumetric and deviatoric strains. The first axle is responsible for the most part of volume changes taking place in the materials (Figure 5.30d), as plastic deformation takes place mainly during the first axle passage. The second axle contributes marginally to the increase in plastic volumetric strain.

It is also important to highlight that both the volumetric and deviatoric strains are of the same order of magnitude (Figure 5.30c). In this sense, it is expected that both volumetric and deviatoric behavior to have an impact on the materials' response.

The stress-strain response of ballast under the sleeper shown in Figure 5.30 can be suitably characterized by an oedometric path. This is a consequence of the load transfer mechanism from the axle load to the ballast imposed by the discrete sleeper support. The track can be viewed as a series of footings, each one representing one sleeper. Different sleepers are loaded at the same time, with different load amplitudes. The lateral displacement of ballast under the sleeper is constrained by the surrounding sleepers, which leads to higher values of lateral stress in points between sleepers. Therefore, under one given sleeper, ballast is subjected to higher vertical stress relatively to lateral and shear stress, whereas between sleepers it presents lower values of vertical stress but higher maximum values of lateral stress. This mechanism is less pronounced at further depth, both by the homogenizing role of the interlayer and the stress radiation into the soil. Evidently, these variations depend on the characteristics of the load repartition over sleepers of the track.

The stress-strain paths of ballast under the sleeper (BUS) and ballast between sleepers (BBS) are compared in Figure 5.31. Maximum mean stress values are similar, as increase on lateral and vertical stresses compensate each other, but BUS is subjected to higher deviatoric stress. The obtained stress paths (Figure 5.31b) are then very different for BUS and BBS. The latter presents mainly three phases for one axle passage: increase of mean and deviatoric stresses, decrease of deviatoric stress with constant mean stress and then decrease of mean stress with a slight decrease of deviatoric stress. Concerning the volumetric response (Figure 5.31d), lower maximum volumetric strain is observed and residual mean stress is lower in the case of BBS. On the other hand, the maximum and residual deviatoric strains are higher for BBS, mainly because of the last part of the

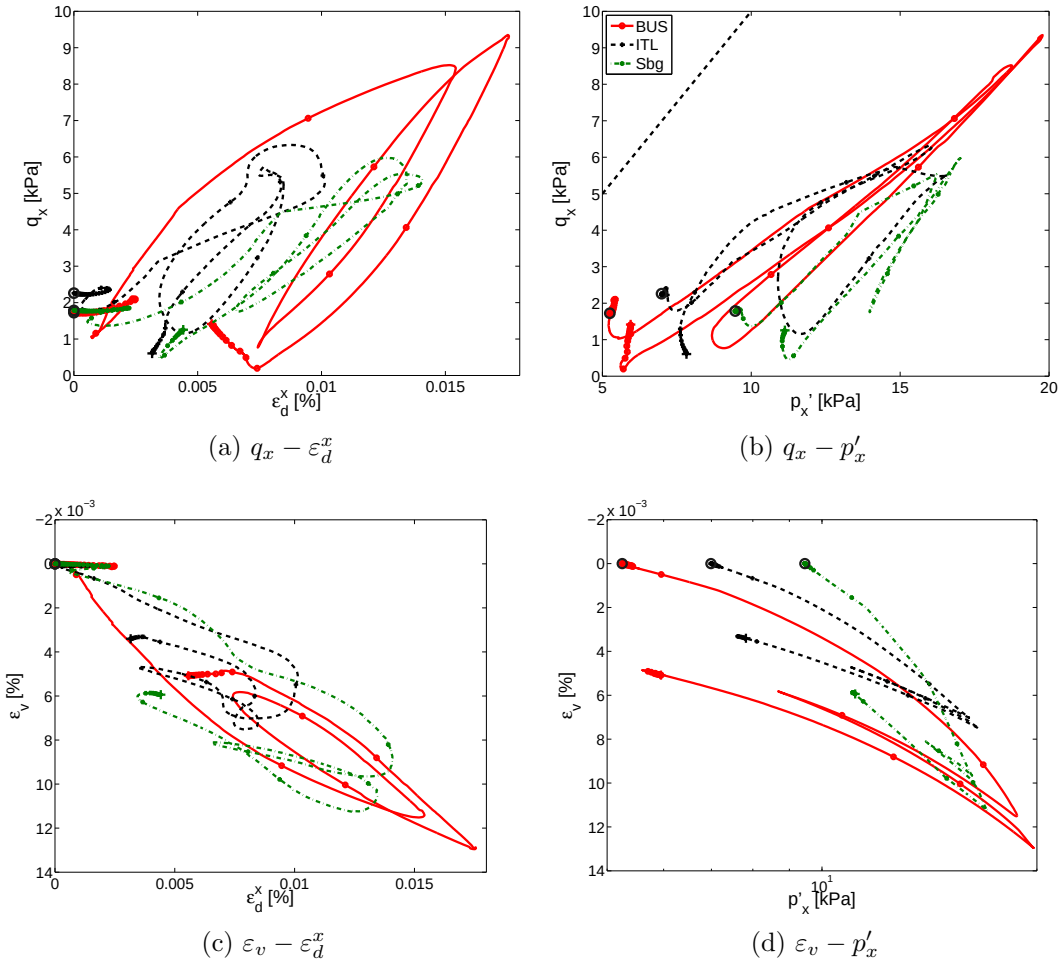

(a) $q_x - \varepsilon_d^x$ (b) $q_x - p'_x$

(c) $\varepsilon_v - \varepsilon_d^x$ (d) $\varepsilon_v - p'_x$

Figure 5.30: Stress-strain response of different materials during the first loading load at 15 km/h. Black dashed line in (b) is the unitary slope (45°). BUS: ballast under the sleeper; ITL: interlayer; Sbg: subgrade.

cycles, when the second axle has passed the considered point. This phase is characterized by a rapid increase of deviatoric strains due to the rapid reduction of mean stress without important variations in deviatoric stress.

From these results, it is then expected that the behavior of ballast under the sleeper and between sleepers to be significantly different in the track. At the grain level, grains under the sleeper are subjected to higher deviatoric stress, but they present lower strains. Inversely, grains between sleepers are expected to be able to rotate and rearrange more often. The present model cannot account for this level of detail, as ballast is modeled as a continuous material. DEM approach can give a further insight in these aspects, as well as in the impact of the discrete sleeper support on ballast response and possibly in the mechanisms behind grain attrition and breakage.

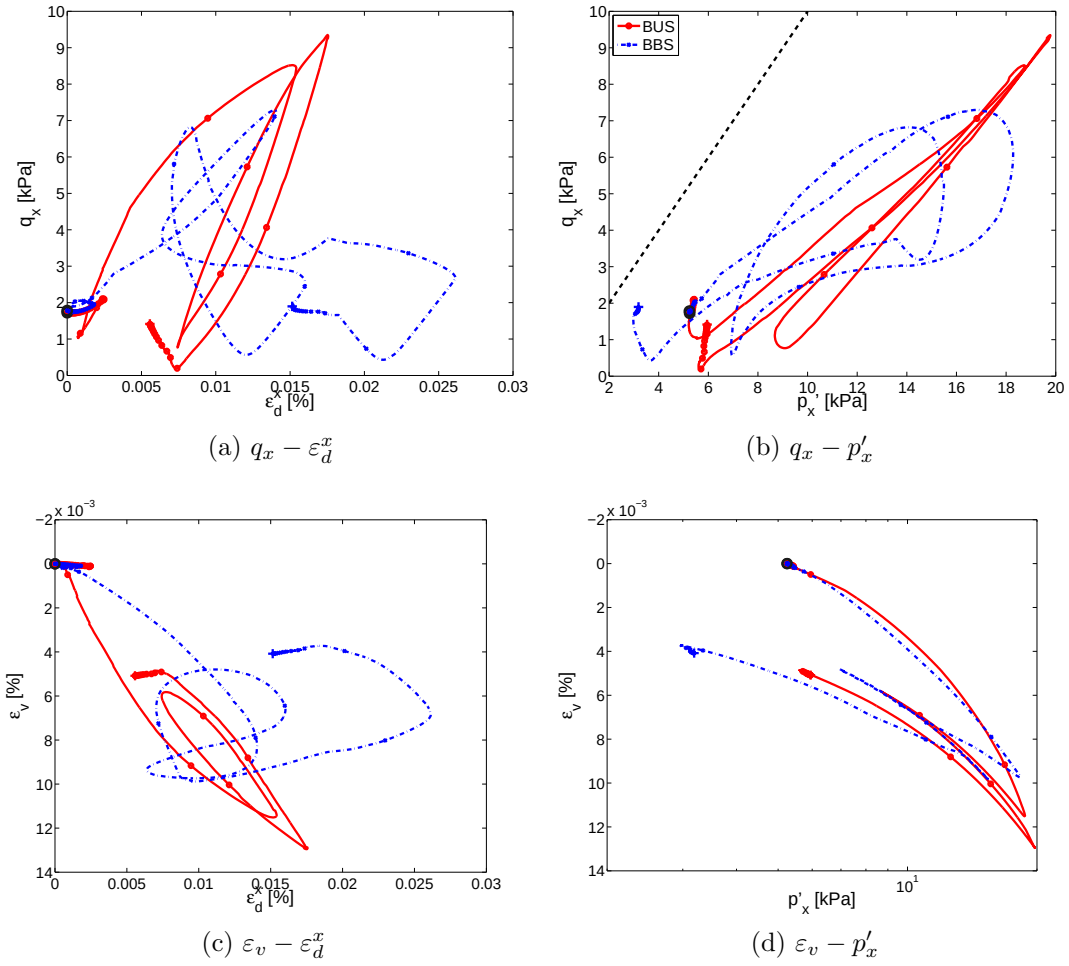

(a) $q_x - \varepsilon_d^x$ (b) $q_x - p'_x$

(c) $\varepsilon_v - \varepsilon_d^x$ (d) $\varepsilon_v - p'_x$

Figure 5.31: Comparison of the stress-strain response of ballast under the sleeper (BUS) and ballast between sleepers (BBS) for load speed of 15 km/h during the first loading cycle. Black dashed line is the unitary slope (45°).

5.5.3 Influence of speed during the first loading cycle

In the previous section, the evolution of stress and strains at the different materials is presented for a stress path imposed by the bogie load at 15 km/h. The performed numerical simulations show that the stress levels on ballast layer depend on the position of the control point relative to the sleepers, these differences not being observed further in depth. The residual stress on materials is characterized by an increase of mean stress and reduction of deviatoric stress, and increase in density is obtained as a consequence of volume reduction.

In this section, the impact of the load speed is analyzed in terms of both the stress-strain response of the materials at the different points of interest. This comparison is obtained by considering a bogie load at 220 km/h instead of 15 km/h as in the previous section.

An overview of the difference in vertical displacements for the speed of 220 km/h relative to 15 km/h is given in Figure 5.32 ($u_{z220km/h}$-$u_{z15km/h}$), for an instant when the bogie is at the same position on the track for both speeds. Higher vertical displacements

are obtained for the load speed at 220 km/h. A maximum difference of 0.12 mm in the ballast layer is obtained, which decreases with increasing depth. As a consequence of nonlinear behavior, the influence of speed on the maximum vertical displacement and permanent settlement is not homogeneous, although differences in a same layer are small. The global profile of vertical displacements and accelerations at the selected control points are given in Figure 5.33. At the rail, a permanent settlement of 0.5 mm is obtained, which is 25% higher than the settlement obtained at 15 km/h. The obtained acceleration levels at the sleeper are of the same order of magnitude as the elastic model (Figure 3.31b) for stiff soils.

Concerning the stress levels, it has been shown that in the case of linear elastic materials, the moving load speed mainly affects the magnitude of shear response, increasing the measured principal stress rotation angle (Section 3.4.2). In this sense, the deviatoric response was more sensitive than the volumetric one with the increase of the load speed. In addition, this effect was more pronounced with soft soils.

For the present case, an important increase of maximum mean and deviatoric stresses with increasing speed in ballast under the sleeper (BUS) is observed (Figure 5.34). The residual mean stress is also higher for the 220 km/h case, which linked with the volume reduction leads to higher compaction and stiffening of the material in this case (Figure 5.34d). The counterpart of rapid material stiffening is that residual deviatoric stress and strain are also higher for the cycle at 220 km/h (Figure 5.34a). Higher stress and strains values can be related to higher grain attrition in the ballast layer.

The comparison for ballast between sleepers (BSB) is presented in Figure 5.35. Stress paths are equivalent on both cases, although the 15 km/h speed case presents higher mean and deviatoric stress (Figure 5.35b). The material presents sensibly lower stiffness during

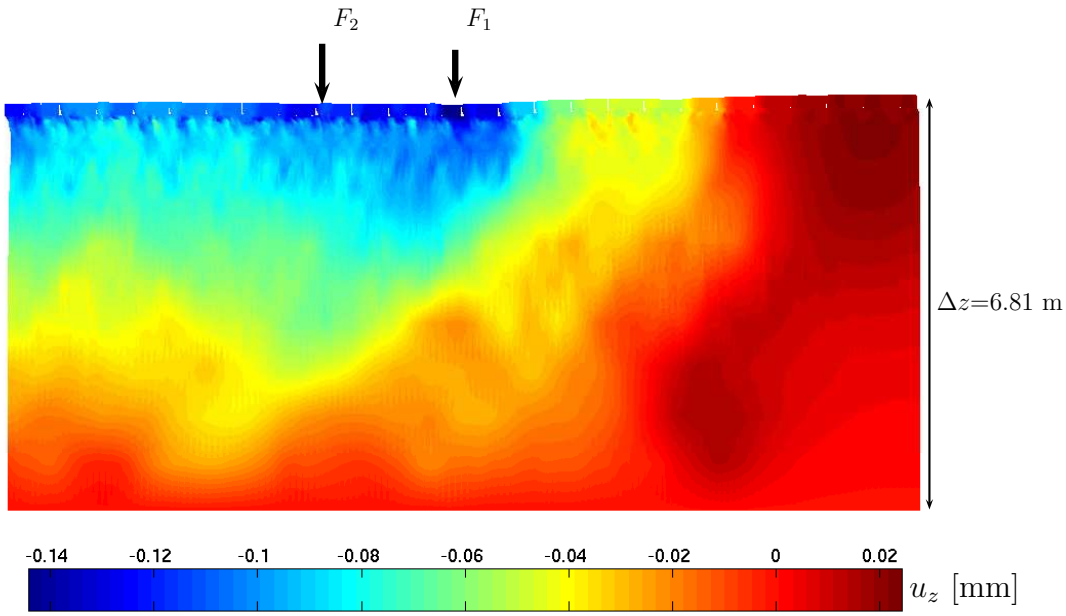

Figure 5.32: Difference in vertical displacements obtained by the model (scaled deformation) for a bogie load at 220km/h relative to 15 km/h ($u_{z220km/h}$-$u_{z15m/h}$).

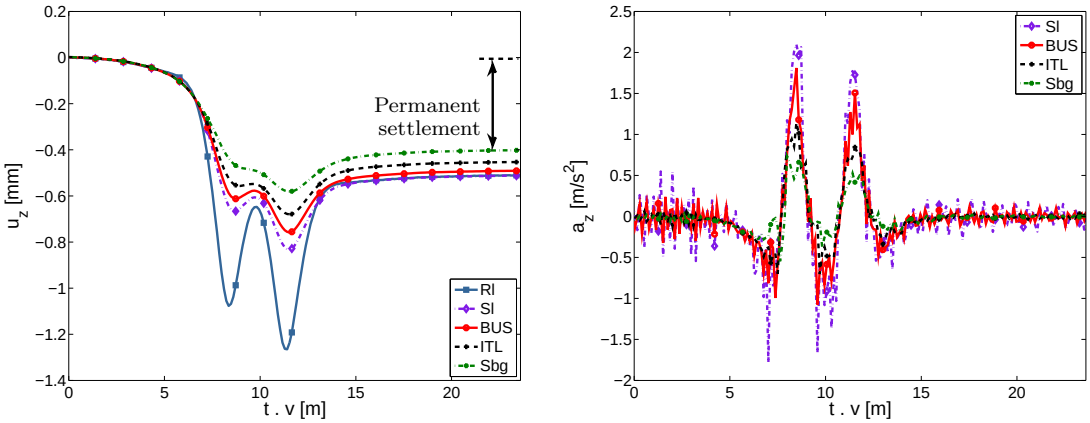

(a) (b)

Figure 5.33: Time scaled response of different materials at 220 km/h. a) Vertical displacement (u_z); b) Vertical acceleration (a_z). Rl: Rail, Sl: sleeper, BUS: ballast under the sleeper, ITL: interlayer, Sbg: subgrade.

the first axle passage (Figure 5.35a), which leads to higher residual deviatoric strain. It is important to highlight that the increase in volumetric strain for the 220 km/h speed case during the reloading phase (Figure 5.35d) is not coherent with the expected volumetric behavior (unloading and reloading phases following the same slope in the (ε_v, p'_x) plane), due possibly to the numerical convergence of the constitutive law.

The stress-strain response of the interlayer material A presented low sensitivity to the load speed. The comparative results are presented in Figure 5.36. The volumetric response is not affected by the bogie speed (Figure 5.36d), whereas the maximum deviatoric strain (Figure 5.36c) is slightly higher for the 220 km/h speed case. The stress paths are very similar (Figure 5.36b), the observed differences in the deviatoric strains appearing mainly after the second axle has passed the considered point.

One reason for the low sensitivity regarding load speed of the interlayer material A is the considered initial state, which is that of the triaxial test. Trinh et al. (2012) estimated from oedometric tests that a vertical stress of 700 kPa is necessary for obtaining the dry density of the soil specimen used in the triaxial test (γ_d=2.01Mg/m^3). Moreover, it is reminded the dry density of the interlayer in tracks was measured by Trinh et al. (2012) as 2.39 Mg/m^3. In this sense, the interlayer material A is less sensible to load speed as a consequence of a denser state regarding the other materials in the track.

Concerning the subgrade, the load speed affects both the volumetric and deviatoric responses. Figure 5.37 shows the comparative stress-strain behavior of the subgrade for the two considered speeds. Maximum values of both mean stress and volumetric strain are higher for 220 km/h load speed (Figure 5.37d), specially because of the higher volumetric strain experimented during the first axle passage. Maximum and residual deviatoric strains are also higher during the cycle at 220 km/h.

These results highlight that the moving load speed differently affects the stress-strain response of the materials during the first cycle. Ballast is more susceptible to variations in speed during the first loading cycle. Under sleeper points being subjected to higher stresses

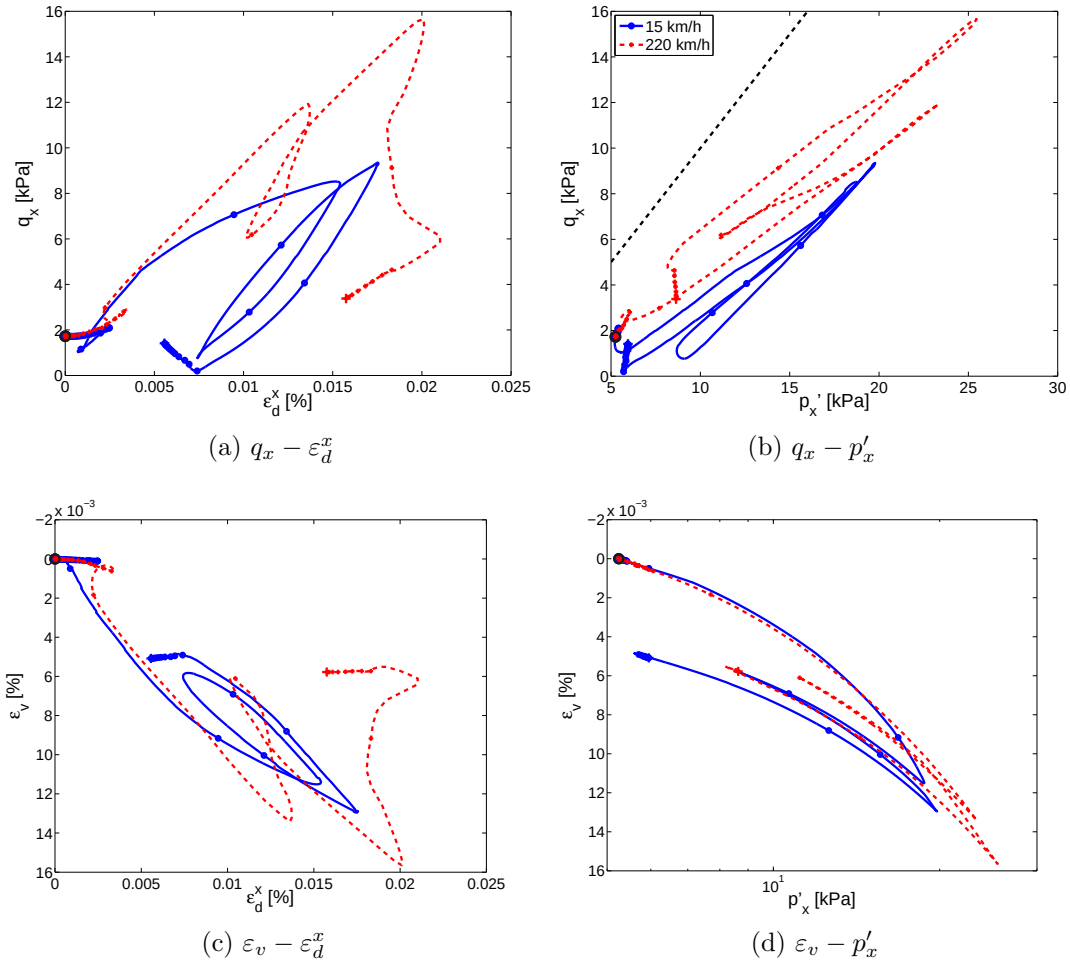

(a) $q_x - \varepsilon_d^x$ (b) $q_x - p'_x$

(c) $\varepsilon_v - \varepsilon_d^x$ (d) $\varepsilon_v - p'_x$

Figure 5.34: Impact of load speed on the stress-strain response of ballast under the sleeper (BUS). Black dashed line is the unitary slope (45°).

and between sleepers points presenting higher strains. In the next section, the effect of speed in the cyclic response of ballast is further discussed. The considered interlayer material presented low sensitivity to the load speed. Finally, speed also affected the stress-strain response of the subgrade, the material being subjected to higher maximum mean stress and residual strains during the load cycle.

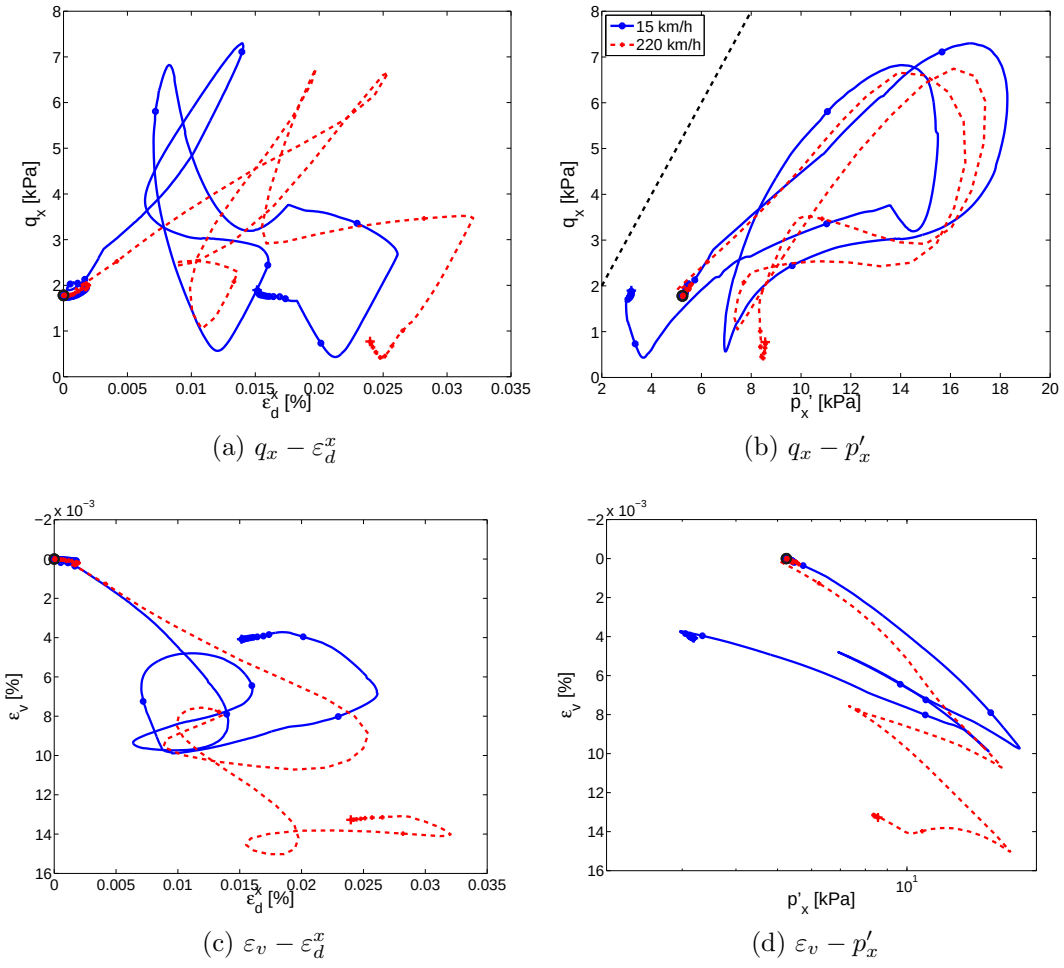

(a) $q_x - \varepsilon_d^x$ (b) $q_x - p'_x$

(c) $\varepsilon_v - \varepsilon_d^x$ (d) $\varepsilon_v - p'_x$

Figure 5.35: Impact of load speed on the stress-strain response of the ballast between sleepers (BBS). Black dashed line is the unitary slope (45°).

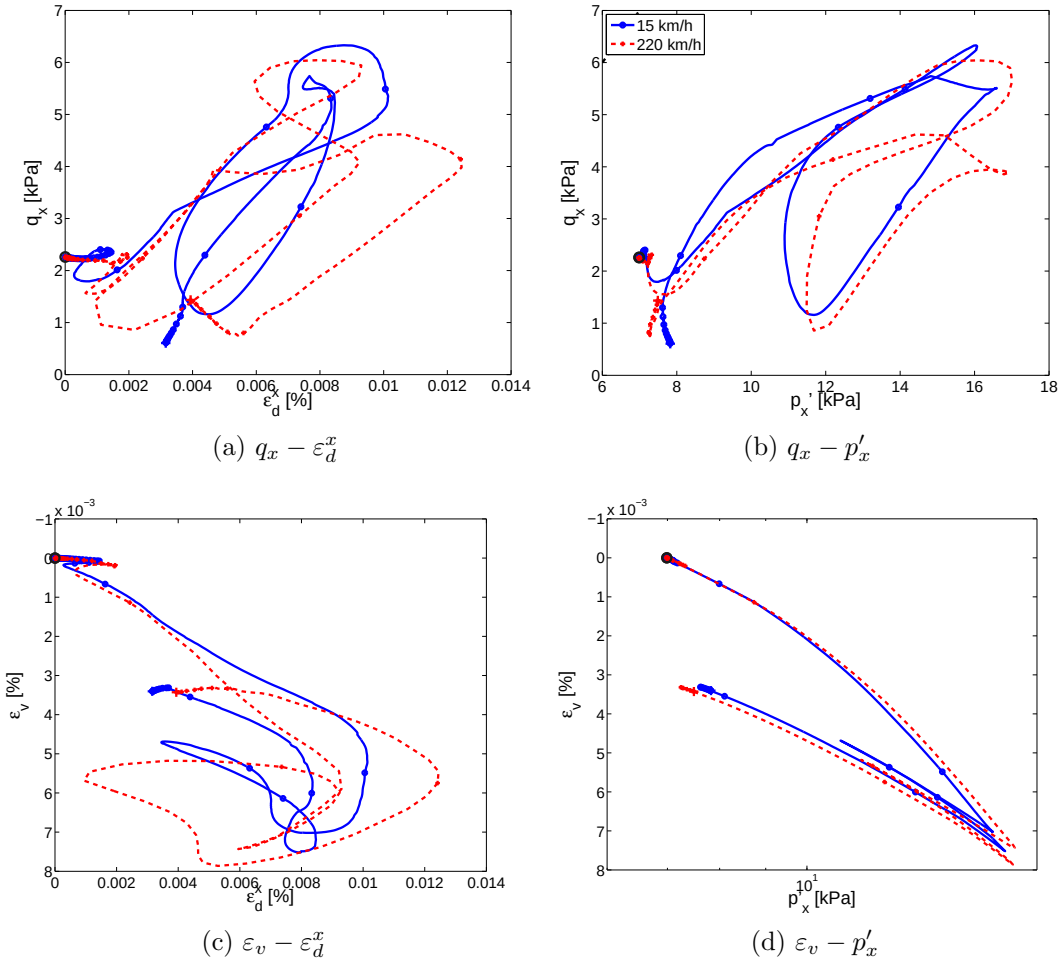

(a) $q_x - \varepsilon_d^x$ (b) $q_x - p'_x$

(c) $\varepsilon_v - \varepsilon_d^x$ (d) $\varepsilon_v - p'_x$

Figure 5.36: Impact of load speed on the stress-strain response of the interlayer.

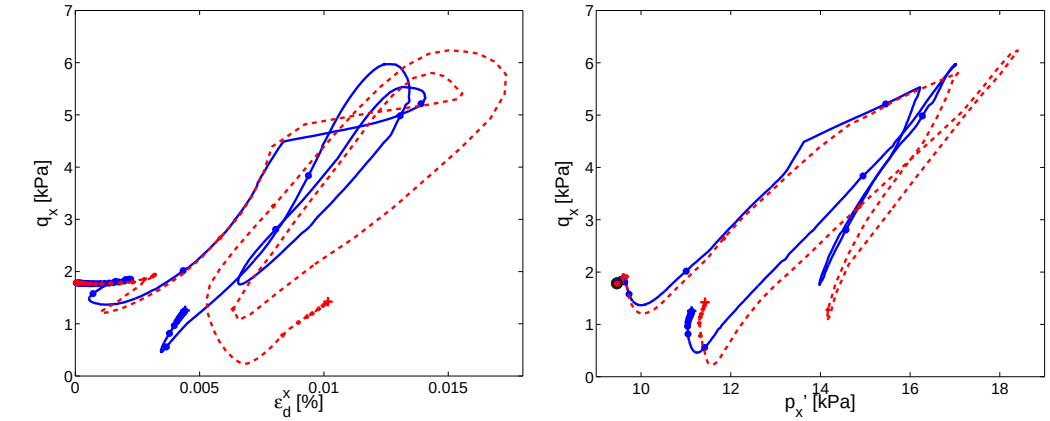

(a) $q_x - \varepsilon_d^x$ (b) $q_x - p'_x$

(c) $\varepsilon_v - \varepsilon_d^x$ (d) $\varepsilon_v - p'_x$

Figure 5.37: Impact of load speed on the stress-strain response of the subgrade soil.

5.5.3.1 Shear response analysis

In earthquake engineering, the imposed load is mainly deviatoric (Δp=0) and in this case the shear response completely describes the behavior of the soil. Therefore, the relations between shear modulus and damping with the cyclic shear strain are the parameters of interest. In this section, these parameters are studied directly from the present numerical model.

Figure 5.38 shows the scaled time response of both shear stress and strain of the interlayer during loading at speed 15 km/h. The full cycle can be decomposed in four steps:

- From the initial state, as the load approaches from a far distance both shear stress and strain slightly increase, before decreasing when the load is near the considered point. Minimum value of shear strain (represented by the number 1 in Figure 5.38) is obtained when the first axle approaches the considered point in the track.

- After this instant, both shear stress and strain increase. The null shear stress corresponds to the moment when the load is maximum over the considered point. The maximum shear strain value (represented by the number 2) is achieved when the first axle has already passed the considered point.

- When the second axle approaches, the same process takes place. The minimum value (represented by the number 3) takes place when the second axle approaches the considered point.

- The last part of the cycle is characterized by the increase of shear stress and strain. The maximum shear strain value (represented by the number 4) takes place after the second axle has passed the considered point. After this instant, both shear stress and strain reduce. However, initial and final values are different as a consequence of nonlinear behavior.

The shear response is usually represented in the (σ_{yz}, γ) plane (γ=2ε_{yz}), as shown in Figure 5.39. Points 1, 2, 3 and 4, representative of the maximum and minimum values of shear strain during the cycle, are also represented. From this representation, both the secant shear modulus (G_{sec} or simply G) and the damping (D) can be suitably measured. The secant shear modulus is obtained for each axle load and for the whole bogie cycle. These are represented by dashed lines in Figure 5.39. The damping can also be estimated for each axle load and for the whole cycle by applying Equation 5.9.

$$D = \frac{A_L}{4\pi A_T} \tag{5.9}$$

where A_L is the area enclosed by the hysteresis loop and A_T the area enclosed by the right triangle whose hypotenuse is defined by the following pair of points: 1-2 for the first axle, 3-4 for the second axle and 1-4 for the whole bogie.

The shear response of the different considered points is summarized in Figure 5.40. The values of the obtained secant shear modulus normalized by the maximum secant shear modulus (G_{max}) and the damping for each material are summarized in Table 5.5. It

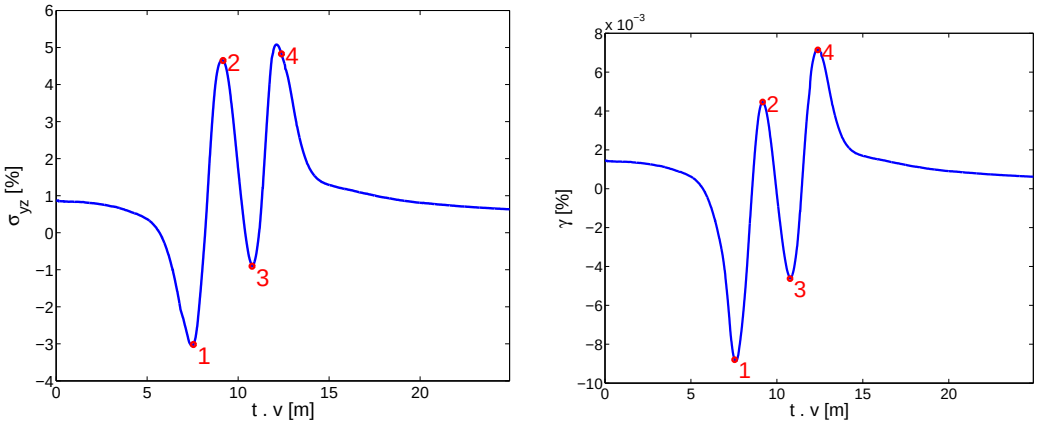

(a) (b)

Figure 5.38: Scaled time response of the interlayer material at first cycle at 15 km/h. a) Shear stress σ_{yz}; b) Shear strain $\gamma = 2\varepsilon_{yz}$.

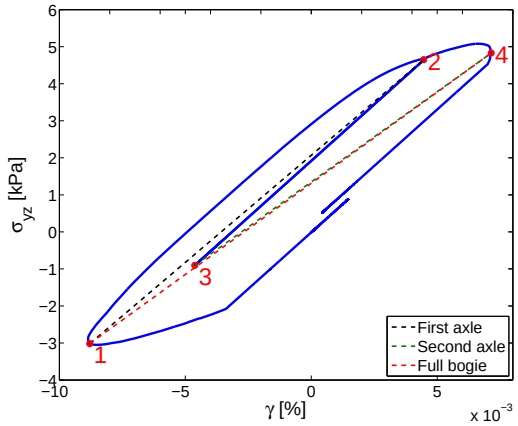

Figure 5.39: Shear response of the interlayer during the first cycle at 15 km/h. Numbered points represent the maximum shear strain value during the cycle and dashed lines the secant shear modulus obtained from these values.

can be seen that ballast and the subgrade are the layers presenting the highest damping characteristics, as expected from Figure 5.40. Both present larger permanent shear strains after load and the obtained higher values of damping for the first loading cycle reflect the dissipated energy through plastic deformation.

Although deviatoric stress is lower at ballast between sleepers, shear stress and strain are higher during both cycles. The obtained shear modulus is then lower for ballast between sleepers than for ballast under the sleeper, although the obtained damping values are similar considering the observed variations between the first and second axle values. From these results, the idea presented by Bodin (2001) of using two different stiffnesses for ballast under the sleeper and between sleepers can be justified as being representative of the stiffness presented by ballast at different points during loading.

As nonlinear elasticity is considered for the subgrade, the soil experiments an increase

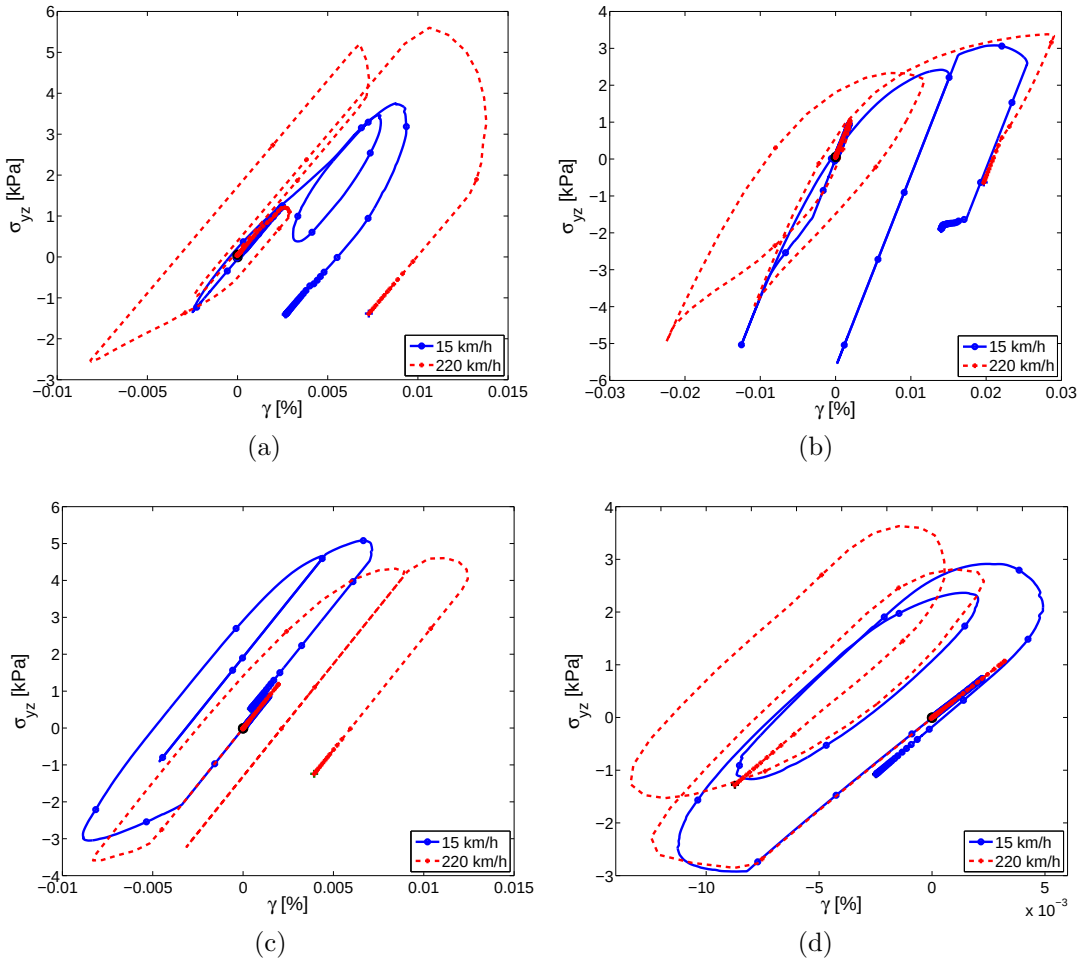

Figure 5.40: Shear response according to load speed for the first loading cycle. a) Ballast under the sleeper; b) Ballast between sleepers; c) Interlayer; d) Subgrade.

in the maximum secant modulus with increasing mean stress. The evolution of mean stress during load will then dictate the variations of maximum secant modulus. The values of G/G_{max} showed in Table 5.5 present the maximum secant modulus calculated with the mean value of the mean stress during the considered load (first axle, second axle or the whole cycle).

These results can be further analyzed by comparing the values of shear modulus reduction and damping curves obtained for the numerical drained cyclic strain-controlled shear test (Appendix G). In Figure 5.41, cross stands for results at 15 km/h and circle at 220 km/h, red representing ballast under the sleeper, blue ballast between sleepers, black the interlayer and green the subgrade. The cyclic shear strain values of ballast under the sleeper, the interlayer and the subgrade considered points are rather equivalent and comprised between 1.10^{-2} and 2.10^{-2}%. As previously discussed, ballast between sleepers is subjected to higher cyclic shear strains, specially at 220 km/h, the obtained range being from 2.10^{-2} to 6.10^{-2}%. Therefore, higher shear modulus degradation is obtained in this case (Figure 5.41a). Moreover, the low influence of speed on the interlayer's damping

		First axle (1-2)		Second axle (3-4)		Full bogie (1-4)	
	Speed [km/h]	G/G_{max} [.]	D [%]	G/G_{max} [.]	D [%]	G/G_{max} [.]	D [%]
BUS	15	0.85	2.5	0.80	9.8	0.73	7.7
	220	0.86	2.5	0.50	13.9	0.51	12.3
BBS	15	0.48	5.8	0.62	6.6	0.36	8.3
	220	0.40	6.8	0.35	7.8	0.31	9.9
ITL	15	0.95	2.8	0.80	3.4	0.81	4.8
	220	0.75	3.6	0.77	4.2	0.60	6.4
Sbg	15	0.9	5.9	0.59	11.2	0.72	14.9
	220	0.8	4.9	0.69	9.9	0.92	20.7

Table 5.5: Secant shear modulus reduction and damping at the different materials during the first loading cycle at 15 km/h and 220 km/h. BUS: ballast under the sleeper; BBS: ballast between sleepers; ITL: interlayer; Sbg: subgrade.

results can be viewed as a consequence of a large elastic domain (Figure 5.41d).

To summarize the observed influence of speed on the shear response during the first loading cycle, both ballast and the subgrade are affected by the load speed and higher shear stress and strains are observed during the cycle at speed of 220 km/h. Shear strains are sensibly higher at speed 220 km/h for BSB. Speed leads to lower shear modulus and higher damping values, according to the obtained numerical results. Concerning the subgrade shear response, shear modulus and damping are rather equivalent in both cases, although strain values are higher at 220 km/h. Load speed has little impact on the shear behavior of the considered interlayer material, in terms of secant modulus reduction, damping and cyclic values of shear stress and strain. This is a consequence of large elastic domain observed for this material from the numerical drained cyclic strain-controlled shear test.

In the next section, the effect of speed in the cyclic response of ballast is further discussed.

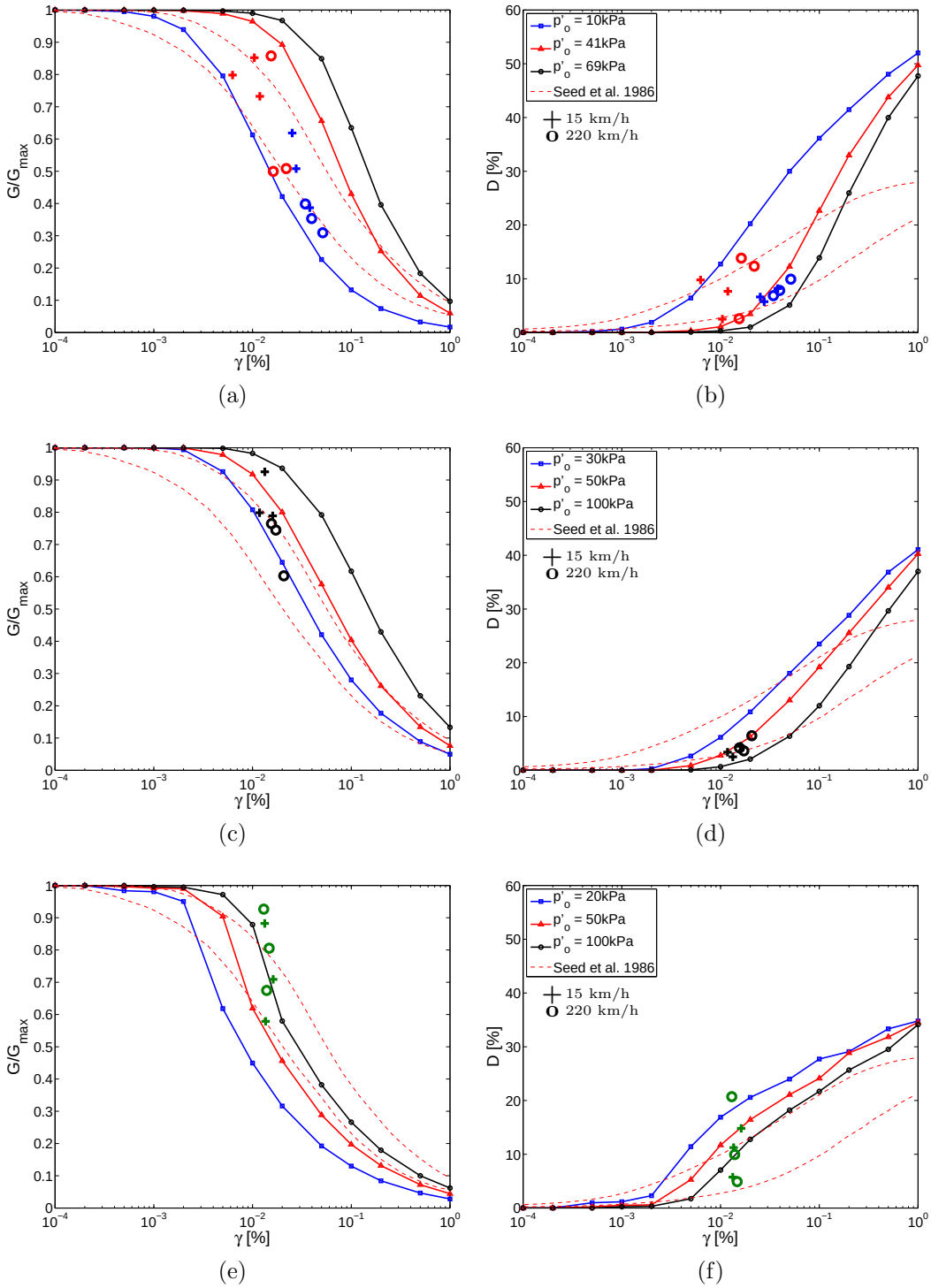

Figure 5.41: Comparison of shear modulus degradation and damping obtained from the numerical model and the results of numerical drained cyclic strain-controlled shear test. Cross stands for results at 15 km/h and circle at 220 km/h. Red: ballast under the sleeper; blue: ballast between sleepers; black: interlayer; green: subgrade. a) Ballast's shear modulus reduction; b) Ballast's damping; c) Interlayer's shear modulus reduction; d) Interlayer's damping; e) Subgrade's shear modulus reduction; f) Subgrade's damping.

5.5.4 Influence of speed on the cyclic response of the track

In the previous sections, the different aspects concerning the first loading cycle were addressed. Permanent settlement was obtained as a consequence of plastic deformation occurring in the materials during load, higher values being obtained for higher moving load speed. In this section, the cyclic response of the track is studied by subsequently applying 5 bogie cycles at 15 km/h and at 220 km/h. These 5 cycles can be viewed as representative of how the materials will cyclically evolve under track loading conditions.

The obtained vertical displacements in the track during the 5^{th} cycle (Δu_z^{5th}) for cycles at 220 km/h are shown in Figure 5.42. Rail and rail pad elements are omitted from this representation for the sake of clarity. Maximum vertical displacements in the ballast are around 0.3 mm, and values are similar under both axles. Differently from the first cycle analysis (Figure 5.17), the zone already loaded by the bogie (left hand-side of forces F_1 and F_2) present small variations on permanent settlement (u_z^p).

After the first loading cycle, u_z^p slowly varies with cycles, depending on the considered load speed (Figure 5.46). For cycles at 15 km/h, small variations are observed after the 2^{nd} cycle on all layers. The reduction in the observed rate of accumulation of permanent settlements after the first loading cycle is a consequence of increase in stiffness due to cyclic hardening in materials. For cycles at 220 km/h, the same tendency is observed for the interlayer and the subgrade, although permanent settlement values are higher. As expected, in this case ballast continues to settle with cyclic load. It was shown in the previous section that ballast was the material presenting the highest stress-strain variations with the load speed. In order to have a better insight on how the cyclic response of ballast during the early stages of the track is linked to the observed increase in settlement for

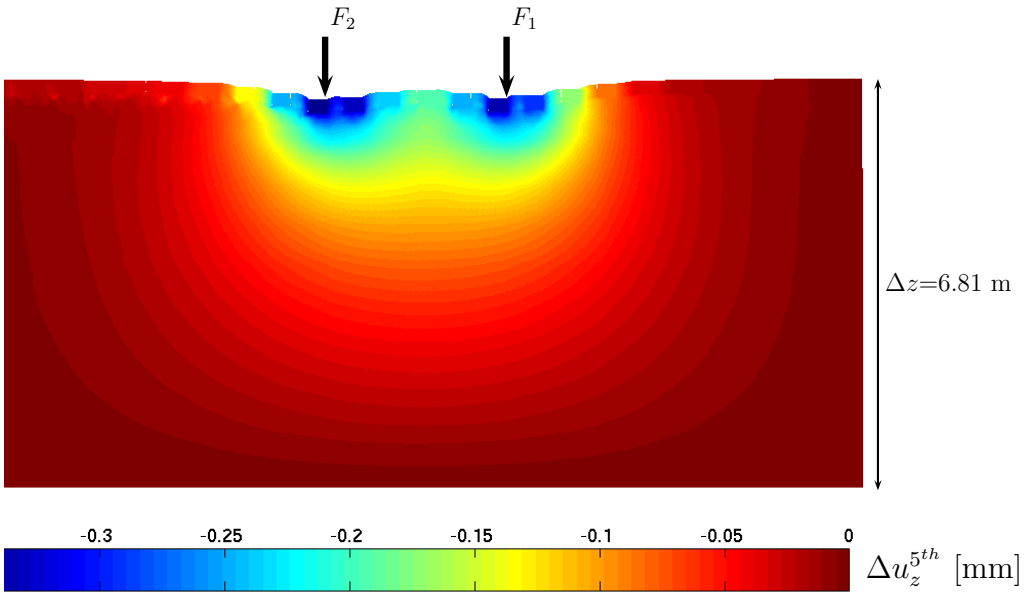

Figure 5.42: Vertical displacements obtained during the 5^{th} loading cycle (Δu_z^{5th}) for speed of 220 km/h.

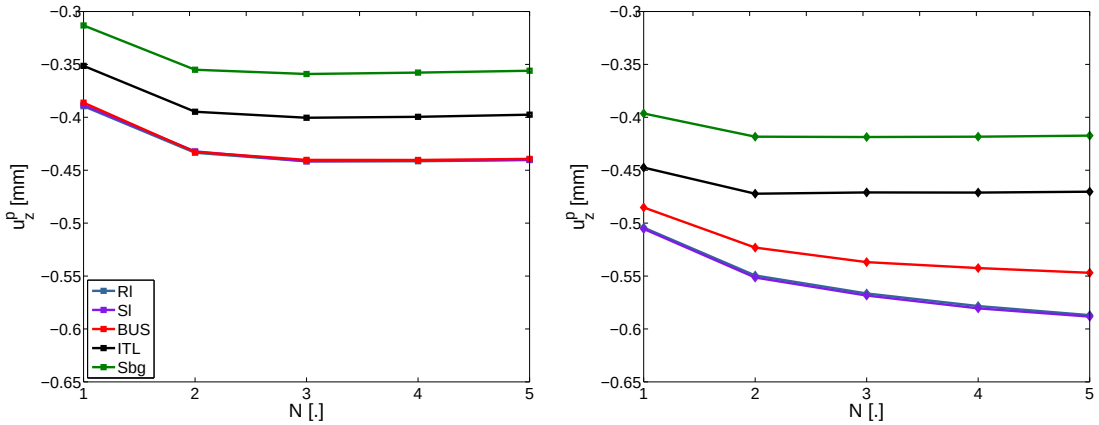

(a) (b)

Figure 5.43: Permanent settlement (u_z^p) in the different materials for 5 loading cycles. a) Cycles at 15 km/h; b) Cycles at 220 km/h. Rl: rail, Sl: sleeper, BUS: ballast under the sleeper, ITL: interlayer, Sbg: subgrade.

loads at 220 km/h, the stress-strain response of ballast under the sleeper is compared for both loading conditions.

Figure 5.44 presents the stress-strain response of ballast under the sleeper for cycles at speed 15 km/h. Cyclic compaction takes place in the material, and hardening is observed by an increase of maximum deviatoric stress developed in the material during loading after the first cycle. Maximum volumetric stress is slighlty affected by the cyclic load, as well as the initial state after each cycle. This slow accumulation of volumetric and deviatoric strains without important changes in the initial state of the material is characteristic for cycles at low speed.

The stress-strain response of ballast under the sleeper for a moving load at speed of 220 km/h is presented in Figure 5.45. From the first cycle analysis, it was shown that stresses were higher for 220 km/h and an important increase in mean stress was observed during the first cycle. With cycles, maximum stresses are sensibly higher in the present case. Higher compaction is obtained as a consequence of higher stresses. The obtained vertical settlement in the ballast layer is a consequence of the cyclic volume reduction. However, increase in mean and deviatoric residual stresses are also observed.

In this sense, with more cycles, it is expected that the stress-path touches the characteristic state line and in this case increase in volume can happen (Section 2.4.2). This is an unwanted situation in tracks, as it can lead to important track settlements as a consequence of increase in strain levels. Strains are expected to be low and materials to evolve slowly with cycles toward reduction in volume and increase in mean stress, without increase in deviatoric stresses.

The previous discussed behavior is avoided in tracks by limiting train speed during the conditioning phase before allowing trains at the nominal speed. In this sense, the increase in shear strains imposed by the load speed is avoided during the first cycles and increase in density can be obtained without increase in stresses. In order to verify the importance of the first loading cycle in the cyclic response, results of numerical simulations considering a

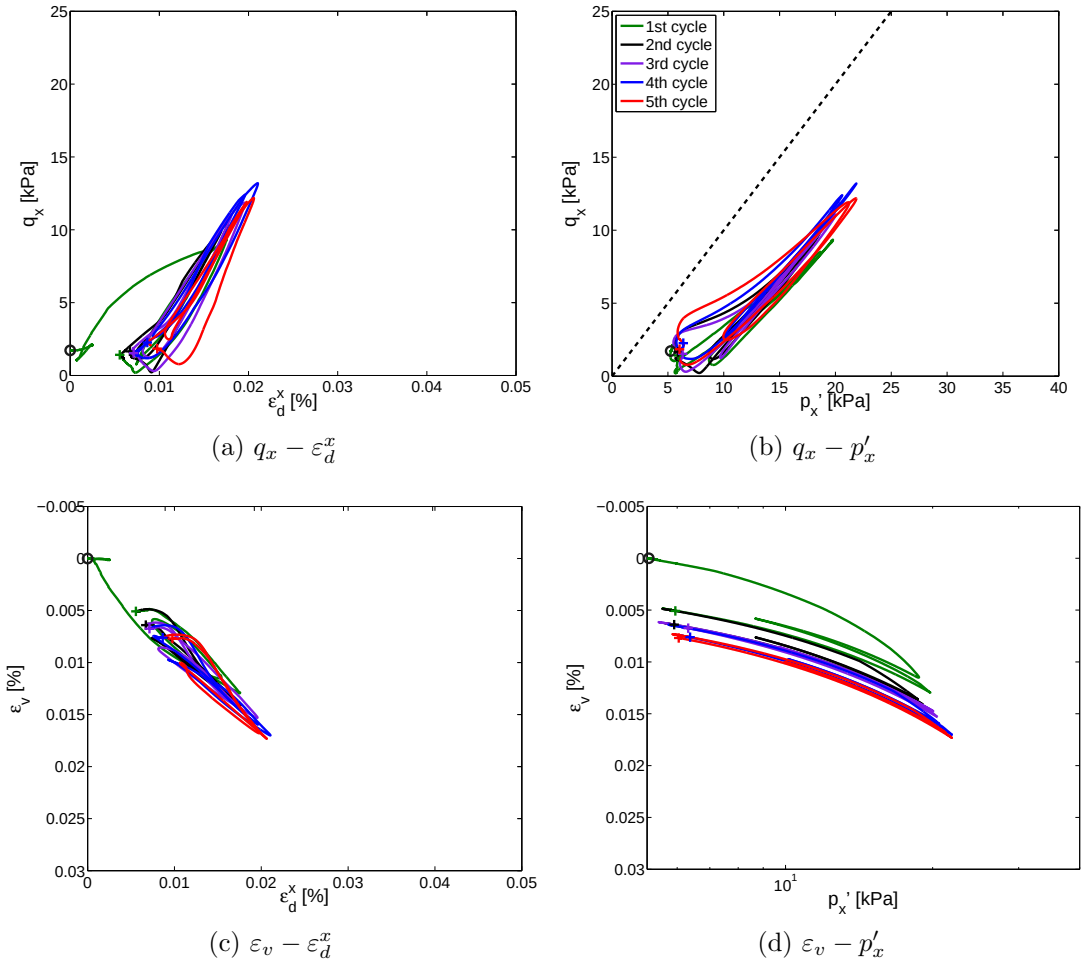

Figure 5.44: Cyclic stress-strain response of under sleeper ballast for load speed of 15 km/h. Black dashed line is the unitary slope (45°).

first cycle at 15 km/h, called preloading cycle, and then cycles at 220 km/h are presented. This method can be viewed as a way to better understand the role of load speed and initial state on material evolution.

The evolution of permanent settlements with cycles at the chosen control points is given in Figure 5.46a. The obtained track settlements is reduced by considering a preloading cycle (first cycle). Indeed, the observed final settlement is 20% lower when the preloading cycle is applied. Figure 5.46b shows the comparative results for the rate of permanent settlement variation (Δu_z^p) at each cycle. Similar trends are observed for both cases, although a more pronounced reduction of Δu_z^p is observed after 5 cycles when no preloading cycle is applied. However, it is expected that Δu_z^p will also reduce with more cycles for the case when a preloading cycle is applied.

Figure 5.47 presents the stress-strain results for this case. Maximum stresses are higher than the 15 km/h but sensibly lower than the 220 km/h case, as well as the observed permanent strains. Material densification and increase in initial mean stress with low accumulation of strains are obtained, which is the expected behavior for stable evolution

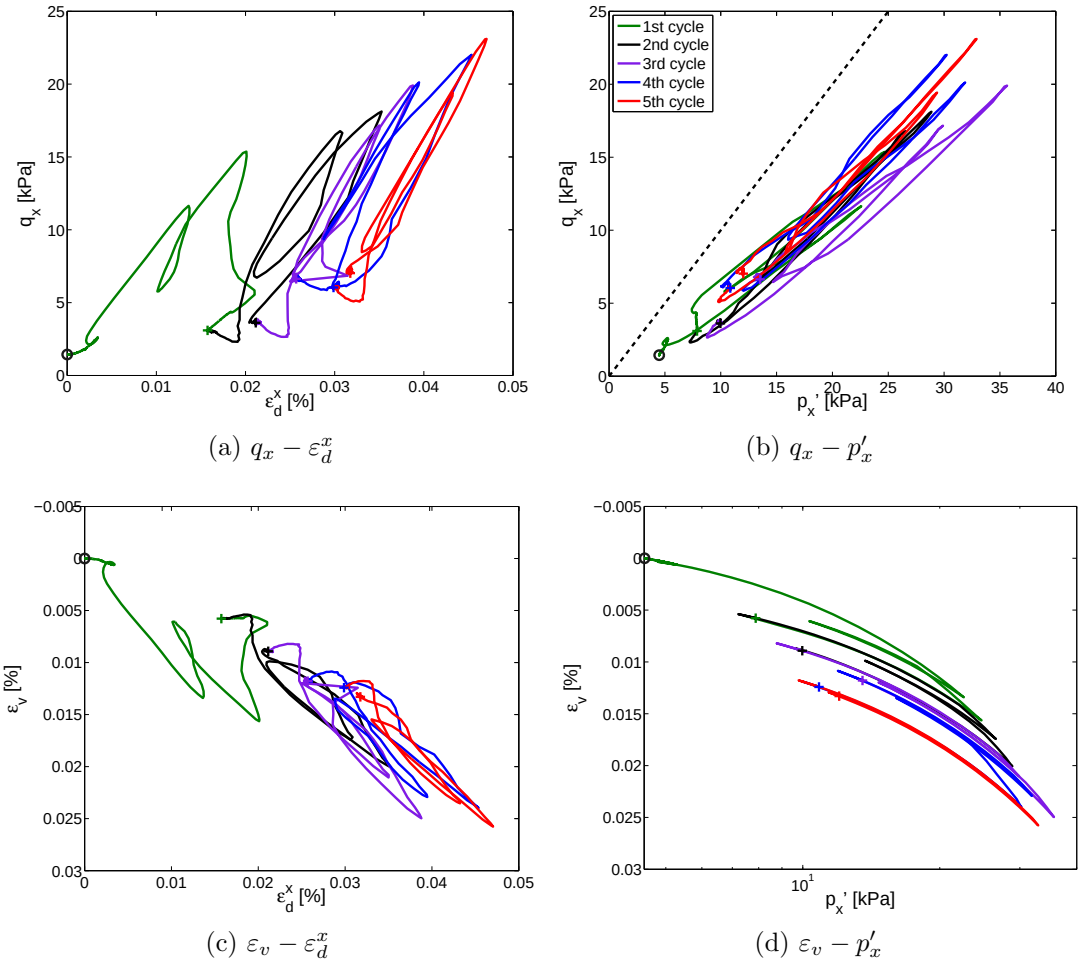

(a) $q_x - \varepsilon_d^x$ (b) $q_x - p'_x$

(c) $\varepsilon_v - \varepsilon_d^x$ (d) $\varepsilon_v - p'_x$

Figure 5.45: Cyclic stress-strain response of under sleeper ballast for load speed of 220 km/h. Black dashed line is the unitary slope (45°).

of the materials on tracks.

For all cases, the observed increase of stresses with cyclic loading is characteristic of material hardening and increase in stiffness due to plastic strains. Higher compaction of ballast under the sleeper is obtained by loads at 220 km/h, but this leads to higher residual deviatoric stress, increase in plastic strains and settlement with cycles. In real tracks, this behavior is avoided by imposing a reduced traffic speed during the conditioning phase of the material. Optimizing the train speed and required tonnage for a certain axle load during this phase in order to ensure good track quality for the long-term behavior is an open challenge, as nowadays standards are mainly based on field feedback.

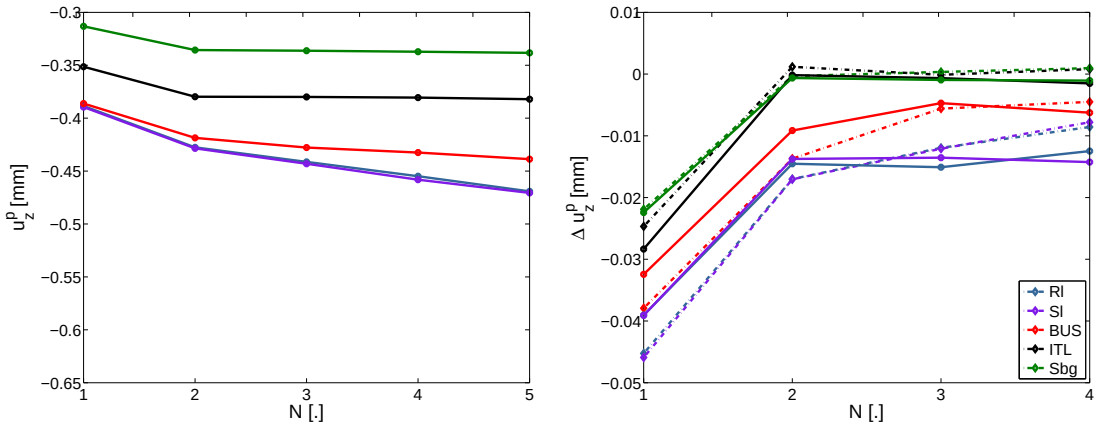

(a) (b)

Figure 5.46: Settlement analysis for 5 loading cycles. a) Permanent settlements (u_z^p) for cycles at 220 km/h after a preloading; b) Rate of permanent settlement variation (Δu_z^p).

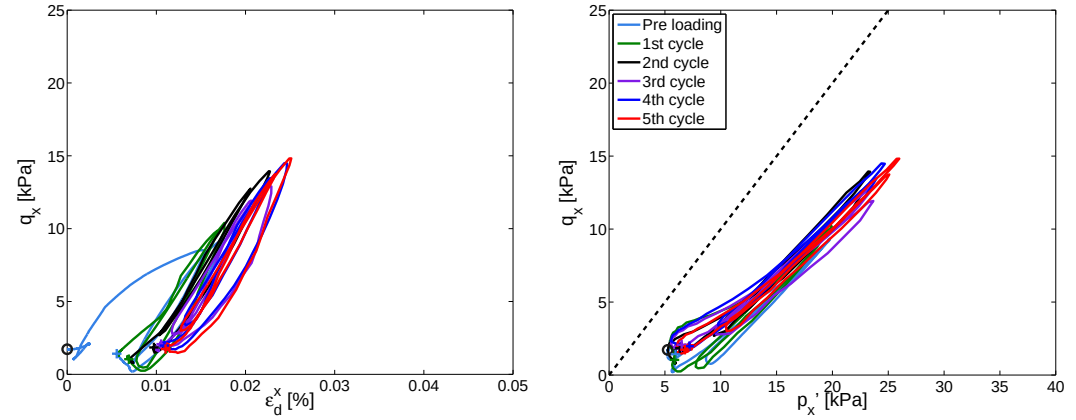

(a) $q_x - \varepsilon_d^x$ (b) $q_x - p'_x$

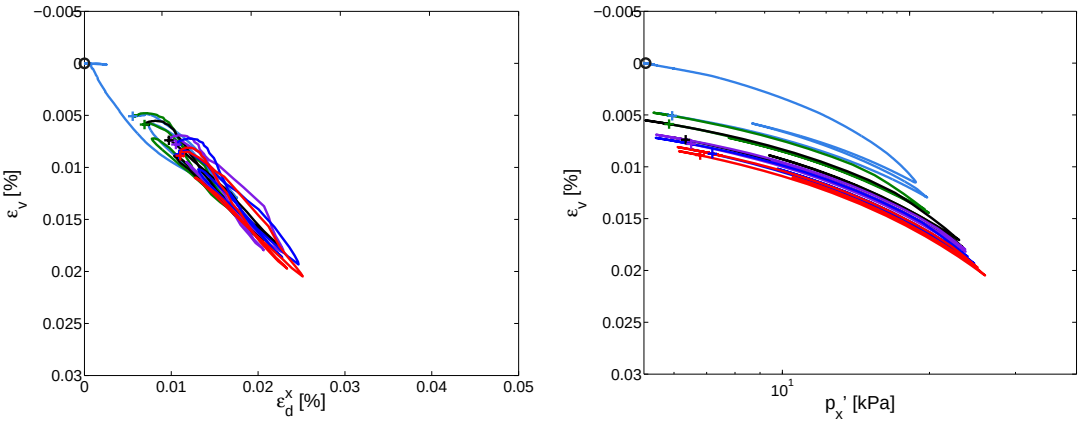

(c) $\varepsilon_v - \varepsilon_d^x$ (d) $\varepsilon_v - p'_x$

Figure 5.47: Cyclic stress-strain response of under sleeper ballast for load speed of 220 km/h with a preloading cycle at 15 km/h. Black dashed line is the unitary slope (45°).

5.6 Influence of subgrade and interlayer materials on the track response

The impact of other track profiles on the mechanical response of the track is studied in this section by considering separately a medium-to-dense sand subgrade and another interlayer material. The preloading cycle, as considered in the previous section (one bogie load at 15 km/h), is used as numerical protocol for comparing the mechanical behavior of the different profiles under loads at 220 km/h.

5.6.1 Influence of subgrade's initial density

Good compaction characteristics are required for the subgrade in railway tracks in order to increase the material stiffness and decrease its deformability by increasing its density, as discussed in Chapter 2. However, in practice it is very difficult to guarantee a homogeneous compaction level everywhere in the subgrade. The impact of variations of the compaction level can be ultimately viewed as variations of material stiffness, and results from Chapter 4 showed the important role played by the subgrade in the track stiffness.

In order to assess the influence of the subgrade's initial relative density on the conditioning phase of the track materials, an extreme case of low initial relative density is considered by modeling the subgrade as a medium-to-dense sand (D_r=40%). All other materials are kept unchanged (ballast, interlayer material A). The numerical protocol proposed in Section 5.5.4 for applying loads at 220 km/h is considered. It consists in applying preloading conditions (a bogie load at 15 km/h) previously to the nominal speed of 220 km/h. As discussed, this procedure better represents the soil history concerning the specific stress-path imposed by the bogie load. The numerical simulations performed considered 5 load cycles at 220 km/h.

Figure 5.48 compares the shear response of the different materials for both subgrade densities during the preloading cycle. The dense sand response is replotted (it was already presented in Figure 5.40) for a better comparison of the influence of the subgrade initial relative density. Shear stress and strains are higher at the subgrade for the medium-to-dense case, specially during the second axle (Figure 5.48d). In this case, the interlayer also presents higher shear strains, although maximum shear stress is equivalent in both cases. Inversely, ballast presents lower shear strains at any position on the track. Particularly for ballast under the sleeper, the material presents an elastic shear response in the case of medium-to-dense sand. Energy dissipation in ballast by damping occurs mainly by the material present between sleepers.

From these results, Figure 5.53 compares the values of damping and shear modulus reduction for the different layers for subgrade soil at relative densities D_r=40% (medium-to-dense sand) and D_r=93% (dense sand). As a consequence of the increase of shear strain in the interlayer, shear modulus reduces (Figure 5.49c) and damping increases (Figure 5.49d). On the other hand, ballast presents lower damping characteristics (Figure 5.49b). Lower damping is also observed in the subgrade (Figure 5.49f).

Figure 5.50 presents the stress-strain response of the subgrade during cyclic load. Solid line represents dense sand and dashed dotted line represents medium-to-dense sand. The preloading cycle and the last performed cycle are highlighted in order to better view the

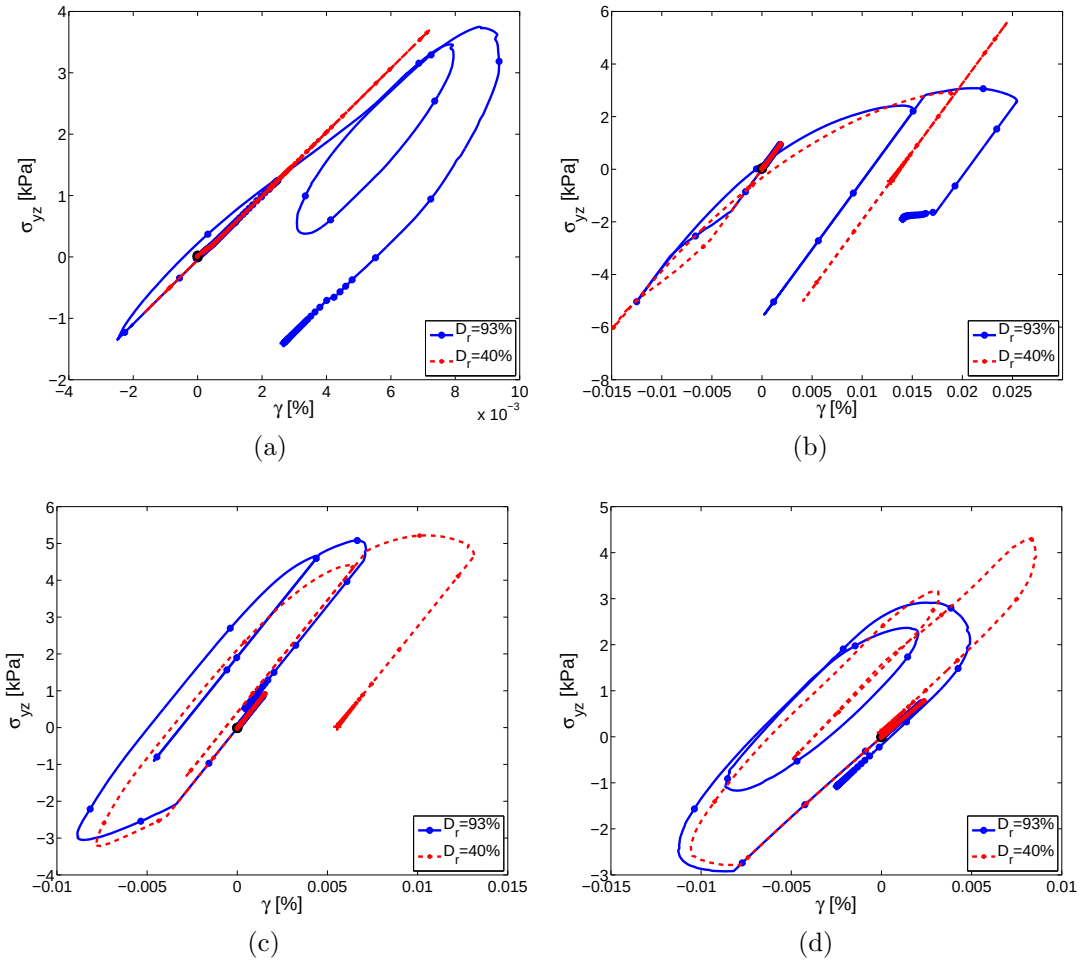

Figure 5.48: Shear response according to subgrade relative density. a) Ballast under the sleeper; b) Ballast between sleepers; c) Interlayer; d) Subgrade.

evolution of stresses and strains with cycles. Initial values of each cycle are represented by a circle, whereas the final value is represented by a cross mark. The stress paths during the preloading cycle are similar (Figure 5.50b), but with cycles at 220 km/h the medium-to-dense soil experiments higher mean stress and lower deviatoric stress.

Slightly higher volumetric and deviatoric strains are observed in the medium-to-dense sand case (Figure 5.50c), but globally the deformation behavior is similar in both cases. It can be concluded that mainly the deviatoric response is affected and that the dense sand case presents higher stiffness with cycles than the medium-to-dense case.

This cyclic increase in stiffness of the subgrade has an important impact on the cyclic response of ballast. Figure 5.51 presents the results for ballast under the sleeper, following the same notation as in Figure 5.50. The deviatoric response is mainly affected by the differences in the subgrade, the lower initial relative density case leading to higher permanent deviatoric strains. Initial state of ballast for the medium-to-dense subgrade case evolves toward higher values of mean and deviatoric stresses.

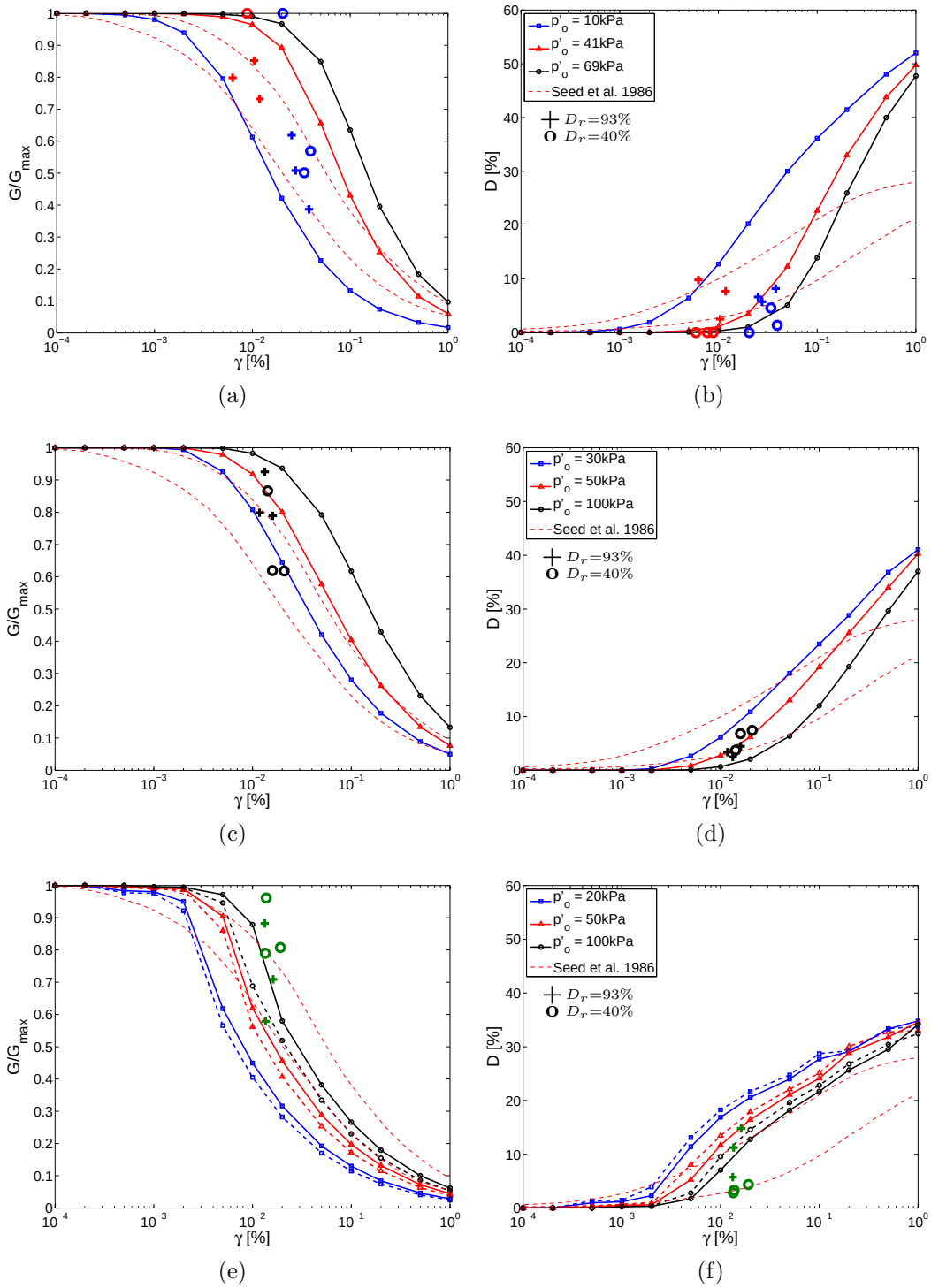

Figure 5.49: Comparison of shear modulus degradation and damping obtained from the numerical model and the results of numerical drained cyclic strain-controlled shear test. Cross stands for results of sand subgrade at relative density D_r=93% and circle at D_r=40%. Red: ballast under the sleeper; blue: ballast between sleepers; black: interlayer; green: subgrade. a) Ballast's shear modulus reduction; b) Ballast's damping; c) Interlayer's shear modulus reduction; d) Interlayer's damping; e) Subgrade's shear modulus reduction (solid line: D_r=93%; dashed line: D_r=40%); f) Subgrade's damping (solid line: D_r=93%; dashed line: D_r=40%).

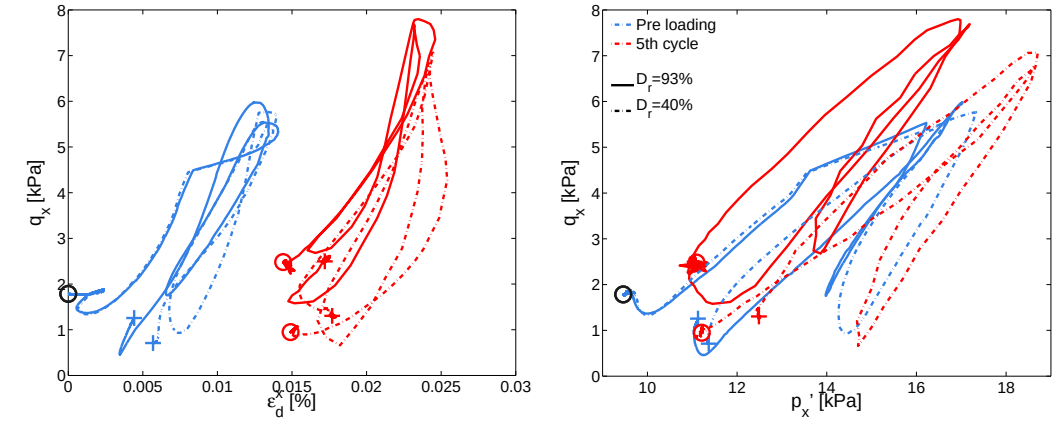

(a) $q_x - \varepsilon_d^x$ (b) $q_x - p'_x$

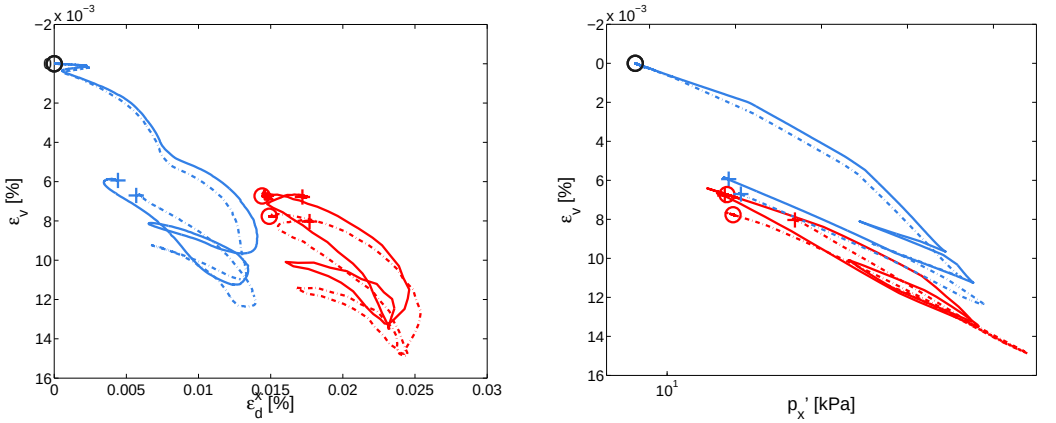

(c) $\varepsilon_v - \varepsilon_d^x$ (d) $\varepsilon_v - p'_x$

Figure 5.50: Impact of the subgrade relative density on its cyclic response. Solid line represents dense sand (D_r=93%) and dashed dotted line medium-to-dense sand (D_r=40%). Circle represents the initial value of the cycle and a cross mark the last value.

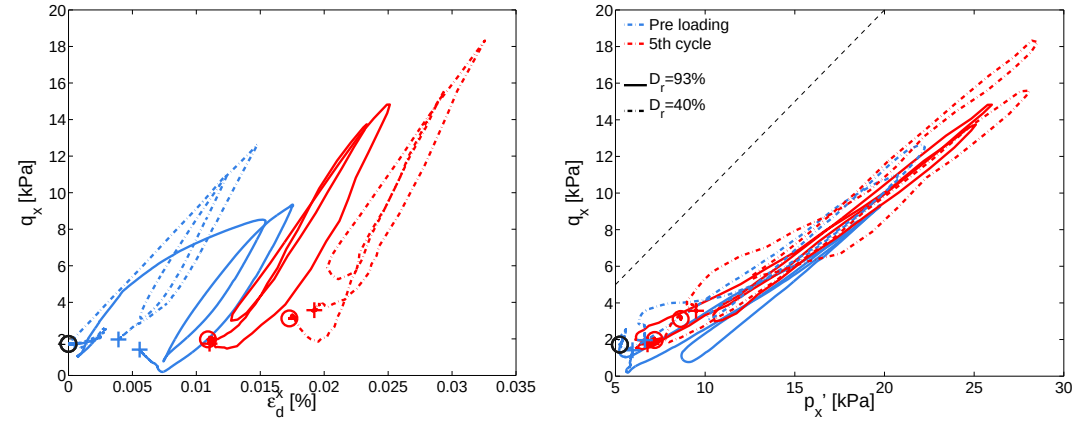

(a) $q_x - \varepsilon_d^x$ (b) $q_x - p'_x$

(c) $\varepsilon_v - \varepsilon_d^x$ (d) $\varepsilon_v - p'_x$

Figure 5.51: Impact of the subgrade relative density on the cyclic response of ballast under the sleeper. Solid line represents dense sand (D_r=40%) and dashed dotted line medium-to-dense sand (D_r=40%). Gray dashed line is the unitary slope (45°).

5.6.2 Influence of interlayer material

In this section, the influence of the interlayer mechanical characteristics on the cyclic response of the materials is assessed by considering a track profile with interlayer material B instead of interlayer material A. Interlayer material B presents lower peak resistance, it has a more contractant volume behavior on the triaxial test at a given confining pressure and it presents higher shear modulus degradation and damping than interlayer material A. All other materials are kept unchanged (ballast, subgrade as dense sand D_r=93%). This section follows the same organization layout as Section 5.6.1. The track's cyclic response is analyzed by considering a preloading cycle at 15 km/h followed by cycles at 220 km/h.

The shear response of the different layers is compared for both interlayer materials in Figure 5.52. As expected, larger cyclic strains are observed for the interlayer when material B is considered (Figure 5.52c). In turn, lower cyclic shear strain amplitudes per axle are observed for the other materials, specially at the ballast layer. This is particularly observed for ballast under the sleeper, which presented lower cyclic shear stress and strain. An increase of permanent shear strain is observed for the interlayer and the subgrade.

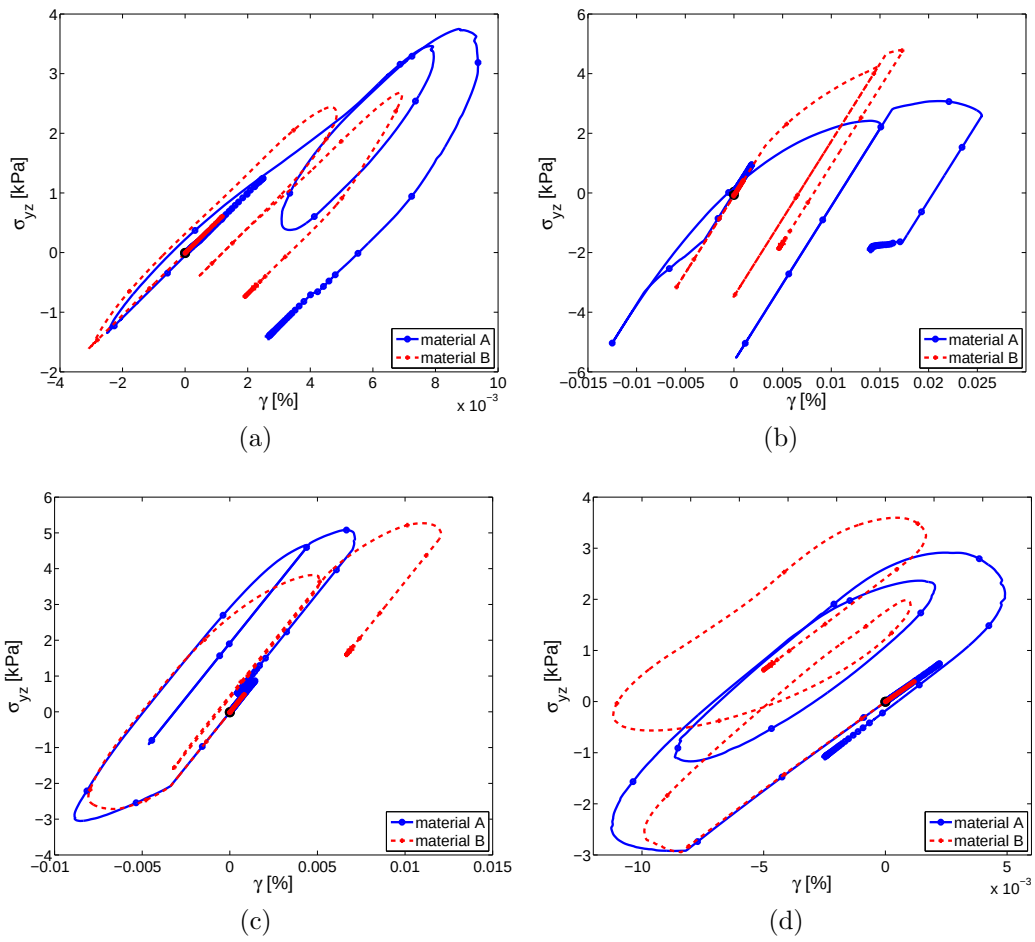

Figure 5.52: Shear response according to interlayer material. a) Ballast under the sleeper; b) Ballast between sleepers; c) Interlayer; d) Subgrade.

Figure 5.53 presents the damping and shear modulus reduction for the different materials during the preloading cycle at 15 km/h, when considering interlayer materials A or B. As expected, shear modulus reduction and damping when the interlayer material B is considered are higher (Figures 5.53c and 5.53d, respectively). In turn, for this case the other layers are submitted to lower shear strains and present smaller shear modulus reduction and damping. Particularly the subgrade, the shear modulus observed for the complete cycle in the case of the interlayer material B is higher than the maximum shear modulus of the material at its mean stress. This is the consequence of the mutual influence of both axles on the subgrade response. It can be seen from Figure 5.52d that the hysteresis loop after the first axle is not closed. This effect is less pronounced in the case of the interlayer material A, as it presents smaller shear modulus degradation. Therefore, the definition of secant shear modulus for the whole cycle cannot be used for the subgrade, as the hypothesis of a closed hysteresis loop is not verified. Therefore, in Figure 5.53e it is represented as no shear modulus degradation (G/G_{max}=1).

The cyclic stress-strain response of the interlayer is first analyzed in Figure 5.54. Solid line represents the interlayer material A and dashed dotted line represents the interlayer material B. The preloading cycle and the last performed cycles are highlighted in order to better view the evolution of stresses and strains with cycles. Cyclic softening of the interlayer material B is observed, characterized by reduction of residual mean stress and stiffness with an increase of permanent strains.

The behavior of interlayer material B presents major consequences for the ballast response. Figure 5.55 compares the stress-strain response for ballast under the sleeper for the two considered interlayer conditions. For both cases, cyclic increase in material's stresses is observed as a consequence from ballast densification and increase in stiffness. However, when the interlayer material B is considered, ballast under the sleeper is subjected to higher residual deviatoric stress and presents higher permanent deviatoric and volumetric strains. The observed cyclic softening leads to an increase in the stresses applied in ballast. From the first cycle analysis, decrease of shear stress was observed for the case with interlayer material B, which means that the increase in deviatoric stress is caused by an increase of vertical stress applied in the material. Moreover, the residual deviatoric stress increase is not followed by mean stress increase and this condition can possibly lead to larger permanent deformations of the ballast layer.

Concerning the subgrade, whose results are presented in Figure 5.56, the main consequence of considering the interlayer material B is the decrease in volumetric strain during the preloading cycle, which is further kept during the following cycles at 220 km/h. The deviatoric response is not affected and stress and strain levels per cycle are very similar in both cases.

From the above results, the interlayer plays an important role in the evolution of stresses and strains on ballast. Depending on the material conditions in the track, ballast can be subjected to higher stresses and strains as a consequence of interlayer's softening during cycles. Therefore, abrasion and breakage of ballast particles are more likely to occur. Although these aspects are not taken into account in the considered ECP model, the stress level which ballast is subjected to during cyclic load for different interlayer conditions can be used as input of specific models for ballast.

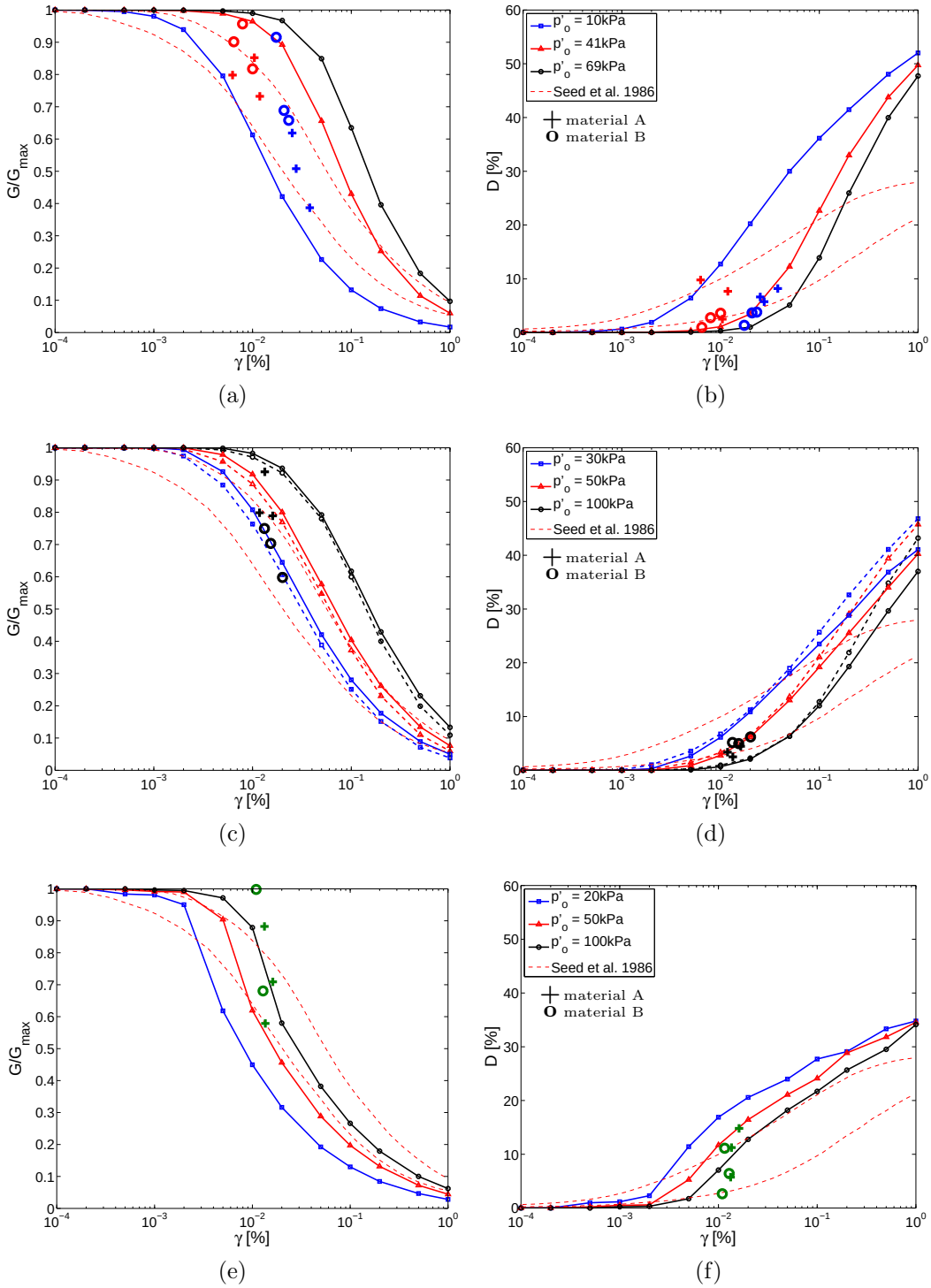

Figure 5.53: Comparison of shear modulus degradation and damping obtained from the numerical model and the results of numerical drained cyclic strain-controlled shear test. Cross stands for results for interlayer material A and circle for interlayer material B. Red: ballast under the sleeper; blue: ballast between sleepers; black: interlayer; green: subgrade. a) Ballast's shear modulus reduction; b) Ballast's damping; c) Interlayer's shear modulus reduction (solid line: material A; dashed line: material B); d) Interlayer's damping (solid line: material A; dashed line: material B); e) Subgrade's shear modulus reduction; f) Subgrade's damping.

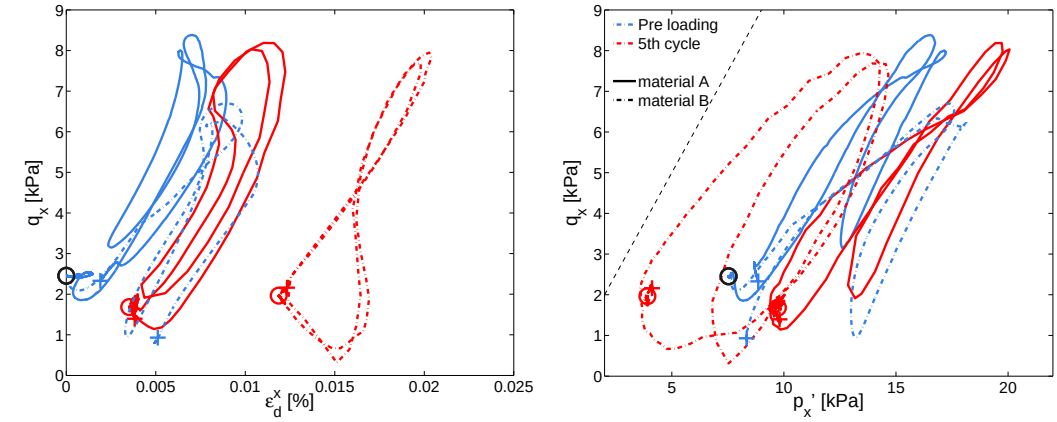

(a) $q_x - \varepsilon_d^x$ (b) $q_x - p'_x$

(c) $\varepsilon_v - \varepsilon_d^x$ (d) $\varepsilon_v - p'_x$

Figure 5.54: Impact of interlayer material on its cyclic response. Solid line represents the interlayer material A and dashed dotted line the interlayer material B. Gray dashed line is the unitary slope (45°).

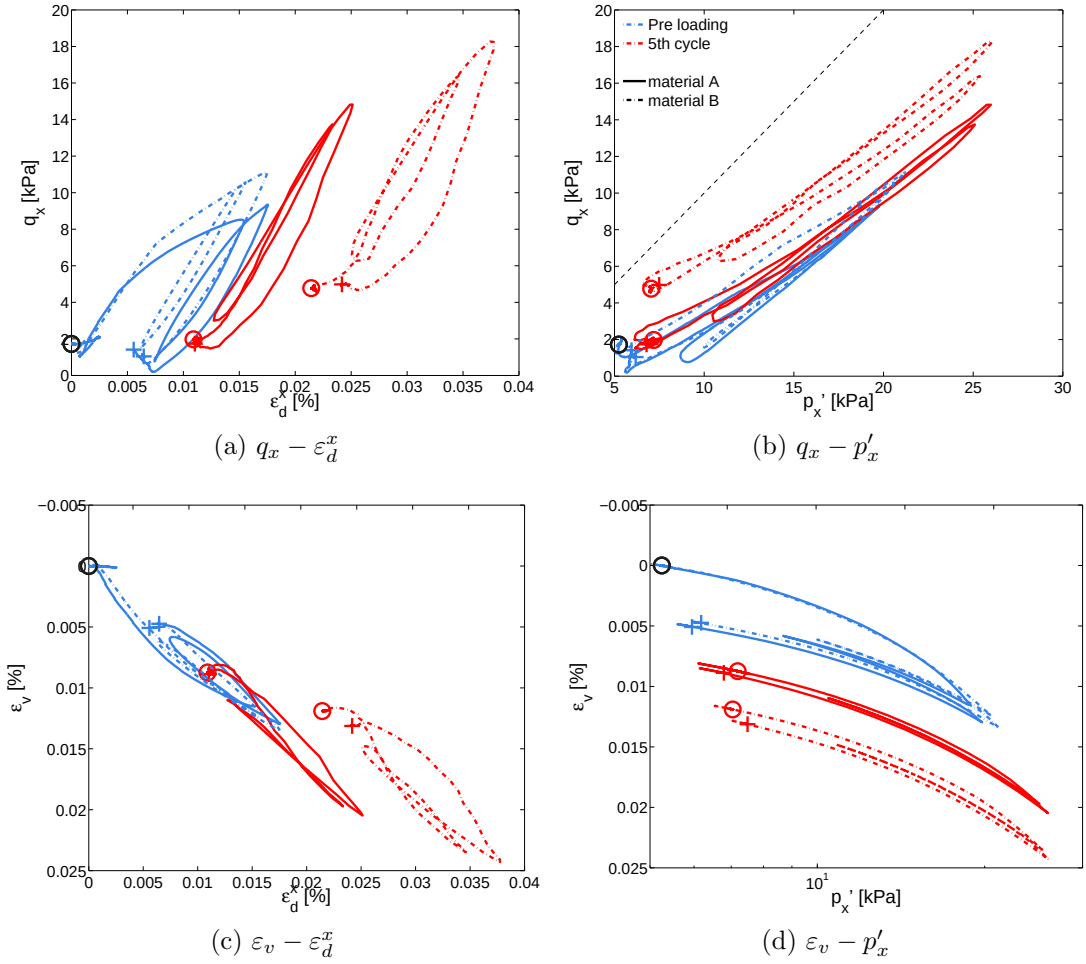

(a) $q_x - \varepsilon_d^x$ (b) $q_x - p'_x$

(c) $\varepsilon_v - \varepsilon_d^x$ (d) $\varepsilon_v - p'_x$

Figure 5.55: Impact of interlayer material on the cyclic response of under sleeper ballast. Solid line represents the interlayer material A and dashed dotted line the interlayer material B. Gray dashed line is the unitary slope (45°).

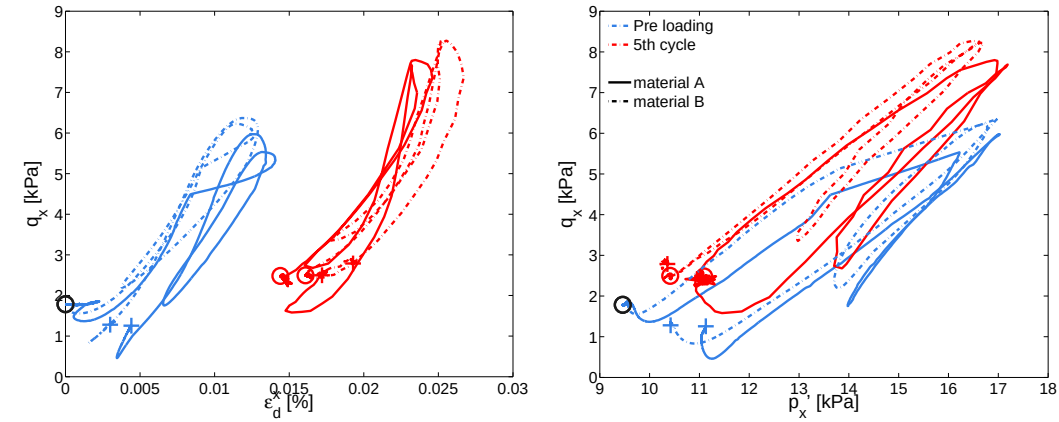

(a) $q_x - \varepsilon_d^x$ (b) $q_x - p'_x$

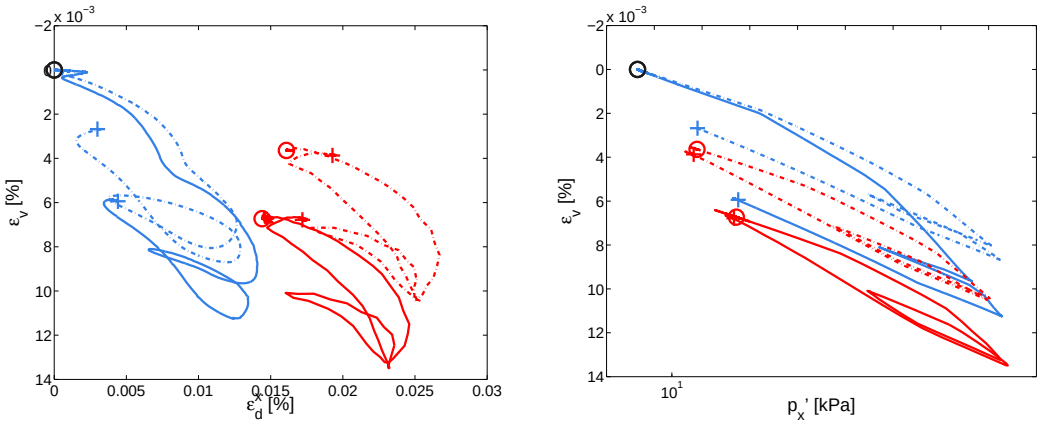

(c) $\varepsilon_v - \varepsilon_d^x$ (d) $\varepsilon_v - p'_x$

Figure 5.56: Impact of interlayer material on the cyclic response of the subgrade. Solid line represents the interlayer material A and dashed dotted line the interlayer material B.

5.7 Concluding remarks

In this section, the impact of nonlinear behavior of granular materials during the conditioning phase of the track is discussed. The elastoplastic nonlinear constitutive law developed at Ecole Centrale, called ECP model, is used in order to model the soil behavior under cyclic load. The model parameters used for ballast and the interlayer are calibrated from triaxial tests available in the literature. An additional verification of the calibrated parameters is proposed for ballast, based on numerical results for cyclic oedometric test.

The numerical model developed in Chapter 3 is adapted for considering nonlinear behavior. The initial stress is obtained by "constructing" the different track layers, and relative displacements between the sleeper and the ballast layer are allowed by the use of mechanical interfaces. These modifications particularly allowed to better represent the initial shear stress at the sleeper/ballast interface.

From the performed simulations and the considered materials' behavior, the following conclusions can be drawn:

1. The load transfer mechanisms during the conditioning phase of the materials are assessed for a moving load at small speed. It is well known that the vertical load is mainly transmitted by ballast zone directly beneath the sleeper, which develops the highest deviatoric stresses. In this zone, the stress path followed by ballast can be interpreted by an oedometric path. The performed simulations showed that the zone between sleepers is then subjected to a different mechanism, as lateral stresses are higher and vertical stresses are lower in this area. Ballast is then subjected to different stress paths and it presents different shear responses according to position of the control point regarding the sleeper. The interlayer plays an important role in homogenizing the vertical and lateral loads observed in the ballast, as the differences in normal stresses are no longer observed in the subgrade. As a consequence of the nonlinear behavior, load is asymmetrically distributed among sleepers for moving loads, sleepers ahead the moving load transmitting lower stresses than the sleeper behind the load.

2. After loading, inhomogeneous track settlement is observed along the track. The variations measured at the rail level are mainly caused by variations of settlement at the subgrade, which can be mainly attributed to the impact of shear stress variations the subgrade is subjected to. These variations should be viewed under a larger context of material inhomogeneities appearing from sleeper/ballast contact conditions and variations in subgrade stiffness. The impact of variations of Young's Modulus in the track stiffness measured at the rail level was extensively discussed in Chapter 4.

3. Cyclic increase in materials' confinement and density is observed from the numerical simulations, as a consequence of both volumetric and deviatoric residual plastic strains. For cycles at low speed, low residual shear and deviatoric stresses are obtained during this phase. Therefore, the accumulation of plastic strains in the materials mainly occurs during the first cycles. Although shear stress values are low

compared to vertical and lateral stresses, the combination of stress variations during load lead to high amplitudes of principal stress axes rotation angle, specially in ballast.

4. The simulations performed confirmed that during the conditioning phase of the materials, load speed has an impact on ballast behavior. Differently from cycles at small speed, ballast settlement continuously increases for cycles at nominal speed as a consequence of higher residual strains. Therefore, higher stresses are developed during loading and the material evolves toward higher stress values. After track maintenance or renewal, this situation is avoided by imposing speed restriction for trains during the first cycles (usually measured in terms of cumulated tonnage). This mechanism is exemplified in the numerical model by considering a preloading cycle at small speed followed by cycles at nominal speed. In this case, the material cumulates lower strains and is subjected to lower stresses for cycles at 220 km/h.

5. The sensitivity of these results to the subgrade soil and the interlayer material was separately assessed. By considering a lower initial density for the subgrade soil, it was shown that ballast is mainly affected by the subgrade behavior. Higher deviatoric stresses and strains are observed for ballast during cyclic load for the subgrade with lower initial density. Concerning the interlayer material, by considering a material presenting higher shear modulus degradation and lower peak resistance, it was shown that ballast also develops higher deviatoric stress and strain during cyclic load. In this particular case, this is a direct consequence of the reduction of mean stress in the interlayer. Therefore, according to the subgrade and interlayer materials, ballast can be subjected to higher grain abrasion and breakage as a consequence of the increased stress level.

The results presented in this chapter illustrate the soil behavior mechanisms during the conditioning phase of the track. Although track settlement and plastic deformation accumulation decrease rapidly after this phase, the strain levels which the materials are subjected to during cyclic load require considering nonlinear behavior. Among the different nonlinear mechanisms inherent of soil behavior, the stress path dependency and cyclic evolution of stiffness are pointed out as important components to be considered by models interested in the track response under train load. When considering the accumulation of settlement for a large number of cycles, the influence of the principal stress axes rotation angle should also be taken into account.

Chapter 6

Conclusions and further research

Contents

6.1 Conclusions

A global framework for geotechnical modeling of the railway track is proposed in the present thesis. It is based on a multi-purpose dynamic finite element model of the railway track, accounting for uncertainty and material nonlinearity. Partial conclusions were already given throughout the dissertation. Thus, the main obtained results are highlighted in this chapter and discussed in the light of their impact on the structure's behavior.

Concerning the numerical model, the choice was made of simplifying the 3D domain by a 2D plane-strain model with a modified width. Therefore, reduction of the computational cost for probabilistic analysis was obtained and the representativeness of the model in the 2D plane was demonstrated. Moreover, a procedure for initializing a moving load on finite discretized domains was also proposed in this work. It permitted to considerably improve the results by reducing spurious wave generation before implementing any appropriate boundary condition. This loading methodology is based on a two-step approach, by first initializing the applied load magnitude and then the load speed, in order to avoid infinite acceleration. In sum, this is a straightforward methodology which can be used for all moving load problems on finite discretized domains.

Concerning Chapter 4, a rational methodology to account for track material's variability was proposed, based on a nonintrusive probabilistic approach. To assess this variability, a probabilistic description of the dynamic cone resistance was obtained, based on statistical analysis from track characterization campaigns performed by SNCF prior to renewal works. Results showed large coefficients of variation for each layer, as a consequence of the material heterogeneity encountered along the track. Finally, empirical relations proposed in the literature were used to link the dynamic cone resistance and the Young's Modulus, which provided the necessary input data for the numerical model. In addition, spatial variations could also be modeled by considering invariant scalar random fields with a prescribed correlation structure.

This methodology was implemented in order to verify the aptitude of the track stiffness measurement in describing spatial variations of material's mechanical properties. From the obtained results, the following conclusions can be drawn:

1. The track stiffness measurement captures the correlation structure imposed in the materials. However, due to the load distribution along the sleepers, the scale of fluctuation of the track stiffness field is higher than the input field. Moreover, small spatial fluctuations of material stiffness (autocorrelation length lower than 1 m) do not lead to variations of the track stiffness. In this sense, the track stiffness measure seems unable to characterize fluctuations smaller than 1 m.

2. The track stiffness' first marginal coefficient of variation presents smaller variations regarding to the large values for the Young's Modulus. The importance of the rail bending stiffness in reducing the output variability is assessed by calculating the foundation stiffness of an analytical solution of beam on elastic foundation loaded by a moving force. Moreover, small autocorrelation distances lead to lower track stiffness' first marginal coefficient of variation.

3. According to the performed sensitivity analysis, the subgrade stiffness variations impact the most the track stiffness. This result was obtained for different track

configurations (conventional and high speed lines) and different load speeds. It was shown that considering the increase of the subgrade Young's Modulus with increasing depth reduces its impact on the track stiffness. Nonetheless, the subgrade was still preponderant regarding the track stiffness. The simulations performed highlight the importance of a homogeneous subgrade's stiffness, as variations of track stiffness are expected to lead to an increased train-track dynamic forces and possibly to track geometry irregularities.

Therefore, the characterization of track's variability through the performed track stiffness measurement is adapted for long autocorrelation distances appearing in the subgrade. This is to say that, short variations (< 1 m) in materials cannot be distinguished by the measurement, which is expected to be the case in the ballast layer. However, it is also expected that short variations appearing from hanging sleepers and variability in rail pads stiffness can be captured by measuring the track stiffness.

The importance of nonlinear behavior and loading history during the conditioning phase of the track materials was also studied in this thesis. The conditioning phase can be viewed as the first loading cycles, when track settlement rapidly increases and materials cumulate the highest plastic strains. Nonlinear behavior of track geomaterials was modeled by the elastoplastic constitutive model ECP, which provides a suitable framework for the description of geomaterials' behavior under cyclic loading. Model parameters were calibrated from triaxial test results available in the literature, following the calibration methodology proposed by Lopez-Caballero and Modaressi-Farahmand-Razavi (2008). From the numerical simulation results presented in Chapter 5, the following conclusions can be drawn:

4. Cyclic increase in density and confinement are obtained as a consequence of the strains accumulation during cycles. Shear modulus decreases and damping increases in materials with increasing speed, as a result of shear strain increase. Principal stress axes rotation was also observed during load caused by shear stress.

5. Different stress paths were observed at different positions relatively to the sleeper. Vertical stress was higher under the sleeper and lateral stress was higher between sleepers. These differences were mainly observed in the ballast layer, which was subjected to the highest increase in stresses during load. This aspect is less important at the subgrade level, as the interlayer homogenizes the normal stresses along the track. Therefore, ballast grains under the sleeper are subjected to higher deviatoric stress, while grains between sleepers are expected to rotate and rearrange more often. This leads to different residual states after load, thus two distinct behaviors are obtained for ballast under cyclic load. Bodin (2001) has pointed out this aspect from heuristic considerations about track construction and possible compaction characteristics of ballast under and between sleepers.

6. Load speed influences decisively the evolution of track's permanent settlement during the conditioning phase and the proposed model is able to capture this aspect. Cyclically applying loads at the nominal speed leads to an increase in ballast settlement, not observed for loads at small speed. As a consequence, residual mean and

deviatoric stresses are also higher, which is unwanted in tracks as ballast is then subjected to higher cyclic stresses and cumulates higher permanent strains.

7. The sensitivity of these results to the interlayer and subgrade materials was assessed by separately considering a subgrade at lower initial density and a softer interlayer. For both cases, ballast was subjected to higher maximum and residual stresses and developed higher residual strains. In the first case, this increase is caused by the lower subgrade stiffness. In the second case, cyclic reduction of the interlayer mean stress is the main cause. Insufficient stiffness of the track formation is well known to increase ballast settlements (Meissonnier, 2000). Moreover, railway standards require sufficient bearing capacity of the track formation below the ballast layer, which is achieved by well compacted materials. The obtained results are then in accordance with the expected behavior of the track under the considered conditions.

After the conditioning phase, the accumulation of residual strains is very low and the resilient behavior of materials can give good results on the track response subjected to moving loads. The obtained results provide some insights on the necessary load transfer mechanisms that a constitutive model should account for. Stress path dependency and material softening are pointed out as important mechanisms for correctly assessing the resilient response of materials in tracks. For the long term response, considering the rotation of principal stress axes in the constitutive model seems necessary, as there are many experimental evidences on the role of this effect in the accumulation of plastic deformation on materials (Chan, 1990; Grabe and Clayton, 2009; Ishikawa et al., 2011, among others).

6.2 Further research topics

In this section some recommendations and topics for further research are discussed in the light of the obtained results in this thesis.

Train-track interaction

The choice is made in this work to not consider train-track interaction aspects. Therefore, the effect of dynamic loads on the obtained results is not assessed, i.e. mainly track geometry irregularities. When no spatial variability is considered (Chapters 3 and 5), the effect of dynamic loads can be considered by Eisenmann or Prud'Homme dynamic amplification factors (DAF) as a first approach (Ferreira, 2010). However, train-track interaction can only be assessed by considering coupled vehicle and track models. A coupled model could be used to verify the crossed influence of track stiffness variability and track geometry irregularities on the vehicle response.

Coupling the probabilistic and nonlinear analysis

Applying the same probabilistic methodology for the nonlinear model is not straightforward. One of the main challenges is in assessing which parameters to vary and their subsequent probabilistic properties, specially for not-directly measurable parameters. First results on how to induce material's response variability for different stress paths (drained and undrained triaxial tests, drained cyclic strain-controlled shear test) and applied to seismic analysis with the ECP model have been presented in the literature (Lopez-Caballero and Modaressi-Farahmand-Razavi, 2010a,b). Transposing these results for railway materials on the present model is one way of considering the impact of material's properties variability.

Another way of tackling this point is in considering binary random fields (Koutsourelakis and Deodatis, 2005, 2006). In this case, the medium is supposed to be composed of two distinct and deterministic materials, which assumes random positions according to a prescribe probability density function and autocorrelation function. This methodology seems more adapted to model material clustering and it has also been extended for multidimensional cases. In this case, the heterogeneity encountered in railway materials such as the interlayer could be finely accounted for.

Water content

The presence of water is not considered in this work. Although the ballast layer is expected to be dry, a water phase exists in the interlayer and the subgrade. Pore water pressure possibly increases during train load, depending on the site drainage conditions, load magnitude and speed. A first step toward considering the water presence is considering these materials under saturated conditions. However, it is well known that unsaturated conditions prevail on compacted soils (Delage and Cui, 2001; Alonso et al., 2013). In this sense, correctly accounting the *in situ* water content requires considering unsaturated soil

behavior. In GEFDyn software, the ECP model formulation for unsaturated soils (Modaressi and Abou-Bekr, 1994) is directly available and can be used for future research on this topic.

Material anisotropy and comparison with resilient models

Experimental evidence discussed in Chapter 2 has showed that compacted materials present an anisotropic behavior called cross-anisotropy, due to the loading history (Kolisoja, 1997; Tatsuoka et al., 1999; Coronado Garcia, 2005, among others). In the ECP model, this aspect is taken into account by the hardening evolution, which is translated by the plastic yield surfaces' evolution of each plastic mechanism. The numerical results presented in this thesis have showed that plastic strains accumulation mainly occur during the first loading cycles, depending on the stress history. For instance, for cycles at low speed or after track preloading, an almost resilient response is obtained after the 5^{th} cycle. Therefore, the ECP model can be used for studying the resilient response of the materials in the track once the plastic strain accumulation is small and the plastic yield surfaces do not evolve. At this state, a comparison of the ECP model and a resilient model such as the Boyce anisotropic model (Hornych et al., 1998) could be performed. Moreover, by modifying the initializing conditions of the ECP model in order to consider the materials after the conditioning phase, numerical laboratory tests could be conducted on materials on a state closer to the state in the track. Such procedure has been applied in other geotechnical context by Salager et al. (2012).

High number of cycles and long-term behavior of the structure

The focus is given in this thesis in studying the material's response during the conditioning phase of the track. Although some insights are given on how this phase affects the subsequent response of the materials, the question on how these affect the long-term response still remains. In Chapter 2, it has been discussed that elastoplastic models with kinematical hardening do not seem adapted for studying high number of cycles, as the predicted plastic strains are higher in this case (Gidel, 2001). For instqnce, such overestimation of plastic strains is observed by Aubry et al. (1999) when simulating around a million bogie passages on ballast, by direct integrating the ECP model in the stress path obtained from the wave propagation software MISS3D (*Modélisation de l'Interaction Sol Structure en 3D*). More recently, interesting results for the long-term behavior of unbound granular materials have been obtained by Chazallon et al. (2006), by considering en elastoplastic model similar to the ECP model but with an elastic domain characterized by the Boyce anisotropic model. The latter could be used in the present model in order to evaluate the long-term behavior of the structure given the considered conditioning phases and track preloading characteristics.

Appendices

Appendix A

ECP multimechanism model

The ECP model or also called Hujeux model is an elastoplastic multimechanism model developed at *Ecole Centrale Paris* (Aubry et al., 1982; Hujeux, 1985). It considers the effective stress concept developed by Terzaghi and is based on a Coulomb type failure criterion and the critical state concept. All irreversible phenomena is modeled by four coupled elementary plastic mechanisms: one isotropic and three plane-strain deviatoric on three orthogonal planes. Hardening is controlled by plastic strain: volumetric plastic strain for the isotropic mechanism and both deviatoric and volumetric plastic strains for the three deviatoric ones. Cyclic behavior uses kinematical hardening based on the state variables at the last load reversal.

The model assumes a complete decomposition of strains on elastic and plastic parts, as proposed by the incremental plasticity theory. The elastic part is supposed to follow a nonlinear elasticity behavior. Bulk (K) and shear (G) moduli are functions of the mean effective stress (p'):

$$K(p') = K_{ref} \left(\frac{p'}{p_{ref}} \right)^{n_{el}} \tag{A.1}$$

$$G(p') = G_{ref} \left(\frac{p'}{p_{ref}} \right)^{n_{el}} \tag{A.2}$$

where K_{ref} and G_{ref} are the bulk and shear moduli measured at the mean reference pressure p_{ref}, and n_{el} is the degree of nonlinearity. The deviatoric primary yield surface on the k plane is given:

$$f_k(\underline{\underline{\sigma}}, \varepsilon_v^p, r_k) = q_k - \sin\phi'_{pp} \cdot p'_k \cdot F_k \cdot r_k \qquad k \in [1, 2, 3] \tag{A.3}$$

with:

$$F_k = 1 - b \ln \left(\frac{p'_k}{p_c} \right) \tag{A.4}$$

$$p_c = p_{c0} \exp(\beta \varepsilon_v^p) \tag{A.5}$$

- ϕ'_{pp} is the friction angle at the critical state or perfect plasticity;

- b controls the form of the yield surface, from a Mohr-Coulomb type yield surface (b=0) to a Cam-Clay type (b=1);
- β is the plasticity compression modulus and it introduces the densification effect of the material after loading;
- p_{c0} represents the critical state stress corresponding to the initial void's ratio.

Each deviatoric plastic mechanism is simply defined by a scalar quantity r_k called degree of mobilized friction and it is associated with the plastic deviatoric strain. Its evolution law is given by:

$$\dot{r}_k = \dot{\lambda}_k^p \frac{(1 - r_k)^2}{a} \tag{A.6}$$

where $\dot{\lambda}_k^p$ is the plastic multiplier of the k mechanism and a is obtained as:

$$a = a_1 + (a_2 - a_1)\alpha_k(r_k) \tag{A.7}$$

with:

$$\alpha_k = 0 \text{ if } r_k^{elas} < r_k < r_k^{hys} \tag{A.8}$$

$$\alpha_k = \left(\frac{r_k - r_k^{hys}}{r_k^{mob} - r_k^{hys}} \right)^m \text{ if } r_k^{hys} < r_k < r_k^{mob} \tag{A.9}$$

$$\alpha_k = 1 \text{ if } r_k^{mob} < r_k < 1 \tag{A.10}$$

where a_1, a_2 and m are model parameters. It allows the decomposition of shear hardening into pseudo-elastic, hysteretic and mobilized domains. The extent of each domain is given by r^{elast}, r^{hyst} and r^{mob}. The model considers an associated flow rule in each deviatoric plane k. Roscoe's dilatancy rule (Roscoe et al., 1958) is assumed to obtain the increment of the volumetric plastic strain of each mechanism:

$$\dot{\varepsilon}_{vk}^p = \dot{\lambda}_k^p \cdot \alpha_\psi \cdot \alpha_k(r_k) \left(\sin\psi - \frac{q_k}{p'_k} \right) \tag{A.11}$$

where ψ is the characteristic angle defining the limit between dilatancy and contractancy on the (q_k, p_k) plan and α_ψ is a constant parameter.

The isotropic mechanism produces only volumetric change. The yield surface is assumed to be:

$$f_{iso} = |p'| - d \cdot p_c \cdot r_{iso} \tag{A.12}$$

with:

$$\dot{r}_{iso} = \dot{\varepsilon}_{viso}^p \frac{(1 - r_{iso})^2}{c_1 \frac{p_c}{p_{ref}}} \tag{A.13}$$

- d defines the distance of the isotropic consolidation line to the critical state line in the plane $(e, \ln p')$ or $(\varepsilon_v^p, \ln p')$;
- c_{mon} controls the volumetric hardening.

The four mechanisms are coupled by the hardening variable ε_v^p as follows:

$$\varepsilon_v^p = \sum_{k=1}^{3} \varepsilon_{vk}^p + \varepsilon_{viso}^p \tag{A.14}$$

Lopez-Caballero and Modaressi-Farahmand-Razavi (2008) proposed to classify the model parameters in terms of their estimation method. This approach separates the parameters in two categories: directly measured (either by in-situ or laboratory tests) and not-directly measured.

	Directly measured	Not-directly measured
Elastic	K_{ref}, G_{ref}, n_{el}, p_{ref}	
Critical state and plasticity	ϕ'_{pp}, β, p_{c0}, d	b
Flow rule and Isotropic hardening	ψ	a_1, a_2, a_ψ, m, c_1, c_2
Threshold domains		r^{ela}, r^{hys}, r^{mob}, r^{ela}_{iso}

Table A.1: Classification of ECP elastoplastic model parameters as proposed by Lopez-Caballero and Modaressi-Farahmand-Razavi (2008).

Appendix B

Analytical solution of infinite beam on elastic foundation

B.1 Formulation of the problem

Consider an infinite Euler beam on an elastic foundation being loaded by a constant force P moving at constant speed c from the infinite to infinite. A Winkler-type elastic foundation is considered. The differential equation of the above problem may be written as follows:

$$EJ\frac{\partial^4\nu(x,t)}{\partial x^4} + \mu\frac{\partial^2\nu(x,t)}{\partial t^2} + 2\mu\omega_b\frac{\partial\nu(x,t)}{\partial t} + k\nu(x,t) = P\delta(x-vt) \tag{B.1}$$

where: x is the length coordinate with the origin at the left-hand end of the beam, t is the time coordinate, $\nu(x,t)$ is the beam deflection at a point x at the instant t, E is the Young's Modulus of the beam [Pa], J is the constant moment of inertia of the beam cross section [m^2], μ is the constant mass per unit length of the beam[kg/m], ω_b is the circular frequency of damping of the beam [Hz], P is the concentrated force of constant magnitude [N], c is the constant speed of the load motion [m/s], k is the coefficient of the Winkler foundation [N/m^2] and $\delta(x-vt)$ is the Dirac function.

Considering an infinite beam and the force, P, coming from the infinite, the deflection, the slope of the deflection line, the bending moment as well as the shear force should be zero at the boundaries at each instant. It can also be considered that these quantities are null as initial conditions. In order to consider a discrete support with constant span rather than a continuous one, the value of the coefficient k can be calculated as:

$$k = \frac{k_t}{L} \tag{B.2}$$

where k_t is stiffness of the discrete support [N/m] and L: span between two supports [m]. Within these conditions, this problem presents a quasi-stationary state, i.e. the beam is at rest in relation to the moving coordinate system. The coordinate system can then be changed and the new dimensionless variable s is adopted:

$$s = \lambda(x-vt) \tag{B.3}$$

$$\lambda = \left(\frac{k}{4EJ}\right)^{1/4} \tag{B.4}$$

For the quasi-stationary state, the solution $\nu(x,t)$ of Equation B.1 will be of the form:

$$\nu(x,t) = \nu_o \nu(s) \tag{B.5}$$

where $\nu(s)$ is dimensionless deflection of the beam given as:

$$\nu_o = \frac{P}{8\lambda^3 EJ} = \frac{P\lambda}{2k} \tag{B.6}$$

Shifting parameters x and t by the dimensionless parameter s in Equation B.1 gives:

$$\frac{\partial^4 \nu(s)}{\partial s^4} + 4\alpha \frac{\partial^2 \nu(s)}{\partial s^2} - 8\alpha\beta \frac{\partial \nu(s)}{\partial s} + 4\nu(s) = P\delta(s) \tag{B.7}$$

where:

$$\alpha = \frac{v}{v_{cr}} = \frac{v}{2\lambda}\left(\frac{\mu}{EJ}\right)^{1/2} \tag{B.8}$$

$$\beta = \left(\frac{\mu}{k}\right)^{1/2} \omega_b \tag{B.9}$$

$$v_{cr} = 2\lambda \left(\frac{EJ}{\mu}\right)^{1/2} \tag{B.10}$$

The parameter α represents the effect of the speed of the load P regarding the critical speed of the beam v_{cr}, and the parameter β represents the effect of the damping of the beam. The solution $\nu(s)$ of the Equation B.7 express the steady-state vibration of the beam, and although it fails to satisfy the initial conditions, it may be shown that the quasi-stationary state is attained in a short period of time once the moving load P is applied.

Equation B.7 will be solved by the method of Fourier integral equations using the following relationships:

$$\nu(s) = \frac{1}{2\pi} \int_{-\infty}^{\infty} V(q) e^{isq} dq \tag{B.11}$$

where:

$$V(q) = \int_{-\infty}^{\infty} \nu(s) e^{-iqs} ds \tag{B.12}$$

It is then obtained:

$$q^4 V(q) - 4\alpha^2 q^2 V(q) - i8\alpha\beta q V(q) + 4V(q) = 8$$

which leads to:

$$V(q) = \frac{8}{q^4 - 4\alpha^2 q^2 - i8\alpha\beta q + 4} \tag{B.13}$$

The solution of the integral equation will be of the form:

$$\nu(s) = \frac{4}{\pi} \int_{\infty}^{\infty} \frac{8}{q^4 - 4\alpha^2 q^2 - i8\alpha\beta q + 4} \tag{B.14}$$

The roots of the denominator $Q(q)$ of Equation B.14 must be obtained. It is assumed that they have the form:

$$\begin{aligned} A_1 &= a_1 + ib \quad A_2 = -a_1 + ib \\ A_3 &= a_2 - ib \quad A_4 = -a_2 - ib \end{aligned} \tag{B.15}$$

which leads to:

$$\begin{aligned} Q(q) =& q^4 - 4\alpha^2 q^2 - i8\alpha\beta q + 4 \\ =& (q - A_1)(q - A_2)(q - A_3)(q - A_4) = 0 \end{aligned} \tag{B.16}$$

After substituting the solutions from B.15 in Equation B.16 and some handling with real and imaginary parts, the following expression is obtained:

$$b^6 + 2\alpha^2 b^4 + (\alpha^4 - 1)b^2 - \alpha^2\beta^2 = 0 \tag{B.17}$$

In order not to loose the sign sense impose on roots of $Q(q)$, only the positive one of the six roots from Equation B.17 is taken. It has always a positive root at $\alpha \geq 0, \beta \geq 0$ according to Descartes rule of signs. This is a third order polynomial equation on b^2 and solutions of a_1 and a_2 may be obtained as:

$$\begin{aligned} a_1^2 =& 2\alpha^2 + b^2 + 2\alpha\beta/b \\ a_2^2 =& 2\alpha^2 + b^2 - 2\alpha\beta/b \end{aligned} \tag{B.18}$$

Approximate or analytic solutions may be obtained for all cases, i.e. no damping ($\beta = 0$), light damping ($\beta \leq 0$), critical damping ($\beta = \beta_{cr}$) and supercritical damping ($\beta \geq \beta_{cr}$), for all values of α ($\alpha \leq 1$, $\alpha = 1$ and $\alpha \geq 1$). However, for the specific case of the railway track, the great difference between values of mechanical properties of the steel rail and the sleeper and soil structure leads to small values of β. Also, the combined effect of the actual vehicle speed c, the steel rail properties E, J, μ and the sleeper plus soil stiffness k leads to small values of α. Considering regular rail properties of Young's Modulus E=210 GPa, moment of inertia J=3.05.10^5 m^2 and constant mass per unit length μ=300 kg/m, and a vehicle at speed c=350 km/h and a typical track stiffness value of k=52.6 MPa (Krylov et al., 2000):

$$\begin{aligned} \alpha =& \frac{c\mu^{1/2}}{2} \left(\frac{4}{kEJ}\right)^{1/4} \\ \alpha \cong& 0.27 \end{aligned} \tag{B.19}$$

Also, considering a circular damping frequency w_b=3Hz as representative of a regular track (Krylov et al., 2000), the following value of β is obtained:

$$\begin{aligned}\beta &= \left(\frac{\mu}{k}\right)^{1/2} \omega_b \\ \beta &= 0.15\end{aligned} \tag{B.20}$$

In the following sessions the full analytical or approximate solutions for the static, no damping and light damping cases will be presented, for which $\beta << 1$ and $\alpha < 1$. In these cases, the values of a_1, a_2 and b are:

- Static Case

$$b = 1,\ a_1 = 1,\ a_2 = 1 \tag{B.21}$$

- Case with no damping($\beta = 0$)

$$\begin{aligned}b &= (1-\alpha^2)^{1/2} \\ a &= a_1 = a_2 = (1+\alpha^2)^{1/2}\end{aligned} \tag{B.22}$$

- Case with light damping ($\beta \leq 1$) - approximative solutions

$$\begin{aligned}b &\approx (1-\alpha^2)^{1/2} \\ a_{1,2} &\approx \left[1+\alpha^2 \pm \frac{2\alpha\beta}{(1-\alpha^2)^{1/2}}\right]^{1/2}\end{aligned} \tag{B.23}$$

B.2 Analytical solution

In order to obtain the analytic solutions of the integral Equation B.14, the Cauchy's residue theorem may be applied over an integral in the counter-clockwise direction around a curve consisting of segments -R,+R and semicircle C_R at $\lim_R = \infty$.

The mathematical development is shown in Fryba (1972). The obtained solution is of the following form:

$$\begin{aligned}\nu(s) &= \frac{1}{a_1(D_1^2+D_2^2)}[(D_1 - D_2 i)e^{iA_1 s} + (D_1 + D_2 i)e^{iA_2 s}] = \\ &= \frac{2}{a_1(D_1^2+D_2^2)} e^{-bs}[D_1 \cos(a_1 s) + D_2 \sin(a_1 s)],\ s \geq 0 \\ \nu(s) &= \frac{1}{a_2(D_3^2+D_4^2)}[(D_3 + D_4 i)e^{iA_3 s} + (D_3 - D_4 i)e^{iA_4 s}] = \\ &= \frac{2}{a_1(D_3^2+D_4^2)} e^{bs}[D_3 \cos(a_2 s) - D_4 \sin(a_2 s)],\ s \leq 0\end{aligned} \tag{B.24}$$

where the coefficients D_1, D_2, D_3 and D_4 are described as:

$$\begin{aligned} D_1 =& a_1 b \\ D_2 =& b^2 - \frac{1}{4}(a_1^2 - a_2^2) \\ D_3 =& a_2 b \\ D_4 =& b^2 + \frac{1}{4}(a_1^2 - a_2^2) \end{aligned} \tag{B.25}$$

The bending moment $M(s)$ and the shear force $T(s)$ may be calculated from the derivatives of the expression of $\nu(s)$:

$$M(x,t) = -EJ\nu''(x,t) = M_o M(s) = \frac{P}{4\lambda} M(s) \tag{B.26}$$

$$T(x,t) = -EJ\nu'''(x,t) = T_o T(s) = P M(s) \tag{B.27}$$

$$\begin{aligned} M(s) = -\frac{1}{2} v''(s) = \\ = \frac{1}{a_1(D_1^2 + D_2^2)} e^{-bs} [(a_1^2 D_1 + 2a_1 b D_2 - b^2 D_1)\cos(a_1 s) \\ + (a_1^2 D_2 - 2a_1 b D_1 - b^2 D_2)\sin(a_1)s], \ s \geq 0 \\ = \frac{1}{a_1(D_3^2 + D_4^2)} e^{bs} [(a_2^2 D_3 + 2a_2 b D_4 - b^2 D_3)\cos(a_2 s) \\ - (a_2^2 D_4 - 2a_2 b D_3 - b^2 D_4)\sin(a_2)s], \ s \leq 0 \end{aligned} \tag{B.28}$$

$$\begin{aligned} T(s) = -\frac{1}{8} v'''(s) \\ = \frac{1}{4a_1(D_1^2 + D_2^2)} e^{-bs} [(a_1^3 D_2 - 3a_1^2 b D_1 - 3a_1 b^2 D_2 + b^3 D_1)\cos(a_1 s) \\ - (a_1^3 D_1 + 3a_1^2 b D_2 - 3a_1 b^2 D_1 - b^3 D_2)\sin(a_1)s], \ s \geq 0 \\ = \frac{1}{4a_2(D_3^2 + D_4^2)} e^{bs} [(a_2^3 D_4 - 3a_2^2 b D_3 - 3a_2 b^2 D_4 + b^3 D_3)\cos(a_2 s) \\ + (a_2^3 D_3 + 3a_2^2 b D_4 - 3a_2 b^2 D_3 - b^3 D_4)\sin(a_2)s], \ s \leq 0 \end{aligned} \tag{B.29}$$

Equations B.24, B.28 and B.29 may be simplified considering the expressions of a_1, a_2 and b obtained above for each particular case.

Static Case

$$\nu(s) = e^{-|s|}(\cos s + \sin|s|) \tag{B.30}$$

$$M(s) = e^{-|s|}(\cos s - \sin|s|) \tag{B.31}$$

$$T(s) = -\operatorname{sign}(s).\frac{1}{2} e^{-|s|}\cos s \tag{B.32}$$

Case with no damping ($\beta = 0$)

$$\nu(s) = \frac{1}{ab} e^{-b|s|} (a \cos(as) + b \sin(a|s|)) \tag{B.33}$$

$$M(s) = \frac{1}{ab} e^{-b|s|} (a \cos(as) - b \sin(a|s|)) \tag{B.34}$$

$$T(s) = -\frac{1}{2ab} e^{-b|s|} (\text{sign}\ (s) ab \cos(as) + \alpha^2 \sin(as)) \tag{B.35}$$

Case with light damping

In this case the full expressions B.24, B.28 and B.29 should be used, as no simplification may be easily obtained.

Appendix C

Boundary conditions for finite models of infinite media

Modeling infinite media by the finite domains imposes fictive boundaries on the continuous medium. Using the Finite Element Method for dynamic applications demands a fine study of boundary conditions. They must ensure that all energy (or as an approximation at least most of it) will pass from the finite model to the exterior through the boundary, i.e. the boundary will absorb most of the incoming energy with no reflection. Correctly modeling wave propagation and dissipation on the finite element context is an actual field of research. Three main different ways of dealing wave reflection on boundaries are discussed in this appendix:

- Boundary conditions: in this case a particular or more general solution of the wave equation is imposed on the boundary. Paraxial approximation (Engquist and Majda, 1977) and Perfectly Matched Layers (PML) (Berenger, 1994) are examples for the first and second cases, respectively. Local conditions and easy computational implementation are often requirements for good boundary conditions.

- Absorbing elements: in this case viscoelastic elements are used to absorb wave energy. Wave reflection on boundaries is not fully avoided, but depending on the complexity and parameter values of the viscoelastic mechanical behavior one could expect high wave absorption and energy dissipation. The Lysmer boundary (Lysmer and Kuhlemeyer, 1969) is a classical example of this type of condition, although other common viscoelastic models can be applied (Kelvin-Voigt, Maxwell).

- Infinite elements: it consists on approximating the element behavior at infinity by a reasonable reflection of the physics of the problem (Bettes, 1992).

In the following a comprehensive development of the above boundary solutions is given in order to present their hypothesis and drawbacks when applied on finite element models.

C.1 Paraxial approximation

The mathematical development presented hereafter follows Engquist and Majda (1977). Consider the 2D scalar wave equation with velocity $c > 0$:

$$\frac{1}{c}\frac{\partial^2 u}{\partial t^2} - \Delta u = 0 \tag{C.1}$$

A family of solutions consisting of plane harmonic waves is of the form:

$$u(x_1, x_2, t) = \exp\left(i(\omega t - k_1 t - k_2 x_2)\right) \tag{C.2}$$

The wave vector $k = (k_1, k_2)$ and the frequency ω satisfying the dispersion relation described in Equation C.3. It defines two frequencies $\omega_+(k)$ and $\omega_-(k)$ for waves traveling in the positive x_2 $(u_+(x,t))$ direction and negative x_2 $(u_-(x,t))$ direction, respectively (Equation C.4).

$$\omega^2 = c^2|k^2| = c^2(k_1^2 + k_2^2) \tag{C.3}$$

$$c\frac{k_2}{\omega_+(k)} = +\left(1 - \left(c\frac{k_1}{\omega_+(k)}\right)^2\right)^{1/2} \tag{C.4}$$

$$c\frac{k_2}{\omega_-(k)} = -\left(1 - \left(c\frac{k_1}{\omega_-(k)}\right)^2\right)^{1/2} \tag{C.5}$$

Solutions $u(x,t)$ may be obtained as the sum of $(u_+(x,t))$ and $(u_-(x,t))$. All solutions with finite energy may be obtained by the superposition of plane waves related to the frequencies $\omega_+(k)$ and $\omega_-(k)$. The ideal dispersion equation would be of the form:

$$c\frac{k_2}{\omega} = +\left(1 - \left(c\frac{k_1}{\omega}\right)^2\right)^{1/2} \tag{C.6}$$

However, Equation C.6 does not correspond to a differential equation. The paraxial approximation proposes an adequate approximation for waves traveling close to the positive x_2 direction:

$$\left|c\frac{k_1}{\omega}\right| = |\sin\theta| \text{ small} \tag{C.7}$$

Applying the Taylor expansion of the term $\left(1 - \left(c\frac{k}{\omega}\right)^2\right)^{1/2}$:

$$\left(1 - \left(c\frac{k_1}{\omega}\right)^2\right)^{1/2} = 1 - c^2\frac{k_1^2}{\omega^2} + O(c^4\frac{k_1^4}{\omega^4}) \tag{C.8}$$

The following dispersion relation is then obtained:

- First-order approximation:

$$c\frac{k_2}{\omega} = 1 \tag{C.9}$$

- Second-order approximation:

$$c\frac{k_2}{\omega} = +\left(1 - \frac{1}{2}c^2\frac{k_1^2}{\omega^2}\right) - \omega^2 + ck_2\omega + \frac{1}{2}c^2k_1^2 \tag{C.10}$$

Leading the the following differential equation:

- First-order approximation:

$$c\frac{\partial u}{\partial x_2} - \frac{\partial u}{\partial t} = 0 \tag{C.11}$$

- Second-order approximation:

$$\frac{\partial^2 u}{\partial t^2} + c\frac{\partial^2 u}{\partial x_2 \partial t} - \frac{1}{2}c^2\frac{\partial^2 u}{\partial x_1^2} = 0 \tag{C.12}$$

The paraxial approximation may be viewed as a parabolic approximation of the wave equation. This approximation is also called 15°-approximation (first-order) or 45°-approximation (second-order). Engquist and Majda (1977) discuss that good boundary conditions should fulfill both the following criteria: locality and to lead to well-posed mixed boundary problem for the wave equation. The first criteria is related to the implementation easiness of the boundary condition. Indeed, although nonlocal conditions lead to perfectly absorbing layers, they are difficult to implement as a point's state is related to all other points on the boundary. The second criteria must always be fulfilled, either by a perfectly or approximated boundary condition. Engquist and Majda (1977) showed that the paraxial approximation satisfies both the above criteria.

C.1.1 Paraxial approximation for heterogeneous media

Bamberger et al. (1988) proposed a further development on the parabolic approximation of the wave equation for heterogeneous media. Consider the scalar wave equation of the form:

$$\frac{1}{c(x)^2}\frac{\partial^2 u}{\partial t^2} - \Delta u = 0 \tag{C.13}$$

In this case the heterogeneity comes from the variation of the wave velocity $c(x)$ along the x direction. The simplest way of tackling the problem is considering that the wave equation is locally homogeneous and the value of c on the parabolic approximation may be directly replaced by the value of $c(x)$. In this case the following equation is obtained:

$$\frac{1}{c(x)^2}\frac{\partial^2 u}{\partial t^2} + \frac{1}{c(x)}\frac{\partial^2 u}{\partial t \partial x_2} - \frac{1}{2}\frac{\partial^2 u}{\partial x_1^2} = 0 \tag{C.14}$$

A second approach using a change of variables on the parabolic equation leads to the following approximation:

$$\frac{1}{c^2}\frac{\partial^2 u}{\partial t^2} + \frac{1}{c^{1/2}}\frac{\partial}{\partial x_2}\left(\frac{1}{c^{1/2}}\frac{\partial u}{\partial t}\right) - \frac{1}{2}\frac{\partial^2 u}{\partial x_1^2} = 0 \tag{C.15}$$

A third approach consists on decomposing the hyperbolic operator $(1/c^2)(\partial^2/\partial t^2) - \Delta$ into a product of two pseudo-differential operators, which is valid in the case of smooth variations of c. In this case the following approximation is obtained for waves traveling in the positive x_2 direction:

$$\frac{1}{c^2}\frac{\partial^2 u}{\partial t^2} + \frac{1}{c^{1/2}}\frac{\partial}{\partial x_2}\left(\frac{1}{c^{1/2}}\frac{\partial u}{\partial t}\right) - \frac{1}{2c}\frac{\partial}{\partial x_1}\left(c\frac{\partial u}{\partial x_1}\right) = 0 \tag{C.16}$$

The three proposed methods may be represented by the following approximation:

$$\frac{1}{c^2}\frac{\partial^2 u}{\partial t^2} + \frac{1}{c\phi(c)}\frac{\partial}{\partial x_2}\left(\phi(c)\frac{\partial u}{\partial t}\right) - \frac{1}{2\psi(c)}\frac{\partial}{\partial x_1}\left(\psi(c)\frac{\partial u}{\partial x_1}\right) = 0 \tag{C.17}$$

where ϕ and ψ are smooth positive functions. When c is constant this equation reduces to the parabolic approximation on homogeneous medium. Functions ϕ and ψ are defined as follows:

- Equation C.14: $\phi(c) = 1$, $\psi(c) = 1$
- Equation C.15: $\phi(c) = c^{1/2}$, $\psi(c) = 1$
- Equation C.16: $\phi(c) = c^{1/2}$, $\psi(c) = c$

However, Bamberger et al. (1988) showed that the above three approximations do not fulfill the following criteria:

1. At null incident angle and normal incidence, the transmission coefficient is equal to the one of the wave equation, up to the second order with respect to $\Delta c/c$.
2. Reflection and transmission coefficients are continuous functions of the incident angle.
3. The Cauchy problem is well-posed for any velocity distribution.

In this case, authors showed that the parabolic Equation C.18 fulfill all the cited criteria and represents a good parabolic approximation of the wave equation on heterogeneous media.

$$\frac{1}{c^2}\frac{\partial^2 u}{\partial t^2} + \frac{1}{c\phi(c)}\frac{\partial}{\partial x_2}\left(\phi(c)\frac{\partial u}{\partial t}\right) - \frac{1}{2\psi(c)\xi(c)}\frac{\partial}{\partial x_1}\left(\psi(c)\frac{\partial}{\partial x_1}(\xi(c)u)\right) = 0 \tag{C.18}$$

They showed that conditions (1) and (2) are satisfied if and only if $\phi(c) = \xi(c) = c^{-1/2}$ and choosing $\psi(c) = c$ then condition (3) is satisfied and the energy-measure stated by Equation C.19 is constant at with respect to time t.

$$E(t) = \frac{1}{2}\int\int \frac{1}{c^2}\left|\frac{\partial u}{\partial t}\right| dx + \frac{1}{4}\int\int c\left|\frac{\partial}{\partial x_1}(c^{-1/2}u)\right|^2 dx \tag{C.19}$$

Using an auxiliary unknown ν the following form is obtained:

$$\nu = c^{-1/2} u \tag{C.20}$$

$$\frac{1}{c}\frac{\partial^2 \nu}{\partial t^2} + \frac{\partial^2 \nu}{\partial t \partial x_2} - \frac{1}{c}\frac{\partial}{\partial x_1}\left(c\frac{\partial \nu}{\partial x_1}\right) = 0 \tag{C.21}$$

C.2 Perfectly Matched Layer

On the context of the electromagnetism, Berenger (1994) introduced the "Perfectly Matched Layer" (PML) to the first order wave equation (speed-displacement equation on the mechanics context). It was called perfectly matched layer as it assure no wave reflection at any incident angle and at any frequency, before equation discretization. Komatitsch and Tromp (2003) presented a mathematical formulation for the second-order wave equation (acceleration-displacement equation), which is more adapted to finite element codes.

C.3 Absorbing elements

The idea of absorbing incoming energy from the system by the boundary can be applied on different type of boundary conditions presenting a damping term.

Lysmer and Kuhlemeyer (1969) proposed an absorbing boundary of the following type:

$$\sigma = a\rho V_p \dot{u}_n \tag{C.22}$$

$$\tau = b\rho V_s \dot{u}_t \tag{C.23}$$

where σ and τ are the normal and shear stress, respectively, $\dot{u}_n$ and $\dot{u}_t$ are the normal and tangential velocities respectively; ρ is the mass density; V_p and V_s are the velocities of S-waves and P-waves in the medium, respectively; and a and b are dimensionless parameters.

In order to verify the ability of the viscous boundary on absorbing incoming elastic waves, they proposed to compare the energy ratio of different a and b values. The energy ratio is defined as the ratio between the energy of the reflected waves over the energy of the incident waves. Its value varies from 0 (full absorption) to 1 (full reflection). The energy transmitted per unit of time through a unit area of the wave front of a P-wave with amplitude A and a S-wave with amplitude B is:

$$W_p = \frac{1}{2}\rho V_p \omega^2 A^2 \tag{C.24}$$

$$W_s = \frac{1}{2}\rho V_s \omega^2 B^2 \tag{C.25}$$

where ω is the wave frequency.

Expressions of the energy ratio have been recently corrected by Kouroussis et al. (2011a) from the original paper of Lysmer and Kuhlemeyer (1969), although the figures showed on the paper are correct. In the case of an incoming P-wave, the energy ratio is given by:

$$\frac{E_r}{E_i} = A^2 + s\frac{\tan\nu}{\tan\theta}B^2 \tag{C.26}$$

where:

$$s^2 = \frac{1-2\mu}{2(1-\mu)} \tag{C.27}$$

$$\cos\nu = s\cos\theta \tag{C.28}$$

θ is the incident angle of the P-wave and ν the reflected angle of the S-wave, both measured from the boundary surface.

The energy ratio depends only on the incident angle θ and the Poisson's ratio μ. Lysmer and Kuhlemeyer (1969) showed that using $a = b = 1$ gives maximum absorption. It presents nearly perfect absorption of incident P-waves with an incident angle higher than 30°. The average product $(E_r/E_i)\sin\theta$ represents the overall ability of the boundary to absorb energy (as the energy at the boundary is proportional to the width of $\sin\theta$).

In the case of an incoming S-wave, the energy ratio may be expressed by:

$$\frac{E_r}{E_i} = B^2 + \frac{\tan\theta}{\tan\nu}A^2 \;\; \nu > \nu_{cr} \tag{C.29}$$

$$\frac{E_r}{E_i} = B_1^2 + B_2^2 \;\; \nu \leq \nu_{cr} \tag{C.30}$$

where ν_{cr} is the critical incident angle defined by $\cos\nu_{cr} = s$ and B_1 and B_2 are the real and complex amplitude of the reflected wave. The meaning of a complex amplitude is that in this case a reflected P-wave do not exist. Instead, a Rayleigh-wave appears traveling along the boundary. Once again using $a = b = 1$ gives maximum absorption.

The same idea of damping on the boundary may be also applied using volume elements presenting visco-elastic mechanical behavior. In this case, the finite medium is composed of an inner medium accounting for all the relevant physical phenomena and materials, and an outer medium where a viscoelastic material is implemented.

C.3.1 Kelvin-Voigt model for boundary damping

The Kelvin-Voigt model is a visco-elastic model commonly used in geomechanics. It consists on an elastic spring of stiffness E connected in parallel to a purely viscous damper of vicosity η. It is used on modeling a solid material with a reversible deformation on long duration, but which may present low deformation on a short duration. The differential equation governing the material behavior is presented in Equation C.31.

$$\sigma(t) = E\varepsilon(t) + \eta\frac{d\varepsilon(t)}{dt} \tag{C.31}$$

Considering suddenly applying a constant stress σ_0 on the material, strain evolves during time following Equation C.32. The rate of relaxation $\lambda = \frac{E}{\eta}$ defines *long* and *short* process according to:

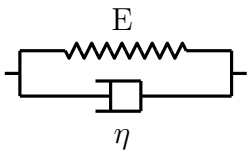

Figure C.1: Kelvin-Voigt mechanical model.

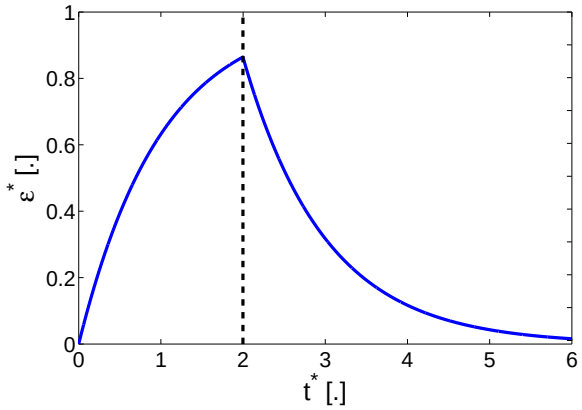

Figure C.2: Loading / unloading cycle for a Kelvin-Voigt material

- $\lambda << 1$: short process, during which the material is almost not deformed.
- $\lambda \approx 1$ midway process, during which the material presents some deformation.
- $\lambda >> 1$: long process, during which the material deformed as elastic material during almost the whole process.

$$\varepsilon(t) = \frac{\sigma_0}{E}\left(1 - e^{-\lambda t}\right) \tag{C.32}$$

Once the applied stress σ_0 vanishes, the material fully recovers its initial state, presenting null deformation. The loading / unloading cycles are fully elastic, although energy is dissipated on the viscous element. In this sense this model is used to represent creep on material behavior. An example is shown in Figure C.2, considering $\lambda = 1$ and the dimensionless time $t^* = \lambda t$ and the dimensionless deformation $\varepsilon^* = E\frac{\varepsilon(t)}{\sigma_0}$.

The dynamic modulus is given by Equation C.33. The imaginary part is directly proportional to the frequency.

$$E^*(\omega) = E + i\eta\omega \tag{C.33}$$

The aptitude of such rheological model to be used as boundary condition in a dynamic model is to be able to dissipate wave incoming energy either by:

- loading/unloading cycles;

- presenting an adapted rate of relaxation λ such that the accumulated energy from the incoming waves is not released in the model during the considered time simulation.

C.4 Infinite elements

The Infinite Element Method consists on approximating the value of the element toward infinity as a reasonable approximation of the physics of the problem (Bettes, 1992). Two main approaches exist:

- Decay function Infinte Elements.
- Mapping Infinite Elements.

The basic idea behind the decay function infinite elements is to multiply the regular finite element shape function by a decaying function. This ensures that the field variable will tend monotonically to its far field value. Consider a parent shape function written as $P_i(\xi, \eta)$ and a decay function $f_i(\xi, \eta)$, where ξ and η are the local coordinates and the subscript denotes the node number. The final shape function is then written as:

$$N_i(\xi, \eta) = P_i(\xi, \eta) f_i(\xi, \eta) \tag{C.34}$$

Two types of decay function are commonly used:

- Exponential: an obvious choice as it decays to zero faster than any polynomial and therefore ensures convergence toward zero in the far field. As an example, the 2D exponential decay function on positive ξ and η directions is given by Equation C.35.

$$f_i(\xi, \eta) = exp\left[\frac{(\xi_i - \eta_i - \xi - \eta)}{L}\right] \tag{C.35}$$

- Reciprocal: in this case the decay is ensured by an inverse function of the form L/r. As an example, the 2D reciprocal decay function on positive ξ and η directions is given by Equation C.36.

$$f_i(\xi) = \left(\frac{\xi_i - \xi_0}{\xi - \xi_0}\right)^l \left(\frac{\eta_i - \eta_0}{\eta - \eta_0}\right)^m \tag{C.36}$$

  ξ_0 and η_0 are the coordinates of an origin point outside the infinite element as to avoid a singularity within the element. l and m are selected bigger than the maximum polynomial degree of the parent shape function $P_i(\xi, \eta)$.

This procedure requires modification on the numerical integration procedures as the integration formula on the infinite element is of the form:

$$\int_0^\infty f(x) exp(-x) dx \tag{C.37}$$

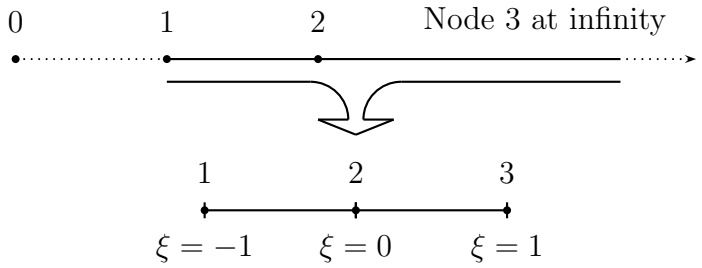

Figure C.3: Infinite Element Mapping (adapted from Kouroussis et al., 2011b).

In the case of mapped infinite elements, the infinite element extends from point x_1 through x_2 to x_3, which is at the infinity. A pole x_0 outside the infinity element is taken as to control the radial behavior. This element is then mapped on the standard finite domain $-1 < \xi < 1$ on 1D direction, as shown in Figure C.3.

Assuming $a = x_2 - x_1 = x_1 - x_0$, a suitable mapping have the form:

$$x = N_0(\xi)x_0 + N_2(\xi)x_2 \tag{C.38}$$

$$N_0(\xi) = \frac{-\xi}{1-\xi} \tag{C.39}$$

$$N_2(\xi) = 1 + \frac{\xi}{1-\xi} \tag{C.40}$$

which gives:

$$x = x_0\frac{2a}{1-\xi} \tag{C.41}$$

$$\xi = 1 - \frac{2a}{x - x_0} \tag{C.42}$$

Using the above obtained mapping, a general polynomial P on the finite χ domain described by Equation C.43 is transformed by the inverse mapping on a new polynomial P' on inverse powers of $r = x - x_0$ (Equation C.44)

$$P = \alpha_0 + \alpha_1\xi + \alpha_2\xi^2 + ... \tag{C.43}$$

$$P' = \beta_0 + \frac{\beta_1}{r} + \frac{\beta_2}{r^2} + ... \tag{C.44}$$

The β coefficients are fully characterized by α_i and a. $\beta_0 = 0$ as in the infinity $P' = 0$. The main advantage of such procedure is that the original numerical integration procedure is maintained. The only change needed on standard Finite Element routines is on obtaining the Jacobian matrix. This approach is implemented in some standard finite element codes and is used when dealing with dynamic problems. For instance, Kouroussis et al. (2011c) successfully used this approach in numerical calculations of track vibrations.

Appendix D

Theoretical background on random field theory

Many physical process exhibits complex patterns of variation on both space and/or time. These may be characterized by random fields in order to complete describe the patterns of a complex random phenomena on which space and/or time are also important. According to Vanmarcke (1983), random field theory may be successfully applied on domains such as:

- Efficient stochastic characterization;
- Prediction of the stochastic response;
- Assessment of the impact of alternative strategies on decision making situations.

Following the definition given by Sudret (2007), a scalar random field $U(u, x)$ is a collection of random variables indexed by a continuous parameter $x \in B$, where B is an open set of $\mathbb{R}^m$ describing the geometry of the system. In this case, each point $x_0 \in B$, $U(u, x_0)$ defines a random variable and $U(u_0, x)$ describes a realization u_0 of the field. A vector-valued random field is defined when each point x defines a random vector. In this case a vector valued random field is characterized by its infinite set of marginal distributions:

$$p(u, x) = p(u_1, ..., u_m; x_1, ..., x_m) \tag{D.1}$$

In the following the simplified notation $U(u, x) = U(x)$ will be used for sake of simplicity. The mean, correlation and covariance are obtained as follows:

$$\bar{u}(x) = E[U(x)] = \int up(u; x)du \tag{D.2}$$

$$R_U(x, x') = R(x, x') = E[U(x) \otimes U(x')] = \int u \otimes u' p(u, u'; x, x')dudu' \tag{D.3}$$

$$C_U(x, x') = C(x, x') = E[(U(x) - \bar{u}(x)) \otimes (U(x') - \bar{u}(x'))] \tag{D.4}$$

$$= \int (u - \bar{u}(x)) \otimes (u' - \bar{u'}(x))p(u, u'; x, x')dudu' \tag{D.5}$$

Some hypothesis and definitions in the random field theory are commonly used when modeling random fields on physical parameters:

- Second-order: random fields with finite energy. This is a broadly used assumption when physical quantities are of interest. This implies on the definition of a second-order random field as having a finite mean energy (either local and instantaneous mean energy) for all points x at all time instants t. Additional constraints are required in order to impose finite total energy.

- Homogeneity, invariance or stationarity: all marginal distributions are invariant when translating the parametric space. The invariance terminology is used mainly on random mediums and the stationarity terminology for random process. In this case, the following conditions hold:

$$E[U(x)] = \bar{u}(x) = u_0 \tag{D.6}$$
$$E[U(x)U(x')] = R(x, x') = R_0(x - x') \tag{D.7}$$

  In this case the mean $\bar{u}(x)$ is constant over the space dimension and the correlation $R(x, x')$ depends only on the distance between two points. A homogeneous field is always indexed on infinite bounds.

- Gaussian random fields: all marginal distributions are Gaussian distributions given by Equation D.8. The field is then fully characterized only by the deterministic function $u(x)$ and a covariance function $C_U(x, x')$.

$$p(u_1, ..., u_m; x_1, ..., x_m) = \frac{\exp\left((u - \bar{u})^T C^{-1}(u - \bar{u})/2\right)}{\sqrt{2\pi}^n \sqrt{\det C}} \tag{D.8}$$

  Non-Gaussian fields may be defined as linear or nonlinear translations of Gaussian fields (Grigoriu, 1984; Liu and Der Kiureghian, 1986).

The simplest purely random field would have independent values taken from identically distributed random variables. In this case it is fully characterized by its first marginal probability density function D.9. This means that the location where observations are made are independent from each other and does not influence probability assessments about nearby values. For random process, it would mean that values of the given process $X(t)$ at each t are independent and identically distributed. Techniques from classical statistics consider that samples are independent and identically distributed. If they are considered to be sampled from a random field, it means that it is unnecessary to retain information about where observations where made on the parametric space.

$$p(u, x) = p(u_1, x_1)p(u_2, x_2), ..., p(u_m, x_m) \tag{D.9}$$

Random process with independent increments considers the accumulation of observations of independent random process. A specific class of random process with independent increments is called Markov process. They are characterized by limited memory: their future state is independent from their past state, given the present state. A Markov

chain is defined as being the discrete-state, discrete-parameter Markov process. At time t, $t = 0, 1, 2, ...$ and a set of discrete states $i = 1, 2, 3, ...$, we define a probability distribution of being at state i at a time t as being:

$$p_i(t) = P[X(t) = i] \tag{D.10}$$

The transitional probability from state i at time t to state j at time $t + \tau$ is:

$$q_{ij}^{(t)}(\tau) = P[X(t + \tau) = j | X(t) = i] \tag{D.11}$$

As a consequence of the Markovian property, the state at time $t + \tau$ may be fully expressed by the probability distribution at time t and the transitional probability distribution:

$$p_j(t + \tau) = \sum_i p_i(t) q_{ij}^{(t)}(\tau) \tag{D.12}$$

For homogeneous Markov chain, all transitional probabilities do not depend on t and the one step ($\tau = 1$) transition probability may be denoted only by q_{ij}. In this case, any transition probability may be obtained by a recursive formulation as:

$$q_{ij}(\tau) = \sum_k q_{ik}(\tau - 1) q_{kj} \tag{D.13}$$

In diffusion theory, the simplest Brownian movement of particles is modeled by a Markov chain often called "random walk". In this case, the marginal probability distribution p_i is a Gaussian distribution with zero mean and a given variance.

As presented by Vanmarcke (1983), the Markovian property does not arise as naturally on the context of random fields as in the context of random process. This is mainly because there are no obvious directionality on spatial coordinates as on time coordinate. There is an obvious past, present and future states for the time coordinate and the independence of the future state from the past given the present is completely defined. However, on the context of spatial coordinates such concepts are not entirely natural. Therefore, other approaches are preferred when dealing with random fields, which will be briefly discussed in the next section.

D.1 Random fields generation and discretization

Generating random fields may be based on different methods, depending on the considered hypothesis and the available information. Second-order invariant fields (stationary processes) are usually obtained from linear or nonlinear transformations of a Gaussian random field. Noninvariant fields (or nonstationary processes) may also be obtained from Gaussian fields, in cases such that it can be decomposed as the sum of a invariant field and a deterministic function. This is the case of many applications where the mean value may vary but the correlation structure is the same at all points. In the general case of noninvariant fields, the Karhunen-Loève Expansion (KLE) is usually deployed as a general method.

Obtaining invariant fields may depend upon the representation given for the field. All generating methods are based on the decomposition of the correlation structure. Three main classes of methods are commonly used in the literature in order to apply random fields on practical numerical applications: point discretization, shape function and series expansion methods. Point discretization methods are among the most direct and easy methods to be used with a nonintrusive approach (Popescu et al., 2005b; Lopez-Caballero and Modaressi-Farahmand-Razavi, 2010a, among others). In the context of finite element modeling, very often the numerical codes allow to give a certain value of the constitutive parameters at each cell mesh, which is a direct transposition of the obtained values of the random field by a point discretization method. However, one important drawback is that this family of methods lead to discontinuities at element boundaries. Shape function methods have the advantage of ensuring a continuous description of the field over the elements, but the shape functions must be coded in the finite element code. Average discretization methods are based on weighted integrals of the random field, for which a better fit is expected due to the averaging process (Huyse and Walters, 2001). Series expansion methods are probably the most complete representation of random fields, as both invariant and noninvariant fields can be equally represented. The Karhunen-Loève Expansion is an example of this category and it is briefly further described in Section D.1.3.

In this work, the midpoint method was chosen over the other methods because: (i) it is a nonintrusive approach and (ii) the random field is considered invariant and both the probability density function and the correlation structure are known and described by parametric functions.

D.1.1 Variance decomposition method

The variance decomposition method is a simple method to generate random fields based on a point discretization method. It consists on the following steps:

- Obtaining the autocorrelation matrix $[R]$ from a considered autocorrelation structure of the random field of dimension m. This matrix gives the correlation coefficient ρ_{ij} between the random variables X_i and X_j for any two locations z_i and z_j. It is represented on Equation D.14.

$$[R] = \begin{pmatrix} 1 & \rho_{12} & \cdots & \rho_{1m} \\ \rho_{21} & 1 & \cdots & \rho_{2m} \\ \vdots & \vdots & \ddots & \vdots \\ \rho_{m1} & \rho_{m2} & \cdots & 1 \end{pmatrix} \tag{D.14}$$

- Calculating the eigenvalues and eigenvectors of the autocorrelation matrix $[R]$. The eigenvectors are a independent uncorrelated basis (by construction) on which the autocorrelation matrix is decomposed. The eigenvalues represent the variance of each component of this base.

- Obtaining N realizations of a standard Gaussian random field of dimension m by multiplying N x m independent standard normal random variables $[G]$ by the matrix $[\Lambda]$ of the square root of the eigenvalues and by the matrix $[B]$ of m independent eigenvectors of the autocorrelation matrix $[R]$, which is summarized in Equation D.15.

$$[P] = [B] \cdot [\Lambda] \cdot [G] \tag{D.15}$$

A non-Gaussian random field $f_B(x)$ may be obtained from a Gaussian random field $f_P(x)$ by the *inverse cdf method* (Grigoriu, 1984), Equation D.16.

$$f_B(x) = F_B^{-1}\{F_G[f_P(x)]\} \tag{D.16}$$

where F_G and F_B are respectively the Gaussian cdf and the non-Gaussian cdf. This method relies on being capable of obtaining the non-Gaussian cdf, which may not always be the case (specially when dealing with *in situ* data).

Some of the common autocorrelation functions used in the literature and presented by Huyse and Walters (2001) are shown in Table D.1, where θ is the autocorrelation length and $\tau = x_i - x_j$. Vanmarcke (1983) proposed the use of a scale of fluctuation (l_c) rather than the correlation length (θ) as to compare two correlation functions. It is defined by the expression given in Equation D.17. Therefore, Table D.1 compares the values of θ and l_c for different autocorrelation functions.

$$l_c = \int_{-\infty}^{\infty} R(x, x')dx \tag{D.17}$$

Correlation model	Autocorrelation function $\rho(\tau)$ [.]	Scale of fluctuation l_c [m]
Exponential	$\rho(\tau) = \exp\left(-2\frac{\lvert\tau\rvert}{\theta}\right)$	l_c=θ
Squared exponential	$\rho(\tau) = \exp\left(-\pi\frac{\tau^2}{\theta^2}\right)$	l_c=θ
Triangular	$\rho(\tau) = 1 - \frac{\lvert\tau\rvert}{\theta}$ if $\tau \leq \theta$, 0 otherwise	l_c=2θ
Cubic	$\rho(\tau) = \frac{\theta^3}{(\theta+\lvert\tau\rvert)^3}$	l_c=$\frac{2\theta}{5}$
Damped sinusoidal	$\rho(\tau) = \frac{\sin\left(\pi\frac{\lvert\tau\rvert}{\theta}\right)}{\pi\frac{\lvert\tau\rvert}{\theta}}$	l_c=θ

Table D.1: Theoretical autocorrelation functions used in the literature.

For a multidimensional random field, the following correlation structures are commonly considered:

- Isotropic: the covariance function depends only in the euclidean distance between two points.

$$\tau = |\tau| = |x - x'| = \sqrt{(\tau_1^2 + ... + \tau_m^2)} \tag{D.18}$$

$$R(\tau) = R(\tau_1, ..., \tau_m) = R(\tau_1, 0, ..., 0) = R^R(\tau) \tag{D.19}$$

  $R^R(\tau)$ is called the radial covariance function and suffices to describe the random variance on any direction from a given point.

- Ellipsoidal: the random field is obtained by scaling and isotropic random field.

$$\tau = \sqrt{\left(\frac{\tau_1}{a_1}\right)^2 + ... + \left(\frac{\tau_m}{a_m}\right)^2} \tag{D.20}$$

- Separable: in this case the correlation structure may be decomposed on unidimensional correlation functions.

$$R(\tau_1, ..., \tau_m) = \sigma^2 \rho_1(\tau_1)...\rho_m(\tau_m) \tag{D.21}$$

  Partially separable random fields are considered when the autocorrelation structure can be expressed as a product of lower dimension correlation structures.

One important drawback from the variance decomposition method is the need of sampling a high number of standard normal random variables. Indeed, the autocorrelation matrix ($[R]$) increases in size with increasing length of the random field thus, increasing the size of $[G]$ and the probabilistic dimension of the problem. In turn, obtaining the requested correlation structure becomes difficult. In the following, the Proper Orthogonalization Decomposition (POD) is presented as a way to reduce the probabilistic dimension by obtaining a compact representation of the autocorrelation matrix ($[R]$).

D.1.2 The Proper Orthogonalization Decomposition (POD)

The main idea behind the Proper Orthogonalization Decomposition (POD) is to retain the maximum available information of the covariance between variables while reducing their number to a much smaller number of uncorrelated variables. The orthogonal basis of the correspondent eigenvectors of the covariance matrix is obtained and then the data are projected in the subspace spanned by the eigenvectors corresponding to the largest eigenvalues. The eigenvalues in this case have the following property:

$$\sum_{i=1}^{m} \lambda_i = 1 \tag{D.22}$$

One important property of this decomposition is that it minimizes the mean-square error. In the case when only a few terms are considered, it is equivalent to the principal component analysis (PCA).

Using the formalism of the variance decomposition method presented above, the POD method leads to a reduced order autocorrelation matrix $[R_d]$ by keeping only the largest eigenvalues and the corresponding eigenvectors. In this case, Equation D.15 may be rewritten as:

$$[P] = [B_d] \cdot [\Lambda_d] \cdot [G_d] \tag{D.23}$$

where $[B_d]$ is the reduced eigenvector basis, $[\Lambda_d]$ the matrix of square root of the largest eigenvalues of matrix $[R]$ and $[G_d]$ are d x N independent random variables, $d < m$ and possibly $d << m$.

Given an admissible error e_{adm} in the energy description given by the eigenvalue distribution by Equation D.24, the value of d depends on the relation between the length of the field L and the correlation length θ for a given autocorrelation function, which defines the autocorrelation structure of the field. Obtaining long weakly correlated fields demands higher values of d, the limiting case being an equal representativeness of each eigenvalue, i.e. every two considered points are uncorrelated.

Results in this sense for the exponential correlation model are presented in Figure D.1a for different cases of θ/L. Figure D.1b presents the evolution of d for different considered e_{adm} values. Increasing e_{adm} reduces the necessary number of uncorrelated variables d for the same θ/L as a consequence of losing information of the autocorrelation structure of the field. Evidently, the higher the admissible error e_{adm}, the more information is lost during the dimension reduction and the simulated field will poorly represent the theoretical field.

From the proposed functions in Table D.1, the squared exponential is the one presenting the fastest dimension reduction for a given error e_{adm}. A comprehensive comparison of each correlation function is shown in Figure D.2. In this thesis, the squared exponential autocorrelation function is chosen and the value of e_{adm}=0.1% is always considered when the Proper Orthogonalization Decomposition is used (Section 4.5.3).

$$e_{adm} = 1 - \sum_{i=1}^{d} \lambda_i \tag{D.24}$$

In the following section the main features of the Karhunen-Loève Expansion (KLE) are presented. Although this method was not directly used in this thesis, the equivalence between the Proper Orthogonalization Decomposition and the Karhunen-Loève expansion is discussed by Liang et al. (2002),Wu et al. (2003) and Kerschen et al. (2005).

D.1.3 The Karhunen-Loève Expansion (KLE)

The Karhunen-Loève Expansion consists of characterizing a random process or random field in terms of deterministic orthogonal functions, provided that the second order moment is available. It may be expressed as follows:

$$U(x) = \bar{u}(x) + \sum_{i=1}^{\infty} \sqrt{\lambda_i} \xi_i(u) \phi_k(x) \tag{D.25}$$

where:

- $\bar{u}(x)$: mean of the random process;

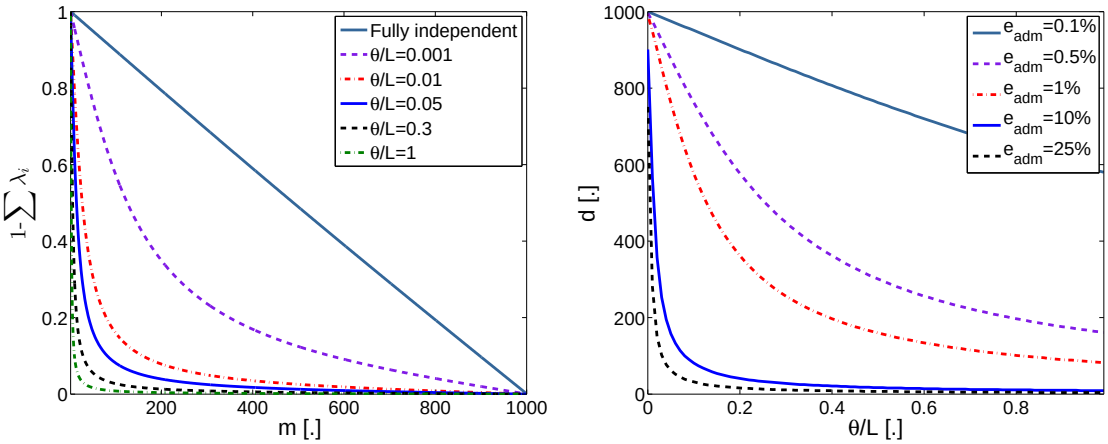

(a) (b)

Figure D.1: Dimension reduction properties in the case of exponential autocorrelation function. a) Evolution of the eigenvalues; b) Value of d for a given error e_{adm}.

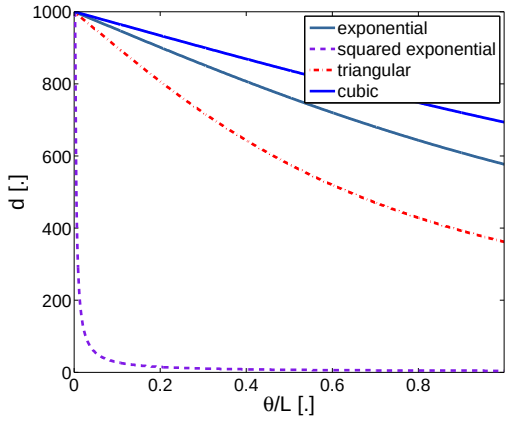

Figure D.2: Comparison of d for different autocorrelation functions for e_{adm}=0.1%.

- $\xi_i(u)$: set of centered unitary and uncorrelated random variables;
- λ_i,$\phi_i(x)$: eigenvalues and eigenfunctions of the covariance operator $C(x, x')$.

The eigenfunctions $\phi_i(u)$ are obtained from the spectral decomposition of the covariance operator, which is mathematically represented by a homogeneous Fredholm integral equation of the second kind:

$$\int_B C(x, x')\phi_i(x')dx' = \lambda_i\phi_i(x) \tag{D.26}$$

The covariance operator is bounded, symmetric and positive definite in the case of random fields with finite total mean energy. Thus, the set of eigenfunctions $\phi_i(x)$ forms a complete orthogonal basis. The spectrum (or eigenvalues) are real, positive and numerable.

$$C_U(x, x') = \sum_{i=1}^{\infty} \lambda_i \phi_i(x) \otimes \phi_i(x') \tag{D.27}$$

This series expansion presents the following interesting properties:

- Eigenvalues are energy decreasing, which motivates the truncation of the series after M-th terms:

$$U(x) = \bar{u}(x) + \sum_{i=1}^{M} \sqrt{\lambda_i} \xi_i(u) \phi_k(x) \tag{D.28}$$

  with an error given by:

$$E[||U - U_M||^2] = \epsilon_M^2 = \sum_{i=M}^{\infty} \lambda_i \; M \overset{\rightarrow}{\rightarrow} \infty \; 0 \tag{D.29}$$

- The covariance eigenfunction basis $\phi_i(x)$ is an optimal basis in the sense of minimizing the mean-square error resulting from the truncation. The error variance is positive and it means that the Karhunen-Loève expansion always under represents the true variance of the field.

Closed form solutions of the Fredholm equation of second kind (Equation D.26) exists for a few covariance functions on certain domains B (Ghanem and Spanos, 1991). Numerical methods may be applied on the general case, such as Galerkin, collocation or Rayleigh-Ritz approximations. Presenting these strategies is outside the scope of this thesis.

D.2 Sampling methods

Many different sampling strategies are used in the literature in order to fully cover the probability density function of a given random variable. The simplest and best-known sampling method is the Monte Carlo Sampling (MCS) method, which consists in generating a large number of random and equally probable samples. Its main drawback is presenting a slow rate of convergence of $O(N^{-1/2})$ (N being the size of the sample). Nonetheless, it has solid mathematical support from the Law of Large Numbers. Different refinements of the MCS method exist, such as importance sampling and Latin Hypercube sampling (LHS). Other methods based on quasi-random numbers also exists and are called quasi-Monte Carlo methods. LHS method and Quasi-Monte Carlo methods will be further developed as an alternative to the standard MCS as to ensure better convergence with lower number of samples.

D.2.1 Monte Carlo Sampling methods (MCS)

Monte Carlo Sampling methods are based on the probabilistic interpretation of an integral (Caflisch, 1998). Indeed, consider the integral over the unitary hypercube I^p,$[0, 1]^p$ of an integrable function f:

$$I[f] = \int_{I^p} f(x)dx \tag{D.30}$$

If x is a random uniformly distributed variable then $I[f] = E[f(x)]$. The empirical approximation of the expectation $E[f(x)]$ is:

$$I_N[f] = \frac{1}{N}\sum_{i=1}^{N} f(x_i) \tag{D.31}$$

Equation D.31 converges to $I[f]$ with probability one according to the Law of Large Numbers. The Monte Carlo integration error is defined as:

$$\epsilon_N[f] = I[f] - I_N[f] \tag{D.32}$$

The bias is defined as $E[\epsilon_N[f]]$ and the root mean square error (RMSE) as $E[\epsilon[f]^2]^{1/2}$ (Caflisch, 1998).

The Central Limit Theorem is useful on establishing the size N and error properties of Monte Carlo integration. To ensure an error ϵ with confidence level c the number of samples N is given by Equation D.33.

$$N = \epsilon^{-2}\sigma^2 s(c) \tag{D.33}$$

σ is the square root of the variance of f and s is the confidence function for normal variable. In order to obtain an approximation of σ (as usually one does not know a priori its value), Hogg and Craig (1995) presented the following method:

1. Performing M computations using x_i independent points, $1 \leq i \leq MN$
2. Obtaining $I_N^{(j)}$ values for $1 \leq j \leq M$. The empirical RMSE is:

$$\tilde{\epsilon_N} = \left(M^{-1} \sum_{j=1}^{M} \left(I_N^{(j)} - \bar{I}_N \right)^2 \right)^{1/2} \tag{D.34}$$

in which:

$$I_N^{(j)} = \frac{1}{N}\sum_{i=1}^{N} f(x_i) \tag{D.35}$$

$$\bar{I}_N = \frac{1}{M}\sum_{j=1}^{M} I_N^{(j)} \tag{D.36}$$

3. The empirical variance is given by Equation D.37. This value may be used on Equation D.33 in order to obtain the number of samples N.

$$\tilde{\sigma} = N^{1/2}\tilde{\epsilon}_N \tag{D.37}$$

D.2.2 Quasi-Monte Carlo methods

Quasi-Monte Carlo methods own their name to the use of quasi-random numbers, instead of random (mathematically) or pseudo-random (numerically) numbers. While pseudo-random sequences try to randomly cover the space, quasi-random sequences are deterministically designed as to provide better uniformity of the number sequence (Sobol, 1998). Such sequences are also called *low discrepancy sequences*, as they minimize the discrepancy measure. It is defined as the measure of the deviation of a sequence's distribution from the ideal uniform distribution Niederreiter (1978). It is commonly used to compare the effectiveness of a certain sampling method to reproduce the uniform distribution. Consider a sequence of N points x_n in the unitary cube I^d and define:

$$R_N(J) = \frac{1}{N}\#\left(x_n \in J\right) - m(J) \tag{D.38}$$

for any subset J of I^d. The discrepancy is defined (Caflisch, 1998) either as the L^∞ norm or the L^2 norm applied to $R_N(J)$:

$$D_N = sup_{J\in E}|R_N(J)| \tag{D.39}$$

$$T_N = \left[\int_{(x,y)\in I^{2d}, x_i<y_i} R_N(J(x,y))^2 dxdy\right] \tag{D.40}$$

Such series are very interesting as they lead to smaller error than standard Monte-Carlo method (Caflisch, 1998). They have a convergence rate of $O((\log N)^k N^{-1})$, while Monte Carlo method has a much slower convergence rate of $O(N^{-1/2})$. Exemples of such sequences are Halton sequences (Halton, 1960), Sobol's sequences (Sobol, 1967), Faure sequence (Faure, 1982), Niederreiter sequence (Niederreiter, 1978). The discrepancy L^∞ norm of all these sequences are bounded by

$$D_N \leq c_d(\log N)^d N^{-1} \tag{D.41}$$

where c_d is a constant depending on the dimension of the problem and the type of sequence. The average discrepancy L^2 norm is:

$$E\left[T_N^2\right]^{1/2} = c_d N^{-1/2} \tag{D.42}$$

However, some important limitations exist when using such sequences instead of Monte Carlo. These are:

- There are no theoretical bases for empirical estimates of accuracy of quasi-Monte Carlo methods (Caflisch, 1998) as the Central Limit Theorem for Monte Carlo methods.

- They are designed for integration rather than simulation (as points in a quasi random sequence are inevitable correlated). However, this may be reduced when one is looking for the expectation of some quantity, which may be written as an integral.

- Quasi-Monte-Carlo effectiveness is lost when dealing with high-dimensional problems. Equation D.41 is controlled by the $(\log N)^d$ term unless $N > 2^d$, which grows rapidly with increasing d.

- Quasi-Monte-Carlo effectiveness is also lost when dealing with nonsmooth integrands (highly nonlinear problems). (Caflisch, 1998) defines as being *smooth enough* something between continuity and differentiability.

D.2.3 Latin Hypercube Sampling method (LHS)

Following Helton et al. (2006), in order to generate a sample of size N from the distributions U_1,U_2,$\cdots$,U_m associated with the elements of $U(x) = [x_1, x_2, \cdots, x_m]$, the cumulative distribution function of each x_i is first divided into N disjoint intervals of equal probability. Then one value x_{ij} is selected randomly from each interval for the first random variable. The values obtained are randomly combined in order to produce another N pairs for the second random variable, and this process continues until a set of N m-tuples $x_i = [x_{i1}, x_{i2}, ..., x_{im}], i = 1, 2, \cdots, N$ is obtained.

In order to select randomly a value for each interval, the sampled cumulative probability can be written as (Wyss and Jorgensen, 1998):

$$Prob_i = \left(\frac{1}{N}\right) r_u + \frac{(i-1)}{N} \tag{D.43}$$

where r_u is uniformly distributed random number ranging from 0 to 1.

In order to better illustrate the procedure, an example is given for two input parameters, x_1 and x_2. Figure D.3 presents a table where dots are the sampling values obtained from the respective probability density function (pdf) of variables x_1 and x_2, which probability density functions's are presented in Figure D.4. This sampling method allows a full coverage of each pdf. However, as it is based in the Monte Carlo Sampling method, its convergence rate is of $O(N^{-1/2})$.

D.2.4 Correlation control technique

Correlation control is an important issue on sampling methods as variables should follow closely a specified correlation structure. If they are independent, the correlation matrix should be close to the identity. However, some authors using LHS mention that this technique may induce an unwanted correlation, even if the probability density function of parameters is well represented (Oscarsson, 2002; Helton et al., 2006). Iman and Conover (1982) developed a procedure in order to impose rank correlation on sample variables. This procedure is based on the Cholesky decomposition of the target correlation matrix and is widely used as it has the following advantages:

- It is independent from the assumed marginal distributions;

- It preserves the intervals from the Latin Hypercube Sampling and is also applicable for simple random sampling;

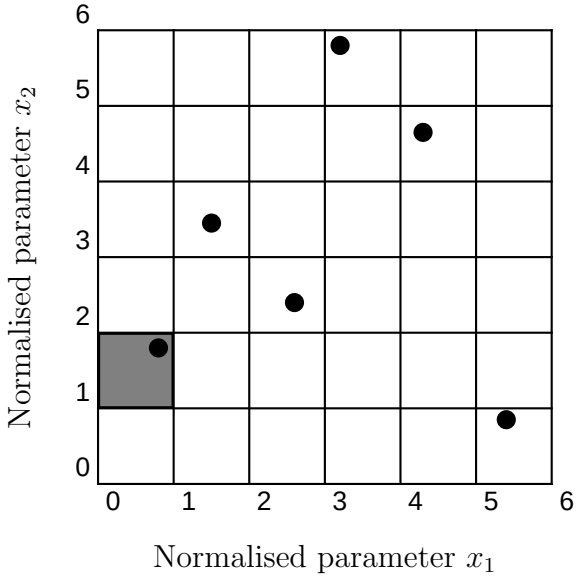

Figure D.3: Latin Hypercube with two parameters, x_1 and x_2 and six samples (adapted from Oscarsson, 2002).

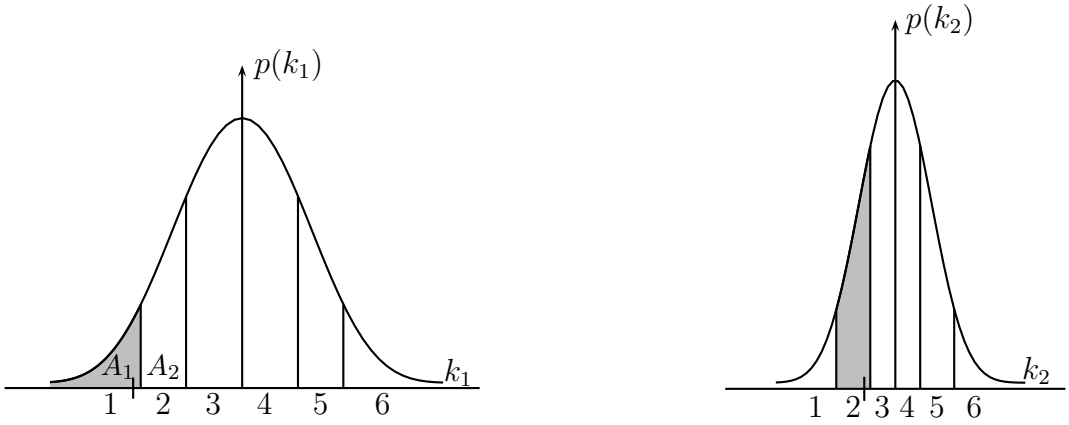

Figure D.4: Example of input to the first sample according to the scheme shown in Figure D.3 (adapted from Oscarsson, 2002).

- It can impose complex correlation structures among variables.

Figure D.5 shows an example of unwanted correlation between two variables induced by sampling and the final configuration after using the correlation control, in the case where the two variables should be independent.

The Cholesky decomposition of the positive definite symmetric matrix $[R]$ is unique and may be written as follows:

$$[R] = [P] \cdot [P]' \tag{D.44}$$

$[P]$ is the lower triangular matrix with strictly positive diagonal entries and $[P]'$ is its conjugate transpose.

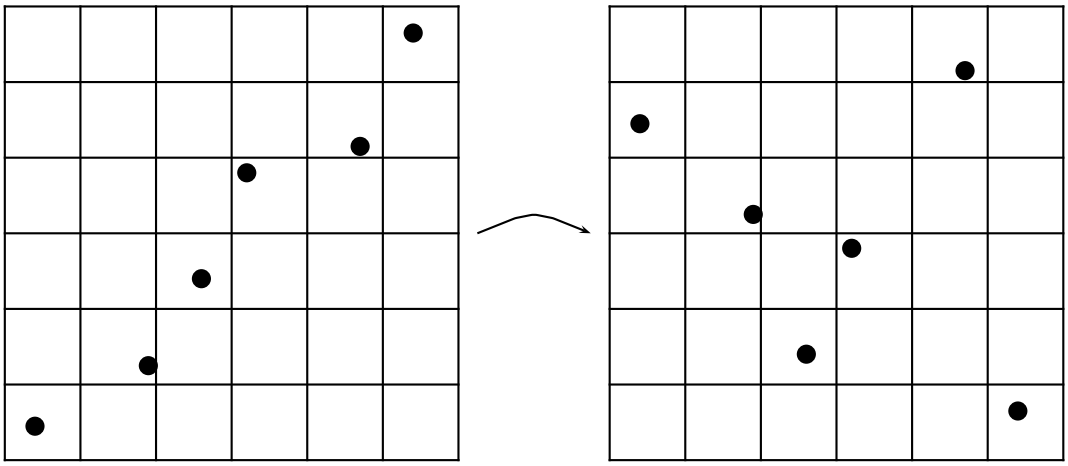

Figure D.5: Example of the induced correlation that may arise from the LHS method and the obtained sample after correlation reduction (Oscarsson, 2002).

The method is developed as follows: first, a sample matrix $[U]$ is generated either by MCS or LHS method. Then, the correlation matrix $[T]$ of the sample matrix $[U]$ is calculated. The Cholesky factorization of the target correlation matrix $[R]$ and of the actual correlation matrix $[T]$ are then calculated and matrix $[P]$ and $[Q]$ are obtained.

$$[R] = [P] \cdot [P]' \tag{D.45}$$
$$[T] = [Q] \cdot [Q]' \tag{D.46}$$

A matrix $[S]$ should then be found such that

$$[S][T][S]' = [R] \tag{D.47}$$

Replacing Equations D.46 and D.45 on Equation D.47 gives:

$$[S][Q][Q]'[S]' = [P][P'] \tag{D.48}$$

One solution of the above system is of the form:

$$[S][Q] = [P] \tag{D.49}$$
$$[S] = [P][Q]^{-1} \tag{D.50}$$

The target matrix $[U]^*$ can be obtained as:

$$[U]^* = [U][S]' \tag{D.51}$$

The last step is to rearrange the values of $[U]$ as that they have the same rank of the target matrix $[U]^*$.

The correlation control technique presents the main advantage of ensuring a very good description of the prescribed correlation structure. However, it imposes the condition on

the number of samples to be greater or at least equal to the probabilistic dimension of the problem m, i.e. dimension of the correlation matrix $[R]$ defined by the correlation structure, as a consequence of the Cholesky decomposition. Although presented as a necessary step on the Latin Hypercube Sampling, this technique can be used also on Monte Carlo Sampling in order to ensure a better description of the autocorrelation structure.

When dealing with time consuming numerical models, it is then necessary to find a compromise between the required number of samples in order to carry out significant statistical studies and the probabilistic dimension of the problem. As discussed in Section D.1.2, the Proper Orthogonalization Decomposition can help on reducing the probabilistic dimension and allowing the use of the correlation control technique presented above.

D.2.5 Comparison of different sampling methods

Bhavsar et al. (1987) presented a numerical procedure in order to evaluate the discrepancy of pseudo-random sequences based on the definition given by Niederreiter (1978) and presented in Section D.2.2. Using this procedure the discrepancy of Sobol sequence, Halton sequence and Latin Hypercube Sampling are compared to standard pseudo-random sampling strategy used on Monte Carlo simulations. Results are presented in Figure D.6. Clearly, low-discrepancy sequences used on quasi-Monte Carlo methods presents very low levels compared to Monte Carlo. However, Latin Hypercube Sampling gives even better results than such sequences, specially with increasing number of samples.

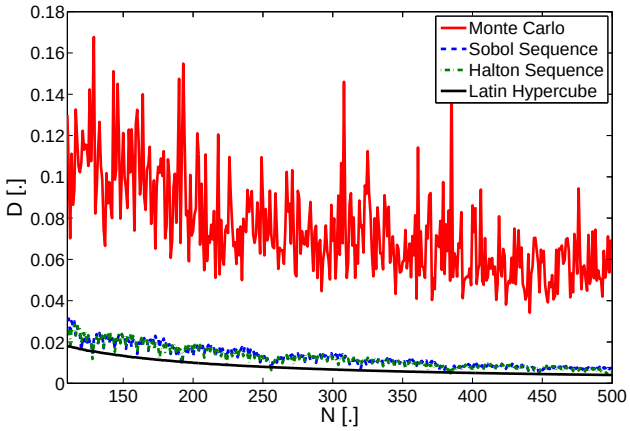

Figure D.6: Discrepancy measure evolution of different sampling strategies.

However, as previously discussed, quasi-Monte Carlo sequences present some important drawbacks with increasing dimensionality. Consider a set of 100 independent uniform random variables. 1000 samples are generated using the the above four different sampling strategies, Monte Carlo, Latin Hypercube, Sobol sequence and Halton sequence. The covariance matrix $[C]$ of the output field is expected to be the identity matrix $[I]$, or at least a good approximation of it, i.e. $c_{ij} \approx 0, i \neq j$. The covariance matrix of the samples obtained by each method are presented in Figure D.7. The Halton sequence presents high values of c_{ij} with increasing dimensionality, spreading more and more over values distant from the main diagonal. The Sobol sequence also presents points for which $c_{ij} \approx 1$. Both Monte Carlo and Latin Hypercube Sampling do not present such drawback.

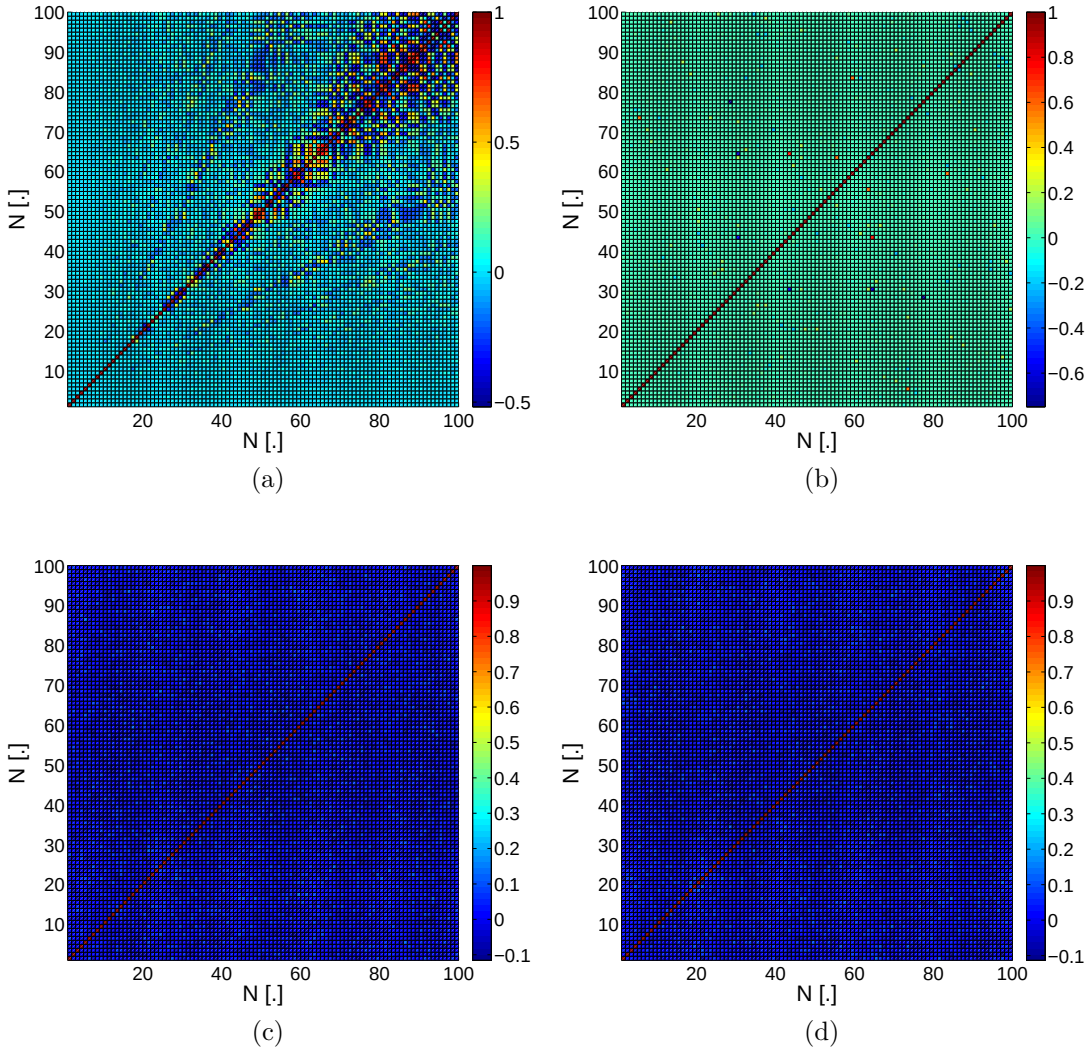

Figure D.7: Covariance matrix $[C]$ for the different considered samples. a) Halton sequence; b) Sobol sequence; c) Monte Carlo Sampling; d) Latin Hypercube Sampling.

The representation of the sampling points in the 2-dimensional space spanned by dimensions i, j, $max(c_{ij}), i \neq j$ is showed in Figure D.8. It can be seen that the quasi-Monte Carlo sequences lead to clustering of the sampling points around some regions in the unitary cube I^p and poor integration results can be expected. Monte Carlo and Latin Hypercube Sampling do not presented such clustering issues in the performed simulations thus, these methods are better fitted as sampling strategies when dealing with weakly correlated random fields.

The high-dimensionality issued of quasi-random sequences is argued by Sobol (1998) as being a problem in the case where all variables are equally important. According to the author, the discrepancy D_N would not be a good measure of irregularity of a distribution, as it is symmetric in all variables. According to Sobol (1998), other type of measures for high-dimensional nets in this case should be set-up.

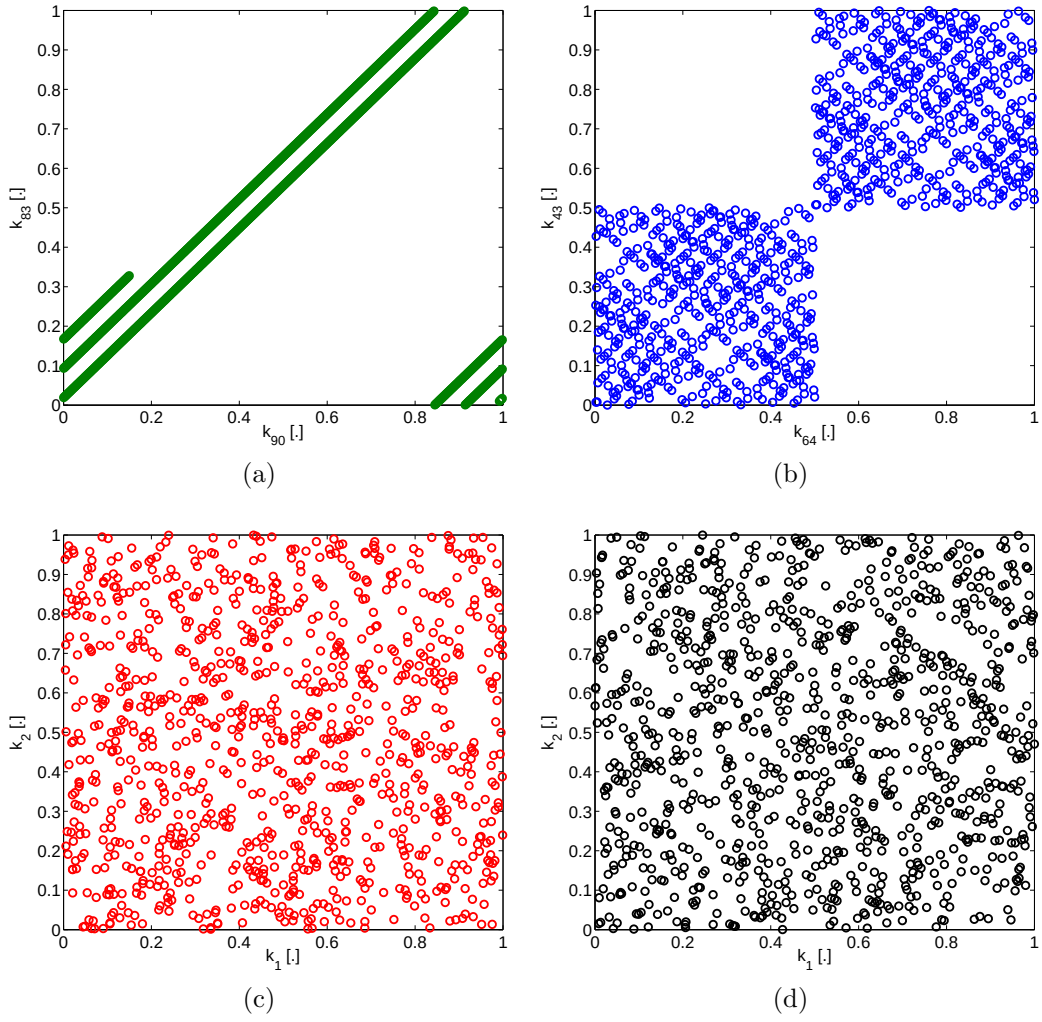

Figure D.8: Sampling points of two different dimensions. a) Halton sequence; b) Sobol sequence; c) Monte Carlo Sampling; d) Latin Hypercube Sampling.

Appendix E

Global Sensitivity Analysis and FAST method

Sensitivity analysis may be divided into two main classes: Local and Global Analysis. Local analysis (also called parametric analysis), consists on verifying the output response when each input parameter is changed separately. In this case, local derivatives may be studied and performance analysis over a nominal point be conducted. On the other hand, Global Analysis captures the impact of the input's variability on the output response. For this goal, all parameters are varied at the same time in other to fully (at a certain degree) cover the parametric space.

Analysis of Variance (ANOVA) methods are a family of Global Sensitivity Analysis methods based on the decomposition of variance proposed by Sobol (1967). The derivation of Sobol Indices or global sensitivity indices is presented in the following section. The Fourier Amplitude Sensitivity Text (FAST) is then presented as an interesting way of obtaining the first-order sensitivity indices.

E.1 Sobol Indices

Consider the model:

$$y = f(x_1, x_2, ..., x_p) \tag{E.1}$$

where $x_1, x_2, ..., x_p$ are independents real random variables belonging to an unitary hypercube I^p, $[0,1]^p$, and Y is an output random variable from the model described by f. Sobol (1967) showed that if f is integrable over I^p, f has a unique decomposition:

$$f(x_1, x_2, ..., x_p) = f_0 + \sum_{i=1}^{p} f_i(x_i) + \sum_{1 \leq i \leq j \leq p} f_{i,j}(x_i, x_j) + ... + f_{1,2,...,p}(x_1, x_2, ..., x_p) \tag{E.2}$$

where f_0 is the mean value of $f(x_1, x_2, ..., x_p)$ and each function of the above decomposition verifies the orthogonality condition expressed in Equation E.3.

$$\int_0^1 f_{i_1,i_2,...,i_s}(x_{i_1}, x_{i_2}, ..., x_{i_s})dx_{i_k} = 0 \ \forall k = 1, ..., s, \ \forall i_1, ..., i_s \subseteq 1, ..., p \tag{E.3}$$

The Total Variance Theorem states that, if $V(Y)$ is finite, then it may be decomposed by the following expression:

$$V(Y) = V(E[Y|X_i]) + E[V(Y|X_i)] \tag{E.4}$$

The second term of Equation E.4 vanishes as all random variables X_i are considered independent. By applying Equation E.4 on the model represented by Equation E.1, Sobol (1967) showed that the decomposition on Equation E.2 and decomposition of variance represented by Equation E.5 are equivalent.

$$V = \sum_{p=1}^{p} V_i + \sum_{1 \leq i \leq j \leq p} V_{ij} + ... + V_{1...p} \tag{E.5}$$

with the two first terms given by:

$$V_i = V(E[Y|X_i]) \tag{E.6}$$
$$V_{ij} = V(E[Y|X_i, X_j]) - V_i - V_j \tag{E.7}$$

The global sensitivity indices (also called Sobol Indices) may be obtained in a straightforward manner once the partial variances are known by the following expression:

$$S_{ij...p} = \frac{V_{i...p}}{V} \tag{E.8}$$

High order indices represent the conjoint effect of variables X_i and X_j over the output variable Y, which is not taken into account when local analysis is performed. For p independent random variables, there are $2^p - 1$ sensitivity index.

(Homma and Saltelli, 1996) proposed the Total Sensitivity Index for global sensitivity analysis. It consists on summing up all the sensitivity indices concerning a particular random variable X_i as follows:

$$S_{T_i} = S_i + S_{ij} + S_{ij...p} \tag{E.9}$$

$$S_{T_i} = 1 - \frac{V(E[Y\|X_{\sim i}])}{V(Y)}$$

The Sobol Indices may be obtained from Monte Carlo simulation. Indeed, considering the model f from Equation E.1, in order to estimate each partial variance, one has to estimate $U_i = E[E[Y|X_i, ..., X_p]^2]$ obtained from:

$$V_{ij...p} = V(E[Y|X_i, ..., X_p]) \tag{E.10}$$
$$= E[E[Y|X_i, ..., X_p]^2] - E[E[Y|X_i, ..., X_p]]^2 \tag{E.11}$$
$$= U_i - E[Y]^2 \tag{E.12}$$

which may be approximated by the following expression:

$$U_i \approx \frac{1}{N}\sum_{k=1}^{N} f(x_1^{k(1)}, x_2^{k(1)}, ..., x_i^{k(1)}, ..., x_p^{k(1)}) \times f(x_1^{k(2)}, x_2^{k(2)}, ..., x_i^{k(1)}, ..., x_p^{k(2)}) \tag{E.13}$$

where (1) and (2) are independent samples of the random variables X. In Equation E.13, only the value x_i of the variable of interest X_i is kept constant. In order to avoid redoubling computation of $f(x)$, random permutation of X may be used.

The Sobol Indices are a very good descriptors of a model's sensitivity to its input's parameters, as no hypothesis of linearity or monotonicity are required. However, computing all indices is most of times computation unfeasible for finite element models, as it requires to compute 2^p Monte Carlo integrals. Other methods have been proposed in the literature to obtain these indices, such as based on the Polynomial Chaos Expansion (PCE) coefficients (Sudret, 2008) and the Fourier Amplitude sensitivity Test (FAST) (Cukier et al., 1973; Saltelli et al., 1999). The last permits to compute the first-order sensitivity indices in a fast and elegant way and has been chosen to be used in this thesis. The main derivation of the method is presented in the next section.

E.2 FAST method

The first-order sensitivity indices may be computed by the Fourier Amplitude Sensitivity Test (FAST). It is based on a multidimensional Fourier transform of $f(x_1, ..., x_p)$ and the application of the ergodic theorem from Weyl (1938), which allows to compute a $p-$dimensional integral by a monodimensional integral. The idea is to explore the Hypercube I^p by a predescribed parametric curve. It is parametrized by a scalar parameter s and represented by Equation E.14:

$$x_i(s) = G_i \sin w_i s \ \forall i = 1, 2, ..., p \tag{E.14}$$

where w_i is a set of independent angular frequencies to be chosen properly (no one is linear combination of the others with integer coefficients), s is the scalar parameter defining the curve and G_i is a transformation function whose optimal form is solution of Equation E.15 as stated by Cukier et al. (1978).

$$\pi(1 - x_i^2)^{1/2} P_i(G_i) \frac{dG(x_i)}{dx_i} = 1 \tag{E.15}$$

The transformation function G_i determines how the parametric space I^p is filled. Different authors have proposed a specific transformation function (Cukier et al., 1973; Koda et al., 1979). In this work, the one proposed by Saltelli et al. (1999) and described by Equation E.16 is used, which results on uniformly distributed values for the random variable X_i.

$$x_i = \frac{1}{2} + \frac{1}{\pi} \arcsin \sin (w_i s) \tag{E.16}$$

When s varies from $-\infty$ to $+\infty$, the $p-$dimensional curve x_i is space-filling. The ergodic theorem from Weyl (1938) states that the moment $\bar{y}^{(r)}$ may be obtained by the following form:

$$\int_{k^p} f^r(x_1(s), x_2(s), ..., x_p(s))ds = \lim_{T\to\infty} \frac{1}{2T} \int_{-T}^{T} f^r(x_1(s), x_2(s), ..., x_p(s))ds \tag{E.17}$$

The multidimensional integral on the left hand side of Equation E.17 is equal to the limit of the monodimensional integral on the right hand side. However, it is numerically impossible to compute Equation E.17 for an incommensurate number of frequencies. As the sets w_i are finite, there exists some T for which the curve will describe a closed-path. Cukier et al. (1973) showed that if w_i's are positive integers, it describes a periodic curve with period 2π.

$$\bar{y}^{(r)} = \frac{1}{2\pi} \int_{-T}^{T} f^r(s)ds \tag{E.18}$$

Then the Total Variance V is obtained from:

$$V = \bar{y}^{(2)} - (\bar{y}^{(1)})^2 \tag{E.19}$$

$$= \frac{1}{2\pi} \int_{-T}^{T} f^2(s)ds - \left[\frac{1}{2\pi} \int_{-T}^{T} f(s)ds\right]^2 \tag{E.20}$$

and $f(s)$ may be expanded on a Fourier basis following Equation E.21:

$$y = f(s) = \sum_{j=-\infty}^{+\infty} A_j \cos js + B_j \sin js \tag{E.21}$$

The Parseval's identity states that:

$$\sum_{j=-\infty}^{+\infty} |c_j|^2 = \frac{1}{2\pi} \int_{-\pi}^{\pi} |f(x)|^2 dx \tag{E.22}$$

where c_j are the composition of the Fourier coefficients A_j and B_j (Equation E.23).

$$c_j^2 = A_j^2 + B_j^2 \tag{E.23}$$

Finally, Cukier et al. (1973) showed that the partial variances V_i, corresponding to each input variable X_i, may be obtained by calculating the variance obtained only at the assigned frequency w_i. The first-order sensitivity indices S_i are then obtained as:

$$S_i = \frac{V_i}{V} = \frac{\sum_{j=1}^{+\infty}(A_{jw_i}^2 + B_{jw_i}^2)}{\sum_{j=1}^{+\infty}(A_j^2 + B_j^2)} \tag{E.24}$$

The minimum sample size N_s is given by the maximum assigned frequency w_{max} and the interference factor M, following Equation E.25. The interference factor represents

the number of harmonics for which the independence of the assigned frequencies w_i is preserved. Saltelli et al. (1999) argues that usually four harmonics are enough to fully capture the response of the model. The maximum frequency w_{max} depends on the number of independent random variables and Saltelli et al. (1999) determined the frequency values for up to 9 independent random variables.

$$N_s = 2Mw_{max} + 1 \tag{E.25}$$

Appendix F

Panda test and empirical relations

F.1 Uncertainty analysis of the dynamic cone resistance measurement

Despite the natural variability of the dynamic cone resistance values obtained from a soil, different hypothesis as well as errors from the Panda sensors can contribute to uncertainties in the Panda measurement. These were studied by different authors (Zhou, 1997; Chaigneau, 2001) both by analytical considerations and from laboratory tests and are briefly summarized below.

F.1.1 Errors from the Hollandais formula

It is reminded from Chapter 2 that the dynamic cone resistance is obtained by the Hollandais formula (Equation F.1). It links the blow energy and the vertical displacement of the tip to the soil resistance. It corresponds to the static load inducing the same settlement as obtained from a hammer blow.

$$q_d = \frac{E}{A.e}\frac{M}{M+P} \tag{F.1}$$

where M is the hammer weight (2.35 kg), P is the dead weight, e is the plastic vertical displacement at each blow (normally between 0.5 and 2 cm), A is the cone cross section and E is the kinetic energy given by the hammer blow.

Figure F.1 presents the force (Q) by the settlement (e) during a hammer blow. Two hypothesis are made in computing the total energy (E): first, the hatched surface in the left, which corresponds to the soil response, is simplified by considering an elastic perfect plastic material, i.e hardening is neglected. Secondly, the elastic component is also neglected, the blow energy being considered equal to the energy absorbed by the soil. In this case the total energy can be obtained directly by the expression:

$$E = Qe \tag{F.2}$$

According to Chaigneau (2001), the error is considered lower than 10% for settlements higher than 2 mm per blow. The author also points out a systematic under evaluation

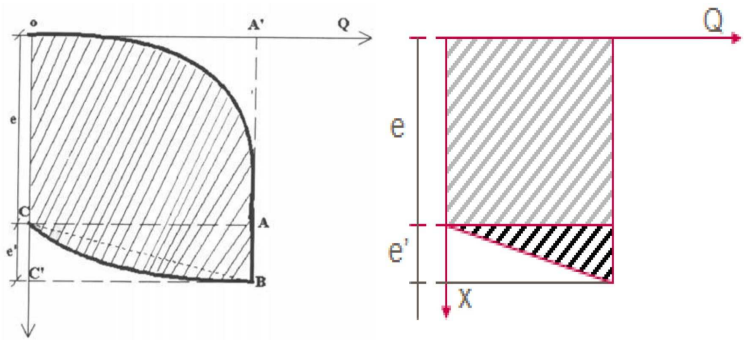

Figure F.1: Energy during penetrometer driving (Zhou, 1997).

of 15% of the soil resistance due to the errors in the estimation of Newton restitution coefficients. This error is systematic to all Panda penetrometers and can be avoided by a better estimation of these coefficients.

F.1.2 Errors from manufacture and sensors

According to Zhou (1997), both mass and sensor position tolerance during the manufacture process of the Panda penetrometer lead to a bias of 6.5% between two equipments. This bias can be avoided if the same equipement is used for all measurements, which is not always the case with large measurement campaigns. The author also points out that errors in the settlement sensor are estimated around 10%.

F.1.3 Errors from the lateral friction

Lateral friction become a critical issue for the Panda penetrometer for depths greater than 1.5 m when using a cone tip of 2 cm^2 (Chaigneau, 2001), but it can be neglected for cone tips of 4 and 10 cm^2.

F.1.4 Conclusions regarding the measurement errors

These different aspects are summarized in Table F.1. According to Chaigneau (2001), summing up the different discussed points, the Panda measurement presents an error of about 10% when using the same equipement and 16% when using different equipements.

Error type	Constant energy penetrometer		Variable energy penetrometer	
	Bias	Error	Bias	Error
Manufacture		3 %		6.5 %
Settlement sensor		20 %		10 %
Hypothesis on estimation of Newton's coefficients	-7 %		-15 %	
Hypothesis on Hollandais formula		10 %	10 %	

Table F.1: Uncertainties on the Panda cone resistance measurement (adapted from Chaigneau, 2001).

F.2 Empirical relations between the dynamic cone resistance (q_d) and Young's Modulus (E)

Different analytical and empirical relations have been proposed in the literature in order to link geotechnical characteristics of soils. Authors have showed that these relations depend both on nature and stress state of the soil, although this last point is less considered in the proposed relations. In the following, different approaches proposed in the literature are presented in order to obtain the Young's Modulus of the soil as a function of the dynamic cone resistance. One drawback of such relations is that it is not always defined at which deformation level the Young's Modulus is obtained.

F.2.1 Direct relations

Chua (1988) proposed an analytical solution to calculate the elastic modulus of a medium from a 1D model for penetration analysis of a rigid projectile into a ideally locking material. A relation between the penetration index and the elastic modulus is therefore obtained for different soil natures. The results from Chua (1988) are transposed to the Panda dynamic cone penetrometer by Haddani et al. (2011), which are presented in Table F.2.

Material	Analytical relation
Crushed graves	$E = 67.8 q_d^{0.55}$
Salty soils	$E = 53.7 \ln qd + 9.1$
Clayed soils	$E = 35.9 \ln q_d + 21.2$
Plastic clayed soils	$E = 23.2 \ln q_d + 12.5$

Table F.2: Different direct relations between the dynamic cone resistance and the Young's Modulus proposed by Chua (1988) (adapted by Haddani et al., 2011).

Bellotti et al. (1989) presented relations for the secant Young Modulus obtained from calibration chamber for an average axial strain of 0.1

$$\begin{aligned} E &= 4 \cdot q_d && \forall q_d \leq 10 && \text{[MPa]} \\ E &= 2 \cdot q_d + 20 && \forall 10 \leq q_d \leq 50 && \text{[MPa]} \end{aligned} \tag{F.3}$$

F.2.2 California Bearing Capacity (CBR)

Correlations between the dynamic cone resistance (q_d) and the California Bearing Ratio (CBR) have been extensively proposed in the literature. Some of these correlations are presented in Table F.3. According to Heukelom and Klomp (1962), the CBR and the Young's Modulus can be related by a simple linear relation:

$$E = A * CBR \tag{F.4}$$

where A is obtained experimentally and depends on both soil nature and the mean effective stress.

Material	Empirical relation	Author
Unknown	$\log CBR = 2.62 - 1.27 \log q_d$	Kleyn (1975)
Granular and cohesive	$\log CBR = 2.56 - 1.16 \log q_d$	Livneh (1987)
Granular and cohesive	$\log CBR = 2.55 - 1.14 \log q_d$	Harison (1987)
Granular and cohesive	$\log CBR = 2.45 - 1.12 \log q_d$	Livneh et al. (1992)
Various soil types	$\log CBR = 2.46 - 1.12 \log q_d$	Webster et al. (1992)
Aggregate base course	$\log CBR = 2.44 - 1.07 \log q_d$	Ese et al. (1994)
Aggregate base course and cohesive	$\log CBR = 2.60 - 1.07 \log q_d$	NCDOT (1998)
Piedmont residual soil	$\log CBR = 2.53 - 1.14 \log q_d$	Coonse (1999)

Table F.3: Different direct relations proposed in the literature between the California Bearing Ration (CBR) and the dynamic cone resistance (q_d) (adapted from Amini, 2003).

F.2.3 Static cone resistance (q_c)

Mohammed et al. (2000) evaluated both *in situ* static cone resistance of different cohesive soils and the Young's Modulus by laboratory tests. The following relation has been proposed:

$$E = a q_c^n + b f_c + c \omega_n + d \rho_d + e \tag{F.5}$$

where E is the Young's Modulus, q_c is the static cone resistance, f_c is the frictional resistance, ω_n is the water content, ρ_d is the dry volumetric mass density, n is an integer (1,2,3) and a,b,c,d,e are regression constants. Simpler direct relations have also been proposed by

Schmertmann (1970) and Trofimenkov (1974), as reported by Amini (2003), according to the following expression:

$$E = B * q_c \tag{F.6}$$

Cassan (1988) proposed to link the static cone resistance (q_c) and the dynamic cone resistance (q_d) for different soils by a linear relation (Equation F.7). Values of C for different materials are summarized in Table F.4.

$$q_c = C * q_d \tag{F.7}$$

Material	Above the water table	Below the water table
Silt	1	1.2 to 3
Sandy clay	0.5 to 0.9	0.1 to 0.4
Sand	1	-
Sand and gravels	1	1 to 2.6

Table F.4: Values of C from Equation F.7 proposed by Cassan (1988)

On the view of these results, some authors have argued that dynamic cone resistance (q_d) can be considered equal to the static cone resistance (q_c) for most soils (Zhou, 1997; Chaigneau et al., 2000).

F.2.4 Oedometric deformation modulus (E_{oed})

Empirical relations have also been proposed between the oedometric deformation modulus (E_{eod}) and the static cone resistance (q_c). Buisman (1940) was the first to propose a linear relation (Equation F.8) between E_{eod} and q_c. The value of α (also called Buisman coefficient) for different soil natures was largely studied by authors. The recommended values are summarized in Table F.5.

$$E_{oed} = \alpha q_c \tag{F.8}$$

Author	Sand	Clayed sand	Compacted clay	Soft clay	Clayed silt	Silt
Sanglerat (1965)	1.5	2 to 5	2 to 5	5 to 10	-	1 to 2
Bachelier and Parez (1965)	1 to 2	2 to 4	3 to 5	-	2.5 to 4	-

Table F.5: Buisman coefficient (α) for different soil natures (adapted from Arbaoui, 2005).

The oedometric deformation modulus and the Young's Modulus are well defined on a linear elastic material by the following relation:

$$E = E_{eod}\frac{(1+\nu)(1-2\nu)}{(1-\nu)} \tag{F.9}$$

The Poisson's ratio of most soils can be considered equal to 0.3. In the railway context, this approach is used by Rhayma et al. (2011, 2013) in order to obtain track geomaterial's Young's Modulus from the Panda dynamic cone resistance (q_d).

F.3 Remarks and conclusions

An overview of empirical relations proposed in the literature linking the static or dynamic cone resistance to the Young's Modulus was presented in the previous section. These relations highlight the importance of soil nature in defining the soil stiffness. However, different Young's Modulus are obtained when considering the same soil nature by different relations, for a given value of the dynamic cone resistance q_d (Figure F.2). Therefore, it is also important to consider the stress state and deformation level imposed on the soil when obtaining such relations. In this work, the relations proposed by Chua (1988) and Lunne et al. (1997) are used, which directly link the Young's Modulus to the dynamic cone resistance. As shown in Figure F.2, they lead to higher values of the Young's Modulus when compared to relations using the Buisman coefficient.

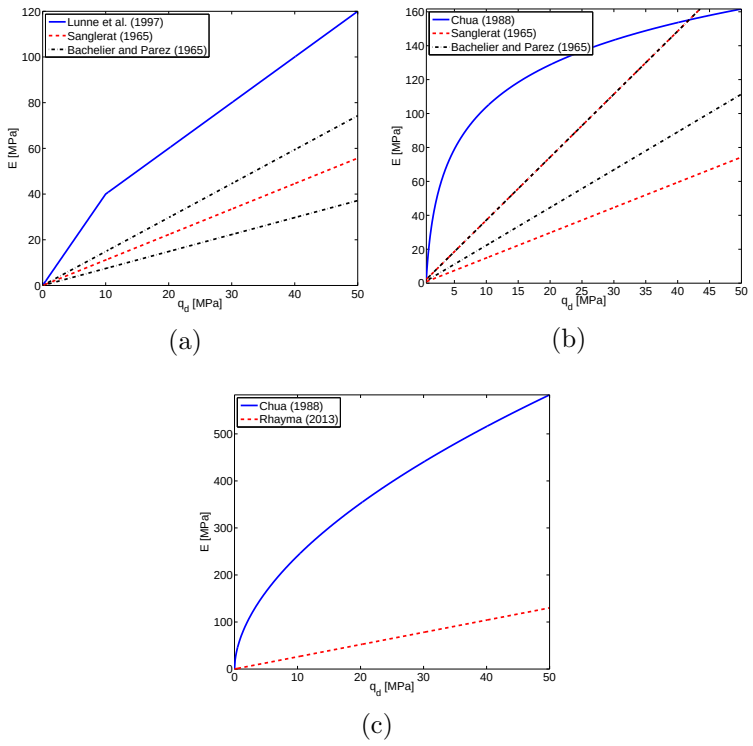

Figure F.2: Comparison of different relations between the Young's Modulus (E) and the dynamic cone resistance (q_d) available in the literature. a) Sand; b) Clay; c) Ballast (considered as gravel).

Appendix G

Material characterization by numerical laboratory tests

Numerical laboratory tests results are presented in order to illustrate the different material's response to the usual stress paths applied on laboratory tests.

G.1 Ballast from Suiker et al. (2005)

G.1.1 Laboratory Test Paths

Several soil mechanics tests are modeled in order to show both a global view of the response of the ECP elastoplastic model Aubry et al. (1982); Hujeux (1985) and the coherence of the set of parameters proposed in this work to simulate the ballast behaviour. Laboratory tests were conducted by Suiker et al. (2005) on this material. The soil mechanics tests concern both monotonic and cyclic paths at different consolidation pressures p'_o.

The used parameters for the sand model are given in Table G.1. All tests are simulated with the same set of parameters. Three initial confinement pressures p'_o (i.e. 10, 41 and 69 kPa) are used in all simulated tests.

Drained triaxial tests

Figures G.1 and G.2 show the response obtained by the model in simulated drained triaxial tests. The response is showed in the $q - \varepsilon_1$, $\varepsilon_v - \varepsilon_1$, $\varepsilon_v - p'$ and $\eta - \varepsilon_1$ planes.

Model parameters	
Elasticity	
$K_{ref}(MPa)$	69.4
$G_{ref}(MPa)$	52.0
n_e	0.00
$p_{ref}(MPa)$	1.0
Critical State and Plasticity	
$\phi'_{pp}(^\circ)$	42
β	10
d	3.00
b	0.06
$p_{co}(MPa)$	0.70
Flow Rule and Isotropic Hardening	
$\psi(^\circ)$	42
α_ψ	3.00
a_1	0.00002
a_2	0.00080
c_1	0.00200
c_2	0.00100
m	1.50
Threshold Domains	
r^{ela}	0.00001
r^{hys}	0.01000
r^{mob}	0.98000
r^{ela}_{iso}	0.00002

Table G.1: ECP model's parameters on ballast material tested by Suiker et al. (2005).

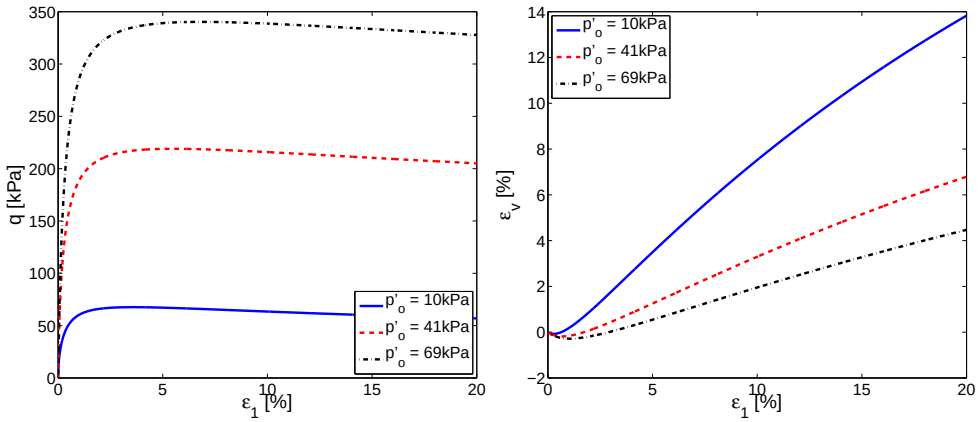

(a) (b)

Figure G.1: Simulated drained triaxial tests. a) $q - \varepsilon_1$; b) $\varepsilon_v - \varepsilon_1$.

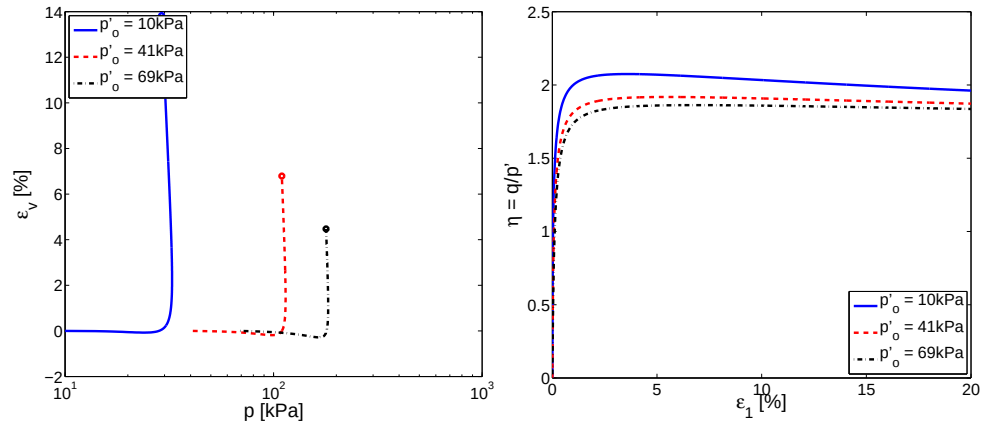

(a) (b)

Figure G.2: Simulated drained triaxial tests. a) $\varepsilon_v - p'$; b) $\eta - \varepsilon_1$.

Consolidation tests

Figure G.3 shows the simulated response of cyclic isotropic and oedometric consolidation tests.

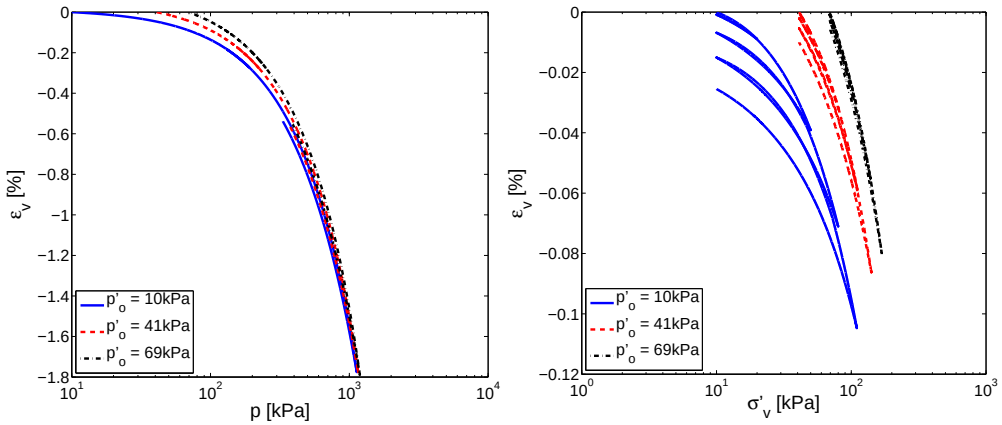

(a) (b)

Figure G.3: Simulated cyclic tests. a) Isotropic consolidation. b) Oedometric consolidation.

Drained cyclic strain-controlled shear test

Figures G.4 and G.5 show the simulated response of drained cyclic strain-controlled shear tests. The obtained $G/G_{max} - \gamma$ and $D - \gamma$ curves are compared to the reference curves given by Seed et al. (1986).

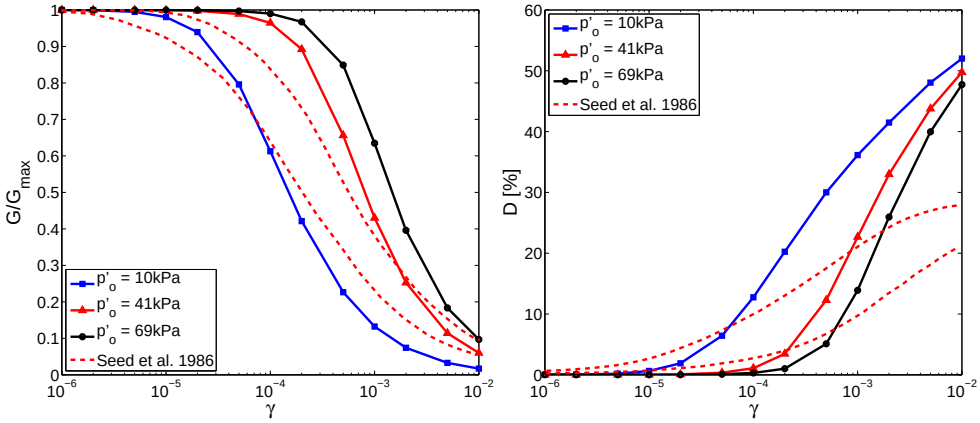

(a) (b)

Figure G.4: Simulated drained cyclic shear test. a) $G/G_{max} - \gamma$; b) $D - \gamma$ curves.

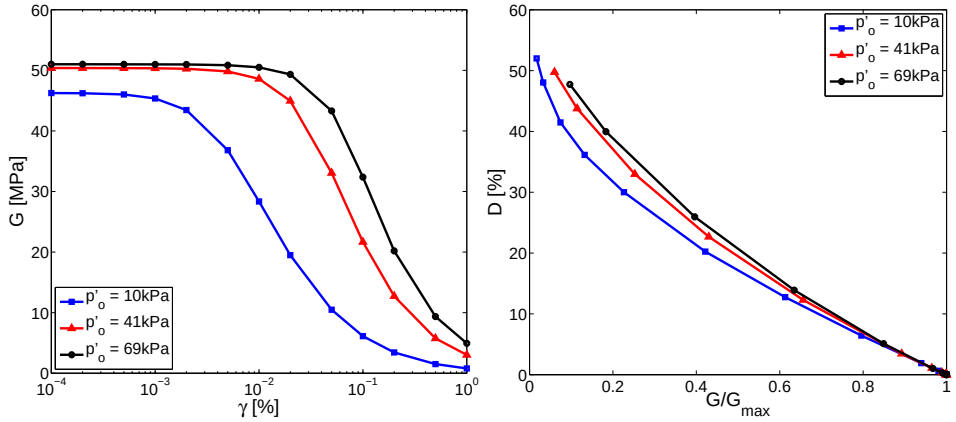

(a) (b)

Figure G.5: Simulated drained cyclic shear test. a) $G - \gamma$; b) $G/G_{max} - D$ curves.

G.2 Ballast from Indraratna et al. (2011)

G.2.1 Laboratory Test Paths

Several soil mechanics tests are modelled in order to show both a global view of the response of the ECP elastoplastic model Aubry et al. (1982); Hujeux (1985) and the coherence of the set of parameters proposed in this work to simulate the ballast behaviour. Laboratory tests were conducted under the work of Indraratna et al. (2011). The soil mechanics tests concern both monotonic and cyclic paths at different consolidation pressures p'_o.

The used parameters for the sand model are given in Table G.2. All tests are simulated with the same set of parameters. Three initial confinement pressures p'_o (i.e. 10, 50 and 100 kPa) are used in all simulated tests.

Model parameters	
Elasticity	
$K_{ref}(MPa)$	87.0
$G_{ref}(MPa)$	60.0
n_e	0.00
$p_{ref}(MPa)$	1.0
Critical State and Plasticity	
$\phi'_{pp}(^\circ)$	43
β	8
d	8.80
b	0.65
$p_{co}(MPa)$	0.50
Flow Rule and Isotropic Hardening	
$\psi(^\circ)$	43
α_ψ	1.20
a_1	0.00002
a_2	0.01500
c_1	0.80000
c_2	0.40000
m	1.20
Threshold Domains	
r^{ela}	0.00001
r^{hys}	0.00400
r^{mob}	0.80000
r^{ela}_{iso}	0.00002

Table G.2: ECP model's parameters for ballast tested by Indraratna et al. (2011).

Drained triaxial tests

Figures G.6 and G.7 show the response obtained by the model in simulated drained triaxial tests. The response is showed in the $q - \varepsilon_1$, $\varepsilon_v - \varepsilon_1$, $\varepsilon_v - p'$ and $\eta - \varepsilon_1$ planes.

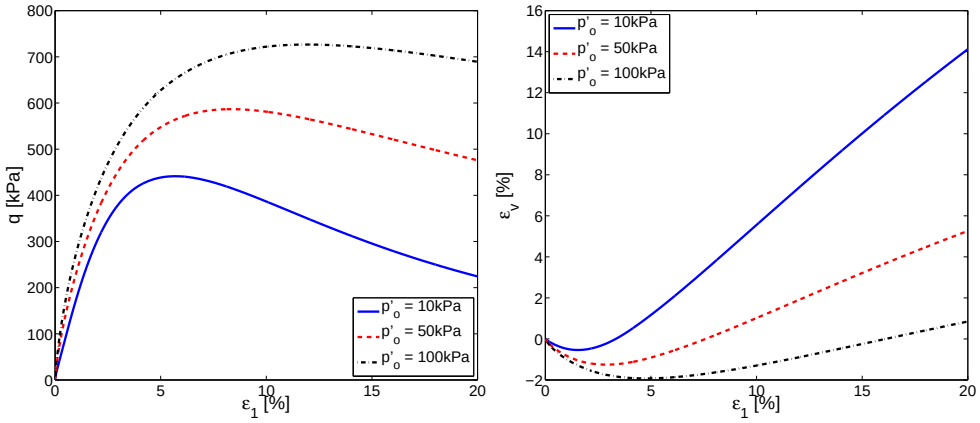

(a) (b)

Figure G.6: Simulated drained triaxial tests. a) $q - \varepsilon_1$; b) $\varepsilon_v - \varepsilon_1$.

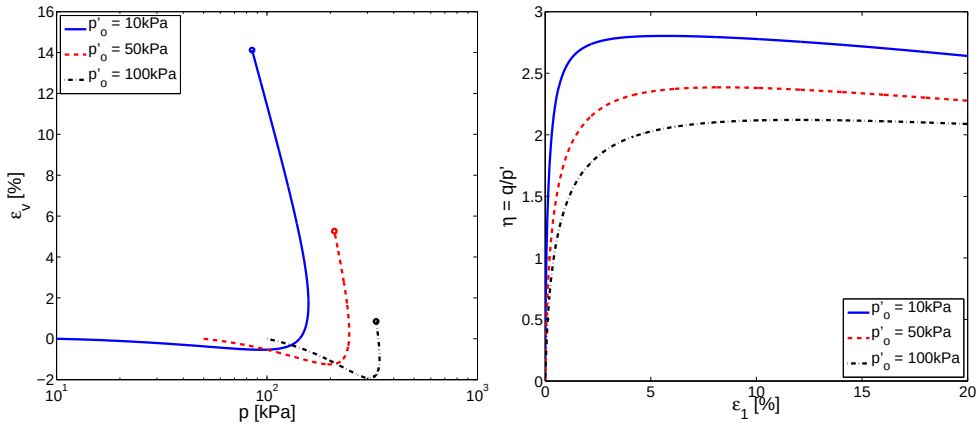

(a) (b)

Figure G.7: Simulated drained triaxial tests. a) $\varepsilon_v - p'$; b) $\eta - \varepsilon_1$.

Consolidation tests

Figure G.8 shows the simulated response of cyclic isotropic and oedometric consolidation tests.

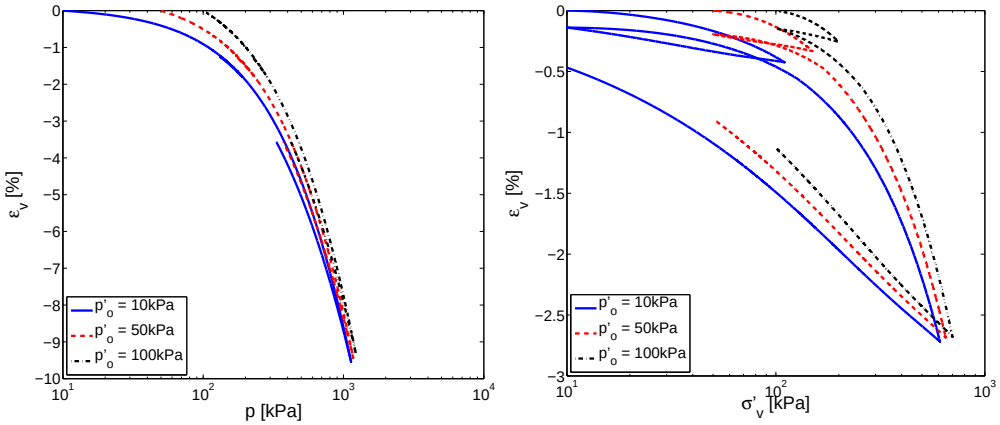

(a) (b)

Figure G.8: Simulated cyclic tests. a) Isotropic consolidation; b) Oedometric consolidation.

Drained cyclic strain-controlled shear test

Figures G.9 and G.10 show the simulated response of drained cyclic strain-controlled shear tests. The obtained $G/G_{max} - \gamma$ and $D - \gamma$ curves are compared to the reference curves given by Seed et al. (1986).

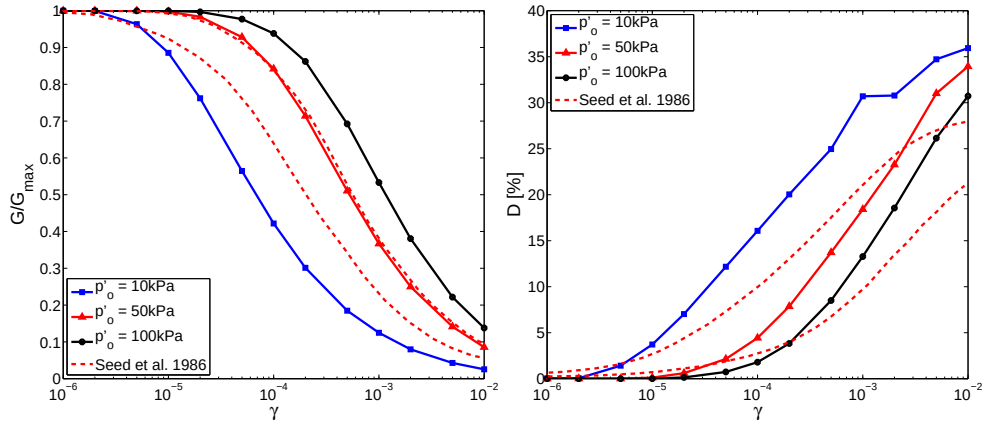

(a) (b)

Figure G.9: Simulated drained cyclic shear test. a) $G/G_{max} - \gamma$; b) $D - \gamma$ curves.

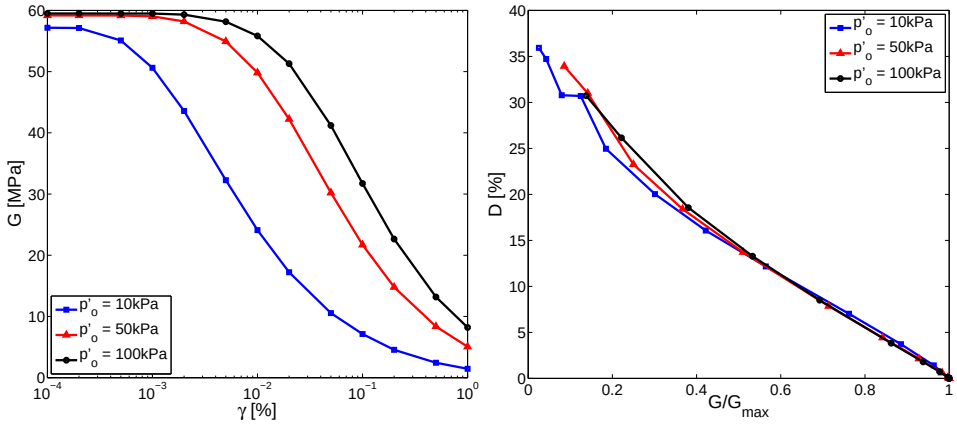

(a) (b)

Figure G.10: Simulated drained cyclic shear test. a) $G - \gamma$; b) $G/G_{max} - D$ curves.

G.3 Interlayer material A tested by Trinh et al. (2012)

G.3.1 Laboratory Test Paths

Several soil mechanics tests are modeled in order to show both a global view of the response of the ECP elastoplastic model Aubry et al. (1982); Hujeux (1985) and the coherence of the set of parameters proposed in this work to simulate the intermediate layer material behavior. Laboratory tests were conducted by Trinh et al. (2012) on this material. The soil mechanics tests concern both monotonic and cyclic paths at different consolidation pressures p'_o.

The used parameters for the sand model are given in Table G.3. All tests are simulated with the same set of parameters. Three initial confinement pressures p'_o (i.e. 30, 50 and 100 kPa) are used in all simulated tests.

Model parameters	
Elasticity	
$K_{ref}(MPa)$	133.0
$G_{ref}(MPa)$	61.0
n_e	0.00
$p_{ref}(MPa)$	1.0
Critical State and Plasticity	
$\phi'_{pp}(^\circ)$	41
β	10
d	1.00
b	0.30
$p_{co}(MPa)$	0.65
Flow Rule and Isotropic Hardening	
$\psi(^\circ)$	41
α_ψ	1.70
a_1	0.00001
a_2	0.00400
c_1	0.00800
c_2	0.00400
m	1.20
Threshold Domains	
r^{ela}	0.00001
r^{hys}	0.02000
r^{mob}	0.90000
r^{ela}_{iso}	0.00002

Table G.3: ECP model's parameters for the interlayer material A.

Drained triaxial tests

Figures G.11 and G.12 show the response obtained by the model in simulated drained triaxial tests. The response is showed in the $q - \varepsilon_1$, $\varepsilon_v - \varepsilon_1$, $\varepsilon_v - p'$ and $\eta - \varepsilon_1$ planes.

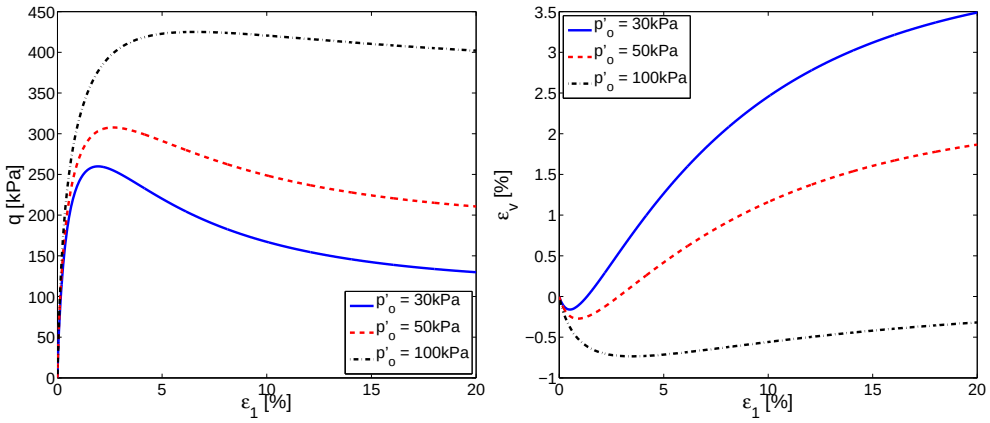

(a) (b)

Figure G.11: Simulated drained triaxial tests a) $q - \varepsilon_1$, b) $\varepsilon_v - \varepsilon_1$.

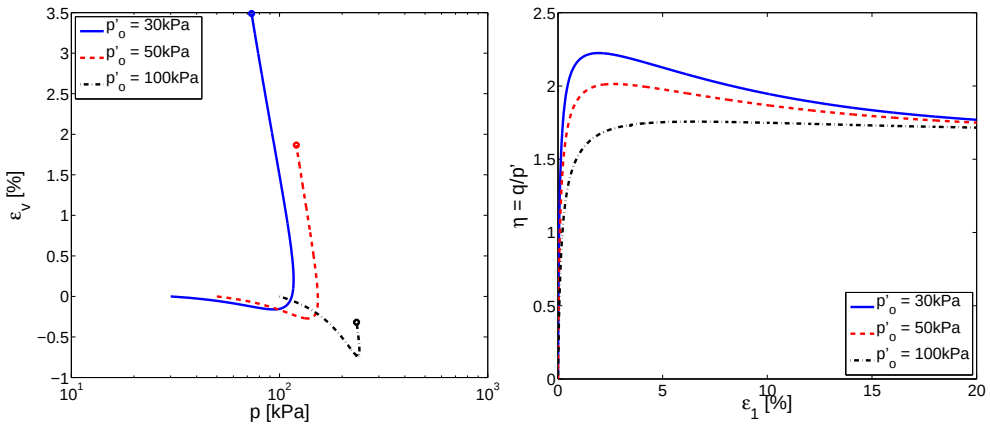

(a) (b)

Figure G.12: Simulated drained triaxial tests a) $\varepsilon_v - p'$, b) $\eta - \varepsilon_1$.

Undrained triaxial tests

Figures G.13 and G.14 show the response obtained by the model in simulated undrained triaxial tests. The response is showed in the $q - \varepsilon_1$, $q - p'$, $\Delta U - \varepsilon_1$ and $\eta - \varepsilon_1$ planes.

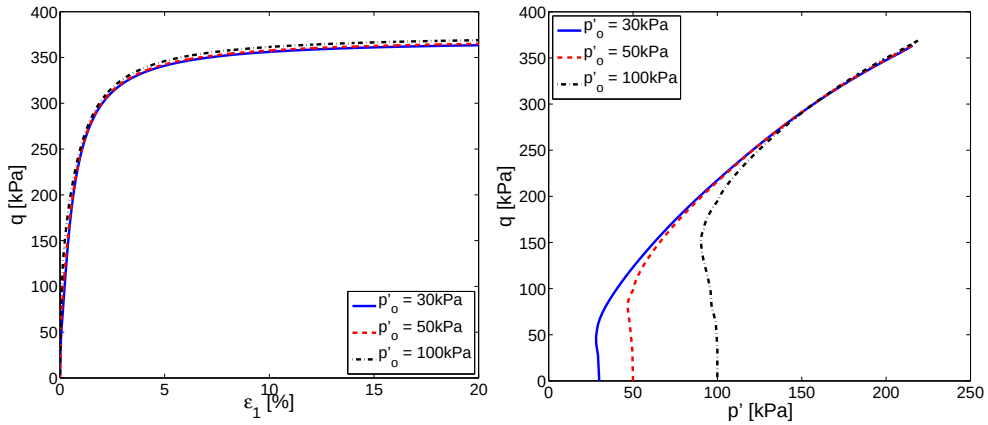

(a) (b)

Figure G.13: Simulated undrained triaxial tests a) $q - \varepsilon_1$, b) $q - p'$.

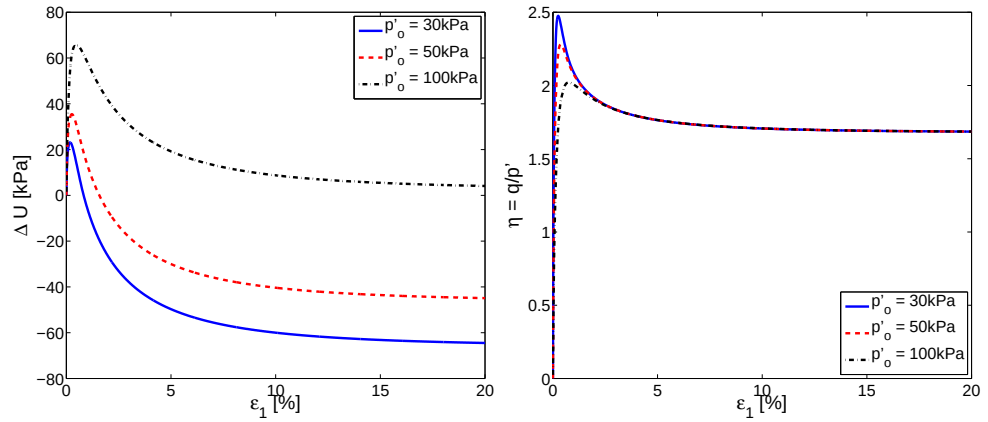

(a) (b)

Figure G.14: Simulated undrained triaxial tests a) $\Delta U - \varepsilon_1$, b) $\eta - \varepsilon_1$.

Consolidation tests

Figure G.15 shows the simulated response of cyclic isotropic and oedometric consolidation tests.

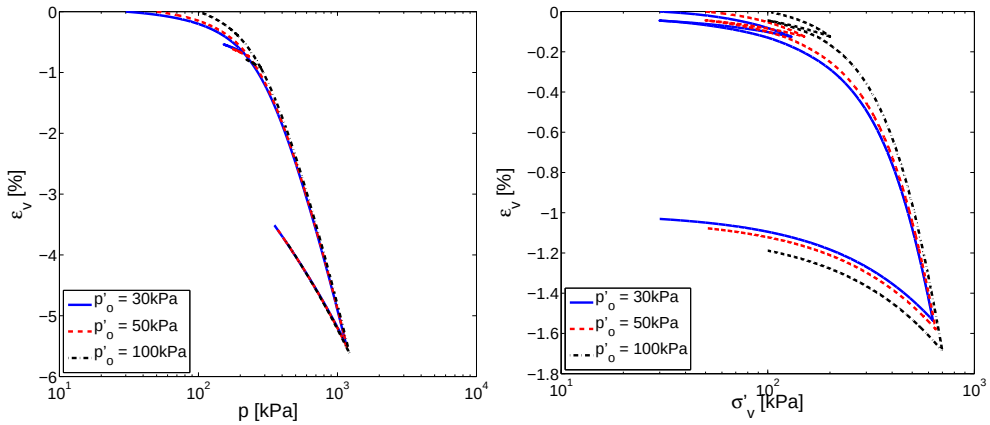

(a) (b)

Figure G.15: Simulated cyclic tests. a) Isotropic consolidation; b) Oedometric consolidation.

Drained cyclic strain-controlled shear test

Figures G.16 and G.17 show the simulated response of drained cyclic strain-controlled shear tests. The obtained $G/G_{max} - \gamma$ and $D - \gamma$ curves are compared to the reference curves given by Seed et al. (1986).

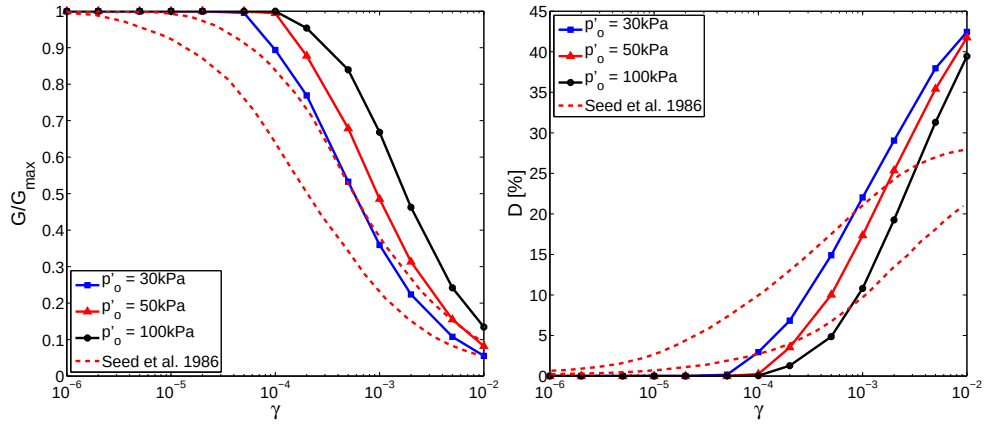

(a) (b)

Figure G.16: Simulated drained cyclic shear test a) $G/G_{max} - \gamma$; b) $D - \gamma$ curves.

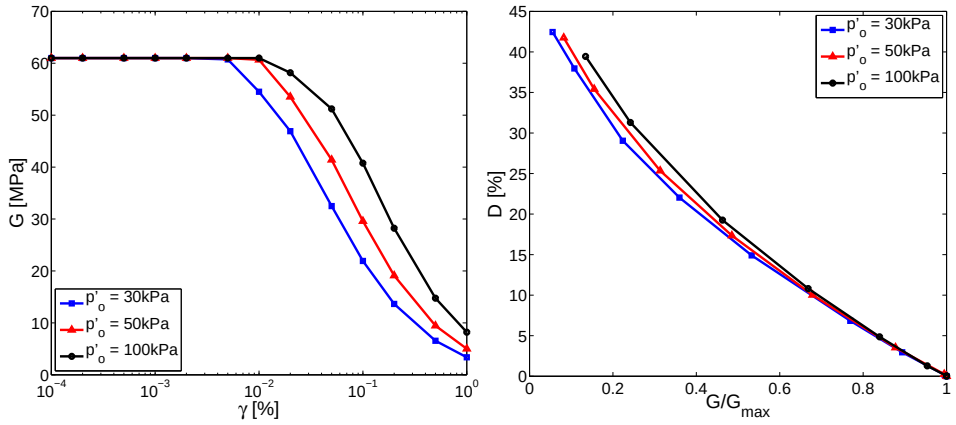

(a) (b)

Figure G.17: Simulated drained cyclic shear test a) $G - \gamma$; b) $G/G_{max} - D$ curves.

G.4 Interlayer material B tested by Trinh et al. (2012)

G.4.1 Laboratory Test Paths

Several soil mechanics tests are modeled in order to show both a global view of the response of the ECP elastoplastic model Aubry et al. (1982); Hujeux (1985) and the coherence of the set of parameters proposed in this work to simulate the intermediate layer material behavior. Laboratory tests were conducted by Trinh et al. (2012) on this material. The soil mechanics tests concern both monotonic and cyclic paths at different consolidation pressures p'_o.

The used parameters for the sand model are given in Table G.4. All tests are simulated with the same set of parameters. Three initial confinement pressures p'_o (i.e. 30, 50 and 100 kPa) are used in all simulated tests.

Model parameters	
Elasticity	
$K_{ref}(MPa)$	133.0
$G_{ref}(MPa)$	61.0
n_e	0.00
$p_{ref}(MPa)$	1.0
Critical State and Plasticity	
$\phi'_{pp}(^\circ)$	41
β	30
d	2.50
b	0.15
$p_{co}(MPa)$	0.18
Flow Rule and Isotropic Hardening	
$\psi(^\circ)$	41
α_ψ	1.10
a_1	0.00001
a_2	0.00120
c_1	0.01000
c_2	0.00500
m	1.00
Threshold Domains	
r^{ela}	0.00001
r^{hys}	0.02000
r^{mob}	0.90000
r^{ela}_{iso}	0.00002

Table G.4: ECP model's parameters for the interlayer material B.

Drained triaxial tests

Figures G.18 and G.19 show the response obtained by the model in simulated drained triaxial tests. The response is showed in the $q - \varepsilon_1$, $\varepsilon_v - \varepsilon_1$, $\varepsilon_v - p'$ and $\eta - \varepsilon_1$ planes.

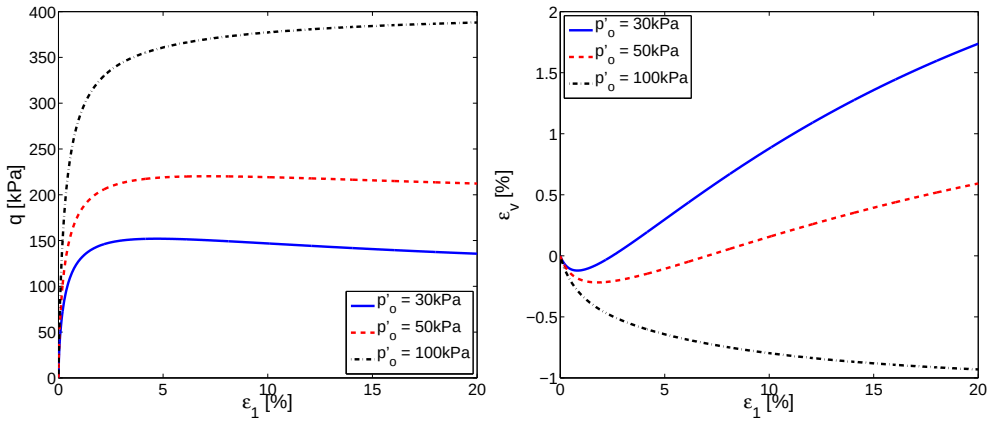

(a) a (b) b

Figure G.18: Simulated drained triaxial tests. a) $q - \varepsilon_1$; b) $\varepsilon_v - \varepsilon_1$.

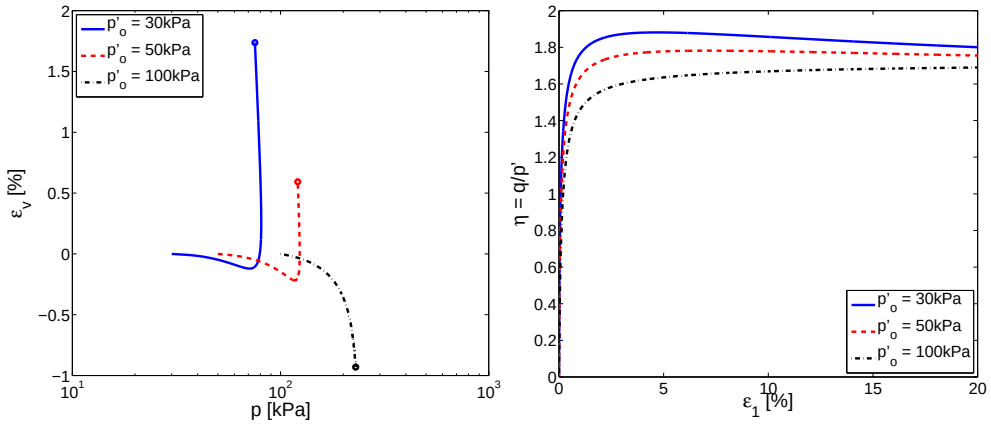

(a) a (b) b

Figure G.19: Simulated drained triaxial tests. a) $\varepsilon_v - p'$; b) $\eta - \varepsilon_1$.

Undrained triaxial tests

Figures G.20 and G.21 show the response obtained by the model in simulated undrained triaxial tests. The response is showed in the $q - \varepsilon_1$, $q - p'$, $\Delta U - \varepsilon_1$ and $\eta - \varepsilon_1$ planes.

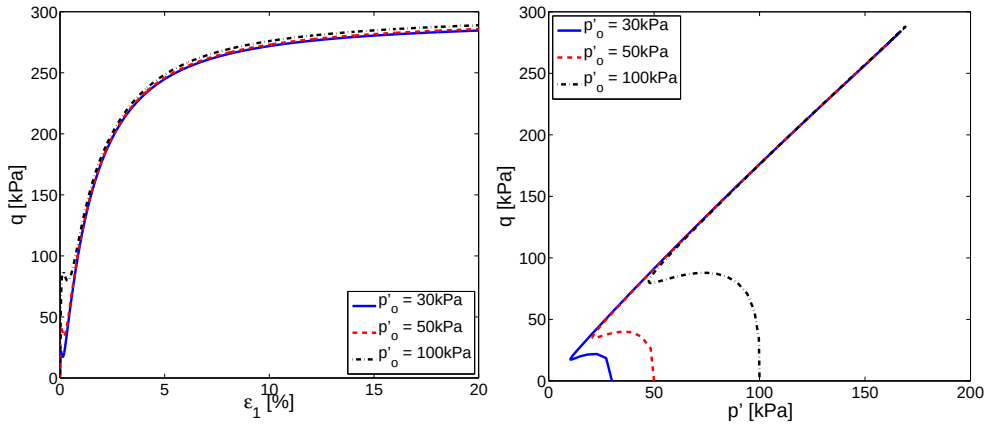

(a) a (b) b

Figure G.20: Simulated undrained triaxial tests. a) $q - \varepsilon_1$; b) $q - p'$.

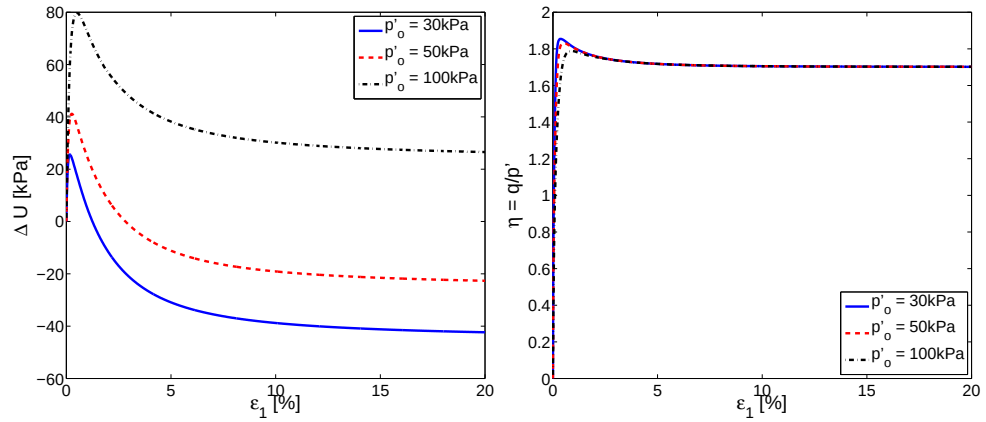

(a) a (b) b

Figure G.21: Simulated undrained triaxial tests. a) $\Delta U - \varepsilon_1$; b) $\eta - \varepsilon_1$.

Consolidation tests

Figure G.22 shows the simulated response of cyclic isotropic and oedometric consolidation tests.

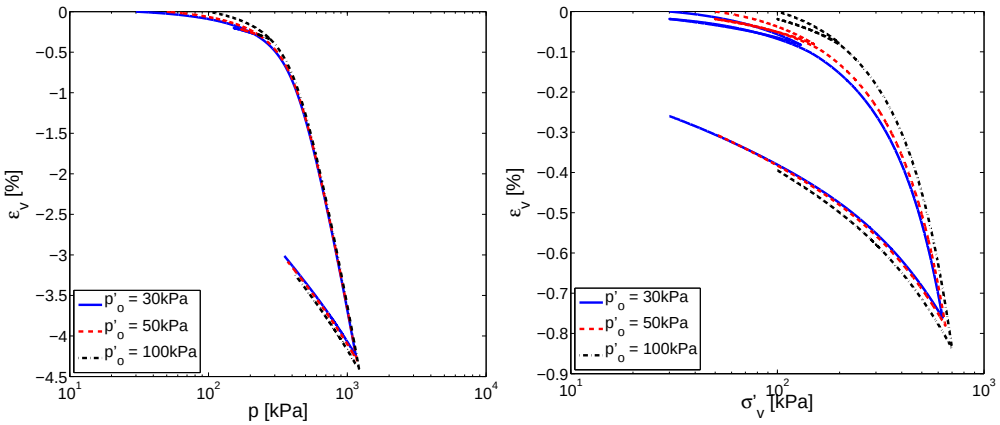

(a) a (b) b

Figure G.22: Simulated cyclic tests. a) Isotropic consolidation; b) Oedometric consolidation.

Drained cyclic strain-controlled shear test

Figures G.23 and G.24 show the simulated response of drained cyclic strain-controlled shear tests. The obtained $G/G_{max} - \gamma$ and $D - \gamma$ curves are compared to the reference curves given by Seed et al. (1986).

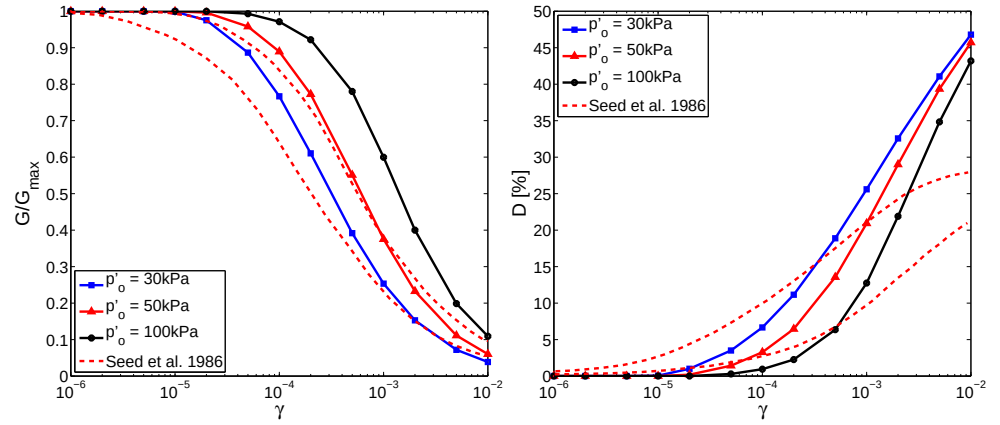

(a) a (b) b

Figure G.23: Simulated drained cyclic shear test. a) $G/G_{max} - \gamma$; b) $D - \gamma$ curves.

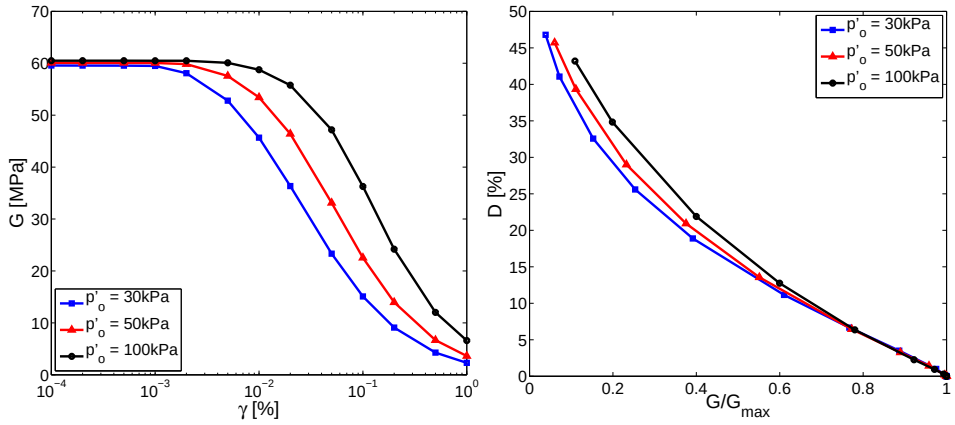

(a) a (b) b

Figure G.24: Simulated drained cyclic shear test. a) $G - \gamma$; b) $G/G_{max} - D$ curves.

G.5 Toyoura sand at D_r=40%

G.5.1 Laboratory Test Paths

Several soil mechanics tests are modeled in order to show both a global view of the response of the ECP elastoplastic model Aubry et al. (1982); Hujeux (1985) and the coherence of the set of parameters proposed in this work to simulate Toyoura sand at relative density D_r=40%. Laboratory tests were conducted by Suiker et al. (2005) on this material. The soil mechanics tests concern both monotonic and cyclic paths at different consolidation pressures p'_o.

The used parameters for the sand model are given in Table G.5. All tests are simulated with the same set of parameters. Three initial confinement pressures p'_o (i.e. 20, 50 and 100 kPa) are used in all simulated tests.

Model parameters	
Elasticity	
$K_{ref}(MPa)$	296.0
$G_{ref}(MPa)$	222.0
n_e	0.40
$p_{ref}(MPa)$	1.0
Critical State and Plasticity	
$\phi'_{pp}(^\circ)$	30
β	43
d	3.50
b	0.22
$p_{co}(MPa)$	1.40
Flow Rule and Isotropic Hardening	
$\psi(^\circ)$	30
α_ψ	1.00
a_1	0.00010
a_2	0.01500
c_1	0.06000
c_2	0.03000
m	1.00
Threshold Domains	
r^{ela}	0.00500
r^{hys}	0.03000
r^{mob}	0.80000
r^{ela}_{iso}	0.00010

Table G.5: ECP model's parameters

Drained triaxial tests

Figures G.25 and G.26 show the response obtained by the model in simulated drained triaxial tests. The response is showed in the $q - \varepsilon_1$, $\varepsilon_v - \varepsilon_1$, $\varepsilon_v - p'$ and $\eta - \varepsilon_1$ planes.

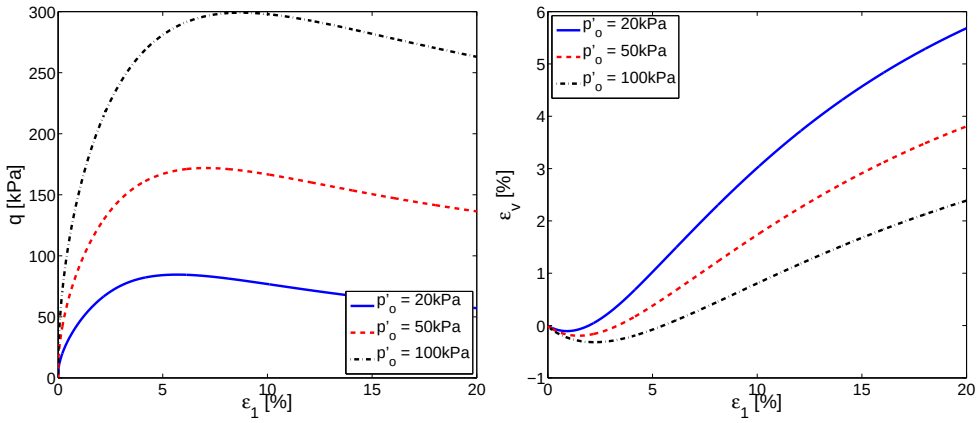

(a) (b)

Figure G.25: Simulated drained triaxial tests. a) $q - \varepsilon_1$; b) $\varepsilon_v - \varepsilon_1$.

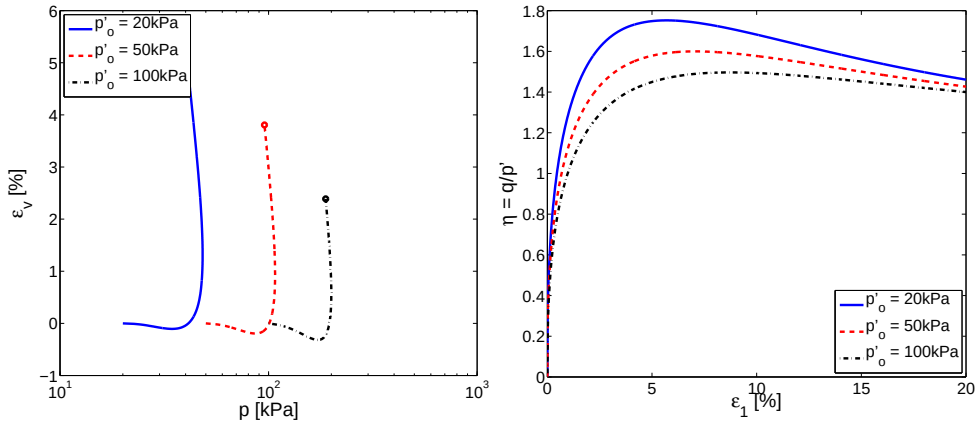

(a) (b)

Figure G.26: Simulated drained triaxial tests. a) $\varepsilon_v - p'$; b) $\eta - \varepsilon_1$.

Undrained triaxial tests

Figures G.27 and G.28 show the response obtained by the model in simulated undrained triaxial tests. The response is showed in the $q - \varepsilon_1$, $q - p'$, $\Delta U - \varepsilon_1$ and $\eta - \varepsilon_1$ planes.

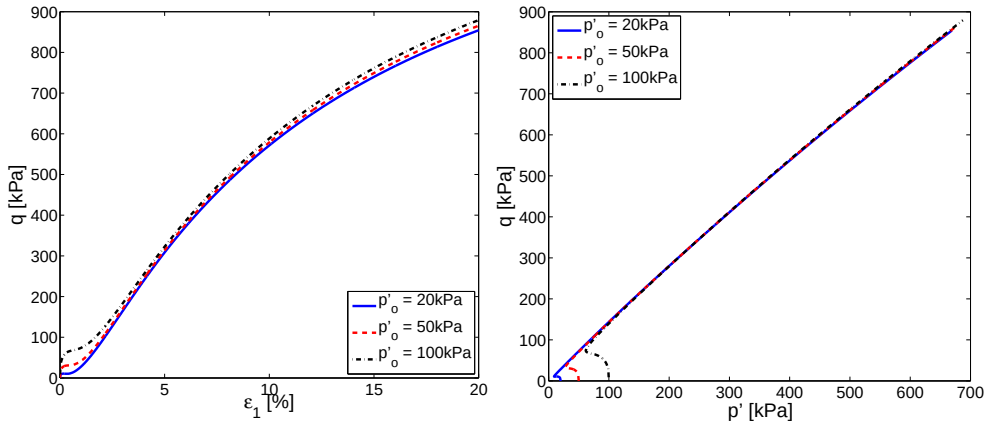

(a) (b)

Figure G.27: Simulated undrained triaxial tests. a) $q - \varepsilon_1$; b) $q - p'$.

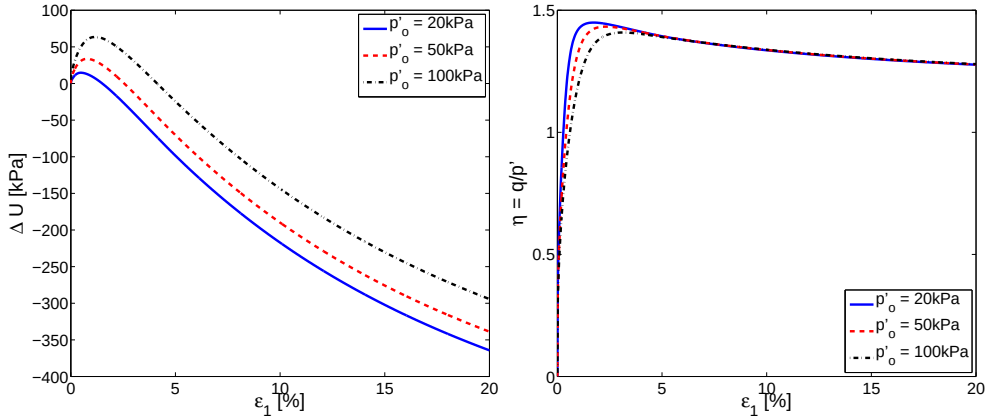

(a) (b)

Figure G.28: Simulated undrained triaxial tests. a) $\Delta U - \varepsilon_1$; b) $\eta - \varepsilon_1$.

Consolidation tests

Figure G.29 shows the simulated response of cyclic isotropic and oedometric consolidation tests.

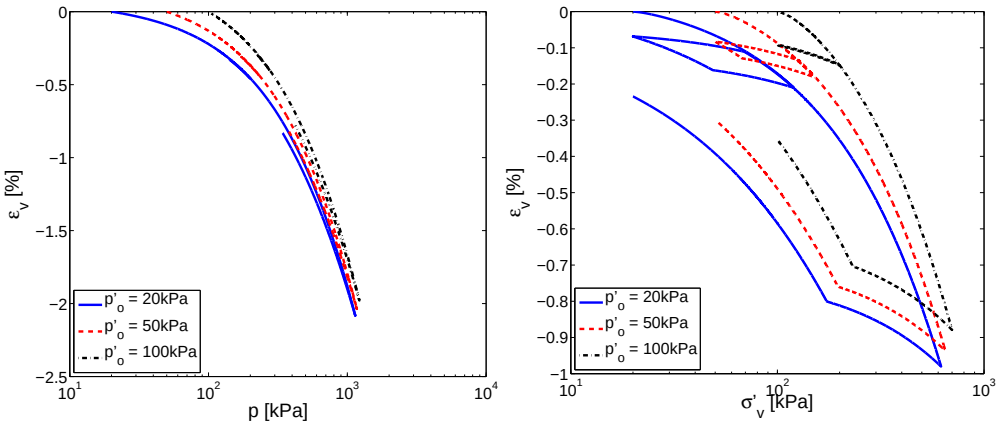

(a) (b)

Figure G.29: Simulated cyclic tests. a) Isotropic consolidation. b) Oedometric consolidation.

Drained cyclic strain-controlled shear test

Figures G.30 and G.31 show the simulated response of drained cyclic strain-controlled shear tests. The obtained $G/G_{max} - \gamma$ and $D - \gamma$ curves are compared to the reference curves given by Seed et al. (1986).

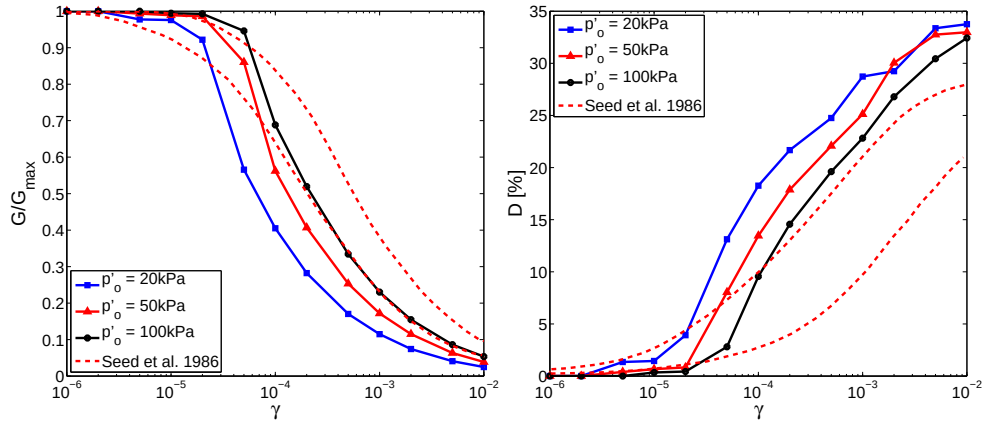

(a) (b)

Figure G.30: Simulated drained cyclic shear test. a) $G/G_{max} - \gamma$; b) $D - \gamma$ curves.

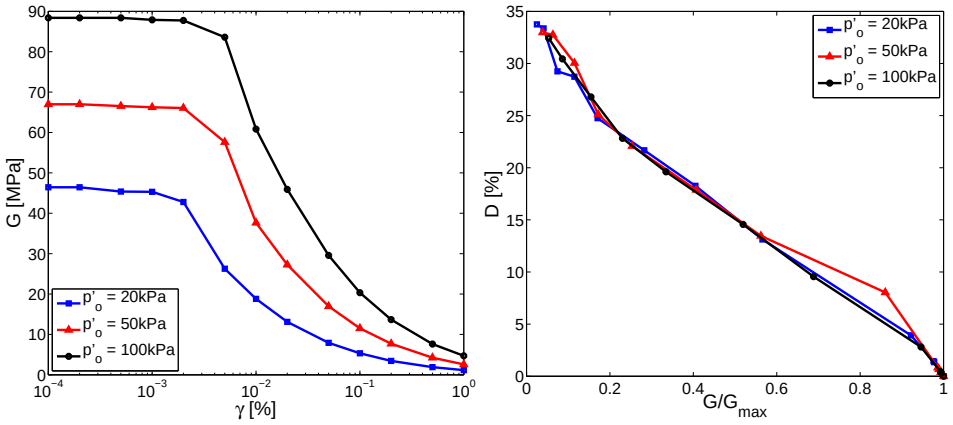

(a) (b)

Figure G.31: Simulated drained cyclic shear test. a) $G - \gamma$; b) $G/G_{max} - D$ curves.

G.6 Toyoura sand at D_r=93%

G.6.1 Laboratory Test Paths

Several soil mechanics tests are modeled in order to show both a global view of the response of the ECP elastoplastic model Aubry et al. (1982); Hujeux (1985) and the coherence of the set of parameters proposed in this work to simulate Toyoura sand at relative density D_r=93%. Laboratory tests were conducted by Suiker et al. (2005) on this material. The soil mechanics tests concern both monotonic and cyclic paths at different consolidation pressures p'_o.

The used parameters for the sand model are given in Table G.6. All tests are simulated with the same set of parameters. Three initial confinement pressures p'_o (i.e. 20, 50 and 100 kPa) are used in all simulated tests.

Model parameters	
Elasticity	
$K_{ref}(MPa)$	296.0
$G_{ref}(MPa)$	222.0
n_e	0.40
$p_{ref}(MPa)$	1.0
Critical State and Plasticity	
$\phi'_{pp}(^\circ)$	30
β	17
d	3.50
b	0.22
$p_{co}(MPa)$	4.90
Flow Rule and Isotropic Hardening	
$\psi(^\circ)$	30
α_ψ	1.00
a_1	0.00010
a_2	0.01500
c_1	0.06000
c_2	0.03000
m	1.00
Threshold Domains	
r^{ela}	0.00500
r^{hys}	0.03000
r^{mob}	0.80000
r^{ela}_{iso}	0.00010

Table G.6: ECP model's parameters

Drained triaxial tests

Figures G.32 and G.33 show the response obtained by the model in simulated drained triaxial tests. The response is showed in the $q - \varepsilon_1$, $\varepsilon_v - \varepsilon_1$, $\varepsilon_v - p'$ and $\eta - \varepsilon_1$ planes.

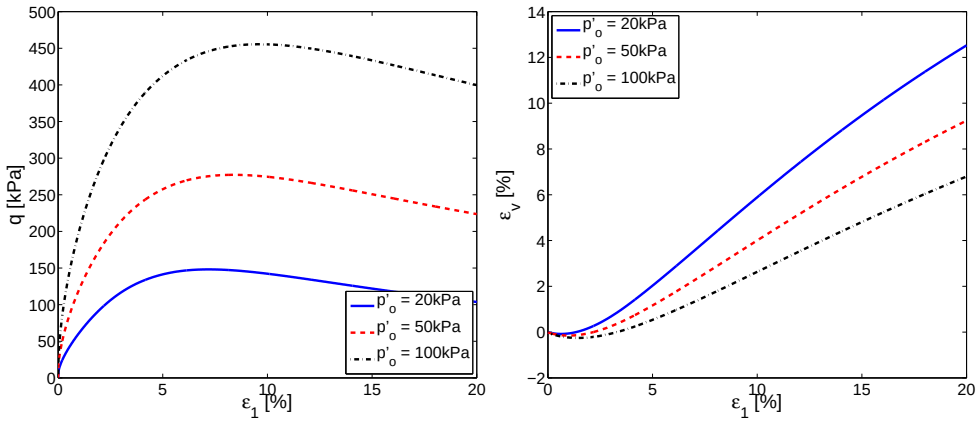

(a) (b)

Figure G.32: Simulated drained triaxial tests. a) $q - \varepsilon_1$; b) $\varepsilon_v - \varepsilon_1$.

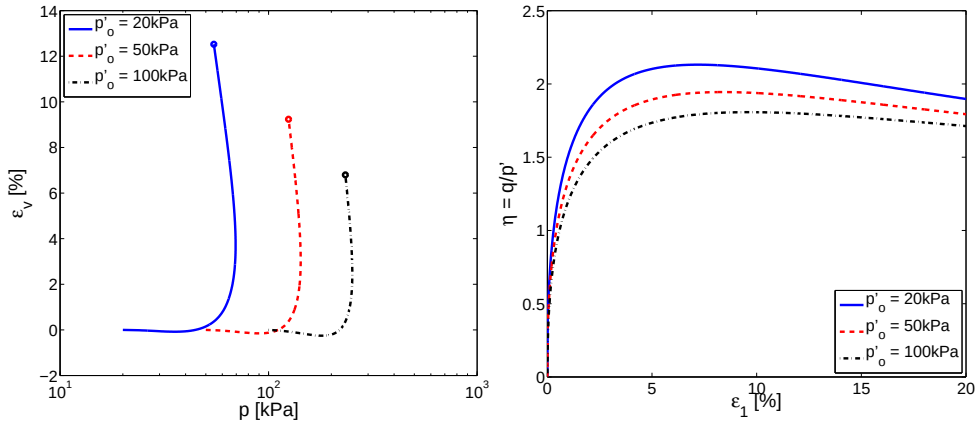

(a) (b)

Figure G.33: Simulated drained triaxial tests. a) $\varepsilon_v - p'$; b) $\eta - \varepsilon_1$.

Undrained triaxial tests

Figures G.34 and G.35 show the response obtained by the model in simulated undrained triaxial tests. The response is showed in the $q - \varepsilon_1$, $q - p'$, $\Delta U - \varepsilon_1$ and $\eta - \varepsilon_1$ planes.

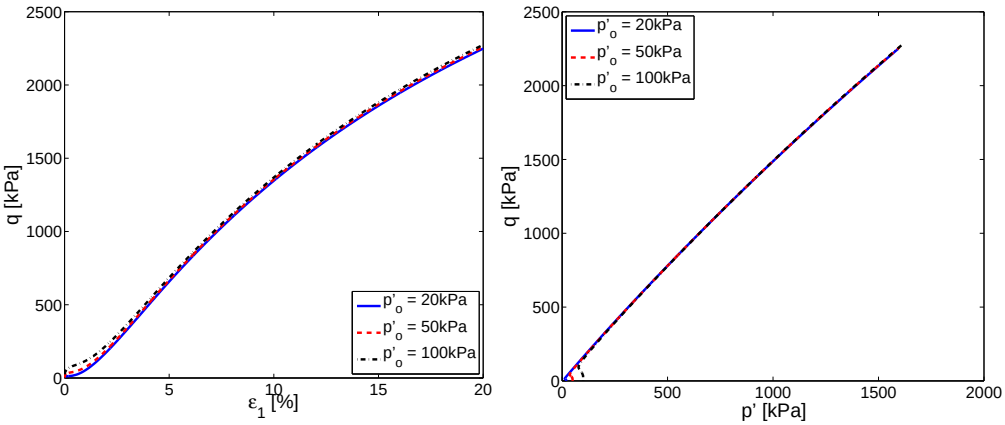

Figure G.34: Simulated undrained triaxial tests. a) $q - \varepsilon_1$; b) $q - p'$.

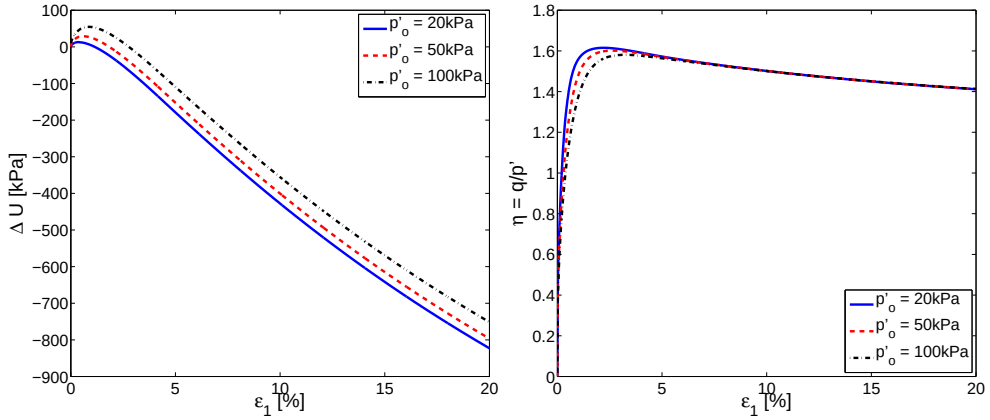

Figure G.35: Simulated undrained triaxial tests. a) $\Delta U - \varepsilon_1$; b) $\eta - \varepsilon_1$.

Consolidation tests

Figure G.36 shows the simulated response of cyclic isotropic and oedometric consolidation tests.

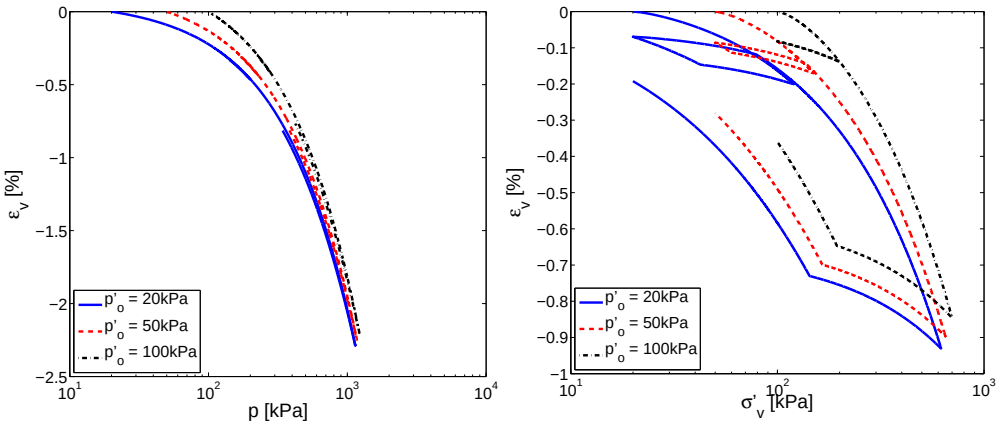

(a) (b)

Figure G.36: Simulated cyclic tests. a) Isotropic consolidation. b) Oedometric consolidation.

Drained cyclic strain-controlled shear test

Figures G.37 and G.38 show the simulated response of drained cyclic strain-controlled shear tests. The obtained $G/G_{max} - \gamma$ and $D - \gamma$ curves are compared to the reference curves given by Seed et al. (1986).

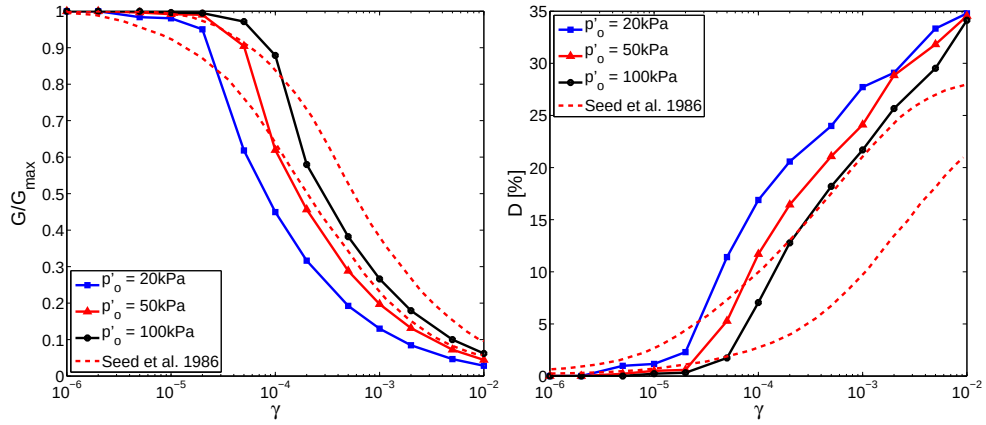

(a) (b)

Figure G.37: Simulated drained cyclic shear test. a) $G/G_{max} - \gamma$; b) $D - \gamma$ curves.

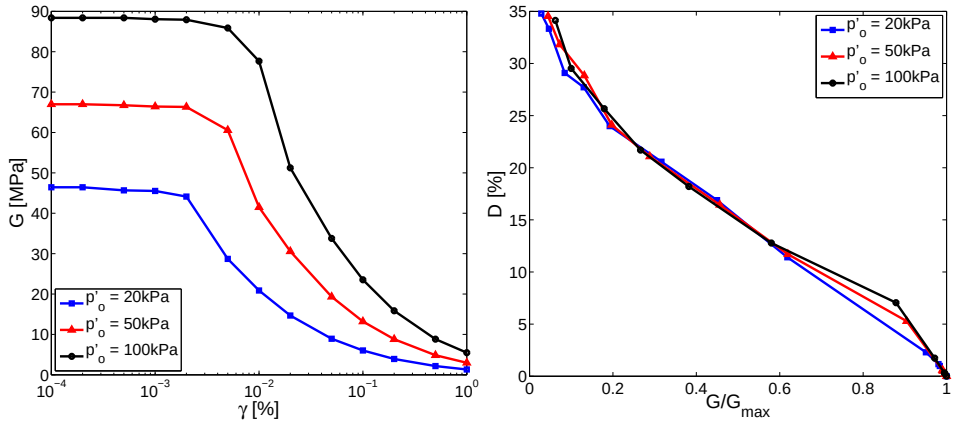

(a) (b)

Figure G.38: Simulated drained cyclic shear test. a) $G-\gamma$; b) $G/G_{max}-D$ curves.

Appendix H

Mechanical interfaces

The interface model is defined in order to take into account discontinuities over the soil-structure interface Σ_{bs}. They are defined in terms of relative displacements and increments of the stress vector in both normal and tangential directions. It is supposed that both the soil domain Ω_s and the structure domain Ω_b are initially in contact and small-strains hypothesis. In terms of the relative displacements, it can be written as:

$$\begin{aligned} [u_n] &= [\underline{u}].\underline{n} \\ [\underline{u_t}] &= [\underline{u}] - [u_n]\underline{n} \end{aligned} \tag{H.1}$$

where $[u_n]$ is the relative gap in the normal direction, $[\underline{u_t}]$ is the relative slide in the tangential direction and $\underline{n}$ is the normal vector over the interface oriented from Ω_b to Ω_s.

In terms of stresses at the interface, considering the effective stress tensor $\underline{\underline{\sigma}}'$ with respect to the interface, the normal σ_n and tangential $\underline{\sigma_t}$ stresses can be obtained as:

$$\begin{aligned} \sigma_n &= \underline{n}.\underline{\underline{\sigma}}'.\underline{n} \\ \underline{\sigma_t} &= \underline{\underline{\sigma}}'.\underline{n} - \sigma_n\underline{n} \end{aligned} \tag{H.2}$$

Three kinematical constrains must be satisfied:

1. Noninterpenetration criterion
$$[u_n] \geq 0$$

2. Uplift and free-surface criterion
$$\text{If } [u_n] > e_{ini} \quad \rightarrow \quad \underline{\underline{\sigma}}.\underline{n} = \underline{0}$$
where e_{ini} is the initial thickness of the interface. The e_{ini} parameter can also be viewed as a regularization parameter, as small fluctuations of the displacement field at the interface lower than this threshold does not lead to uplift.

3. Contact-compression criterion
$$\text{If } [u_n] \leq e_{ini} \quad \rightarrow \quad \sigma_n = 0 \text{ and } |\underline{\sigma_t}| \neq \underline{0}$$
where the operator $|\cdot|$ denotes the modulus.

An elastic perfectly plastic Mohr-Coulomb failure criterion is chosen in order to link the stress field and the displacement field at the interface. From the elastoplasticity framework, the normal and tangential jump increments can be decomposed in elastic and plastic contributions as follows:

$$\begin{aligned}[\dot{u}_n] &= [\dot{u}_n^e] + [\dot{u}_n^p] \\ [\underline{\dot{u}}_t] &= [\underline{\dot{u}}_t^e] + [\underline{\dot{u}}_t^p]\end{aligned} \tag{H.3}$$

where the superscript e denotes elastic contribution and p the plastic contribution. The elastic displacement increments are related to the stress field increments as follows:

$$\begin{aligned}\dot{\sigma}_n &= E[\dot{u}_n^e] \\ \underline{\dot{\sigma}}_t &= G[\underline{\dot{u}}_t^e]\end{aligned} \tag{H.4}$$

where E and G are the normal stiffness and tangent stiffness modulus of the interface. These can be also viewed as penalization parameters, in order to regularize the stress jump appearing from the noninterpenetration criterion. The plastic contribution is obtained from the Mohr-Coulomb failure criterion. Normal σ_n and tangential $\underline{\sigma}_t$ stresses are linked as follows:

$$|\underline{\sigma}_t| \leq |\sigma_n| \tan\phi + c \tag{H.5}$$

where ϕ is the friction angle and c is the cohesion of the interface. From these criteria, two kinematical situations may occur once contact is verified at the interface ($[u_n] \leq e_{ini}$):

- No plastic sliding condition:

$$\text{If } |\underline{\sigma}_t| < |\sigma_n| \tan\phi + c \rightarrow [\underline{\dot{u}}_t^p] = \underline{0} \text{ and } [\underline{\dot{u}}_n^p] = 0$$

- Plastic sliding condition:

$$\text{If } |\underline{\sigma}_t| = |\sigma_n| \tan\phi + c \quad \rightarrow \quad \exists \dot{\lambda}^p \geq 0 \text{ t.q.}$$

$$\begin{aligned}[\underline{\dot{u}}_t^p] &= \dot{\lambda}^p \frac{\underline{\sigma}_t}{|\underline{\sigma}_t|} \\ [\underline{\dot{u}}_n^p] &= \dot{\lambda}^p \tan\psi\end{aligned} \tag{H.6}$$

  where $\dot{\lambda}^p$ is the plastic multiplier, $\dot{\lambda}^p \leq 0$, and ψ is the dilatancy angle of the interface. Taking ψ=0 completely decouples the vertical and tangential response. The model is considered associated when ψ=ϕ.

The plastic multiplier $\dot{\lambda}^p$ is obtained by the following expression:

$$\dot{\lambda}^p = \frac{\frac{G}{|\underline{\sigma}_t|}(\underline{\sigma}_t.[\underline{\dot{u}}_t]) + E[\dot{u}_n]\tan\phi}{G + E\tan\phi\tan\psi} \tag{H.7}$$

Parameter	Description	Considered value
E [MPa]	Normal stiffness modulus	870 MPa
G [MPa]	Tangent stiffness modulus	5 Pa
ϕ [°]	Friction angle	10°
ψ [°]	Dilatancy angle	0°
c [MPa]	Interface cohesion	1 kPa
e_{ini} [m]	Interface thickness	0.01 mm

Table H.1: Parameters of the interface model with an elastic perfectly plastic Mohr-Coulomb failure criterion.

Table H.1 summarizes the necessary model parameters for the the presented formulation.

Bibliography

Adam, D., Brandl, H., and Paulmichl, I. (2010). Dynamic aspects of rail tracks for high-speed railways. *International Journal of Pavement Engineering*, 11(4):281–291.

Al Shaer, A., Duhamel, D., Sab, K., Foret, G., and Schmitt, L. (2008). Experimental settlement and dynamic behavior of a portion of ballasted railway track under high speed trains. *Journal of Sound and Vibration*, 316(1-5):211–233.

Alias, J. (1984). *La voie ferrée*. Eyrolles.

Alonso, E., Pinyol, N., and Gens, A. (2013). Compacted soil behaviour: initial state, structure and constitutive modelling. *Géotechnique*, 63(6):463–478.

Amini, F. (2003). Potential applications of dynamic and static cone penetrometers in MDOT pavement design and construction. Technical Report September, Jackson State University.

Andersen, L. and Nielsen, S. (2003). Vibrations of a track caused by variation of the foundation stiffness. *Probabilistic Engineering Mechanics*, 18(2):171–184.

Ang, K. K. and Dai, J. (2013). Response analysis of high-speed rail system accounting for abrupt change of foundation stiffness. *Journal of Sound and Vibration*, 332(12):2954–2970.

Ansari, M., Esmailzadeh, E., and Younesian, D. (2011). Frequency analysis of finite beams on nonlinear Kelvin-Voight foundation under moving loads. *Journal of Sound and Vibration*, 330(7):1455–1471.

Apsel, R. J. and Luco, J. E. (1983). On the Green's functions for a layered half-space. Part II. *Bulletin of Seismological Society of America*, 73:931–951.

Araújo, N. M. F. (2010). *High-speed trains on ballasted railway track - Dynamic stress field analysis*. PhD thesis, Universidade do Minho.

Arbaoui, H. (2005). *Mesure de la déformabilité du sol en place avec un pénétromètre*. PhD thesis, Université Blaise Pascal - Clermont-Ferrand II.

AREMA (2002). Manual for railway engineering - Sect. 2.4.4, Gradations. Technical report.

Aubry, D., Baroni, A., Cloteau, D., Fodil, A., and Modaressi, A. (1999). Modélisation du comportement du ballast en voie. In *12th International Conference on Soil Mechanics and Foundation Engineering, Vol. 3*, pages 1733–1736.

Aubry, D., Chouvet, D., Modaressi, A., and Modaressi, H. (1986). GEFDYN: Logiciel d'Analyse de Comportement Mécanique des Sols par Eléments Finis avec Prise en Compte du Couplage Sol-Eau-Air. Technical report, Ecole Centrale Paris, LMSS-Mat.

Aubry, D., Hujeux, J.-C., Lassoudière, F., and Meimon, Y. (1982). A double memory model with multiple mechanisms for cyclic soil behaviour. In *Int. Symp. Num. Mod. Geomech.*, pages 3–13. Balkema.

Aubry, D. and Modaressi, A. (1996). GEFDYN, Manuel Scientifique. Technical report, Ecole Centrale Paris, LMSS-Mat.

Auersch, L. (2008). The effect of critically moving loads on the vibrations of soft soils and isolated railway tracks. *Journal of Sound and Vibration*, 310(3):587–607.

Aursudkij, B. (2007). *A Laboratory Study of Railway Ballast Behaviour under Traffic Loading and Tamping Maintenance*. PhD thesis, University of Nottingham.

Azéma, E. (2007). *Etude numérique des matériaux granulaires à grains polyédriques : rhéologie quasi-statique, dynamique vibratoire, application au procédé de bourrage du ballast*. PhD thesis, Université de Montpellier 2.

Bachelier, M. and Parez, L. (1965). Contribution à l'étude de la compressibilité des sols à l'aide du pénétromètre à cône. In *6ème Congrès International de Mécanique des Sols et des Travaux de Fondations*, pages 3–7, Montreal. University of Toronto Press.

Baessler, M. and Ruecker, W. (2003). Track settlement due to cyclic loading with low minimum pressure and vibrations. In *System Dynamics and Long-Term behaviour of Railway Vehicles, Track and Subgrade*, pages 337–356.

Balay, J., Gomes-Correia, A., Jouve, P., Hornych, P., and Paute, J.-L. (1998). Etude expérimentale et modélisation du comportement mécanique des graves non traitées et des sols supports de chaussées. Dernières avancées. *Bulletin des laboratoires des Ponts et Chaussées*, 216:3–18.

Balmès, E. (1996). Use of generalized interface degrees of freedom in component mode synthesis. In *XIV International Modal Analysis Conference*, Dearborn.

Bamberger, A., Engquist, B., Halpern, L., and Joly, P. (1988). Parabolic wave equations approximations in heterogeneous media. *Journal of Applied Mathematics*, 48(1):99–128.

Banimahd, M. (2008). *Advanced Finite Element Modelling of coupled train-track systems: A geotechnical perspective*. PhD thesis, Heriot-Watt University.

Barksdale, R. D. (1972). Laboratory evaluation of rutting in base course materials. In *3rd International Conference on Structural Design of Asphalt Pavements*, pages 161–174, London, UK.

Bellotti, R., Ghionna, V., Jamiolkowski, M., and Robertson, P. K. (1989). Shear strength of sand from CPT. In *12th International Conference on Soil Mechanics and Foundation Engineering, Vol. 1*, pages 179–184, Rio de Janeiro.

Berenger, J. (1994). A perfectly matched layer for the absorption of electromagnetic waves. *Journal of Computational Physics*, 114(2):185–200.

Berenguer Todo Bom, L. A. (2014). *Numerical modelling of soil-pile interaction considering grain breakage in finite deformations*. PhD thesis, Ecole Centrale Paris / Instituto Superior Técnico de Lisboa.

Berggren, E. G. (2005). *Dynamic Track Stiffness Measurements - A new tool for Condition Monitoring of Track Substructure*. PhD thesis, KTH Royal Institute of Technology.

Berggren, E. G., Kaynia, A. M., and Dehlbom, B. (2010). Identification of substructure properties of railway tracks by dynamic stiffness measurements and simulations. *Journal of Sound and Vibration*, 329(19):3999–4016.

Beskou, N. D. and Theodorakopoulos, D. D. (2011). Dynamic effects of moving loads on road pavements: A review. *Soil Dynamics and Earthquake Engineering*, 31(4):547–567.

Bettes, P. (1992). *Infinite Elements*. Penshaw Press.

Bhavsar, V. C., Lambrou, L. A., Horton, J. D., and Gujar, U. G. (1987). Evaluation of the discrepancy of the linear congruential pseudo-random number sequences. Technical Report October, University of New Brunswick, Fredericton, New Brunswick, Canada.

Biarez, J. and Hicher, P.-Y. (1994). *Elementary Mechanics of Soil Behaviour*. A. A. Balkema.

Biot, A. M. (1937). Bending of an Infinite Beam on Elastic Foundation. *Journal of Applied Mechanics*, 4:A1–A7.

Bodin, V. (2001). *Comportement du ballast des voies ferrées soumises à un chargement vertical et lateral*. PhD thesis, Ecole Nationale des Ponts et Chaussées.

Bolton, M. D. and Wilson, J. M. R. (1989). An experimental and theoretical comparison between static and dynamic torsional soil tests. *Géotechnique*, 39(4):585–599.

Bolton, M. D. and Wilson, J. M. R. (1990a). Discussion - An experimental and theoretical comparison between static and dynamic torsional soil tests. *Géotechnique*, 40(4):659–664.

Bolton, M. D. and Wilson, J. M. R. (1990b). Soil stiffness and damping. In *International Conference on Structural Dynamics*, pages 209–216, Bochum, Gemrany.

Bonnans, J.-F., Gilbert, J. C., Lemaréchal, C., and Sagastizabal, C. A. (2006). *Numerical optimization*. Springer.

Boyce, J. R. (1980). A non-linear model for the elastic behaviour of granular materials under repeated loading. In *International Symposium on Soils under cyclic and transient loading*, pages 285–294, Swansea, UK.

Brecciaroli, F. and Kolisoja, P. (2006). Deformation behaviour of railway embankment materials under repeated loading. Technical report, Finnish Rail Administration, Helsinki.

Bressolette, P., Fogli, M., and Chauvière, C. (2010). A stochastic collocation method for large classes of mechanical problems with uncertain parameters. *Probabilistic Engineering Mechanics*, 25(2):255–270.

Brough, M., Ghataora, G., Stirling, A., Madelin, K., Rogers, C., and Chapman, D. (2003). Investigation of railway track subgrade. Part 1: In situ assessment. *Proceedings of the Institute of Civil Engineering Transportation*, 156(3):145–154.

Brough, M., Ghataora, G., Stirling, A., Madelin, K., Rogers, C., and Chapman, D. (2006). Investigation of railway track subgrade. Part 2: case study. *Proceedings of the Institute of Civil Engineering Transportation*, 159(2):83–92.

Brown, S. F. (1974). Repeated load testing of granular materials. *Journal of Geotechnical Engineering Division*, 100:825–841.

Brown, S. F. (1996). Soil mechanics in pavement engineering. *Géotechnique*, 46(3):383–426.

Brown, S. F. and Hyde, A. F. L. (1975). Significance of cyclic confining stress in repeated-load triaxial testing of granular material. *Transportation Research Record*, 537:49–58.

Brown, S. F. and Pappins, J. W. (1985). Modeling of granular materials in pavements. *Transportation Research Record*, 1022:45–51.

Buisman, A. S. K. (1940). *Groundmechanica*. Waltman, Delft.

Caflisch, R. E. (1998). Monte Carlo and quasi-Monte Carlo methods. *Acta Numerica*, 7:1–49.

Cai, Y., Cao, Z., Sun, H., and Xu, C. (2010). Effects of the dynamic wheel-rail interaction on the ground vibration generated by a moving train. *International Journal of Solids and Structures*, 47(17):2246–2259.

Cai, Y., Sun, H., and Xu, C. (2008). Response of railway track system on poroelastic half-space soil medium subjected to a moving train load. *International Journal of Solids and Structures*, 45(18-19):5015–5034.

Caicedo, B., Ocampo, M., Vallejo, L., and Monroy, J. (2012). Hollow cylinder apparatus for testing unbound granular materials of pavements. *Road Materials and Pavement Design*, 13(3):455–479.

Canou, J., Benahmed, N., Dupla, J.-C., and De Gennaro, V. (2002). Instabilités de liquéfaction et phénomène de mobilité cyclique dans les sables. *Revue Française de Géotechnique*, 98:29–46.

Carter, F. W. (1916). The electric locomotive. *Minutes of the Proceedings*, 201:221–252.

Cassan, M. (1988). Réalisations et interprétations. In *Les essais in situ en mécanique des sols. 1 - Réalisation et Interprétation*, pages 509–573. Eyrolles, Paris, 2ème edition.

Çelebi, E. and Göktepe, F. (2012). Non-linear 2-D FE analysis for the assessment of isolation performance of wave impeding barrier in reduction of railway-induced surface waves. *Construction and Building Materials*, 36:1–13.

Cekerevac, C., Girardin, S., Klubertanz, G., and Laloui, L. (2006). Calibration of an elasto-plastic constitutive model by a constrained optimisation procedure. *Computers and Geotechnics*, 33(8):432–443.

Chaigneau, L. (2001). *Caractérisation des milieux granulaires de surface à l'aide d'un pénétromètre*. PhD thesis, Université Blaise Pascal - Clermont-Ferrand II.

Chaigneau, L., Bacconnet, C., and Gourvès, R. (2000). Penetration test coupled with geotechnical classification for compacting control. In *International Conference on Geotechnical and Geotechnical Engineering*, Melbourne, Australia.

Chan, F. W. K. (1990). *Permanent deformation resistance of granular layers in pavements*. PhD thesis, University of Nottingham.

Chan, F. W. K. and Brown, S. F. (1994). Significance of principal stress rotation in pavements. In *13th International Conference on Soil Mechanics and Foundation Engineering*, pages 1823–1826, New Delhi, Inde.

Chang, K.-T., Ge, L., and Sture, S. (2012). Evaluation of the Stiffness and Volumetric Behaviors of Medium Dense Sand under Principal Stress Rotations. *Journal of Testing and Evaluation*, 38(3):1–5.

Chazallon, C., Hornych, P., and Mouhoubi, S. (2006). Elastoplastic Model for the Long-Term Behavior Modeling of Unbound Granular Materials in Flexible Pavements. *International Journal of Geomechanics*, 6(4):279–289.

Chebli, H., Clouteau, D., and Schmitt, L. (2008). Dynamic response of high-speed ballasted railway tracks : 3D periodic model and in situ measurements. *Soil Dynamics and Earthquake Engineering*, 28(2):118–131.

Chebli, H., Othman, R., and Clouteau, D. (2006). Response of periodic structures due to moving loads. *Comptes Rendus Mécanique*, 334(6):347–352.

Chen, C., Mcdowell, G. R., and Thom, N. H. (2013). A study of geogrid-reinforced ballast using laboratory pull-out tests and discrete element modelling. *Geomechanics and Geoengineering: An International Journal*, 8(4):244–253.

Christie, D., Lackenby, J., Indraratna, B., and McDowell, G. (2007). Effect of confining pressure on ballast degradation and deformation under cyclic triaxial loading. *Géotechnique*, 57(6):527–536.

Chua, K. M. (1988). Determination of CBR and elastic modulus of soils using a portable pavement dynamic cone penetrometer. In Ruiter, D., editor, *1st International Symposium on Penetration Testing, ISOPT-1*, pages 407–414, Orlando. Balkema.

Clouteau, D., Arnst, M., Alhussaini, T., and Degrande, G. (2005). Freefield vibrations due to dynamic loading on a tunnel embedded in a stratified medium. *Journal of Sound and Vibration*, 283(1-2):173–199.

Clouteau, D., Cottereau, R., and Lombaert, G. (2013). Dynamics of structures coupled with elastic media - A review of numerical models and methods. *Journal of Sound and Vibration*, 332(10):2415–2436.

Connolly, D., Giannopoulos, A., and Forde, M. C. (2013). Numerical modelling of ground borne vibrations from high speed rail lines on embankments. *Soil Dynamics and Earthquake Engineering*, 46:13–19.

Connolly, D. P., Kouroussis, G., Giannopoulos, A., and Verlinden, O. (2014). Assessment of railway vibrations using an efficient scoping model. *Soil Dynamics and Earthquake Engineering*, 58:37–47.

Coonse, J. W. (1999). *Estimating California Bearing Ratio of cohesive Piedmont residual soil using the Scala dynamic cone penetrometer*. Msc. thesis, The North Carolina State University.

Coronado Garcia, O. (2005). *Etude du comportement mécanique de matériaux granulaires compactés non saturés sous chargement cyclique*. PhD thesis, Ecole Centrale Paris.

Costa, P. A., Calc, R., and Cardoso, A. S. (2012a). Track-ground vibrations induced by railway traffic: In-situ measurements and validation of a 2.5D FEM-BEM model. *Soil Dynamics and Earthquake Engineering*, 32(1):111–128.

Costa, P. A., Calçada, R., and Cardoso, A. S. (2012b). Ballast mats for the reduction of railway traffic vibrations . Numerical study. *Soil Dynamics and Earthquake Engineering*, 42:137–150.

Costa, P. A., Calçada, R., Cardoso, A. S., and Bodare, A. (2010). Influence of soil nonlinearity on the dynamic response of high-speed railway tracks. *Soil Dynamics and Earthquake Engineering*, 30(4):221–235.

Costa d'Aguiar, S. (2008). *Numerical modelling of soil-pile axial load transfer mechanisms in granular soils*. PhD thesis, Ecole Centrale Paris / Instituto Superior Técnico de Lisboa.

Cottereau, R., Costa d'Aguiar, S., Quezada, J. C., Perales, R., and Saussine, G. (2011). Stochastic continuum modeling of the ballast. In *9th World Congress on Railway Research - May 22-26*, Lille.

Cui, Y.-J., Lamas-lopez, F., Nam, V., Calon, N., Costa, S., Aguiar, D., Dupla, J.-C., Minh, A., Canou, J., and Robinet, A. (2014). Investigation of interlayer soil behaviour by field monitoring. *Transportation Geotechnics*, 1(3):91–105.

Cukier, R. I., Fortuin, C. M., Shuler, K. E., Petschek, A. G., and Schaibly, J. H. (1973). Study of the sensitivity of coupled reaction systems to uncertainties in rate coefficients. I Theory. *Chemical Physics*, 59(8):3873–3878.

Cukier, R. I., Levine, H. B., and Shuler, K. E. (1978). Nonlinear sensitivity analysis of multiparameter model systems. *Journal of Computational Physics*, 26:1–42.

Cundall, P. A. and Strack, O. D. L. (1979). A discrete numerical model for granular assemblies. *Géotechnique*, 29(1):47 – 65.

Cunha, J. (2013). *Modelling of ballasted railway tracks for high-speed trains*. PhD thesis, Universidade do Minho.

Dahlberg, T. (2010). Railway Track Stiffness Variations - Consequences and Countermeasures. *International Journal of Civil Engineering*, 8(1):1–12.

Delage, P. and Cui, Y.-J. (2001). Comportement mécanique des sols non saturés. *Techniques de l'Ingénieur*, Constructi(C302):1–19.

Desai, C. S. and Siriwardane, H. J. (1982). Numerical models for track support structures. *Journal of the Geotechnical Engineering Division*, 108(3):461 – 480.

Dieterman, H. A. and Metrikine, A. V. (1996). The equivalent stiffness of a half space interacting with a beam. Critical velocities of a moving load along the beam. *European Journal Mechanics A/Solids*, 15(1):67–90.

Dieterman, H. A. and Metrikine, A. V. (1997). Steady-state displacements of a beam on an elastic half-space due to a uniformly moving constant load. *European Journal Mechanics A/Solids*, 16(2):295–306.

Dimitrovová, Z. and Varandas, J. (2009). Critical velocity of a load moving on a beam with a sudden change of foundation stiffness: Applications to high-speed trains. *Computers & Structures*, 87(19-20):1224–1232.

Donzé, F. V., Richefeu, V., and Magnier, S.-A. (2009). Advances in Discrete Element Method Applied to Soil , Rock and Concrete Mechanics. *Electronic Journal of Geotechnical Engineering*, pages 1–44.

Duong, T. V., Cui, Y.-J., Minh, A., Dupla, J.-C., Canou, J., Calon, N., and Robinet, A. (2014a). Investigating the mud pumping and interlayer creation phenomena in railway sub-structure. *Engineering Geology*, 171:45–58.

Duong, T. V., Cui, Y.-J., Tang, A. M., Calon, N., and Robinet, A. (2014b). Assessment of conventional French railway sub-structure : a case study. *Bulletin of Engineering Geology and the Environment*, pages 1–12.

Duong, T. V., Tang, A. M., Cui, Y.-J., Trinh, V. N., Dupla, J.-C., Calon, N., Canou, J., and Robinet, A. (2013). Effects of fines and water contents on the mechanical behavior of interlayer soil in ancient railway sub-structure. *Soil and Foundations*, 53(6):868–878.

Ekberg, A. and Paulsson, B. (2010). INNOTRACK - Concluding Technical Report. Technical report, International Union of Railways, Paris.

El Kacimi, A., Woodward, P., Laghrouche, O., and Medero, G. (2012). Time domain 3D finite element modelling of train-induced vibration at high speed. *Computers & Structures*, 118:66–73.

Elkateb, T., Chalaturnyk, R., and Robertson, P. K. (2003). An overview of soil heterogeneity: quantification and implications on geotechnical field problems. *Canadian Geotechnical Journal*, 40(1):1–15.

Engquist, B. and Majda, A. (1977). Absorbing boundary conditions for numerical simulation of waves. *Mathematics of Computation*, 31(139):629–651.

Ese, D., Myre, J., Noss, P. M., and Vaernea, E. (1994). The use of dynamic cone penetrometer (DCP) for road strengthening design in Norway. In *International Conference on Bearing Capacity of Roads and Airfield*, pages 3–22.

Estorff, O. V. and Hagen, C. (2005). Iterative coupling of FEM and BEM in 3D transient elastodynamics. *Engineering Analysis with Boundary Elements*, 29:775–787.

Faure, H. (1982). Discrépance de suites associées à un système de numérotation (en dimension s). *Acta Arithmetica*, 41:337–351.

Ferellec, J.-F. and McDowell, G. R. (2012). Modelling of ballast-geogrid interaction using the discrete-element method. *Geosynthetics International*, 19(6):470–479.

Ferreira, J. N. V. d. S. (2013). *Long-term behavior of railway transitions under dynamic loading*. PhD thesis, Universidade Nova de Lisboa.

Ferreira, P. A. A. D. (2010). *Modelling and prediction of the dynamic behaviour of railway infrastructures at very high speeds*. PhD thesis, Instituto Superior Técnico de Lisboa.

Fortin, J. P. (1983). Dynamic Track Deformation. *French Railway Review*, 1(1):3–12.

Fortunato, E. (2005). *Renovação de plataformas ferroviarias - Estudos relativos à capacidade de carga*. PhD thesis, Universidade do Porto, Portugal.

Fortunato, E., Pinelo, A., and Fernandes, M. M. (2010). Characterization of the fouled ballast layer in the substructure of a 19th century railway track under renewal. *Soils and Foundations*, 50(1):55–62.

François, S., Schevenels, M., Galvín, P., Lombaert, G., and Degrande, G. (2010). A 2.5D coupled FE-BE methodology for the dynamic interaction between longitudinally invariant structures and a layered halfspace. *Computer Methods in Applied Mechanics and Engineering*, 199:1536–1548.

Frohling, R. D. (1997). *Deterioration of railway track due to dynamic vehicle loading and spatially varying track stiffness*. PhD thesis, University of Pretoria, South Africa.

Fryba, L. (1972). *Vibration of solids and structures under moving loads*. ThomasTelford.

Fryba, L., Nakagiri, S., and Yoshikawa, N. (1993). Stochastic finite elemens for a beam on a random foundation with uncertain damping under a moving force. *Journal of Sound and Vibration*, 163:31–45.

Fukushima, S. and Tatsuoka, F. (1984). Strength and deformation characteristics of saturated sand at extremely low pressures. *Soils and Foundations*, 24(4):30–48.

Galvín, P. and Domínguez, J. (2009). Experimental and numerical analyses of vibrations induced by high-speed trains on the Córdoba-Málaga line. *Soil Dynamics and Earthquake Engineering*, 29(4):641–657.

Galvín, P., François, S., Schevenels, M., Bongini, E., Degrande, G., and Lombaert, G. (2010a). A 2.5D coupled FE-BE model for the prediction of railway induced vibrations. *Soil Dynamics and Earthquake Engineering*, 30(12):1500–1512.

Galvín, P., Romero, A., and Domínguez, J. (2010b). Fully three-dimensional analysis of high-speed train-track-soil-structure dynamic interaction. *Journal of Sound and Vibration*, 329(24):5147–5163.

Gamboa, C. J. N. (2011). *Mechanical behavior of rockfill materials. Application to concrete face rockfill dams*. PhD thesis, Ecole Centrale Paris.

Gao, G. Y., Chen, Q. S., He, J. F., and Liu, F. (2012). Investigation of ground vibration due to trains moving on saturated multi-layered ground by 2.5D finite element method. *Soil Dynamics and Earthquake Engineering*, 40:87–98.

Ghanem, R. G. and Spanos, P. D. (1991). *Stochastic Finite Elements: A spectral approach*. Springer-Verlag.

Gidel, M. G. (2001). *Comportement et valorisation des graves non-traitées calcaires utilisées pour les assises de chaussées souples*. PhD thesis, Université de Bordeaux I.

Gourvès, R. (1991). Le PANDA - pénétromètre dynamique léger à énergie variable. Technical report, LERMES CUST, Université Blaise Pascal, Clermont-Ferrand.

Grabe, P. J. and Clayton, C. R. I. (2009). Effects of Principal Stress Rotation on Permanent Deformation in Rail Track Foundations. *Journal of Geotechnical and Geoenvironmental Engineering*, 135(4):555.

Griffiths, D. V., Huang, J., and Fenton, G. A. (2009). Influence of Spatial Variability on Slope Reliability Using 2-D Random Fields. *Journal of Geotechnical and Geoenvironmental Engineering*, 135(10):1367.

Grigoriu, M. (1984). Crossings of non-Gaussian translation processes. *Journal of Engineering Mechanics*, 100:610–620.

Haddani, Y., Saussine, G., Breul, P., Navarrete, M. B., and Gourvès, R. (2011). Estimation de la portance et de la raideur des plateformes ferroviaires par couplage d'essai Panda et géondoscope. In *Symposium International GEORAIL*, Paris, France.

Hall, L. (2003). Simulations and analyses of train-induced ground vibrations in finite element models. *Soil Dynamics and Earthquake Engineering*, 23:403–413.

Halton, J. H. (1960). On the efficiency of a certain quasi-random sequences of points in evaluating multi-dimensional integrals. *Numerical Mathematics*, 2(2):84–90.

Hardin, B. O. and Drnevich, V. P. (1972). Shear modulus and damping in soils: design equations and curves. *Journal of Soil Mechanics*, 98(SM7):667 – 692.

Harison, J. A. (1987). Correlation between California Bearing Ratio and Dynamic Cone Penetrometer strength measurement of soils. *Institution of Civil Engineers Proceedings*, 83(4):833 – 844.

Haskell, N. (1953). The dispersion of surface waves on multilayered media. *Bulletin of Seismological Society of America*, 73:17–43.

Heelis, M., Dawson, A., Collop, A., Chapman, D., and Krylov, V. (1999). Resilient Modulus of Soft Soil Beneath High-Speed Rail Lines. *Transportation Research Record*, 1687(3):39–46.

Helton, J., Johnson, J., Sallaberry, C., and Storlie, C. (2006). Survey of sampling-based methods for uncertainty and sensitivity analysis. *Reliability Engineering & System Safety*, 91(10-11):1175–1209.

Hertz, H. (1896). On the contact of elastic solids. In *Miscellaneous Papers*, pages 146–162.

Heukelom, W. and Klomp, A. J. G. (1962). Dynamic testing as a means of controlling pavements during and after construction. In *First International Conference on the Structural Design of Asphalt Pavements*, pages 667–697, Ann Arbor, Michigan.

Hicks, R. G. (1970). *Factors influencing the resilient properties of granular materials*. PhD thesis, University of California.

Hoang, T. M. P., Saussine, G., Dureisseix, D., and Alart, P. (2012). Domain decomposition with discrete element simulations using shared- memory parallel computing for railways applications. *European Journal Of Computational Mechanics*, 21(3-6):242 – 253.

Hogg, R. V. and Craig, A. T. (1995). *Introduction to mathematical statistics*. Prentice Hall.

Homma, T. and Saltelli, A. (1996). Importance measures in global sensitivity analysis of non linear models. *Reliability Engineering and System Safety*, 55:1–17.

Hornych, P., Kazai, A., and Piau, J. M. (1998). Study of the resilient behaviour of unbound granular materials. In *5th International Conference on the Bearing Capacity of Roads and Airfields*, pages 1277–1287, Trondhein, Norway.

Hosseingholian, M., Levacher, D., and Khay, M. (2011). Mesure en continu de la raideur dynamique d une voie ferrée. *Canadian Geotechnical Journal*, 48(3):439–450.

Hughes, T. J. R. (2000). *The Finite Element Method - Linear Static and Dynamic Finite Element Analysis*. Dover Publications.

Hujeux, J. C. (1985). Une loi de comportement pour le chargement cyclique des soils. In Davidovici, V., editor, *Génie Parasismique*, pages 278–302. Presses ENPC, France.

Hung, H. H., Chen, G. H., and Yang, Y. B. (2013). Effect of railway roughness on soil vibrations due to moving trains by 2.5D finite / infinite element approach. *Engineering Structures*, 57:254–266.

Hunt, G. (1994). Analysis of Requirements for Railway Construction os Soft Soils. Technical report, British Railway Report No. LR TM 031. British Railway Research, Derby, U.K.

Huyse, L. and Walters, R. W. (2001). Random Field Solutions Including Boundary Condition Uncertainty for the Steady-state Generalized Burgers Equation. Technical report, NASA/CR-2001-211239, Hampton, Virginia.

Iman, R. L. and Conover, W. J. (1982). A distribution-free approach to inducing rank correlation among input variables. *Communications in Statistics - Simulation and Computation*, 11(3):311–334.

Indraratna, B. and Nimbalkar, S. (2011). Implications of ballast breakage on ballasted railway track based on numerical modeling. In *13th International Conference for Computer Methods and Advances in Geomechanics*, number May, pages 1085–1092, Sydney, Australia.

Indraratna, B., Salim, W., and Rujikiatkamjorn, C. (2011). *Advanced Rail Geotechnology - Ballasted Track*. CRC Press/Balkema.

Ishihara, K. (1993). Liquefaction and flow failure during earthquakes. *Géotechnique*, 43(3):351–415.

Ishihara, K., Tatsuoka, F., and Yasuda, S. (1975). Undrained deformation and liquefaction of sand under cyclic stress. *Soil and Foundations*, 15(1):29–44.

Ishikawa, T., Sekine, E., and Miura, S. (2011). Cyclic deformation of granular material subjected to moving-wheel loads. *Canadian Geotechnical Journal*, 48(5):691–703.

Iwan, W. D. (1966). A distributed element model for hysteresis and its steady state dynamic response. *Journal of Applied Mechanics*, 88(4):893–900.

Iwan, W. D. (1967). On a class of models for the yielding behaviour of continous and composite systems. *Journal of Applied Mechanics*, 89(3):612–617.

Iwasaki, T., Tatsuoka, F., and Takagi, Y. (1978). Shear moduli of sands under cyclic torsional shear loading. *Soils and Foundations*, 18(1):39–56.

Jack, R. and Jackson, P. (1999). Imaging attributes of railway track formation and ballast using ground probing radar. *NDT&E International*, 32(8):457–462.

Jacobsson, L. (1998). Review of research on railway ballast behaviour - Experimental findings and constitutive models. Technical report, Chalmers University of Technology.

Jean, M. and Moreau, J. J. (1992). Unilaterality and dry friction in the dynamics of rigid body collections. In *Contact Mechanics International Symposium*, pages 31–48, Lausanne, Switzerland. Presse Polytechnique et Universitaire Romandes.

Jeffs, T. and Marich, S. (1987). Ballast characteristics in the laboratory. In Barton, editor, *Conference on Railway Engineering*, pages 141–147, Perth, WA, Australia. ACT: Institution of Engineers.

Jeremic, B. and Yang, Z. (2002). Template elastic-plastic computations in geomechanics. *International Journal for Numerical and Analytical Methods in Geomechanics*, 26(14):1407–1427.

Ju, S. H., Ho, Y. S., and Leong, C. C. (2012). A finite element method for analysis of vibration induced by maglev trains. *Journal of Sound and Vibration*, 331:3751–3761.

Ju, S. H. and Li, H. C. (2011). Dynamic interaction analysis of trains moving on embankments during earthquakes. *Journal of Sound and Vibration*, 330(22):5322–5332.

Ju, S. H. and Lin, H. T. (2004). Analysis of train-induced vibrations and vibration reduction schemes above and below critical Rayleigh speeds by finite element method. *Soil Dynamics and Earthquake Engineering*, 24(12):993–1002.

Kaewunruen, S. and Remennikov, A. M. (2009). State dependent properties of rail pads. *Transport Engineering in Australia*, 12(1):17–24.

Kalker, J. J. (1990). *Three-dimensional elastic bodies in rolling contact*. Kluwer Academic Publishers.

Karraz, K. (2008). *Comportement cyclique à long terme d un matériau granulaire modèle pour application aux infrastructures ferroviaires*. PhD thesis, Université Paris-Est.

Katona, M. G. and Zienkiewicz, O. C. (1985). A unified set of single step algorithms Part 3: the Beta-m method, a generalization of the Newmark scheme. *International Journal for Numerical Methods in Engineering*, 21(7):1345–1359.

Kausel, E. and Roesset, J. M. (1981). Stiffness matrices for layered soils. *Bulletin of the Seismological Society of America*, 71(6):1743 – 1761.

Kerschen, G., Golinval, J.-C., Vakakis, A. F., and Bergman, L. A. (2005). The Method of Proper Orthogonal Decomposition for Dynamical Characterization and Order Reduction of Mechanical Systems : An Overview. *Nonlinear Dynamics*, 41:147–169.

Kleiber, M. and Hien, T. D. (1992). *The stochastic finite element method - A basic perturbation technique and computer implementation*. John Wiley & Sons Ltd.

Kleyn, E. G. (1975). The use of dynamic cone penetrometer (DCP). Technical report, Transvl Roads Departement, Pretoria, South Africa.

Knothe, K. L. and Grassie, S. L. (1993). Modelling of Railway Track and Vehicle/track Interaction at High Frequencies. *Vehicle System Dynamics*, 22(3-4):209–262.

Koda, M., McRae, G. J., and Seinfeld, J. H. (1979). Automatic sensitivity analysis of kinetic mechanisms. *International Journal of Chemical Kinetics*, 11(4):427–444.

Kolisoja, P. (1997). *Resilient deformation characteristics of granular materials*. PhD thesis, Tampere University of Technology, Publ. No 223, Tampere, Finland.

Komatitsch, D. and Tromp, J. (2003). A perfectly matched layer absorbing boundary condition for the second-order seismic wave equation. *Geophysical Journal International*, 154(1):146–153.

Korpanec, I., Rebeyrotte, E., Guigon, M., and Tordai, L. (2005). Increasing axle load in Europe - state of art and perspectives. In *8th International Heavy Haul Conference*, pages 227–235, Rio de Janeiro, Brazil.

Kouroussis, G., Gazetas, G., Anastasopoulos, I., Conti, C., and Verlinden, O. (2011a). Discrete modelling of vertical track-soil coupling for vehicle-track dynamics. *Soil Dynamics and Earthquake Engineering*, 31(12):1711–1723.

Kouroussis, G., Parys, L. V., Conti, C., and Verlinden, O. (2011b). Prediction of Environmental Vibrations Induced by Railway Traffic using a Three-Dimensional Dynamic Finite Element Analysis. In Topping, B. H. V. and Tsompanakis, Y., editors, *13th International Conference on Civil, Structural and Environmental Engineering Computing*. Civil-Comp Press.

Kouroussis, G., Verlinden, O., and Conti, C. (2011c). Free field vibrations caused by high-speed lines: Measurement and time domain simulation. *Soil Dynamics and Earthquake Engineering*, 31(4):692–707.

Koutsourelakis, P.-S. and Deodatis, G. (2005). Simulation of Binary Random Fields with Applications to Two-Phase Random Media. *Journal of Engineering Mechanics*, 131(4):397–412.

Koutsourelakis, P.-S. and Deodatis, G. (2006). Simulation of Multidimensional Binary Random Fields with Application to Modeling of Two-Phase Random Media. *Journal of Engineering Mechanics*, 132(6):619–631.

Kramer, S. L. (1996). *Geotechnical Earthquake Engineering*. Prentice-Hall, Upper Saddle River, New Jersey.

Krylov, V. V., Dawson, A. R., Heelis, M. E., and Collop, A. C. (2000). Rail movement and ground waves caused by high-speed trains approaching track-soil critical velocities. *Proceedings of the Institution of Mechanical Engineers, Part F: Journal of Rail and Rapid Transit*, 214(2):107–116.

Kumaran, G., Menon, D., and Nair, K. K. (2003). Dynamic studies of railtrack sleepers in a track structure system. *Journal of Sound and Vibration*, 268(3):485–501.

Kwan, C. C. J. (2006). *Geogrid reinforcement of railway ballast*. PhD thesis, University of Nottingham.

Lade, P. V. (1992). Static instability and liquefaction of loose fine sandy slopes. *Journal of Geotechnical Engineering*, 118(1):51–71.

Lade, P. V. and Ibsen, L. B. (1997). A study of phase transformation and the characteristic lines of sand behaviour. In *International Symposium on Deformation and Progressive Failure in Geomechanics*, pages 353–359, Nagoya, Japan.

Lanier, J., di Prisco, D., and Nova, R. (1991). Etude expérimentale et analyse théorique de l'anisotropie induite dans un sable d'Hostun. *Revue Française de Géotechnique*, 57:59–74.

Le Pen, L. (2008). *Track behaviour: The importance of the sleeper to ballast interface*. PhD thesis, University of Southampton.

Lefeuve-Mesgouez, G. and Mesgouez, A. (2010). Three-dimensional dynamic response of a porous multilayered ground under moving loads of various distributions. *Advances in Engineering Software*, 46(1):75–84.

Lei, X. and Noda, N. A. (2002). Analysis of dynamic response of vehicle and track coupling system with random irregularity of track vertical profile. *Journal of Sound and Vibration*, 258(1):147–165.

Lekarp, F., Isacsson, U., and Dawson, A. (2000a). State of the Art. I: Resilient response of unbound aggregates. *Journal of Transportation Engineering*, 126(1):66–75.

Lekarp, F., Isacsson, U., and Dawson, A. (2000b). State of the art. II: Permanent strain response of unbound aggregates. *Journal of Transportation Engineering*, 126(1):76–83.

Liang, Y. C., Lee, H. P., Lim, S. P., Lin, W. Z., Lee, K. H., and Wu, C. G. (2002). Proper orthogonal decomposition and its applications - Part I: Theory. *Journal of Sound and Vibration*, 252(3):527–544.

Lim, W. L. (2004). *Mechanics of Railway Ballast Behaviour*. PhD thesis, University of Nottingham.

Lim, W. L. and McDowell, G. R. (2005). Discrete element modelling of railway ballast. *Granular Matter*, 7(1):19–29.

Liu, P.-L. and Der Kiureghian, A. (1986). Multivariate distribution models with prescribed marginals and covariances. *Probabilistic Engineering Mechanics*, 1(2):105–112.

Livneh, M. (1987). Validation of correlations between a number of penetration tests and in situ California Bearing Ratio Tests. *Transportation Research Records*, 1219:56–67.

Livneh, M., Ishai, I., and Livneh, N. A. (1992). Automated DCP Device versus manual DCP device. *Road and Transport Reseach*, 1(4):48–61.

Lombaert, G. (2001). *Development and experimental validation of a numerical model for the free field vibrations induced by road traffic*. PhD thesis, Katholieke Universiteit te Leuven.

Lombaert, G., Degrande, G., Kogut, J., and François, S. (2006). The experimental validation of a numerical model for the prediction of railway induced vibrations. *Journal of Sound and Vibration*, 297(3-5):512–535.

Lopez-Caballero, F. (2003). *Influence du Comportement Non-Linéaire du Sol sur les Mouvements Sismiques Induits dans des Géo-Structures*. PhD thesis, Ecole Centrale Paris.

Lopez-Caballero, F., Gaspar, A. P. T., and Gomes-Correia, A. (2011). Uncertainty and Sensitivity Analysis of FWD test. In *GeoHunan International Conference II*, Hunan, China.

Lopez-Caballero, F. and Modaressi-Farahmand-Razavi, A. (2008). Numerical simulation of liquefaction effects on seismic SSI. *Soil Dynamics and Earthquake Engineering*, 28(2):85–98.

Lopez-Caballero, F. and Modaressi-Farahmand-Razavi, A. (2010a). Assessment of variability and uncertainties effects on the seismic response of a liquefiable soil profile. *Soil Dynamics and Earthquake Engineering*, 30(7):600–613.

Lopez-Caballero, F. and Modaressi-Farahmand-Razavi, A. (2010b). Uncertainty and sensitivity analysis of laboratory test simulations using an elastoplastic model. In *7th European Conference on Numerical Methods in Geotechnical Engineering*, pages 131–136.

Luco, J. E. and Apsel, R. J. (1983). On the Green's functions for a layered half-space. Part I. *Bulletin of Seismological Society of America*, 73:909 – 929.

Lunne, T., Robertson, P. K., and Powell, J. J. M. (1997). *Cone penetration testing*. Blackie Academic and Professional.

Luong, M. P. (1980). Phénomènes cycliques dans les sols pulvérulants. *Revue Française de Géotechnique*, 10(1):39 – 53.

Lysmer, J. and Kuhlemeyer, R. L. (1969). Finite Dynamic Model for Infinite Media. *Journal of Engineering Mechanics Division*, 95(EM4):859–877.

Madshus, C. and Kaynia, A. M. (2000). High-Speed Railway Lines on Soft Ground: Dynamic Behaviour At Critical Train Speed. *Journal of Sound and Vibration*, 231(3):689–701.

Martins, J. P. (2011). *Compaction and its influence on the structural behaviour of high speed railways*. PhD thesis, Universidade do Minho.

Meissonnier, F. (2000). European Research for an Optimised Ballasted Track: Final Report, Synthesis Part. Technical report, European Union, Contract number: BRPR-CT97-0455. Project number: BE96-3263.

Miranda, T. F. S. (2007). *Geomechanical Parameters Evaluation in Underground Structures. Artificial Intelligence, Bayesian Probabilities and Inverse Methods.* PhD thesis, Universidade do Minho.

Miura, K., Miura, S., and Toki, S. (1986). Deformation behaviour of anisotropic dense sand under principal stress axes rotation. *Soils and Foundations*, 26(1):36 – 52.

Modaressi, A. and Abou-Bekr, N. (1994). A unified approach to model the behaviour of saturated and unsaturated soils. In *8th International Conference on Computer Methods and Advances in Geomechanics*, pages 1507–1513, Rotterdam. Balkema.

Mohammed, L. N., Titi, H. H., and Herath, A. (2000). Evaluation of resilient modulus of subgrade soil by cone penetration test. *Transportation Research Records*, 1652:236–245.

Mok, Y.-J., Park, I.-B., and Park, C.-S. (2011). Evaluation of Resilient Moduli for Recycled Crushed-Rock-Soil-Mixtures Using Nonlinear Dynamic Properties. In *90th Annual Meeting of the Transportation Research Board*, number January, Washington DC.

NCDOT (1998). Pavement conditions survey manual. Technical report, North Carolina Department of Transportation, Raleigh, N.C.

Nguyen, T. D. (2006). *Modélisation du comportement cyclique des sols. Application aux barrages en terre.* PhD thesis, Ecole Centrale Paris.

Niederreiter, B. Y. H. (1978). Quasi-Monte Carlo methods and pseudo-random numbers. *Bulletin of the American Mathematical Society*, 84(6):957–1041.

Nielsen, J. (1995). Vertical Dynamic Interaction Between Train and Track Influence of Wheel and Track Imperfections. *Journal of Sound and Vibration*, 187(5):825–839.

Nielsen, J., Berggren, E., Lolgen, T., Muller, R., Stallaert, B., and Pesqueux, L. (2013). RIVAS Project. D2.5: Overview of Methods for Measurement of Track Irregularities Important for Ground-Borne Vibration. Technical report.

Nitka, M., Combe, G., Dascalu, C., and Desrues, J. (2011). Two-scale modeling of granular materials: a DEM-FEM approach. *Granular Matter*, 13(3):277–281.

Olhoeft, G. R. and Selig, E. T. (2002). Ground penetrating radar evaluation of railway track substructure conditions. In Lee, S. K. K. and H., editors, *9th International Conference on Ground Penetrating Radar*, pages 48–53, Santa Barbara, CA.

Oscarsson, J. (2002). Dynamic Train-Track Interaction: Variability Attributable to Scatter in the Track Properties. *Vehicle System Dynamics*, 37(1):59–79.

Paderno, C. (2010). *Comportement du ballast sous l'action du bourrage et du trafic ferroviaire.* PhD thesis, Ecole Polytechnique de Lausanne.

Pappin, J. W. and Brown, S. F. (1980). Resilient stress-strain behaviour of crushed rock. In *International Symposium on Soils under cyclic and transient loading*, pages 169–177, Swansea, UK.

Pappin, J. W., Brown, S. F., and O'Reilly, M. P. (1992). Effective stress behaviour of saturated and partially saturated granular material subjected to repeated loading. *Géotechnique*, 42(3):485–497.

Paulsson, B. and Berggren, S. (2005). Introducing heavy haul on existing lines - the swedish approach and experience. In *8th International Heavy Haul Conference*, pages 213–219, Rio de Janeiro, Brazil.

Pender, M. J. (1978). A model for the behaviour of overconsolidated soil. *Géotechnique*, 28(1):1–25.

Perales, R., Saussine, G., Milesi, N., and Radjai, F. (2011). Tamping process optimization. In *9th World Congress on Railway Research - May 22-26*, Lille.

Perrin, G. (2013). *Random fields and associated statistical inverse problems for uncertainty quantification - Application to railway track geometries for high-speed trains dynamical responses and risk assessment*. PhD thesis, Université Paris Est.

Perzyna, P. (1966). Fundamental problems in viscoplasticity. *Recent Advances in Applied Mechanics*, 9:243–377.

Phoon, K.-K. and Kulhawy, F. H. (1999a). Characterization of geotechnical variability. *Canadian Geotechnical Journal*, 36:612 – 624.

Phoon, K.-K. and Kulhawy, F. H. (1999b). Evaluation of geotechnical property variability. *Canadian Geotechnical Journal*, 36:625 – 639.

Popescu, R., Deodatis, G., and Nobahar, A. (2005a). Effects of random heterogeneity of soil properties on bearing capacity. *Probabilistic Engineering Mechanics*, 20:324–341.

Popescu, R., Prevost, J. H., and Deodatis, G. (2005b). 3D effects in seismic liquefaction of stochastically variable soil deposits. *Géotechnique*, 55(1):21–31.

Poulos, S. J. (1981). The steady state of deformation. *Journal of Geotechnical Engineering*, 107(GT5):553 – 562.

Powrie, W., Yang, L. a., and Clayton, C. R. I. (2007). Stress changes in the ground below ballasted railway track during train passage. *Proceedings of the Institution of Mechanical Engineers, Part F: Journal of Rail and Rapid Transit*, 221(2):247–262.

Priest, J., Powrie, W., Grabe, P., Clayton, C., and Yang, L. (2010). Measurements of transient ground movements below a ballasted railway line. *Géotechnique*, 60(9):667–677.

Prisco, C. D. and Zambelli, C. (2003). Cyclic and dynamic mechanical behaviour of granular soils : experimental evidence and constitutive modelling. *Revue Française de Génie Civil*, 7(7-8):881 – 910.

Profillidis, V. (1982). *La voie et sa fondation. Modélisation mathématique.* PhD thesis, ENPC.

Quezada, J. C. (2012). *Mécanismes de tassement du ballast et sa variabilité.* PhD thesis, Université de Montpellier 2.

Raymond, G. P. (1979). Railroad ballast prescription: state-of-the-art. *Journal of Geotechnical Engineering Division*, 105(GT2):305–322.

Rhayma, N. (2010). *Contribution à l'évolution des méthodologies de caractérisation et d'amélioration des voies ferrées.* PhD thesis, Université Blaise Pascal - Clermont II.

Rhayma, N., Bressolette, P., Breul, P., Fogli, M., and Saussine, G. (2011). A probabilistic approach for estimating the behavior of railway tracks. *Engineering Structures*, 33(7):2120–2133.

Rhayma, N., Bressolette, P., Breul, P., Fogli, M., and Saussine, G. (2013). Reliability analysis of maintenance operations for railway tracks. *Reliability Engineering & System Safety*, 114:12–25.

Ribeiro, A. C. C. A. (2012). *Transições aterro - Estrutura em linhas ferroviarias em alta velocidade: Análise experimental e numérica.* PhD thesis, Universidade do Porto.

Ricci, L., Nguyen, V. H., Sab, K., Duhamel, D., and Scmitt, L. (2005). Dynamic behaviour of ballasted railway tracks : A discrete / continuous approach. *Computer & Structures*, 83:2282–2292.

Rondon, H. A., Wichtmann, T., Triantafyllidis, T., and Lizcano, A. (2009). Comparison of cyclic triaxial behavior of unbound granular material under constant and variable confining pressure. *Journal of Transportation Engineering*, 135(7):467–478.

Roney, M. (2005). Common elements of successful heavy haul railways: a worldwide perspective. In *8th International Heavy Haul Conference*, pages 221–225, Rio de Janeiro, Brazil.

Roscoe, K. H., Schofield, A. N., and Wroth, C. P. (1958). On the yielding of soils. *Géotechnique*, 8(1):22–52.

Sadeghi, J. and Fesharaki, M. (2013). Importance of Nonlinearity of Track Support System in Modeling of Railway Track Dynamics. *International Journal of Structural Stability and Dynamics*, 13(1):1–16.

Sáez, E. (2009). *Dynamic Nonlinear soil-structure interaction.* PhD thesis, Ecole Centrale Paris.

Sáez, E., Lopez-Caballero, F., and Modaressi-Farahmand-Razavi, A. (2013). Inelastic dynamic soil-structure interaction effects on moment-resisting frame buildings. *Engineering Structures*, 51:166–177.

Saïm, R. (1997). *Des comportements repères des grains sans colle à un exemple de sol réel*. PhD thesis, Ecole Centrale Paris.

Salager, S., François, B., Nuth, M., and Laloui, L. (2012). Constitutive analysis of the mechanical anisotropy of Opalinus Clay. *Acta Geotechnica*, 8(2):137–154.

Saltelli, A., Tarantola, S., and Chan, K. P.-S. (1999). A quantitative model-independent method for global sensitivity analysis of model output. *Technometrics*, 41(1):39–56.

Sanglerat, G. (1965). *Le pénétromètre et la reconnaissance des sols: intérpretation des diagrammes de pénétration, théorie et pratique*. Dunod.

Saussine, G., Allain, E., Paradot, N., and Gaillot, V. (2011). Ballast flying risk assessment method for high speed line. In *9th World Congress on Railway Research - May 22-26*, Lille.

Saussine, G., Azéma, E., Gautier, P. E., Peyroux, R., and Radjai, F. (2008). Numerical modeling of the damping operation by Discrete Element Approach. In *8th World Congress on Railway Research*, Seoul.

Saussine, G., Cholet, C., Gautier, P. E., Dubois, F., Bohatier, C., and Moreau, J. J. (2006). Modelling ballast behaviour under dynamic loading . Part 1 : A 2D polygonal discrete element method approach. *Computer Methods in Applied Mechanics and Engineering*, 195:2841–2859.

Sauvage, G. (1993). Railway track vertical static behaviour. Technical report, INRETS/LTN.

Schmertmann, J. H. (1970). Guidelines for cone penetration test, performance and design. *Journal of Soil Mechanics and Foundations Divison*, 96(SM3):1011–1043.

Seed, H. B. and Idriss, I. M. (1970). Soil moduli and damping factors for dynamic response analysis. Technical report, University of California, Berkeley, CA.

Seed, H. B., Mitry, F. G., Monismith, C. L., and Chan, C. K. (1967). Prediction of flexible pavement deflections from laboratory repeated load tests. Technical report, NCHRP Rep. No. 35, National Cooperative Highway Research Program.

Seed, H. B., Wong, R. T., Idriss, I. M., and Tokimatsu, K. (1986). Moduli and damping factors for dynamic analyses of cohesionless soils. *Journal of Geotechnical Engineering*, 112(11):1016 – 1032.

Selig, E. and Waters, J. (1994). *Track Geotechnology and Sub-structure management*. ThomasTelford, London, UK.

Selig, E. T., Yoo, T. S., Adegoke, C. W., and Stewart, H. E. (1981). Status report - Ballast experiments, Intermediate (175 mgt), Substructure stress and strain data. Technical report, Tech. Rep. FAST/TTC/TM-81/03, University of Massachusetts, Cambridge.

Shan, Y., Albers, B., and Savidis, S. A. (2013). Influence of different transition zones on the dynamic response of track-subgrade systems. *Computers and Geotechnics*, 48:21–28.

Sheng, X., Jones, C. J. C., and Petyt, M. (1999). Ground Vibration Generated By a Harmonic Load Acting on a Railway Track. *Journal of Sound and Vibration*, 225(1):3–28.

Sheng, X., Jones, C. J. C., and Thompson, D. J. (2003). A comparison of a theoretical model for quasi-statically and dynamically induced environmental vibration from trains with measurements. *Journal of Sound and Vibration*, 267(3):621–635.

Sheng, X., Jones, C. J. C., and Thompson, D. J. (2004a). A theoretical model for ground vibration from trains generated by vertical track irregularities. *Journal of Sound and Vibration*, 272(3-5):937–965.

Sheng, X., Jones, C. J. C., and Thompson, D. J. (2004b). A theoretical study on the influence of the track on train-induced ground vibration. *Journal of Sound and Vibration*, 272(3-5):909–936.

Shenton, M. J. (1984). Ballast deformation and track deterioration. In *Track Technology*, Nottingham, UK.

Singh, A. (2005). Increasing productivity through heavy haul operation on indian railways. In *8th International Heavy Haul Conference*, pages 237–243, Rio de Janeiro, Brazil.

Sladen, J. A., D'Hollander, R. D., and Krahn, J. (1985). The liquefaction of sands, a collapse surface approach. *Canadian Geotechnical Journal*, 22(4):564 – 578.

SNCF (2009). La direction de la communication: Chiffres infrastrucures et gares.

SNCF (2010). Ballasts neufs pour voies ferrées. Technical report, Direction de l'Ingénierie - CT IGEV 001 - Indice B.

Sobol, I. M. (1967). On the distribution of points in a cube and the approximative evaluation of integrals. *U.S.S.R. Comput. Math. and Math. Phys.*, 7:86–112.

Sobol, I. M. (1998). On quasi-Monte Carlo integrations. *Mathematics and Computers in Simulation*, 47(2-5):103–112.

Steenbergen, M. J. M. M. (2008). Quantification of dynamic wheel-rail contact forces at short rail irregularities and application to measured rail welds. *Journal of Sound and Vibration*, 312(4-5):606–629.

Steenbergen, M. J. M. M. (2013). Physics of railroad degradation: The role of a varying dynamic stiffness and transition radiation processes. *Computer & Structures*, 124:102–111.

Steenbergen, M. J. M. M., Metrikine, A. V., and Esveld, C. (2007). Assessment of design parameters of a slab track railway system from a dynamic viewpoint. *Journal of Sound and Vibration*, 306(1-2):361–371.

Stewart, H. E., Selig, E. T., and Norman-Gregory, G. M. (1985). Failure Criteria and Lateral Stresses in Track Foundations. *Transportation Research Record*, 1022:59–64.

Su, L.-J., Rujikiatkamjorn, C., and Indraratna, B. (2010). An Evaluation of Fouled Ballast in a Laboratory Model Track Using Ground Penetrating Radar. *Geotechnical Testing Journal*, 33(5):103045.

Sudret, B. (2007). *Uncertainty propagation and sensitivity analysis in mechanical models and stochastic spectral methods*. Habilitation à diriger des recherches, Université Blaise Pascal - Clermont II.

Sudret, B. (2008). Global sensitivity analysis using polynomial chaos expansions. *Reliability Engineering & System Safety*, 93(7):964–979.

Suiker, A. S. J. (2002). *The Mechanical Behaviour of Ballasted Railway Tracks*. PhD thesis, Delft University of Technology.

Suiker, A. S. J., Chang, C. S., de Borst, R., and Esveld, C. (1999). Surface waves in a stratified half space with enhanced continuum properties. Part 1: Formulation of the boundary value problem. *European Journal Mechanics A/Solids*, 18(5):749–768.

Suiker, A. S. J., Selig, E. T., and Frenkel, R. (2005). Static and Cyclic Triaxial Testing of Ballast and Subballast. *Journal of Geotechnical and Geoenvironmental Engineering*, 131(6):771–783.

Sun, Y. (2002). A dynamic model for the vertical interaction of the rail track and wagon system. *International Journal of Solids and Structures*, 39(5):1337–1359.

Takemiya, H. and Bian, X. (2005). Substructure Simulation of Inhomogeneous Track and Layered Ground Dynamic Interaction under Train Passage. *Journal of Engineering Mechanics*, 131(7):699–711.

Tatsuoka, F., Modoni, G., Jiang, G. L., Anh Dan, L. Q., Flora, A., Matsushita, M., and Koseki, J. (1999). Stress-strain behaviour at small strains of unbound granular materials and its laboratory test. In Correia, A. G., editor, *Modelling and Advanced testing for Unbound Granular Materials*, pages 17–61. A. A. Balkema.

Tatsuoka, F., Sakamoto, M., Kawamura, T., and Fukushima, S. (1986). Strength and deformation characteristics of sand in plane strain compression at extremely low pressures. *Soils and Foundations*, 26(1):63–84.

Thach, P.-N., Liu, H.-L., and Kong, G.-Q. (2013). Vibration analysis of pile-supported embankments under high-speed train passage. *Soil Dynamics and Earthquake Engineering*, 55:92–99.

Thomson, W. T. (1950). Transmission of Elastic Waves through a Stratified Solid Medium. *Journal Applied Pysics*, 21:89–93.

Trinh, V.-N. (2011). *Comportement hydromécanique des matériaux constitutifs de plate-formes ferroviaires anciennes*. PhD thesis, Université Paris-Est.

Trinh, V. N., Tang, A. M., Cui, Y.-J., Dupla, J.-C., Canou, J., Calon, N., Lambert, L., Robinet, A., and Schoen, O. (2012). Mechanical characterisation of the fouled ballast in ancient railway track substructure by large-scale triaxial tests. *Soils and Foundations*, 52(3):511–523.

Trofimenkov, J. G. (1974). Penetration testing in URSS - State of Art Report. In *European Symposium on Penetration Testing*, Stockholm.

Tutumluer, E. and Seyhan, U. (1999). Stress path loading effects on granular material resilient response. In Correia, A. G., editor, *Unbound granular materials: Laboratory testing, in-situ testing and modelling*, pages 109–121. A.A. Balkema.

Uzan, J. (1985). Characterization of granular materials. *Transportation Research Record*, 1022:52–59.

Vanmarcke, E. H. (1983). *Random fields: analysis and synthesis*. MIT Press.

Vesic, A. S. (1963). Beams on Elastic Subgrade and the Winkler Hypothesis. In *5th International Conference on Soil Mechanics and Foundation Engineering*, pages 845–850, Paris, France.

Vlaslov, V. L. and Leontiev, N. H. (1956). *Beams, Plates and Shells on Elastic Foundations*. Fizmatgiz, Moscow.

Voivret, C., Perales, R., Saussine, G., Costa d'Aguiar, S., Laurans, E., and Petit, P. (2013). Multi-unit tamping machine: beyond the linear performance. In *10th World Congress on Railway Research*, Sydney, Australia.

Vostroukhov, A. V. and Metrikine, A. V. (2003). Periodically supported beam on a visco-elastic layer as a model for dynamic analysis of a high-speed railway track. *International Journal of Solids and Structures*, 40(21):5723–5752.

Vucetic, M. and Dobry, R. (1991). Effect of soil plasticity in cyclic response. *Journal of Geotechnical Engineering*, 117(1):89–107.

Webster, S. L., Grau, R. H., and Williams, T. P. (1992). Description and application of dual mass dynamic cone penetrometer. Technical report, Department of Army, Waterways Experiment Station, Vicksburg, MS.

Weyl, H. (1938). Mean Motion. *American Journal of Mathematics*, 60(4):889–896.

Wickens, A. H. (2003). *Fundamentals of Rail Vehicle Dynamics*. Swets & Zeitlinger.

Wu, C. G., Liang, Y. C., Lin, W. Z., Lee, H. P., and Lim, S. P. (2003). A note on equivalence of proper orthogonal decomposition methods. *Journal of Sound and Vibration*, 265:1103–1110.

Wu, S., Gray, D. H., and Richart, F. E. J. (1984). Capillary effects on dynamic modulus of sands and silts. *Journal of Geotechnical Engineering*, 110(9):1188 – 1203.

Wyss, G. D. and Jorgensen, K. H. (1998). A user's guide to LHS: Sandia's Latin Hypercube Sampling software. Technical report, Sandia National Laboratories, Albuquerque, NM.

Xie, G. and Iwnicki, S. (2008). Simulation of wear on a rough rail using a time-domain wheel-track interaction model. *Wear*, 265(11-12):1572–1583.

Xu, B., Lu, J.-f., and Wang, J.-h. (2007). Dynamic response of an infinite beam overlying a layered poroelastic half-space to moving loads. *Journal of Sound and Vibration*, 306:91–110.

Yang, L. a., Powrie, W., and Priest, J. a. (2009). Dynamic Stress Analysis of a Ballasted Railway Track Bed during Train Passage. *Journal of Geotechnical and Geoenvironmental Engineering*, 135(5):680.

Yang, Y. B. and Hung, H. H. (2001). A 2.5D finite/infinite element approach for modeling visco-elastic bodies subjected to moving loads. *International Journal of Numerical Methods in Engineering*, 51(11):1317 – 1336.

Yang, Y. B. and Hung, H. H. (2008). Soil Vibrations Caused by Underground Moving Trains. *Journal of Geotechnical and Geoenvironmental Engineering*, 134(11):1633–1644.

Zhai, W., Wang, K., and Cai, C. (2009). Fundamentals of vehicle - track coupled dynamics. *Vehicle System Dynamics*, 47(11):1349–1376.

Zhai, W., Wang, K., and Lin, J. (2004). Modelling and experiment of railway ballast vibrations. *Journal of Sound and Vibration*, 270(4-5):673–683.

Zhou, S. (1997). *Caractérisation des sols de surface à l'aide du pénétromètre dynamique léger de type Panda*. PhD thesis, Université Blaise Pascal - Clermont Ferrand.

Zhou, T., Hu, B., Sun, J., and Liu, Z. (2013). Discrete Element Method Simulation of Railway Ballast Compactness During Tamping Process. *The Open Electrical & Eletronic Engineering Journal*, 7:103–109.